Lecture Notes in Physics

Pietro Faccioli
Carlos Lourenço

Particle Polarization in High Energy Physics

An Introduction and Case Studies on Vector Particle Production at the LHC

OPEN ACCESS

Springer

Lecture Notes in Physics

Volume 1002

The series Lecture Notes in Physics (LNP), founded in 1969, reports new developments in physics research and teaching - quickly and informally, but with a high quality and the explicit aim to summarize and communicate current knowledge in an accessible way. Books published in this series are conceived as bridging material between advanced graduate textbooks and the forefront of research and to serve three purposes:

- to be a compact and modern up-to-date source of reference on a well-defined topic;
- to serve as an accessible introduction to the field to postgraduate students and non-specialist researchers from related areas;
- to be a source of advanced teaching material for specialized seminars, courses and schools.

Both monographs and multi-author volumes will be considered for publication. Edited volumes should however consist of a very limited number of contributions only. Proceedings will not be considered for LNP.

Volumes published in LNP are disseminated both in print and in electronic formats, the electronic archive being available at springerlink.com. The series content is indexed, abstracted and referenced by many abstracting and information services, bibliographic networks, subscription agencies, library networks, and consortia.

Proposals should be sent to a member of the Editorial Board, or directly to the responsible editor at Springer:

Dr Lisa Scalone
Springer Nature
Physics
Tiergartenstrasse 17
69121 Heidelberg, Germany
lisa.scalone@springernature.com

Pietro Faccioli · Carlos Lourenço

Particle Polarization in High Energy Physics

An Introduction and Case Studies on Vector Particle Production at the LHC

Springer

Pietro Faccioli
LIP, Laboratório de Instrumentação
e Física Experimental de Partículas
Lisbon, Portugal
Pietro.Faccioli@cern.ch

Carlos Lourenço
CERN, European Organization
for Nuclear Research
Geneva, Switzerland
Carlos.Lourenco@cern.ch

ISSN 0075-8450 ISSN 1616-6361 (electronic)
Lecture Notes in Physics
ISBN 978-3-031-08874-2 ISBN 978-3-031-08876-6 (eBook)
https://doi.org/10.1007/978-3-031-08876-6

This Springer imprint is published by the registered company Springer Nature Switzerland AG
The registered company address is: Gewerbestrasse 11, 6330 Cham, Switzerland

To Giacomo Battista, for his persistent curiosity in seeing the outcome of this work.

P.F.

To Christina, for her enthusiastic interest and encouragement over the long time she saw me working on this project.

C.L.

Foreword

The spin is a fundamental feature of elementary particles, together with their mass and gauge charges. Spin reflects the quantum mechanical behaviour of particles under space-time symmetry transformations, with profound implications ranging from their statistical properties to their potential role in presence of higher symmetries, such as supersymmetry. That the measurement of a new particle's spin is a top priority following a discovery, is therefore totally obvious. Spin being a discrete variable, its measurement, contrary to that of masses and couplings, does not require unlimited precision, but just enough to guarantee its accurate determination. Nevertheless, measurements sensitive to a particle's spin and to its polarization state provide unique probes for a large variety of independent studies, where precision is the key expected outcome. For example, the polarizations of W and Z bosons produced at the LHC are crucial to extract precision measurements of the W mass, of the weak mixing angle, and even of the partonic structure of the proton.

Polarization measurements, furthermore, highlight dynamical features that might hide behind inclusive measurements. For example, while the study of charmonium inclusive production at large transverse momentum led, in the mid 90's, to the development of a highly satisfactory theoretical framework based on non-relativistic QCD (NRQCD), the subsequent measurements of charmonium polarization unveiled discrepancies suggestive of a more complex and richer dynamics, which is still being explored today.

It was precisely the challenge of interpreting puzzling charmonium polarization data that prompted the authors to undertake their voyage into the subtleties of these effects in high-energy experiments, becoming world authorities. The result is this book, an indispensable and unique field guide for experimentalists and theorists interested in measurements sensitive to polarization phenomena. The book fulfils a double role. First, it underscores, with a multitude of real-life examples, the interplay between polarization and the detector properties in sculpting production distributions, distorting them from their theoretical shape, and potentially compromising a correct interpretation. In parallel, it provides all tools to disentangle this interplay, and extract maximal information from the available data. Along the way, we are informed about the state of the art in a large number of LHC physics studies, with a

behind-the-scenes perspective on their complexity and on the traps that they might conceal.

Whether the reader is interested in studies of QCD dynamics, in precision electroweak measurements, or in new tools to increase the efficiency of searches for beyond the Standard Model particles, the book will provide invaluable guidance and technical support to undertake the experimental analyses, and to properly interpret the results.

CERN, March 2022 *Michelangelo Mangano*

Preface

The subject of this book can be briefly summarised: it addresses studies of angular distributions of the decay products of a particle, discussing methodological aspects that should be taken into account to ensure accurate measurements, as well as reliable and unambiguous physical interpretations.

The angular decay distribution is directly determined by the physical properties of the decaying particle and by how it interacts with the other particles involved in the process. Above all, it reflects the particle's polarization, i.e., the angular momentum state in which it was created, as defined by the production mechanism in the specific physical conditions of the experiment (the colliding particles, the collision energy, the covered phase space window, etc.). By directly probing the nature of the studied particles, polarization measurements offer detailed insights into the mechanisms behind particle production, providing a window into the underlying fundamental interactions.

On the other hand, it is more challenging to measure polarizations than, for example, cross sections. To start with, we need larger event samples because the analyses are performed as a function of additional variables: the decay angles. Precise measurements of the kinematics of the decay particles are also needed, as they have a direct impact on the quality of the polarization results. These are not major limiting factors in the case of the LHC experiments, which operate with record-breaking integrated luminosities and relatively large cross sections (given the high-energy of the collisions), associated with very efficient triggers, state-of-the-art data-acquisition systems, high-performance offline computing infrastructures, and more powerful detector technologies and reconstruction techniques than those used in any previously-operating high-energy physics experiment. We are left with the most delicate step of the polarization measurements: the definition of the data-analysis method. There are many potential hurdles in the path between the high-precision data and the high-accuracy physics results, and care must be taken to avoid the use of approximate or biased analysis methods, which can lead to ambiguous and puzzling results. Indeed, precision does not mean accuracy: a precise result (small uncertainties) can be wrong, if it is obtained through the use of biased analysis techniques.

The purpose of this book is to help ensuring that graduate students, post-docs, and other young researchers turn high-quality data (collected at the LHC or elsewhere) into crystal-clear physical results, interpretable without ambiguities. The text should also be understandable by interested readers familiar with some basic concepts of quantum mechanics and particle physics. After briefly introducing the topic, we present the ideas and tools necessary to achieve accurate measurements of decay angular distributions and corresponding interpretations in terms of the polarization of the decaying particle. In particular, we discuss in detail several aspects of polarization measurements that are often underestimated or ignored in the data analyses, such as the importance of the choice (and reproducible definition) of all axes of the reference frame and the usefulness of frame-independent representations of the angular distribution. We address concrete problems that a researcher might face when starting an experimental analysis, or when trying to interpret existing measurements. The explored topics include the exceptionality of an "unpolarized" observation, the unavoidable residual dependence of measurements of the polarizations of indirectly produced particles on the experimental selections, and the pitfalls introduced when the intrinsic multidimensionality of the problem is neglected in exchange for a simplified approach. The concepts are presented gradually and, in general, it is assumed that later chapters are read once the subjects covered in the previous ones are understood. For pedagogical reasons, each chapter starts with a list of the main questions that will be addressed and ends with a wrap-up section that recapitulates the main messages.

The decays of vector states (Drell–Yan, Z and W bosons, J/ψ mesons and other quarkonia, etc.) into lepton-antilepton pairs, which are among the most frequently analysed processes in LHC experiments, play the central role in the progressive exposition of the concepts and methods. We start by deriving, from basic principles, the general expression for the dilepton decay distribution of a vector particle, in the parity-conserving and parity-violating cases (in Chapter 1). We also discuss the meaning of the observable anisotropy parameters, as well as the crucial and challenging effects of event selection criteria commonly applied in the data analyses, and we show that vector particles are never produced unpolarized. We then describe (in Chapter 2) the most commonly adopted definitions for the system of reference axes, highlighting the physical relevance of each of them for different kinds of processes. We also show how the parametrization of the angular distribution strongly depends on the reference frame, so that its choice, while in principle arbitrary, can actually affect the simplicity of the interpretation of the results. We follow up (in Chapters 3 and 4) with a detailed description of the parameter space and of how the angular distribution can be characterized and studied with numerically frame-independent observables, also presenting their advantages (and limitations) in measurements and theoretical calculations. The Lam–Tung relation for Drell–Yan and vector boson production is also discussed in detail. Chapters 5 and 6 are mostly devoted to effects that irrecoverably smear the magnitude of the observable polarization, occurring when it is not possible to approximate the natural polarization with experimentally-definable reference directions. In particular, we consider cases of "non-planar" production processes, like those where the particle under study is

accompanied by more than one recoil particle or where the intrinsic longitudinal momentum of the colliding partons is not negligible, and we address the consequent violations of the Lam–Tung relation, precisely observed at the LHC, and how the relation can be generalized. We then focus on a detailed description of cascade decays, where the vector particle is a daughter of another particle. The case in which the mother has zero angular momentum provides examples of maximal smearing effects, possibly leading to the observation of a seemingly unpolarized vector particle, of which the LHC quarkonium polarization measurements might be a natural (albeit exceptional) example. Finally, we describe (in Chapter 7) a general method for calculating angular distributions, before offering a survey of typical angular distributions of particles of any integer or half-integer spin into various final states.

Many of the topics are presented and discussed through pedagogical examples based on real measurements, gedankenexperiments, or realistic simulations. Mathematical tools are presented in a pragmatic way, suitable for down-to-earth applications in hands-on analyses of real data. For example, the Wigner matrices are defined as depending only on two rotation angles, a reduced form that is perfectly sufficient for the calculations of two-body decay distributions. More importantly, the concepts are explained, as much as possible, with the help of graphical illustrations. By reporting the spatial shapes of most angular distributions and by illustrating geometrically the effects of frame rotations and those of mixing and smearing phenomena, for example, we provide a much more direct and intuitive view of the physical and experimental effects than usually found in scientific articles. Given our hands-on contributions to several polarization measurements, in HERA-B or CMS, as well as to a few phenomenological studies, we know that the use of such visual representations is also helpful to find solutions to problems that can be encountered in experimental or theoretical analyses.

The preparation of this book was seeded by two pedagogical seminars that one of us (P.F.) gave in April 2013, at CERN, Geneva, and at HEPHY, Vienna, on the topic “Angular momentum and decay distributions in high energy physics: an introduction and use cases for the LHC”. We were encouraged by friendly interactions with several colleagues, including Roberto Spighi, Chris Fabjan, Gigi Rolandi, João Seixas, Ian Shipsey, Claudia Wulz, Wolfgang Adam, Hermine Wöhri, Valentin Knünz, Ilse Krätschmer, Thomas Madlener, Helena Santos, and Mariana Araújo. The text and figures evolved with time and reflect work that we presented and discussed in numerous articles and/or in scientific workshops, university seminars, and courses on “Physics at the LHC” for graduate students. We would also like to acknowledge fruitful interactions with physicists from the E866, HERA-B, CDF, ALICE, ATLAS, CMS, and LHCb Collaborations, as well as interesting discussions with Sergey Baranov, Geoff Bodwin, Eric Braaten, Fabio Maltoni, Michelangelo Mangano, Helmut Satz, and Ramona Vogt, among many other people. Finally, we thank the Scientific Information Service at CERN, especially Jens Vigen, for providing the budget needed to have this book published in open access.

Lisbon and Meyrin,
March 2022

Pietro Faccioli
Carlos Lourenço

Contents

Foreword vii

Preface ix

1 Dilepton decays of vector particles 1
1.1 Why vector particles? 2
1.2 Helicity conservation in dilepton decays 4
1.3 Rotation of angular momentum eigenstates 6
1.4 Parity properties 10
1.5 Introductory remarks on polarization measurements 12
1.6 Correlation between cross sections and polarizations 19
1.7 The two-dimensional angular distribution 22
1.8 Addition rules for the polarization parameters 24
1.9 Alternative determinations of the anisotropy parameters 25
1.10 The "unpolarized" case 27
1.11 Parity-violating decay distribution 30
1.12 Recapitulation 33
References 36

2 Reference frames and transformations 39
2.1 The choice of the reference frame 40
2.2 The Gottfried–Jackson frame 42
2.3 The Collins–Soper frame 46
2.4 The centre-of-mass helicity frame 47
2.5 The perpendicular helicity frame 48
2.6 The definition of the y axis 49
2.7 Dependence of the measurement on the polarization frame 50
2.8 Two interesting limit cases 51
2.9 Effect of production kinematics on the angular distribution 55
2.10 The meaning of $\lambda_{\vartheta\varphi}$ 60
2.11 The role of the azimuthal anisotropy 66

2.12 Frame-dependence of the experimental acceptance 68
2.13 Caveats of one-dimensional analyses 71
2.14 The importance of being lucky 73
2.15 More general frame transformations 76
2.16 Recapitulation 79
References 83

3 A frame-independent study of the angular distribution 85
3.1 Is polarization a relative concept? 86
3.2 The borders of the physical domain 86
3.3 Inside the parameter domain 90
3.4 An absolute definition of "longitudinal" and "transverse" 93
3.5 A more fundamental derivation of the invariant polarization 94
3.6 Frame-independent angular distribution 95
3.7 The parameter domain of the general dilepton decay 97
3.8 The "canonical form" of the angular distribution 97
3.9 Other parity-conserving frame-independent parameters 104
3.10 Frame-independent parity-violating asymmetry 110
3.11 The frame-independent counterpart of λ_ϑ 111
3.12 Searching for biases using $\tilde{\lambda}$ 112
3.13 Recapitulation 117
References 120

4 Meaning and interpretation of the frame-independent polarization . . 121
4.1 Addition rules for invariant shape parameters 122
4.2 When $\tilde{\lambda}$ is "simpler" than λ_ϑ in every polarization frame 123
4.3 Drell–Yan and W / Z boson polarizations 128
4.4 The Lam–Tung relation 135
4.5 The quasi-invariants 136
4.6 Recapitulation 142
References 145

5 Smearing effects in non-planar processes 147
5.1 When the natural axis escapes experimental observation 148
5.2 Non-planar processes: violations of the Lam–Tung relation 149
5.3 A generalization of the Lam–Tung relation 156
5.4 Effects of the parton transverse momentum 163
5.5 Recapitulation 169
References 171

6 Polarization in cascade decays 173
6.1 Observing unpolarized vector-particle production 174
6.2 Kinematics of cascade decays 180
6.3 A wide spectrum of possible observations 190
6.4 The unique case of J/ψ production 204
6.5 Non-prompt charmonium production 210

6.6 Decays from $J > 0$ particles and the "cloning" effect 215
6.7 The importance of the reference frame 227
6.8 A counterexample for the cloning effect 229
6.9 Recapitulation 234
References 238

7 Two-body decay distributions beyond the dilepton case 243
7.1 Wigner rotation matrices 244
7.2 Generic formulas for two-body decay distributions 249
7.3 The polar projection of the decay distribution 252
7.4 The general $J = 1$ two-body decay distribution 254
7.5 Polar anisotropy of the $J = 2$ two-body decay distribution 258
7.6 Case study: spin characterization of a heavy di-photon resonance . . 263
7.7 Decay distributions of half-integer spin particles 270
7.8 When "polarized" and "anisotropic" are seemingly not equivalent . . 274
7.9 Recapitulation 277
References 280

A Alternative parametrization of the dilepton decay distribution 283
References 290

B Angular distributions of $O \to V\gamma$, with $J(O) = J(V) = 1$ and $V \to \ell^+\ell^- \,|\, \pi\gamma \,|\, \pi\pi \,|\, \ldots$ 291
References 298

Index 299

Chapter 1
Dilepton decays of vector particles

This chapter introduces the basic notions used in the measurement of the polarization of a particle and in its interpretation. We use as a prototype the case of a vector particle (the J/ψ meson, a virtual photon, the Z boson, etc.) decaying into a lepton-antilepton pair, frequently studied in high-energy physics because of the high quality of the experimental signals and the simplicity of the involved physics principles.

We will address the following questions.

- How is the polarization of a particle defined and how can it be measured by observing its decay distribution? What principles are used in the determination of this distribution? What are the relevant angular variables and shape parameters? Are there different kinds of polarizations and, if so, what are their meanings?
- How is the sample of decay events concretely translated into a polarization measurement? What important aspects and systematic effects should be considered in the analysis with particular care? Can the (differential) production cross sections of the observed particles be reliably measured if the polarization dimension is not carefully considered in the analysis?
- How do particles produced by different mechanisms combine their different polarizations into the average value that can be measured in the collected data sample? Can a particle be produced "unpolarized" and, if so, what would that indicate?
- What additional observables can be defined to study parity-violating effects in production and decay?

P. Faccioli and C. Lourenço, *Particle Polarization in High Energy Physics*,
Lecture Notes in Physics 1002,
https://doi.org/10.1007/978-3-031-08876-6_1

1.1 Why vector particles?

Polarization measurements provide deep insights into the mechanisms of particle production and interaction in high-energy physics. In fact, no measurement comes closer to "seeing" the shape of the wave function of a particle produced in an experiment than the determination of the angular distribution of its decay and, therefore, of its polarization. The intimate connection between angular momentum properties and decay angular distribution can also provide tools for the characterization of newly discovered particles, as will be exemplified in Section 7.6.

Vector particles are the lead characters on the stage of experimental polarization studies. The "spin alignments" of elementary vector particles (Z, W, photon), produced ether directly in the hard scattering process, or from the decays of heavier particles, directly reflect the mechanisms of their couplings to leptons, light quarks, top quark, Higgs boson, etc., in the Standard Model and beyond.

Polarizations are also an important probe to test the predictions of quantum chromodynamics (QCD) for hadron production in elementary collisions. For example, the production of lepton-antilepton pairs produced from a virtual photon (Drell–Yan [1]) is theoretically the simplest and cleanest hadron-hadron scattering process and, therefore, the ideal case study for proving and testing the QCD factorization theorem [2–4], as well as a crucial source of information for the determination of the parton distribution functions of hadrons. Studies of the polarizations of heavy quarkonium vector mesons (J/ψ, ψ(2S), Υ) play a major role in the understanding of the still mysterious mechanisms of hadron bound-state formation, as will be explained in Section 6.4.

Most importantly, vector particles can be reconstructed in their decays to lepton-antilepton pairs, a particularly convenient channel for the accuracy of its experimental detection and the directness of its theoretical interpretation. Even when the particle under study is not a vector particle and does not decay into leptons, it is often seen through its decay chain to vector particles, with the latter further decaying into dileptons. Also the study of its angular momentum properties benefits from the analysis of the dilepton decay distribution of its vector daughters. For instance, the first direct evidences that the recently discovered Higgs boson candidate was indeed a spin-parity $J^P = 0^+$ particle were provided by studies using data on the decay $\mathrm{H} \to \mathrm{Z}\mathrm{Z}^* \to \ell^+\ell^-\,\ell^+\ell^-$, besides $\mathrm{H} \to \mathrm{W}\,\mathrm{W}^* \to \ell\nu\,\ell\nu$ and $\mathrm{H} \to \gamma\gamma$, as main ingredients [5, 6]. Another example, described in Section 6.6, is the polarization measurement of the $J = 1$ and $J = 2$ χ_c mesons, which can be performed by simply observing the dilepton decay of the J/ψ produced by their radiative decays.

Many experiments are optimized for the detection of muons and/or electrons, so that particularly accurate and precise measurements can be performed by observing vector particles in their dilepton decays. Figure 1.1 offers a glimpse of the wide range of studies that can be performed by the LHC experiments thanks to their impressive capabilities in the reconstruction of particles in the dimuon decay channel. Besides the extensive coverage in invariant mass, from a few 100 MeV to a few 100 GeV, we see that the measurement resolution is sufficiently good to separate the three close-by Υ states.

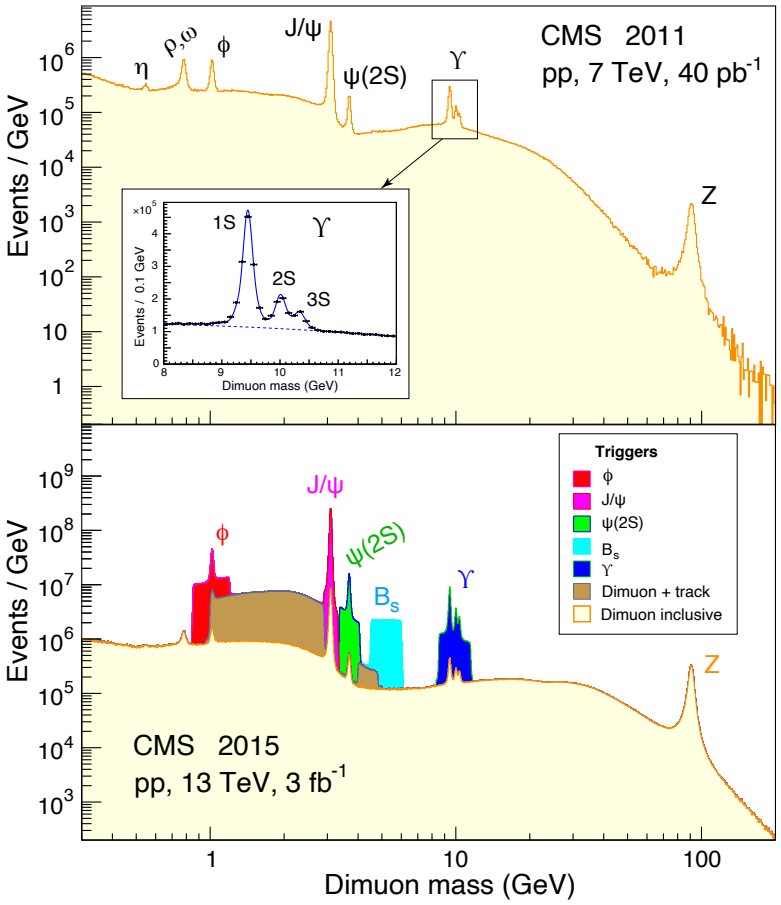

Fig. 1.1 Dimuon mass distributions measured by CMS in pp collisions at 7 TeV (top) in 2011 [7] and at 13 TeV (bottom) in 2015 [8]. The significantly larger instantaneous luminosity of the LHC in 2015 resulted in a collision rate that was too high for the data acquisition bandwidth, so that the inclusive double muon trigger used in 2011 had to be replaced by a set of more exclusive triggers, to retain as many interesting events as possible. In particular, a trigger path was dedicated to the collection of events used to search for the rare $B_s \to \mu^+\mu^-$ decay (in cyan).

A vector particle, V, is eigenstate of the angular momentum operator, $\mathbf{J}^2 |V\rangle = J(J+1)|V\rangle$, with the corresponding quantum number J being 1 (natural units, with $c = \hbar = 1$, are used throughout this book). A "polar" vector particle, such as the "vector mesons" ρ, ϕ and J/ψ, has negative parity, that is, its wave function changes sign with inversion of the coordinates, just like a polar vector flips within the geometrical space (whereas a pseudo- or axial-vector maintains its sign/orientation). This latter property allows the particle to be produced through the annihilation of a quark and its antiquark, and/or decay into a lepton-antilepton pair. V can be any of three eigenstates of the angular momentum component J_z along a chosen quantiza-

tion axis z, $J_z|V\rangle = M|V\rangle$, with $M = -1, 0$ or $+1$, as well as a superposition of those three states.

The word "polarization" refers to how these three base eigenstates are combined to form the observed state of V. The combination is determined by the mechanism that produces V in the considered experimental conditions. To measure the polarization of a particle effectively means to measure the *average* J_z composition of the particles in the collected event sample. The measurement exploits the fact that the particle tends to emit its decay products in different characteristic directions, strongly correlated to its actual J_z projection. The experiment collects and identifies many such decays and builds the statistical distribution of the emission angles, as seen in the particle's rest frame. A shape analysis of this distribution reveals the particle's polarization.

As mentioned above, the analysis of the dilepton decay represents the cleanest way, from both the experimental and theoretical perspectives, of measuring and interpreting the production yield and polarization of the parent particle. In this chapter we discuss how to determine experimentally the polarization of a vector particle by measuring its decay angular distribution in this channel. To provide a concrete example, we take the J/ψ meson as the decaying particle, but all the considerations and results are equally valid for any other vector particle.

The shape of the observable decay angular distribution is determined by a few basic principles, examined in the next sections: 1) the conservation of "helicity", satisfied by fermions in electroweak and strong forces under certain limit conditions; 2) the rotational covariance of angular momentum eigenstates, i.e. how the J_z composition changes when the definition of the quantization axis changes; 3) the conservation of parity (in cases where only the electromagnetic or strong forces determine the decay) or its violation (when the weak force is also involved). While the first principle represents a constraint specific to the dilepton decay of vector particles, the other two are completely general considerations, applying to the angular distribution of any particle decay.

1.2 Helicity conservation in dilepton decays

The electroweak and strong forces preserve the chirality of fermions. The dynamics of the coupling of electrons to photons, for example, is described by terms of the form $\overline{u}\gamma^\mu u = \overline{u}_\mathrm{L}\gamma^\mu u_\mathrm{L} + \overline{u}_\mathrm{R}\gamma^\mu u_\mathrm{R}$, where γ^μ are the Dirac matrices, u is the electron spinor, and L (R) indicates its left-handed (right-handed) chiral component. Terms containing both opposite chiral components are absent, meaning that the fermion chirality is preserved in the interaction with the photon. When the fermions are assumed to have zero mass, so that the direction of their momenta cannot be reversed by any Lorentz transformation, left-handed and right-handed chiral components become eigenstates of the helicity operator $h = \mathbf{S}\cdot\mathbf{p}/|\mathbf{p}|$, corresponding to the projection of the spin on the momentum direction. In this case, chirality conservation becomes helicity conservation.

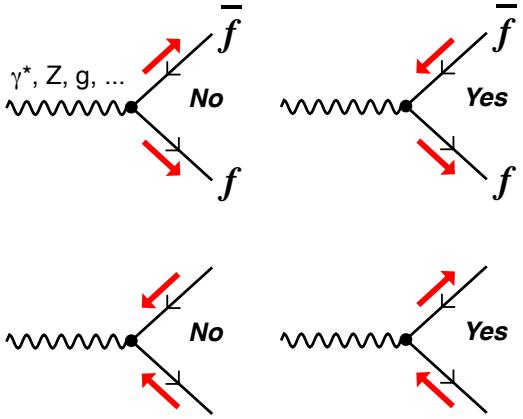

Fig. 1.2 Illustration of helicity conservation in the decay of a gauge boson (γ^*, Z, g, ...) into a fermion-antifermion pair ($f\bar{f}$). The red arrows indicate the spin orientations of the outgoing f and $\bar{f}$, while the black arrows represent the direction of the fermion flux.

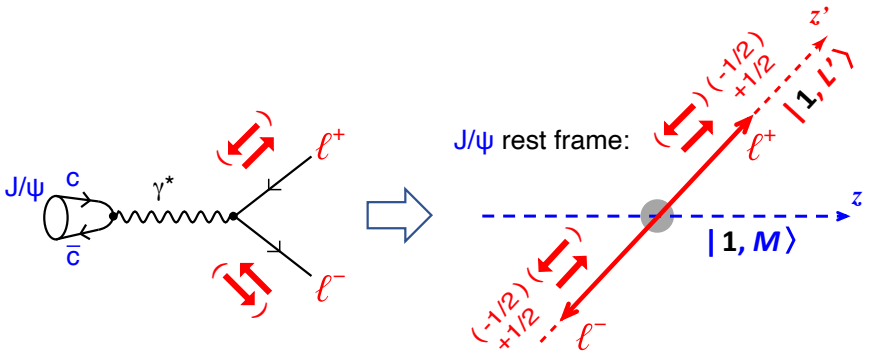

Fig. 1.3 Helicity conservation in the decay J/$\psi \to \ell^+\ell^-$ (left) and its effect on the total angular momentum of the dilepton system as seen in the J/ψ rest frame (right).

As illustrated in Fig. 1.2, this rule implies that the fermion and antifermion resulting from the decay of a virtual photon (or a gluon, or another gauge boson) must have opposite helicities, because the boson has zero (fermion) helicity. In other words, if in the Feynman diagram we follow the fermion flux (along the orientation of the fermion momentum and opposite to the antifermion momentum), the fermion spin never flips in the coupling to the photon.

Figure 1.3 shows the consequence of helicity conservation using the example of the dilepton decay of the J/ψ meson, where the pair of c and $\bar{c}$ quarks composing the J/ψ annihilates into a virtual photon, transforming in turn into the observed lepton-antilepton pair. In the J/ψ rest frame, the leptons have anti-parallel momenta; to have opposite helicities, as required by the conservation law, they must have the same spin orientation. The total angular momentum component of the dilepton system along

the direction z' is, therefore, $L' = +1$ or -1, while the case $L' = 0$ is forbidden (in the limit of massless leptons).

To evaluate the precision of this prediction of quantum electrodynamics (QED), we can consider that the observable contribution of the helicity-changing process, where $L' = 0$, is, in relative terms, of order $(m_f/E_f)^2 = 4(m_f/m_{J/\psi})^2$, being m_f and E_f the fermion mass and energy (in the J/ψ rest frame) and $m_{J/\psi}$ the J/ψ mass. In the case of the decay into a pair of muons this component is $\simeq 5 \times 10^{-3}$, being even smaller for decays of Υ mesons or into electron-positron pairs.

In summary, helicity conservation "polarizes" the dilepton system, giving it maximal angular momentum projection along the emission axis in the J/ψ rest frame. We are not yet referring to any specific polarization state of the J/ψ, for which we considered a generic angular momentum component M along the chosen polarization axis z.

While this chapter is devoted to the dilepton decay, different causes and mechanisms will, in general, "polarize" different final states in different ways, as will be discussed in Section 7.4. But we can already anticipate in here that a final state of the kind $S + \gamma$, where S is a $J = 0$ particle, is polarized with $L' = \pm 1$ along the emission axis z', just as what happens in the dilepton system. This is, for example, the case of the decay $J/\psi \to \eta_c \gamma$, which has exactly the same angular distribution as our prototype decay $J/\psi \to \ell^+\ell^-$. It can be kept in mind, therefore, that all considerations concerning the geometrical properties of the "dilepton" angular distribution, in this and the following chapters, will be equally valid for radiative decays to $J = 0$ particles.

1.3 Rotation of angular momentum eigenstates

We will discuss in the next chapter how the polarization frame is concretely defined in the experiments with respect to known reference directions (for example, the directions of the colliding beams). Here, to start with, we use a completely generic and arbitrary Cartesian system of axes (x, y, z), defined in the decaying particle's rest frame.

The angular distribution is naturally expressed in spherical coordinates, with the polar angle ϑ determined by the direction of one of the two decay products (the positive lepton in this case, according to the most common convention) with respect to the chosen polar axis z, and the azimuthal angle φ measured with respect to the zx plane, as illustrated in Fig. 1.4.

In Fig. 1.3-right the decay process is sketched as the transition from the initial J/ψ state, with angular momentum defined along z, to the final dilepton state, with angular momentum defined (and constrained by helicity conservation) along the quantization axis z'. To calculate the decay angular distribution we must impose angular momentum conservation between the initial and final states. This cannot be trivially achieved by equating L' with M in Fig. 1.3, because these are projections referred to two intrinsically different quantization axes. While it is not forbidden to

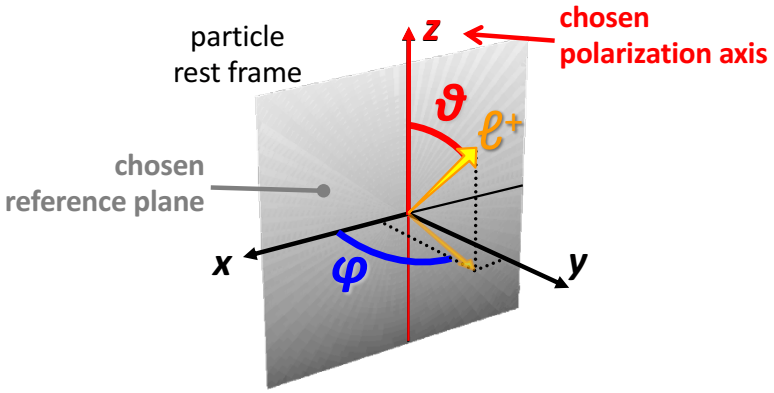

Fig. 1.4 The coordinate system for the measurement of a two-body decay angular distribution, with axes and angles defined in the rest frame of the decaying particle. In the decay into a lepton-antilepton pair, ϑ and φ conventionally indicate the direction of the *positive* lepton. Common definitions of the axes, relative to physical directions, are discussed in the next chapter.

choose the J/ψ quantization axis z (in principle arbitrary) as coincident with the z' axis, this choice is not appropriate for the description of the decay angular distribution, which is just determined by how the relative orientation of z' (direction of emission of the positive lepton) *changes event by event* with respect to the arbitrary (but conveniently fixed) reference direction z.

Instead, we rather need to *re-express* the angular momentum of the final state by *rotating its quantization axis* until it coincides with the one of the initial state. In other words, the question to be answered is: if an object has angular momentum projection L' along z', what is its angular momentum projection along z? The answer is not as definite in quantum mechanics as in the classical case, where it reduces to finding the geometrical projection of a vector over an axis. In general, all projection components are possible, with probability amplitudes expressed by elements of the Wigner rotation matrix [9], $\mathcal{D}^J_{LL'}(\vartheta, \varphi)$.

As illustrated in Fig. 1.5-left, an eigenstate $|J, L'\rangle$ of $J_{z'}$ can be expressed as a superposition of the eigenstates $|J, L\rangle$ of J_z through the rotation transformation [10]

$$|J, L'\rangle = \sum_{L=-J}^{+J} \mathcal{D}^J_{LL'}(\vartheta, \varphi)\, |J, L\rangle\,. \tag{1.1}$$

The angles ϑ and φ, defined in Fig. 1.4, represent here the rotation that brings the quantization axis z into coincidence with z', as well as x with x', and y with y'. The transformed system of axes (x', y', z'), like the original one (x, y, z), is naturally orthogonal and right-handed.

The (complex) rotation matrix elements $\mathcal{D}^J_{LL'}$ are defined as

$$\mathcal{D}^J_{LL'}(\vartheta, \varphi) = e^{-iL\varphi}\, d^J_{LL'}(\vartheta)\, e^{iL'\varphi} \tag{1.2}$$

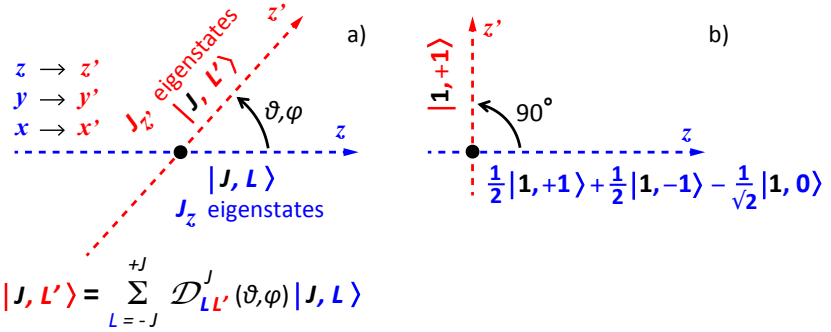

Fig. 1.5 Transformation of an angular momentum eigenstate by change of the quantization axis, for a generic rotation (left) and for a rotation by $\vartheta = 90°$ (right, for $\varphi = 0$).

in terms of the (real) "reduced" matrix elements

$$d^J_{LL'}(\vartheta) = \sum_{t=\max(0,L-L')}^{\min(J+L,J-L')} (-1)^t \times \frac{\sqrt{(J+L)!\,(J-L)!\,(J+L')!\,(J-L')!}}{(J+L-t)!\,(J-L'-t)!\,t!\,(t-L+L')!} \times \left(\cos\frac{\vartheta}{2}\right)^{2J-(L'-L+2t)} \left(\sin\frac{\vartheta}{2}\right)^{L'-L+2t} . \tag{1.3}$$

Swapping L with L' or flipping the signs of both, the reduced matrix element changes sign if $L - L'$ is odd and remains unchanged otherwise:

$$d^J_{L',L}(\vartheta) \;=\; (-1)^{L-L'}\, d^J_{L,L'}(\vartheta) \;=\; (-1)^{L-L'}\, d^J_{-L',-L}(\vartheta)\,. \tag{1.4}$$

A more detailed discussion of rotation transformations, including explicit expressions of $d^J_{L,L'}(\vartheta)$ for several values of J, are provided in Chapter 7. A coherent convention must be maintained for the definition of the angles and the consequent direction of the rotation throughout the calculations. At the risk of being repetitive, we emphasize that the above definitions are valid when the pure angular momentum eigenstate (the object to be "projected") is defined with respect to the *final* quantization axes, while its resulting decomposition into the full basis of states (components of the "projection") refers to the *initial* system. This is the convention defining the *positive* direction of the rotation in Eq. 1.1. The convention is chosen in analogy with the classical concept of projection of a vector, where the angle is measured with respect to the projection axis, as in a rotation *from* that axis *to* the vector.

The analogy only serves as guidance, the reality of quantum mechanics being very different. One example illustrating the difference with the classical case is

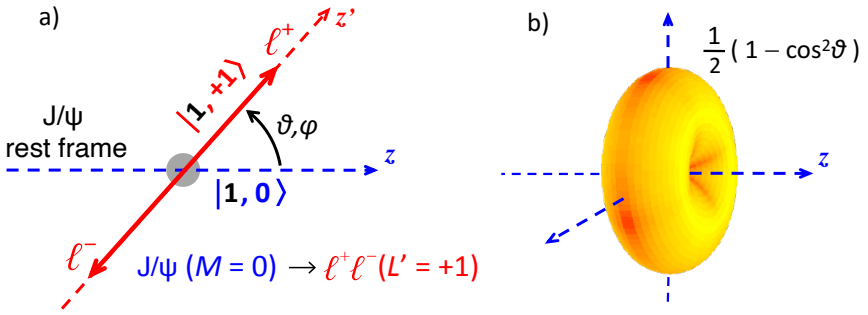

Fig. 1.6 A specific example of angular momentum configuration for the decay J/$\psi \to \ell^+\ell^-$, where the J/ψ has component $J_z = 0$ with respect to the chosen quantization axis (left), leading to the characteristic "donut" shape of the angular distribution (right).

shown in Fig. 1.5-right: the eigenstate $|1, +1\rangle$ of $J_{z'}$ becomes a superposition of all three J_z eigenstates with respect to a quantization axis perpendicular to the original one, while the classical expectation would simply be $|1, 0\rangle$, as the geometrical projection of the vector **J** along z is zero if it is maximal along z'.

We have now all the necessary ingredients to calculate a first example of a decay angular distribution in a specific case. We assume that the decaying particle, a J/ψ, was produced in the angular momentum state $|J, M\rangle_z = |1, 0\rangle_z$ with respect to a given quantization axis z. We want to calculate the shape of the angular distribution of its decay into leptons. We know from Section 1.2 that the system of the two leptons can be in one of only two possible angular momentum states with respect to their common direction in the J/ψ rest frame: $|J, L'\rangle_{z'} = |1, +1\rangle_{z'}$ or $|1, -1\rangle_{z'}$.

Let us start by considering the individual subprocess represented in Fig. 1.6-left, where $|J, L'\rangle_{z'} = |1, +1\rangle_{z'}$. We use Eq. 1.1 to "project" the dilepton angular momentum state onto the J/ψ quantization axis z, i.e. to express it as a combination of terms of eigenstates of J_z:

$$\begin{aligned} |\ell^+\ell^-; 1, +1\rangle_{z'} &= \mathcal{D}^1_{-1,+1}(\vartheta, \varphi)\, |\ell^+\ell^-; 1, -1\rangle_z \\ &+ \mathcal{D}^1_{0,+1}(\vartheta, \varphi)\, |\ell^+\ell^-; 1,\ 0\rangle_z \\ &+ \mathcal{D}^1_{+1,+1}(\vartheta, \varphi)\, |\ell^+\ell^-; 1, +1\rangle_z\ . \end{aligned} \tag{1.5}$$

The dilepton configuration contains, therefore, the J_z eigenstate $|1, 0\rangle_z$ with component amplitude $\mathcal{D}^1_{0,+1}(\vartheta, \varphi)$. This is the same as the eigenstate of the initial J/ψ and is therefore *the* component contributing to the transition probability: it is the one satisfying angular momentum conservation. The other two components are, instead, orthogonal to the J/ψ configuration, so that they cannot be reached from the initial state without violating angular momentum conservation.

The probability amplitude of the process is, therefore,

$$_z\langle \ell^+\ell^-; 1, 0\,|\,\mathcal{B}\,|\,\mathrm{J}/\psi; 1, 0\rangle_z \ \propto \mathcal{D}^{1*}_{0,+1}(\vartheta, \varphi)\ ,$$

where $\mathcal{B}$ is a transition operator. The probability is obtained as its square modulus, where the φ-dependent factors cancel out (Eq. 1.2), a usual feature when the initial state is a pure eigenstate — as in the simple case here considered — rather than a superposition of different eigenstates.

Using $d^1_{0,+1} = \sin\vartheta/\sqrt{2}$ (from Eq. 1.3 or Table 7.3), we find that the angular distribution is proportional to $\frac{1}{2}(1-\cos^2\vartheta)$. It can be easily verified that an identical result is obtained, in this specific case, also with the complementary choice of the dilepton polarization, $|J, L'\rangle_{z'} = |1,-1\rangle_{z'}$. The distribution is, therefore, characteristic of the dilepton decay of a $J_z = 0$ eigenstate. Its shape, resembling a "donut", is represented in Fig. 1.6-right, where the distance of the surface from the origin of the system of axes is proportional to the probability of the direction of emission. Most of the leptons tend to be emitted close to the plane perpendicular to the quantization axis z, while the emission along z is forbidden: in the one-dimensional representation as a function of $\cos\vartheta$, the distribution tends to zero as $\cos\vartheta \to \pm 1$. As already mentioned, this is an azimuthally isotropic distribution; it does not have φ-dependent modulations, which are present in the general case considered in Section 1.7.

1.4 Parity properties

To illustrate the next concept, we repeat the calculation of the dilepton decay angular distribution, assuming now that the decaying particle is produced in the angular momentum state $|J, M\rangle_z = |1,+1\rangle_z$. We consider at the same time both cases of dilepton polarization, $|J, L'\rangle_{z'} = |1,-1\rangle_{z'}$ and $|1,+1\rangle_{z'}$, illustrated in Fig. 1.7-a on the left and right, respectively.

Using Eq. 1.5, together with the similarly obtainable expression for $|\ell^+\ell^-; 1,-1\rangle_{z'}$, the transition probabilities of the two configurations can be written as

$$|_z\langle \ell^+\ell^-; 1,+1 \,|\, \mathcal{B} \,|\, \mathrm{J}/\psi; 1,+1\rangle_z|^2 \;\propto |\mathcal{D}^{1*}_{+1,\pm 1}(\vartheta,\varphi)|^2 \,,$$

where only the dilepton J_z component $L = M = +1$ contributes and the index ± 1 corresponds to the two dilepton polarizations. Since $d^1_{+1,\pm 1} = (1 \pm \cos\vartheta)/2$, the corresponding angular distributions are proportional to $1 + \cos^2\vartheta \pm 2\cos\vartheta$. As represented in Fig. 1.7-b, the dilepton polarizations $|J, L'\rangle_{z'} = |1,+1\rangle_{z'}$ and $|1,-1\rangle_{z'}$ lead in this case to two different decay distributions that are mirror reflections of each other. Reversing the angular momentum projection of the mother particle, from $|J, M\rangle_z = |1,+1\rangle_z$ to $|1,-1\rangle_z$, further exchanges the two shapes. The orientation of the distribution depends, therefore, on the sign of the product $M \cdot L'$.

While at first sight the distributions may look approximately spherical, it should be noted that they exhibit a strong asymmetry in the z direction. In addition to the small valleys that they have around their extremes located at the origin along the z axis, making them rather resemble an orange, for $M \cdot L' > 0$ the decay emission in the "forward" direction ($z > 0$) is much more favoured than the one in the "backward" direction ($z < 0$), and the opposite happens in the $M \cdot L' < 0$ case.

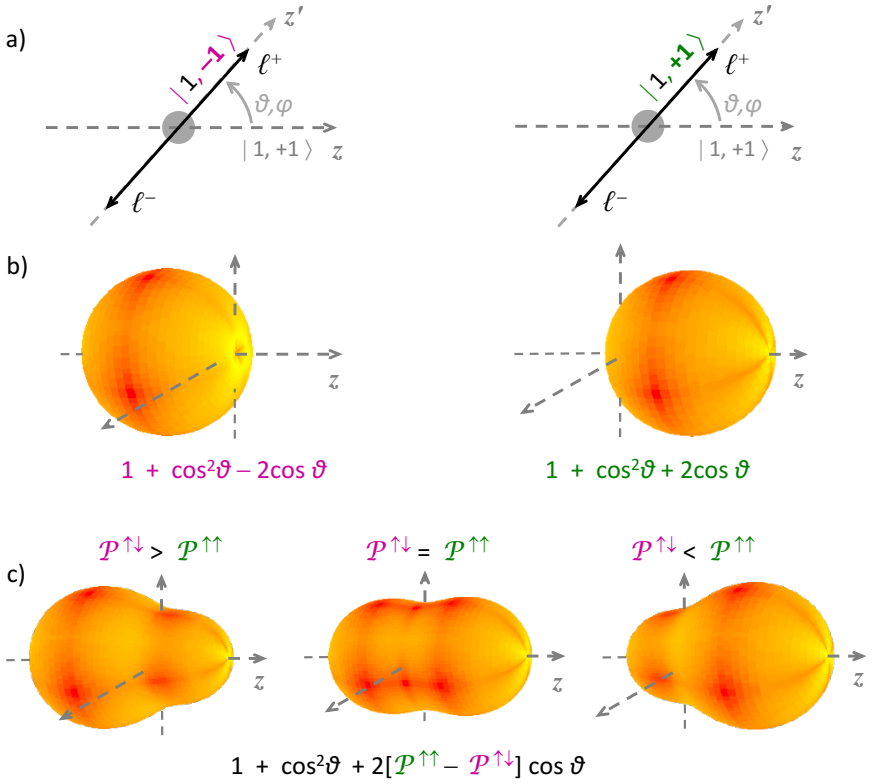

Fig. 1.7 (a) Sketches of the dilepton decay of a $J = 1$ particle having angular momentum projection $M = +1$ along the chosen quantization axis z, with two opposite polarizations of the dilepton system, $|J, L'\rangle_{z'} = |1, -1\rangle_{z'}$ (left) and $|1, +1\rangle_{z'}$ (right). (b) The geometrical shapes of the corresponding angular distributions; taking a parent particle with projection $M = -1$ instead of $M = +1$ has the effect of changing "forward" into "backward" emission, and vice-versa. (c) Observable distributions for different relative contributions of the two configurations, in two parity-violating cases (left and right) and in the parity-conserving case (middle).

The two orientations are reciprocally related by the transformation of parity, involving the sign change $z \to -z$, that is $\cos\vartheta \to -\cos\vartheta$, in addition to the transformations $x \to -x$ and $y \to -y$, which imply $\varphi \to \pi + \varphi$ and are thus irrelevant in the current, azimuthally isotropic case. Therefore, we can see that, while the $J_z = 0$ configuration produces a decay distribution that is always parity-invariant (Fig. 1.6-right), the $J_z = \pm 1$ case *is* sensitive to the parity properties of the system: in the presence of parity-violating effects, leading to different probabilities for the forward and backward emissions, the angular distribution is represented by pear-shaped distributions of the kind shown in the left and right panels of Fig. 1.7-c, globally described by the function $1 + \cos^2\vartheta \pm 2\mathcal{A}\cos\vartheta$, where $\mathcal{A}$ is proportional to the "forward-backward asymmetry" (see Section 1.11). The parity conserving

case, where $\mathcal{A} = 0$ and the two specular configurations have identical weights, has a typical peanut-like shape (Fig. 1.7-c, middle panel).

Addressing the basic polarization cases of vector particles using food metaphors (donuts, peanuts, oranges, pears) may not seem very appropriate. As a matter of fact, a commonly recognized terminology exists and we will adopt it also in here. In order to minimize confusion, however, we should emphasize how possibly misleading are those "standard" definitions.

"Polar" vector particles share the quantum numbers of the photon and are therefore said, by analogy with the photon, to be "transversely" polarized when they have spin projection $J_z = \pm 1$. The denomination is motivated by the fact that the electromagnetic field carried by the photon oscillates in the transverse plane with respect to the photon momentum; however, the photon *spin* is aligned *along* the momentum, making such terminology counterintuitive when the focus of the discussion is on angular momentum.

In the case of the decay of vector particles, when we refer to a "transverse" polarization not only is the particle angular momentum vector aligned in the *longitudinal* direction with respect to z but also, at least in the parity conserving case, the two leptons are emitted in a preferred longitudinal alignment with the z axis, resulting in the characteristic peanut-shape of the distribution. In the same terminology, "longitudinal" polarization indicates the angular momentum configuration $J_z = 0$, classically representing a *transverse* alignment of the vector $\mathbf{J}$ with respect to z and leading to a preferred lepton emission in the transverse plane (donut-shaped distribution). By further extension, the same terms are also used to describe vector-particle polarizations not only with respect to their own momenta, but also with respect to any other reference direction z (such as the beam directions in a collider experiment), where the analogy with the photon is completely lost.

1.5 Introductory remarks on polarization measurements

Before considering more complex (and realistic) cases, we will use the examples of angular distributions derived in the previous sections to address the following question: what is, in practical terms, a polarization measurement? For simplicity, we will only consider two extreme polarization scenarios: we want to establish whether a sample of J/ψ mesons is "transversely" or "longitudinally" polarized with respect to the quantization axis z represented by its own direction in the laboratory, commonly referred to as the "helicity axis". In general, these are not the only possible options (as will become clearer in the following chapters of this book), but it is more convenient to start with a simple illustration and two different scenarios are sufficient to present the main messages of this section.

The core of the measurement consists in building the distribution of the dilepton events as a function of the variable $\cos\vartheta$, where ϑ is the angle between the positive lepton in the J/ψ rest frame and the direction of the J/ψ itself in the laboratory, and verify whether it has a shape consistent with $1 + \cos^2\vartheta$ (i.e. $J_z = \pm 1$, transverse

case, considering only the parity-conserving term) or with $1 - \cos^2\vartheta$ (i.e. $J_z = 0$, longitudinal case). In reality, these functional shapes are not expected to straightforwardly describe the $\cos\vartheta$ distributions of the dileptons in the collected experimental samples, which are affected by inevitable limitations of the detectors. Leaving aside the (also quite important) problem of background subtractions, a crucial difficulty in the measurement of the $\cos\vartheta$ distribution is that the detection acceptance of the experiments depends very significantly on the momentum of the leptons. In the case of the CMS LHC experiment, for example, muons that are produced in the so-called "barrel region" of the detector, roughly corresponding to the angular region defined by $|\eta| \lesssim 1$, where η is the particle's pseudorapidity, must have transverse momentum, p_{T}, larger than ~ 3.3 GeV to be identified as muons. Lower p_{T} muons fail to reach the (innermost) muon stations, because the curl induced by the 3.8 T solenoidal field is too strong in that case; they are, therefore, indistinguishable from pions and other charged particles that are only reconstructed in the (inner) tracker system. This means, for example, that J/ψ mesons produced in the barrel (with rapidity $|y| \lesssim 1$) will only trigger the detector's readout and acquisition system if *both* decay daughters are identified as muons, which means that almost all the J/ψ dimuons written to permanent storage will have J/ψ p_{T} larger than ~ 6.5 GeV. The low trigger and reconstruction efficiency of low momentum muons induces "acceptance and efficiency effects" that distort the measured kinematical distributions.

Naturally, the cause and the magnitude of these effects depend on the experiment and, more specifically, on the region of the detector under consideration. In the "endcap regions" of CMS, for instance, the magnetic field effect loses relevance and the acceptance becomes determined by energy loss in the material budget of the detector that the muons need to traverse, which imposes a minimum threshold on the *total* momentum of the muons. Analogous effects are also present in the detection of electrons. In summary, only events where both leptons pass certain thresholds in momentum (longitudinal or transverse) are collected by the experiments. For the purpose of our discussion, the most important aspect is that these conditions affect the $\cos\vartheta$ distributions: the dilepton detection acceptance depends on $\cos\vartheta$.

In collider experiments, for example, when $\cos\vartheta \to +1$ or -1 the two leptons are emitted along the J/ψ direction and the one emitted backwards in the J/ψ rest frame often has a small laboratory momentum (especially when the J/ψ momentum itself is not large), resulting in a low detection efficiency. The configurations maximizing the chances that the event is detected are, hence, those with $\cos\vartheta \sim 0$, where the two muons are emitted transversely to the J/ψ momentum and have comparable laboratory momenta, none of them being below the detection threshold, if the J/ψ is not too soft. Different and/or additional effects may be present in fixed-target experiments with forward detectors, where the non-uniform angular coverage and even possible discontinuities (for example in the region of the beam pipe) can influence the detection efficiency as a function of the momenta and relative angle of the two leptons, sculpting the decay angular distribution.

For illustration purposes we will consider J/ψ mesons produced in the $9 < p_{\mathrm{T}} < 12$ GeV and $|y| < 1$ phase space window, in a collider "gedankenexperiment" with a muon trigger and reconstruction efficiency that depends on the muon p_{T} accord-

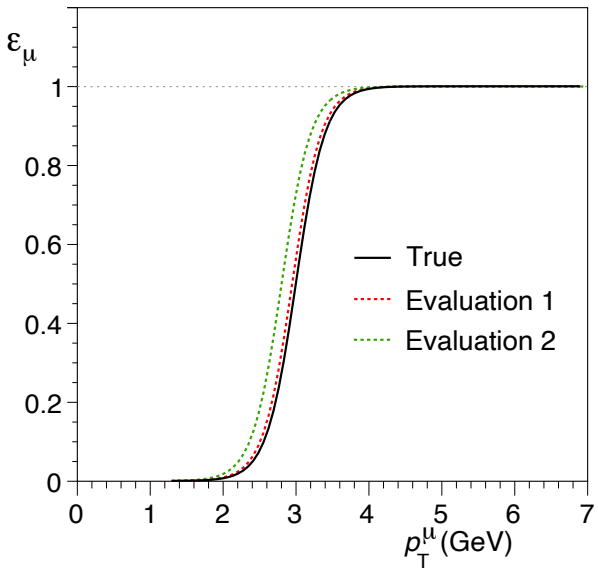

Fig. 1.8 Examples of typical single-muon detection efficiencies, ϵ_μ, as a function of p_T. The black curve represents the true efficiency of our "gedankenexperiment", reflecting limitations in the trigger, track reconstruction, muon identification, etc., while the red and green dashed curves represent two alternative evaluations, mimicking what one would get through simulation studies, using standard Monte Carlo techniques.

ing to the function shown as a black solid curve in Fig. 1.8. This curve shows the typical "turn-on" behaviour of detection efficiencies as p_T increases, represented by a smoothly increasing function followed by a saturation plateau. The slope of the "turn-on" part can be more or less steep but it never happens that a detection efficiency is represented by a step function, which would reflect a sharp cut at some well-defined p_T value. In our hypothetical example, the efficiency crosses the 50% value at $p_T \simeq 3$ GeV.

The left panel of Fig. 1.9 shows how this function translates into a data histogram of the $\cos\vartheta$ dimuon distribution, in a sample of events where the J/ψ is assumed to be transversely polarized: no events are recorded above a certain value of $|\cos\vartheta|$. The distribution drops drastically, strongly departing from the parabolic shape expected for a physical distribution. An acceptance correction must be applied to the data and only the corrected distribution can be compared to the physical templates corresponding to transverse and longitudinal polarization scenarios.

The result of an ideal measurement outcome is shown in the right panel of Fig. 1.9, where the data distribution was corrected by the ratio between the reconstructed and the generated $\cos\vartheta$ distributions obtained with a sample of simulated events, analogous to the Monte Carlo simulations frequently used in analyses of experimental data. It might be worth emphasising that, in this section, whenever we use the words "data" and "simulated events" we are referring to samples of pseudo-

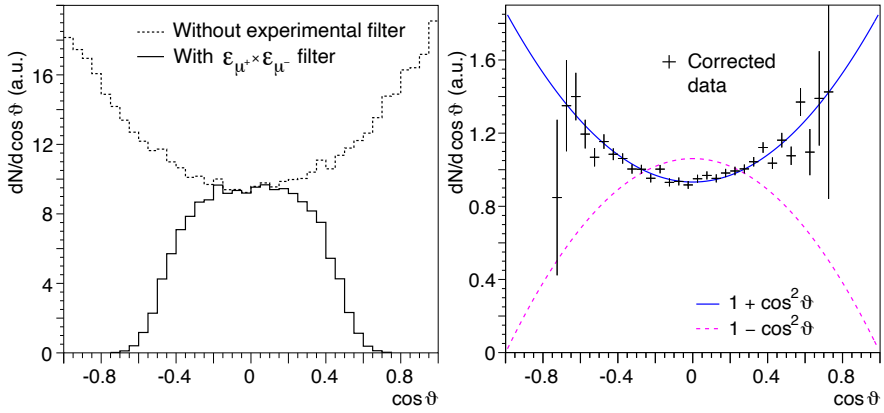

Fig. 1.9 Illustration of an ideal polarization measurement. Left: The dimuon $\cos\vartheta$ distribution seen if the experiment had 100% detection efficiency for all muons (grey dashed histogram) and in the data collected by our hypothetical detector (black solid histogram), affected by the muon-pair detection efficiency $\epsilon_{\mu^+} \times \epsilon_{\mu^-}$. Right: The data distribution after efficiency correction, using a perfectly simulated Monte Carlo sample, exactly reproducing the true efficiency shape (black curve in Fig. 1.8). While not extending to the full angular domain (most events in the $|\cos\vartheta| > 0.6$ range are not detected), the shape of the corrected distribution, in this ideal illustration, is perfectly compatible with the $1 + \cos^2\vartheta$ function, in agreement with the simulated transverse polarization hypothesis.

events generated by a very simple software code and not to data collected by real experiments or to events simulated with complex Monte Carlo event generators. The correction is perfect because, for this "ideal illustration", which one could call a calibration or debugging step, we made the event simulation with exactly the correct efficiency curve (the black curve in Fig. 1.8), therefore precisely accounting for the detection efficiency effects.

We should note here that, in this section, we assume, for simplicity, that this "reconstructed over generated ratio" is independent of the polarization scenario included in the generation of the Monte Carlo event sample: the generation was made with a flat $\cos\vartheta$ distribution, reflecting the fact that, in principle, we ignore the polarization that we are going to measure. In reality, as will be discussed in Chapter 2 (e.g. in Section 2.13), this assumption is not valid in all polarization scenarios, and higher-dimensional corrections, considering also the azimuthal angular component, are needed for a reliable result in more general cases.

We conclude that, with a perfectly faithful simulation of the detection efficiency, the corrected distribution (represented by the black markers) reproduces well the $1 + \cos^2\vartheta$ shape (solid blue curve) denoting transverse polarization (the hypothesis injected in the generation of the data-like sample) and strongly disfavours the longitudinal scenario (dashed magenta curve). As a consequence of the muon acceptance limitations, the corrected distribution is restricted to the more central region, the external bins showing large statistical fluctuations (that do not represent a problem in these fully ideal conditions).

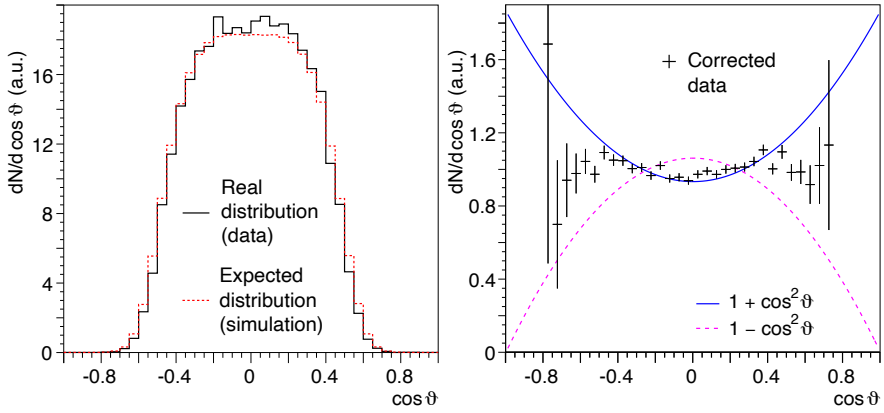

Fig. 1.10 Illustration of a realistic polarization analysis using an imperfect evaluation of the lepton detection efficiency. Left: The event distribution in the "collected data" (black solid histogram), reflecting the true detection efficiency shape (black curve in Fig. 1.8), compared to the distribution obtained in (transversely polarized) simulated events (red dashed histogram) filtered using a slightly mis-evaluated efficiency shape (red dashed curve in Fig. 1.8). Right: The data distribution after correction for the estimated efficiency, seemingly contradicting the transverse polarization hypothesis used in this exercise.

In reality, the efficiency correction is never an exact procedure, at the very least because its dependence on the muon p_T (and on p_L, rapidity, etc) is never known as a perfectly faithful analytical function, but rather as a binned histogram affected by fluctuations caused by the limited size of the simulated event sample. More importantly, the detector description in the simulation software is necessarily affected by approximations needed to speed up the computations, replacing the measured magnetic field maps by analytical parametrizations, neglecting some material in the detector description, etc. Furthermore, the real data are collected over a period of several months, with alignment and calibration parameters that vary with time (e.g. because of accumulated radiation damage), while, in general, one single event sample is simulated, corresponding to a suitable average of parameters.

Even in the best cases, there will always be some residual differences between the collected events and the simulated ones. Perfection is out of reach and the important question to ask is if the accuracy of the physics measurement is significantly affected by the efficiency corrections. It is a question that needs to be quantitatively answered through the evaluation of the sensitivity of the result of the measurement to the precision with which the detection efficiency is known.

Figure 1.10 illustrates a realistic experimental situation. The analysis is made correcting the "collected data" with an estimated detection efficiency, represented by the red dashed curve in Fig. 1.8, which is slightly shifted towards lower p_T values with respect to the true efficiency. This means that the simulated sample will include (low p_T) events that are not present in the collected data.

The overestimation of the low-p_T muon efficiency leads to an underestimation of the corrected dimuon yield (i.e. of the production cross section). The bias rep-

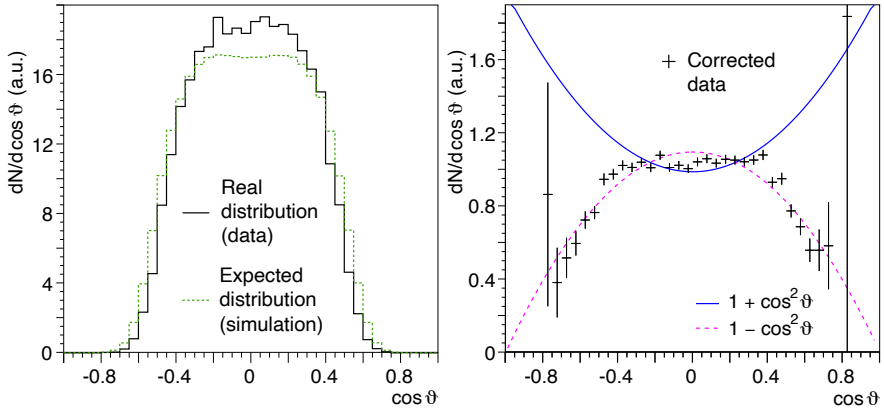

Fig. 1.11 A measurement scenario analogous to the one shown in the previous figure, but using a simulated muon efficiency (shown in Fig. 1.8 by the green dashed curve) departing more significantly from the real one. The expected $\cos\vartheta$ distribution (green dashed histogram) is considerably broader than it should, leading to an acceptance-corrected distribution with a shape that clearly favours the longitudinal polarization hypothesis.

resented in Fig. 1.10 is not very strong, so that the measured cross section is only 2.3% smaller than the true value.

The effect is much more significant on the shape of the $\cos\vartheta$ distribution. The events that survive the efficiency filter used in the simulation while being rejected in the "real experiment" are located at high $|\cos\vartheta|$ values, as illustrated by the broader simulated distribution shown by the red dashed histogram in Fig. 1.10-left. This means that, after the efficiency correction is applied, the "acceptance-corrected" physical physical distribution, shown by the black markers in the right panel, has a shape remarkably different from the real one, indicated by the blue curve.

If a physical conclusion had to be derived from such a measurement, with its intermediate shape between those of the transverse and longitudinal cases, it would be that the J/ψ event sample is not fully transversely polarized, having a component of longitudinally polarized events. A critical look at the wavy-shaped corrected distribution shown in Fig. 1.10-right, which does not resemble any physical shape, should alert to the presence of a problem in the analysis. However, a measurement based on a smaller number of events would lead to a less precise pattern, not so obviously unphysical and likely to resemble the typical flat distribution of an isotropic decay: the result would suggest the wrong conclusion that the analysed sample of J/ψ mesons provides evidence of "unpolarized" production (a case further discussed in Section 1.10).

Figure 1.11 shows how a sufficiently biased efficiency curve (in this case, represented in Fig. 1.8 by the green dashed curve) can even lead to a conclusion opposite to the correct one: the acceptance-corrected $\cos\vartheta$ distribution tends to vanish for $\cos\vartheta \to \pm 1$, resembling the shape expected for a fully longitudinally polarized

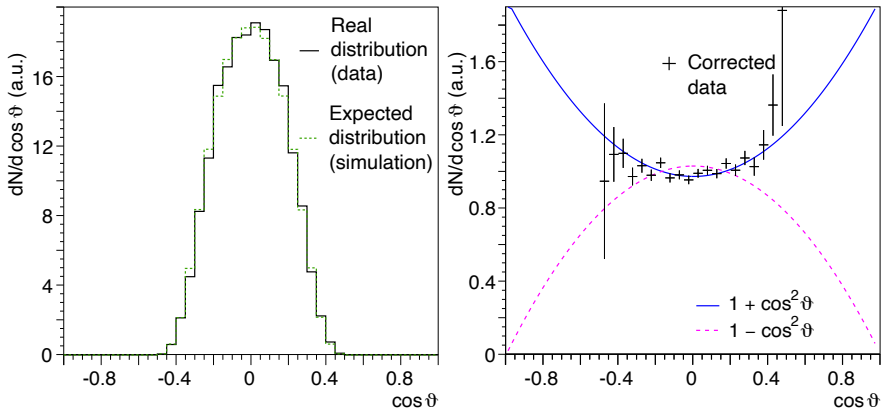

Fig. 1.12 The same hypothetical measurement as shown in the previous figure but now performed with a fiducial selection of events, imposing that the muons must have $p_T > 4$ GeV. By excluding the delicate turn-on region of the detection efficiency, the compatibility with the transverse polarization hypothesis is restored, at the expense of a decrease in the statistical precision of the measurement.

particle (magenta dashed curve). If taken at face value, such a measurement would clearly exclude the true interpretation of transverse polarization.

Even in unfortunate cases like these, where the detector effects cannot be simulated with sufficient accuracy, safer measurements can be made by avoiding the steep turn-on region of the muon efficiency curve. Figure 1.12 shows the result of the same analysis (still using the biased muon efficiency represented by the green dashed curve in Fig. 1.8) but now only selecting events where both muons have $p_T > 4$ GeV. Applying this sharp selection of events makes the analysis insensitive to the exact shape of the efficiency function, as all the selected muons are on "the plateau" and the magnitude of the efficiency in that region is not relevant for polarization measurements, as it only affects the normalization of the distribution.

The vastly improved agreement between the acceptance-corrected (green dashed histogram) and the real (black histogram) $\cos\vartheta$ distributions, with respect to the case shown in Fig. 1.11, comes with a price: the precision and discriminatory power of the measurement is considerably reduced, not so much because the number of selected events is reduced to half, but because the covered $|\cos\vartheta|$ domain becomes narrower, and the central data points are the least effective in distinguishing between different physical scenarios (in the $|\cos\vartheta| \lesssim 0.3$ window, the transverse and longitudinal polarization curves are barely distinguishable).

In summary, polarization measurements are delicate procedures because of their strong sensitivity to the *shapes* of the functional dependences of the detection efficiencies on the relevant kinematic variables. The data analyses must find a good balance between using the largest possible data sample, leading to maximal statistical precision, and selecting a restricted phase space domain, where the efficiency correction can be safely applied within controllable systematic uncertainties.

1.6 Correlation between cross sections and polarizations

The discussion of the previous section can also be used to illustrate another important concept: to measure the production cross section of a particle, one needs to know its polarization. As we can see in Figs. 1.9–1.12, selecting events where both leptons have momenta above a certain threshold reduces the visible angular domain of the decay distribution. Obviously, the acceptance correction cannot influence the distribution in the $\cos\vartheta$ domain where *zero* events were accepted, since the correction is nothing more than a multiplication. Therefore, the measurement of the total corrected yield of the particle, in a given p_{T} and rapidity range, implies an extrapolation beyond the $\cos\vartheta$ domain covered by the experiment, effectively introducing a dependence on the (assumed) polarization. In fact, what the analysis can effectively determine by applying the acceptance/efficiency correction is the yield of particles decaying with a polar angle satisfying the relation $|\cos\vartheta| < C$, with $[-C, +C]$ being the region where the event distribution is not zero (its support). Of course, the physical cross section for the production of a particle does not depend on how the particle decays, nor on experiment-dependent cuts applied to the decay angles. A physically meaningful cross section measurement implies, therefore, an extrapolation to the full angular range $-1 < \cos\vartheta < +1$. This procedure requires knowing how the variable $\cos\vartheta$ is distributed outside of the experimentally limited support of the $\cos\vartheta$ distribution; in other words, it requires knowing the particle's polarization.

Denoting by σ_C the corrected cross section obtained in the visible range $[-C, +C]$ and by $w(\cos\vartheta)$ the "true" distribution, then the full (extrapolated) cross section is computed as

$$\sigma = \frac{\int_{-1}^{+1} w(\cos\vartheta)\,\mathrm{d}\cos\vartheta}{\int_{-C}^{+C} w(\cos\vartheta)\,\mathrm{d}\cos\vartheta}\,\sigma_C\,. \tag{1.6}$$

In the specific case where the particle is always produced with either transverse or longitudinal polarizations, $w(\cos\vartheta) \propto 1 \pm \cos^2\vartheta$, we get

$$\sigma = \frac{3 \pm 1}{C\,(3 \pm C^2)}\,\sigma_C\,, \tag{1.7}$$

where the alternative + or − signs correspond, respectively, to the transverse and longitudinal polarization cases.

For example, if the lepton detection imposes $|\cos\vartheta| < 0.6$ as the visible $\cos\vartheta$ window, the extrapolation to full phase space is represented by a scaling factor of 2.0 or 1.3, depending on which of the two extreme polarization scenarios we are considering. These are not small effects: using one or the other polarization hypothesis leads to cross section measurements that differ by around 50%.

In reality, the angular acceptance window strongly depends on the particle's p_{T} and on how large the lepton momentum cut values are, with respect to the particle's mass. The examples considered above addressed J/ψ mesons of p_{T} around 10 GeV, decaying to muons that needed to have p_{T} larger than a threshold value similar

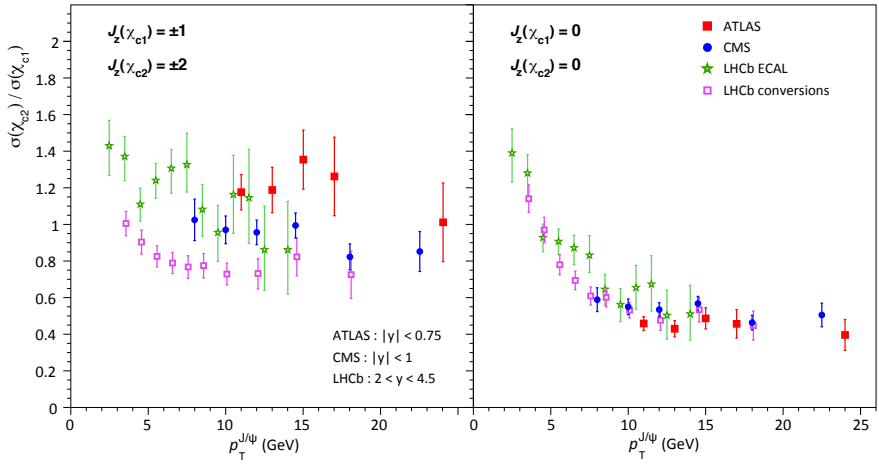

Fig. 1.13 The χ_{c2}/χ_{c1} cross section ratio measured in pp collisions at 7 TeV by ATLAS [11], CMS [12], and LHCb [13, 14], as a function of the J/ψ p_T, with acceptance corrections calculated under two extreme polarization hypotheses, one assuming the angular momentum projections $J_z(\chi_{c1}) = \pm 1$ and $J_z(\chi_{c2}) = \pm 2$ (left panel), and the other $J_z(\chi_{c1}) = J_z(\chi_{c2}) = 0$ (right panel).

to the particle's mass. In these conditions, the acceptance/efficiency effects are very important, as we have just seen. Their relevance decreases as one studies J/ψ mesons of larger and larger p_T. Much smaller effects, of the order of a few percent, are expected in measurements of the cross section of Z bosons, if the lepton momentum thresholds are at the level of 10–20% of the mass, as is the case in typical analyses reported by the LHC experiments.

It is clear from these examples that the polarization dimension, that is, the decay's angular degrees of freedom, cannot be ignored in the measurement of the cross section, a quantity by definition independent of the decay channel. Measurements of differential cross sections as a function of p_T and rapidity, ignoring the angular coordinates of the decay (including the azimuthal variable φ, which also plays a role in the realistic cases of more complex polarization scenarios), implicitly (and sometimes blindly) assume a certain polarization of the particle: the one coded in the Monte Carlo simulation program used for the determination of the acceptance correction. This is not a minor oversight, if the particle's polarization is not known a priori (or not implemented in the simulation), as is often the case in studies of production properties.

The best way to illustrate the sizeable magnitude that this effect can have is through the use of existing measurements. Figure 1.13 shows the ratio between the χ_{c2} and the χ_{c1} production cross sections measured in pp collisions at 7 TeV by ATLAS [11], CMS [12], and LHCb [13, 14], as a function of the J/ψ p_T. Both particles were reconstructed in the decay channel $\chi_{cJ} \to J/\psi\,\gamma$.

The cross-section ratios presented in the figure were corrected for detection acceptances according to two different scenarios for the χ_{c1} and χ_{c2} polarizations,

which were completely unknown when the experimental analyses were made (and still today remain only weakly constrained). The comparison is possible thanks to the availability, in the experimental publications, of tables from which the values corresponding to any assumed polarizations can be obtained.

For the "pseudovector" and "tensor" quarkonia χ_{c1} and χ_{c2}, the relations between the angular momentum projections J_z along a given axis and the shapes of the angular distributions of their decays to J/$\psi\,\gamma$ are different with respect to the J/$\psi \to \ell^+\ell^-$ case considered until now, besides being different among the two χ_{cJ} states. This is a topic that will be discussed in detail in Section 6.6. Nevertheless, it is easy to understand, by analogy with the previous discussion, that the acceptance limitations imposed by the minimum p_{T} requirements on the muons of the J/ψ decay, as well as, in this case, on the radiated photon, sculpt the angular acceptance of the decay products and lead to a dependence of the phase-space-corrected χ_{c1} and χ_{c2} yields on the polarization states assumed for the two particles. There are two possible pure polarization states for the χ_{c1}, $J_z = 0$ or ± 1, and three for the χ_{c2}, which can also have $J_z = \pm 2$. The assumed quantization axis is, in this case, the particle momentum direction in the laboratory (helicity axis).

As can be seen in Fig. 1.13, selecting one or the other of these two scenarios leads to results that differ from each other by around a factor of two (or even more than a factor of 2.5, in the case of the ATLAS points). This is a much larger variation than that corresponding to the combined statistical and systematic uncertainties reported for the measurements. The remaining combinations of χ_{c1} and χ_{c2} pure polarizations lead to intermediate results.

It is particularly remarkable to realize that even the level of consistency between independent measurements changes significantly, because the experimental selection criteria defining the acceptances, and therefore the polarization dependences, are different from one measurement to another. If the hypothesis $J_z(\chi_{c1}) = \pm 1$, $J_z(\chi_{c2}) = \pm 2$ were the correct one, it should be concluded that the ATLAS and CMS measurements, obtained in very similar rapidity ranges ($|y| < 0.75$ and $|y| < 1$, respectively), are inconsistent with each other.

Even more surprisingly, two measurements reported by one single experiment, LHCb, mostly differing by the method used to detect the photon, are also significantly different. In the first measurement [13], the photons are reconstructed from energy deposits in the electromagnetic calorimeter ("LHCb ECAL", green stars in Fig. 1.13). In the second [14], the photon converts to a e^+e^- pair that is then reconstructed from the hits left in the tracker layers ("LHCb conversions", pink squares in the figure). The first result is around a factor of 1.4 higher than the second. These differences reflect the fact that the detection acceptance corrections (i.e. the factors needed to extrapolate the fiducial measurements, made in regions defined by the photon kinematics, to the reported χ_c phase space window) depend on the minimum energy that the photons must have in order to be accepted by the analyses and on the coverage of the detectors used in the measurement. In particular, converted photons emitted at relatively large angles often lead to e^+e^- pairs where one of the electrons is outside of the detection area. The polarization hypothesis $J_z(\chi_{c1}) = J_z(\chi_{c2}) = 0$, on the other hand, provides a much more consistent account of the experimental

picture, also being better in this respect than any of the remaining $J_z(\chi_{c1}), J_z(\chi_{c2})$ combinations (not shown in the figure).

Therefore, perhaps surprisingly, the strong correlation between acceptance correction and polarization effectively turns this set of cross section measurements into an experimental constraint on the χ_{c1} and χ_{c2} polarizations: the requirement of mutual compatibility between measurements strongly favours one scenario over the others, in a way that can be quantitatively evaluated through an analysis that simultaneously considers all the experimental measurements, properly accounting for (correlated and uncorrelated) systematic and statistical uncertainties, as well as other relevant details. Interestingly, this indirect indication was confirmed and strengthened by the first (and as yet unique) direct experimental constraints on the χ_{c1} and χ_{c2} polarizations, recently obtained by CMS in an analysis devoted to the study of the decay angular distributions of these two mesons [15].

1.7 The two-dimensional angular distribution

In the previous sections we presented simple "base" cases, where the decaying state is a pure angular momentum eigenstate and the resulting decay distributions depend on $\cos\vartheta$ but not on φ. We will now move to a more general case, leading also to a possible azimuthal anisotropy, using the same notations and definitions as before and limiting the discussion to the parity conserving case, here illustrated with the dilepton decay of a J/ψ meson.

We consider the case of a J/ψ formed as a generic superposition of the three $J = 1$ eigenstates, $J_z = +1, -1, 0$, with respect to the polarization axis z,

$$|\mathrm{J}/\psi\rangle = \sum_{M=0,\pm1} a_M \, |\mathrm{J}/\psi; 1, M\rangle_z \, . \tag{1.8}$$

The dilepton system, eigenstate of $J_{z'}$ with eigenvalue $L' = +1$ or -1 for helicity conservation, is a superposition of eigenstates of J_z, according to the relation (Eq. 1.5 in compact form)

$$|\ell^+\ell^-; 1, L'\rangle_{z'} = \sum_{L=0,\pm1} \mathcal{D}^1_{L\,L'}(\vartheta, \varphi) \, |\ell^+\ell^-; 1, L\rangle_z \, . \tag{1.9}$$

The amplitude $\mathcal{A}_{L'} = {}_{z'}\langle \ell^+\ell^-; 1, L' \,|\, \mathcal{B} \,|\, \mathrm{J}/\psi\rangle_z$ of the process $\mathrm{J}/\psi \to \ell^+\ell^-(L')$ is, therefore,

$$\begin{aligned} \mathcal{A}_{L'} \;&=\; \sum_{M=0,\pm1} a_M \sum_{L=0,\pm1} \mathcal{D}^{1*}_{LL'}(\vartheta, \varphi) \;\; {}_z\langle \ell^+\ell^-; 1, L \,|\, \mathcal{B} \,|\, \mathrm{J}/\psi; 1, M\rangle_z \\ &\propto \sum_{M=0,\pm1} a_M \, \mathcal{D}^{1*}_{ML'}(\vartheta, \varphi) \, , \end{aligned} \tag{1.10}$$

where the transition operator $\mathcal{B}$ has the main effect of imposing angular momentum conservation,

$$ {}_z\langle \ell^+\ell^-; 1, L \,|\, \mathcal{B} \,|\, \mathrm{J}/\psi; 1, M\rangle_z = B\,\delta_{ML} \,, $$

with B independent of M because of rotational invariance.

The transition probability is obtained by squaring Eq. 1.10 and summing over the (unobserved) spin alignments ($L' = \pm 1$) of the dilepton system, with equal weights attributed to the two configurations, to respect parity conservation. Using Eq. 1.2, with

$$ \begin{aligned} d^1_{0,\pm1} &= \pm \sin\vartheta/\sqrt{2} \,, \\ d^1_{\pm1,\pm1} &= (1 + \cos\vartheta)/2 \,, \text{ and} \\ d^1_{\pm1,\mp1} &= (1 - \cos\vartheta)/2 \end{aligned} \tag{1.11} $$

(from Eq. 1.3 or Table 7.3), we obtain the angular distribution

$$ \begin{aligned} W(\cos\vartheta, \varphi) \propto \sum_{L'=\pm1} |\mathcal{A}_{L'}|^2 \;\propto\; \frac{\mathcal{N}}{(3 + \lambda_\vartheta)} \times \\ \Big(1 \;+\; \lambda_\vartheta \,\cos^2\vartheta \;+\; \lambda_\varphi \,\sin^2\vartheta\,\cos 2\varphi \;+\; \lambda_{\vartheta\varphi} \,\sin 2\vartheta\,\cos\varphi \\ + \lambda^\perp_\varphi \,\sin^2\vartheta\,\sin 2\varphi \;+\; \lambda^\perp_{\vartheta\varphi} \,\sin 2\vartheta\,\sin\varphi\Big) \,, \end{aligned} \tag{1.12} $$

with $\mathcal{N} = |a_0|^2 + |a_{+1}|^2 + |a_{-1}|^2$ and

$$ \begin{aligned} \lambda_\vartheta &= \frac{\mathcal{N} - 3|a_0|^2}{\mathcal{N} + |a_0|^2} \,, \\ \lambda_\varphi &= \frac{2\,\mathrm{Re}[a^*_{+1}a_{-1}]}{\mathcal{N} + |a_0|^2} \,, \\ \lambda_{\vartheta\varphi} &= \frac{\sqrt{2}\,\mathrm{Re}[a^*_{+1}a_0 - a^*_0 a_{-1}]}{\mathcal{N} + |a_0|^2} \,, \\ \lambda^\perp_\varphi &= \frac{2\,\mathrm{Im}[a^*_{+1}a_{-1}]}{\mathcal{N} + |a_0|^2} \,, \\ \lambda^\perp_{\vartheta\varphi} &= \frac{\sqrt{2}\,\mathrm{Im}[a^*_{+1}a_0 - a^*_0 a_{-1}]}{\mathcal{N} + |a_0|^2} \,. \end{aligned} \tag{1.13} $$

The resulting angular distribution has, therefore, five λ shape parameters, a number consistent with the three complex amplitudes defining the decay state of Eq. 1.8: three moduli and two of the three complex phases, which can be arbitrarily redefined by applying any common offset. Only two relative phases are physically relevant (for instance, those of a_{+1} and a_{-1} with respect to that of a_0).

The parameters λ_φ, $\lambda_{\vartheta\varphi}$, $\lambda_\varphi^\perp$, and $\lambda_{\vartheta\varphi}^\perp$ describe the azimuthal anisotropy of the distribution. In particular, the two parameters carrying the superscript $\perp$ represent asymmetries with respect to the yz plane (see Fig. 1.4), which is *perpendicular* to the plane (zx) providing the reference to measure φ. As will be further emphasized in Section 1.11 and Chapter 2, in most experiments, where no possibility exists to detect physical asymmetries with respect to the yz plane, these parameters are completely suppressed because of event-by-event smearing and become unobservable. The parameters λ_ϑ, λ_φ, and $\lambda_{\vartheta\varphi}$ are always observable (with suitable experimental definitions of the reference axes) and are the only ones considered in the majority of the measurements.

1.8 Addition rules for the polarization parameters

The expression of the angular distribution derived in the previous section is valid when the decaying particle is always produced, in each event of the observed sample, in the *same* angular momentum state, defined by Eq. 1.8.

More generally, however, the particles composing the sample can result from the superposition of different production processes, corresponding to more or less different physics mechanisms, each one yielding J/ψ mesons in a specific angular momentum state.

In the presence of n contributing production processes, with corresponding weights $f^{(i)}$, the observable distribution is the weighted sum of the normalized "elementary" decay distributions, $W^{(i)}(\cos\vartheta,\varphi)$, corresponding to single subprocesses producing definite angular momentum states $\sum_{M=0,\pm1} a_M^{(i)}\,|1,\,M\rangle_z$,

$$W(\cos\vartheta,\varphi) \;=\; \sum_{i=1}^{n} f^{(i)}\, W^{(i)}(\cos\vartheta,\varphi)\,, \tag{1.14}$$

where

$$\begin{aligned} W^{(i)}(\cos\vartheta,\varphi) \;\propto\; & \frac{\mathcal{N}^{(i)}}{3+\lambda_\vartheta^{(i)}} \Big(1+\lambda_\vartheta^{(i)}\,\cos^2\vartheta \\ & + \lambda_\varphi^{(i)}\,\sin^2\vartheta\,\cos 2\varphi + \lambda_{\vartheta\varphi}^{(i)}\,\sin 2\vartheta\,\cos\varphi \\ & + \lambda_\varphi^{\perp(i)}\,\sin^2\vartheta\,\sin 2\varphi + \lambda_{\vartheta\varphi}^{\perp(i)}\,\sin 2\vartheta\,\sin\varphi\Big) \end{aligned} \tag{1.15}$$

and the expressions of the anisotropy parameters, $\lambda_\vartheta^{(i)}$, $\lambda_\varphi^{(i)}$, $\lambda_{\vartheta\varphi}^{(i)}$, etc., are the same as in Eq. 1.13 with the index (i) added to decay parameters and component amplitudes $a_M^{(i)}$. Expanding Eq. 1.14 and collecting the terms with the same angular dependence, we see that the resulting angular distribution, describing the decay of the considered mixture of particles, formally maintains the same shape as for one

individual process,

$$W(\cos\vartheta,\varphi) \propto \frac{1}{3+\lambda_\vartheta}\Big(1+\lambda_\vartheta\cos^2\vartheta + \lambda_\varphi\sin^2\vartheta\cos 2\varphi + \lambda_{\vartheta\varphi}\sin 2\vartheta\cos\varphi + \lambda_\varphi^\perp\sin^2\vartheta\sin 2\varphi + \lambda_{\vartheta\varphi}^\perp\sin 2\vartheta\sin\varphi\Big), \tag{1.16}$$

but the meaning of the observable parameters is obviously different. Now, each of the five parameters, $X = \lambda_\vartheta$, λ_φ, $\lambda_{\vartheta\varphi}$, $\lambda_\varphi^\perp$, and $\lambda_{\vartheta\varphi}^\perp$, is a weighted average of the corresponding parameters characterizing the single subprocesses, $X^{(i)}$:

$$X = \sum_{i=1}^{n} \frac{f^{(i)}\mathcal{N}^{(i)}}{3+\lambda_\vartheta^{(i)}}\,X^{(i)} \Bigg/ \sum_{i=1}^{n} \frac{f^{(i)}\mathcal{N}^{(i)}}{3+\lambda_\vartheta^{(i)}}\ . \tag{1.17}$$

It should be noted that, in this general "addition rule" for the five anisotropy parameters, the weight always contains the factor $1/(3+\lambda_\vartheta^{(i)})$, which depends on the *polar* anisotropy.

1.9 Alternative determinations of the anisotropy parameters

There are situations where, for several possible reasons, it is not convenient to determine the anisotropy parameters of the angular distribution through a multi-parameter fit of the measured data to Eq. 1.12. In such cases, it might be better to use one of the formulas presented in this section.

To start with, the integration over either φ or $\cos\vartheta$ leads to the one-dimensional angular distributions

$$w(\cos\vartheta) \propto 1 + \lambda_\vartheta\cos^2\vartheta \tag{1.18}$$

and

$$w(\varphi) \propto 1 + \frac{2\lambda_\varphi}{3+\lambda_\vartheta}\cos 2\varphi + \frac{2\lambda_\varphi^\perp}{3+\lambda_\vartheta}\sin 2\varphi\ , \tag{1.19}$$

from which λ_ϑ, λ_φ and $\lambda_\varphi^\perp$ can be determined in two independent steps, possibly improving the stability of the fits in analyses of small event samples. The "diagonal" terms, $\lambda_{\vartheta\varphi}$ and $\lambda_{\vartheta\varphi}^\perp$, vanish in both these integrations. They can be extracted, for example, through the angular variable $\tilde{\varphi}$, defined as

$$\tilde{\varphi} = \begin{cases} \varphi - \frac{3}{4}\pi & \text{for } \cos\vartheta < 0 \\ \varphi - \frac{\pi}{4} & \text{for } \cos\vartheta > 0 \end{cases} \tag{1.20}$$

(adding 2π if $\tilde{\varphi} < -\pi$, when $\tilde{\varphi}$ is defined in the range $[-\pi, \pi]$), by measuring the distribution

$$w(\tilde{\varphi}) \propto 1 + \frac{\sqrt{2}\,\lambda_{\vartheta\varphi}}{3+\lambda_\vartheta} \cos\tilde{\varphi} + \frac{\sqrt{2}\,\lambda^{\perp}_{\vartheta\varphi}}{3+\lambda_\vartheta} \sin\tilde{\varphi}\,. \tag{1.21}$$

The five anisotropy parameters can also be determined from the asymmetries between the event populations of two complementary angular topologies (which are equiprobable in the unpolarized case):

$$\begin{aligned}
\frac{P(|\cos\vartheta| > 1/2) - P(|\cos\vartheta| < 1/2)}{P(|\cos\vartheta| > 1/2) + P(|\cos\vartheta| < 1/2)} &= \frac{3}{4}\,\frac{\lambda_\vartheta}{3+\lambda_\vartheta}\,,\\
\frac{P(\cos 2\varphi > 0) - P(\cos 2\varphi < 0)}{P(\cos 2\varphi > 0) + P(\cos 2\varphi < 0)} &= \frac{2}{\pi}\,\frac{2\lambda_\varphi}{3+\lambda_\vartheta}\,,\\
\frac{P(\sin 2\varphi > 0) - P(\sin 2\varphi < 0)}{P(\sin 2\varphi > 0) + P(\sin 2\varphi < 0)} &= \frac{2}{\pi}\,\frac{2\lambda^{\perp}_{\varphi}}{3+\lambda_\vartheta}\,,\\
\frac{P(\sin 2\vartheta\cos\varphi > 0) - P(\sin 2\vartheta\cos\varphi < 0)}{P(\sin 2\vartheta\cos\varphi > 0) + P(\sin 2\vartheta\cos\varphi < 0)} &= \frac{2}{\pi}\,\frac{2\lambda_{\vartheta\varphi}}{3+\lambda_\vartheta}\,,\\
\frac{P(\sin 2\vartheta\sin\varphi > 0) - P(\sin 2\vartheta\sin\varphi < 0)}{P(\sin 2\vartheta\sin\varphi > 0) + P(\sin 2\vartheta\sin\varphi < 0)} &= \frac{2}{\pi}\,\frac{2\lambda^{\perp}_{\vartheta\varphi}}{3+\lambda_\vartheta}\,.
\end{aligned} \tag{1.22}$$

In analyses applying efficiency corrections to the reconstructed angular spectra, the use of these formulas may require an iterative re-weighing of the Monte Carlo data, in order to compensate for the effect of the non-uniformity of those experimental corrections. In "perfect" experiments, with uniform acceptance and efficiencies over $\cos\vartheta$ and φ (such as in Monte Carlo studies at the generation level), the parameters can be obtained from the average values of the one-dimensional distributions of suitable angular combinations, by inverting the following relations:

$$\begin{aligned}
\langle \cos^2\vartheta \rangle &= \frac{1+\frac{3}{5}\lambda_\vartheta}{3+\lambda_\vartheta}\,,\\
\langle \cos 2\varphi \rangle &= \frac{\lambda_\varphi}{3+\lambda_\vartheta}\,,\\
\langle \sin 2\varphi \rangle &= \frac{\lambda^{\perp}_{\varphi}}{3+\lambda_\vartheta}\,,\\
\langle \sin 2\vartheta\,\cos\varphi \rangle &= \frac{4}{5}\,\frac{\lambda_{\vartheta\varphi}}{3+\lambda_\vartheta}\,,\\
\langle \sin 2\vartheta\,\sin\varphi \rangle &= \frac{4}{5}\,\frac{\lambda^{\perp}_{\vartheta\varphi}}{3+\lambda_\vartheta}\,.
\end{aligned} \tag{1.23}$$

1.10 The "unpolarized" case

An interesting feature of the expressions shown in Eq. 1.13 is that it is impossible to choose the component amplitudes a_M such that all λ parameters in Eq. 1.12 vanish simultaneously. For the following discussion we will adopt the convenient (and always possible) definition where the $M = 0$ component a_0 is real. We can see from Eq. 1.13 that the condition $\lambda_{\vartheta\varphi} = \lambda^{\perp}_{\vartheta\varphi} = 0$ (that is, $a_0(a^*_{+1} - a_{-1}) = 0$) implies that either $a_0 = 0$ or $a^*_{+1} = a_{-1}$. The first case leads to $\lambda_\vartheta = +1$. In the second case, to obtain also $\lambda_\varphi = \lambda^{\perp}_{\varphi} = 0$ ($a^*_{+1}a_{-1} = 0$) we need that both a_{+1} and a_{-1} vanish, in which case $\lambda_\vartheta = -1$.

This means that the angular distribution of the dilepton decay of a $J = 1$ state produced *always in a single* angular momentum state, defined by the three component amplitudes a_M, is never isotropic (that is, spherical). This fact can be formalized with the following theorem [16, 17]:

> **Theorem 1.1.** *For any production mechanism where a $J = 1$ particle is produced as a single, completely generic angular momentum state*
>
> $$|V\rangle = a_{-1}\,|1, -1\rangle + a_0\,|1, 0\rangle + a_{+1}\,|1, +1\rangle\,, \tag{1.24}$$
>
> *there always exists a quantization axis, $z^\star$, along which the $J_z = 0$ component a_0 vanishes.*

For its mathematical verification we continue to use the convention of a real a_0. It can then be checked directly, using the formalism of the Wigner matrices, how the state of Eq. 1.24 changes by the rotation defined by the angles $\varphi^\star$ and $\vartheta^\star$, with

$$\begin{aligned} \cos\vartheta^\star &= \frac{R_+R_- + I_+I_-}{\sqrt{2a_0^2(R_+^2 + I_-^2) + (R_+R_- + I_+I_-)^2}}\,, \\ \cos\varphi^\star &= \frac{R_+}{\sqrt{R_+^2 + I_-^2}}\,, \quad \sin\varphi^\star = -\frac{I_-}{\sqrt{R_+^2 + I_-^2}}\,, \end{aligned} \tag{1.25}$$

where $R_\pm = \mathrm{Re}(a_{+1} \pm a_{-1})$ and $I_\pm = \mathrm{Im}(a_{+1} \pm a_{-1})$. The a_0 component indeed vanishes after this new choice of polarization axis. This means, in particular, according to Eq. 1.13, that with this rotation we obtain $\lambda_\vartheta = +1$, because the state will have only $J_z = \pm 1$ components. In other words, there is always a quantization axis along which the polarization of a vector state is *transverse*. This result is, in fact, a natural consequence of the "vectorial" nature of the particle, and a nice illustration of the correspondence to the classical case: a unit-modulus vector will always have projection ± 1 along some reference axis.

The theorem does not imply that it is physically *impossible* to observe isotropic decay distributions of a vector particle. An *ensemble* of different states suitably mixed together *can* produce a globally isotropic decay distribution. To illustrate

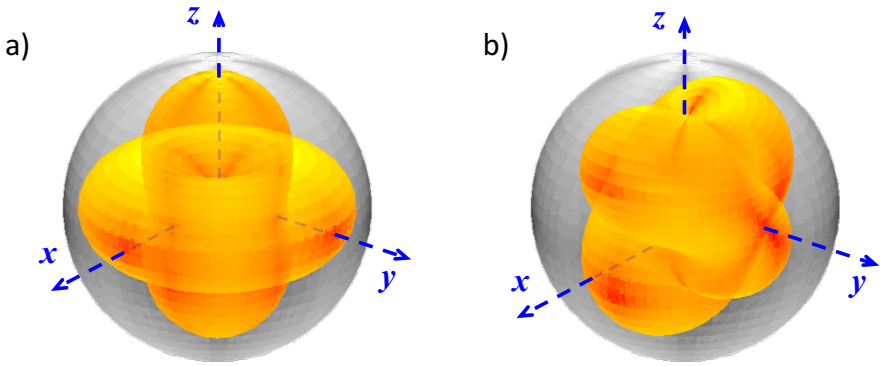

Fig. 1.14 Examples of isotropic angular distributions produced by the dilepton decay of a vector state. Left: Sum of transverse and longitudinal cases, in 2-to-1 proportions. Right: Sum of the distributions, proportional to $1 \pm \frac{1}{2} \sin 2\vartheta \cos\varphi$, produced by the states $|\mathrm{J}/\psi\rangle = \sqrt{2/3}\,|1, +1\rangle_z + \sqrt{1/3}\,|1, 0\rangle_z$ and $|\mathrm{J}/\psi\rangle = \sqrt{2/3}\,|1, -1\rangle_z + \sqrt{1/3}\,|1, 0\rangle_z$. In both mixtures, the $J_z = +1, -1$ and 0 projections are equally probable.

this observation, we will now consider a few examples of angular distributions resulting from the superposition of different production processes, each one yielding J/ψ mesons in a specific angular momentum state.

Using the addition rules introduced in the previous section, we can realize that a simple way to obtain an isotropic decay distribution is to consider a mixture of pure "longitudinal" and "transverse" eigenstates, $|\mathrm{J}/\psi\rangle = |1, 0\rangle_z$, $|1, +1\rangle_z$, and $|1, -1\rangle_z$, the first one giving $W(\cos\vartheta, \varphi) \propto 1 - \cos^2\vartheta$, i.e. $\lambda_\vartheta = -1$, and the other two giving $W(\cos\vartheta, \varphi) \propto 1 + \cos^2\vartheta$, i.e. $\lambda_\vartheta = +1$, with all other parameters being zero.

The "democratic" choice of taking an equal mixture of these three states gives the desired result. This corresponds to having two λ_ϑ parameters, $\lambda_\vartheta^{(1)} = -1$ with weight $f^{(1)} = 1/3$ and $\lambda_\vartheta^{(2)} = +1$ with weight $f^{(2)} = 2/3$, to be summed using the rule of Eq. 1.17, here rewritten in the $n = 2$ case:

$$\lambda_\vartheta = \left(\frac{f^{(1)}\lambda_\vartheta^{(1)}}{3 + \lambda_\vartheta^{(1)}} + \frac{f^{(2)}\lambda_\vartheta^{(2)}}{3 + \lambda_\vartheta^{(2)}} \right) \Bigg/ \left(\frac{f^{(1)}}{3 + \lambda_\vartheta^{(1)}} + \frac{f^{(2)}}{3 + \lambda_\vartheta^{(2)}} \right). \tag{1.26}$$

The result is that λ_ϑ vanishes, as do all the other parameters. This condition is referred to as "unpolarized" production: the particle is a superposition of the three pure polarization states with equal probabilities and, consequently, the decay distribution is isotropic, as illustrated in Fig. 1.14-left.

However, this is not the only possible choice that gives an isotropic decay distribution. For example, the two states $|\mathrm{J}/\psi\rangle = \sqrt{2/3}\ |1, +1\rangle_z + \sqrt{1/3}\ |1, 0\rangle_z$ and $|\mathrm{J}/\psi\rangle = \sqrt{2/3}\ |1, -1\rangle_z + \sqrt{1/3}\ |1, 0\rangle_z$ yield, respectively, angular distributions proportional to $1 + 1/2 \sin 2\vartheta \cos\varphi$ and $1 - 1/2 \sin 2\vartheta \cos\varphi$ (that is, $\lambda_{\vartheta\varphi} = +1$ and -1, all other parameters being zero), and the superposition of two such distributions is isotropic, as shown in Fig. 1.14-right. Note that, in the ensemble of the two

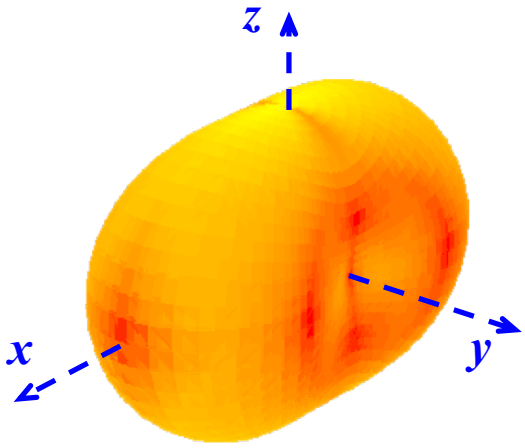

Fig. 1.15 Anisotropic shape of the decay distribution proportional to $1 + 1/2\ \sin^2\vartheta\ \cos 2\varphi$, produced by the state $|\mathrm{J}/\psi\rangle = \sqrt{1/3}\,|1,\,+1\rangle_z + \sqrt{1/3}\,|1,\,-1\rangle_z + \sqrt{1/3}\,|1,\,0\rangle_z$.

states, the components $J_z = +1, -1$, and 0 have identical total probabilities. Experimentally, it is generally not possible to distinguish between these two examples of resulting isotropic distribution, and both are equally considered to represent "unpolarized" production.

It is interesting to see that a state definition as "democratic" as the one of the first example above, but this time concerning the components of a *single* angular momentum state, does not produce an isotropic distribution. Indeed, according to Eq. 1.13, the state $|\mathrm{J}/\psi\rangle = \sqrt{1/3}\,|1,\,+1\rangle_z + \sqrt{1/3}\,|1,\,-1\rangle_z + \sqrt{1/3}\,|1,\,0\rangle_z$, with identical probabilities (squared amplitudes) for the three J_z components, produces a very anisotropic distribution, shown in Fig. 1.15, with all parameters vanishing except for $\lambda_\varphi = 1/2$. We certainly need the superposition of at least two different angular momentum configurations, produced together, in order to obtain an "unpolarized particle". The example just considered shows that the very definition of the concept of "unpolarized particle" is not straightforward, if we try to give it in terms of the angular momentum configuration of the decaying particle. In practice, the most reasonable and intuitive definition is the one based on the condition that the resulting angular distribution is isotropic.

We can conclude that the dilepton decay distribution produced by a vector particle is intrinsically *anisotropic*. Even if it is possible that a superposition of different production processes leads to a cancellation of all decay parameters, as in the examples shown above, this is, in general, a non-trivial physical scenario. Unpolarized production is, therefore, a very peculiar physics case.

On the other hand, it can also happen that an intrinsically polarized production process is *observed* as exactly unpolarized, because of a peculiar choice of the polarization frame. When the latter is defined in a way that is completely decorrelated from the "natural" polarization direction (or from the direction of the $z^\star$ axis of

the above theorem), a randomization effect is created, making all observable shape parameters vanish.

We will see in Chapter 6 that the measurement of (seemingly) unpolarized production becomes possible in certain kinds of experimental analyses, where some degrees of freedom of the decay process are integrated over (for example, in cascade decays with unobserved intermediate states).

It is also important to remark that, strictly speaking, the statement "the decay distribution of an individual $J = 1$ particle configuration is alway anisotriopic" should be considered in the context of the dilepton decay case. More generally, a necessary condition for the observability of the polarization state of the decaying particle it that the final state, system of the two decay products, is "polarized". That is the case of the dilepton decays, where helicity conservation effectively means that the dilepton system has $J_{z'} = \pm 1$.

As will be discussed in detail in Chapter 7, most cases of physical interest are indeed represented by decays to "polarized" final states (i.e. non-democratic superpositions of spin orientations) and it is thanks to this condition that the polarization of the mother particle is fully reflected in an anisotropy of the decay angular distribution. Indeed, we will see that the specific relation between the anisotropy parameters and the polarization of the mother particle is completely different for different decay channels.

1.11 Parity-violating decay distribution

In the most general case, the decay of a vector particle into a fermion-antifermion pair contains parity-violating terms. Its derivation is very similar to the one of the parity-conserving case, seen in Section 1.7. The only modification consists in keeping track of the *sign* of L' (which can be either $+1$ or -1) in Eq. 1.10: the amplitudes a_M are now replaced with L'-dependent ones, $a_{M,L'}$, describing the angular momentum configuration of the decaying state (having J_z eigenvalue equal to M) *and* of the two-fermion system (with $J_{z'}$ eigenvalue L').

Beginning with the case of a single production "subprocess", denoted by the index (i), the decay angular distribution is, then,

$$\begin{aligned} W^{(i)}(\cos\vartheta,\varphi) \propto \frac{\mathcal{N}^{(i)}}{(3+\lambda_\vartheta^{(i)})}\,(1+\lambda_\vartheta^{(i)}\cos^2\vartheta + \\ +\lambda_\varphi^{(i)}\sin^2\vartheta\cos 2\varphi + \lambda_{\vartheta\varphi}^{(i)}\sin 2\vartheta\cos\varphi \\ +\lambda_\varphi^{\perp(i)}\sin^2\vartheta\sin 2\varphi + \lambda_{\vartheta\varphi}^{\perp(i)}\sin 2\vartheta\sin\varphi \\ +2A_\vartheta^{(i)}\cos\vartheta + 2A_\varphi^{(i)}\sin\vartheta\cos\varphi + 2A_\varphi^{\perp(i)}\sin\vartheta\sin\varphi)\,, \end{aligned} \tag{1.27}$$

with

$$
\begin{aligned}
\lambda_{\vartheta}^{(i)} &= 1/D^{(i)} \times [\mathcal{N}^{(i)} - 3(|a_{0,+1}^{(i)}|^2 + |a_{0,-1}^{(i)}|^2)]\,, \\
\lambda_{\varphi}^{(i)} &= 2/D^{(i)} \times \mathrm{Re}[a_{+1,+1}^{(i)*} a_{-1,+1}^{(i)} + a_{+1,-1}^{(i)*} a_{-1,-1}^{(i)}]\,, \\
\lambda_{\varphi}^{\perp(i)} &= 2/D^{(i)} \times \mathrm{Im}[a_{+1,+1}^{(i)*} a_{-1,+1}^{(i)} + a_{+1,-1}^{(i)*} a_{-1,-1}^{(i)}]\,, \\
\lambda_{\vartheta\varphi}^{(i)} &= \sqrt{2}/D^{(i)} \times \mathrm{Re}[a_{+1,+1}^{(i)*} a_{0,+1}^{(i)} + a_{+1,-1}^{(i)*} a_{0,-1}^{(i)} - a_{0,+1}^{(i)*} a_{-1,+1}^{(i)} - a_{0,-1}^{(i)*} a_{-1,-1}^{(i)}]\,, \\
\lambda_{\vartheta\varphi}^{\perp(i)} &= \sqrt{2}/D^{(i)} \times \mathrm{Im}[a_{+1,+1}^{(i)*} a_{0,+1}^{(i)} + a_{+1,-1}^{(i)*} a_{0,-1}^{(i)} - a_{0,+1}^{(i)*} a_{-1,+1}^{(i)} - a_{0,-1}^{(i)*} a_{-1,-1}^{(i)}]\,, \\
A_{\vartheta}^{(i)} &= 1/D^{(i)} \times [|a_{+1,+1}^{(i)}|^2 + |a_{-1,-1}^{(i)}|^2 - |a_{+1,-1}^{(i)}|^2 - |a_{-1,+1}^{(i)}|^2]\,, \\
A_{\varphi}^{(i)} &= \sqrt{2}/D^{(i)} \times \mathrm{Re}[a_{+1,+1}^{(i)*} a_{0,+1}^{(i)} - a_{+1,-1}^{(i)*} a_{0,-1}^{(i)} + a_{0,+1}^{(i)*} a_{-1,+1}^{(i)} - a_{0,-1}^{(i)*} a_{-1,-1}^{(i)}]\,, \\
A_{\varphi}^{\perp(i)} &= \sqrt{2}/D^{(i)} \times \mathrm{Im}[a_{+1,+1}^{(i)*} a_{0,+1}^{(i)} - a_{+1,-1}^{(i)*} a_{0,-1}^{(i)} + a_{0,+1}^{(i)*} a_{-1,+1}^{(i)} - a_{0,-1}^{(i)*} a_{-1,-1}^{(i)}]\,,
\end{aligned}
\tag{1.28}
$$

where $\mathcal{N}^{(i)} = \sum_{M,L'} |a_{M,L'}^{(i)}|^2$ and $D^{(i)} = \mathcal{N}^{(i)} + |a_{0,+1}^{(i)}|^2 + |a_{0,-1}^{(i)}|^2$.

Parity-violating effects are parametrized by the coefficients $A_{\vartheta}^{(i)}$, $A_{\varphi}^{(i)}$, and $A_{\varphi}^{\perp(i)}$ now appearing in the expression when $a_{M,+1}^{(i)} \neq a_{M,-1}^{(i)}$. These parameters vanish when the produced state has a pure $J_z = 0$ angular momentum projection along the chosen axis (that is, all coefficients $a_{\pm 1,L'}^{(i)}$ are zero), as expected from the description made in Section 1.3, where we saw that the shape of the decay distribution is in that case a perfectly symmetric "donut", invariant by reflection about any of the principal planes (Fig. 1.6). This symmetry is lost (Fig. 1.7-c) only when at least one of the $J_z = +1$ or $J_z = -1$ components is nonzero and they are different from one another.

In the presence of n contributing production processes with weights $f^{(i)}$, the resulting observable distribution has a general expression formally analogous to Eq. 1.27:

$$
\begin{aligned}
W(\cos\vartheta, \varphi) \propto\ & \frac{1}{(3 + \lambda_{\vartheta})} (1 + \lambda_{\vartheta} \cos^2\vartheta \\
& + \lambda_{\varphi} \sin^2\vartheta \cos 2\varphi + \lambda_{\vartheta\varphi} \sin 2\vartheta \cos\varphi \\
& + \lambda_{\varphi}^{\perp} \sin^2\vartheta \sin 2\varphi + \lambda_{\vartheta\varphi}^{\perp} \sin 2\vartheta \sin\varphi \\
& + 2A_{\vartheta} \cos\vartheta + 2A_{\varphi} \sin\vartheta \cos\varphi + 2A_{\varphi}^{\perp} \sin\vartheta \sin\varphi)\,.
\end{aligned}
\tag{1.29}
$$

The observable coefficients, $X = \lambda_{\vartheta}$, λ_{φ}, $\lambda_{\vartheta\varphi}$, $\lambda_{\varphi}^{\perp}$, $\lambda_{\vartheta\varphi}^{\perp}$, A_{ϑ}, A_{φ}, and $A_{\varphi}^{\perp}$ are weighted averages of the corresponding single-subprocess parameters, $X^{(i)}$, calculated according to the rule of Eq. 1.17.

In inclusive production studies, where the decaying particle is the only observed object (together with its decay products), the zx (production) plane, containing the directions of the colliding hadrons as seen in the particle's rest frame, represents a symmetry plane for the angular distribution if parity-violating effects are absent: the observed *event distribution* must be symmetric by reflection with respect to it. Therefore, not only the coefficients A_{ϑ}, A_{φ}, and $A_{\varphi}^{\perp}$, but also $\lambda_{\varphi}^{\perp}$ and $\lambda_{\vartheta\varphi}^{\perp}$, multiplying terms that are asymmetric by the reflection transformation $\varphi \to \varphi + \pi$, are unobservable, because they vanish on average.

In these considerations we are, actually, excluding an entire category of experimental studies, performed using collisions involving polarized beams and/or targets. When, for example, the target contains polarized nucleons, their preferred spin direction effectively defines an *additional* plane, besides the production plane, providing a reference for physically meaningful azimuthal anisotropies. With two distinct physical reference planes, angular distribution terms proportional to $\sin^2\vartheta \sin 2\varphi$ and $\sin 2\vartheta \sin\varphi$ become observable and possibly significant, even in fully parity-conserving processes.

These anisotropies, corresponding to those here parametrized by $\lambda_\varphi^\perp$ and $\lambda_{\vartheta\varphi}^\perp$, are the main focus of vector boson and Drell–Yan measurements in polarized collisions [18, 19], which address several aspects of perturbative and nonperturbative QCD, including the measurement of p_T dependent parton distribution functions [20, 21]. In most of the examples and discussions presented in this book we will, however, neglect the possible existence of such effects and assume that $\lambda_\varphi^\perp = \lambda_{\vartheta\varphi}^\perp = 0$, implicitly referring to cases where the decaying particle is produced in unpolarized collisions.

In the more general case when parity is not conserved, as in the $\mathrm{Z}/\gamma^* \to \ell\ell$ and $\mathrm{W} \to \ell\nu$ decays, event-by-event topological asymmetries with respect to the experimental production plane can result in nonzero values of the observed $\lambda_\varphi^\perp$ and $\lambda_{\vartheta\varphi}^\perp$, even if these coefficients, as well as $A_\varphi^\perp$, are expected to remain negligible because of the kinematic averaging. This should be true at least at midrapidity, where the measurement is completely insensitive to the direction of the valence quark in quark-antiquark and quark-gluon scattering, the only direction that may provide a possible reference for an asymmetry with respect to the production plane.

In summary, in inclusive measurements the observable di-fermion distribution is described, in first approximation, by five coefficients: the three "spin-alignment" parameters λ_ϑ, λ_φ and $\lambda_{\vartheta\varphi}$, containing information about the average angular momentum composition of the decaying particle, and the two "parity-asymmetry" parameters A_ϑ and A_φ, expressing the parity properties of the decay. The remaining three parameters represent second-order corrections.

It can be experimentally convenient, when the detector itself does not induce "parity-violating" acceptance effects on the distributions of the decay fermions, to measure the following simple asymmetries between integrated event yields, related to A_ϑ, A_φ, and $A_\varphi^\perp$:

$$\begin{aligned}
\mathcal{A}_{\cos\vartheta} &= \frac{N(\cos\vartheta > 0) - N(\cos\vartheta < 0)}{N(\cos\vartheta > 0) + N(\cos\vartheta < 0)} = \frac{3\,A_\vartheta}{3 + \lambda_\vartheta}\,, \\
\mathcal{A}_{\cos\varphi} &= \frac{N(\cos\varphi > 0) - N(\cos\varphi < 0)}{N(\cos\varphi > 0) + N(\cos\varphi < 0)} = \frac{3\,A_\varphi}{3 + \lambda_\vartheta}\,, \\
\mathcal{A}_{\sin\varphi} &= \frac{N(\sin\varphi > 0) - N(\sin\varphi < 0)}{N(\sin\varphi > 0) + N(\sin\varphi < 0)} = \frac{3\,A_\varphi^\perp}{3 + \lambda_\vartheta}\,.
\end{aligned} \tag{1.30}$$

These quantities are physically constrained between $-3/4$ and $3/4$. They cannot reach the extreme values -1 or $+1$ because the distribution of, for example, $\cos\vartheta$ can never be fully restricted to one of the two hemispheres, $\cos\vartheta < 0$ or $\cos\vartheta > 0$. In fact, the function $1+\cos^2\vartheta \pm 2\cos\vartheta$, polar projection of W when parity violation is maximum, remains nonzero for all $\cos\vartheta$ values between -1 and $+1$; even if it is peaked at ± 1, its "tail" reaches ∓ 1.

The observable $\mathcal{A}_{\cos\vartheta}$ is the so-called forward-backward asymmetry, $\mathcal{A}_{\rm FB}$, studied, for example, in experimental analyses of direct Z/γ^* and W production. It is worth emphasizing that the parameters λ_ϑ, A_ϑ, etc., need to be determined from the analysis of the angular distributions, measured with a sufficiently large number of bins (the minimum number of bins being four in the case of the $\cos\vartheta$ distribution and two if we resort to the $|\cos\vartheta|$ distribution). Ideally, also the forward-backward asymmetry, $\mathcal{A}_{\rm FB}$, should be extracted from a differential $\cos\vartheta$ pattern, just as it is done for A_ϑ (Eq. 1.30): $\mathcal{A}_{\rm FB} = 3A_\vartheta / (3+\lambda_\vartheta)$.

Instead, evaluating $\mathcal{A}_{\rm FB}$ as the asymmetry in the event yields among only two $\cos\vartheta$ bins ($\cos\vartheta > 0$ and $\cos\vartheta < 0$) is equivalent to fitting the $\cos\vartheta$ distribution between -1 and $+1$ using only two bins, each of them of width unity: the polar anisotropy λ_ϑ remains undetermined. This simplification can lead to biased results, depending on necessary hypotheses regarding the distributions of the variables that have been integrated out. This potentially risky procedure should be complemented by a series of careful systematic studies, as in all cases where a detailed differential measurement is replaced by the simpler determination of integrated distributions or quantities. Possible pitfalls of simplified analysis approaches integrating out relevant degrees of freedom are discussed in Section 2.13.

1.12 Recapitulation

By measuring the shape of the dilepton decay distribution of a vector particle we can determine the angular momentum state (J_z projection) in which it was produced, that is, its polarization.

The measurement is performed by collecting many dilepton events and building the statistical distribution of the spherical coordinates $\cos\vartheta$ and φ of the lepton direction in the particle's rest frame. The several possible choices of reference defining the coordinate system will be discussed in detail in the next chapter.

The relation between angular distribution and state of polarization simply descends from angular momentum conservation and, in the case of the dilepton decay, helicity conservation, according to which the dilepton system has $J_{z'} = \pm 1$ (never 0) along the common lepton-antilepton direction in the rest frame of the decaying particle (Fig. 1.3).

The two simplest cases of polarization are the so called "transverse" ($J_z = \pm 1$) and "longitudinal" ones, characterized by distributions of the kind $1+\cos^2\vartheta$ and $1-\cos^2\vartheta$ with respect to the chosen quantization axis, when parity-violating effects are absent (Figs. 1.6 and 1.7).

More generally, when the decaying particle is a superposition of different J_z eigenstates (or, as will be seen in the next chapter, when the polarization is naturally transverse or longitudinal along an axis different from the one adopted for the measurement), the angular distribution can assume a continuous variety of shapes (Eq. 1.16), with one term describing the polar-angle dependence, $1+\lambda_\vartheta \cos^2\vartheta$ (with $-1 < \lambda_\vartheta < +1$), and additional terms representing azimuthal anisotropies (that vanish by integration over the azimuthal angle φ).

The number of observable azimuthal parameters depends on the geometrical symmetry of the experiment: they are two, λ_φ and $\lambda_{\vartheta\varphi}$, when there is no other symmetry plane than the production plane, and can become four, including also $\lambda_\varphi^\perp$ and $\lambda_{\vartheta\varphi}^\perp$, when further external physical references exist, as in collisions between polarized hadrons or in indirect production via cascade decays.

In the presence of parity-violating effects, the maximum number of shape parameters becomes eight, adding to the count the asymmetries A_ϑ, A_φ, and $A_\varphi^\perp$ (Eq. 1.29).

Different production mechanisms can coexist, each leading to a different angular momentum configuration of the observed decaying particle. A non-linear sum rule (Eq. 1.17) gives the resulting overall anisotropy parameters as a function of those of the individual processes.

The superposition of at least two different angular momentum configurations (Fig. 1.14) is necessary to explain the hypothetical case of a completely isotropic decay distribution, where all eight parameters vanish ("unpolarized case"). Vector states are, in fact, always intrinsically polarized (Theorem 1.1), as also suggested by the analogy with the classical case of the angular momentum vector, which has always nonzero projection along some axis (provided that its modulus is not zero). With respect to the hypothesis of a superposition of processes conspiring to exactly cancel the anisotropy effects, a more natural way of explaining the observation of a fully isotropic distribution is through smearing or randomization phenomena, due to limitations or peculiarities of the observation process rather than to intrinsic properties of the production mechanism, as will be discussed in Chapter 6.

In the data analyses it is necessary to take into account the sculpting effects created by the minimum-momentum requirements imposed by experimental constraints (Figs. 1.8 and 1.9), including the detection acceptance and efficiency limitations (caused by the magnetic field, material budget, angular coverage, trigger and data-acquisition bandwidth, etc.), as well as by the "offline" analysis selection criteria applied to the decay leptons, aimed, for instance, at improving the signal purity by rejecting background events.

These spurious modulations must be reproduced with accurate simulations and corrected for. The shape of the resulting angular distribution is extremely sensitive to even small biases in the description of the detection efficiency, especially if the applied lepton momentum thresholds are of the same order or larger than the mass of the decaying particle. Seemingly small inaccuracies, which would produce an almost unnoticeable change in the measurement of an integrated particle yield (production cross section) can have a large effect on the measured angular distribution, to the point that wrong physical conclusions might be derived from the measurement, regarding the particle's polarization: a transversely polarized particle could be seen

as longitudinal, or vice versa, and unphysical results could be obtained (Figs. 1.10–1.12).

Lepton acceptance limitations are also responsible for a strong dependence of the cross section measurements on the polarization assumed in the generation of the simulated event samples used to evaluate their correction (Eq. 1.7). If the polarization is not known or well measured, the arbitrary assumption of a given polarization scenario (for example, the unpolarized one that is often chosen to report results) does not lead, in general, to a correct physical result and may even create apparent experimental inconsistencies between measurements adopting the same (wrong) hypothesis (Fig. 1.13).

Difficulties often faced by the experimental analyses, and non-trivial pitfalls to be avoided, will continue to be mentioned throughout the remainder of the book.

References

[1] S. D. Drell and T.-M. Yan, "Massive lepton pair production in hadron-hadron collisions at high-energies", *Phys. Rev. Lett.* **25** (1970) 316, doi:10.1103/PhysRevLett.25.316. [Erratum: *Phys. Rev. Lett.* **25** (1970) 902].

[2] J. C. Collins, D. E. Soper, and G. F. Sterman, "Factorization for short distance hadron-hadron scattering", *Nucl. Phys. B* **261** (1985) 104, doi:10.1016/0550-3213(85)90565-6.

[3] G. T. Bodwin, "Factorization of the Drell–Yan cross-section in perturbation theory", *Phys. Rev. D* **31** (1985) 2616, doi:10.1103/PhysRevD.34.3932. [Erratum: *Phys. Rev. D* **34** (1986) 3932].

[4] J. C. Collins, D. E. Soper, and G. F. Sterman, "Factorization of hard processes in QCD", *Adv. Ser. Direct. High Energy Phys.* **5** (1989) 1, doi:10.1142/9789814503266_0001, arXiv:hep-ph/0409313.

[5] ATLAS Collaboration, "Observation of a new particle in the search for the Standard Model Higgs boson with the ATLAS detector at the LHC", *Phys. Lett. B* **716** (2012) 1, doi:10.1016/j.physletb.2012.08.020, arXiv:1207.7214.

[6] CMS Collaboration, "Observation of a new boson at a mass of 125 GeV with the CMS experiment at the LHC", *Phys. Lett. B* **716** (2012) 30, doi:10.1016/j.physletb.2012.08.021, arXiv:1207.7235.

[7] CMS Collaboration, "Performance of CMS muon reconstruction in pp collision events at $\sqrt{s}$ = 7 TeV", *JINST* **7** (2012) P10002, doi:10.1088/1748-0221/7/10/P10002, arXiv:1206.4071.

[8] CMS Collaboration, "Performance of the CMS muon detector and muon reconstruction with proton-proton collisions at $\sqrt{s}$ = 13 TeV", *JINST* **13** (2018) P06015, doi:10.1088/1748-0221/13/06/P06015, arXiv:1804.04528.

[9] E. P. Wigner, "Group theory and its application to the quantum mechanics of atomic spectra". Pure and applied physics. Academic Press, New York, USA, 1959. ISBN 0127505504.

[10] D. M. Brink and G. R. Satchler, "Angular momentum". Oxford science publications. Clarendon Press, third edition, 1993. ISBN 0198517599.

[11] ATLAS Collaboration, "Measurement of χ_{c1} and χ_{c2} production with $\sqrt{s}$ = 7 TeV pp collisions at ATLAS", *JHEP* **07** (2014) 154, doi:10.1007/JHEP07(2014)154, arXiv:1404.7035.

[12] CMS Collaboration, "Measurement of the relative prompt production rate of χ_{c2} and χ_{c1} in pp collisions at $\sqrt{s}$ = 7 TeV", *Eur. Phys. J. C* **72** (2012) 2251, doi:10.1140/epjc/s10052-012-2251-3, arXiv:1210.0875.

[13] LHCb Collaboration, "Measurement of the cross-section ratio $\sigma(\chi_{c2}) / \sigma(\chi_{c1})$ for prompt χ_c production at $\sqrt{s}$ = 7 TeV", *Phys. Lett. B* **714** (2012) 215, doi:10.1016/j.physletb.2012.06.077, arXiv:1202.1080.

[14] LHCb Collaboration, "Measurement of the relative rate of prompt χ_{c0}, χ_{c1} and χ_{c2} production at $\sqrt{s} = 7$ TeV", *JHEP* **10** (2013) 115, doi:10.1007/JHEP10(2013)115, arXiv:1307.4285.

[15] CMS Collaboration, "Constraints on the χ_{c1} versus χ_{c2} polarizations in proton-proton collisions at $\sqrt{s} = 8$ TeV", *Phys. Rev. Lett.* **124** (2020) 162002, doi:10.1103/PhysRevLett.124.162002, arXiv:1912.07706.

[16] P. Faccioli, C. Lourenço, and J. Seixas, "Rotation-invariant relations in vector meson decays into fermion pairs", *Phys. Rev. Lett.* **105** (2010) 061601, doi:10.1103/PhysRevLett.105.061601, arXiv:1005.2601.

[17] P. Faccioli, C. Lourenço, J. Seixas, and H. K. Wöhri, "Model-independent constraints on the shape parameters of dilepton angular distributions", *Phys. Rev. D* **83** (2011) 056008, doi:10.1103/PhysRevD.83.056008, arXiv:1102.3946.

[18] STAR Collaboration, "Measurement of the transverse single-spin asymmetry in $p^{\uparrow} + p \to W^{\pm}/Z^0$ at RHIC", *Phys. Rev. Lett.* **116** (2016) 132301, doi:10.1103/PhysRevLett.116.132301, arXiv:1511.06003.

[19] COMPASS Collaboration, "First measurement of transverse-spin-dependent azimuthal asymmetries in the Drell–Yan process", *Phys. Rev. Lett.* **119** (2017) 112002, doi:10.1103/PhysRevLett.119.112002, arXiv:1704.00488.

[20] S. Arnold, A. Metz, and M. Schlegel, "Dilepton production from polarized hadron hadron collisions", *Phys. Rev. D* **79** (2009) 034005, doi:10.1103/PhysRevD.79.034005, arXiv:0809.2262.

[21] S. Mert Aybat and T. C. Rogers, "TMD parton distribution and fragmentation functions with QCD evolution", *Phys. Rev. D* **83** (2011) 114042, doi:10.1103/PhysRevD.83.114042, arXiv:1101.5057.

Chapter 2
Reference frames and transformations

In the previous chapter, the particle's polarization state and the resulting shape of the decay distribution were referred to an abstract set of axes, without specifying their relations to physical directions. We will now discuss the possible physical choices of reference frames in a real experiment. In particular, we review different options for defining the polarization axis z, reflecting the topologies of different kinds of production mechanisms. We also call attention to the convention on the orientation of the y axis and its often neglected consequences on the observable value of $\lambda_{\vartheta\varphi}$. We then explain how the observed anisotropy parameters of the decay distribution of a vector particle depend on the choice of the polarization frame, as well as, in general, on the particle's laboratory momentum.

With several examples, including simulated experiments reproducing the conditions of real measurements, we will address the following questions.

- What are the disadvantages of a simple measurement only determining the polar anisotropy and integrating out the azimuthal dimension? In what ways can the possibility of physically interpreting the results be limited by this shortcut? Are there also consequences on the very reliability of the analysis results?
- If it is true that the choice of the reference frame is arbitrary, does this mean that it can be done blindly, because, irrespectively of it, the result will provide the same immediate physical indications?
- Moreover, are all reference frames completely equivalent from the point of view of the acceptance and efficiency sculpting effects mentioned in the previous chapter, or can there be a frame offering advantages for the analysis?

The chapter ends reporting frame transformation relations that are more general than the ones between experimentally relevant polarization frames, to be used in later chapters.

P. Faccioli and C. Lourenço, *Particle Polarization in High Energy Physics*,
Lecture Notes in Physics 1002,
https://doi.org/10.1007/978-3-031-08876-6_2

2.1 The choice of the reference frame

In the two-body decay of a vector particle, the shape of the angular distribution of the back-to-back decay products directly reflects the particle polarization, as seen in the previous chapter. The measurement of the shape parameters λ_ϑ, λ_φ, $\lambda_{\vartheta\varphi}$, etc., of the distribution (Eq. 1.16) requires the choice of a coordinate system in the particle rest frame, with respect to which the momentum of one of the two decay products is expressed in spherical coordinates (Fig. 1.4). While the choice is arbitrary, it can have a strong influence on the numerical results of the measurement and, therefore, on their interpretation.

The observation frame is built using physical reference directions, as seen in the particle rest frame. The variety of the usable directions depends on the experiment and on the process under consideration. In this chapter we will consider the case of an experiment measuring the "inclusive" production of a vector particle V, that is, processes of the kind $\mathrm{h_1h_2} \to V + X$, where $\mathrm{h_1h_2}$ is the collision system and X represents whatever ensemble of particles is produced together with V. The particles X are ignored in the analysis and no distinction is made between processes producing V directly in the collision and those where V is actually coming from the decay of another particle. This is, for example, the case of most measurements of quarkonium, Drell–Yan and Z boson production in proton-(anti)proton, proton-nucleus, pion-nucleus, and nucleus-nucleus collisions, based on data collected in fixed-target or collider experiments conducted at, for example, Fermilab and CERN. Specific frame definitions are needed for more detailed process descriptions, such as, for instance, when explicitly considering cascade decay sequences, a topic we will address in Chapter 6.

In inclusive production measurements using events from unpolarized hadron collisions (i.e. not involving polarized beams nor polarized targets), the only reasonable physical reference directions are those provided by the momenta of the two colliding beams (or of beam and target) as seen from the V rest frame. These are two distinct directions (if V is produced with a non-negligible transverse momentum) and form the "production plane", which imposes itself as *the* reference plane of Fig. 1.4. The y axis is then fixed in the direction perpendicular to this plane, with a certain convention for its orientation (more details in Section 2.6). The polarization axis z can be any axis belonging to the production plane, its unit vector being a linear combination of the unit vectors of the $\mathrm{h_1}$ and $\mathrm{h_2}$ momenta. Finally, the x axis completes the Cartesian system in a right-handed way.

Before discussing possible definitions of z, we note that in the observation of inclusive parity-conserving processes in symmetric (and unpolarized) collisions (such as J/ψ production in pp collisions at the LHC), choosing a reference frame based on observed physical directions effectively *changes* the shape of the most general decay distribution, simplifying its mathematical expression with respect to the one derived in the previous chapter. The last two terms in Eq. 1.16, containing the factors $\sin\varphi$ and $\sin 2\varphi$, change sign by reflection across the production plane ($\varphi \to -\varphi$, with ϑ unchanged) and therefore introduce an observable asymmetry. While not violating parity invariance (both terms remain unchanged in the transformation $\varphi \to \pi + \varphi$ and

$\cos\vartheta \rightarrow -\cos\vartheta$) and being a possible property of individual categories of events and subprocesses, this asymmetry with respect to the production plane cannot survive the sum over all events.

In (unpolarized) proton-proton collisions, the symmetry by reflection across the production plane must be a property of the observed *global event distribution*. In fact, an excess of events on one side of the production plane with respect to the other would have no physical justification, because it would not be possible to reverse the effect by reversing the point of view, i.e. by exchanging the two beams, given that they are identical. In summary, the terms in $\sin^2\vartheta \sin 2\varphi$ and $\sin 2\vartheta \sin\varphi$ are on average unobservable and the most general distribution is simply of the form

$$W(\cos\vartheta,\varphi) = \frac{1}{4\pi}\,\frac{3}{3+\lambda_\vartheta} \times \left(1 + \lambda_\vartheta \cos^2\vartheta + \lambda_\varphi \sin^2\vartheta\cos 2\varphi + \lambda_{\vartheta\varphi} \sin 2\vartheta\cos\varphi\right), \tag{2.1}$$

where, to define an absolute scale of W for later use in graphical representations, we have now included the normalization factor, defined by

$$\int_{-\pi}^{+\pi}\int_{-1}^{+1} W(\cos\vartheta,\varphi)\,\mathrm{d}\cos\vartheta\,\mathrm{d}\varphi = 1\,. \tag{2.2}$$

As we mentioned in Section 1.11, measurements involving polarized beams or targets can lead to nonzero values of the shape parameters $\lambda_\varphi^\perp$ and $\lambda_{\vartheta\varphi}^\perp$ (Eq. 1.16). But even in unpolarized collisions there are specific kinematic conditions, in the presence of parity-violating processes, where such azimuthal anisotropies can also be observed.

For example, when the observed particle flies away from the collision point with a high longitudinal momentum (p_L) in the laboratory, the partons coming from the two beams have on average rather different longitudinal momenta. If the two colliding partons are different, a quark and an antiquark, say, it becomes possible to distinguish them, on a statistical basis, given the different longitudinal momentum distributions characterizing, for example, valence and sea quarks. In a proton, quarks tend to have larger longitudinal momentum than antiquarks and, therefore, a particle coming from a quark-antiquark interaction in a proton-proton collision flies more often into the same hemisphere as the quark. In this situation, the invariance by exchange of the two beams is effectively broken, because we are "observing" the collision between two *distinguishable* objects and we can give a physically meaningful (conventional, but reproducible) definition of the "orientation" of the collision direction. If, moreover, the elementary production process violates parity conservation, leading to different average kinematic distributions when the quark and antiquark are exchanged, we *can* observe an asymmetry of the decay distribution with respect to the production plane, that is, between the "left" and "right" half-spaces cut by this plane.

We will devote the next sections to the presentation of several conventions that have been used in past polarization measurements for the definition of the polariza-

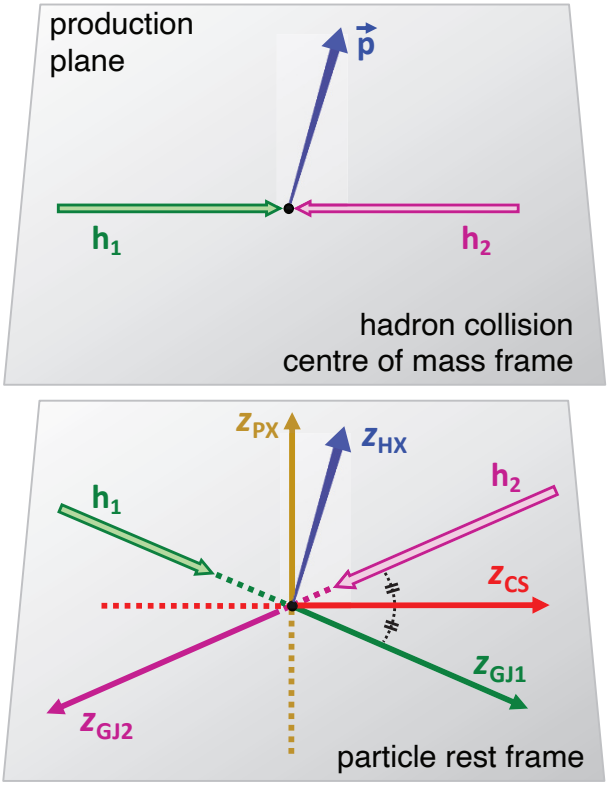

Fig. 2.1 Illustration of several definitions of the polarization axis z with respect to the directions of motion of the colliding hadrons (h_1 and h_2) in the particle rest frame: Gottfried–Jackson (GJ), Collins–Soper (CS), centre-of-mass helicity (HX), and perpendicular helicity (PX).

tion axis, shown in Fig. 2.1: Gottfried–Jackson (GJ), Collins–Soper (CS), centre-of-mass helicity (HX), and perpendicular helicity (PX). These frame definitions differ in the way the momenta of the colliding hadrons, h_1 and h_2, are used as reference directions. We denote by $\hat{\jmath}_1 = \mathbf{p}_1/|\mathbf{p}_1|$ and $\hat{\jmath}_2 = \mathbf{p}_2/|\mathbf{p}_2|$ the unit vectors representing those directions, where $\mathbf{p}_1$ and $\mathbf{p}_2$ are the momenta of h_1 and h_2 in the rest frame of the particle under study, V.

2.2 The Gottfried–Jackson frame

In the Gottfried–Jackson (GJ) frame [1], the z axis is "simply" the direction of the momentum of one of the two colliding hadrons. The corresponding unit vector is

$$\hat{z}_{\mathrm{GJ}} = \hat{\jmath}_1 \quad \text{or} \quad \hat{\jmath}_2 \,. \tag{2.3}$$

While the choice is simple, the adoption of this frame requires care. There are, in fact, two possible choices, which we call GJ1 and GJ2, associated respectively to the colliding hadrons h_1 and h_2, where the labels "1" and "2" identify each of the two beams in a given experiment. In Fig. 2.1, the polarization axes in the GJ1 and GJ2 frames are represented by the green and pink arrows, respectively.

As we will show later in this chapter, analyses using the GJ1 and GJ2 frames do not lead, in general, to the same measured angular distribution parameters, for a given laboratory momentum of the decaying particle V (and, in particular, for a given sign of p_L), even when the physics processes being studied are perfectly invariant by exchange of the two colliding particles, as in the proton-proton case. In fact, $\hat{\jmath}_1$ and $\hat{\jmath}_2$, indicating the beam directions in the *boosted* frame of V, are neither parallel nor anti-parallel (except in very specific kinematic conditions, when the particle transverse momentum approaches either zero or much larger values than the mass).

A reflection of the z axis simply swaps the $J_z = +1$ and -1 projections without affecting the $J_z = 0$ component. As can be seen from the expressions of the anisotropy parameters in Eq. 1.13, when a_{+1} and a_{-1} are swapped, λ_ϑ and λ_φ remain unchanged (the $\lambda_{\vartheta\varphi}$ case is discussed in Section 2.10). Instead, going from GJ1 to GJ2 implies a rotation of the quantization axis that is almost never a reflection, and changes, hence, the J_z composition of the V angular momentum state in a significant way. All three parameters of Eq. 2.1 can change in a non-trivial way by such a rotation. Therefore, the choice between GJ1 and GJ2, seemingly innocuous in collisions between identical proton beams, can lead to misleading results in comparisons between experiments, or between data and theoretical predictions, if the two analyses do not use the same beam naming convention. To ensure a correct comparison, the beam "labels" and the definition of the positive sign for the longitudinal momentum p_L (that is, the laboratory z axis) must be consistent in the two analyses.

Apart from the risk of ambiguity, it is, a priori, not the most natural choice to use the "asymmetric" frames GJ1 or GJ2 when the collision system is symmetric. For example, it could happen that the anisotropy parameters, in certain physics scenarios, would be significantly different for $p_L > 0$ and $p_L < 0$, a very unusual observation in proton-proton production measurements, where the two hemispheres of the particle momentum space should rightfully be considered as equivalent. Before continuing, it is worth saying that all considerations made in this chapter regarding the sign of p_L are equally valid in terms of the more frequently used variables rapidity, $y = 1/2\ \ln[(E + p_L) / (E - p_L)]$, where E is the particle energy, and Feynman-x, $x_F = 2p_L / \sqrt{s}$, where $\sqrt{s}$ is the centre-of-mass collision energy.

Choosing one of the two GJ frames may be appropriate when the colliding particles are different and the experiment focuses on the effects of such differences. For example, in fixed-target experiments, the projectile (e.g. a proton) is different from the target (typically an atomic nucleus) and part of the interest of the measurement is to study the influence of the nuclear structure of the target on the elementary parton-parton hard-scattering process, by comparing the results with those of symmetric proton-proton collisions. In this case, where the asymmetry of the collision is physically meaningful, the choice of the "asymmetric" GJ frame is justified.

Actually, also in proton-proton collisions, being the parton process itself often asymmetric, there are situations in which the GJ frame, in either of the two variants, can be considered as the one most closely reflecting the topology of the production process. We will illustrate the usefulness of the GJ frame, and of other frame definitions, in the following sections, using the example of Drell–Yan production, where the virtual photon emitted by a quark, in quark-antiquark annihilation ($q\bar{q}$) or quark-gluon scattering (qg) processes, leads to a lepton-antilepton pair detected experimentally.

Figure 2.2 shows the basic processes that contribute to the production of Drell–Yan dileptons at the lowest perturbative orders. We will indifferently indicate with V the dilepton system or the virtual photon; analogous considerations also apply if V represents a Z or W boson. We start by considering the $q\bar{q}$ annihilation diagrams (a) and the qg scattering ones (b), shown in each case in the t-channel (left) as well as in the u-channel (right) variants.

The polarization of V can be deduced by applying helicity conservation along the line of the quark that emits the virtual photon, as illustrated in Fig. 2.3: the quark helicity never flips when we move along that line, which in the V rest frame is the common direction of the incoming quark and the virtual quark. With respect to this direction, V is always transversely polarized. In the case of the diagrams (a) and (b), therefore, the "natural polarization axis" is defined by the direction of the incoming quark, as seen in the V rest frame. These diagrams are complemented by analogous versions, where all quarks are exchanged with antiquarks; in those cases, the natural polarization axis is the direction of the incoming antiquark.

The GJ frame, with polarization axis defined by the beam carrying the incoming quark (or antiquark) coupling to the photon, can, therefore, be seen as a natural frame choice for the experiment, under the assumption that the parton and proton have approximately the same direction (that is, neglecting the intrinsic transverse momentum of the parton, k_{T}).

While we cannot match the incoming quark (or antiquark) with its beam of origin on an event-by-event basis, this is possible on average, for events where V has sufficiently high $|p_{\mathrm{L}}|$. Indeed, as already mentioned, in a proton the quarks have higher average longitudinal momenta than the antiquarks and the gluons, so that the beam going into the same hemisphere as V has a higher probability of contributing a quark than an antiquark or a gluon.

When V is produced by $q\bar{q}$ annihilation, diagrams (a) of Fig. 2.2, we will always have the superposition of processes where V is transverse with respect to the incoming quark direction (as in the diagrams shown) with the equally probable ones where V is transverse with respect to the incoming antiquark (diagrams with the q and $\bar{q}$ exchanged), so that in this case there is an automatic symmetrization of the results of the polarization measurement, independently of the proton beam selected as reference. The qg scattering case (b) is different because the photon always couples to the quark or antiquark (with qg dominating over $\bar{q}g$), never to the gluon, thereby leading to a predominant transverse polarization along the beam going in the same direction as V. In this latter case and, therefore, in general, it is more appropriate to slightly change the definition of the GJ frames, as explained in the next lines, to

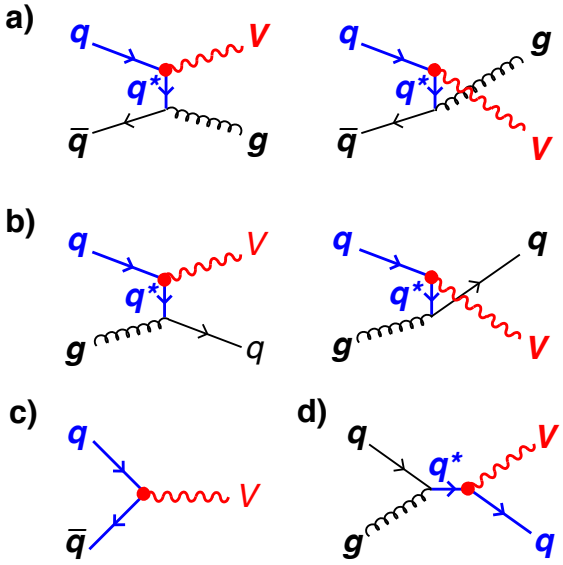

Fig. 2.2 Feynman diagrams for Drell–Yan production, always leading to transverse polarizations but along different specific quantization axes: $q\bar{q}$ (a) and qg (b) scattering with natural polarizations along the incoming quark direction, approximated by the Gottfried–Jackson frame; $q\bar{q}$ annihilation with natural polarization along the relative motion direction of the quark and antiquark, approximated by the Collins–Soper frame (c); and qg scattering with natural polarization along the outgoing quark, approximated by the centre-of-mass helicity frame (d).

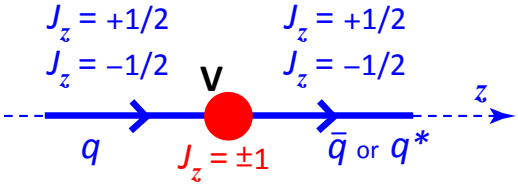

Fig. 2.3 Illustration of helicity conservation along the quark lines in the V rest frame, leading to transverse polarization.

avoid a seemingly unphysical change of results between the $p_{\mathrm{L}} > 0$ and $p_{\mathrm{L}} < 0$ phase space domains.

The GJ1 and GJ2 axis definitions permanently introduce an orientation towards one of the two hemispheres, defined by the colliding hadron directions, opposite to each other. In the case of the collision of two identical proton beams, the two hemispheres are a priori indistinguishable and such an orientation is arbitrary and unphysical. If there is no explicit intention of introducing possible consequences of an asymmetric definition in the results of the measurement, the choice of one or the other direction for the z axis should rather be done taking into account the laboratory direction of the decaying particle V, which effectively breaks the symmetry. In this

way, the experiment becomes the ensemble of two identical sub-experiments oriented in opposite directions, each one collecting only the events where the particle has either "positive" or "negative" p_{L} in the centre-of-mass system of the collision.

In the proton-proton case, both sub-experiments, in the lack of a specific motivation to force the contrary, must give compatible results. The proper symmetry can be ensured automatically by labelling, in each event, h_1 as the colliding hadron travelling into the same hemisphere as the decaying particle and h_2 as the other hadron, independently of the experiment-specific naming conventions. In this "symmetrized" version of the GJ frame, the direction of the z axis is defined on an event-by-event basis, depending on the particle momentum, and measurements in symmetric collisions should provide identical results for $p_{\mathrm{L}} > 0$ and $p_{\mathrm{L}} < 0$. But even in this case it remains necessary to specify, to avoid ambiguities in comparisons between different analyses, how the association between one beam and the corresponding sign of p_{L} is made, that is, whether the polarization axis is chosen as the *same*-hemisphere beam (as described in the lines above) or as the *opposite*-hemisphere beam, another equally appropriate choice, potentially leading to different results.

2.3 The Collins–Soper frame

The Collins–Soper (CS) frame [2] represents an intrinsically "symmetric" frame definition, suitable for the analysis of data collected in collisions of identical beams, obtained by geometrically averaging the two beam directions. One often reads in the literature that the z axis of the CS frame has the direction of "the" bisector of the angle formed by the h_1 and h_2 momentum directions in the particle rest frame. However, it is possible to define *two* different bisectors between two non-oriented directions. Considering the two momenta with their orientations, the CS frame is the one defining z in the direction of the bisector between one beam momentum and the *opposite* of the other,

$$\hat{z}_{\mathrm{CS}} = \frac{\hat{j}_1 - \hat{j}_2}{|\hat{j}_1 - \hat{j}_2|} \,. \tag{2.4}$$

In Fig. 2.1 the CS polarization axis is represented by the red arrow, which is the bisector between the h_1 momentum and the opposite of the h_2 momentum. This definition uses the fact that the bisector of two *unit* vectors has the direction of the sum of the two. Again, as in the GJ case, two alternative definitions are possible, depending on how the labels "1" and "2" are assigned, and it is appropriate to adopt, at least in proton-proton collisions, the p_{L}-dependent definition described above, exchanging $\hat{j}_1$ and $\hat{j}_2$ when going from one hemisphere to the other (and explicitly declaring the adopted convention). However, while in the GJ case all measured parameters can, in certain scenarios, depend on this kind of precise definition, in the case of the CS frame the change only affects parity-violating asymmetries, which are not considered in this chapter.

Indeed, inverting the orientation of the polarization axis is equivalent to defining the angles using the negative decay lepton, instead of the positive one, having no ef-

fect in parity-conserving decays. The ordering of the two colliding hadrons remains important for the definition of the y axis and has consequences on the sign of $\lambda_{\vartheta\varphi}$, as discussed in Sections 2.6 and 2.10.

The CS z axis coincides with the direction of the relative motion of the colliding partons, when their transverse momenta are neglected (the validity and limits of this approximation will be discussed in Chapter 5). This choice reflects the natural polarization axis of a particle P in the kinematic limit where it is produced without any recoiling particle, that is, in so-called "$2 \to 1$" processes of the kind $\mathrm{h_1 h_2} \to P$, and is relevant when the p_T of P is not large with respect to its mass. One example is Drell–Yan production by quark-antiquark annihilation at the leading order in the perturbative description of the process, corresponding to the diagram Fig. 2.2-c. Helicity conservation translates, again, into a transverse polarization, this time along the relative direction of the colliding quark and antiquark, which are back-to-back in the V rest frame, therefore having opposite helicities, i.e. identical signs of their $J_z = \pm 1/2$ projections. Another example is the category of partonic processes of the kind $gg \to P$. In the assumption that gluons are mostly transversely polarized, i.e. each of them has projection $J_z = \pm 1$ along its own direction, the total projection along z can only be $J_z = 0$ or ± 2. Since P is the only produced particle, it inherits this property and, by lacking the $J_z = \pm 1$ component, is polarized. In particular, a $J = 1$ particle must always be produced in the $J_z = 0$ state.

2.4 The centre-of-mass helicity frame

In the centre-of-mass helicity (HX) frame the quantization axis is taken along the flight direction of V itself. The name "helicity" refers, in fact, to the projection of the spin of a particle along its own momentum. The momentum of V, and therefore its flight direction, *depends*, in both modulus and orientation, on the chosen external reference for the motion of V. In inclusive production studies the only reasonable choice for such external reference is the "centre of mass" of the system of the colliding hadrons, coinciding with the laboratory in symmetric proton-proton collisions, as illustrated in Fig. 2.1, where the HX polarization axis is represented by the blue arrow.

The polarization axis direction can be defined in terms of either the V momentum ($\mathbf{p}$) in the hadron rest frame or the hadron momenta $\mathbf{p}_1$ and $\mathbf{p}_2$ in the V rest frame, remembering, in this latter case, that V recognizes its own flight direction by "seeing" the system of the colliding hadrons receding with momentum $-(\mathbf{p}_1 + \mathbf{p}_2)$:

$$\hat{z}_\mathrm{HX} = \frac{\mathbf{p}}{|\mathbf{p}|} = -\frac{\mathbf{p}_1 + \mathbf{p}_2}{|\mathbf{p}_1 + \mathbf{p}_2|} \,. \tag{2.5}$$

The choice of the HX axis tends to reflect the natural polarization direction in processes like Drell–Yan production in s-channel qg scattering, represented by the diagram (d) of Fig. 2.2, where V is emitted from a quark line having the same direction as V itself, given that V and the outgoing q are emitted back-to-back in the

rest frame of the partonic collision. Again, V will be transversely polarized, but this time along its own momentum.

It is important to realize that the experimentally-definable HX axis is only an approximation of the true ("natural") polarization direction. Experiments measuring inclusive V production, without detecting the recoil system X, coming, for example, from the hadronization of the outgoing quark or gluon shown in Fig. 2.2, have no access to the motion of the interacting partons. It is the centre-of-mass of that parton-parton system, rather than of the system of colliding hadrons, that should ideally be taken as reference for the V momentum direction used in the HX definition. The parton-parton and proton-proton centre-of-mass frames do not coincide event by event; the effect of their relative motion can only be simulated statistically (using existing sets of parton distribution functions), not on a per-event basis.

We have already mentioned that the intrinsic *transverse* motion of the parton system, k_{T}, affects how well the GJ and CS frames approximate the most natural polarization frames, whose axes are defined by the colliding parton directions. We have now seen that also the *longitudinal* motion of the parton-parton system, with respect to the proton-proton system, smears the correspondence between the HX frame used in analyses of experimental data and the true natural axis, relevant for the physics processes under study.

2.5 The perpendicular helicity frame

When defining the CS frame we took one of the two bisectors of the hadron momentum directions as reference z axis. If we take the other bisector, we obtain the perpendicular helicity (PX) frame [3]. This is the case where the z axis is properly defined along the bisector between the two beam momenta, taking the sum (rather than the difference) of their unit vectors,

$$\hat{z}_{\mathrm{PX}} \;=\; \pm \frac{\hat{\jmath}_1 + \hat{\jmath}_2}{|\hat{\jmath}_1 + \hat{\jmath}_2|} \,. \tag{2.6}$$

In Fig. 2.1, the PX polarization axis is shown by the yellow arrow.

The adjective in the denomination comes from the fact that the z axis is, by definition, always exactly perpendicular to the CS z axis, while the noun reflects the fact that the PX axis approaches asymptotically the HX axis, in the limit of high transverse momentum and small longitudinal momentum of V in the laboratory frame ($p_{\mathrm{T}}/|p_{\mathrm{L}}| \gg 1$). In this limit, in fact, the CS and HX axes become perpendicular to each other, differing by a rotation of 90° around the y axis. With the choice of the minus sign in Eq. 2.6, the PX axis has the same orientation as the HX axis when they assume the same direction. Towards the opposite limit, $p_{\mathrm{T}}/p_{\mathrm{L}} \to 0$, the GJ, CS, and HX frames become progressively coincident. This is a physical necessity, as in this limit the scattering process becomes "one-dimensional": the outgoing V and X are emitted along the scattering direction (apart for the parton momentum smearing) and no other direction provides a uniquely identifiable reference. At the

same time, it is clear that there is no physical reference *plane* in this condition: for symmetry reasons, any azimuthal dependence of the decay distribution is physically forbidden.

The PX axis, instead, continues to remain (exactly) perpendicular to the CS axis and, therefore, (approximately) to all other frames, when we gradually approach the low-p_{T} limit. For $p_{\mathrm{T}} \to 0$ it is no longer univocally defined, as there are infinite directions perpendicular to a line without the constraint of a reference plane where the axis should belong.

A purely conventional perpendicular direction can be chosen if one wants to use the PX frame in experiments reaching very low $p_{\mathrm{T}}/p_{\mathrm{L}}$ regions, with the consequence that an equally conventional reference plane is induced by this definition and azimuthal anisotropies become mathematically allowed. We will show in Section 4.2 how the PX frame can be used, together with the CS frame, to maximise the observed polar anisotropy in Drell–Yan production when it is dominated by the t- and u-channel diagrams (b) of Fig. 2.2.

2.6 The definition of the y axis

We have seen that the use of the GJ and CS frames requires some care in order to avoid ambiguities implied by the beam naming convention, given that the direction (GJ frame) or the orientation (CS frame) of the z axis depend on the ordering of the two beams (Eqs. 2.3 and 2.4). This problem does not seem to affect the HX and PX cases, for which the z axis definition is invariant by exchange of the two hadrons (Eqs. 2.5 and 2.6). However, the definition of the y axis, always taken in the direction perpendicular to the production plane for any of the frames discussed so far, implies an arbitrary choice of orientation. Looking at the mathematical definition of the axis,

$$\hat{y} \;=\; \hat{\jmath}_1 \times \hat{\jmath}_2 \,, \tag{2.7}$$

we immediately see that the vector product implies a dependence on the ordering of the two hadrons.

We will further discuss in Section 2.10 how the chosen convention, which does not affect λ_ϑ or λ_φ, determines the sign of $\lambda_{\vartheta\varphi}$ and whether or not this parameter changes sign at positive and negative p_{L}. A flip of the sign of $\lambda_{\vartheta\varphi}$ is produced, when going from p_{L} to $-p_{\mathrm{L}}$, as an artefact of the frame definitions if one fixed ordering, disregarding the sign of p_{L}, is assumed in Eq. 2.7. Such a definition is anyhow inappropriate in symmetric collisions, since it introduces an arbitrary space orientation in a physically fully rotation-symmetric system.

Moreover, when $\lambda_{\vartheta\varphi}$ changes sign with the sign of p_{L} and, at the same time, the measurement does not distinguish between positive and negative p_{L}, as often happens in measurements using proton-proton data from symmetric collider experiments, the effectively measured value of $\lambda_{\vartheta\varphi}$ is actually always *zero*, irrespectively of the true angular momentum composition determined by the underlying processes.

Indeed, when this happens the corresponding relation in Eq. 1.13 is forcefully violated, for all participating processes where the amplitude combination $a^*_{+1}a_0 - a^*_0 a_{-1}$ is actually not zero, and physical information is lost. This is one more reason for using a $p_{\rm L}$-dependent ordering of the two beam labels in all the definitions of the y and z axes mentioned above. Even in this case, it remains necessary to explicitly report which specific convention is used, because the sign of $\lambda_{\vartheta\varphi}$, resulting from a measurement or a calculation, will depend on that choice.

2.7 Dependence of the measurement on the polarization frame

As discussed above, all possible *experimentally definable* polarization axes in inclusive measurements belong to the production plane. We can, therefore, parametrize the transformation from an observation frame to another by a single angle, describing a rotation around the y axis. A possible method consists in determining how a generic angular momentum state vector changes by such a rotation, using the Wigner matrix, and calculate the corresponding "rotated" decay angular distribution, as we have done in Chapter 1. Here, instead, we apply a geometrical transformation directly to the momentum vector of the (positive) decay lepton.

The rotation matrix

$$R_y(\delta) = \begin{pmatrix} \cos\delta & 0 & -\sin\delta \\ 0 & 1 & 0 \\ \sin\delta & 0 & \cos\delta \end{pmatrix} \tag{2.8}$$

transforms the components of a vector, reproducing the effect of a rotation of the z and x axes in the production plane. The direction of the rotation is anticlockwise when δ is positive and the (fixed) y axis points towards the observer. We will discuss in Section 2.9 how the sign of δ depends, in an observable way, on the conventions chosen for the orientation of the z and y axes, and how its value depends, in general, on the momentum of V in the laboratory. The coordinates of the unit vector indicating the positive lepton direction in the *old* frame,

$$\hat{r} \;=\; (\sin\vartheta\,\cos\varphi,\ \sin\vartheta\,\sin\varphi,\ \cos\vartheta)\,, \tag{2.9}$$

can be expressed as a function of the coordinates in the new frame by inverting the rotation,

$$\hat{r} = R_y^{-1}(\delta)\,\hat{r}' = R_y^{\rm T}(\delta)\,\hat{r}'\,, \tag{2.10}$$

that is,

$$\begin{aligned} \sin\vartheta\,\cos\varphi &= \cos\delta\,\sin\vartheta'\,\cos\varphi' \;+\; \sin\delta\,\cos\vartheta'\,, \\ \sin\vartheta\,\sin\varphi &= \sin\vartheta'\,\sin\varphi'\,, \\ \cos\vartheta &= -\sin\delta\,\sin\vartheta'\,\cos\varphi' \;+\; \cos\delta\,\cos\vartheta'\,. \end{aligned} \tag{2.11}$$

Substituting Eq. 2.11 into Eq. 2.1, we obtain the angular distribution in the rotated frame,

$$W'(\cos\vartheta', \varphi') \propto \frac{1}{(3+\lambda'_\vartheta)} \times \left(1 + \lambda'_\vartheta \cos^2\vartheta' + \lambda'_\varphi \sin^2\vartheta' \cos 2\varphi' + \lambda'_{\vartheta\varphi} \sin 2\vartheta' \cos\varphi'\right), \tag{2.12}$$

where

$$\lambda'_\vartheta = \frac{\lambda_\vartheta - 3\Lambda}{1+\Lambda}, \quad \lambda'_\varphi = \frac{\lambda_\varphi + \Lambda}{1+\Lambda},$$

$$\text{and} \quad \lambda'_{\vartheta\varphi} = \frac{\lambda_{\vartheta\varphi} \cos 2\delta - \frac{1}{2}(\lambda_\vartheta - \lambda_\varphi) \sin 2\delta}{1+\Lambda}, \tag{2.13}$$

$$\text{with} \quad \Lambda = \frac{1}{2}(\lambda_\vartheta - \lambda_\varphi) \sin^2\delta - \frac{1}{2}\lambda_{\vartheta\varphi} \sin 2\delta.$$

2.8 Two interesting limit cases

To illustrate the importance of the choice of the observation frame, we will now consider two specific examples assuming, for simplicity, that the chosen polarization axis is perpendicular to the natural axis ($\delta = \pm 90°$). These cases are physically relevant: when the decaying particle is produced with high transverse momentum ($p_T \gg |p_L|$), a frequent kinematic configuration in midrapidity collider experiments like ATLAS and CMS, the CS and HX axes become perpendicular to one another; and the CS and PX axes are always perpendicular to each other, by definition.

When $\delta = 90°$, a natural "transverse" polarization ($\lambda_\vartheta = +1$ and $\lambda_\varphi = \lambda_{\vartheta\varphi} = 0$) transforms (see Eq. 2.13) into an observed polarization of opposite sign, $\lambda'_\vartheta = -1/3$. At the same time, a significant azimuthal anisotropy appears, quantified by the parameter $\lambda'_\varphi = 1/3$. As shown in Fig. 2.4, in the rotated frame the geometrical shape of the distribution loses its original cylindrical symmetry around the z axis. Figure 2.5 represents the same effect in a way closer to what experiments observe, showing the measured angular distribution as a two-dimensional function (Eq. 2.1) and in its one-dimensional projections, obtained by averaging over φ or $\cos\vartheta$:

$$\frac{1}{2\pi}\int_{-\pi}^{+\pi} W(\cos\vartheta, \varphi)\, \mathrm{d}\varphi = \frac{1}{4\pi}\frac{3}{3+\lambda_\vartheta}\left(1 + \lambda_\vartheta \cos^2\vartheta\right), \tag{2.14}$$

$$\frac{1}{2}\int_{-1}^{+1} W(\cos\vartheta, \varphi)\, \mathrm{d}\cos\vartheta = \frac{1}{4\pi}\left(1 + \frac{2\lambda_\varphi}{3+\lambda_\vartheta}\cos 2\varphi\right). \tag{2.15}$$

In terms of angular momentum wave functions, a state that is fully "transverse" with respect to one quantization axis becomes, when observed in a frame rotated by

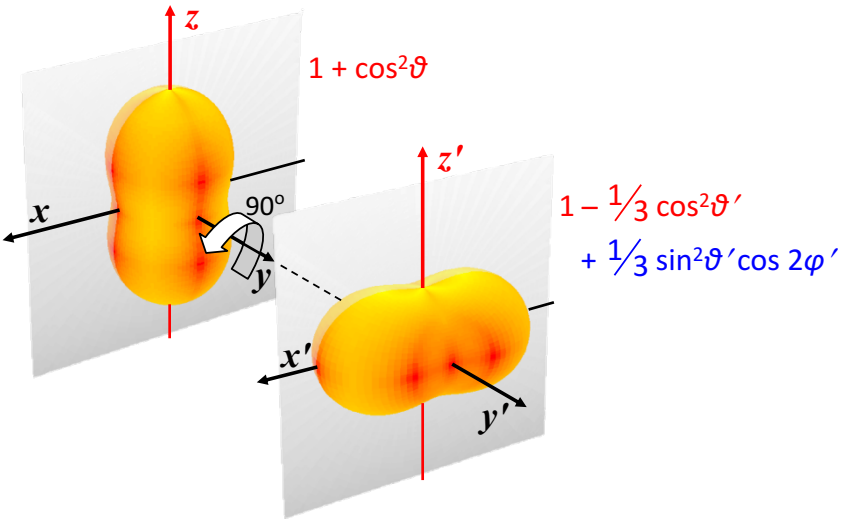

Fig. 2.4 Illustration of how the rotation of the polarization frame by an angle $\delta = 90°$ changes the shape parameters of the decay distribution of a transversely polarized vector particle.

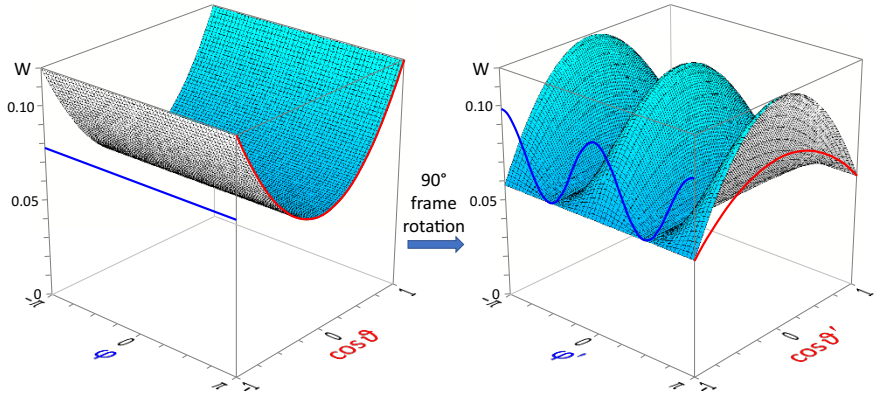

Fig. 2.5 The angular decay distribution $W(\cos\vartheta, \varphi)$ of a transversely polarized vector particle in its "natural" frame and its transformation to a polarization frame rotated by an angle $\delta = 90°$. The red and blue curves on the faces of the cube are the polar and azimuthal projections.

90°, a coherent superposition of equally-probable "transverse" and "longitudinal" components,

$$|1,\pm1\rangle \quad \xrightarrow{90°} \quad \frac{1}{2}\,|1,+1\rangle \;+\; \frac{1}{2}\,|1,-1\rangle \;\mp\; \frac{1}{\sqrt{2}}\,|1,0\rangle\,, \tag{2.16}$$

a result obtained from Eqs. 1.1, 1.4 and 1.11, keeping in mind the convention that the positive rotation is the one *towards* the state to be "projected" into its components

(in this case, the *inverse* of the considered frame rotation). The amplitude of the transition of this mixed state to the "rotated" dilepton state in Eq. 1.9 contains three terms with *relative* phases (due to the φ dependence of the rotation matrix) giving rise to the observable azimuthal dependence.

An identical polar anisotropy parameter, $\lambda'_\vartheta = -1/3$, would also be measured in the presence of an equal mixture of naturally "transverse" processes and naturally "longitudinal" ones, but in this case we would not see any azimuthal anisotropy, given that $\lambda_\varphi = 0$ in both categories of processes. This observation shows how the study of the azimuthal dimension can help in the discrimination between two very different physical scenarios, such as a scenario reflecting a certain superposition of processes and one where there is only a single process, naturally polarized in a frame different from the one used in the analysis.

As a second example, illustrated in Figs. 2.6 and 2.7, we note that a fully "longitudinal" natural polarization ($\lambda_\vartheta = -1$) translates, in a frame rotated by 90° with respect to the natural one, into a fully "transverse" polarization ($\lambda'_\vartheta = +1$), accompanied by a maximal azimuthal anisotropy ($\lambda'_\varphi = -1$).

In terms of angular momentum, the measurement in the rotated frame is performed on a coherent admixture of states,

$$|1,0\rangle \quad \xrightarrow{90^\circ} \quad \frac{1}{\sqrt{2}}\,|1,+1\rangle - \frac{1}{\sqrt{2}}\,|1,-1\rangle\,, \tag{2.17}$$

while a *natural* "transverse" polarization would originate from the statistical superposition of uncorrelated $|1,+1\rangle$ and $|1,-1\rangle$ states.

It is important to appreciate the relevance of this observation: the two physically very different cases of a natural transverse polarization observed in its natural frame (Fig. 2.4-left) and a natural longitudinal polarization observed in a rotated frame (Fig. 2.6-right) are experimentally indistinguishable when the azimuthal anisotropy is ignored. Measurements are sometimes limited by the lack of a sufficiently large number of events properly populating the two-dimensional $(\cos\vartheta, \varphi)$ variable space. In order to circumvent this problem, it might be tempting to focus on the determination of the polar anisotropy parameter λ_ϑ, which characterizes "natural" polarizations (if measured in the natural frame), by integrating out the φ dependence (Eq. 2.14) to reduce the problem to a one-dimensional analysis, removing λ_φ and $\lambda_{\vartheta\varphi}$ from the equation.

As one can easily see by browsing through the literature, this solution has been applied in several analyses of experimental data, which only report the values of λ_ϑ, probably because the simultaneous measurement of the three anisotropy parameters was not a viable option. However, the examples presented above show that a measurement (or theoretical calculation) consisting only in the determination of the polar parameter λ_ϑ in a single frame contains an ambiguity that prevents a fundamental (model-independent) interpretation of the results. The polarization is only fully determined when *both* the polar and azimuthal components of the decay distribution are known, or when the distribution is analysed in at least two geometrically complementary frames. Section 2.11 further develops this discussion and

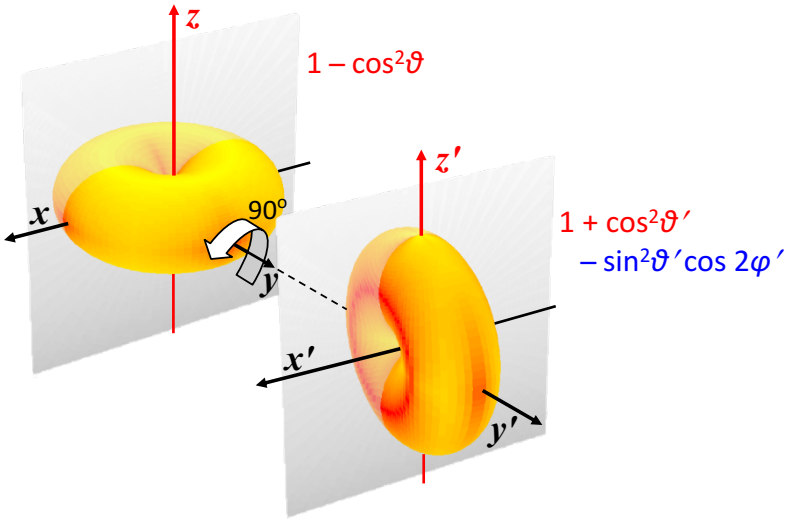

Fig. 2.6 Illustration of how the rotation of the polarization frame by an angle $\delta = 90°$ changes the shape parameters of the decay distribution of a longitudinally polarized vector particle.

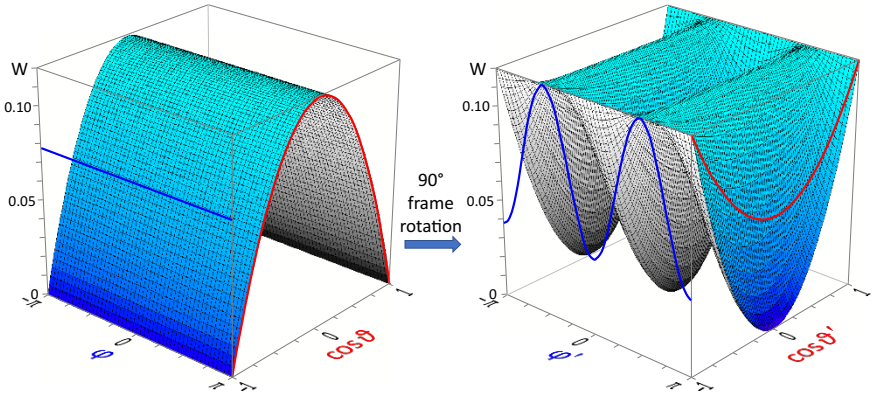

Fig. 2.7 The angular decay distribution $W(\cos\vartheta, \varphi)$ of a longitudinally polarized vector particle in its "natural" frame and its transformation to a polarization frame rotated by an angle $\delta = 90°$. The red and blue curves on the front faces of the cube are the polar and azimuthal projections.

illustrates some conceptual pitfalls triggered by neglecting the full dimensionality of the physics problem, while Section 2.13 shows how the measurement itself can be significantly biased by an artificial reduction of the dimensionality of the problem.

The reader must have noticed in Figs. 2.4 and 2.6 that, while the transformation of polarization frame changes considerably the numerical values of the measurable parameters, the *shapes* of the decay distributions remain obviously unchanged, as they are unaffected by geometrical rotations. While this consideration might seem

rather elementary, it was only very recently that it triggered the realization that it is possible to define parameters characterizing the shape of the decay distribution in a frame-independent way. This topic will be developed in Chapters 3 and 4.

2.9 Effect of production kinematics on the angular distribution

While the above example, where $\delta = \pm 90°$, shows that the adoption of one or the other polarization frame has a large effect on the measured parameters, it does not properly reflect the full complexity of the patterns that can be observed in real measurements. In fact, the angle δ between the polarization axis chosen for the analysis of the data and the "natural axis" depends, in general, on the laboratory momentum of the decaying particle. Therefore, the polarization parameters λ_ϑ, λ_φ, and $\lambda_{\vartheta\varphi}$ can show a strong kinematic dependence, not because of a physical change of the angular momentum configuration in which the particle is produced but simply as a consequence of the purely geometrical effect induced by the frame choice.

To calculate the directions of the polarization axes as functions of the particle kinematics, we need the expressions of the momenta of the colliding particles, h_1 and h_2, as seen in the V rest frame. Since we are interested in *relative* angles between the directions of different axis definitions, we are free to choose a convenient basis of unit vectors for the calculation. In view of the boost from the "laboratory" frame (centre-of-mass of the collision) to the V rest frame, a good choice is to express all considered vectors in longitudinal and transverse components with respect to the direction of V in the laboratory, knowing that only the longitudinal component will be modified by the boost.

The h_1 and h_2 momenta in the laboratory, $\mathbf{P}_1$ and $\mathbf{P}_2$, with $|\mathbf{P}_1| = |\mathbf{P}_2| = P$, are

$$\mathbf{P}_1 = -\mathbf{P}_2 = P\cos\Theta\,\hat{\imath}_\parallel + P\sin\Theta\,\hat{\imath}_\perp\,, \tag{2.18}$$

where Θ is the angle between the V momentum, $\mathbf{p}$, with $|\mathbf{p}| = p$, and the beam axis,

$$p_\mathrm{L} = p\,\cos\Theta\,, \quad p_\mathrm{T} = p\,\sin\Theta\,. \tag{2.19}$$

When boosted to the V rest frame, they become (neglecting the h_1 and h_2 masses)

$$\begin{aligned} \mathbf{p}_1 &= \;\;(\gamma P\cos\Theta - \beta\gamma P)\,\hat{\imath}_\parallel + P\sin\Theta\,\hat{\imath}_\perp\,, \\ \mathbf{p}_2 &= (-\gamma P\cos\Theta - \beta\gamma P)\,\hat{\imath}_\parallel - P\sin\Theta\,\hat{\imath}_\perp\,, \end{aligned} \tag{2.20}$$

where $\gamma = E/m$ (Lorentz factor of V) and $\beta = p/E = \sqrt{1 - 1/\gamma^2}$, E being the energy of V. The corresponding unit vectors, $\hat{\jmath}_1 = \mathbf{p}_1/|\mathbf{p}_1|$ and $\hat{\jmath}_2 = \mathbf{p}_2/|\mathbf{p}_2|$, define the directions of the different polarization frames, according to Eqs. 2.3–2.6. The direction of the unit vector $\hat{\imath}_\parallel$, parallel to the V momentum, is nothing else than the direction of the HX axis. Given that the momenta of V, h_1, and h_2 belong to the same plane (the production plane zx, unchanged by the boost), we can adopt the x axis of the HX frame, with its orientation, to define the "transverse" dimension:

$$\hat{t}_{\parallel} = \hat{z}_{\mathrm{HX}}\,, \quad \hat{t}_{\perp} = \hat{x}_{\mathrm{HX}}\,. \tag{2.21}$$

We can now express the directions of the other polarization axes (Eqs. 2.3, 2.4, and 2.6) using Eqs. 2.20 and 2.21:

$$\hat{z}_{\mathrm{GJ1}} = \frac{(\cos\Theta - \beta)\ \hat{z}_{\mathrm{HX}} + \sqrt{1-\beta^2}\sin\Theta\ \hat{x}_{\mathrm{HX}}}{1-\beta\cos\Theta}\,, \tag{2.22}$$

$$\hat{z}_{\mathrm{GJ2}} = \frac{(-\cos\Theta - \beta)\ \hat{z}_{\mathrm{HX}} - \sqrt{1-\beta^2}\sin\Theta\ \hat{x}_{\mathrm{HX}}}{1+\beta\cos\Theta}\,, \tag{2.23}$$

$$\hat{z}_{\mathrm{CS}} = \frac{\sqrt{1-\beta^2}\cos\Theta\ \hat{z}_{\mathrm{HX}} + \sin\Theta\ \hat{x}_{\mathrm{HX}}}{\sqrt{1-\beta^2\cos^2\Theta}}\,, \tag{2.24}$$

$$\hat{z}_{\mathrm{PX}} = \frac{\sin\Theta\ \hat{z}_{\mathrm{HX}} - \sqrt{1-\beta^2}\cos\Theta\ \hat{x}_{\mathrm{HX}}}{\sqrt{1-\beta^2\cos^2\Theta}}\,. \tag{2.25}$$

For the PX axis, we have taken the negative sign in Eq. 2.6, corresponding to the condition that the PX and HX frames have identical axis orientations in the $p_{\mathrm{L}}/p_{\mathrm{T}} \to 0$ limit (that is, $\cos\Theta \to 0$, being $\sin\Theta$ always positive by definition). The y axis, the same for all frames, is defined in Eq. 2.5. To explicitly illustrate the previously discussed p_{L}-asymmetric behaviours possibly induced by this definition, we will derive all relations for the case $p_{\mathrm{L}} > 0$ ($\cos\Theta > 0$) and extend them to $p_{\mathrm{L}} < 0$ without applying the symmetrizing convention mentioned in Sections 2.2 and 2.6. In Section 2.10 we will then discuss the resulting asymmetries. The x axis for frame A is defined as

$$\hat{x}_{\mathrm{A}} = \hat{y} \times \hat{z}_{\mathrm{A}}\,. \tag{2.26}$$

The equations above fully determine the angle $\delta_{\mathrm{A}\to\mathrm{B}}$ for a given transformation from frame A to frame B, the rotation being positive ($\sin\delta > 0$) if the product $\hat{z}_{\mathrm{A}} \times \hat{z}_{\mathrm{B}}$ is oriented towards the positive direction of $\hat{y}$ (and vice-versa):

$$\cos\delta_{\mathrm{A}\to\mathrm{B}} = \hat{z}_{\mathrm{A}} \cdot \hat{z}_{\mathrm{B}}\,, \tag{2.27}$$

$$\sin\delta_{\mathrm{A}\to\mathrm{B}} = (\hat{z}_{\mathrm{A}} \times \hat{z}_{\mathrm{B}}) \cdot \hat{y}\,. \tag{2.28}$$

The signs of the rotations between the frames here considered are illustrated in Fig. 2.8, where the circular arrows indicate the positive rotations to or from the CS frame.

Table 2.1 lists, for all possible transformations, the resulting expressions of $\cos\delta$ and $\sin\delta$ in terms of the kinematic variables of the decaying particle, for three different sets of such variables: 1) $\cos\Theta$ and β; 2) E, p, p_{T}, p_{L}, m, and m_{T}, where m denotes the mass and $m_{\mathrm{T}}^2 = m^2 + p_{\mathrm{T}}^2$; 3) y and ξ, where $\xi = p_{\mathrm{T}}/m$. After substituting the expressions of $\sin\delta$ and $\sin 2\delta = 2\sin\delta\cos\delta$ for the relevant case in Eq. 2.13, the frame transformation contains explicit functions of the energy and momentum of the decaying particle.

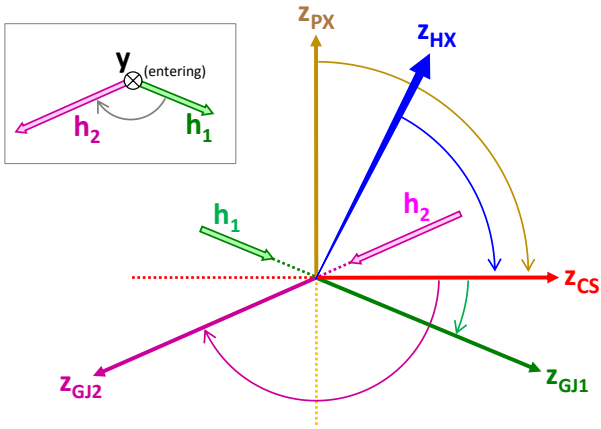

Fig. 2.8 Reference frame transformations. All considered z axes belong to the production plane and the transformations are rotations around the y axis. In the represented kinematic configuration and given the assumed convention, the y axis *enters* the plane (see inset), establishing clockwise rotations as the positive ones. For example, rotations from the PX and HX frames to the CS frame are positive, while those from the GJ1 and GJ2 frames to the CS frame are negative.

The observed polarization parameters, λ_ϑ, λ_φ, and $\lambda_{\vartheta\varphi}$, become, therefore, dependent on the particle kinematics when the measurement is not performed in the "natural" frame. Examples are shown in Figs. 2.9, 2.10, and 2.11, adopting four different illustrative scenarios of natural transverse or longitudinal polarizations in the HX or CS frame.

For simplicity (i.e. to keep the discussion exclusively devoted to geometric considerations) these illustrations neglect differences between the parton-parton and proton-proton rest frames, which, as mentioned in Sections 2.2–2.4, can affect the definition of natural reference frame. This approximation will be revisited and discussed in more detail in Sections 4.3 and 5.4.

The kinematic ranges are inspired by the phase space regions covered in Drell–Yan measurements made by the ATLAS and CMS experiments at the LHC, for dilepton mass lower than the Z boson mass. The considered kinematic variables are the dilepton mass, p_{T}, and rapidity. Each observable is varied independently, the other two being fixed to representative values.

Even with polarizations that are intrinsically well defined and constant, as in the considered examples, the *choice* of the observation frame induces strong variations with the mass and momentum of the state. This is a serious difficulty in polarization measurements, because a simple change of "point of view" can mask and/or mimic more fundamental and interesting kinematic dependences, reflecting a varying mixture of different production mechanisms. It should be even more clear from these examples that a polarization analysis should always consider alternative choices of the polarization frame.

Finding the existence of one frame where the measured polarization parameters show a reduced kinematic dependence, more closely resembling what would

Table 2.1 The angle δ of the polarization frame transformation (Eq. 2.13) for different combinations of initial and final frames, as a function of the kinematic variables of the particle under study. Expressions for three sets of variables are shown, in distinct columns. The plus and minus signs in each $\sin\delta$ expression correspond, in their order, to the two directions of the transformation.

CS $\rightleftarrows$ HX	$\cos\delta$	$\frac{\sqrt{1-\beta^2}\,\cos\Theta}{\sqrt{1-\beta^2\cos^2\Theta}}$	$\frac{m\,p_\mathrm{L}}{p\,m_\mathrm{T}}$	$\frac{\sinh y}{\sqrt{\sinh^2 y+\xi^2\cosh^2 y}}$
	$\sin\delta$	$(\mp)\,\frac{\sin\Theta}{\sqrt{1-\beta^2\cos^2\Theta}}$	$(\mp)\,\frac{E\,p_\mathrm{T}}{p\,m_\mathrm{T}}$	$(\mp)\,\frac{\xi\,\cosh y}{\sqrt{\sinh^2 y+\xi^2\cosh^2 y}}$
CS $\rightleftarrows$ PX	$\cos\delta$	0	0	0
	$\sin\delta$	$(\mp)\,1$	$(\mp)\,1$	$(\mp)\,1$
CS $\rightleftarrows$ GJ1	$\cos\delta$	$\frac{\sqrt{1-\beta^2}}{\sqrt{1-\beta^2\cos^2\Theta}}$	$\frac{m}{m_\mathrm{T}}$	$\frac{1}{\sqrt{1+\xi^2}}$
	$\sin\delta$	$(\pm)\,\frac{\beta\,\sin\Theta}{\sqrt{1-\beta^2\cos^2\Theta}}$	$(\pm)\,\frac{p_\mathrm{T}}{m_\mathrm{T}}$	$(\pm)\,\frac{\xi}{\sqrt{1+\xi^2}}$
CS $\rightleftarrows$ GJ2	$\cos\delta$	$-\frac{\sqrt{1-\beta^2}}{\sqrt{1-\beta^2\cos^2\Theta}}$	$-\frac{m}{m_\mathrm{T}}$	$-\frac{1}{\sqrt{1+\xi^2}}$
	$\sin\delta$	$(\pm)\,\frac{\beta\,\sin\Theta}{\sqrt{1-\beta^2\cos^2\Theta}}$	$(\pm)\,\frac{p_\mathrm{T}}{m_\mathrm{T}}$	$(\pm)\,\frac{\xi}{\sqrt{1+\xi^2}}$
HX $\rightleftarrows$ PX	$\cos\delta$	$\frac{\sin\Theta}{\sqrt{1-\beta^2\cos^2\Theta}}$	$\frac{E\,p_\mathrm{T}}{p\,m_\mathrm{T}}$	$\frac{\xi\,\cosh y}{\sqrt{\sinh^2 y+\xi^2\cosh^2 y}}$
	$\sin\delta$	$(\mp)\,\frac{\sqrt{1-\beta^2}\,\cos\Theta}{\sqrt{1-\beta^2\cos^2\Theta}}$	$(\mp)\,\frac{m\,p_\mathrm{L}}{p\,m_\mathrm{T}}$	$(\mp)\,\frac{\sinh y}{\sqrt{\sinh^2 y+\xi^2\cosh^2 y}}$
HX $\rightleftarrows$ GJ1	$\cos\delta$	$\frac{\cos\Theta-\beta}{1-\beta\cos\Theta}$	$\frac{E\,p_\mathrm{L}-p^2}{E\,p-p\,p_\mathrm{L}}$	$\frac{1}{\sqrt{1+\xi^2}}\,\frac{\sinh y-\xi^2\cosh y}{\sqrt{\sinh^2 y+\xi^2\cosh^2 y}}$
	$\sin\delta$	$(\pm)\,\frac{\sqrt{1-\beta^2}\,\sin\Theta}{1-\beta\cos\Theta}$	$(\pm)\,\frac{m\,p_\mathrm{T}}{E\,p-p\,p_\mathrm{L}}$	$(\pm)\,\frac{\xi}{\sqrt{1+\xi^2}}\,\frac{\cosh y+\sinh y}{\sqrt{\sinh^2 y+\xi^2\cosh^2 y}}$
HX $\rightleftarrows$ GJ2	$\cos\delta$	$\frac{-\cos\Theta-\beta}{1+\beta\cos\Theta}$	$\frac{-E\,p_\mathrm{L}-p^2}{E\,p+p\,p_\mathrm{L}}$	$\frac{1}{\sqrt{1+\xi^2}}\,\frac{-\sinh y-\xi^2\cosh y}{\sqrt{\sinh^2 y+\xi^2\cosh^2 y}}$
	$\sin\delta$	$(\mp)\,\frac{\sqrt{1-\beta^2}\,\sin\Theta}{1+\beta\cos\Theta}$	$(\mp)\,\frac{m\,p_\mathrm{T}}{E\,p+p\,p_\mathrm{L}}$	$(\mp)\,\frac{\xi}{\sqrt{1+\xi^2}}\,\frac{\cosh y-\sinh y}{\sqrt{\sinh^2 y+\xi^2\cosh^2 y}}$
PX $\rightleftarrows$ GJ1	$\cos\delta$	$\frac{-\beta\,\sin\Theta}{\sqrt{1-\beta^2\cos^2\Theta}}$	$-\frac{p_\mathrm{T}}{m_\mathrm{T}}$	$-\frac{\xi}{\sqrt{1+\xi^2}}$
	$\sin\delta$	$(\pm)\,\frac{\sqrt{1-\beta^2}}{\sqrt{1-\beta^2\cos^2\Theta}}$	$(\pm)\,\frac{m}{m_\mathrm{T}}$	$(\pm)\,\frac{1}{\sqrt{1+\xi^2}}$
PX $\rightleftarrows$ GJ2	$\cos\delta$	$\frac{-\beta\,\sin\Theta}{\sqrt{1-\beta^2\cos^2\Theta}}$	$-\frac{p_\mathrm{T}}{m_\mathrm{T}}$	$-\frac{\xi}{\sqrt{1+\xi^2}}$
	$\sin\delta$	$(\mp)\,\frac{\sqrt{1-\beta^2}}{\sqrt{1-\beta^2\cos^2\Theta}}$	$(\mp)\,\frac{m}{m_\mathrm{T}}$	$(\mp)\,\frac{1}{\sqrt{1+\xi^2}}$
GJ1 $\rightleftarrows$ GJ2	$\cos\delta$	$\frac{-(1-\beta^2)+\beta^2\sin^2\Theta}{1-\beta^2\cos^2\Theta}$	$\frac{p_\mathrm{T}^2-m^2}{p_\mathrm{T}^2+m^2}$	$\frac{-1+\xi^2}{1+\xi^2}$
	$\sin\delta$	$(\pm)\,\frac{2\beta\sqrt{1-\beta^2}\,\sin\Theta}{1-\beta^2\cos^2\Theta}$	$(\pm)\,\frac{2\,m\,p_\mathrm{T}}{p_\mathrm{T}^2+m^2}$	$(\pm)\,\frac{2\xi}{1+\xi^2}$

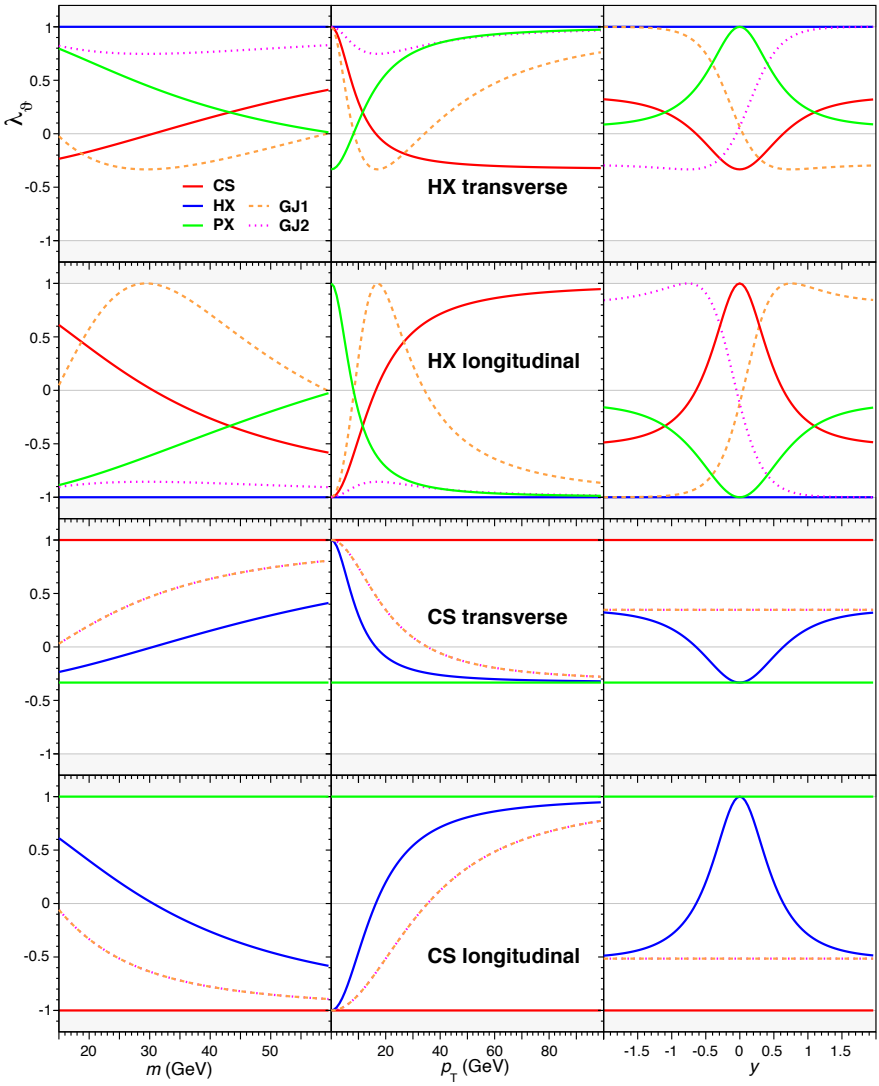

Fig. 2.9 Values of λ_ϑ observed in the five frames indicated in the legends, as a function of three kinematical observables (m, p_T, and y), when the particle is produced with a pure transverse or longitudinal polarization in the HX or CS frame. For each kinematical dependence, the other two variables are fixed to suitable values: m = 25 GeV, p_T = 20 GeV, and y = +0.5.

be observed in a "natural" frame, is as important as measuring the values of the parameters themselves, in view of ensuring unambiguous progress in the physics understanding. Furthermore, if different experimental or theoretical analyses adopt different "points of view", the resulting variations in the results can make a rigorous comparison very difficult or even impossible, as will be discussed in Section 2.14.

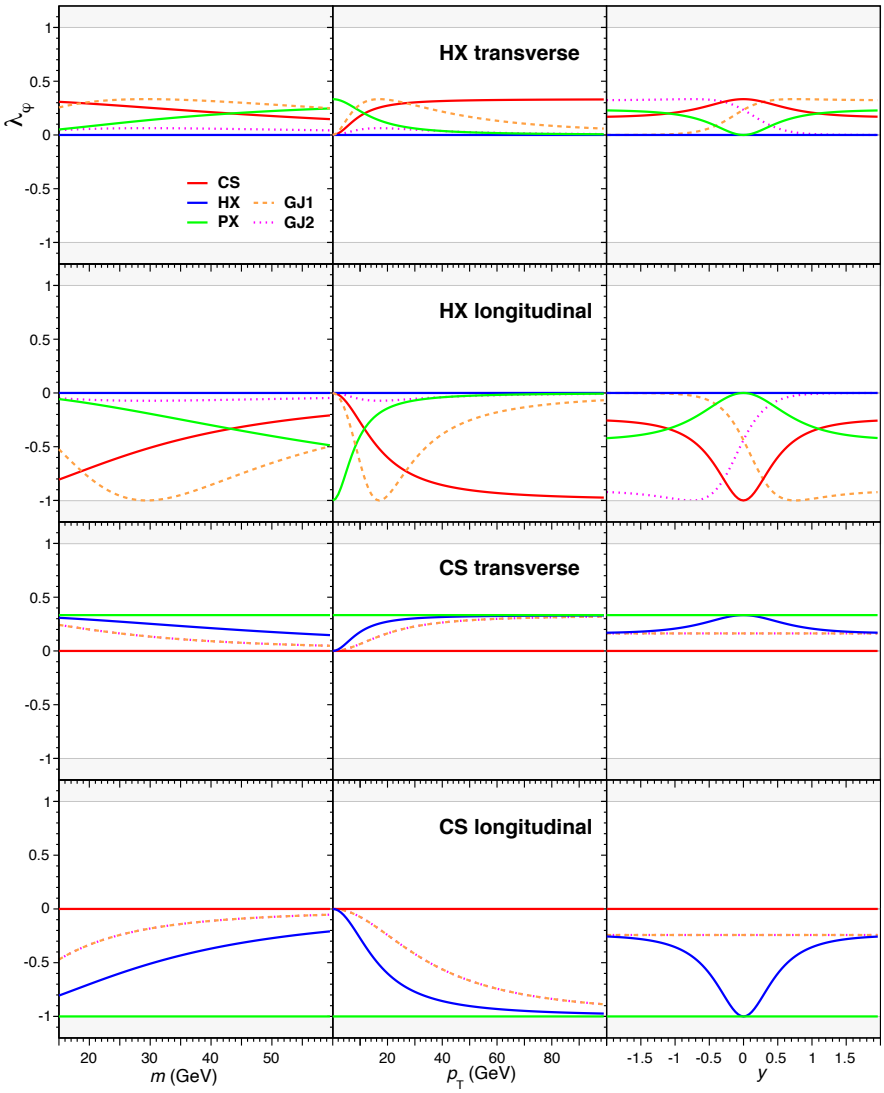

Fig. 2.10 Values of λ_φ observed in five reference frames, for the same scenarios and conditions of Fig. 2.9.

2.10 The meaning of $\lambda_{\vartheta\varphi}$

It is easy to recognize in Figs. 2.9, 2.10, and 2.11 examples of the previously-mentioned artificial p_L-asymmetries, arising from the convention that the "first" beam is always the one positively oriented in the laboratory, at both positive and negative p_L. All shape parameters measured in the GJ1 and GJ2 frames change sig-

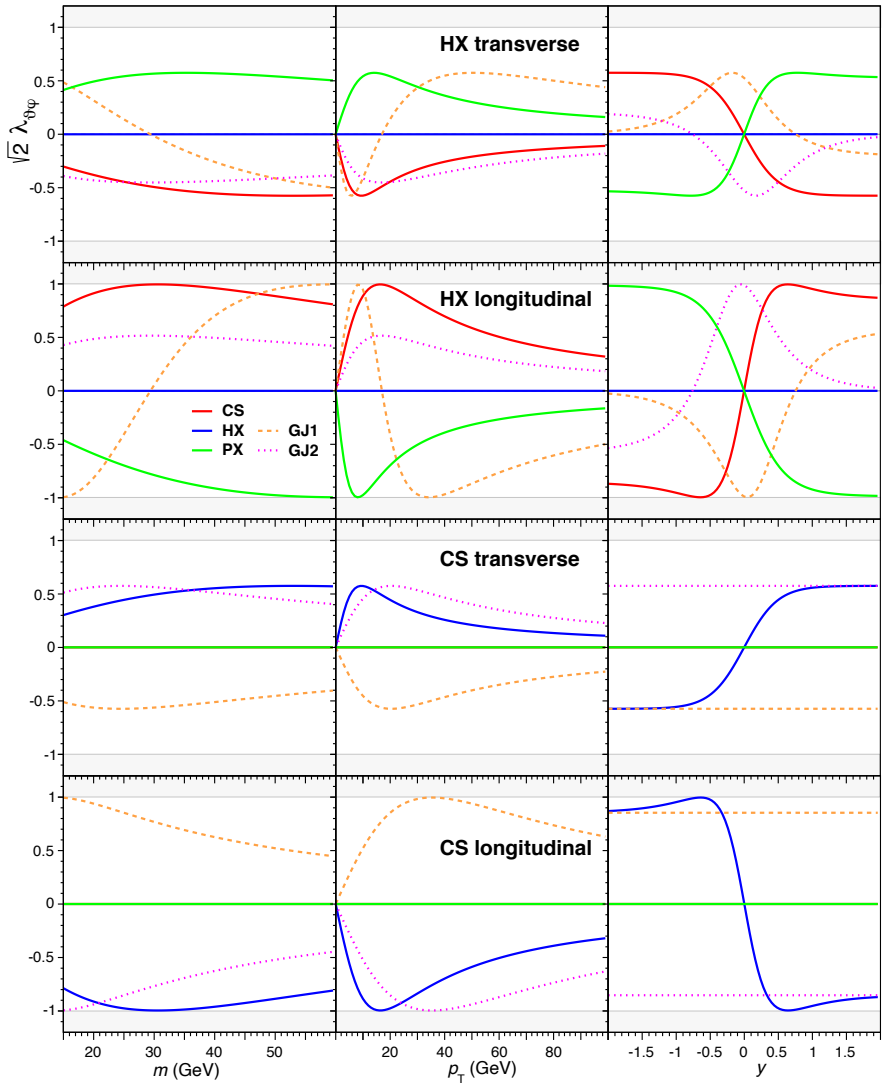

Fig. 2.11 Values of $\lambda_{\vartheta\varphi}$ observed in five reference frames, for the same scenarios and conditions of Fig. 2.9.

nificantly from positive to negative rapidity when the natural frame is the HX frame, because the angle δ with respect to the HX axis is not only different for the GJ1 and GJ2 axes, but also (not only for a sign) for y and $-y$, according to the formulas of Table 2.1. If, instead, the polarization is natural in the CS or PX frames, the GJ1 and GJ2 frames are completely equivalent, given that the CS and PX axes are (the two orthogonal) bisectors of the GJ1 and GJ2 polarization axes.

One feature common to all frames is the potential change of sign of $\lambda_{\vartheta\varphi}$ from positive to negative rapidity. All these p_{L}-asymmetries can be eliminated with the symmetrization procedure described in Section 2.2, consisting in the exchange of roles of the two colliding hadrons when going from positive to negative rapidity. The result, illustrated in Fig. 2.12, is that the negative-rapidity part of each function becomes the mirror reflection of the positive-rapidity part.

As mentioned in Section 2.6, this symmetrization does not eliminate the dependence of the sign of $\lambda_{\vartheta\varphi}$ on the y axis convention, so that it remains necessary to report the convention used in the measurement or computation. Besides ensuring that we are not missing a minus sign when comparing several results, in certain situations the symmetrization procedure is a mandatory step.

Indeed, analyses of particle polarizations made by experiments at high-energy colliders, such as ATLAS and CMS, are frequently made in kinematic intervals defined in terms of *absolute* rapidity, $|y|$, merging events from the symmetric ranges $-y_2 < y < -y_1$ and $y_1 < y < y_2$. In these cases, the p_{L}-asymmetry leads to an exact cancellation of $\lambda_{\vartheta\varphi}$, preventing the experiment from providing relevant information on this polarization parameter. This artificial elimination of $\lambda_{\vartheta\varphi}$ from the data analysis represents a significant loss of information and a distortion of the physical content of the measurement.

To illustrate this fact, we will study a simple case of frame rotation leading to a nonzero $\lambda_{\vartheta\varphi}$ value. This was not the case in the examples of Figs. 2.4–2.7, where the 90° rotation maintained the initial $\lambda_{\vartheta\varphi} = 0$ (Eq. 2.13). Any other rotation angle produces the desired effect. Choosing for example $\delta = -45°$ and a natural transverse polarization, we obtain in the new frame the "tilted" shape represented in Fig. 2.13-left.

In fact, as will be discussed in Chapter 3, $\lambda_{\vartheta\varphi}$ can be seen to parametrize a *tilt* of the distribution with respect to a configuration where the reference axes xyz are principal axes of symmetry of its shape. This explains why an originally "symmetric" distribution, like the one corresponding to a natural polarization, does not acquire a $\lambda_{\vartheta\varphi} \neq 0$ value with a 90° rotation.

The angular momentum composition of the state changes in the following way in the transformation (remembering that, for a frame rotation of −45°, the "projection" operation defined in Eq. 1.1 requires considering an angle $\vartheta = +45°$ with respect to the projection axis):

$$|1,\pm1\rangle \quad \xrightarrow{-45°} \quad \frac{1}{2}\left(1 \pm \frac{\sqrt{2}}{2}\right)|1,+1\rangle \pm \frac{1}{2}|1,0\rangle + \frac{1}{2}\left(1 \mp \frac{\sqrt{2}}{2}\right)|1,-1\rangle\,. \quad (2.29)$$

The comparison with Eqs. 2.16 and 2.17 illustrates how the existence of a "tilt" is related to the conditions $a_0 \neq 0$ and $a_{+1} \neq a_{-1}$, which lead, as seen in Eq. 1.13, to $\lambda_{\vartheta\varphi} \neq 0$. Using either Eq. 1.13, with the component amplitudes just shown, or Eq. 2.13, one finds $\lambda'_{\vartheta} = \lambda'_{\varphi} = 1/5$ and $\lambda'_{\vartheta\varphi} = 2/5$.

Figure 2.13-right shows the effect of the exact cancellation of $\lambda'_{\vartheta\varphi}$ that occurs artificially when the measurement is made integrating over p_{L}-symmetric intervals, without a corresponding re-definition of the orientation of the y' axis when going

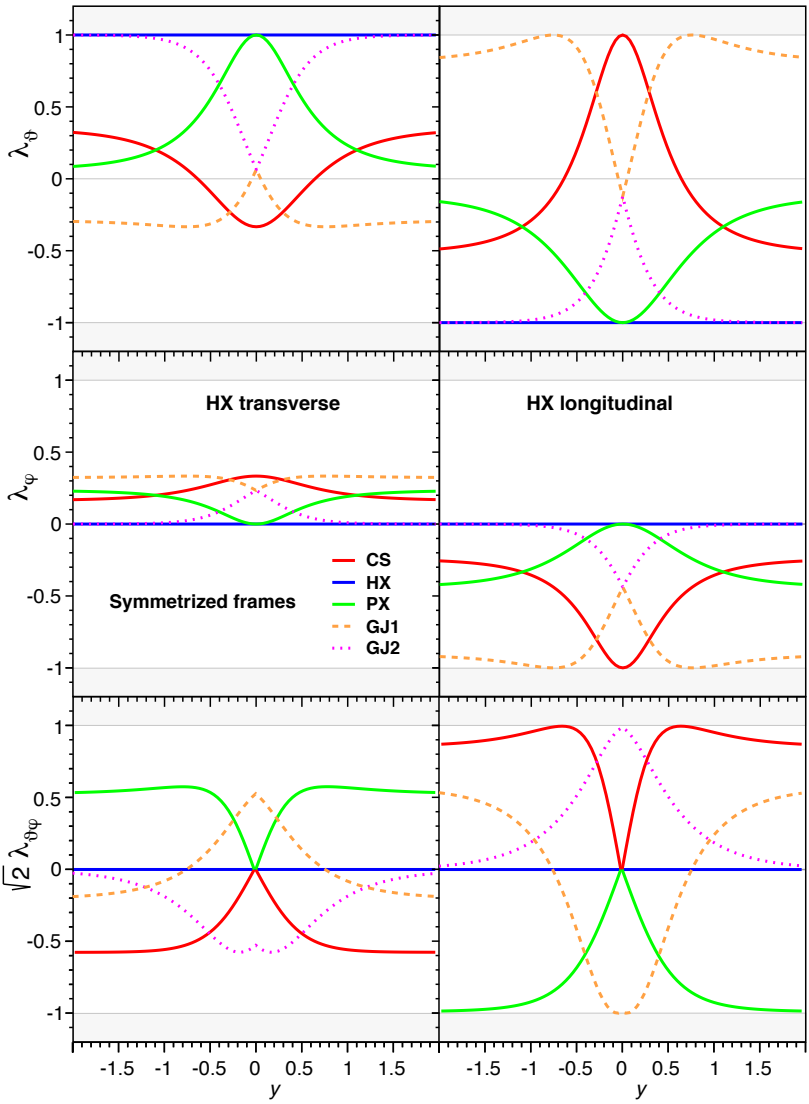

Fig. 2.12 Rapidity dependences of λ_ϑ, λ_φ, and $\lambda_{\vartheta\varphi}$ in the five polarization frames, re-defined by exchanging the names of h_1 and h_2 when going from positive to negative rapidity. The curves are the same as in the previous figures for $y > 0$, while for $y < 0$ they become a mirror reflection of the positive-rapidity part.

from $p_L > 0$ to $p_L < 0$. With vanishing $\lambda'_{\vartheta\varphi}$, no "tilt" is visible. Above all, the shape of the distribution changes dramatically.

The corresponding change in the $W(\cos\vartheta', \varphi')$ distribution, as can be measured by an experiment, is shown in Fig. 2.14. The original distribution, correctly reflect-

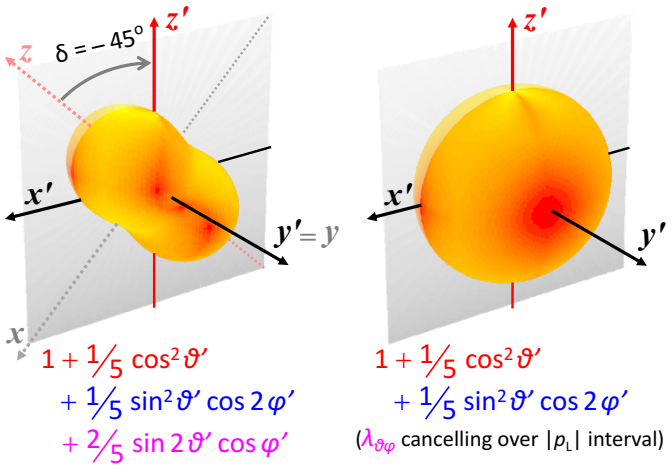

Fig. 2.13 The decay distribution of a transversely polarized vector particle as seen in the frame $x'y'z'$, rotated by $\delta = -45°$ with respect to the natural polarization frame xyz. We show the full three-parameter physical distribution on the left and, on the right, the distribution with $\lambda'_{\vartheta\varphi}$ artificially set to zero, characterized by a rotational invariance with respect to the y' axis.

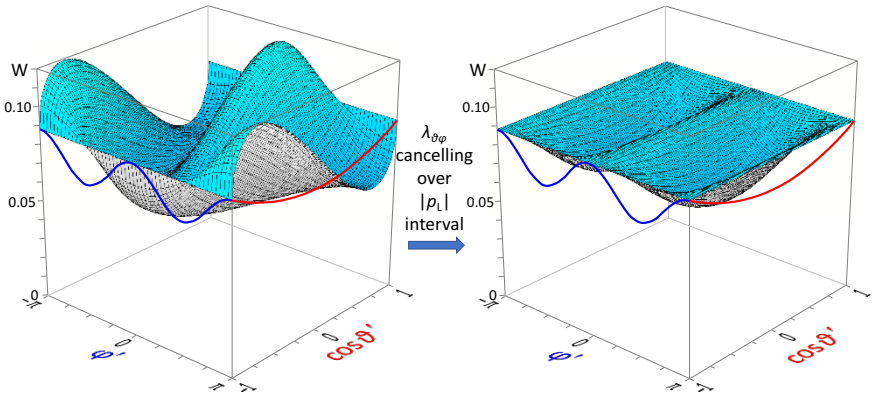

Fig. 2.14 The angular decay distributions $W(\cos\vartheta', \varphi')$ (with their one-dimensional projections) corresponding to the two cases shown in the previous figure.

ing the underlying angular momentum configuration of the decaying state, shows a strong correlation between the $\cos\vartheta'$ and φ' functional dependences. For example, when sliced at fixed values of φ', the distribution changes very significantly its $\cos\vartheta'$ pattern, varying from $\propto 1 + 1/3 \sin 2\vartheta'$ at $\varphi = 0$ to $\propto 1 - 1/3 \sin 2\vartheta'$ at $\varphi = \pm\pi$. In fact, $\lambda_{\vartheta\varphi}$ can also be interpreted as the parameter that describes the *intercorrelated* changes of modulations of the polar and azimuthal angle dependences, which is what motivates its notation. The "artificial" distribution in Fig. 2.14-right no longer reflects those correlations: for any fixed value of φ', the polar dependence remains

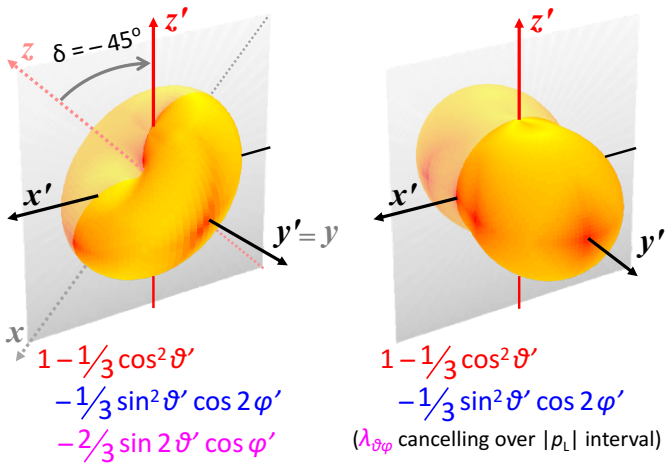

Fig. 2.15 Same as Fig. 2.13, for the case of a natural longitudinal polarization.

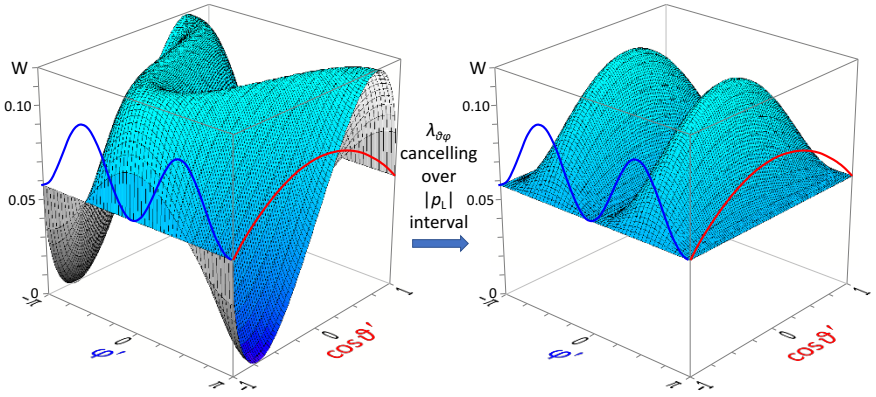

Fig. 2.16 Same as Fig. 2.14, for the case of a natural longitudinal polarization.

of the kind $\propto 1 + \alpha \cos^2 \vartheta'$, with a φ'-dependent coefficient α. The projected polar and azimuthal distributions remain identical before and after the $|p_L|$-integration "mistake", as they do not depend on $\lambda_{\vartheta\varphi}$ (Eqs. 2.14 and 2.15).

Figures 2.15 and 2.16 show the effects of the $\lambda'_{\vartheta\varphi}$ cancellation in the case of a longitudinally polarized state, which transforms as

$$|1,0\rangle \quad \xrightarrow{-45^\circ} \quad -\frac{1}{2}\,|1,+1\rangle \;+\; \frac{\sqrt{2}}{2}\,|1,0\rangle \;+\; \frac{1}{2}\,|1,-1\rangle\,, \tag{2.30}$$

leading to a decay distribution with $\lambda'_\vartheta = \lambda'_\varphi = -1/3$ and $\lambda'_{\vartheta\varphi} = -2/3$.

We mentioned how the peculiar $\cos\vartheta'$ vs. φ' correlation is lost when $\lambda_{\vartheta\varphi}$ is cancelled, but it is also interesting to note that the maximum variation of the

$W(\cos\vartheta', \varphi')$ function is significantly reduced. For example, the function presented in Fig. 2.16-left retains the same maximum, $3/(8\,\pi)$, and minimum, zero, of the distribution before rotation (Fig. 2.7-left), while the distribution in Fig. 2.16-right has a much higher minimum, $3/(16\,\pi)$; the physical modulations were *smeared* because of the loss of $\lambda_{\vartheta\varphi}$. This means that, contrary to what one could naively expect, an analysis of experimental data that reduces the number of free parameters from three to two by allowing for the cancellation of $\lambda_{\vartheta\varphi}$ will not achieve a more significant measurement. On the contrary, the result will be, in general, a *less* significant experimental characterization of the decay distribution.

The artificial cancellation of $\lambda_{\vartheta\varphi}$ is above all a conceptual problem, for both experimental and theoretical analyses. In fact, it can even be seen as a violation of the basic principle of rotational invariance. The number of events where the lepton is emitted within a given solid angle cannot change by spatial rotation and, therefore, the maximum and minimum of the distribution are rotation invariants. The artificial redistribution of events in the $\lambda_{\vartheta\varphi}$-suppressed distribution violates such invariance, leading to a serious loss of physical information and preventing meaningful interpretations of the results.

In both examples considered, the rotation leads to $\lambda'_{\vartheta} = \lambda'_{\varphi}$. If, moreover, we now impose $\lambda'_{\vartheta\varphi} = 0$, a *further* rotation of the axes *by any angle* δ will lead to *unchanged* anisotropy parameters, because $\Lambda' = 0$: the distribution becomes artificially frame-independent. We conclude that, without the knowledge of the value of $\lambda_{\vartheta\varphi}$, it is not possible to transform the angular distribution measured in one frame into what would be measured in another frame, and attempts to do so will lead to paradoxical results.

It should be clear from these examples that when the parameter $\lambda_{\vartheta\varphi}$ is ignored, in analyses opting for one-dimensional determinations of λ_{ϑ} and λ_{φ} (Eqs. 2.14 and 2.15) or considering $|p_{\mathrm{L}}|$ intervals without suitably adjusting the y-axis orientation, the result of the measurement will only represent a smeared picture of reality and its physical interpretation will be limited or ambiguous.

2.11 The role of the azimuthal anisotropy

We will now consider a concrete experimental example to illustrate the practical relevance of some of the concepts presented in the previous sections. Our aim is to show how measurements that ignore the intrinsic multidimensionality of the decay angular distribution, in particular by only reporting the polar angle distribution, and only in one single reference frame, might lead to ambiguous physical interpretations regarding the polarization of the particle.

The measurement of the polarization of J/ψ mesons promptly produced in pp collisions at 1.96 TeV, reported by the CDF Collaboration [4], provides a good example to illustrate the importance of measuring both the polar and the azimuthal anisotropies. The CDF analysis only considered the polar angle dimension, $\cos\vartheta$,

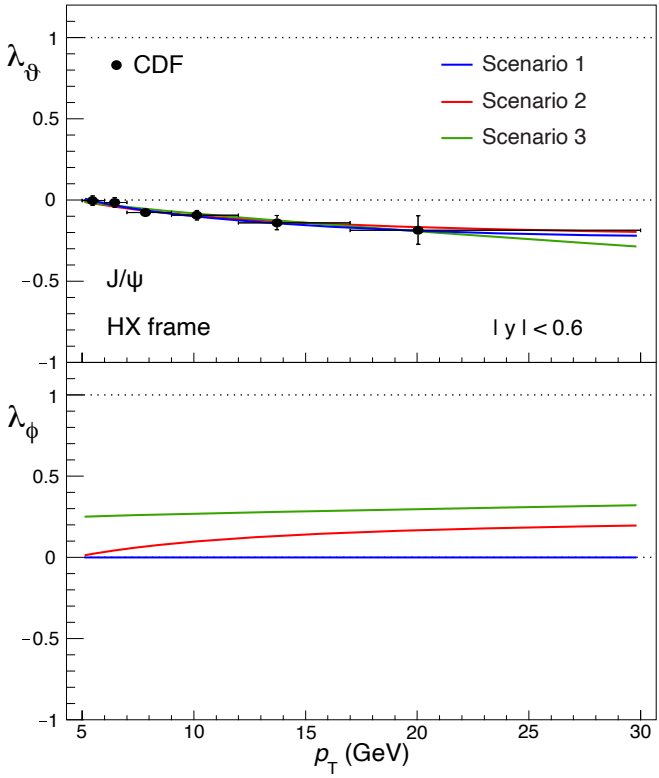

Fig. 2.17 Top: the polar anisotropy parameter in the helicity frame, $\lambda_\vartheta^{\rm HX}$, of promptly produced J/ψ mesons, as a function of $p_{\rm T}$ and in the $|y| < 0.6$ range, as reported by CDF [4] (circles) and as determined in the three fundamentally different production scenarios described in the text (curves). Bottom: the azimuthal anisotropy parameter computed in the same three production scenarios.

integrating over the azimuthal component of the decay; furthermore, the results were exclusively presented in the helicity frame.

The top panel of Fig. 2.17 presents the $p_{\rm T}$ dependence of the parameter λ_ϑ in the helicity frame, $\lambda_\vartheta^{\rm HX}$, as reported by CDF, in the rapidity range $|y| < 0.6$. Overlaid in the same figure we show three curves, representing three rather different physical scenarios. The first scenario, represented by the blue curve, assumes that the J/ψ polarization is natural in the HX frame, so that the decay angular distribution has no azimuthal anisotropy, $\lambda_\varphi^{\rm HX} = 0$. In the second scenario, represented by the red curve, the polarization is assumed to be natural in the CS frame, $\lambda_\varphi^{\rm CS} = 0$, with $\lambda_\vartheta^{\rm CS}$ varying from zero to +0.5 as $p_{\rm T}$ increases from zero to 30 GeV. Without an accompanying measurement of the azimuthal anisotropy, these two scenarios, leading to identical λ_ϑ trends vs. $p_{\rm T}$, are indistinguishable. The third scenario assumes that a certain fraction of the J/ψ mesons is produced fully transversely polarized with respect to the HX frame, the remaining fraction also being fully transversely polarized, but

with respect to the CS frame. The green curve represents this third scenario, in the case where the fraction of transversely polarized mesons in the HX frame decreases with p_T, from 30% to 15% in the p_T range from 5 to 20 GeV. All three options are perfectly compatible with the published data points. The bottom panel of Fig. 2.17 shows the parameter λ_φ in the helicity frame, calculated for each of the three scenarios. The significantly different trends vs. p_T illustrates how a measurement of λ_φ would resolve these three scenarios and allow us to know the true nature of the polarization.

Given that no azimuthal anisotropy measurement was reported and that only one frame was considered in the analysis, the experimental result is equally well compatible with physical interpretations representing very different fundamental scenarios of quarkonium production. In particular, the weak longitudinal polarization measured in the HX frame may actually be the reflection of a natural transverse polarization (as in the scenarios 2 and 3, represented by the red and green curves).

When the event sample is small, it may be tempting to opt for a simplified analysis using only the one-dimensional polar projection of the decay distribution. However, it is important to keep in mind that this choice implicitly imposes some hypothesis regarding the distribution of the integrated azimuthal variable and might lead to an ambiguous measurement, preventing model-independent interpretations.

2.12 Frame-dependence of the experimental acceptance

As anticipated in Section 1.5, one of the difficulties of an experimental analysis is that the low detection efficiency of low-momentum leptons strongly reduces the population of accepted events in certain regions of the angular phase space and an accurate efficiency correction is needed.

With respect to the simplified, one-dimensional example seen in the previous chapter, the reality of a polarization measurement is even more challenging, because the correction must reflect correlations, induced by the experimental selections, between the two angular coordinates $\cos\vartheta$ and φ; moreover, the acceptance sculpting of the event distribution depends, like the physical polarization, on the reference frame and on the kinematic domain (p_T and rapidity).

Figure 2.18 illustrates these features by showing, in three different frames, the two-dimensional efficiency maps corresponding to the same experimental filter already considered in the example of Section 1.5, where we only addressed the polar anisotropy in the HX frame. As in that case, both leptons from the J/ψ decay are required to have p_T larger than approximately 3 GeV, following the efficiency described by the "ideal" curve of Fig. 1.8. The J/ψ mesons are generated in the p_T range $9 < p_T < 12$ GeV and in two different rapidity windows, $|y| < 1$ and $3 < |y| < 4$.

The acceptance maps in the three frames are very different, regarding the shapes and the kinematic dependences. In the midrapidity bin, the HX and PX maps (very similar to one another, as expected in this limit) depend on the two angular coordinates in an almost uncorrelated way: in these frames the main effect of the ex-

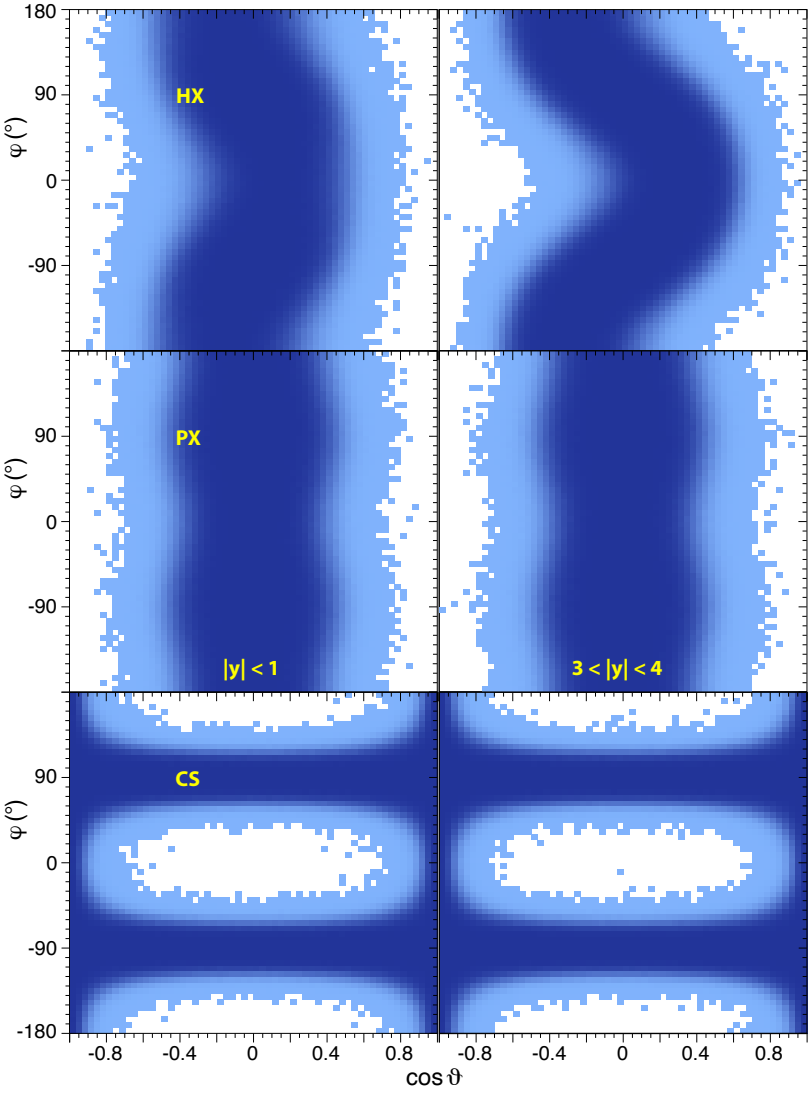

Fig. 2.18 Two-dimensional acceptance and efficiency maps in the HX (top), PX (middle), and CS (bottom) frames, for J/ψ mesons produced with $9 < p_{\mathrm{T}} < 12$ GeV and $|y| < 1$ (left) or $3 < |y| < 4$ (right). The decay leptons must have $p_{\mathrm{T}} \gtrsim 3$ GeV to be detected. The darker is the shade of a cell, the higher is its population.

perimental selections is a strong modulation in the variable $\cos\vartheta$, whose domain becomes restricted to the central range, while almost no dependence on φ is induced.

In remarkable contrast, in the CS frame the regions of zero acceptance are "internal" to the angular domain and centred at specific combinations of the two variables,

($\cos\vartheta = 0, \varphi = 0$) and ($\cos\vartheta = 0, \varphi = \pm 180°$, so that an integration over either $\cos\vartheta$ or φ seemingly removes such "holes": when the two projected one-dimensional distributions are observed, one gets the false impression that a better coverage is obtained in the CS frame than in the HX frame. On the contrary, this characteristic actually makes the CS frame a more difficult case for the measurement, because, as will be discussed in the next section, neglecting such strongly correlated acceptance limitations can produce much more important biases than in the HX frame, reducing the sensitivity to the true underlying polarization. At more forward rapidity, also the map in the HX frame shows a definite correlation between the modulations of the two variables.

Interestingly, the PX frame remains immune to such correlations and, moreover, the map is practically rapidity-independent (like the one in the CS frame). These features make the PX frame a particularly useful choice from the point of view of the experimental analysis. Applying the corrections to the observed event distribution using the PX efficiency maps, as per-event lookup tables (independently of what frame is used for the determination of the physical angular distribution) has the advantage that the rapidity dimension does not need to be scanned as finely as in the HX frame, while the almost total independence of the $\cos\vartheta$ coverage on φ attenuates residual correlation effects: in the CS frame, the minimization of such effects requires the use of maps with a fine binning in the two variables (especially in φ).

It remains true that the dependence on p_{T} is significant and not removable with a simple choice: the lower the J/ψ p_{T} (for a given requirement on the lepton p_{T}), the larger become the zero-acceptance regions. Figure 2.19 illustrates this fact, showing how the efficiency map in the PX frame for $|y| < 1$ changes inside the p_{T} interval

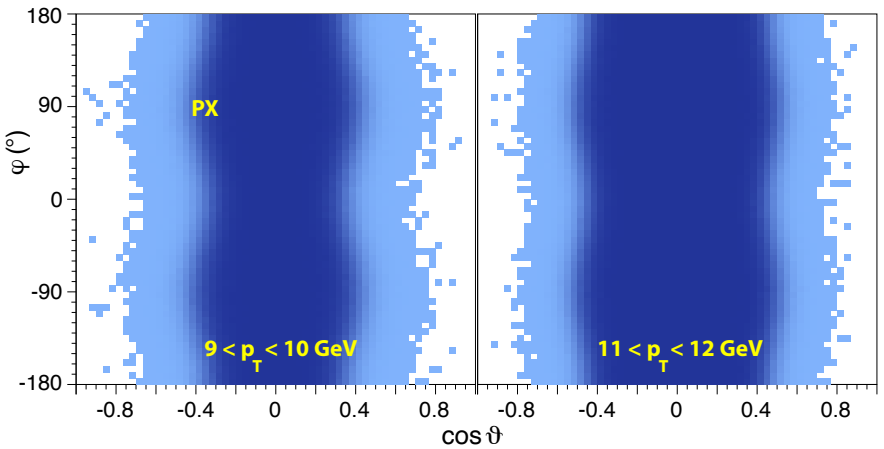

Fig. 2.19 Two-dimensional acceptance and efficiency maps in the PX frame, for J/ψ mesons produced in the kinematic domain $|y| < 1$, with $9 < p_{\mathrm{T}} < 10$ GeV (left) and $11 < p_{\mathrm{T}} < 12$ GeV (right). The decay leptons must have $p_{\mathrm{T}} \gtrsim 3$ GeV to be detected. The darker is the shade of a cell, the higher is its population.

considered in the example of Fig. 2.18: towards the lower end of the interval ($9 < p_T < 10$ GeV), the $\cos\vartheta$ coverage is visibly narrower than towards the higher end ($11 < p_T < 12$ GeV).

This observation reinforces a consideration found more than once in this book: it is important to minimize the size of the integrated kinematic domain where the angular distribution is measured. In fact, correcting the event distribution by an average acceptance value when the shape of the acceptance function, and even its support, vary inside the considered kinematic interval should only be considered as a first approximation to reduce the complexity of the analysis: its effects on the resulting angular distribution, especially towards the most critical regions at the border of the acceptance coverage, must be carefully checked with detailed systematic studies.

2.13 Caveats of one-dimensional analyses

We will now see that, besides the problems of ambiguous interpretations mentioned in Section 2.11, experimental data analyses ignoring the azimuthal dimension can actually lead to *wrong* results. The reason is that, as we have just seen in the previous section, the detection acceptance is usually a strongly intercorrelated function of the two variables, $\cos\vartheta$ and φ. In other words, the experimental efficiency relevant for the projected $\cos\vartheta$ distribution depends on the φ distribution, i.e. on λ_φ, and vice-versa.

If the φ dimension is integrated out and ignored, the resulting λ_ϑ measurement becomes strongly dependent on the specific "prior hypothesis" (implicitly) made for the angular distribution in the Monte Carlo simulation. Since we do not know which distribution should be used in the generation of the acceptance maps, as this is one of the observables that we should be measuring, it is clear that the raw measured data will be wrongly corrected, leading to a wrong result.

Figure 2.20 offers a concrete and quantitative illustration of this kind of mistake, using the J/ψ scenario considered in Section 2.12, with $9 < p_T < 12$ GeV and $|y| < 1$. The starting point is the generation of J/ψ events with fully longitudinal polarization in the HX frame, $\lambda_\vartheta^{HX} = -1$ and $\lambda_\varphi^{HX} = 0$. As we have shown in Fig. 2.6, if we generate J/ψ mesons with fully longitudinal polarization in one frame (the HX frame, in our example) and then measure the angular distributions in another frame, approximately perpendicular to the first one (the CS frame), then we should see a distribution with λ_ϑ^{CS} and λ_φ^{CS} approaching, respectively, $+1$ and -1. This is expected, of course, under the assumption that the measurement is correctly done.

If, instead, the $\cos\vartheta$ acceptance correction is made using a one-dimensional projection, using Monte Carlo events generated with a flat azimuthal dependence, we get the blue points shown in the top panels of Fig. 2.20, well compatible with unpolarized production. The rather strong anisotropies that we should see (and are seen if the measurement is made in the HX frame, as shown in the bottom panels) were completely smeared away by the incorrect analysis procedure. The result is a reflec-

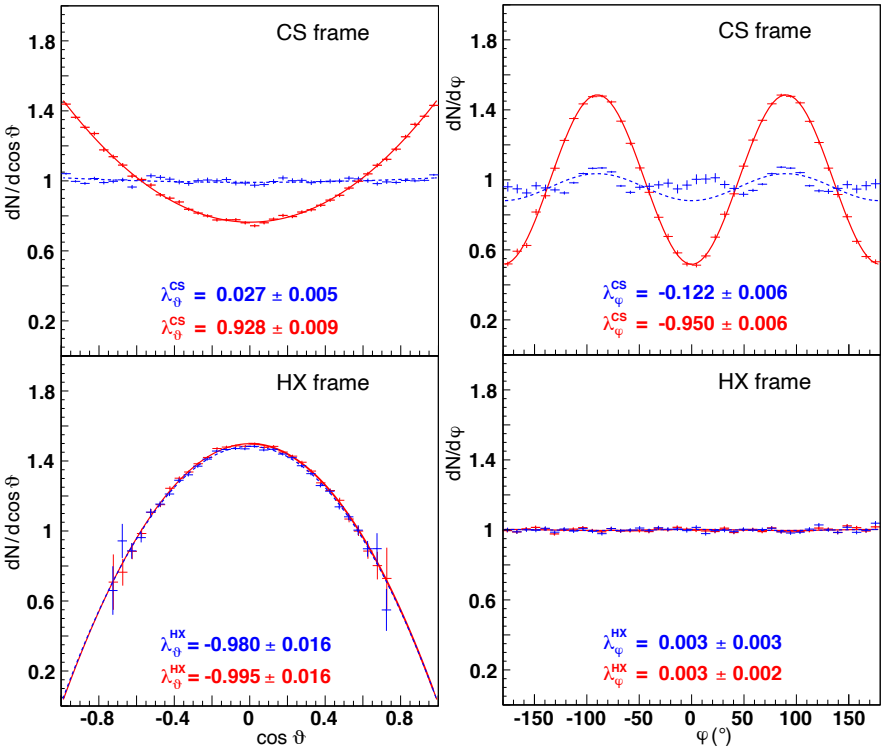

Fig. 2.20 Angular distributions, in $\cos\vartheta$ (left) and φ (right), measured in the CS (top) and HX (bottom) frames, for J/ψ mesons generated as fully longitudinal in the HX frame, $\lambda_\vartheta^{HX} = -1$ and $\lambda_\varphi^{HX} = 0$, using one-dimensional projections with acceptance corrections without (blue) and with (red) iterative reweighing.

tion of the polarization assumption used in the Monte Carlo simulation and not of the real physics we would like to probe.

Analyses that, for some reason, need to use one-dimensional projections rather than the two-dimensional distribution can still provide correct results, under the condition of using the correct distributions in the generation of the acceptance map. That is something that can be achieved through an iterative procedure, where the Monte Carlo simulation is repeated, each time using the previously measured distributions as inputs for the new iteration.

The procedure is effective only if the measurement is sufficiently precise to clearly indicate the polarization to be assumed in the first step of the iteration. In this case, the successful application of this iterative acceptance correction leads to the results shown by the red points in Fig. 2.20, indicating, as expected, a strong transverse polarization in the CS frame. The small difference between the obtained values ($\lambda_\vartheta^{CS} = 0.93$ and $\lambda_\varphi^{CS} = -0.95$) and the values expected in a frame exactly orthogonal to the natural one ($\lambda_\vartheta^{CS} = 1$ and $\lambda_\varphi^{CS} = -1$) reflects the fact that the angle

between the two frames, for the phase space domain used in the example ($|y| < 1$ and $9 < p_{\mathrm{T}} < 12$ GeV), is around 83°.

The iterative reweighing procedure means that, effectively, a two-dimensional acceptance correction is being made, avoiding the bias mentioned above. In other words, when only a one-dimensional projected distribution is measured, the detector acceptance description must, nevertheless, be maintained multi-dimensional. One-dimensional acceptance corrections or "template" fits should be avoided, unless the Monte Carlo is (when possible and effective) iteratively re-generated with the correct distribution of the variables that have been integrated out (which has, therefore, to be measured anyway).

Concrete examples of data analyses where the one-dimensional approach should be avoided are searches for physics beyond the Standard Model (SM). Precision measurements of the parity-violating asymmetry in Drell–Yan production have been made at the LHC [5–7], using simulations based on the SM to account for the detector's acceptance and efficiency, and to integrate over the unobserved azimuthal dimension. Given the high level of theory-data agreement, these analyses can be considered as successful tests of the SM. But can one then proceed and translate these precision measurements into limits on the existence of "new physics" (e.g. a Z' resonance), expected to be found in the form of *small* deviations with respect to the standard Drell–Yan distributions? If the detection acceptance as a function of $\cos\vartheta$ depends on the generated φ distribution, and the searched-for new phenomenon leads to a distribution (slightly) different from the one assumed in the simulation, then the acceptance correction will be (slightly) biased, hampering the sensitivity of this kind of analyses, given that, as shown in the example above, the results will be "attracted" to the distributions assumed in the event generation. Statistically meaningful limits on models predicting new physics should be provided by one-dimensional analyses only after careful consideration of suitable variations of the assumed azimuthal anisotropies

2.14 The importance of being lucky

We will now develop a concept introduced at the end of Section 2.9: the way the observed polarization depends on the frame and, consequently, on the production kinematics has important consequences when the results reported by several experiments are compared to each other. Comparisons between experiments are common practice to verify the reliability of the measurements in high-energy physics and one of the main reasons justifying the existence of several similar experiments at particle accelerators, such as CDF and D0 at the Tevatron, or ATLAS and CMS at the LHC. However, they are not immune to difficulties and require some care, especially when the experiments cover different acceptance windows in rapidity and/or p_{T}.

We will illustrate this problem by considering a toy Monte Carlo simulation where we generated events with J/ψ and Υ(1S) mesons naturally polarized in the CS frame: $\lambda_{\varphi}^{\mathrm{CS}} = \lambda_{\vartheta\varphi}^{\mathrm{CS}} = 0$. For each meson, we consider in turn the two cases of extreme

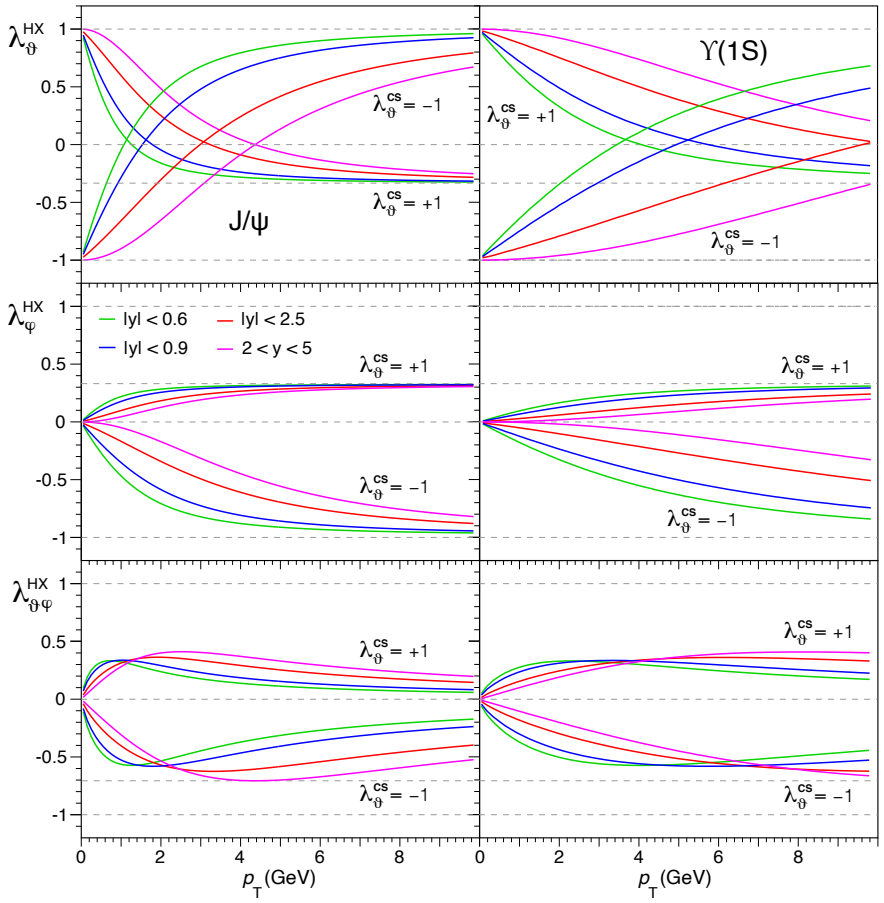

Fig. 2.21 Polarization parameters λ_ϑ (top), λ_φ (middle), and $\lambda_{\vartheta\varphi}$ (bottom) measured in the HX frame, as a function of p_T and for several rapidity ranges (different line colours), for J/ψ (left) and Υ(1S) (right) mesons generated with natural transverse ($\lambda_\vartheta^\mathrm{CS} = +1$) or longitudinal ($\lambda_\vartheta^\mathrm{CS} = -1$) polarizations in the CS frame. As a function of p_T over mass, the two columns would look identical.

polarizations: fully transverse ($\lambda_\vartheta^\mathrm{CS} = +1$) and fully longitudinal ($\lambda_\vartheta^\mathrm{CS} = -1$). Obviously, if the experiments perform their measurements in the CS frame, they should all measure identical values, $\lambda_\varphi = \lambda_{\vartheta\varphi} = 0$ and either $\lambda_\vartheta = +1$ or -1, depending on the sample, independently of p_T and rapidity. But what will the measurements look like if the experiments, covering several different rapidity windows, decide to use the HX frame in their analyses?

Figure 2.21 shows the results obtained, as a function of p_T, by four hypothetical experiments, covering the rapidity intervals $|y| < 0.6$, $|y| < 0.9$, $|y| < 2.5$, and $2 < y < 5$, respectively corresponding to the acceptances of CDF, ALICE (central barrel), ATLAS/CMS, and LHCb. Only at $p_\mathrm{T} = 0$, an extreme limit where the HX and CS frames coincide, would the experiments agree with each other. For other p_T

regions, each experiment would obtain a different result, not only in magnitude but also in the trends vs. p_{T}.

Furthermore, the rapidity distributions of the events collected ("reconstructed") by the experiments are affected by detection efficiencies, so that it is very difficult to infer the (original) λ_ϑ value that would have been observed in the CS frame. In other words, it is not easy to transform the λ parameters measured in one frame into those that would have been measured in another frame, given that this transformation can only be accurately made if one accounts for the rapidity distribution of the detected particles. It is much more accurate (and easier) to directly provide the measurements in two frames.

The spread among the four patterns displayed in Fig. 2.21 for each generated case shows that an "unlucky" choice of the frame used in the analyses of the data may lead to very misleading conclusions regarding the consistency of the experimental results. Results that are perfectly identical in the "right frame" (the frame closest to the "natural" one) will, instead, look completely inconsistent with each other when the analyses are made in the "wrong frame". We also recognize the "extrinsic" kinematic dependences created by a specific frame choice, already seen in Section 2.9, which produce a misleadingly complex view of the underlying constant-polarization scenario and would, moreover, mask or strongly distort a possible intrinsic momentum dependence of the natural polarization.

The example now described shows, furthermore, that these spurious effects are even detector-dependent, given that they change with the kinematical range covered by the detector; additionally, in a real measurement the result should also reflect the variation of the detection efficiencies within that acceptance window (a detail not explicitly considered in here).

If we reverse the roles of the frames, so that the events are generated in the CS frame and the measurements are made in the HX frame, the figures showing the λ_ϑ and λ_φ parameters remain identical, as already seen in Figs. 2.9 and 2.10.

Only the $\lambda_{\vartheta\varphi}$ parameter changes, flipping its sign, because it depends on the sign of the rotation angle, δ, between the two frames, as shown in the frame-transformation relations reported in Eq. 2.13, in Section 2.7. As already mentioned in Section 2.9, it is because the transformation relations depend on the production kinematics that we see the ("extrinsic") acceptance-dependent kinematic behaviours; in the case of transformations between the CS and HX frames, in particular, the kinematic dependence can be found on the first row of Table 2.1.

Naturally, the effects of the acceptances and efficiencies of the experiments are not only relevant when comparing multiple measurements with each other but also when comparing measurements with theory calculations. The polarization results reported by the experiments reflect the specific population of events that they have collected, which will depend on the detection and trigger efficiencies, and on the event selection criteria used in the analysis. When the polarization depends significantly on the kinematics, two experiments covering the same phase space window may find different average polarizations, if their differential acceptances are sufficiently different. This problem can be minimized by providing the measurements, and the corresponding theoretical predictions, in several narrow kinematic intervals.

2.15 More general frame transformations

Even if it is true that, in inclusive production studies, a change of polarization frame is always a rotation in the production plane (around the y axis) — because experimentally the only possible and/or sensible choices of polarization axis belong to this plane — for theoretical and modelling considerations it can sometimes be useful to also know what happens to the parameters of the angular distribution under the other two kinds of rotations, those around the x and z axes.

In this section we provide the mathematical expressions of these transformations, also extending those seen in Section 2.7 to consider all eight coefficients of the general distribution of a possibly parity-violating decay (Section 1.11). Besides the rotation matrix $R_y(\delta)$, reported in Eq. 2.8, the derivation also uses the corresponding matrices of the rotations around the x and z axes, defined with the conventions already discussed:

$$R_x(\delta) = \begin{pmatrix} 1 & 0 & 0 \\ 0 & \cos\delta & \sin\delta \\ 0 & -\sin\delta & \cos\delta \end{pmatrix}, \quad R_z(\delta) = \begin{pmatrix} \cos\delta & \sin\delta & 0 \\ -\sin\delta & \cos\delta & 0 \\ 0 & 0 & 1 \end{pmatrix}. \tag{2.31}$$

All angular expressions appearing in Eq. 1.29 are suitable combinations of the components of the vector $\hat{r} = (\sin\vartheta\cos\varphi, \sin\vartheta\sin\varphi, \cos\vartheta)$. The corresponding components in terms of the coordinates in the new frame are obtained from the inverse rotation $\hat{r} = R^{\mathrm{T}}_{x|y|z}(\delta)\,\hat{r}'$. After these are replaced in Eq. 1.29, the resulting expression can be ordered by collecting the eight terms in $\cos^2\vartheta'$, $\sin^2\vartheta'\cos 2\varphi'$, $\sin 2\vartheta'\cos\varphi'$, $\sin^2\vartheta'\sin 2\varphi'$, $\sin 2\vartheta'\sin\varphi'$, $\cos\vartheta'$, $\sin\vartheta'\cos\varphi'$, and $\sin\vartheta'\sin\varphi'$, whose coefficients, divided by the $\cos\vartheta'$- and φ'-independent term, give the expressions of the eight transformed shape parameters.

The result of a rotation around the y axis, extending the relations of Eq. 2.13, can be shown using a matrix form to describe the linear part of the parameter transformation, scaled by an overall factor, common to all transformed parameters, expressing the nonlinear part.

The "parity-conserving parameters" transform as

$$\begin{pmatrix} \lambda'_\vartheta \\ \lambda'_\varphi \\ \lambda'_{\vartheta\varphi} \\ \lambda^{\perp\prime}_\varphi \\ \lambda^{\perp\prime}_{\vartheta\varphi} \end{pmatrix} = \frac{1}{1+\Lambda_y} \begin{pmatrix} 1-\frac{3}{2}\sin^2\delta & \frac{3}{2}\sin^2\delta & \frac{3}{2}\sin 2\delta & 0 & 0 \\ \frac{1}{2}\sin^2\delta & 1-\frac{1}{2}\sin^2\delta & -\frac{1}{2}\sin 2\delta & 0 & 0 \\ -\frac{1}{2}\sin 2\delta & \frac{1}{2}\sin 2\delta & \cos 2\delta & 0 & 0 \\ 0 & 0 & 0 & \cos\delta & -\sin\delta \\ 0 & 0 & 0 & \sin\delta & \cos\delta \end{pmatrix} \begin{pmatrix} \lambda_\vartheta \\ \lambda_\varphi \\ \lambda_{\vartheta\varphi} \\ \lambda^\perp_\varphi \\ \lambda^\perp_{\vartheta\varphi} \end{pmatrix}, \tag{2.32}$$

while the "parity-violating parameters" transform as

$$\begin{pmatrix} A'_\vartheta \\ A'_\varphi \\ A^{\perp\prime}_\varphi \end{pmatrix} = \frac{1}{1+\Lambda_y} \begin{pmatrix} \cos\delta & \sin\delta & 0 \\ -\sin\delta & \cos\delta & 0 \\ 0 & 0 & 1 \end{pmatrix} \begin{pmatrix} A_\vartheta \\ A_\varphi \\ A^\perp_\varphi \end{pmatrix}, \tag{2.33}$$

with

$$\Lambda_y = \frac{1}{2}(\lambda_\vartheta - \lambda_\varphi)\sin^2\delta - \frac{1}{2}\lambda_{\vartheta\varphi}\sin 2\delta\,. \tag{2.34}$$

The coefficients of the parity-conserving terms and those of the parity-violating terms follow two decoupled transformations, except for the common $1/(1+\Lambda_y)$ factor, which depends on the λ_ϑ, λ_φ, and $\lambda_{\vartheta\varphi}$ parameters.

The corresponding equations for a rotation around the x axis are

$$\begin{pmatrix} \lambda'_\vartheta \\ \lambda'_\varphi \\ \lambda'_{\vartheta\varphi} \\ \lambda^{\perp\prime}_\varphi \\ \lambda^{\perp\prime}_{\vartheta\varphi} \end{pmatrix} = \frac{1}{1+\Lambda_x} \begin{pmatrix} 1-\frac{3}{2}\sin^2\delta & -\frac{3}{2}\sin^2\delta & 0 & 0 & -\frac{3}{2}\sin 2\delta \\ -\frac{1}{2}\sin^2\delta & 1-\frac{1}{2}\sin^2\delta & 0 & 0 & -\frac{1}{2}\sin 2\delta \\ 0 & 0 & \cos\delta & -\sin\delta & 0 \\ 0 & 0 & \sin\delta & \cos\delta & 0 \\ \frac{1}{2}\sin 2\delta & \frac{1}{2}\sin 2\delta & 0 & 0 & \cos 2\delta \end{pmatrix} \begin{pmatrix} \lambda_\vartheta \\ \lambda_\varphi \\ \lambda_{\vartheta\varphi} \\ \lambda^\perp_\varphi \\ \lambda^\perp_{\vartheta\varphi} \end{pmatrix} \tag{2.35}$$

and

$$\begin{pmatrix} A'_\vartheta \\ A'_\varphi \\ A^{\perp\prime}_\varphi \end{pmatrix} = \frac{1}{1+\Lambda_x} \begin{pmatrix} \cos\delta & 0 & -\sin\delta \\ 0 & 1 & 0 \\ \sin\delta & 0 & \cos\delta \end{pmatrix} \begin{pmatrix} A_\vartheta \\ A_\varphi \\ A^\perp_\varphi \end{pmatrix}, \tag{2.36}$$

with

$$\Lambda_x = \frac{1}{2}(\lambda_\vartheta + \lambda_\varphi)\sin^2\delta + \frac{1}{2}\lambda^\perp_{\vartheta\varphi}\sin 2\delta\,. \tag{2.37}$$

Finally, a rotation around the z axis transforms the shape parameters as

$$\begin{pmatrix} \lambda'_\vartheta \\ \lambda'_\varphi \\ \lambda'_{\vartheta\varphi} \\ \lambda^{\perp\prime}_\varphi \\ \lambda^{\perp\prime}_{\vartheta\varphi} \end{pmatrix} = \begin{pmatrix} 1 & 0 & 0 & 0 & 0 \\ 0 & \cos 2\delta & 0 & \sin 2\delta & 0 \\ 0 & 0 & \cos\delta & 0 & \sin\delta \\ 0 & -\sin 2\delta & 0 & \cos 2\delta & 0 \\ 0 & 0 & -\sin\delta & 0 & \cos\delta \end{pmatrix} \begin{pmatrix} \lambda_\vartheta \\ \lambda_\varphi \\ \lambda_{\vartheta\varphi} \\ \lambda^\perp_\varphi \\ \lambda^\perp_{\vartheta\varphi} \end{pmatrix} \tag{2.38}$$

and

$$\begin{pmatrix} A'_\vartheta \\ A'_\varphi \\ A^{\perp\prime}_\varphi \end{pmatrix} = \begin{pmatrix} 1 & 0 & 0 \\ 0 & \cos\delta & \sin\delta \\ 0 & -\sin\delta & \cos\delta \end{pmatrix} \begin{pmatrix} A_\vartheta \\ A_\varphi \\ A^\perp_\varphi \end{pmatrix}. \tag{2.39}$$

The rotation around the z axis is a linear and orthogonal transformation of the parameters. Contrary to what happens in the rotations around the y and x axes, no parameter-dependent factor $1\,/\,(1+\Lambda)$ appears in front of the matrices and the transformation of the parity-violating coefficients is now completely independent of the values of the parity-conserving ones. In fact, an equivalent way to obtain the expression of the transformed distribution is to simply transform the angle φ, leaving unchanged the values of the shape parameters, given that a rotation around z is a shift in the azimuthal orientation:

$$\begin{aligned} W(\cos\vartheta',\varphi') \propto\ & \frac{1}{(3+\lambda_\vartheta)}\Big[1+\lambda_\vartheta\cos^2\vartheta' \\ & +\lambda_\varphi\sin^2\vartheta'\cos 2(\varphi'+\delta)+\lambda_{\vartheta\varphi}\sin 2\vartheta'\cos(\varphi'+\delta) \\ & +\lambda_\varphi^\perp\sin^2\vartheta'\sin 2(\varphi'+\delta)+\lambda_{\vartheta\varphi}^\perp\sin 2\vartheta'\sin(\varphi'+\delta) \\ & +2A_\vartheta\cos\vartheta'+2A_\varphi\sin\vartheta'\cos(\varphi'+\delta)+2A_\varphi^\perp\sin\vartheta'\sin(\varphi'+\delta)\Big]. \end{aligned} \tag{2.40}$$

Several of the relations reported above — actually, all of them in the case of Eqs. 2.38 and 2.39 — are orthogonal or have orthogonal components (the linear parts, excluding the factor $1\,/\,(1+\Lambda)$), suggesting the existence of combinations of parameters that remain unchanged in the transformation and, therefore, characterize the decay distribution in a frame-independent way. These "invariant" shape parameters are very interesting and their meanings and possible uses will be the subjects of Chapters 3 and 4.

The most general frame transformation, changing the directions of all three reference axes, can be parametrized as the sequence of three rotations, which can be chosen according to different conventions. We will consider the convention illustrated in Fig. 2.22.

All rotations are applied to the axes of the frame being transformed. The first one is made around the z axis, by an angle ψ, defined so that the rotated y axis becomes perpendicular to the final z axis and will now belong to the final xy plane (a). Then follows a rotation around the new y axis, by an angle ζ, bringing the initial and final polarization axes (z) and, therefore, the two xy planes, to coincide (b). A rotation around z by ω completes the transformation, giving the x and y axes their wanted directions (c).

The order of the sequence of rotations is important because, in general, rotations do not commute. In order to describe all possible rotations with a $1:1$ correspondence, the angles ψ, ζ, and ω must belong to, respectively, the domains $[-\pi,\pi]$, $[0,\pi]$, and $[-\pi,\pi]$, that is, ζ can be seen as a "polar" variable and the other two as "azimuthal" variables.

The overall transformation of the shape parameters can be calculated as a function of the angles with the usual procedure, considering now the product matrix $R_z(\omega)\,R_y(\zeta)\,R_z(\psi)$, or by applying, in the correct sequence, the parameter transformations given by Eqs. 2.32, 2.33, 2.38, and 2.39. The resulting transformations for the parity-conserving and parity-violating parameters are presented in Table 2.2.

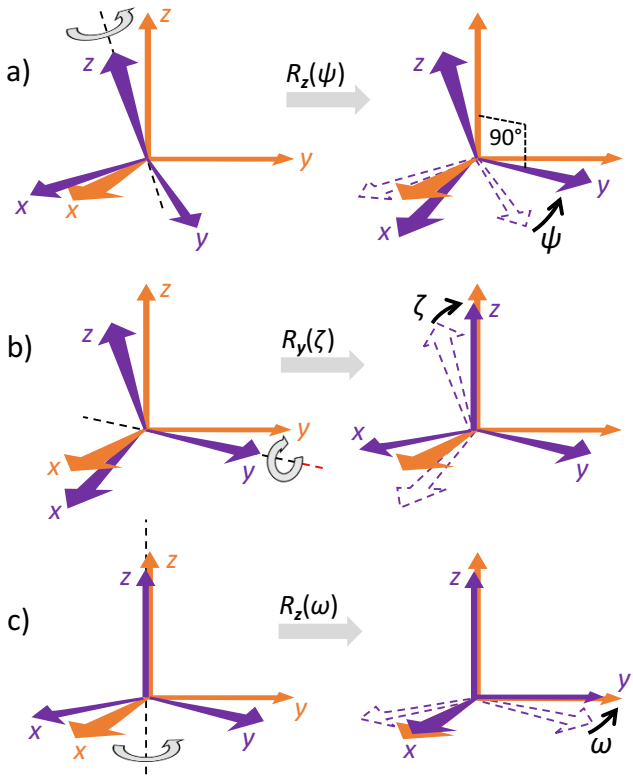

Fig. 2.22 The three consecutive steps of a generic transformation that brings a given initial polarization frame (violet) to coincide with the final one (orange).

2.16 Recapitulation

When the decaying particle is observed in "inclusive" production processes of the kind $h_1h_2 \to V + X$, with unpolarized targets and/or beams, and without including any information on X in the analysis, the polarization axis z is naturally defined by the experiment as belonging to the production plane, formed by the h_1 and h_2 momentum directions in the V rest frame (Fig. 2.1). The y axis is taken perpendicular to this plane, which, therefore, coincides with the zx plane.

The different options for defining the z axis reflect the simplest topologies of the elementary production processes, as seen in the V rest frame (Figs. 2.2 and 2.3): the two Gottfried–Jackson (GJ1 and GJ2) axes (defined as the momentum directions of h_1 and h_2) approximate the natural quantization axes in certain t/u-channel processes, the helicity (HX) axis (direction of V itself) the one of s-channel processes, and the Collins–Soper (CS) axis (direction of the relative motion of h_1 and h_2) is best suited for $2 \to 1$ processes (where no X is produced); the perpendicular helicity (PX) axis is exactly perpendicular to the CS axis.

Table 2.2 Matrix presenting the rotated parity-conserving (λ_i', top rows) and parity-violating (A_i', bottom rows) parameters of the decay distribution as linear combinations of the initial parameters (λ_i and A_i, columns). For instance, $A_\vartheta' = A_\vartheta/(1+\Lambda) \times \cos\zeta + A_\varphi/(1+\Lambda) \times \sin\zeta\cos\psi + A_\varphi^\perp/(1+\Lambda) \times \sin\zeta\sin\psi$. In the $1/(1+\Lambda)$ factor, the term Λ is a function of the λ_i parameters: $\Lambda = 1/2\left(\lambda_\vartheta - \lambda_\varphi\cos 2\psi - \lambda_\varphi^\perp \sin 2\psi\right)\sin^2\zeta - 1/2\left(\lambda_{\vartheta\varphi}\cos\psi + \lambda_{\vartheta\varphi}^\perp \sin\psi\right)\sin 2\zeta$.

	$\frac{\lambda_\vartheta}{1+\Lambda}\times$	$+\frac{\lambda_\varphi}{1+\Lambda}\times$	$+\frac{\lambda_{\vartheta\varphi}}{1+\Lambda}\times$	$+\frac{\lambda_\varphi^\perp}{1+\Lambda}\times$	$+\frac{\lambda_{\vartheta\varphi}^\perp}{1+\Lambda}\times$
$\lambda_\vartheta' =$	$1-\frac{3}{2}\sin^2\zeta$	$\frac{3}{2}\sin^2\zeta\cos 2\psi$	$\frac{3}{2}\sin 2\zeta\cos\psi$	$\frac{3}{2}\sin^2\zeta\sin 2\psi$	$\frac{3}{2}\sin 2\zeta\sin\psi$
$\lambda_\varphi' =$	$\frac{1}{2}\sin^2\zeta\cos 2\omega$	$\left(1-\frac{1}{2}\sin^2\zeta\right)\cos 2\omega\cos 2\psi$ $-\cos\zeta\sin 2\omega\sin 2\psi$	$-\frac{1}{2}\sin 2\zeta\cos 2\omega\cos\psi$ $+\sin\zeta\sin 2\omega\sin\psi$	$\left(1-\frac{1}{2}\sin^2\zeta\right)\cos 2\omega\sin 2\psi$ $+\cos\zeta\sin 2\omega\cos 2\psi$	$-\frac{1}{2}\sin 2\zeta\cos 2\omega\sin\psi$ $-\sin\zeta\sin 2\omega\cos\psi$
$\lambda_{\vartheta\varphi}' =$	$-\frac{1}{2}\sin 2\zeta\cos\omega$	$\frac{1}{2}\sin 2\zeta\cos\omega\cos 2\psi$ $-\sin\zeta\sin\omega\sin 2\psi$	$\cos 2\zeta\cos\omega\cos\psi$ $-\cos\zeta\sin\omega\sin\psi$	$\frac{1}{2}\sin 2\zeta\cos\omega\sin 2\psi$ $+\sin\zeta\sin\omega\cos 2\psi$	$\cos 2\zeta\cos\omega\sin\psi$ $+\cos\zeta\sin\omega\cos\psi$
$\lambda_\varphi^{\perp\prime} =$	$-\frac{1}{2}\sin^2\zeta\sin 2\omega$	$-\left(1-\frac{1}{2}\sin^2\zeta\right)\sin 2\omega\cos 2\psi$ $-\cos\zeta\cos 2\omega\sin 2\psi$	$\frac{1}{2}\sin 2\zeta\sin 2\omega\cos\psi$ $+\sin\zeta\cos 2\omega\sin\psi$	$-\left(1-\frac{1}{2}\sin^2\zeta\right)\sin 2\omega\sin 2\psi$ $+\cos\zeta\cos 2\omega\cos 2\psi$	$\frac{1}{2}\sin 2\zeta\sin 2\omega\sin\psi$ $-\sin\zeta\cos 2\omega\cos\psi$
$\lambda_{\vartheta\varphi}^{\perp\prime} =$	$\frac{1}{2}\sin 2\zeta\sin\omega$	$-\frac{1}{2}\sin 2\zeta\sin\omega\cos 2\psi$ $-\sin\zeta\cos\omega\sin 2\psi$	$-\cos 2\zeta\sin\omega\cos\psi$ $-\cos\zeta\cos\omega\sin\psi$	$-\frac{1}{2}\sin 2\zeta\sin\omega\sin 2\psi$ $+\sin\zeta\cos\omega\cos 2\psi$	$-\cos 2\zeta\sin\omega\sin\psi$ $+\cos\zeta\cos\omega\cos\psi$

	$\frac{A_\vartheta}{1+\Lambda}\times$	$+\frac{A_\varphi}{1+\Lambda}\times$	$+\frac{A_\varphi^\perp}{1+\Lambda}\times$
$A_\vartheta' =$	$\cos\zeta$	$\sin\zeta\cos\psi$	$\sin\zeta\sin\psi$
$A_\varphi' =$	$-\sin\zeta\cos\omega$	$\cos\zeta\cos\omega\cos\psi - \sin\omega\sin\psi$	$\cos\zeta\cos\omega\sin\psi + \sin\omega\cos\psi$
$A_\varphi^{\perp\prime} =$	$\sin\zeta\sin\omega$	$-\cos\zeta\sin\omega\cos\psi - \cos\omega\sin\psi$	$-\cos\zeta\sin\omega\sin\psi + \cos\omega\cos\psi$

The convention for the positive orientation of the z axis must be specified in the presence of parity-violating effects, because it determines the resulting sign of the asymmetry parameter A_ϑ. More generally, the y axis orientation must be part of the definition of the polarization frame, as the sign of $\lambda_{\vartheta\varphi}$ depends on it and even changes from the positive to the negative p_{L} (or rapidity) hemispheres if the y axis does not, at the same time, flip its orientation: any integration over a symmetric p_{L} range would artificially suppress $\lambda_{\vartheta\varphi}$, creating serious ambiguities of interpretation (Figs. 2.13–2.16), as well as incompatibilities between measurements and/or predictions using different conventions. In collisions between identical hadrons, or whenever the underlying processes are insensitive to the exchange of the colliding objects, the GJ1 and GJ2 frames have to be carefully defined and used: in each of them, the values of all anisotropy parameters can change radically, not only in sign, with the change of sign of p_{L}, as a consequence of having arbitrarily chosen one or the other beam to define the z axis (Figs. 2.9–2.11). "Symmetrised" versions of these two frames, changing the beam taken as reference when p_{L} changes sign, may be adopted to eliminate this spurious asymmetry (Fig. 2.12). It is anyhow essential, for any faithful comparison to models or to other measurements, that all adopted conventions are well indicated.

Any change of polarization frame, among the ones above defined, is a rotation in the production plane (around the y axis) by an angle δ (Eq. 2.13), which depends on the transverse and longitudinal momentum components of V, normalized by its mass m. The anisotropy parameters depend strongly on the frame. For example, a fully longitudinal polarization ($\lambda_\vartheta = -1$, $\lambda_\varphi = \lambda_{\vartheta\varphi} = 0$) in the HX frame becomes transverse ($\lambda_\vartheta = +1$) in the CS frame (or vice versa) when, for $p_{\mathrm{T}} >> m$, the two z axes are almost perpendicular (Figs. 2.6 and 2.7). Importantly, a strong azimuthal anisotropy (in this case, $\lambda_\varphi = -1$ in the frame where $\lambda_\vartheta = +1$) clearly denotes that the chosen frame is not providing the simplest and more natural physical picture. This means that the azimuthal anisotropy is a crucial observable: when it is integrated out (a compromise adopted in some measurements based on relatively small data samples) it is generally not possible to establish if the measured polar anisotropy (λ_ϑ) represents the "natural" polarization characterizing the production of V in the given conditions, unless the measurement is repeated in different frames.

More generally, the measurement of a moderate and p_{T}-dependent λ_ϑ, as the one that was reported by CDF in the HX frame (Fig. 2.17), may be interpreted, without an accompanying λ_φ measurement, with an infinite and continuous range of fundamental polarization hypotheses involving different natural frames.

Neglecting the azimuthal dimension also affects the reliability of the result, because, in the presence of acceptance correlations between the variables $\cos\vartheta$ and φ, the integration over φ can lead to completely different acceptance-corrected $\cos\vartheta$ distributions (and measured λ_ϑ values), depending on the hypothesis on the value of λ_φ used in the determination of the acceptance (Fig. 2.20).

The importance of these effects depends on the experiment. Moreover, not all frames are equally susceptible to them. For example, the minimum-lepton-p_{T} requirements sculpt the two-dimensional distribution in such a way that the HX frame (at high p_{T}) and the PX frame (also down to low p_{T}) show a minimal level of corre-

lation between the two angular variables (Figs. 2.18 and 2.19). A two-dimensional study of the acceptance effects should always be made, at least to assess or exclude possible correlations. Actually, the problem should be addressed in its even higher dimensionality, given that the $\cos\vartheta, \varphi$ acceptance sculpting depends on p_{T} and rapidity, and the correction of the data by a strongly non-uniform acceptance function, should be made avoiding integrations as much as possible.

Being the frame-rotation angle δ a function of the particle's laboratory momentum (Table 2.1), the anisotropy parameters have very different kinematic dependences in different frames. A constant polarization $\lambda_\vartheta = \pm 1$, $\lambda_\varphi = \lambda_{\vartheta\varphi} = 0$ observed when the measurement is made in the natural frame transforms into a complex pattern of p_{T} and rapidity dependent λ_ϑ, λ_φ, and $\lambda_{\vartheta\varphi}$ values, when a different frame is chosen (Figs. 2.9–2.11). Moreover, two experiments choosing the same frame, different from the natural one, will observe, in general, different results as a function of p_{T} if they integrate over rapidity (or vice versa), as a consequence of different rapidity (p_{T}) coverages and/or different detection efficiencies as function of rapidity (p_{T}): not only the simplicity of the underlying polarization scenario escapes observation, but seeming incompatibilities are found between measurements (Fig. 2.21). While, in principle, the choice of the frame is arbitrary, in practice there can exist a frame leading to significantly clearer and more informative physics results. This example shows the importance of using at least two alternative frame definitions in the analysis.

Frame transformations corresponding to rotations around an axis not coinciding with the y axis are not directly relevant for experimental analyses (for inclusive observations), but were provided in Section 2.15 for future reference in descriptions of phenomena involving deviations from purely planar processes, as when more than two final states are produced or the intrinsic transverse momentum of partons is taken into account (Chapter 5), as well as in indirect production via cascade decays (Chapter 6).

References

[1] K. Gottfried and J. D. Jackson, "On the connection between production mechanism and decay of resonances at high-energies", *Nuovo Cim.* **33** (1964) 309, doi:10.1007/BF02750195.

[2] J. C. Collins and D. E. Soper, "Angular distribution of dileptons in high-energy hadron collisions", *Phys. Rev. D* **16** (1977) 2219, doi:10.1103/PhysRevD.16.2219.

[3] E. Braaten, D. Kang, J. Lee, and C. Yu, "Optimal spin quantization axes for the polarization of dileptons with large transverse momentum", *Phys. Rev. D* **79** (2009) 014025, doi:10.1103/PhysRevD.79.014025, arXiv:0810.4506.

[4] CDF Collaboration, "Polarization of J/ψ and ψ(2S) mesons produced in $p\bar{p}$ collisions at $\sqrt{s}$ = 1.96 TeV", *Phys. Rev. Lett.* **99** (2007) 132001, doi:10.1103/PhysRevLett.99.132001, arXiv:0704.0638.

[5] CMS Collaboration, "Forward-backward asymmetry of Drell–Yan lepton pairs in pp collisions at $\sqrt{s}$ = 7 TeV", *Phys. Lett. B* **718** (2013) 752, doi:10.1016/j.physletb.2012.10.082, arXiv:1207.3973.

[6] ATLAS Collaboration, "Measurement of the forward-backward asymmetry of electron and muon pair-production in pp collisions at $\sqrt{s}$ = 7 TeV with the ATLAS detector", *JHEP* **09** (2015) 049, doi:10.1007/JHEP09(2015)049, arXiv:1503.03709.

[7] CMS Collaboration, "Forward-backward asymmetry of Drell–Yan lepton pairs in pp collisions at $\sqrt{s}$ = 8 TeV", *Eur. Phys. J. C* **76** (2016) 325, doi:10.1140/epjc/s10052-016-4156-z, arXiv:1601.04768.

Chapter 3
A frame-independent study of the angular distribution

In this chapter we continue our study of the dilepton decay distribution of a vector particle, introducing general frame-independent relations between the observable anisotropy parameters. Some of these relations reflect the geometrical properties of the distribution, including inequalities that delimit the allowed phase space of the anisotropy parameters, and the representation of the distribution in a "canonical" form.

The most interesting relation defines a rotation-invariant parameter expressing the intrinsic nature of the polarization, independently of the reference frame and even (as will be seen in the next chapter) of shape variations caused by the superposition of production processes.

We will address the following questions.

- What extreme physical values can be assumed by the anisotropy parameters λ_ϑ, λ_φ, $\lambda_{\vartheta\varphi}$, etc., and what angular momentum configurations do they correspond to?
- By what "trajectory" is the transformation from one frame to another represented inside the physical parameter space? What are the parameter combinations preserved by the transformation?
- How can the angular distribution, as a geometrical shape, be represented in terms of "absolute" shape parameters, independent of the reference axes?
- How can the concepts of "transverse" and "longitudinal" polarization (which, as defined in the previous chapter, seem to strongly depend on the reference frame) be expressed in a rotation-invariant way?
- Is it possible to define a frame-independent parity asymmetry?
- How can the repetition of the same measurement in more than one frame provide a cross check of the analysis procedure?

P. Faccioli and C. Lourenço, *Particle Polarization in High Energy Physics*,
Lecture Notes in Physics 1002,
https://doi.org/10.1007/978-3-031-08876-6_3

3.1 Is polarization a relative concept?

The careful definition of a system of reference axes is the first ingredient of a polarization measurement. The choice among several possible definitions is *arbitrary* in the sense that, regardless of how it is (properly) made, it always leads to a measurement retaining, at least potentially, the same amount of physical information. However, it must not be a random choice. As illustrated in the previous chapter, the measured values of the shape parameters defining the decay angular distribution depend strongly on the chosen frame and, consequently, on the decay particle's laboratory momentum, since the angle between two different frames is explicitly kinematics-dependent. One choice may lead to results showing a simpler kinematic pattern and allowing for a cleaner and more immediate physical interpretation, with respect to other choices. In the case of the decay of vector particles, the denominations themselves of transverse and longitudinal polarization, where a characteristic angular momentum projection originates from a specific kind of couplings between the involved particles, become *relative* to the chosen observation frame and can even switch their roles if the frame choice is particularly "unfortunate". As mentioned in Chapter 2, to provide all necessary ingredients for an unambiguous physical interpretation the analysis must consider alternative choices of the polarization frame and avoid blind simplifications (integrations, cancellations), which, especially in the less favourable frames, can lead to significant losses of information.

While the multidimensional and multi-frame method must remain the core of the measurement, we consider now a complementary approach, based on the existence of rotation-invariant relations between the shape parameters [1–7]. Such relations characterize the angular distribution independently of the chosen frame, directly reflecting the angular momentum projection along the natural quantization axis, even if a different axis was chosen for the measurement. In fact, the *natural* polarization of a particle is not a "relative" concept. In particular, as hereafter illustrated, it is possible to qualify the nature of the polarization of a vector particle as transverse or longitudinal in *absolute* terms, as an intrinsic property of the production mechanism and, as such, unaffected by the arbitrary choice of the quantization axis.

3.2 The borders of the physical domain

In the first part of this chapter we will consider, for simplicity, the case of a parity-conserving dilepton decay, exclusively and fully described by the λ_ϑ, λ_φ, and $\lambda_{\vartheta\varphi}$ parameters. We start by discussing the magnitude scale of the shape parameters, until here not explicitly addressed. For λ_ϑ, the values -1 and $+1$, corresponding to the fully longitudinal ($J_z = 0$) and transverse ($J_z = \pm 1$) cases, respectively, are the extremes of the physically allowed interval, as can be seen from the relation (Eq. 1.13)

$$\lambda_\vartheta = \frac{1 - 3\,|a_0|^2}{1 + |a_0|^2}\,, \tag{3.1}$$

where $|a_0|^2$ is the fraction of longitudinal polarization (with respect to the total sum of transverse and longitudinal components), thereby necessarily in the range 0–1.

Figures 2.10 and 2.11 suggest that also $|\lambda_\varphi|$ and $\sqrt{2}\,|\lambda_{\vartheta\varphi}|$ reach at most unity, while not demonstrating it in general, because they represent rather specific physics cases. Moreover, the three-dimensional $(\lambda_\vartheta, \lambda_\varphi, \sqrt{2}\,\lambda_{\vartheta\varphi})$ parameter domain certainly does not occupy the full cube $[-1,+1]^3$. The fully longitudinal polarization case provides a clear illustration of this statement. As seen in Eq. 1.13, when $\lambda_\vartheta = -1$, i.e. $|a_0| = 1$ and $a_{+1} = a_{-1} = 0$, λ_φ and $\lambda_{\vartheta\varphi}$ are necessarily zero: no azimuthal anisotropies are allowed when a fully longitudinal polarization is measured, meaning, moreover, that the analysis has "luckily" chosen an observation frame coinciding with the natural frame. Instead, in the transverse polarization case we already know, from the example of Eq. 2.17, that a measurement of $\lambda_\vartheta = +1$ may be accompanied by a large azimuthal anisotropy, $\lambda_\varphi = -1$, meaning that the polarization is natural, and actually fully transverse, in a frame perpendicular to the chosen one.

The shape of the allowed three-dimensional parameter space can be determined from Eq. 1.13. For each single subprocess (i) producing V in one given angular momentum composition, we obtain the following identities and inequalities (the latter two using the Schwarz inequality):

$$\begin{aligned}
1 \pm \lambda_\varphi^{(i)} &= (|a_{+1}^{(i)} \pm a_{-1}^{(i)}|^2 + 2\,|a_0^{(i)}|^2) \,/\, (\mathcal{N}^{(i)} + |a_0^{(i)}|^2)\,, \\
\lambda_\vartheta^{(i)} \pm \lambda_\varphi^{(i)} &= (|a_{+1}^{(i)} \pm a_{-1}^{(i)}|^2 - 2\,|a_0^{(i)}|^2) \,/\, (\mathcal{N}^{(i)} + |a_0^{(i)}|^2)\,, \\
|\lambda_{\vartheta\varphi}^{(i)}| &\le \sqrt{2}\;|a_0^{(i)}|\,|a_{+1}^{(i)} - a_{-1}^{(i)}| \,/\, (\mathcal{N}^{(i)} + |a_0^{(i)}|^2)\,, \\
|\lambda_{\vartheta\varphi}^{\perp(i)}| &\le \sqrt{2}\;|a_0^{(i)}|\,|a_{+1}^{(i)} + a_{-1}^{(i)}| \,/\, (\mathcal{N}^{(i)} + |a_0^{(i)}|^2)\,.
\end{aligned} \tag{3.2}$$

These, in turn, imply the following relations between the coefficients of the angular distribution:

$$\begin{aligned}
(1 - \lambda_\varphi^{(i)})^2 - (\lambda_\vartheta^{(i)} - \lambda_\varphi^{(i)})^2 &\ge 4\lambda_{\vartheta\varphi}^{(i)2}\,, \\
(1 + \lambda_\varphi^{(i)})^2 - (\lambda_\vartheta^{(i)} + \lambda_\varphi^{(i)})^2 &\ge 4\lambda_{\vartheta\varphi}^{\perp(i)2}\,.
\end{aligned} \tag{3.3}$$

To reach expressions valid for a generic superposition of production processes, we use Eq. 1.17 and the Schwarz inequality,

$$\left(\frac{\sum_{i=1}^n g^{(i)}\,X^{(i)}}{\sum_{i=1}^n g^{(i)}}\right)^2 \;\le\; \frac{\sum_{i=1}^n g^{(i)}\,X^{(i)2}}{\sum_{i=1}^n g^{(i)}}\,, \tag{3.4}$$

valid for $g^{(i)} > 0$. To eliminate from the expressions the parameter $\lambda_{\vartheta\varphi}^{\perp}$, assumed to be unobservable (as we are considering parity conserving processes in unpolarized collisions), we use the obvious relation $\lambda_{\vartheta\varphi}^{\perp(i)2} \ge 0$. In this way we obtain the following completely general inequalities:

$$\begin{aligned}
(1 - \lambda_\varphi)^2 - (\lambda_\vartheta - \lambda_\varphi)^2 &\ge 4\lambda_{\vartheta\varphi}^2\,, \\
1 + \lambda_\vartheta + 2\lambda_\varphi &\ge 0\,.
\end{aligned} \tag{3.5}$$

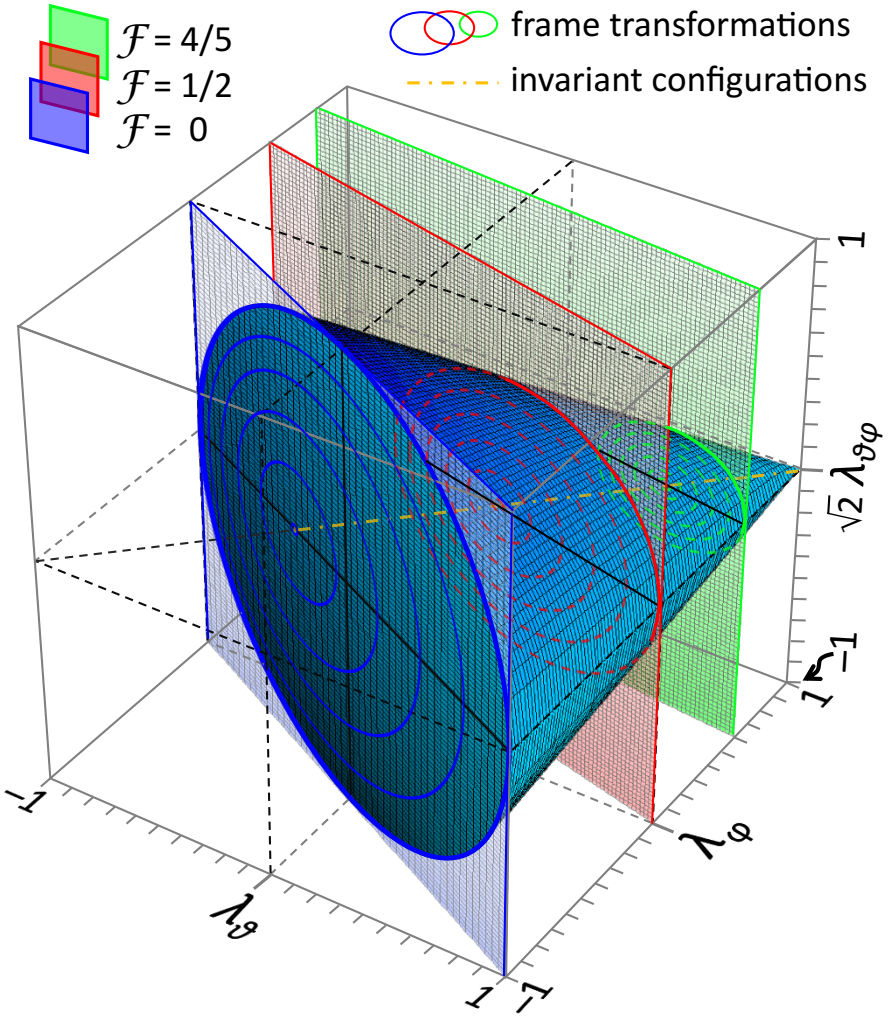

Fig. 3.1 The "invariant cone", defined by Eq. 3.5, enclosing the physically allowed values of the decay angular parameters λ_ϑ, λ_φ, and $\lambda_{\vartheta\varphi}$ in any reference frame. The three intersecting planes are defined by Eq. 3.7 for $\mathcal{F} = 0$ ("plane of the longitudinal polarizations", in blue, corresponding to the base of the cone), $\mathcal{F} = 1/2$ ("plane of the transverse polarizations", in red), and $\mathcal{F} = 4/5$ (green). Several possible frame-transformation trajectories belonging to the three planes are drawn in matching colours. The "line of the invariant configurations", in yellow, is the locus of points (Eq. 3.8) representing angular distributions that are identical in all polarization frames.

The first relation defines the space inside a circular conic surface, while the second selects the half-space on one side of a plane. Their intersection defines an oblique solid cone contained in the cube $[-1, +1]^3$, as shown in Fig. 3.1. The projections of this conic volume on the $(\lambda_\vartheta, \lambda_\varphi)$, $(\lambda_\vartheta, \sqrt{2}\,\lambda_{\vartheta\varphi})$, and $(\lambda_\varphi, \sqrt{2}\,\lambda_{\vartheta\varphi})$ planes are shown as grey areas in Fig. 3.2. They are described by the following sets of

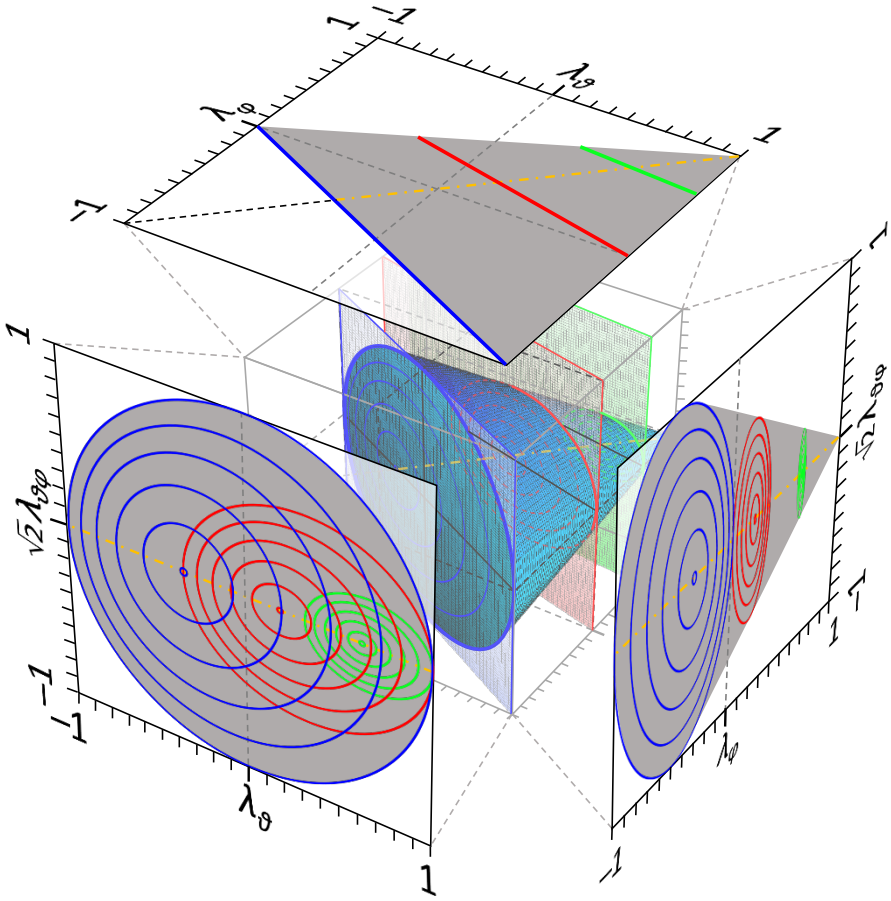

Fig. 3.2 The invariant parameter space as seen in the $(\lambda_\vartheta, \lambda_\varphi)$, $(\lambda_\vartheta,\ \sqrt{2}\lambda_{\vartheta\varphi})$ and $(\lambda_\varphi,\ \sqrt{2}\lambda_{\vartheta\varphi})$ planes. The projections of the invariant line and of the invariant planes and transformation trajectories shown in Fig. 3.1 are also drawn.

inequalities, in the three respective cases:

$$
\begin{aligned}
&|\lambda_\varphi| \le \frac{1}{2}\,(1+\lambda_\vartheta) \quad \text{and} \quad |\lambda_\vartheta| \le 1\,; \\
&\lambda_\vartheta^2 + 2\,\lambda_{\vartheta\varphi}^2 \le 1\,; \\
&|\lambda_{\vartheta\varphi}| \le \frac{1}{2}\,(1-\lambda_\varphi) \quad \text{and} \quad |\lambda_\varphi| \le 1\,, \\
&\qquad\qquad \text{with} \;\; (1+2\,\lambda_\varphi)^2 + 2\,\lambda_{\vartheta\varphi}^2 \le 1 \;\; \text{for} \;\; \lambda_\varphi < -1/3\,.
\end{aligned}
\tag{3.6}
$$

The relations of Eq. 3.5 are frame-independent, that is, the oblique cone of Figs. 3.1 and 3.2 represents the allowed parameter space in *any* polarization frame.

In other words, no frame rotation around the y axis ever leads to $(\lambda_\vartheta, \lambda_\varphi, \sqrt{2}\,\lambda_{\vartheta\varphi})$ values outside that volume.

3.3 Inside the parameter domain

A closer insight into the structure of the invariant domain can be obtained by studying the transformation of the shape parameters from one frame to another. The frame rotation described by Eq. 2.13 can be seen as a "trajectory" in the $(\lambda_\vartheta, \lambda_\varphi, \lambda_{\vartheta\varphi})$ space, parametrized by the variation of the rotation angle δ. While in principle δ can vary from 0 to 2π, it can be seen in Eq. 2.13 that the results of the transformation are fully invariant by a simultaneous change of sign of $\cos\delta$ and $\sin\delta$: therefore, the half interval $[0, \pi]$, for example, parametrizes all $(\lambda'_\vartheta, \lambda'_\varphi, \lambda'_{\vartheta\varphi})$ points reached by the transformation. This is due to the fact that in the considered, parity-conserving, case a parity-flip of the polarization axis has no observable consequence. As seen in the more general transformations reported in Section 2.15, with observable parity violating effects, the δ intervals $[0, \pi]$ and $[\pi, 2\pi]$ no longer represent equivalent families of transformations.

There is one and only one trajectory passing through a given $(\lambda_\vartheta, \lambda_\varphi, \lambda_{\vartheta\varphi})$ point: it represents the infinite number of "views" of the same physical distribution that are obtained by continuously varying the orientation of the polarization axis (in the production plane). Figures 3.1 and 3.2 show several examples of such trajectories in the three-dimensional parameter space, as well as their projections in the three planes. All trajectories are, as expected, fully contained in the invariant cone. A feature can be recognized from this representation: the trajectories do not "spiral" through the parameter space, but form circumferences belonging to fixed *planes*. Also this is expected: they represent rotations around one fixed axis, depending only on $\cos\delta$ and $\sin\delta$, and must therefore be closed circular (or elliptic) trajectories, with coinciding start and end points. Each "invariant plane" is defined by the equation

$$\frac{1 + \lambda_\vartheta + 2\,\lambda_\varphi}{3 + \lambda_\vartheta} = \mathcal{F} \tag{3.7}$$

for a given value of $\mathcal{F}$, between 0 and 1, with $\mathcal{F} = 0$ representing the base of the invariant cone and $\mathcal{F} = 1$ its vertex. The value of $\mathcal{F}$, identical in all frames, has an interesting physical meaning that will be discussed in the next sections.

In each invariant plane, larger circular trajectories correspond to larger differences between λ_ϑ and λ_φ, and larger values of $\lambda_{\vartheta\varphi}$. In fact, the trajectories reduce to points in the limit condition

$$\begin{cases} \lambda_\vartheta = \lambda_\varphi \\ \lambda_{\vartheta\varphi} = 0 \end{cases}, \tag{3.8}$$

defining a line that represents the locus of fixed points of the frame rotation: when the shape parameters belong to this "invariant line", they remain identical in all reference frames.

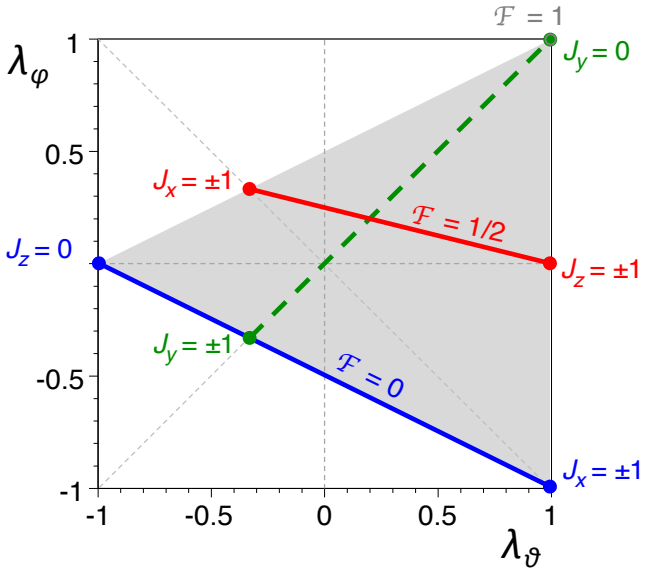

Fig. 3.3 The projection of the invariant parameter space over the plane $\lambda_{\vartheta\varphi} = 0$. The six coloured points, all belonging to the $\lambda_{\vartheta\varphi} = 0$ plane, indicate combinations of observable parameters corresponding to pure eigenstates of J_x, J_y, and J_z with eigenvalues 0 or ±1.

Specific angular momentum configurations of the decaying particle are shown in Fig. 3.3, within the triangle projected by the cone onto the $(\lambda_\vartheta, \lambda_\varphi)$ plane. The two points in blue, for which nonzero $\lambda_{\vartheta\varphi}$ values are forbidden, correspond to pure eigenstates of J_z and J_x, with eigenvalue 0. They both represent possible experimental observations of fully longitudinal polarizations, but with respect to two different polarization axes (z and x), related by a 90° rotation in the production plane. All transformations of these two configurations to any other frame remain inside the same "invariant plane", having the blue line as projection. This means that all possible configurations representing fully longitudinal polarizations (along quantization axes rotated by any angle δ within the production plane, and this time with varying values of $\lambda_{\vartheta\varphi}$) belong to the $\mathcal{F} = 0$ invariant plane, which can, therefore, be seen as "the plane of the longitudinal polarizations".

Analogously, the two points in red (for which $\lambda_{\vartheta\varphi}$ necessarily vanishes), represent fully transverse polarizations with respect to the x and z axes, while transverse configurations in any other polarization frame belong (with $\lambda_{\vartheta\varphi}$ no longer necessarily zero) to what can be called "the plane of the transverse polarizations", where $\mathcal{F} = 1/2$, having the red line as projection.

It is important to emphasise that the frame transformation relations in Eq. 2.13 and all considerations in the previous chapter and in the present one only concern rotations around the y axis. We do not contemplate in our discussion rotations where, for example, the y axis transforms into the z' axis. While taking y as polarization axis is geometrically possible, its direction, perpendicular to the production plane, is not

an obvious candidate for a *natural* polarization axis, at least in inclusive production studies and at least in the case of fully planar processes, such as the $h_1h_2 \to V$ and $h_1h_2 \to V + X$ topologies mentioned in the previous chapter. In fact, it is difficult to imagine that, in such conditions, a spin alignment would naturally arise along a direction perpendicular to the plane where all particle momenta belong.

Nevertheless, the physical phase space formally includes an entire family of angular distributions "oriented" along the y axis, that is, having a cylindrical symmetry with respect to it. These are the above-mentioned cases of distributions that are invariant with respect to rotations around the y axis and appear identical in the HX, CS, and GJ frames, and any other frame having the zx plane coinciding with the production plane. These configurations, all with $\lambda_{\vartheta\varphi} = 0$, belong to the green line shown in Fig. 3.3. Given their peculiar symmetry, they have a simple representation in terms of J_y components. The extreme cases are indicated by the two green points. The one at $\lambda_\vartheta = \lambda_\varphi = -1/3$ is identical to the "peanut" shape shown in Fig. 2.15-right, a hypothetical case of fully transverse ($J_y = \pm 1$) polarization along the y axis. The $\lambda_\vartheta = \lambda_\varphi = +1$ point, vertex of the invariant cone, touching the frontier plane defined by $\mathcal{F} = 1$, represents a fully longitudinal distribution ($J_y = 0$), a "donut" having as symmetry axis the y axis. All other points along this "invariant line" can be seen as intermediate cases, obtainable as mixtures of these two base cases and always maintaining their rotational symmetry along the y axis. One example, with $\lambda_\vartheta = \lambda_\varphi = +1/5$, is a distribution identical to the one in Fig. 2.13-right.

Obviously, even if theoretically allowed as angular momentum states, these cases do not necessarily represent real configurations in which the decaying particle may actually be produced in the considered physical conditions. When the outcome of a measurement is interpreted, the comparison to the mathematical constraints represented by the invariant cone should be complemented, when possible, by further considerations about how the measured distribution is related to possible symmetries imposed by the production mechanism and by the observation conditions. In fact, while we just mentioned, as examples of peculiar frame-independent distributions, two cases effectively encountered in the previous chapter, there they were meant to illustrate possible "artefacts" of an incorrect use of the polarization frame definitions, resulting in significantly distorted versions of the physical distributions of, respectively, Fig. 2.15-left and Fig. 2.13-left.

A further clarification is needed for the example of Fig. 2.15. One may find it contradictory that the seemingly "transverse" $\lambda_\vartheta = \lambda_\varphi = -1/3$ case (right) actually belongs to the plane of the longitudinal polarizations $\mathcal{F} = 0$. The way this case was obtained, starting from the fully longitudinal distribution on the left, shows that there is actually no contradiction. The "peanut" on the right is the result of a full rotational smearing of the distribution on the left: it can be seen as the superposition of infinite "donuts" rotated around the y axis by all possible angles. Each rotated donut (i) remains, like the original one, in the *invariant plane* $\mathcal{F} = 0$ and its parameters satisfy, therefore, the condition $1 + \lambda_\vartheta^{(i)} + 2\,\lambda_\varphi^{(i)} = 0$. This linear relation, summed over $i = 1, \ldots \infty$ using the sum rule of Eq. 1.17, remains unchanged in form: $1 + \lambda_\vartheta + 2\,\lambda_\varphi = 0$. The superposition of any number of $\mathcal{F} = 0$ distributions is a $\mathcal{F} = 0$ distribution: $\mathcal{F}$ can be interpreted as the "intrinsic" polarization of the decay

distribution, a property maintained in any frame rotation and in the superposition of rotated distributions.

This is only one illustration of the interesting concept of "invariant polarization" that will be developed in the following sections.

3.4 An absolute definition of "longitudinal" and "transverse"

As we saw in the previous chapter, for instance in Figs. 2.4 and 2.6, a transformation of polarization frame, being nothing else than a rotation, leaves the *shape* of the decay distribution unchanged. While the shape itself is rotation invariant, the shape parameters λ_ϑ, λ_φ, and $\lambda_{\vartheta\varphi}$ are not. In particular, the concepts of "longitudinal" and "transverse", when defined as, respectively, $\lambda_\vartheta < 0$ and $\lambda_\vartheta > 0$, depend, just like λ_ϑ, on the reference frame. However, it is possible to define one or more parameters, in terms of λ_ϑ, λ_φ, and $\lambda_{\vartheta\varphi}$, to reflect the characteristic shape of the distribution, independently of the chosen reference frame. We have encountered one possible definition of such kind of observable in the previous section: the parametric equation of the invariant planes, Eq. 3.7, can be read as the definition of the invariant polarization parameter $\mathcal{F}$, which has the same value, included between 0 and 1, in all polarization frames. In particular, $\mathcal{F}$ assumes the characteristic values 0, 1/3, and 1/2 when (even if not exclusively) the polarization is, respectively, fully longitudinal, zero (two thirds transverse, one third longitudinal), and fully transverse with respect to a given (not necessarily known) polarization axis.

The very existence of such a parameter is interesting: it means that it is *possible* to identify the natural alignment of the angular momentum vector in *absolute* terms, that is, independently of the direction of the quantization axis and even when the latter is unknown. The words "longitudinal" and "transverse", classically referred to a specific, known direction in space, acquire a rotation-invariant meaning.

More generally, using the general frame-transformation relations in Eq. 2.13 the reader can verify that $3 + \lambda_\vartheta$ and $1 - \lambda_\varphi$ transform covariantly,

$$\begin{aligned} 3 + \lambda'_\vartheta &= \frac{1}{1+\Lambda}\,(3 + \lambda_\vartheta)\,, \\ 1 - \lambda'_\varphi &= \frac{1}{1+\Lambda}\,(1 - \lambda_\varphi)\,, \end{aligned} \tag{3.9}$$

and, therefore, any quantity $\mathcal{F}_{\{c_i\}}$ defined by the linear relation

$$\mathcal{F}_{\{c_i\}} \;=\; \frac{c_1\,(3 + \lambda_\vartheta) + c_2\,(1 - \lambda_\varphi)}{c_3\,(3 + \lambda_\vartheta) + c_4\,(1 - \lambda_\varphi)}\,, \tag{3.10}$$

where c_1, c_2, c_3, and c_4 are real numbers, is left unchanged by the transformation: $\mathcal{F}'_{\{c_i\}} = \mathcal{F}_{\{c_i\}}$. All these definitions of invariant shape parameters are equivalent: each one can be expressed as a function of the others. The parameter $\mathcal{F}$ defining the invariant planes corresponds to: $c_1 = c_3 = 1$; $c_2 = -2$; and $c_4 = 0$.

3.5 A more fundamental derivation of the invariant polarization

The existence of a rotation-invariant relation among the parameters of the decay distribution is rooted on the rotational covariance properties of angular momentum states. In fact, the frame-invariance of $\mathcal{F}$, seen in the previous section to be a consequence of how the observable parameters of the decay distribution transform from one frame to another, can also be demonstrated starting from the transformations of the (not directly observed) angular momentum components of the decaying particle.

As discussed in Chapter 1, for successive rotations about the z and y axes, respectively by the angles φ and ϑ, a pure $J = 1, J_z = M$ angular momentum eigenstate $|1,\, M\rangle$ transforms according to the relation (analogous to Eq. 1.1 but describing the inverse rotation)

$$|1,\, M\rangle = \sum_{M'=0,\pm1} \mathcal{D}^{1*}_{MM'}(\vartheta,\varphi)\, |1,\, M'\rangle\,. \tag{3.11}$$

For a generic superposition

$$|V\rangle = \sum_{M=0,\pm1} a_M\, |1,\, M\rangle\,, \tag{3.12}$$

the components transform, therefore, as

$$a'_K = \sum_{M=0,\pm1} a_M\, \mathcal{D}^{1*}_{MK}(\vartheta,\varphi)\,. \tag{3.13}$$

For a rotation in the production plane (about the y axis; $\varphi = 0$),

$$a'_{+1} + a'_{-1} = \sum_{M=0,\pm1} a_M\, [d^1_{M,+1}(\vartheta) + d^1_{M,-1}(\vartheta)] = a_{+1} + a_{-1}\,, \tag{3.14}$$

where we have used $d^1_{\pm1,+1}(\vartheta) + d^1_{\pm1,-1}(\vartheta) = 1$ and $d^1_{0,+1}(\vartheta) + d^1_{0,-1}(\vartheta) = 0$ (Eq. 1.3 or Table 7.3).

In other words, *the amplitude combination $a_{+1} + a_{-1}$ is invariant by rotation around the y axis*, that is, for a transformation between polarization frames. Therefore, given also the obvious rotation invariance of the state normalization $|a_0|^2 + |a_{+1}|^2 + |a_{-1}|^2$, we can write the following frame-independent quantity, now explicitly considered for one individual subprocess i, producing a state with component amplitudes $a^{(i)}_{+1}$, $a^{(i)}_{-1}$, and $a^{(i)}_0$:

$$h^{(i)} = \frac{1}{2}\, \frac{\left|a^{(i)}_{+1} + a^{(i)}_{-1}\right|^2}{\left|a^{(i)}_0\right|^2 + \left|a^{(i)}_{+1}\right|^2 + \left|a^{(i)}_{-1}\right|^2}\,. \tag{3.15}$$

It can easily be seen that this expression is always positive and assumes its maximum value, 1, when $a^{(i)}_{+1} = a^{(i)}_{-1}$ and $a^{(i)}_0 = 0$.

Using Eq. 1.13, summing over n subprocesses with fractional contributions $f^{(i)}$, and then using Eq. 1.17, a few algebra manipulations finally lead to

$$\frac{\sum_{i=1}^{n} f^{(i)} \mathcal{N}^{(i)} h^{(i)}}{\sum_{i=1}^{n} f^{(i)} \mathcal{N}^{(i)}} = \frac{1 + \lambda_\vartheta + 2\,\lambda_\varphi}{3 + \lambda_\vartheta}\,. \tag{3.16}$$

This expression is frame-independent, being the sum of n frame-independent terms, and gives values between 0 and $\sum_{i=1}^{n} f^{(i)} \mathcal{N}^{(i)} = 1$. It can be recognized from Eq. 3.7 that it is equal to $\mathcal{F}$.

While the rotation around the y axis is the one relevant for a change among experimentally-definable polarization frames (in inclusive production studies), for completeness and curiosity we can wonder what observable quantities are invariant by hypothetical rotations around other directions. Following an analogous procedure and using the same notation as above, we find that the quantity

$$\mathcal{G} = \frac{\sum_{i=1}^{n} f^{(i)} \mathcal{N}^{(i)} \mathcal{G}^{(i)}}{\sum_{i=1}^{n} f^{(i)} \mathcal{N}^{(i)}} = \frac{1 + \lambda_\vartheta - 2\,\lambda_\varphi}{3 + \lambda_\vartheta}\,, \tag{3.17}$$

with

$$\mathcal{G}^{(i)} = \frac{1}{2}\,\frac{\left|a_{+1}^{(i)} - a_{-1}^{(i)}\right|^2}{\left|a_0^{(i)}\right|^2 + \left|a_{+1}^{(i)}\right|^2 + \left|a_{-1}^{(i)}\right|^2}\,, \tag{3.18}$$

is invariant by rotation about the x axis.

Finally, it is immediate to understand that the parameter λ_ϑ is in itself invariant by rotation about z: such a rotation simply corresponds to a change of the value of the azimuthal coordinate φ, leaving completely unchanged, in form and value, the polar-angle dependent term, $(1 + \lambda_\vartheta \cos^2\vartheta) \,/\, (3 + \lambda_\vartheta)$, of the full angular distribution (Eq. 2.1).

3.6 Frame-independent angular distribution

The frame-invariant polarization observable $\mathcal{F}$ can be determined through the measurement of the two-dimensional, three-parameters angular distribution of Eq. 2.1. A convenient procedure, adoptable in an analysis of experimental data, is to fit the event distribution (after considering acceptance and efficiency corrections) to the expected functional form, where either λ_ϑ or λ_φ is re-expressed in terms of $\mathcal{F}$. In the latter case, for example,

$$\begin{aligned} W(\cos\vartheta, \varphi) \;=\; & \frac{1}{4\,\pi}\,\frac{3}{3 + \lambda_\vartheta} \times \Big\{ 1 \;+\; \lambda_\vartheta\, \cos^2\vartheta \;+\; \lambda_{\vartheta\varphi}\, \sin 2\vartheta\, \cos\varphi \\ & + \frac{1}{2}\Big[(3 + \lambda_\vartheta)\,\mathcal{F} - (1 + \lambda_\vartheta)\Big]\, \sin^2\vartheta\, \cos 2\varphi \Big\}\,, \end{aligned} \tag{3.19}$$

This method obviously requires the prior choice of one of the several possible reference frames, because the angles ϑ and φ depend on it; however, the resulting determination of $\mathcal{F}$ will not depend on that choice. Actually, the latter statement is more properly written as "the resulting determination of $\mathcal{F}$ *should* not depend on

that choice", given that, as discussed in Section 3.12, systematic variations caused by experimental biases may lead to a violation of the invariance of $\mathcal{F}$. It is, therefore, very useful and important to perform the experimental analysis in two sufficiently-different reference frames, in order to *probe* such effects and verify whether identical values of $\mathcal{F}$ are indeed measured in both frames, in spite of the different values of λ_ϑ and λ_φ.

On the other hand, it can sometimes be convenient to determine $\mathcal{F}$ directly from a one-dimensional, single-parameter angular distribution. That such a distribution exists, and what it is, can be inferred with simple reasoning. The distribution must necessarily be, as its (only) shape parameter $\mathcal{F}$, invariant by rotation about the y axis. In other words, it must be a function of a frame-independent angular variable. This restricts the possibilities for the definition of the corresponding angular variable to one single case,

$$\cos\alpha \;=\; \sin\vartheta\,\sin\varphi\,, \tag{3.20}$$

where α is the angle formed by the direction of the decay lepton with the y axis (the axis perpendicular to the production plane). The $\cos\alpha$ distribution can only be of the form

$$w(\cos\alpha) \;\propto\; 1 + \lambda_\alpha \cos^2\alpha\,, \tag{3.21}$$

just as any parity-conserving distribution of the angle formed with respect to an axis must be, when only $J = 1$ wave functions are involved. Finally, the coefficient λ_α can be specified as a function of $\mathcal{F}$ by imposing the condition

$$\begin{aligned}\langle\cos^2\alpha\rangle &= \int_{-1}^{+1} \cos^2\alpha\; w(\cos\alpha)\;\mathrm{d}(\cos\alpha) \\ &= \int_0^{2\pi}\int_{-1}^{+1} (\sin\vartheta\,\sin\varphi)^2\; W(\cos\vartheta,\varphi)\;\mathrm{d}(\cos\vartheta)\;\mathrm{d}\varphi\,,\end{aligned} \tag{3.22}$$

with the result

$$\lambda_\alpha \;=\; -\frac{\lambda_\vartheta + 3\,\lambda_\varphi}{2 + \lambda_\vartheta + \lambda_\varphi} \;=\; \frac{1 - 3\,\mathcal{F}}{1 + \mathcal{F}}\,. \tag{3.23}$$

The similarity between the latter equality and the expression of λ_ϑ as a function of the longitudinal polarization fraction $|a_0|^2$ (Eq. 3.1) reveals that $\mathcal{F}$ also represents a longitudinal polarization fraction, determined in this case taking as quantization axis the axis perpendicular to the production plane.

The $\cos\alpha$ distribution should be used with care because it has similar limitations to those of the projected one-dimensional $\cos\vartheta$ and φ distributions, previously discussed in Section 2.13. While its reduced variable dimensionality with respect to the the full angular distribution (Eq. 3.19) can offer advantages in an experimental analysis, especially when limited data samples are available, it can also lead to a biased measurement if correlation effects induced by the limited experimental coverage and detection efficiencies are not properly taken into account. Such effects must be corrected in their full dimensionality (that is, as a function of $\cos\vartheta$ and φ) when the $\cos\alpha$ event distribution is produced.

3.7 The parameter domain of the general dilepton decay

The relations in Eq. 3.5, defining the allowed parameter space for the inclusive observation of a parity-conserving decay in unpolarized collisions, can be made more general to include the effects of parity violating processes and/or polarizations of the colliding hadrons. Five combinations of the eight shape parameters enter the generalized inequalities, which formally represent the intersection of volumes defined by three conical surfaces (relations of the kind $(1 + X)^2 - (Y + X)^2 = 4K^2$) and a pair of planes (one relation of the same kind, with $K = 0$) in the five dimensional space of the coordinates λ_ϑ, λ_φ, $\sqrt{\lambda_{\vartheta\varphi}^{\perp 2} + A_\varphi^2}$, $\sqrt{\lambda_{\vartheta\varphi}^2 + A_\varphi^{\perp 2}}$, and $\sqrt{\lambda_\varphi^{\perp 2} + A_\vartheta^2}$:

$$
\begin{aligned}
(1 - \lambda_\varphi)^2 - (\lambda_\vartheta - \lambda_\varphi)^2 &\geq 4(\lambda_{\vartheta\varphi}^2 + A_\varphi^{\perp 2})\,, \\
(1 + \lambda_\varphi)^2 - (\lambda_\vartheta + \lambda_\varphi)^2 &\geq 4(\lambda_{\vartheta\varphi}^{\perp 2} + A_\varphi^2)\,, \\
\left(1 + \sqrt{\lambda_\varphi^{\perp 2} + A_\vartheta^2}\right)^2 - \left(\lambda_\vartheta + \sqrt{\lambda_\varphi^{\perp 2} + A_\vartheta^2}\right)^2 &\geq 4\left[(\lambda_{\vartheta\varphi}^2 + A_\varphi^{\perp 2}) + (\lambda_{\vartheta\varphi}^{\perp 2} + A_\varphi^2)\right]\,, \\
\left(1 - \sqrt{\lambda_\varphi^{\perp 2} + A_\vartheta^2}\right)^2 - \left(\lambda_\vartheta - \sqrt{\lambda_\varphi^{\perp 2} + A_\vartheta^2}\right)^2 &\geq 0\,.
\end{aligned}
\tag{3.24}
$$

Figure 3.4 shows the two-dimensional projections of the physical parameter domain defined by these relations. The inequalities of Eq. 3.24 become equivalent to those of Eq. 3.5 when only the three parity-conserving observables λ_ϑ, λ_φ, and $\lambda_{\vartheta\varphi}$ are nonzero.

It is worth noting that, while the polar component of the parity asymmetry, A_ϑ, is bounded between -1 and $+1$, like λ_ϑ, the azimuthal counterparts A_φ and $A_\varphi^\perp$ have magnitudes limited to $|A_\varphi^{(\perp)}| < \sqrt{2}/2$, just like $\lambda_{\vartheta\varphi}$ and $\lambda_{\vartheta\varphi}^\perp$.

3.8 The "canonical form" of the angular distribution

According to Theorem 1.1, presented in Section 1.10, for any angular momentum state $|V\rangle = a_{-1}\,|1, -1\rangle + a_0\,|1, 0\rangle + a_{+1}\,|1, +1\rangle$ of a $J = 1$ particle it is always possible to make the $J_z = 0$ component vanish by performing a well defined rotation of the system of axes. The redefined state, written as

$$
|V\rangle = a_{-1}^\star\,|1, -1\rangle + a_{+1}^\star\,|1, +1\rangle \tag{3.25}
$$

with respect to the new polarization axis $z^\star$, has a dilepton decay angular distribution simpler than its most general form in Eq. 1.27. In fact, it can be seen in Eq. 1.28 that the parameters $\lambda_{\vartheta\varphi}$, $\lambda_{\vartheta\varphi}^\perp$, A_φ, and $A_\varphi^\perp$ (the index indicating the individual subprocess is omitted for simplicity), containing amplitudes of the kind $a_{0,L'}$, all become zero.

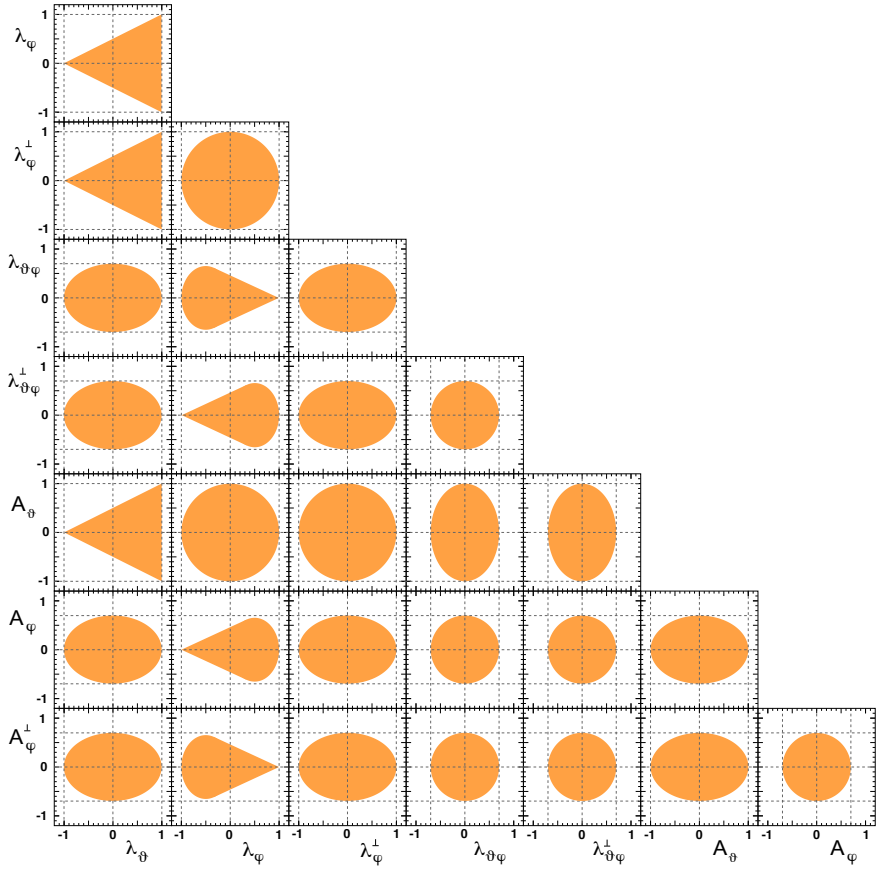

Fig. 3.4 Two-dimensional projections of the allowed parameter space for the angular distribution of the dilepton decay of a vector particle.

Of the remaining ones, we notice that λ_φ and $\lambda_\varphi^\perp$ do not need to be both nonzero: if they are, a further rotation around the $z^\star$ axis by a suitable angle δ (determined by $\tan 2\delta = \lambda_\varphi^\perp / \lambda_\varphi$) can always bring $\lambda_\varphi^\perp$ to zero, according to the following relations (a subset of the relations in Eq. 2.38):

$$\begin{pmatrix} \lambda'_\varphi \\ \lambda_\varphi^{\perp\prime} \end{pmatrix} = \begin{pmatrix} \cos 2\delta & \sin 2\delta \\ -\sin 2\delta & \cos 2\delta \end{pmatrix} \begin{pmatrix} \lambda_\varphi \\ \lambda_\varphi^\perp \end{pmatrix} . \tag{3.26}$$

The same rotation, as seen in Eq. 2.38, leaves λ_ϑ and A_ϑ unchanged, while it would change $\lambda_{\vartheta\varphi}$, $\lambda_{\vartheta\varphi}^\perp$, A_φ, and $A_\varphi^\perp$ only if they were not zero; but they are zero, after the first rotation. Therefore, considering also that $a_0^\star = 0$ implies $\lambda_\vartheta = +1$, we can reformulate Theorem 1.1, for the specific case of a dilepton decay, in the following form.

Theorem 3.1. *For any production mechanism where a vector particle is consistently produced in the same angular momentum state, expressed as a linear combination of the $J_z = -1$, 0, and $+1$ eigenstates, there always exists a system of axes, $x^\star y^\star z^\star$, with respect to which the dilepton decay distribution has the shape*

$$W^\star(\cos\vartheta,\varphi) \;=\; \frac{3}{8\pi}\left(\,1+\cos^2\vartheta+\lambda_\varphi^\star\sin^2\vartheta\cos 2\varphi+2A_\vartheta^\star\cos\vartheta\,\right). \tag{3.27}$$

The distribution has only two shape parameters, $\lambda_\varphi^\star$ and $A_\vartheta^\star$, given by

$$\begin{aligned}\lambda_\varphi^\star \;&=\; 2\,\mathrm{Re}[(a^\star_{+1,+1})^* a^\star_{-1,+1}] \;+\; 2\,\mathrm{Re}[(a^\star_{+1,-1})^* a^\star_{-1,-1}]\\ &=\; |a^\star_{+1,+1}+a^\star_{-1,+1}|^2 \;+\; |a^\star_{+1,-1}+a^\star_{-1,-1}|^2 \;-\; 1\\ &=\; 2\mathcal{F}^\star-1\,,\\ A_\vartheta^\star \;&=\; |a^\star_{+1,+1}|^2+|a^\star_{-1,-1}|^2-|a^\star_{+1,-1}|^2-|a^\star_{-1,+1}|^2\,,\end{aligned} \tag{3.28}$$

where $a^\star_{M,L'}$ are the amplitudes for the general (possibly parity-violating) dilepton decay process, previously defined in Section 1.11 but now referred to the frame ($x^\star$, $y^\star$, $z^\star$). The amplitudes are normalized according to $|a^\star_{+1,+1}|^2+|a^\star_{-1,-1}|^2+|a^\star_{+1,-1}|^2+|a^\star_{-1,+1}|^2=1$ (since $a^\star_{0,\pm1}=0$).

The quantity $\mathcal{F}^\star$ is formally identical to the invariant polarization parameter $\mathcal{F}$, which, for one individual subprocess, is defined, extending the parity-conserving case of Eq. 3.15, as

$$\mathcal{F}=\frac{1}{2}\;\frac{\left|a_{+1,+1}+a_{-1,+1}\right|^2+\left|a_{+1,-1}+a_{-1,-1}\right|^2}{\left|a_{0,+1}\right|^2+\left|a_{0,-1}\right|^2+\left|a_{+1,+1}\right|^2+\left|a_{-1,+1}\right|^2+\left|a_{+1,-1}\right|^2+\left|a_{-1,-1}\right|^2}\,. \tag{3.29}$$

Also in the most general parity-violating case, and after summing over all subprocesses, $\mathcal{F}$ maintains its dependence on (only) λ_ϑ and λ_φ, as defined in Eq. 3.16.

Coming back to the particular view of the distribution referred to the axes $x^\star, y^\star, z^\star$, the parameter $\mathcal{F}^\star$ becomes $(1+\lambda_\vartheta^\star+2\lambda_\varphi^\star)\,/\,(3+\lambda_\vartheta^\star)=\frac{1}{2}\,(1+\lambda_\varphi^\star)$. The difference in notation, $\mathcal{F}^\star$ instead of $\mathcal{F}$, is a reminder that this parameter now expresses the polarization as it would be measured in the ($x^\star$, $y^\star$, $z^\star$) frame, which is not always experimentally accessible. In fact, if $z^\star$ does not belong to the production plane, the parameters $\lambda_\varphi^\perp$, $\lambda_{\vartheta\varphi}^\perp$, and $A_\varphi^\perp$ are, in general, nonzero, but may be suppressed in the average over all events in certain situations, when not all particles participating in the production and decay process are observed, as previously mentioned ("inclusive" observation). In these conditions, the distribution is, to some extent, smeared out: it effectively *changes shape*. This also changes the "natural" value of $\mathcal{F}^\star$ (i.e. of $\lambda_\varphi^\star$), which reflects the full shape of the unsmeared distribution, into an "effective" $\mathcal{F}$, characterizing the *observable* distribution.

Even if $\lambda_\vartheta=+1$ in the ($x^\star$, $y^\star$, $z^\star$) frame, natural polarizations different from the transverse one are included in this parametrization: for example, as seen in Section 2.8, the condition $a^\star_{+1,\pm1}+a^\star_{-1,\pm1}=0$ corresponds to a longitudinal polarization

with respect to an axis *perpendicular* to $z^\star$ (Eq. 2.17), and, in fact, Eq. 3.28 gives $\mathcal{F}^\star = 0$.

The quantities $\mathcal{F}^\star$ and $A_\vartheta^\star$ represent, respectively, the *natural* polarization and parity asymmetry characterizing the production and decay process. Interestingly, these parameters, which obviously do not depend on the chosen frame, are both invariant by *any* rotation, not only around the y axis, with the caveat mentioned above: they are not always fully observable.

The existence of a simpler, "canonical" form of the distribution, identified by two shape parameters independently of its orientation in space, is sometimes of more theoretical than practical interest. First, as discussed above, the $z^\star$ axis may not belong to the production plane and may, therefore, not be approximated well enough by any of the polarization axes adoptable in the analysis of the experimental data. Second, we have assumed that there is no superposition of different production processes. In the most general case, where a mixture of different angular momentum states is produced, we can still, at least in principle, characterize the shape of the overall distribution with a small number of geometrical parameters independent of the chosen frame. However, in general, it is not possible to simultaneously reduce the parity-conserving term, parametrized by λ_ϑ, λ_φ, $\lambda_\varphi^\perp$, $\lambda_{\vartheta\varphi}$, and $\lambda_{\vartheta\varphi}^\perp$, and the parity-violating one, described by A_ϑ, A_φ, and $A_\varphi^\perp$, to their simplest possible forms.

To illustrate this fact it is convenient to start by assuming that the latter three parameters are zero. The resulting (parity-conserving) angular distribution can be written as a quadratic form:

$$\begin{aligned}
&\frac{1}{3+\lambda_\vartheta}\Big(1+\lambda_\vartheta\cos^2\vartheta+\lambda_\varphi\sin^2\vartheta\cos 2\varphi+\lambda_{\vartheta\varphi}\sin 2\vartheta\cos\varphi \\
&\qquad +\lambda_\varphi^\perp\sin^2\vartheta\sin 2\varphi+\lambda_{\vartheta\varphi}^\perp\sin 2\vartheta\sin\varphi\Big) \\
&\qquad = \hat{r}^{\mathrm{T}}\,\mathcal{M}\,\hat{r}\,, \\
&\text{with}\quad \hat{r} = (\sin\vartheta\cos\varphi,\ \sin\vartheta\sin\varphi,\ \cos\vartheta) \\
&\text{and}\quad \mathcal{M} = \frac{1}{3+\lambda_\vartheta}\begin{pmatrix} 1+\lambda_\varphi & \lambda_\varphi^\perp & \lambda_{\vartheta\varphi} \\ \lambda_\varphi^\perp & 1-\lambda_\varphi & \lambda_{\vartheta\varphi}^\perp \\ \lambda_{\vartheta\varphi} & \lambda_{\vartheta\varphi}^\perp & 1+\lambda_\vartheta \end{pmatrix}.
\end{aligned} \tag{3.30}$$

The real and symmetric matrix $\mathcal{M}$ can always be diagonalized: the parameters $\lambda_{\vartheta\varphi}$, $\lambda_{\vartheta\varphi}^\perp$, and $\lambda_\varphi^\perp$ represent off-diagonal terms that can be set to zero with a suitable rotation. In the rotated frame, the axes x, y, and z of the reference frame will coincide with the principal axes of the geometrical shape of the distribution: that is, the planes xy, yz, and zx will be symmetry planes, bisecting the distribution into halves that are mirror images of each other. The distribution will then be described by only two parameters, $\lambda_\vartheta^\star$ and $\lambda_\varphi^\star$, or $\lambda_\vartheta^\star$ and $\mathcal{F}^\star$.

As far as parity-conserving processes are concerned, we can, therefore, condense the above considerations in the form of the diagonal matrix representing, in a suitable and always existing frame of axes, the decay distribution in its "canonical" shape.

For a single subprocess producing always the same angular momentum state, the matrix has one parameter, $\mathcal{F}^\star$,

$$\overline{\mathcal{M}} = \begin{pmatrix} \frac{\mathcal{F}^\star}{2} & 0 & 0 \\ 0 & \frac{1-\mathcal{F}^\star}{2} & 0 \\ 0 & 0 & \frac{1}{2} \end{pmatrix}, \tag{3.31}$$

while in the most general case it has two parameters, $\mathcal{F}^\star$ and $\lambda_\vartheta^\star$,

$$\overline{\mathcal{M}} = \begin{pmatrix} \frac{1}{2}\left(\frac{1-\lambda_\vartheta^\star}{3+\lambda_\vartheta^\star} + \mathcal{F}^\star\right) & 0 & 0 \\ 0 & \frac{1-\mathcal{F}^\star}{2} & 0 \\ 0 & 0 & \frac{1+\lambda_\vartheta^\star}{3+\lambda_\vartheta^\star} \end{pmatrix} = \begin{pmatrix} \frac{1+\lambda_\varphi^\star}{3+\lambda_\vartheta^\star} & 0 & 0 \\ 0 & \frac{1-\lambda_\varphi^\star}{3+\lambda_\vartheta^\star} & 0 \\ 0 & 0 & \frac{1+\lambda_\vartheta^\star}{3+\lambda_\vartheta^\star} \end{pmatrix}. \tag{3.32}$$

Incidentally, this means that the measurement is not sensitive to the existence of more than two underlying processes: the distribution created by a superposition of n different processes can always be reproduced as the sum of only two components.

It is not possible to include the parity-violating parameters, together with the parity conserving ones, to build a 3×3 matrix that can be diagonalized through an ordinary space rotation. However, the subset of the parity-violating parameters has a simple transformation property, resembling a rotation. Table 2.2 shows that, under a generic rotation $R_z(\omega)\,R_y(\zeta)\,R_z(\psi)$, as defined in Section 2.15, the parameters A_ϑ, A_φ, and $A_\varphi^\perp$ transform like the vector (z, x, y), besides acquiring the factor $1/(1+\Lambda)$:

$$\begin{pmatrix} A'_\vartheta \\ A'_\varphi \\ A_\varphi^{\perp\prime} \end{pmatrix} = \frac{1}{1+\Lambda} \begin{pmatrix} \mathrm{c}\,\zeta & \mathrm{s}\,\zeta\,\mathrm{c}\,\psi & \mathrm{s}\,\zeta\,\mathrm{s}\,\psi \\ -\mathrm{s}\,\zeta\,\mathrm{c}\,\omega & \mathrm{c}\,\zeta\,\mathrm{c}\,\omega\,\mathrm{c}\,\psi - \mathrm{s}\,\omega\,\mathrm{s}\,\psi & \mathrm{c}\,\zeta\,\mathrm{c}\,\omega\,\mathrm{s}\,\psi + \mathrm{s}\,\omega\,\mathrm{c}\,\psi \\ \mathrm{s}\,\zeta\,\mathrm{s}\,\omega & -\mathrm{c}\,\zeta\,\mathrm{s}\,\omega\,\mathrm{c}\,\psi - \mathrm{c}\,\omega\,\mathrm{s}\,\psi & -\mathrm{c}\,\zeta\,\mathrm{s}\,\omega\,\mathrm{s}\,\psi + \mathrm{c}\,\omega\,\mathrm{c}\,\psi \end{pmatrix} \begin{pmatrix} A_\vartheta \\ A_\varphi \\ A_\varphi^\perp \end{pmatrix},$$

where $\mathrm{c}\,\alpha$ and $\mathrm{s}\,\alpha$ are condensed abbreviations of $\cos\alpha$ and $\sin\alpha$, respectively.

It is always possible, therefore, to choose a suitable rotation that brings the "vector" $(A_\vartheta, A_\varphi, A_\varphi^\perp)$ to lie on one of the three "axes" of the parameter space, that is, to transform it to a vector of, for example, the kind $(A'_\vartheta, 0, 0)$. According to Theorem 3.1, in the case of a single angular momentum state, the rotation leading to the canonical form of Eq. 3.31 for the parity conserving parameters automatically performs, at the same time, the "projection" of the vector of the parity asymmetries over the polar direction. That does not always happen, however, in the presence of an ensemble of states characterized by different production mechanisms and/or decay properties. In general, while a rotation diagonalizing the parity conserving part and another "projecting" the parity-violating part of the distribution always exist, they are not necessarily the same rotation.

This concept can be visually clarified through an example scenario where the measured angular distribution results from the superposition of two hypothetical

production mechanisms; the first creates a natural polarization along the z axis, the second along an axis forming a 45° angle with z, in the production plane. The two mechanisms account, respectively, for 70% and 30% of the events. Three variants of this scenario are considered, differing for the polarizations of the two processes and leading to the shapes seen in the three panels of Fig. 3.5.

The first two cases only include parity conserving processes and are mixtures of either two fully transverse polarizations (a) or one longitudinal and one transverse (b). In the case (c), both polarizations are transverse but the first component, polarized along the z axis, is of the kind $1 + \cos^2\vartheta - 2\cos\vartheta$ (the shape shown on the left side of Fig. 1.7-b), corresponding to $A_\vartheta = -1$. The observable shapes in the cases (a) and (b) have a clear "directionality": for each of them there are three orthogonal directions in space representing its principal axes. The major axis, for example, is indicated by the green dashed line.

The preservation of this "ellipsoidal" symmetry is not a trivial result of peculiarly "symmetric" cases selected as examples: we intentionally chose the relative contributions of the two components to be significantly asymmetric and in the case (b) the two contributing distributions have maximally different shapes. In fact, these are illustrations of a general result: a parity-conserving decay distribution always assumes a canonical form with respect to a certain system of axes.

Instead, no directionality can be seen in the third distribution, which has a parity-violating component along an axis *different* from z. Its geometrical shape has no principal axes. More generally, distributions lacking axes of symmetry are obtained in the presence of two essential conditions: the existence of more than one "natural" axis in the superposition of processes and the presence of at least one parity-violating process.

It is worth repeating this same message using different words: as long as all processes are parity conserving, their superposition leads to a diagonalizable distribution; and a superposition of parity-violating processes, having individual asymmetries with different signs and magnitudes, will also lead to a shape that retains a well defined axis of symmetry, as long as they all share the same reference direction. The latter situation was illustrated in Fig. 1.7-c and is contemplated by Theorem 3.1.

Actually, we can generalize that theorem by summing Eq. 3.27 over any number of subprocesses, with the *additional hypothesis* that the $z^\star$ axis is the same for all of them. In that case, the overall distribution can be written, in its canonical form, as

$$W^\star(\cos\vartheta,\varphi) = \frac{3}{4\pi}\,\frac{1}{3+\lambda^\star_\vartheta}\left[1+\lambda^\star_\vartheta\cos^2\vartheta + \left(1-\frac{(1-\mathcal{F}^\star)\left(3+\lambda^\star_\vartheta\right)}{2}\right)\sin^2\vartheta\,\cos 2\varphi + 2A^\star_\vartheta\,\cos\vartheta\right], \tag{3.33}$$

where $\lambda^\star_\vartheta$ and $\mathcal{F}^\star$ result from the diagonalization of the parity-conserving part of the distribution, Eq. 3.32, and $A^\star_\vartheta$ is the largest measurable parity asymmetry, that is, the maximum projection of the $(A_\vartheta, A_\varphi, A^\perp_\varphi)$ vector.

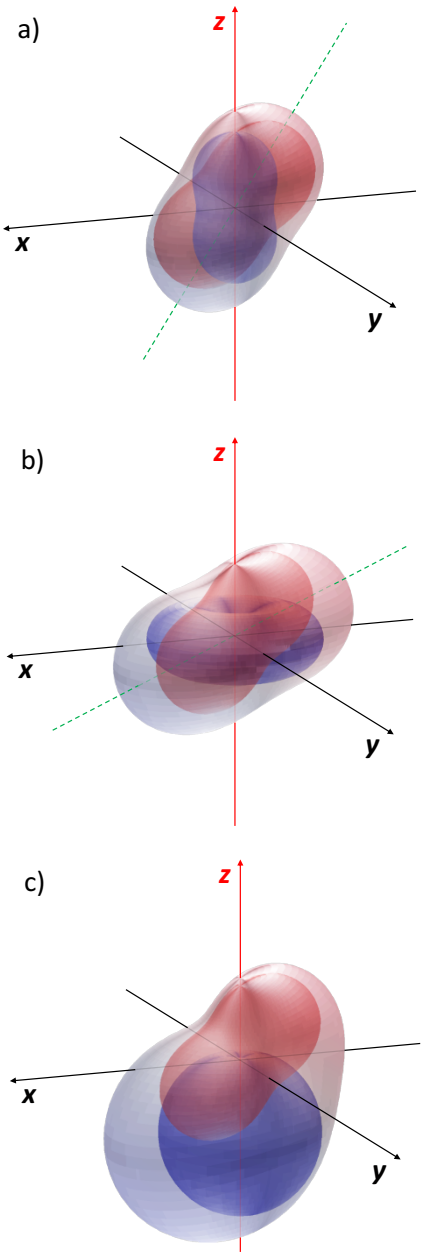

Fig. 3.5 Three examples of dilepton angular distributions resulting from the superpositions of two mechanisms with natural polarizations along two different directions: (a) both processes are parity conserving and transversely polarized; (b) both are parity conserving, with one being longitudinally and the other transversely polarized; (c) both are transversely polarized, but one of the two violates parity, making the overall distribution lose any “directionality”.

3.9 Other parity-conserving frame-independent parameters

An outcome of the considerations in the previous section is that $\mathcal{F}$ is not the only parameter that is invariant by rotation of the reference frame. We discuss here in more detail the further frame-independent parameters describing the parity-conserving part of the distribution and how they are related to the frame-dependent shape parameters, while the parity-violating asymmetry will be the subject of the next section.

We will start by assuming that it is *possible* to observe the full angular distribution, with an experimental procedure sensitive to all physical reference directions relevant for the process under study and, therefore, immune to event-averaging effects that would partially smear the observed shape. This ideal scenario is certainly worth considering; in order to quantify smearing effects and interpret the physical indications lying behind the blurred picture, it is important to have a baseline perspective of what happens in ideal conditions, when such effects can be neglected.

We have seen that the parameters $\lambda_\vartheta^\star$ and $\lambda_\varphi^\star$ are necessary and sufficient for defining the *shape* of the distribution when parity asymmetries are absent (Eqs. 3.30–3.32). One of the two can be optionally replaced by $\mathcal{F}^\star = (1 + \lambda_\vartheta^\star + 2\lambda_\varphi^\star) / (3 + \lambda_\vartheta^\star)$, which identifies the nature of the polarization (transverse, longitudinal, or a mixture of the two cases). Moreover, $\lambda_\vartheta^\star$ can always be chosen to be 1 if only one elementary process contributes to the production of the decaying particle. In this case, there is only one essential shape parameter, $\lambda_\varphi^\star$ or $\mathcal{F}^\star$. For whatever fully reconstructed dilepton distribution it is always possible to determine these parameters as a function of λ_ϑ, λ_φ, $\lambda_\varphi^\perp$, $\lambda_{\vartheta\varphi}$, and $\lambda_{\vartheta\varphi}^\perp$, as measured in *any* rotated frame. Their expressions can be obtained by diagonalizing the matrix $\mathcal{M}$, that is, by solving the following cubic equation in κ:

$$\det(\mathcal{M} - \kappa\,\mathbb{I}) = 0\,. \tag{3.34}$$

The three solutions provide the diagonal elements of $\overline{\mathcal{M}}$ (Eq. 3.32), only two of which are independent. Since $\mathcal{M}$ is real and symmetric, the equation has always three real solutions, which can be determined analytically, leading to expressions containing nested trigonometric functions of the kind $\sin[\,(\arcsin(K)+n\pi)\,/\,3\,]$ (with integer n), and similar ones. The resulting formulas, while not particularly illuminating, are reported here explicitly, so that the following discussion becomes less abstract:

$$\begin{aligned}
\kappa_1 &= \frac{1}{3} - \frac{1}{3}\frac{1}{3+\lambda_\vartheta}\left\{2A^{1/2}\sin\left[\frac{1}{3}\arcsin\left(\frac{B}{2A^{3/2}}\right)\right]\right\}\,,\\
\kappa_2 &= \frac{1}{3} + \frac{1}{3}\frac{1}{3+\lambda_\vartheta}\left\{2A^{1/2}\sin\left[\frac{1}{3}\arcsin\left(\frac{B}{2A^{3/2}}\right)+\frac{\pi}{3}\right]\right\}\,,\\
\kappa_3 &= 1-\kappa_1-\kappa_2\,,
\end{aligned} \tag{3.35}$$

where the last relation uses the property that $\mathcal{M}$ has unit trace. The parameters A and B are:

$$
\begin{aligned}
A &= \lambda_\vartheta^2 + 3\left(\lambda_\varphi^2 + \lambda_\varphi^{\perp 2} + \lambda_{\vartheta\varphi}^2 + \lambda_{\vartheta\varphi}^{\perp 2}\right), \\
B &= 2\lambda_\vartheta^3 + 9\lambda_\vartheta\left[\lambda_{\vartheta\varphi}^2 + \lambda_{\vartheta\varphi}^{\perp 2} - 2\left(\lambda_\varphi^2 + \lambda_\varphi^{\perp 2}\right)\right] \\
&\quad + 27\left[\lambda_\varphi\left(\lambda_{\vartheta\varphi}^2 - \lambda_{\vartheta\varphi}^{\perp 2}\right) + 2\,\lambda_{\vartheta\varphi}\,\lambda_{\vartheta\varphi}^{\perp}\,\lambda_\varphi^{\perp}\right].
\end{aligned}
\tag{3.36}
$$

It is important to note that the three solutions are interchangeable, that is, there are three diagonal forms of the distribution, corresponding to the three combinations of "names" ($x^\star y^\star z^\star$, $y^\star z^\star x^\star$, or $z^\star x^\star y$) given to the principal axes of the angular distribution:

$$
\left(\frac{1+\lambda_\vartheta^\star}{3+\lambda_\vartheta^\star}, \frac{1+\lambda_\varphi^\star}{3+\lambda_\vartheta^\star}, \frac{1-\lambda_\varphi^\star}{3+\lambda_\vartheta^\star}\right) = \begin{cases} (\kappa_1, \kappa_2, \kappa_3) \\ (\kappa_2, \kappa_3, \kappa_1) \\ (\kappa_3, \kappa_1, \kappa_2) \end{cases}. \tag{3.37}
$$

The choice among the three options is conventional, but it can be driven by physical considerations. One option is to make the canonical form converge towards the one characterized by $\lambda_\vartheta^\star = 1$ (Eq. 3.27) when one underlying process dominates. For this, it is sufficient to choose the combination giving the largest positive $\lambda_\vartheta^\star$ value. In this case, the following procedure can be used. The first step is to define $\lambda_\vartheta^\star = \max_i \left\{\frac{3\kappa_i - 1}{1-\kappa_i}\right\}$, where the function of κ_i is the inverse of the one in the first diagonal element in Eq. 3.37. Let us assume, for discussion purposes, that κ_3 is the solution yielding such maximum. The subsequent alternative choices of either $\lambda_\varphi^\star = (3+\lambda_\vartheta^\star)\,\kappa_1 - 1$ or $\lambda_\varphi^\star = (3+\lambda_\vartheta^\star)\,\kappa_2 - 1$ differ only for the *sign* of $\lambda_\varphi^\star$, given that $(3+\lambda_\vartheta^\star)(\kappa_1+\kappa_2) - 2 = 0$, as implied by the unit-trace property, $\kappa_1 + \kappa_2 = 1 - \kappa_3$, and by the definition of $\lambda_\vartheta^\star$ as $(3\kappa_3 - 1)\,/\,(1-\kappa_3)$. This ambiguity is due to the fact that until here we are dealing with a purely geometrical representation, abstracting from the physical reference frame.

In fact, as seen in Eq. 3.26, $\lambda_\varphi^\star$ changes sign (and $\lambda_\vartheta^\star$ is invariant, while $\mathcal{F}^\star$ changes to $\frac{2(1+\lambda_\vartheta^\star)}{3+\lambda_\vartheta^\star} - \mathcal{F}^\star$) for a rotation by $\pi/2$ around the $z^\star$ axis, i.e. when the reference plane for the measurement of φ changes from the $z^\star x^\star$ plane to its perpendicular one, the $y^\star z^\star$ plane. Only when the principal axes are identified with physical directions, the sign of $\lambda_\varphi^\star$ will become unambiguously determined.

Figure 3.6 represents the $\lambda_\varphi^\star$ vs. $\lambda_\vartheta^\star$ two-dimensional domain of all possible distributions in canonical form. In fact, the two parameters satisfy the same positivity constraints of Eqs. 3.6 with $\lambda_{\vartheta\varphi} = 0$:

$$
|\lambda_\varphi^\star| \le \frac{1}{2}(1+\lambda_\vartheta^\star), \quad |\lambda_\vartheta^\star| \le 1. \tag{3.38}
$$

The six points marked on the border of the triangle represent the cases of natural longitudinal or transverse polarizations along the three axes. The sign ambiguity of $\lambda_\varphi^\star$ in this abstract frame-independent representation is well illustrated by the longitudinal cases. The diagonalization in this case reveals a "donut"-like shape, in one of its three orientations (red, blue or green), depending on the assumed order of the eigenvalues. The choice of the solution with the largest $\lambda_\vartheta^\star$ selects not one but two cases, the blue and the green orientations, both having $\lambda_\vartheta^\star = +1$. With the

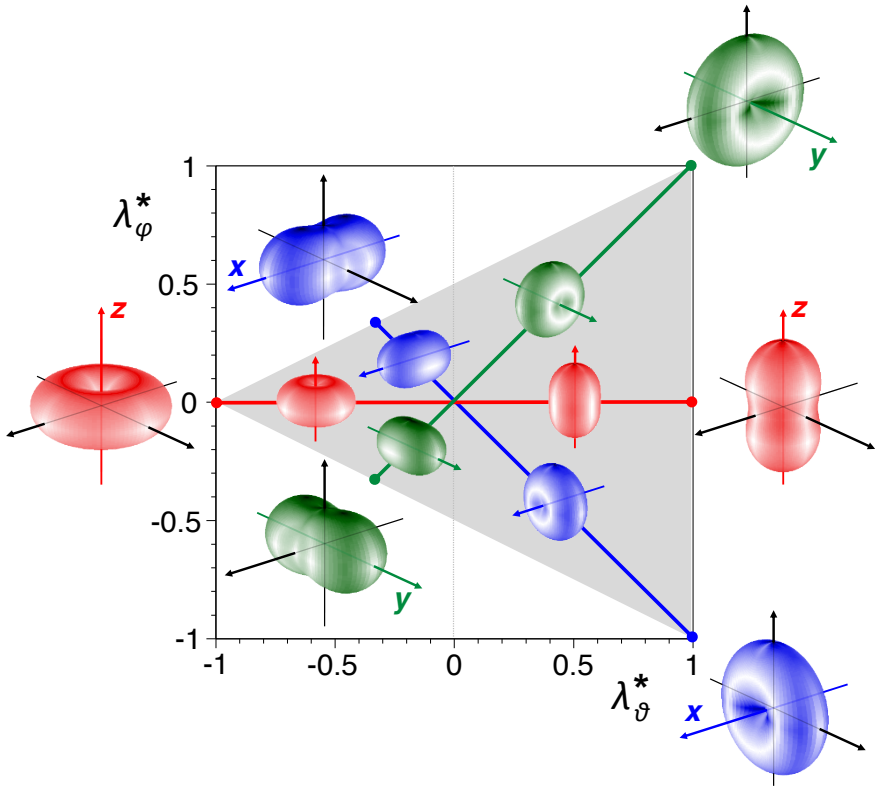

Fig. 3.6 The parameter space of the dilepton decay angular distribution in its canonical form, with $\lambda^\star_{\vartheta\varphi} = \lambda^{\perp\star}_{\vartheta\varphi} = \lambda^{\perp\star}_{\varphi} = 0$, i.e. having the $x^\star$, $y^\star$, and $z^\star$ axes as principal axes. The six points on the border correspond to natural transverse ($J_{z|x|y} = \pm 1$) or longitudinal ($J_{z|x|y} = 0$) polarizations, with distributions having the characteristic "peanut" and "donut" shapes. Those points are connected by coloured lines representing mixtures of processes that are longitudinal or transverse along the $z^\star$ (red), $x^\star$ (blue) or $y^\star$ (green) axes; "intermediate" shapes are shown inside the triangle. Each of these distributions has cylindrical symmetry with respect to its respective natural axis, so that, if we assume that axis as a new quantization direction $z^\star$, we will see that $\lambda^\star_\varphi$ vanishes.

specific axis orientations chosen in the figure, the blue shape has $\lambda^\star_\varphi = -1$ ($\mathcal{F}^\star = 0$) and the green one $\lambda^\star_\varphi = +1$ ($\mathcal{F}^\star = 1$). The alternative axis definition exchanging the $x^\star$ and $y^\star$ directions would exchange the signs of $\lambda^\star_\varphi$ and the values of $\mathcal{F}^\star$ between the two cases. Note that, instead, with the adopted diagonalization criterion, there is no ambiguity in the case of the "peanuts": the solution with maximal $\lambda^\star_\vartheta$, equal to +1 also this time, is now unique and the red shape is the one univocally selected (the other two have $\lambda^\star_\vartheta = -1/3$). In fact, this is a limit case where $\lambda^\star_\varphi = 0$, that is, the two alternative solutions coincide.

This suggests an alternative criterion, where the chosen canonical form is the one minimizing $|\lambda^\star_\varphi|$. In the limit $\lambda^\star_\varphi \to 0$, the distribution acquires a cylindrical

symmetry: two of the eigenvalues become identical. The procedure in this case consists in determining the pair of eigenvalues κ_i, κ_j minimizing the difference $|\kappa_i - \kappa_j|$ and defining $\lambda_\vartheta^\star$ from the *other* eigenvalue. The three coloured lines in the figure represent all configurations where this procedure leads to a univocal result (with $\kappa_i - \kappa_j = 0$), because $\lambda_\varphi^\star$ vanishes for a certain choice of $z^\star$ (the one coinciding with the axis of cylindrical symmetry). Along such axis the decay distribution results from the superposition of an ensemble of pure angular momentum eigenstates, in part longitudinally and in part transversely polarized, and its shape is intermediate between those of the two extremes, as can be seen in the examples shown inside the triangle, at their approximate coordinates.

The configurations deviating from the coloured lines often lose the cylindrical symmetry and, when this happens, two opposite $\lambda_\varphi^\star$ solutions appear. Also this criterion is, therefore, not immune to the seeming ambiguity in the sign of $\lambda_\varphi^\star$. In both procedures, the eigenvector corresponding to the eigenvalue chosen to define $\lambda_\vartheta^\star$ provides the direction of the new $z^\star$ axis with respect to the original axes (those of the frame where the angular distribution is measured). The other two eigenvectors provide the $x^\star$ and $y^\star$ directions: $x^\star$ and $y^\star$ cease to be "names" and become physical directions well defined in the experiment. If the distribution has an intrinsic azimuthal anisotropy, i.e. it has no cylindrical symmetry, $\lambda_\varphi^\star$ will be nonzero and its sign will indicate unambiguously how the shape is oriented around the $z^\star$ axis.

The main outcome of the previous discussion is that all possible *shapes* of a parity-conserving dilepton decay angular distribution can be classified with only *two* parameters, which are frame-independent and can, in principle, always be determined from the data. The *five* shape parameters of the angular distribution (Eq. 3.30) contain the additional information of how the shape is *oriented* in the three-dimensional space. The three additional degrees of freedom correspond to the three angles, ψ, ζ and ω, necessary to define the generic rotation of a rigid body (as in Fig. 2.22). Average values of such angles can, in principle, be determined from the observed distribution together with $\lambda_\vartheta^\star$ and $\lambda_\varphi^\star$, using the relations of Table 2.2 to express the vector of parameters $(\lambda_\vartheta, \lambda_\varphi, \lambda_{\vartheta\varphi}, \lambda_\varphi^\perp, \lambda_{\vartheta\varphi}^\perp)$ in terms of $(\lambda_\vartheta^\star, \lambda_\varphi^\star, 0, 0, 0)$ and of the rotation angles. In conclusion, $\lambda_\vartheta^\star$, $\lambda_\varphi^\star$, ψ, ζ and ω become the new parameters of the analysis.

Most measurements are made in less ideal conditions, where the process producing the decaying particle is only partially reconstructed, as is the case of inclusive-production studies, so that only λ_ϑ, λ_φ, and $\lambda_{\vartheta\varphi}$ survive the event-averaging effect and are observable. When $\lambda_\varphi^\perp$ and $\lambda_{\vartheta\varphi}^\perp$ are not seen, the observed shape is the "symmetrized" version of the original one: it is invariant by reflection about the production plane. Just like any other smearing effect, this symmetrization prevents the experiment from reconstructing the original, asymmetric shape. The canonical form of such event-averaged distribution can still be defined and still depends on the *two* shape parameters $\lambda_\vartheta^\star$ and $\lambda_\varphi^\star$, but only on one angle, defining the orientation of the shape in the plane of symmetry, that is, a rotation around the y axis, perpendicular to the plane.

The expressions of the invariant parameters in this simpler case can be derived by noticing that Eq. 2.32 can be rewritten in terms of an orthogonal matrix:

$$\begin{pmatrix} \lambda'_\vartheta - \lambda'_\varphi \\ \lambda'_{\vartheta\varphi} \\ \lambda^{\perp\prime}_\varphi \\ \lambda^{\perp\prime}_{\vartheta\varphi} \end{pmatrix} = \frac{1}{1+\Lambda_y} \begin{pmatrix} \cos 2\delta & \sin 2\delta & 0 & 0 \\ -\sin 2\delta & \cos 2\delta & 0 & 0 \\ 0 & 0 & \cos\delta & -\sin\delta \\ 0 & 0 & \sin\delta & \cos\delta \end{pmatrix} \begin{pmatrix} \lambda_\vartheta - \lambda_\varphi \\ \lambda_{\vartheta\varphi} \\ \lambda^\perp_\varphi \\ \lambda^\perp_{\vartheta\varphi} \end{pmatrix} . \tag{3.39}$$

This implies two new covariance relations, complementing those in Eq. 3.9:

$$\begin{aligned} \sqrt{\lambda^{\perp\prime 2}_\varphi + \lambda^{\perp\prime 2}_{\vartheta\varphi}} &= \frac{1}{1+\Lambda_y} \sqrt{\lambda^{\perp 2}_\varphi + \lambda^{\perp 2}_{\vartheta\varphi}} , \\ \sqrt{(\lambda'_\vartheta - \lambda'_\varphi)^2 + 4\lambda'^2_{\vartheta\varphi}} &= \frac{1}{1+\Lambda_y} \sqrt{(\lambda_\vartheta - \lambda_\varphi)^2 + 4\lambda^2_{\vartheta\varphi}} . \end{aligned} \tag{3.40}$$

Since there are three covariant quantities, $3 + \lambda_\vartheta$, $1 - \lambda_\varphi$, and $\sqrt{(\lambda_\vartheta - \lambda_\varphi)^2 + 4\lambda^2_{\vartheta\varphi}}$, depending on λ_ϑ, λ_φ, and $\lambda_{\vartheta\varphi}$, it is possible to define *two* invariant quantities, as ratios of linear combinations of those. This operation is similar to how we defined one invariant, $\mathcal{F}_{\{c_i\}}$, from the two covariants $3 + \lambda_\vartheta$ and $1 - \lambda_\varphi$ (in Section 3.4).

Incidentally, the fact that the ratio $(1 - \lambda_\varphi)\,/\,(3 + \lambda_\vartheta)$, equal to $(1 - \mathcal{F})\,/\,2$, is invariant, is also immediately visible in the expression of $\mathcal{M}$ (Eq. 3.32), where it appears as the middle diagonal element, which remains constant in rotations around the y axis.

To find the combination of covariants giving $\lambda^\star_\vartheta$ and $\lambda^\star_\varphi$, we can impose that the rotation brings to a frame where the "diagonal" element $\lambda_{\vartheta\varphi}$ vanishes and, therefore, the distribution becomes $\propto 1 + \lambda^\star_\vartheta \cos^2\vartheta + \lambda^\star_\varphi \sin^2\vartheta \cos 2\varphi$. From Eq. 2.13, we see that this happens when $\tan 2\delta = 2\lambda_{\vartheta\varphi}\,/\,(\lambda_\vartheta - \lambda_\varphi)$, or when $\delta = \pi/4$, if $\lambda_\vartheta = \lambda_\varphi$. Substituting this angle in the λ_ϑ and λ_φ transformations of that same equation, we obtain

$$\begin{aligned} \lambda^\star_\vartheta &= \frac{\lambda_\vartheta - 3\Lambda^\star}{1+\Lambda^\star} , \\ \lambda^\star_\varphi &= \frac{\lambda_\varphi + \Lambda^\star}{1+\Lambda^\star} , \\ \text{with} \quad \Lambda^\star &= \frac{1}{4}\left(\lambda_\vartheta - \lambda_\varphi \pm \sqrt{(\lambda_\vartheta - \lambda_\varphi)^2 + 4\lambda^2_{\vartheta\varphi}} \right). \end{aligned} \tag{3.41}$$

The two possible solutions (plus or minus sign) correspond to the cases in which the new z axis coincides with one or the other of the principal axes of symmetry belonging to the production plane. For example, if the vector particle is fully longitudinally polarized with respect to a certain quantization axis in that plane, the two solutions are $(\lambda^\star_\vartheta, \lambda^\star_\varphi) = (-1, 0)$ and $(+1, -1)$. If, instead, the polarization is fully transverse, then the solutions are $(\lambda^\star_\vartheta, \lambda^\star_\varphi) = (+1, 0)$ and $(-1/3, +1/3)$.

As discussed above, the definition of the absolute shape parameter $\lambda_\vartheta^\star$ can be made univocal by always choosing either the solution with larger positive $\lambda_\vartheta^\star$ or the one giving the smaller $|\lambda_\varphi^\star|$. Moreover, in this case, since frame rotations around an axis different from the y axis are no longer foreseen, the $\lambda_\varphi^\star$ sign ambiguity seen in the most general case disappears. It is, therefore, always possible to define both $\lambda_\vartheta^\star$ and $\lambda_\varphi^\star$ univocally. Then, $\lambda_\vartheta^\star$ represents the best possible approximation of either — depending on the convention — the polar anisotropy with respect to the $z^\star$ axis of Theorem 3.1, or the natural polarization, when it exists and is uniquely definable.

The rotation invariants $\lambda_\vartheta^\star$ and $\lambda_\varphi^\star$ are related to λ_ϑ, λ_φ and to the invariant $\mathcal{F}$ by the expression

$$\frac{1+\lambda_\vartheta^\star+2\lambda_\varphi^\star}{3+\lambda_\vartheta^\star} = \mathcal{F} = \frac{1+\lambda_\vartheta+2\lambda_\varphi}{3+\lambda_\vartheta}\,. \tag{3.42}$$

It should be noted that the second equality is not valid, in general, for the previously defined $\mathcal{F}^\star$ parameter, which, being invariant for *any* rotation, actually depends, just like $\lambda_\vartheta^\star$ and $\lambda_\varphi^\star$ in that case, on all five parameters of the distribution.

It is possible to obtain $\lambda_\vartheta^\star$ and $\lambda_\varphi^\star$ directly, by fitting the observed angular distribution performing the following substitutions in Eq. 2.1:

$$\begin{aligned}
\lambda_\vartheta &\longrightarrow \frac{\lambda_\vartheta^\star - 3\overline{\Lambda}}{1+\overline{\Lambda}}\,,\\
\lambda_\varphi &\longrightarrow \frac{\lambda_\varphi^\star + \overline{\Lambda}}{1+\overline{\Lambda}}\,,\\
\lambda_{\vartheta\varphi} &\longrightarrow \frac{-\frac{1}{2}\,(\lambda_\vartheta^\star - \lambda_\varphi^\star)\sin 2\overline{\delta}}{1+\overline{\Lambda}}\,,\\
&\text{with}\quad \overline{\Lambda} = \frac{1}{2}\,(\lambda_\vartheta^\star - \lambda_\varphi^\star)\sin^2\overline{\delta}\,.
\end{aligned} \tag{3.43}$$

The third parameter of the fit, $\overline{\delta}$, is the angle by which the shape of the angular distribution is tilted with respect to the principal axes of symmetry, in the specific kinematic conditions considered. While in the most general case three rotation angles would be necessary to define an alternative set of parameters, as previously mentioned, here $\overline{\delta}$, representing a rotation in the zx plane, forms a complete set together with $\lambda_\vartheta^\star$ and $\lambda_\varphi^\star$. A fit performed using this parametrization has two solutions, in which the two values of $\overline{\delta}$ differ by $\pi/2$, corresponding to the two canonical forms of the angular distribution. The criteria discussed above help choosing between the two.

As a final remark, we note that the existence of a diagonal form of the distribution clarifies why the invariant polarization parameter $\mathcal{F}$ depends only on λ_ϑ and λ_φ. In fact, $\lambda_{\vartheta\varphi}$ can be interpreted as a measure of the "tilt" of the chosen system of axes with respect to the principal axes of symmetry of the distribution, while $\mathcal{F}$ represents an intrinsic (rotation-independent) characteristic of the *shape* of the angular distribution.

3.10 Frame-independent parity-violating asymmetry

We will now study the rotational properties of the parity-violating coefficients A_ϑ, A_φ, and $A_\varphi^\perp$. The matrix expression of the most general transformation in Table 2.2 implies the following covariance relation, valid for *any* rotation (while those given in Eqs. 3.9 and 3.40 only refer to rotations around the y axis):

$$\sqrt{A_\vartheta'^2 + A_\varphi'^2 + A_\varphi^{\perp\prime 2}} \;=\; \frac{1}{1+\Lambda}\,\sqrt{A_\vartheta^2 + A_\varphi^2 + A_\varphi^{\perp 2}}\,. \tag{3.44}$$

Moreover, from the transformation for λ_ϑ, it can be verified that $3 + \lambda_\vartheta$ is another completely general covariant quantity:

$$3 + \lambda_\vartheta' \;=\; \frac{1}{1+\Lambda}\,(3 + \lambda_\vartheta)\,. \tag{3.45}$$

Therefore, the following quantity is fully rotation-invariant:

$$\mathcal{A}^\star \;=\; \frac{4}{3+\lambda_\vartheta}\,\sqrt{A_\vartheta^2 + A_\varphi^2 + A_\varphi^{\perp 2}}\,. \tag{3.46}$$

It takes values between 0 and 1, and represents the magnitude of the *maximum* parity-violating effect that can be observed in any polarization frame. It is related to the three asymmetries of Eq. 1.30 by the relation

$$\mathcal{A}^\star \;=\; \frac{4}{3}\,\sqrt{\mathcal{A}^2_{\cos\vartheta} + \mathcal{A}^2_{\cos\varphi} + \mathcal{A}^2_{\sin\varphi}}\,. \tag{3.47}$$

The parameter $A_\varphi^\perp$ and the corresponding asymmetry $\mathcal{A}_{\sin\varphi}$ should be small, as a consequence of the approximate symmetry with respect to the production plane expected for the decay distribution of inclusively produced vector bosons. In any case, these parameters can be neglected without affecting the exactness of the frame-independent formalism. In fact, the "reduced" invariant asymmetry

$$\begin{aligned}\mathcal{A}^\star_{\mathrm{R}} \;&=\; \frac{4}{3+\lambda_\vartheta}\,\sqrt{A_\vartheta^2 + A_\varphi^2} \\ &=\; \frac{4}{3}\,\sqrt{\mathcal{A}^2_{\cos\vartheta} + \mathcal{A}^2_{\cos\varphi}}\end{aligned} \tag{3.48}$$

is exactly invariant under rotations about the y axis (while $\mathcal{A}^\star$ is invariant under *any* rotation) and is, therefore, independent of the choice of a polarization axis belonging to the production plane.

The rotation-invariant parameter $\mathcal{A}^\star$ can be determined directly from a fit of the measured angular distribution (taking into account the detection acceptance and efficiencies) with *any* choice of polarization frame, through a suitable substitution of parameters in Eq. 1.29. For example:

$$A_\vartheta \;\to\; \frac{(3+\lambda_\vartheta)\,\mathcal{A}^\star}{4}\cos\xi\,,$$

$$A_\varphi \;\to\; \frac{(3+\lambda_\vartheta)\,\mathcal{A}^\star}{4}\sin\xi\cos\chi\,, \tag{3.49}$$

$$A_\varphi^\perp \;\to\; \frac{(3+\lambda_\vartheta)\,\mathcal{A}^\star}{4}\sin\xi\sin\chi\,.$$

The fit also yields the values of the angles ξ and χ, which represent the rotation of the current polarization axis to the one with respect to which the maximum partity-violation effect would be observed, i.e., the axis of maximum projection of the vector $(A_\vartheta, A_\varphi, A_\varphi^\perp)$. With $A_\varphi^\perp$ being negligible, the χ angle may be set to zero.

3.11 The frame-independent counterpart of λ_ϑ

Another possible definition of the invariant polarization parameter (Eq. 3.10) has a particularly intuitive and useful meaning. The observable

$$\tilde{\lambda} \;\equiv\; \mathcal{F}_{\{1,-3,0,1\}} \;=\; \frac{\lambda_\vartheta + 3\,\lambda_\varphi}{1-\lambda_\varphi} \tag{3.50}$$

can be considered as a frame-independent version of the polar anisotropy parameter λ_ϑ: when the polarization is naturally fully longitudinal or fully transverse with respect to whatever axis (even an unknown one), it assumes the values -1 and $+1$, respectively, while it is zero in the unpolarized case, that is, when the transverse component is twice as large as the longitudinal one [3]. Contrary to λ_ϑ, it can, however, assume values larger than $+1$, corresponding to the region of invariant parameter space delimited by the $\mathcal{F} = 1/2$ plane on the side of the vertex of the cone (Fig. 3.3). Towards that vertex, while $\mathcal{F}$ remains finite and between $1/2$ and 1, the variable $\tilde{\lambda}$ tends to ∞.

The determination of the invariant polarization is immune to the "extrinsic" kinematic dependences of λ_ϑ, λ_φ, and $\lambda_{\vartheta\varphi}$, illustrated in Figs. 2.9, 2.10, and 2.11, which are due to nothing else than a change in observation perspective with respect to the "natural" frame (where the polarization is constant). In the scenarios considered in those figures, a measurement will always yield, in the absence of experimental biases, the values $\tilde{\lambda} = +1$ ($\mathcal{F} = 1/2$) for the transverse case (natural in either the HX or CS frame) and $\tilde{\lambda} = -1$ ($\mathcal{F} = 0$) for the longitudinal one, both results being completely independent of p_T, y, and m: the value of $\tilde{\lambda}$ is identical to the value of λ_ϑ in the natural polarization frame.

This is also true for the J/ψ and Υ(1S) examples illustrated in Fig. 2.21: the measurement would in these cases yield $\tilde{\lambda} = +1$ for all experiments, independently of the choice of the frame and of the rapidity range, indicating that the significant variations seen for the frame-dependent λ_ϑ, λ_φ, and $\lambda_{\vartheta\varphi}$ parameters are not caused by

experimental biases, nor by strong physically-relevant ("intrinsic") dependences of the underlying production processes on the particle's rapidity, but rather by the "extrinsic" kinematic dependences generated by how polarizations transform from one frame to another. It is also interesting to note that, when the underlying physics is not intrinsically momentum dependent, the frame-independent polarization, $\tilde{\lambda}$, remains immune not only to changes in the overall acceptance window ("geometrical coverage") but also to variations in the kinematic dependences of the detection efficiencies within those windows.

While it is correct to say that the value of $\tilde{\lambda}$ always represents, irrespectively of its measurement frame, the intrinsic "nature" of polarization, assuming the value $+1$ or -1 if the particle is, in each event, produced as a $J = \pm 1$ or $J = 0$ state along some quantization axis, it can happen, in some cases, that there is no uniquely defined "natural" frame where the measurement can be performed. An interesting example is the case of Drell–Yan production, where the main contributing processes lead to transverse polarizations with respect to significantly different quantization axes, as seen in Fig. 2.2. In the presence of such a superposition of topologically different processes, no individual choice of the polarization frame leads to a simple observation of a constant, "natural" polarization. It is in more complex cases like this that the use of the invariant polarization provides the biggest advantage in terms of immediate understanding of the underlying physics. This concept is the main subject of Chapter 4.

3.12 Searching for biases using $\tilde{\lambda}$

Polarization measurements are clearly not simple to perform and many examples can be found of difficulties related to experimental hurdles, among which we can cite the effects introduced by detection efficiencies on the measured distributions, as discussed in Section 1.5. It should be kept in mind that polarization measurements are directly based on the correlations between two particles, such as the two muons emitted in the decay of a J/ψ, so that we need to be very careful about effects that might affect the detection of the *pair* and the measurement of their (correlated) kinematical variables.

We have already shown in Section 2.13 how the dependence of the detector acceptance on the momenta of the decay products creates strong $\cos\vartheta$–φ modulations. It might also happen that the efficiency of the experiment to detect one of the two daughter particles depends on the kinematics of the other one. For instance, a detector might be inefficient when the two particles (the two muons, say) cross the same detection elements, at least in a section of their trajectories. Such inefficiencies will directly affect the probability that the pair of muons is detected, therefore sculpting the angular distributions that are needed to measure polarizations. If the detector performance is not known with sufficiently good accuracy, maybe because the Monte Carlo simulations do not faithfully reproduce the data collection conditions (material budget, magnetic field map, detector calibrations, geometric alignment,

etc.), then the final measurement, not fully corrected for the detector effects, may be biased, sometimes even showing unphysical distributions.

Another frequent source of potential problems is the treatment of the background inevitably associated to all polarization measurements. The vector quarkonia J/ψ, ψ(2S), and Υ(nS), in particular, are usually detected using the dimuon decay channel, which is ideal for the measurement of their polarizations, as long as the analyses include a reliable subtraction of the underlying continuum background due to pairs of uncorrelated muons. These background muon pairs, if not accurately subtracted, will bias the polarization measurements, especially in the cases where the peaks have a poor signal to background ratio, which is usually the case of the ψ(2S) and Υ(3S) states. This problem is particularly important in experiments that suffer from poor measurement resolutions, where the background "under the peak" is correspondingly larger, since it is integrated over a broader mass range. Poor mass resolutions also lead to a different kind of background, the cross-feed between two close-by peaks, as is often the case of the Υ(2S) and Υ(3S) mesons.

The measurement of the frame-invariant parameter $\tilde{\lambda}$ can be used as a tool to probe the existence of systematic effects not properly covered by the reported uncertainties. For example, it is easy to understand that the values of $\tilde{\lambda}$ measured in two different frames will likely *not* be identical if the probed dimuon sample is dominated by uncorrelated muon pairs, which are not the daughters of a vector particle. In fact, the angular distribution of these pairs, observed in their rest frame, is not expected to have a physical shape and, in particular, not the characteristic shape of the two-body decay of a vector state, with parameters satisfying the constraints described in Section 3.2 and transforming from frame to frame according to the corresponding covariance relations (Sections 3.4–3.5).

As an illustration, we will consider the case of two experiments that study the polarization of a given particle, using the same colliding particles, the same collision energy, in the same decay channel, and in the same kinematic domain. The only difference is that the λ_ϑ and λ_φ parameters are measured in the HX frame by the first experiment and in the CS frame by the second. Let us assume that these hypothetical experiments report the λ_ϑ and λ_φ values shown in Fig. 3.7. What can we say about the compatibility of the two measurements? This question can be answered by evaluating $\tilde{\lambda}$ for each of the two frames. The result, on the right panel of Fig. 3.7, shows a clear discrepancy for the lowest p_{T} measurement, which can be considered as evidence that one of the two experiments (or both) reported systematic uncertainties (for that kinematic interval) that are significantly smaller than the real ones. Since $\tilde{\lambda}$ is "homogeneous" to λ_ϑ, we can also deduce that the error is quantitatively equivalent to a bias of order 0.4 in the polar anisotropy.

This example shows the importance of measuring the frame-independent parameter $\tilde{\lambda}$ in two frames as a valuable tool to reveal unaccounted residual systematic effects biasing the experimental results. The two chosen frames should be as "orthogonal" as possible, to maximize the possibility that their sensitivities to analysis biases are quantitatively different. For example, we have seen in Section 2.12 that the shape of the efficiency as a function of $\cos\vartheta$ and φ is very different in the CS and HX frames, so that, for example, the effects due to an improper integration over

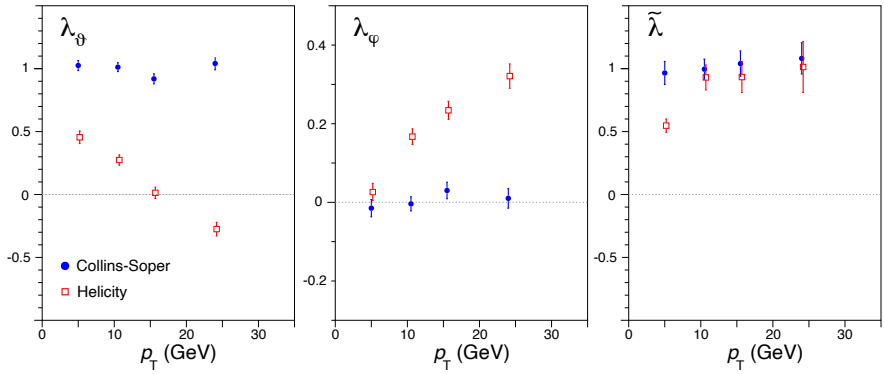

Fig. 3.7 Illustration of a case where the λ_ϑ and λ_φ polarization parameters measured by two experiments, in two different frames, are inconsistent with each other (in the lowest p_{T} bin).

the azimuthal variable in a one-dimensional analysis will be quantitatively different in the two frames. The combination of the CS and PX frames may be, from this point of view, an even better choice, given that the two efficiency maps maintain the strongest shape difference at every value of p_{T} and rapidity, with the CS frame showing the maximum and the PX frame the minimum correlation between the two variables.

The use of $\tilde{\lambda}$ as a tool to check the reliability of the systematic uncertainties implies that exactly the same event sample is used in its measurement in the two (sufficiently different) polarization frames, so that the statistical uncertainties cancel in the comparison. In that way, the differences between the *central values* of the two $\tilde{\lambda}$ evaluations can be used to see if certain steps of the analysis should be revisited (correction of the detection efficiencies, background subtraction, etc.). For this purpose, figures showing $\tilde{\lambda}$ vs. p_{T} as measured in the HX and CS frames with their *total* uncertainties are not as informative as when the systematic uncertainties are presented separately. An even better method for the verification of residual systematic effects consists in determining the variations directly for the *difference* between the two sets of $\tilde{\lambda}$ values. The resulting values of, say, $\tilde{\lambda}^{\mathrm{CS}} - \tilde{\lambda}^{\mathrm{HX}}$ would then be compared with zero within their purely systematic uncertainty, properly taking into account that some of the variations may be correlated or anti-correlated in the the two frames.

Figure 3.8 shows recent measurements of λ_ϑ and λ_φ, in the HX and CS frames, reported by the LHCb [8] and ALICE [9] Collaborations for J/ψ mesons produced in pp and Pb-Pb collisions, respectively. We can deduce from these results that the $\tilde{\lambda}$ values corresponding to the three highest p_{T} bins of LHCb change from around -0.20 in the HX frame to around -0.11 in the CS frame, a difference that does not seem to be negligible with respect to the reported uncertainties. The difference in the $\tilde{\lambda}$ values that can be inferred from the ALICE points is similar, around 0.1 in the intermediate p_{T} bin, a variation that also seems to be quite large, in comparison to the reported (systematic) uncertainties. These are qualitative observations, only

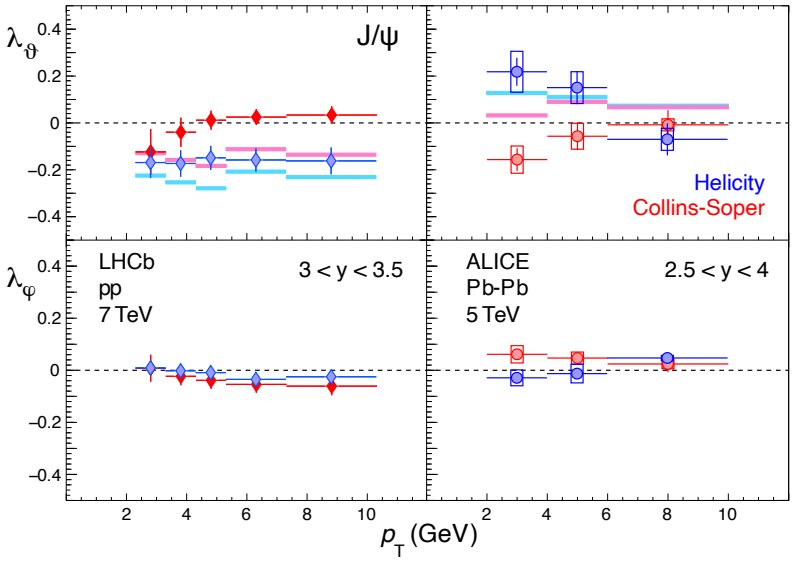

Fig. 3.8 Values of the polarization parameters λ_ϑ (top) and λ_φ (bottom) reported by the experiments LHCb [8] (left) and ALICE [9] (right), in the HX (blue) and CS (red) frames. The corresponding central values of $\tilde{\lambda}$ are shown as cyan (HX) and magenta (CS) horizontal bars.

meant to illustrate the importance of proper measurements of the *difference* between two sets of $\tilde{\lambda}$ values, including a reliable evaluation of its uncertainty, as a tool to eliminate doubts regarding potential biases.

Figure 3.9 shows an example of $\tilde{\lambda}$ measurements made in the HX and CS frames, as a function of p_{T}. They were reported by the CDF Collaboration [10] and correspond to Υ(nS) polarizations in pp collisions at 1.96 TeV. In general, the two sets of $\tilde{\lambda}$ values are in good agreement for the Υ(1S) state, while the Υ(2S) and Υ(3S) patterns do not show such a good overlap, especially in the lowest and highest p_{T} bins. It is probably not a coincidence that the signal to background ratio is better for the 1S state than for the 2S and 3S states. The biggest "fluctuations" are seen in the lowest p_{T} bin, which is where the background under the signal peaks is the largest. The $\tilde{\lambda}$ values measured for the lowest p_{T} Υ(3S) mesons are particularly outstanding, being significantly larger than +1.

To further illustrate the application of the frame-independent formalism as a practical tool to spot problems in experimental data analyses, we refer again to the J/ψ pseudo-experiments described in Section 2.13, generated with fully longitudinal polarization in the HX frame, $\lambda_\vartheta^{\mathrm{HX}} = -1$ and $\lambda_\varphi^{\mathrm{HX}} = 0$. In Fig. 2.20 we showed what happens if one applies one-dimensional acceptance corrections, computed assuming unpolarized production, when measuring the parameters λ_ϑ and λ_φ, in the CS and HX frames. From the four one-dimensional values obtained without iterative reweighing (corresponding to the distributions shown in blue in the four panels), we obtain, using Eq. 3.50, $\tilde{\lambda}^{\mathrm{CS}} \simeq -0.30$ and $\tilde{\lambda}^{\mathrm{HX}} \simeq -0.97$. The large difference between

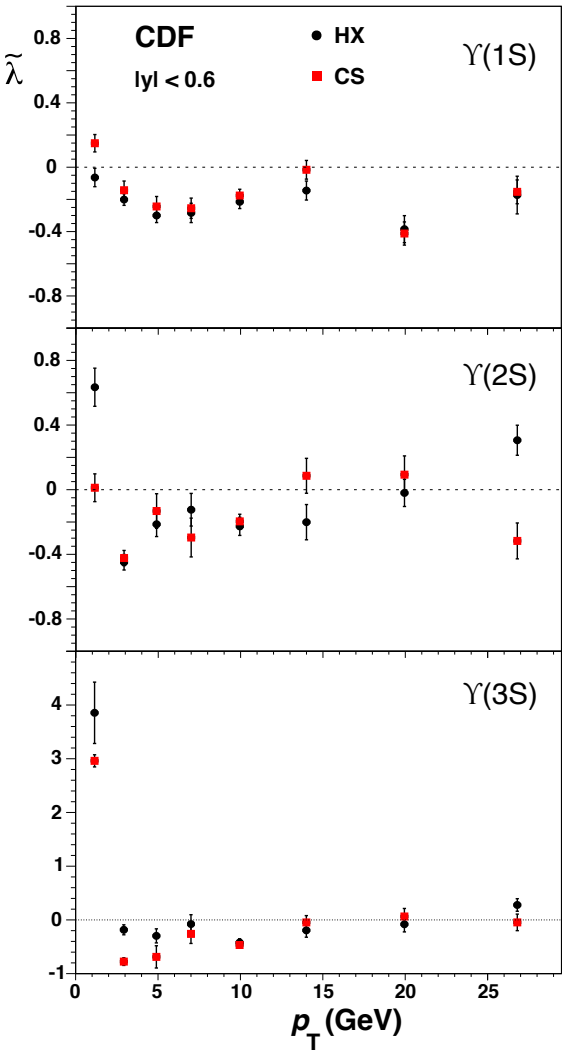

Fig. 3.9 Values of the $\tilde{\lambda}$ polarization parameter reported by CDF [10] in the HX (black circles) and CS (red squares) frames, for the Υ(1S) (top), Υ(2S) (middle), and Υ(3S) (bottom).

the two values is an unequivocal signal of a mistake in the analysis. Instead, using the distributions (represented in red) obtained by reweighing the Monte Carlo with the "correct" polarization, iteratively inferred by successively choosing as "generation frame" the one showing the strongest polarization modulations (the HX frame in this case), both $\tilde{\lambda}$ values approach -1, as expected in this specific exercise.

We also see from this example that the correct $\tilde{\lambda}$ value is generally not *included* between the ones found in two different frames, in the presence of not completely

corrected systematic effects. It is not recommendable, therefore, to use as best value of $\tilde{\lambda}$ the *average* between the values obtained in different frames. In the example just discussed, the best value of $\tilde{\lambda}$ is the one found in the frame showing the smallest acceptance correlations between $\cos\vartheta$ and φ (the HX frame, in this case, as can be seen in Fig. 2.18). For the same reason, it is not always a correct practice to impose $\tilde{\lambda}^{\mathrm{CS}} = \tilde{\lambda}^{\mathrm{HX}}$ as a constraint in a simultaneous fit of the angular distributions observed in two frames (a method that has been used in the literature), without previously investigating reasonable causes of the discrepancy.

3.13 Recapitulation

While the parameters λ_ϑ, λ_φ, $\lambda_{\vartheta\varphi}$, etc., of the dilepton decay distribution of a vector particle depend on the reference frame, general frame-independent relations exist between them.

A first category of such relations is a set of inequalities delimiting the allowed phase space of the anisotropy parameters: Eq. 3.5 for the case of the inclusive observation of the particle V in processes of the kind $\mathrm{h}_1\,\mathrm{h}_2 \to V + X$ and, more generally, Eq. 3.24.

The physical domain for the parameters λ_ϑ, λ_φ and $\lambda_{\vartheta\varphi}$ is an oblique cone (Figs. 3.1 and 3.2), whose intersections with the planes $(1+\lambda_\vartheta+2\lambda_\varphi)\,/\,(3+\lambda_\vartheta) = \mathcal{F}$, with $0 < \mathcal{F} < 1$, contain the elliptical trajectories representing all possible rotations from one reference frame to another (around the y axis). Each transformation preserves, therefore, the value of $\mathcal{F}$. When the polarization is transverse or longitudinal in the "natural" frame, $\mathcal{F}$ equals, respectively, 0 and 1 in *any* other frame. This implies that the intrinsic nature of the polarization can be defined in an absolute, rotation-invariant fashion.

This result is interesting because, while the underlying elementary production processes and the involved interaction couplings usually lead to a distinctive polarization signature, the measurement of the frame-dependent parameters may not immediately reflect it, if the chosen frame is different from the natural one. As will be discussed in detail in the next chapter, the production of Drell–Yan lepton pairs is an emblematic example: helicity conservation in the coupling between light quarks and gluons represents a strongly polarizing mechanism leading to an unmistakable transverse polarization, even if along more than one possible direction, depending on the topology of the process (as seen in Fig. 2.2).

Except for the "one-dimensional" $p_{\mathrm{T}} \to 0$ limit, where all polarization directions tend to coincide, or when only one natural quantization direction exists and the analysis chooses it as reference axis, the measurement of λ_ϑ may fail to provide an evidence of the underlying fully transverse polarization. As will be seen, this evidence is fully recovered when the frame-independent polarization parameter is measured.

The parameter $\mathcal{F}$, defined as a combination of λ_ϑ and λ_φ, can be determined directly from the measurement of the two-dimensional $\cos\vartheta, \varphi$ angular distribution

(Eq. 3.19), or even from the distribution of one suitably defined angle (Eqs. 3.21 and 3.23), provided that the caveats of one-dimensional analyses are taken into account.

While $\mathcal{F}$ represents an intrinsic polarization and does not directly parametrize the different possible shapes of the distribution, other frame-independent relations exist, reflecting purely geometrical properties.

As a three-dimensional solid figure, the distribution can be written in a "canonical" form, depending on "absolute" shape parameters and, in principle, three rotation angles describing the spatial orientation of the shape. In particular, it is always possible to "diagonalize" the parity conserving term of the distribution (depending on λ_ϑ, λ_φ, $\lambda_{\vartheta\varphi}$, $\lambda_\varphi^\perp$, and $\lambda_{\vartheta\varphi}^\perp$) to a two-parameter shape (Eqs. 3.30 and 3.32), by taking as axes its principal axes of symmetry. Moreover, with a suitable rotation it is possible to simplify the parity violating term (depending on A_ϑ, A_φ, $A_\varphi^\perp$) so that only the polar component of the asymmetry survives. Not always, however, the two terms can be diagonalized simultaneously, as exemplified in Fig 3.5. These considerations, reported with somewhat technical details in Sections 3.8 and 3.9, refer to the hypothetical case where the full geometry of the decay (including the direction of the recoiling particle X) is reconstructed event after event, preventing the parameters $\lambda_\varphi^\perp$, $\lambda_{\vartheta\varphi}^\perp$ and $A_\varphi^\perp$ from being suppressed by rotational smearing and event symmetrization effects.

In the more usual case of an "inclusive" production measurement, where those parameters effectively vanish, the diagonalization of the parity-conserving term reduces to a rotation in the production plane, providing simple mathematical relations for the two frame-independent polar- and azimuthal-anisotropy parameters $\lambda_\vartheta^\star$ and $\lambda_\varphi^\star$ (Eq. 3.41). These are related to $\mathcal{F}$ by the same expression valid for the frame-dependent parameters, Eq. 3.42. Two of these three rotation-invariant parameters, together with the rotation angle between the observation frame and the "canonical" one, form, therefore, a complete set of observables, replacing λ_ϑ, λ_φ and $\lambda_{\vartheta\varphi}$ (Eq. 3.43).

Additionally, the parity-violating part of the distribution can be represented with one absolute asymmetry, $\mathcal{A}^\star$ (Eq. 3.46), representing the modulus of the maximum parity asymmetry that can be observed by varying the orientation of the polarization axis. Also this parameter can be determined directly with a fit of the (acceptance- and efficiency-corrected) event distribution to a functional shape, also depending on one or two orientation angles (Eq. 3.49).

Some limitations in the effective frame-transformation invariance of the parameters $\lambda_\vartheta^\star$, $\lambda_\varphi^\star$ and $\mathcal{A}^\star$, due to their non linear dependence on the coefficients of the angular terms of the distribution, will be discussed in the next chapter, where they will be renamed as "quasi-invariants".

The parameter $\tilde{\lambda} = (\lambda_\vartheta + 3\lambda_\varphi) / (1 - \lambda_\varphi)$, related to the invariant $\mathcal{F}$ by the relation $\tilde{\lambda} = -(1-3\mathcal{F}) / (1-\mathcal{F})$, provides, in any frame, the value of the "natural" polarization (a pure polar anisotropy in the natural frame), when it exists. The crucial difference between $\lambda_\vartheta^\star$ and $\tilde{\lambda}$, and the general advantage of the latter, will be understood in the next chapter, where superpositions of processes having natural polarizations along different axes (as in the Drell–Yan case) will be considered.

The frame-independence of $\mathcal{F}$ or $\tilde{\lambda}$ (and, with some limitations to be discussed, of $\lambda_\vartheta^\star$ and/or $\lambda_\varphi^\star$) can be exploited as a test condition to be verified during the experimental analysis, repeating the measurement in at least two sufficiently "orthogonal" frames: when it is not exactly satisfied (within systematic uncertainties, but not considering the statistical ones, if the two measurements use the same events), it must be concluded that one or more steps of the analysis procedure are affected by biases that have not been fully accounted for.

References

[1] P. Faccioli, C. Lourenço, and J. Seixas, "Rotation-invariant relations in vector meson decays into fermion pairs", *Phys. Rev. Lett.* **105** (2010) 061601, doi:10.1103/PhysRevLett.105.061601, arXiv:1005.2601.

[2] P. Faccioli, C. Lourenço, J. Seixas, and H. K. Wöhri, "Rotation-invariant observables in parity-violating decays of vector particles to fermion pairs", *Phys. Rev. D* **82** (2010) 096002, doi:10.1103/PhysRevD.82.096002, arXiv:1010.1552.

[3] P. Faccioli, C. Lourenço, and J. Seixas, "A new approach to quarkonium polarization studies", *Phys. Rev. D* **81** (2010) 111502, doi:10.1103/PhysRevD.81.111502, arXiv:1005.2855.

[4] P. Faccioli, C. Lourenço, J. Seixas, and H. K. Wöhri, "Towards the experimental clarification of quarkonium polarization", *Eur. Phys. J. C* **69** (2010) 657, doi:10.1140/epjc/s10052-010-1420-5, arXiv:1006.2738.

[5] P. Faccioli, C. Lourenço, J. Seixas, and H. K. Wöhri, "Model-independent constraints on the shape parameters of dilepton angular distributions", *Phys. Rev. D* **83** (2011) 056008, doi:10.1103/PhysRevD.83.056008, arXiv:1102.3946.

[6] S. Palestini, "Angular distribution and rotations of frame in vector meson decays into lepton pairs", *Phys. Rev. D* **83** (2011) 031503, doi:10.1103/PhysRevD.83.031503, arXiv:1012.2485.

[7] W.-C. Chang, R. E. McClellan, J.-C. Peng, and O. Teryaev, "Lepton angular distributions of fixed-target Drell–Yan experiments in perturbative QCD and a geometric approach", *Phys. Rev. D* **99** (2019) 014032, doi:10.1103/PhysRevD.99.014032, arXiv:1811.03256.

[8] LHCb Collaboration, "Measurement of J/ψ polarization in pp collisions at $\sqrt{s}$ = 7 TeV", *Eur. Phys. J. C* **73** (2013) 2631, doi:10.1140/epjc/s10052-013-2631-3, arXiv:1307.6379.

[9] ALICE Collaboration, "First measurement of quarkonium polarization in nuclear collisions at the LHC", *Phys. Lett. B* **815** (2021) 136146, doi:10.1016/j.physletb.2021.136146, arXiv:2005.11128.

[10] CDF Collaboration, "Measurements of angular distributions of muons from Υ meson decays in $p\bar{p}$ collisions at $\sqrt{s}$ = 1.96 TeV", *Phys. Rev. Lett.* **108** (2012) 151802, doi:10.1103/PhysRevLett.108.151802, arXiv:1112.1591.

Chapter 4
Meaning and interpretation of the frame-independent polarization

The invariant polarization observable $\mathcal{F}$ (or $\tilde{\lambda}$) introduced in the previous chapter is particularly interesting in certain physics scenarios, where none of the adoptable polarization frames would provide a particularly simple picture in terms of λ_ϑ, λ_φ and $\lambda_{\vartheta\varphi}$. One such case is the production of Drell–Yan dileptons. Their polarization parameters, when calculated including perturbative QCD corrections, satisfy the Lam–Tung identity (reported in 1978), a frame-independent relation maintaining its seemingly surprising simplicity even when the polar and azimuthal anisotropies have strong dependences on the particle momentum. The notion of invariant polarization allows us to reinterpret this relation in a geometrical way, explaining it as a mere consequence of helicity conservation and rotational invariance.

In the illustration of these concepts, we will go through the following questions.

- How are the measurable $\mathcal{F}$ and $\tilde{\lambda}$ parameters related to those of the individual underlying production subprocesses, possibly having different natural polarization axes?
- Which advantages offer the invariant polarization in the interpretation of Drell–Yan, Z and W measurements?
- How should the geometrical invariants $\lambda^\star_\vartheta$ and $\lambda^\star_\varphi$, as well as the invariant parity asymmetry $\mathcal{A}^\star$, be interpreted and used?

P. Faccioli and C. Lourenço, *Particle Polarization in High Energy Physics*,
Lecture Notes in Physics 1002,
https://doi.org/10.1007/978-3-031-08876-6_4

4.1 Addition rules for invariant shape parameters

We have seen in Chapter 3 that, when a particle is produced with a natural transverse or longitudinal polarization along one well defined quantization axis, this property can immediately be recognized even if the measurement has chosen *another* quantization axis and even if the "natural" polarization axis is unknown: it is sufficient to determine the value of the invariant polarization parameter.

Natural transverse and longitudinal polarizations are revealed in any chosen frame by the respective conditions $\tilde{\lambda} = +1$ and -1, or, equivalently, $\mathcal{F} = 1/2$ and 0. This also means that, in such extreme physical cases, while an "arbitrary" frame choice can show complicated patterns of kinematic dependences for λ_ϑ, λ_φ, and $\lambda_{\vartheta\varphi}$, as those seen in Figs. 2.9, 2.10, and 2.11, even creating seeming discrepancies between experiments covering different rapidity ranges, as seen in Fig. 2.21, the same choice, whatever it is, will always show the same, simple scenario of an extreme, constant value of $\tilde{\lambda}$ or $\mathcal{F}$.

In this chapter we consider a more complex hypothesis, where several, rather than *one*, natural polarization axes exist, each one reflecting the topology of a category of subprocesses contributing to the particle's production. This hypothesis has at least one important physical counterpart, the one of Drell–Yan production, where, as anticipated in Chapter 2 (Fig. 2.2) and hereafter discussed in more detail (in Section 4.3), different process configurations, all simultaneously contributing to the observed distributions in some proportions, are best reflected by different definitions of the polarization axis.

We will, therefore, consider examples where the observed particles result from a superposition of production mechanisms, characterized by different natural polarizations along different quantization axes. It was shown in Section 1.8 (Eq. 1.17) how the frame-dependent polarization parameters for the observed mixture of processes are related to those of the individual processes. We have seen that λ_ϑ, λ_φ, and $\lambda_{\vartheta\varphi}$ do not sum linearly, as comprehensible since they are akin to asymmetries, not to yields: the sum, reported here for clarity in the case of λ_ϑ,

$$\lambda_\vartheta = \sum_{i=1}^{n} \frac{f^{(i)}}{3+\lambda_\vartheta^{(i)}} \lambda_\vartheta^{(i)} \Big/ \sum_{i=1}^{n} \frac{f^{(i)}}{3+\lambda_\vartheta^{(i)}}, \tag{4.1}$$

requires the use of a further weight, $1/(3+\lambda_\vartheta^{(i)})$, besides the fractional contribution $f^{(i)}$ of the process to the particle yield. To determine the analogous addition rule for the invariant parameters, it is convenient to start by considering $\mathcal{F}$.

It is possible to define anisotropy parameters that represent fractional yields and, therefore, sum linearly. For example, the longitudinal fraction $|a_0|$ appearing in Eq. 3.1 is by definition the *fraction of events* where the particle is produced in the $J_z = 0$ state. In the superposition of two or more subprocesses such fraction gets averaged linearly. Similarly, from Eq. 3.23 we see that $\mathcal{F}$ itself is a longitudinal fraction: specifically, it is the fraction of events where the particle is produced, this time, in the $J_y = 0$ state. The addition rule for $\mathcal{F}$ is, therefore, simply linear:

$$\mathcal{F} = \frac{\sum_{i=1}^{n} f^{(i)}\mathcal{F}^{(i)}}{\sum_{i=1}^{n} f^{(i)}}\,, \tag{4.2}$$

so that, for example, if half of the processes have $\mathcal{F} = 1/2$ (as in the fully transverse case) and half $\mathcal{F} = 0$ (the longitudinal case), the measurement yields the intermediate $\mathcal{F} = 1/4$.

The analogous rule for $\tilde{\lambda}$ can be derived using the relations

$$\begin{aligned} 1 - 3\mathcal{F} &= -2\tilde{\lambda} \,/\, (3 + \tilde{\lambda}) \\ 1 - \mathcal{F} &= 2 \,/\, (3 + \tilde{\lambda})\,, \end{aligned} \tag{4.3}$$

leading to

$$\begin{aligned} \tilde{\lambda} &= -\frac{1 - 3\mathcal{F}}{1 - \mathcal{F}} = -\frac{\sum_{i=1}^{n} f^{(i)}(1 - 3\mathcal{F}^{(i)})}{\sum_{i=1}^{n} f^{(i)}(1 - \mathcal{F}^{(i)})} \\ &= \sum_{i=1}^{n} \frac{f^{(i)}}{3 + \tilde{\lambda}^{(i)}}\tilde{\lambda}^{(i)} \Big/ \sum_{i=1}^{n} \frac{f^{(i)}}{3 + \tilde{\lambda}^{(i)}}\,. \end{aligned} \tag{4.4}$$

The observable $\tilde{\lambda}$ is, therefore, a weighted sum with weights $1/(3 + \tilde{\lambda}^{(i)})$, formally identical to the sum giving the value of the average λ_ϑ (Eq. 4.1). Just as in that case, an equal mixture of transverse ($\tilde{\lambda} = +1$) and longitudinal ($\tilde{\lambda} = -1$) processes yields $\tilde{\lambda} = -1/3$. The analogy in addition rule is a further reason to consider $\tilde{\lambda}$ as the frame-invariant counterpart of λ_ϑ.

In the special case when the observed distribution is the superposition of n elementary distributions of the kind $1+\lambda_0^{(i)} \cos^2\vartheta$ with respect to n different polarization axes ($n - 1$ of which, at least, do not have the same orientation as the experimental polarization axis), $\tilde{\lambda}$ represents a weighted average of the n $\lambda_0^{(i)}$ parameters, made *without* transforming these "natural" polarizations from their respective natural axes to the actual observation frame:

$$\tilde{\lambda} = \sum_{i=1}^{n} \frac{f^{(i)}}{3 + \lambda_0^{(i)}}\lambda_0^{(i)} \Big/ \sum_{i=1}^{n} \frac{f^{(i)}}{3 + \lambda_0^{(i)}}\,. \tag{4.5}$$

It is important to emphasize the difference between this expression and the addition rule for λ_ϑ, Eq. 4.1, where the individual $\lambda_\vartheta^{(i)}$ are all measured with respect to the *same* polarization axis, the experimental one.

4.2 When $\tilde{\lambda}$ is "simpler" than λ_ϑ in every polarization frame

In the examples of Figs. 2.9, 2.10, and 2.11, the use of $\tilde{\lambda}$ provides benefits that, in principle, can also be obtained by repeating the measurement in several frames and realising that one of them provides the most "natural" view of the angular distribution. This is only possible, however, when the natural frame coincides with a frame

that can be experimentally defined, a condition not always established in practice. For example, in proton-proton (or, more generally, hadron-hadron) collisions, the polarization measurement is made in a frame defined in terms of the proton-proton system (e.g. at rest in the laboratory, in the case of symmetric colliding beams), but the particle under study is produced in a parton-parton interaction, and the momentum of the parton-parton system can be significantly different from that of the proton-proton system. The description of such effects, related to the parton motion inside the protons, will be developed in Sections 4.3 and 5.4.

Moreover, it can happen that the observed mixture of production processes is characterized by *more than one* natural polarization axis. It is in such cases that the measurement of $\tilde{\lambda}$ is particularly helpful for understanding and characterizing the underlying physics.

As a hypothetical illustration, we can consider a physics case analogous to the one considered in Figs. 2.9, 2.10, and 2.11, but now assuming a mixture of processes such that 50% of the particles are produced with transverse polarization in the CS frame and 50% with longitudinal polarization in the HX frame. The resulting dependences of the parameters λ_ϑ, λ_φ, and $\lambda_{\vartheta\varphi}$ in several frames are shown in the Figs. 4.1, 4.2, and 4.3, corresponding in order and notations to Figs. 2.9, 2.10, and 2.11. A second scenario is also shown, exchanging the two polarizations (longitudinal in the CS frame, transverse in the HX frame).

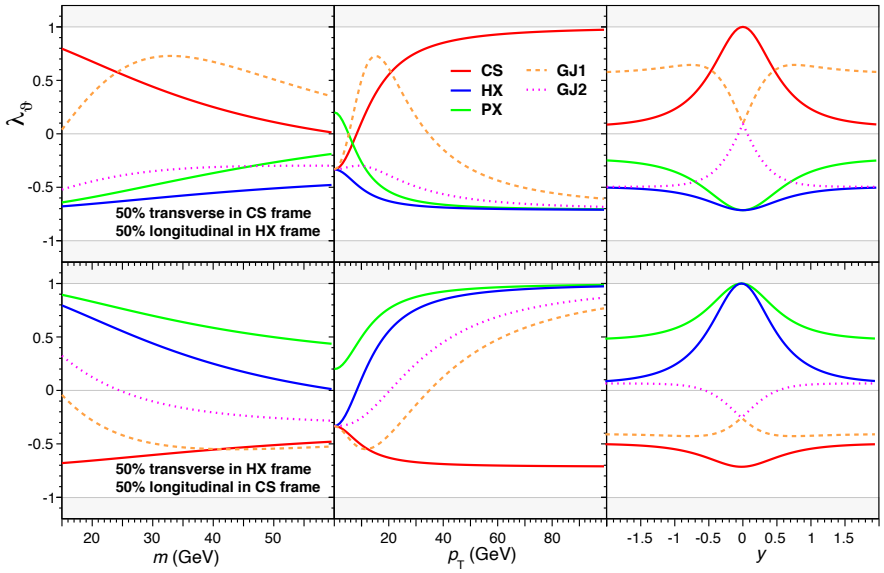

Fig. 4.1 Values of λ_ϑ measured in the five frames indicated in the legends, as a function of three kinematical observables (m, p_T, and y), when the particle is produced with an equal and constant mixture of purely transverse polarization in the CS (or HX) frame and purely longitudinal polarization in the HX (or CS) frame. For each kinematical dependence, the other two variables are fixed to suitable values: m = 25 GeV, p_T = 20 GeV, and y = +0.5.

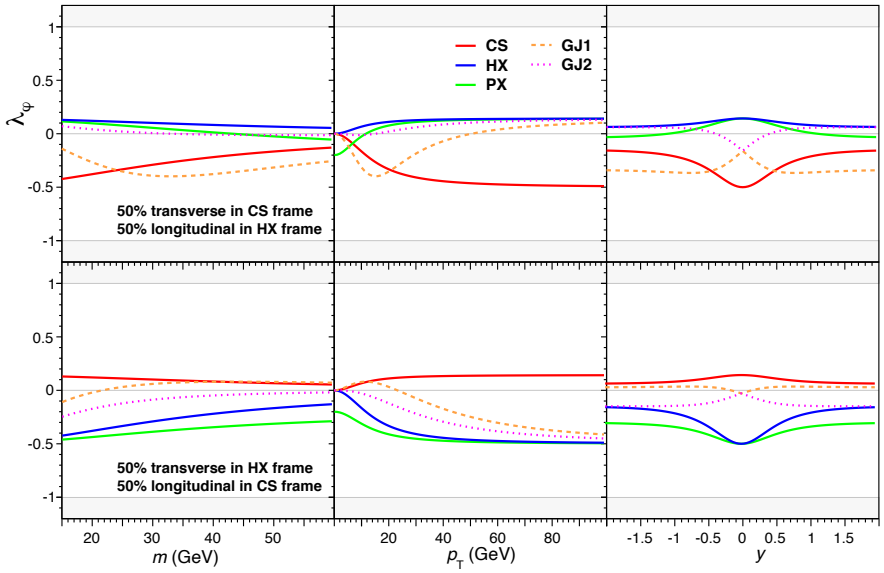

Fig. 4.2 Same as previous figure, for λ_φ.

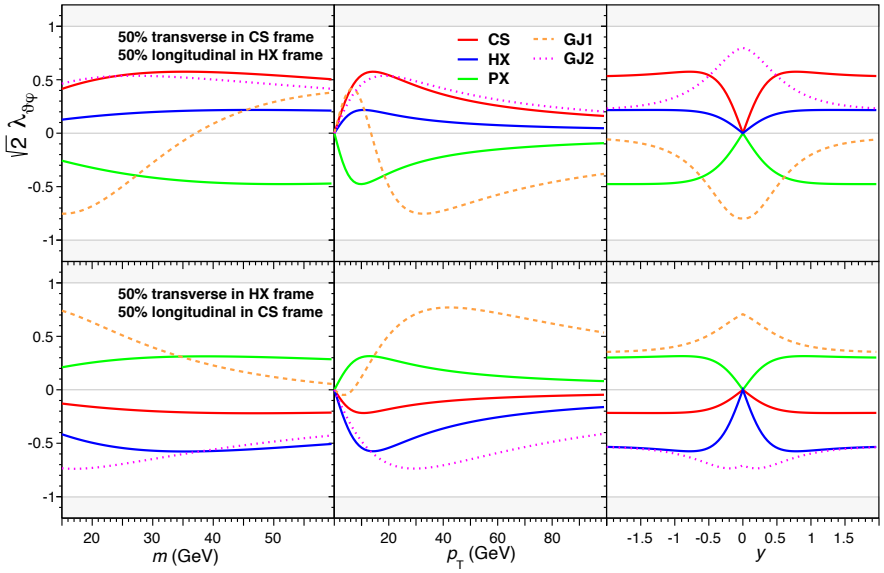

Fig. 4.3 Same as previous figure, for $\lambda_{\vartheta\varphi}$.

As can be easily seen, in these cases there is never an observation frame offering a simple point of view, with a constant λ_ϑ and zero λ_φ and $\lambda_{\vartheta\varphi}$, as it happened by

definition in the example with *one* natural frame: here the kinematic dependences are always strong and complex.

It is just in physical conditions like these that the measurement of the invariant polarization is particularly revealing, as it provides the numerical average of the natural polarizations, each one considered along its own natural axis. In the present example, $\mathcal{F} = 0.5 \times 1/2 + 0.5 \times 0 = 1/4$, independently of p_T, y and mass, while applying the non-linear addition rule of Eq. 4.5 provides a constant $\tilde{\lambda} = -1/3$.

We will now illustrate the possible effects of different experimental acceptances by considering J/ψ polarization measurements made by gedanken experiments covering different rapidity windows, analogous to those considered in Fig. 2.21. We assume that J/ψ production proceeds through the superposition of two processes: in 60% of the events, the mesons have full transverse polarization in the CS frame, $\lambda_\vartheta^{CS} = +1$, while in the remaining fraction the production is also fully transverse but this time in the HX frame: $\lambda_\vartheta^{HX} = +1$. The polarizations of the two event subsamples are intrinsically independent of the production kinematics, as in the examples we considered in the Fig. 2.21.

However, as shown in Fig. 4.4, none of the frames, CS or HX, will allow the several experiments to find simple and mutually compatible results; it is surely not evident from these patterns that we are studying production processes that are exactly identical for all considered experimental conditions and always fully transversely polarized.

The measurement of $\tilde{\lambda}$ will, instead, yield the "universal" value +1, immediately revealing the simplicity of the underlying production scenario and the consistency between the experimental results, a result not achievable in terms of the frame-dependent parameters in any chosen experimental frame. On the other hand, it remains true that $\tilde{\lambda}$ should not replace the measurement of the frame-dependent parameters, since it is by itself "blind" to some underlying physical information. In the present examples, the measurements of λ_ϑ, λ_φ, and $\lambda_{\vartheta\varphi}$ contain the indication that we are indeed in the presence of a *superposition* of (at least) two processes. In fact, they can even be used to infer the relative contribution of the two processes, since the observed patterns depend on that factor.

It should now be clear that the measurement of $\tilde{\lambda}$ complements the frame-dependent observables λ_ϑ, λ_φ, and $\lambda_{\vartheta\varphi}$, allowing us to better understand the production processes behind the experimental results. In fact, it sometimes represents the only way to obtain the immediate experimental indication of a constant and maximal underlying polarization, a fact that can help in the discrimination of different physics scenarios. As an example, we refer again to the possible interpretations of the ambiguous J/ψ polarization measurement reported by CDF [1], discussed in Section 2.11 and presented in Fig. 2.17. In the scenarios 1 and 2, with one single participating subprocess having, respectively, $\lambda_\varphi^{HX} = 0$ and $\lambda_\varphi^{CS} = 0$, the corresponding $\tilde{\lambda}$ parameters are immediately obtained as $\tilde{\lambda} = \lambda_\vartheta^{HX}$ and $\tilde{\lambda} = \lambda_\vartheta^{CS}$. The scenario 3, instead, corresponds to the superposition of two processes, both having full transverse polarizations, natural in either the CS or the HX frames, so that we need to use the Eq. 4.5, introduced in the previous section, to see that the frame-invariant polarization parameter is $\tilde{\lambda} = +1$.

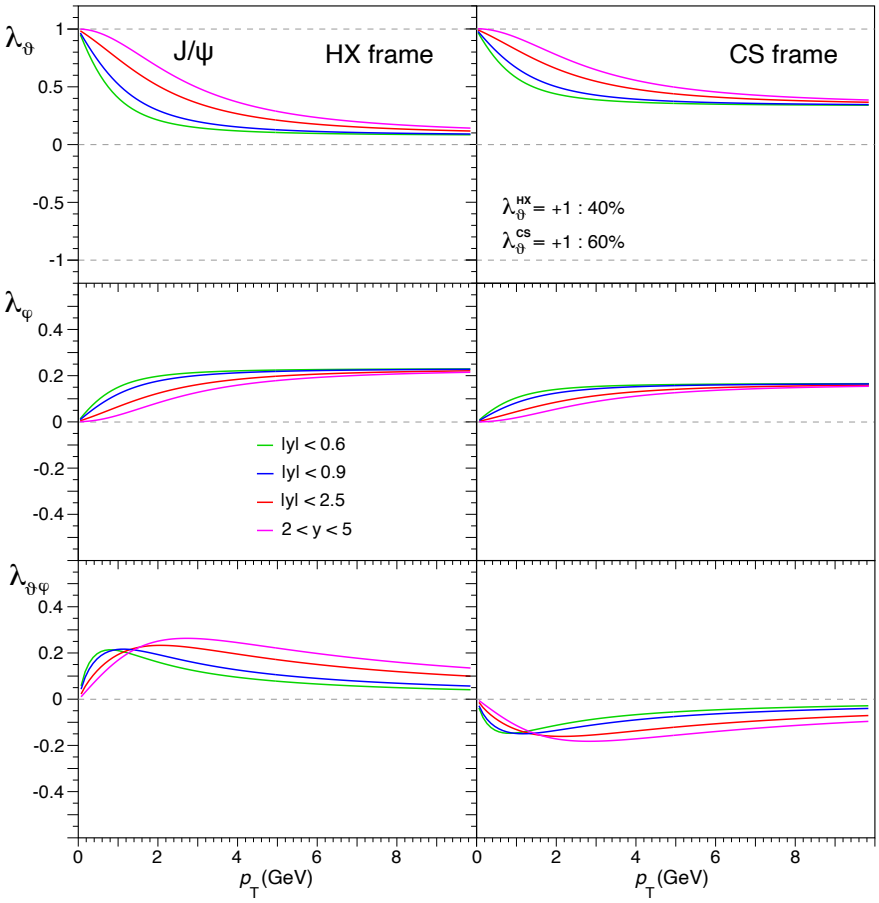

Fig. 4.4 Polarization parameters λ_ϑ (top), λ_φ (middle), and $\lambda_{\vartheta\varphi}$ (bottom) measured in the HX (left) and CS (right) frames, as a function of $p_{\rm T}$ and for several rapidity ranges (different line colours), for J/ψ mesons generated with a superposition of transverse polarizations along the HX (40%) and CS (60%) axes.

Figure 4.5 shows the $p_{\rm T}$ dependence of $\tilde{\lambda}$ for each of the three scenarios. The three curves are very different from each other, confirming that, as foresseable, a measurement of $\tilde{\lambda}$ provides a remarkable level of discrimination between hypotheses that are indistinguishable when only $\lambda_\vartheta^{\rm HX}$ is measured.

In the pedagogical examples considered above we used hypotheses involving two natural polarizations coexisting with relative probabilities independent of $p_{\rm T}$, y, and m, to provide simple, even if not completely realistic, illustrations. A practical case where polarizations along two distinct quantization axes do indeed contribute equally in all kinematic conditions is represented by certain t/u-channel processes, like the ones shown in Fig. 2.2-a. There the observed particle is produced with angular momentum aligned along the direction of one or the other incoming parti-

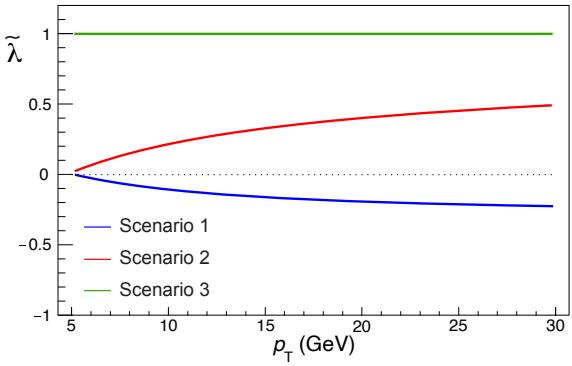

Fig. 4.5 The frame-independent parameter $\tilde{\lambda}$ determined in the three fundamentally different production scenarios described in the text and previously shown in Fig. 2.17.

cle (a quark or an antiquark). These two distinct natural quantization directions, approximated experimentally by the GJ1 and GJ2 axes (as defined in Chapter 2), are equiprobable in symmetric collision systems (such as pp collisions) and in the absence of parity-violating effects. Therefore, considering the GJ as the "natural" frame effectively means to consider 50% of the particle yield as naturally polarized along the GJ1 axis, and the other 50% as polarized along the GJ2 axis.

Two scenarios of this kind are illustrated in Figs. 4.6, 4.7, and 4.8, for transverse and longitudinal polarizations. As can be seen, no individual observation frame shows the fully transverse or fully longitudinal nature of the polarization.

An "optimal" frame for the observation of these t/u-channel processes appears to be the "composite" frame having the identity of the CS frame for $p_T/m < 1$ and of the PX frame for $p_T/m > 1$: the diagrams of the p_T and m dependences show that λ_ϑ is always maximal (and λ_φ minimal) in this frame (the transition point $p_T = m$ being indicated by a vertical dashed line). However, only the invariant polarization reveals immediately the full natural polarization ($\tilde{\lambda} = +1$ or -1).

More generally, the superposition of production processes can itself be a function of p_T, y or m, reflecting the different kinematic behaviours of the coexisting mechanisms. The invariant polarization continues to provide the average of the natural polarizations; if such "absolute" polarizations are constant in value, the invariant polarization remains constant, despite the presence of an evolving mixture of processes. Realistic examples of process superpositions, possibly also changing with p_T, are considered in the next section.

4.3 Drell–Yan and W / Z boson polarizations

In the previous section we illustrated the difference between frame-dependent and frame-independent parameters in the presence of hypothetical superpositions of pro-

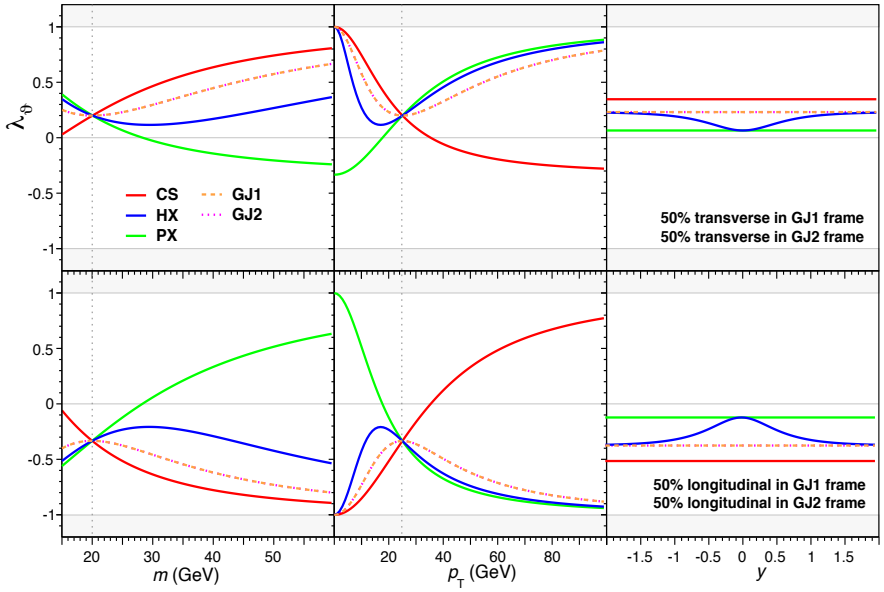

Fig. 4.6 Values of λ_ϑ measured in the five frames indicated in the legends, as a function of three kinematical observables (m, p_T, and y), when the particle is produced with fully transverse or fully longitudinal polarization in the GJ frame (that is, in the GJ1 and GJ2 frames with equal probability). For each kinematical dependence, the other two variables are fixed to suitable values: $m = 25$ GeV, $p_T = 20$ GeV, and $y = +0.5$.

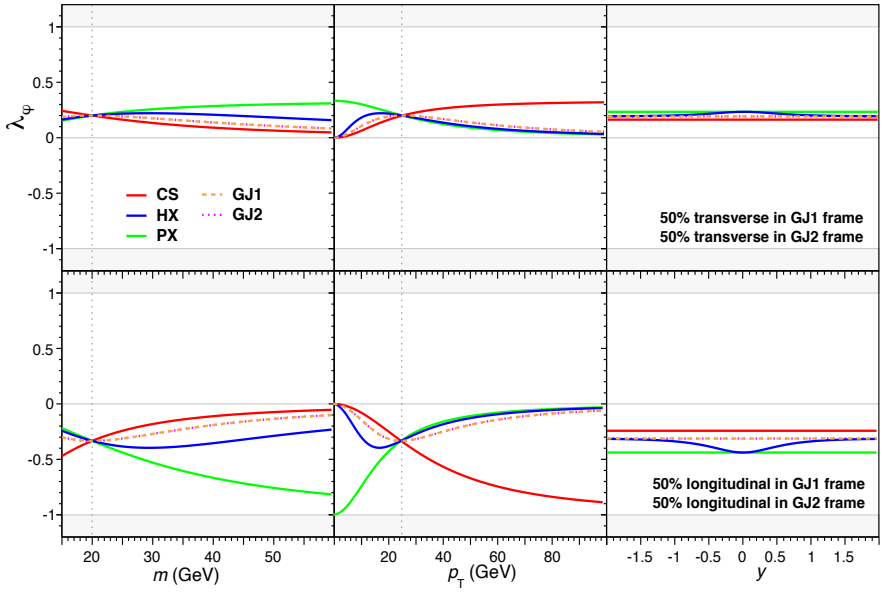

Fig. 4.7 Same as previous figure, for λ_φ.

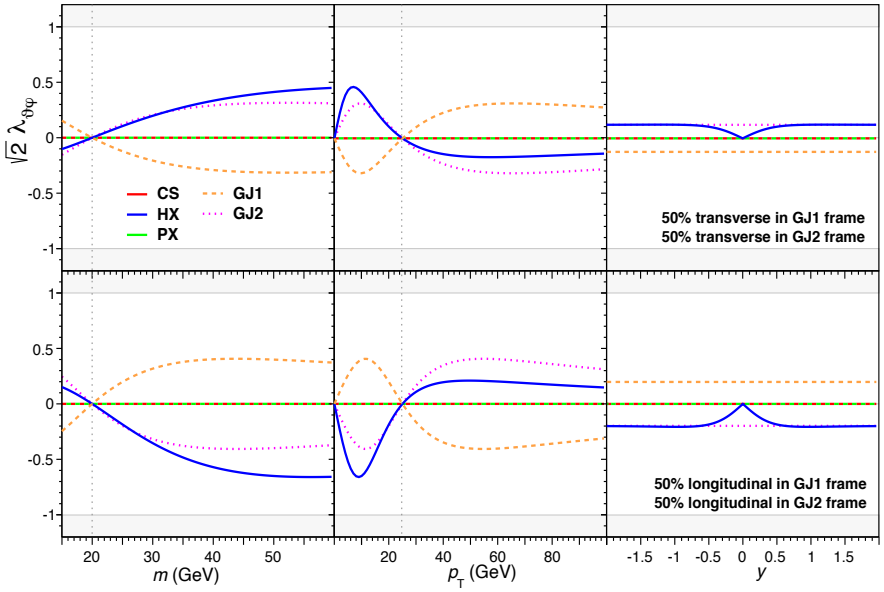

Fig. 4.8 Same as previous figure, for $\lambda_{\vartheta\varphi}$.

cesses having natural polarizations along different quantization axes. We now turn our attention to the interesting case of the direct production of Drell–Yan lepton pairs and of the vector bosons W and Z. The partonic processes contributing at the lowest perturbative orders were shown in Fig. 2.2 and it was already discussed in there how their different topologies lead to polarizations that are always transverse, but along different axes.

The purely electromagnetic (order α_s^0) $q\bar{q}$ annihilation process (Fig. 2.2-c) is characterized by a constant and transverse polarization in the CS frame. This process alone, where the lepton pair is produced at rest in the frame of the parton-parton system ($2 \to 1$ process), explains well the observations of the E866 experiment [2], which collected data at p_T values of the same order as the intrinsic parton momentum, for which the contribution of $2 \to 2$ topologies is expected to be small. The E866 results are presented in Fig. 4.9, as a function of the dilepton p_T (left panel) and x_F (right panel). The variable x_F is commonly used (instead of rapidity) in fixed target experiments. It is defined as $x_F = 2\,p_L/\sqrt{s}$, where p_L is the longitudinal momentum of the dilepton in the rest frame of the colliding hadrons (the proton-nucleon rest frame, in the case here considered).

To illustrate what happens in the presence of a *superposition* of different processes, it is particularly interesting to study the case of W and Z production, as measured, at much higher p_T, by Tevatron and LHC experiments. Here we consider the results for the polar anisotropies of the two decays distributions (W in lepton-neutrino and Z in dilepton). The Z results use an alternative parametrization of the angular distribution (given in its complete form in Appendix A),

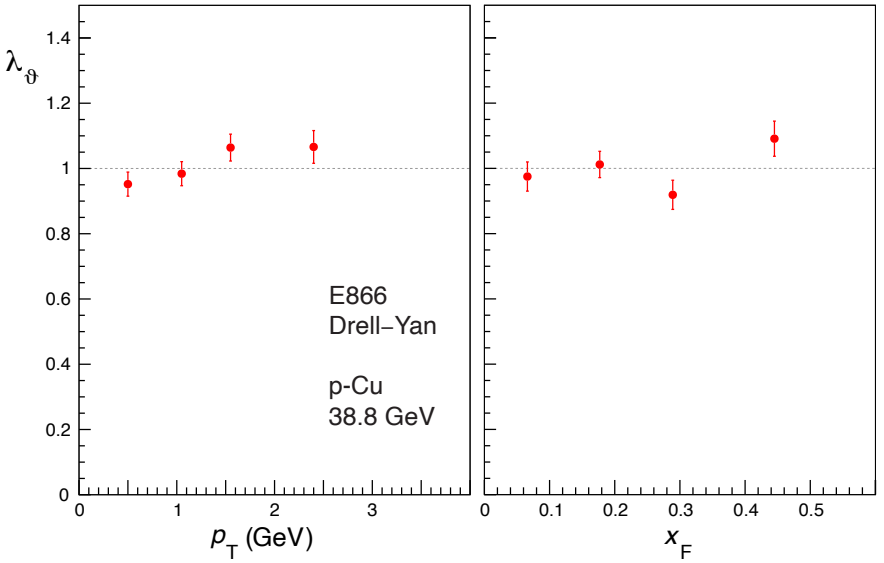

Fig. 4.9 Measurement of the polarization (λ_ϑ in the CS frame) of Drell–Yan lepton pairs of invariant masses $8.1 < m < 8.45$ and $11.1 < m < 15$ GeV, produced in proton-copper collisions at $\sqrt{s} = 38.8$ GeV [2].

$$W(\cos\vartheta) \;\propto\; 1 + \cos^2\vartheta \;+\; \frac{1}{2}\,A_0\,(1 - 3\cos^2\vartheta)\,, \tag{4.6}$$

where transverse and longitudinal polarizations are indicated by $A_0 = 0$ and $A_0 = 2$, respectively, so that $\lambda_\vartheta = (1 - \frac{3}{2}\,A_0) \,/\, (1 + \frac{1}{2}\,A_0)$, i.e. $\frac{1}{2}\,A_0$ is the longitudinal fraction.

To describe high-p_{T} production, it is necessary to consider processes with the presence of a recoil system produced back-to-back to the dilepton system. A recoiling quark or gluon appears for example in the diagrams (a), (b), and (d) of Fig. 2.2, which include order-α_s^1 QCD corrections due to one gluon emission/absorption by the quark line. These terms contribute with polarizations that are naturally transverse along the HX axis (s-channel qg scattering diagram in panel (d)) and both the GJ1 and GJ2 axes (t/u-channel $q\bar{q}$ and qg diagrams in panels (a) and (b)). When observed in the CS frame, these $2 \to 2$ processes show polarizations changing from transverse to longitudinal values, depending on the dilepton momentum, as it was shown, in the two respective cases, in Figs. 2.9 and 4.6. In fact, the main motivation of the parametrization of Eq. 4.6 is that A_0, when considered in the CS frame, measures directly the effect of the QCD corrections causing the deviation from the zero-order, fully transverse and momentum-independent, $1 + \cos^2\vartheta$ distribution.

For a realistic and accurate interpretation of the measured patterns, shown in Figs. 4.10 and 4.11, it is important to have a deeper understanding of the impact that the quantization direction has on the observations of polarizations that are natural in the HX frame. For simplicity of illustration, we have until now neglected an important detail in the definition of this kind of polarizations: the natural quantization

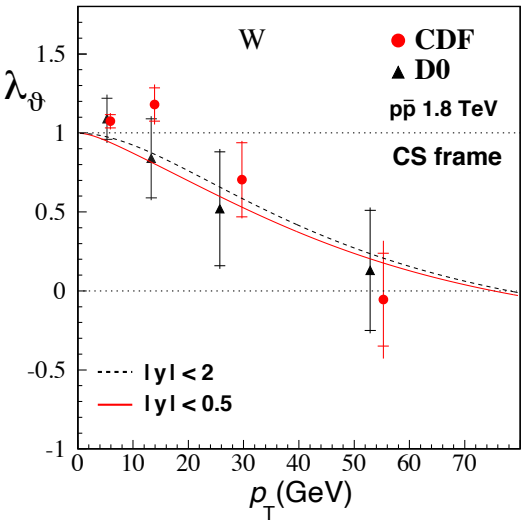

Fig. 4.10 Polar anisotropy parameter, λ_ϑ, measured by the CDF [3] and D0 [4] Collaborations, in the CS frame, for W bosons produced in $p\bar{p}$ collisions at 1.8 TeV. The vertical bars represent the total uncertainties while the horizontal tick marks represent the statistical-only uncertainties. The curves represent the analytical model described in the text, for the $|y| < 0.5$ (solid) and $|y| < 2$ (dashed) rapidity ranges.

axis is the (unobservable) direction of the decaying particle with respect to the rest frame of the parton-parton system (parton-parton-HX axis), which is not the same as the one seen in the proton-proton system (experimental HX axis). To transform such intrinsic polarizations in predictions for λ_ϑ, λ_φ, and $\lambda_{\vartheta\varphi}$, as measurable in an experimentally definable frame, it is necessary to use an additional piece of information on the process: how the parton-parton system is boosted with respect to the proton-proton system (which is the laboratory frame in the case of symmetric collisions in collider experiments). For W and Z production, we can safely neglect the effects of parton motion in the direction transverse to the beam, since the transverse momentum of a parton (of order 1 GeV) is negligible with respect to its longitudinal momentum, which is of order $m_{Z|W}/2$ already in the limit $p_T, y \to 0$.

A look at the formulas in Table 2.1 reminds us that the rotation angle between frames, δ, only depends on p_T (actually, on $\xi = p_T/m$) and y; rotations between the parton-parton HX frame and the others can then be obtained by simply replacing the rapidity measured with respect to the proton-proton system, y, with the (unmeasured) one referred to the parton-parton system, $\hat{y}$, while the corresponding replacement of p_T with $\hat{p}_T$ has a negligible effect in the case considered. It can also be seen in the table that, for a measurement performed in the CS frame, only the polarizations that are natural in the HX frame are indeed sensitive to y and, therefore, to its difference with respect to $\hat{y}$. To interpret the data of Figs. 4.10 and 4.11 we need, therefore, some knowledge of $\hat{y}$, that is, of the (average) rapidity boost y_0 of the parton-parton system in the laboratory ($\hat{y} = y - y_0$), when calculating the observable

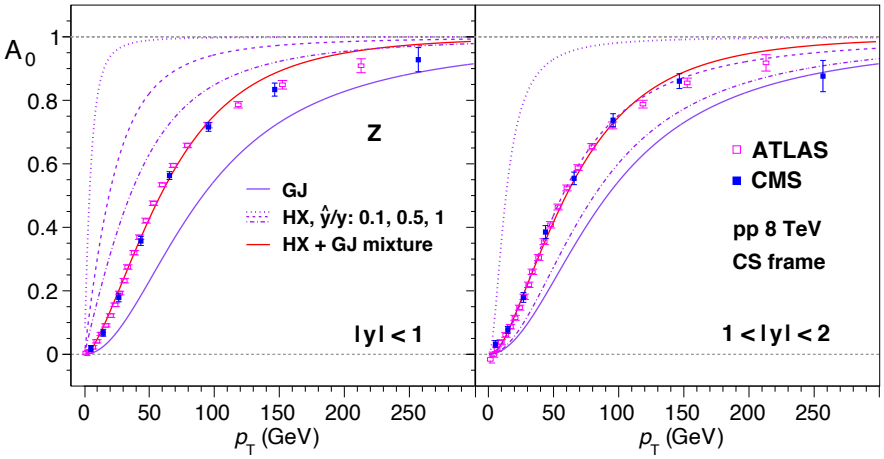

Fig. 4.11 Polarization (A_0 in the CS frame) of Z bosons produced in proton-proton collisions at $\sqrt{s}$ = 8 TeV [5, 6] in two ranges of rapidity: $|y| < 1$ (left) and $1 < |y| < 2.1$ (right). The curves represent the analytical model described in the text, for those two specific rapidity ranges.

polarizations of the s-channel qg scattering process, while such additional ingredient is not necessary in the case of the t/u-channel $q\bar{q}$ and qg processes. The study of y_0 in the relevant conditions requires the use of parton distribution functions and of specific calculations of the partonic cross sections. Here we limit ourselves to assuming that (the average) $\hat{y}$ is roughly proportional to y. Figure 4.11 shows, for different fixed values of $\hat{y}/y$ (0.1, 0.5, and 1.0), how the polarization of the s-channel processes would be observed in the CS frame as a function of p_{T}, in two rapidity ranges. All individual t/u-channel and s-channel components change polarization, in the CS frame, from fully transverse at $p_{\mathrm{T}} = 0$ to 50% longitudinal in the $p_{\mathrm{T}} \gg m$ limit ($\lambda_\vartheta \to -1/3$, $A_0 \to 1$).

It can be seen in Figs. 4.10 and 4.11 that a specific combination of the two kinds of $2 \to 2$ processes, with $\hat{y}/y = 0.2$ for the s-channel one, is able to reproduce well the data. In that combination, the relative proportions of the s- and t/u-channel terms has been assumed to depend on p_{T}, changing from 1 : 3 at around $p_{\mathrm{T}} = 50$ GeV to 3 : 1 at around $p_{\mathrm{T}} = 220$ GeV, in the same way, for simplicity, for both the W and the Z, and in all rapidity ranges. In these calculations, the masses are fixed to the W or Z pole masses, as applicable.

Figure 4.12 shows, for one of the rapidity domains considered in the previous figure, $|y| < 1$, how the observed polarization (corresponding to the combination best describing the data) would look like in different frames; the results are given for both A_0 and λ_ϑ. For p_{T} larger than the particle mass the CS frame, commonly chosen by the experiments, turns out to be the one showing the largest departure from transverse polarization (largest A_0, smallest λ_ϑ), while the HX and PX frames are the ones closest to the natural frame, as they show the largest polar anisotropies. We remind that the magnitude of A_0 in the parametrization chosen by CMS and ATLAS is not related to the strength of the anisotropy. In fact, $A_0/2$ is the "longitu-

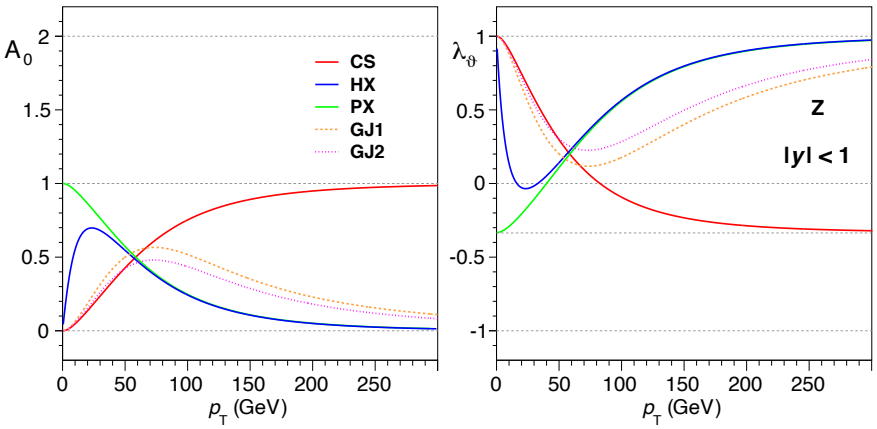

Fig. 4.12 The parameter A_0, already shown in Fig. 4.11-left by the black curve ($|y| < 1$, CS frame), now also shown in four other reference frames (left panel). The corresponding λ_ϑ curves are shown on the right panel. We remind that A_0 can take values between 0 and 2, with $A_0 = 1$ being equivalent to $\lambda_\vartheta = -1/3$ and $A_0 = 0$ corresponding to $\lambda_\vartheta = +1$.

dinal fraction". The maximal polar anisotropies are obtained when the longitudinal fraction is $A_0/2 = 0$ or $A_0/2 = 1$, while $A_0/2 = 1/3$ corresponds to the absence of polar anisotropy (flat $\cos\vartheta$ distribution). The value $A_0/2 = 1/2$ asymptotically approached by the data represents, hence, a mild anisotropy. On the contrary, λ_ϑ is a geometrical anisotropy parameter and large $|\lambda_\vartheta|$ values correspond to large experimentally recognizable anisotropies.

In general, therefore, the several $2 \to 1$ and $2 \to 2$ processes contributing to Drell–Yan, W, and Z production have different angular distributions, with momentum-dependent shapes, and their superposition is itself a function of momentum. Therefore, the observable angular distribution, determined by that superposition, is strongly momentum-dependent, so that its measurement, in whatever frame, does not provide straightforward evidence, if not in the $p_T \to 0$ limit, of the actually fully transverse and momentum-independent polarization intrinsically characterizing each of the individual processes.

Such fundamental information is, instead, immediately provided by the invariant polarization: each subprocess has $\tilde{\lambda}^{(i)} = +1$ ($\mathcal{F}^{(i)} = 1/2$) and any event mixture, therefore, maintains the property $\tilde{\lambda} = +1$ ($\mathcal{F} = 1/2$). An important notion in reaching this conclusion deserves being emphasized: the transformations between the (experimentally undefinable) parton-parton-HX frame and the "experimental" frames (CS, HX, GJ, PX) follow the same rules as those between two experimental frames, being described by the relations of Eq. 2.13 for some (unobservable) value of δ. Therefore, also such transformations *preserve* the invariance of $\tilde{\lambda}$ ($\mathcal{F}$). This happens because they are all represented by rotations applied *within the production plane*, at least at not too low p_T, so that intrinsic parton momentum effects can be neglected.

The importance of these conditions, and their limitations, will be discussed in Chapter 5. Here we want to remark another advantage of the measurement of $\tilde{\lambda}$ with respect to the one of the frame-dependent λ_ϑ: it usually provides information on the underlying polarization with no need to worry about the *longitudinal* motion of the partons within the colliding hadrons, i.e. without invoking the parton distribution functions.

4.4 The Lam–Tung relation

It is known since 1978 that Drell–Yan dilepton production, calculated at order α_s in perturbative QCD, obeys a relation between the helicity structure functions of the produced virtual photon or, equivalently, between the coefficients λ_ϑ and λ_φ of the lepton angular distribution measured in the dilepton rest frame:

$$\lambda_\vartheta + 4\,\lambda_\varphi = 1. \tag{4.7}$$

This identity, known as the Lam–Tung relation [7], is valid not only for Drell–Yan production, but also for the direct production of elementary vector bosons, Z and W, decaying into lepton-antilepton or lepton-neutrino.

The Lam–Tung relation can be seen as the analogous, for dilepton production, of the Callan–Gross relation in deep inelastic scattering, $F_2(x) - 2xF_1(x) = F_\mathrm{L}(x) = 0$, where the Bjorken scaling functions, F_1 and F_2, are connected by the condition that the longitudinal structure function, F_L, of the virtual photon vanishes identically. The Callan–Gross relation is affected by substantial $O(\alpha_s)$ corrections, due to gluon radiation. Similarly, also the Drell–Yan production cross section and the corresponding λ_ϑ and λ_φ coefficients (considered individually) change significantly from the order-α_s^0 calculation. The theoretical relevance of the Lam–Tung relation resides in the fact that the specific combination of Eq. 4.7 is, instead, unchanged by $O(\alpha_s^1)$ corrections. Moreover, it is invariant under rotations in the dilepton rest frame around the axis perpendicular to the production plane.

The existence of such a relation has been described as “remarkable” and even “surprising” because, while it is the outcome of perturbative QCD calculations, the ingredients of its derivation (magnitudes of the contributing partonic cross sections, shapes of the parton distribution functions, and the identity of the colliding partons) unexpectedly disappear from the final expression. It has been found, not long ago, that the relation remains valid, or is only affected by small corrections, when subsequent orders in α_s are taken into account [8, 9], as will be discussed in Chapter 5. In fact, the Lam–Tung relation is generally assumed to be such a solid result of perturbative QCD that its violation is considered as a strong signal of non-perturbative effects.

Experimentally, the Lam–Tung relation has been shown to be violated in pion-nucleus collisions [10, 11], triggering discussions about effects of intrinsic parton k_T [12, 13] or of higher twist contributions [14]. Saturation effects have also been

proposed as a cause of violations of the Lam–Tung relation, in proton-nucleus and deuteron-nucleus collisions at RHIC and at the LHC [15].

As the reader may have already noticed, there is a direct connection between the Lam–Tung relation and the frame-independent polarization parameter $\tilde{\lambda}$, which was introduced three decades later [16]. In fact, the condition $\tilde{\lambda} = +1$ (or, equivalently, $\mathcal{F} = 1/2$) *is precisely* the Lam–Tung relation:

$$\tilde{\lambda} = \frac{\lambda_\vartheta + 3\lambda_\varphi}{1 - \lambda_\varphi} = +1 \quad \Rightarrow \quad \lambda_\vartheta + 4\,\lambda_\varphi = 1. \tag{4.8}$$

The Lam–Tung relation is, therefore, a *special* case of the more general frame-independent polarization relations for vector particles, denoting a physics scenario where all underlying processes produce a vector state with an intrinsic *transverse* polarization. This latter condition is verified in all $2 \to 1$ and $2 \to 2$ processes, including, in particular, when leading QCD corrections are considered.

In other words, the Lam–Tung relation, just like $\tilde{\lambda} = +1$, is not really a "QCD relation" but rather a consequence of the rotational covariance of $J = 1$ angular momentum eigenstates and of the properties of the electroweak coupling between quarks and elementary bosons (photon, Z, W), i.e. of helicity conservation. In fact, all the "QCD details" *disappear* from it: the partonic cross sections, including the distribution of how the vector state is emitted in the parton-parton rest frame, the p_{T} dependences of the different contributing processes and their relative mixture, the identity of the colliding partons and their density functions (PDFs), and even the mass of the produced state (be it a Z boson or a low-mass Drell–Yan pair). All of these aspects, necessary ingredients and features of the QCD calculations, leave no trace in the Lam–Tung identity.

On the other hand, this interesting observation also denotes, in a particularly illuminating way, the limitation of the frame-independent approach: we lose significant physics information if its measurement is not accompanied by the simultaneous determination the frame-dependent parameters, which provide, through their trends as functions of p_{T} and y, fundamental information about the underlying elementary processes (even if, sometimes, in a somewhat hidden or cryptic way).

4.5 The quasi-invariants

We will now discuss the meaning of the frame-invariants $\lambda_\vartheta^\star$ and $\mathcal{A}^\star$ introduced in Sections 3.9 and 3.10. In the first example, we consider the superposition of two processes characterized by transverse polarizations along two different polarization axes, with half of the events naturally polarized in the CS frame and the other half in the HX frame.

For simplicity of illustration, in the case of the HX frame we neglect effects of the longitudinal motion of the partons within the colliding hadrons and assume the proton-proton centre-of-mass HX axis as natural axis.

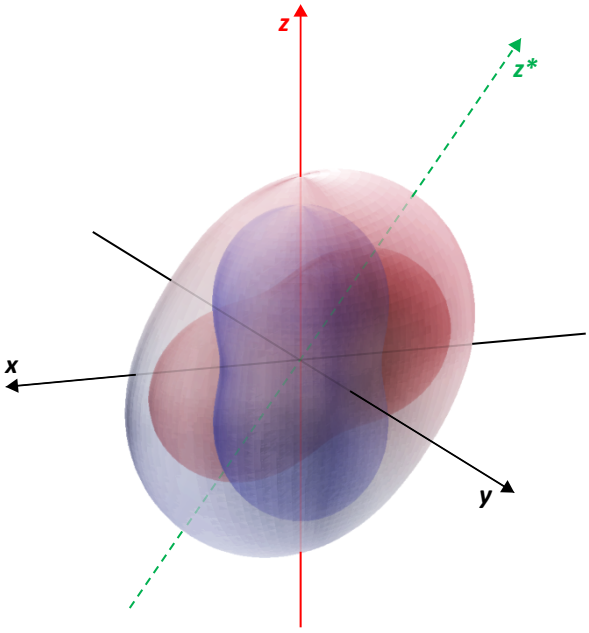

Fig. 4.13 The shape of the dilepton angular distribution resulting from the superposition of two processes, both transversely polarized but with respect to significantly different natural axes. The green axis $z^\star$ represents the polar axis of the frame where the distribution is in its canonical form and has minimal azimuthal anisotropy, as discussed in Section 3.9.

The angular distribution resulting from this mixture, for a kinematic condition where the HX and CS axes are significantly different (but not fully perpendicular, as it happens at very high p_{T}), is shown in Fig. 4.13. Looking at this figure we can easily recognize that the invariants $\tilde{\lambda}$ and $\lambda_\vartheta^\star$ have different meanings. In fact, the former is equal to +1, as in the examples seen in the previous sections, while the latter represents the value that λ_ϑ assumes in the frame where the distribution becomes "diagonal". According to the discussion of Section 3.9, two of such frames, orthogonal to one another, can be defined with a rotation in the production plane, but we can make the choice univocal by selecting as new polar axis, $z^\star$, the one minimizing the azimuthal anisotropy. In the present case, this selection leads to the axis indicated in the figure by the green dashed line.

The corresponding $\lambda_\vartheta^\star$ value is strictly smaller than 1 (it would be even smaller with the other possible choice of the polar axis), as can be recognized from the identity

$$\frac{\lambda_\vartheta^\star + 3\,\lambda_\varphi^\star}{1 - \lambda_\varphi^\star} \equiv \tilde{\lambda}\,, \tag{4.9}$$

considering that the shape in the figure has a visible azimuthal anisotropy, $\lambda_\varphi^\star > 0$, in the diagonalizing frame.

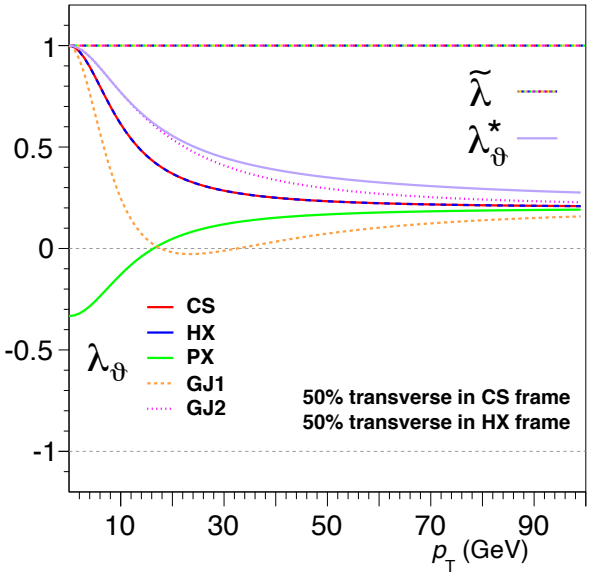

Fig. 4.14 The parameters $\lambda^\star_\vartheta$, $\tilde{\lambda}$ and λ_ϑ, as a function of p_T, as seen in the five frames indicated in the legends, when the decaying state, of $m = 25$ GeV and $y = +0.5$, is produced with an equal and constant mixture of purely transverse polarizations in the CS and HX frames. Both $\lambda^\star_\vartheta$ and $\tilde{\lambda}$ are identical in all frames.

The positive sign of $\lambda^\star_\varphi$ can be deduced from the fact that the shape flattens against the reference plane zx, instead of protruding perpendicularly to it. The condition $\tilde{\lambda} = \lambda^\star_\vartheta$ is only verified when there is a frame where the distribution has the shape $\propto 1 + \lambda_\vartheta \cos^2\vartheta$, without any azimuthal anisotropy, this frame being the "natural" one for all involved processes.

Figure 4.14 illustrates quantitatively, for $m = 25$ GeV and $y = +0.5$ (the same kinematic conditions as used in the examples of Section 4.2), the difference between $\lambda^\star_\vartheta$ (always chosen according to the above-mentioned convention), $\tilde{\lambda}$, and λ_ϑ as measurable in different polarization frames (in this specific case, given the chosen symmetry of the processes, the HX and CS frames provide identical observations). While not constant (unlike $\tilde{\lambda}$), the parameter $\lambda^\star_\vartheta$ is identical in all frames. It is also always larger, in magnitude, than λ_ϑ: it represents, in fact, the maximum observable polar anisotropy.

The parameters $\lambda^\star_\vartheta$ and $\lambda^\star_\varphi$ are *geometrical* invariants, describing the absolute *shape* of the distribution. In the presence of a superposition of processes characterized by different natural axes, they become dependent of the kinematics, following the variation of the (p_T/M and y-dependent) angle between those natural frames; in the example of Fig. 4.13, this is the angle between the two superimposed "peanut" shapes. Clearly, the *shape* of the resulting distribution depends on such an angle.

On the other hand, $\tilde{\lambda}$, like $\mathcal{F}$, denotes the *nature* of the polarization and, in the case of a superposition of production processes, it equals the average of the natural

polarizations, independently of possibly different directions of the several natural axes and, therefore, with no direct correlation to the shape resulting from the superposition. In fact, in the present example only $\tilde{\lambda}$ is completely independent of the production kinematics.

The two different natures of the $\tilde{\lambda}$ and $\lambda_\vartheta^\star$ invariants also affects how they should be used, both in measurements and in calculations. As seen in the discussion of the Drell–Yan and Z/W boson decay distributions in Section 4.3, the invariance of $\tilde{\lambda}$ survives any integration over kinematic ranges. For example, the Lam–Tung relation $\tilde{\lambda} = +1$, when verified for fixed values of p_T, mass and y or x_F, continues to hold even if the angular distribution is measured integrating over the largest possible ranges of such variables, provided that the underlying physics does not change inside the integration domain. This is not true for $\lambda_\vartheta^\star$ and $\lambda_\varphi^\star$, which, actually, should rather be called "quasi-invariants". Because of the non-linearity of their dependence on λ_ϑ, λ_φ, and $\lambda_{\vartheta\varphi}$ (Eq. 3.41), when the angular distribution is averaged over a large kinematic domain, $\lambda_\vartheta^\star$ and $\lambda_\varphi^\star$ can lose their exact frame independence; only the combination $(\lambda_\vartheta^\star + 3\,\lambda_\varphi^\star) / (1 - \lambda_\varphi^\star)$, equal to $\tilde{\lambda}$, is immune to the averaging effect.

This fact is illustrated in Fig. 4.15, prepared for the case of Drell–Yan dileptons with invariant mass in a narrow window around 25 GeV. For simplicity, we only consider a single scenario, where the dileptons are produced with a fully transverse polarization in the HX frame, with no process superpositions: as mentioned above, we straightforwardly expect $\lambda_\vartheta^\star = \tilde{\lambda} = +1$ and $\lambda_\varphi^\star = 0$. The parameters are shown as a function of p_T, in two hypothetical measurements performed around the same average rapidity, $\langle y \rangle = 1$, but integrating events in two different ranges: $0 < y < 2$ and $0.5 < y < 1.5$.

The results are not shown for the HX frame, where, naturally, $\lambda_\vartheta^\star = \tilde{\lambda} = \lambda_\vartheta = +1$ and $\lambda_\varphi^\star = \lambda_\varphi = 0$. In the CS frame, $\tilde{\lambda}$ confirms its invariance, remaining exactly +1, while the parameter λ_ϑ is, not surprisingly, slightly different when measured in rapidity intervals of different widths, as already seen in previous examples. More interestingly, the parameter $\lambda_\vartheta^\star$ departs from +1, with a deviation that increases when measured over a broader rapidity interval. Analogous observations can be made for the variable $\lambda_\varphi^\star$, seen to depart from zero when the integration is made in the broader $\Delta y = 2$ range.

The violation of the invariance of these parameters can, in principle, be made negligible with respect to the experimental precision of the measurement, by suitably reducing the width of the integration intervals. In the example of Fig. 4.15, the effect becomes almost invisible when the width of the integration interval, Δy, is reduced from 2 to 1. The integration over large kinematic intervals is, in general, a hazardous practice for more than one reason. As discussed in Section 2.14, different experimental acceptances, and even different efficiency shapes inside a given acceptance, have a direct influence on how the anisotropy parameters transform from one frame to another and the same effects, including a different dependence of the detector efficiency on p_T and rapidity among different experiments (even inside the same dilepton kinematic range), can lead to slightly different values of $\lambda_\vartheta^\star$ and $\lambda_\varphi^\star$.

Similar considerations apply to the frame-independent parity-violating asymmetry $\mathcal{A}^\star$ introduced in Section 3.10. The measurement of this parameter is interesting

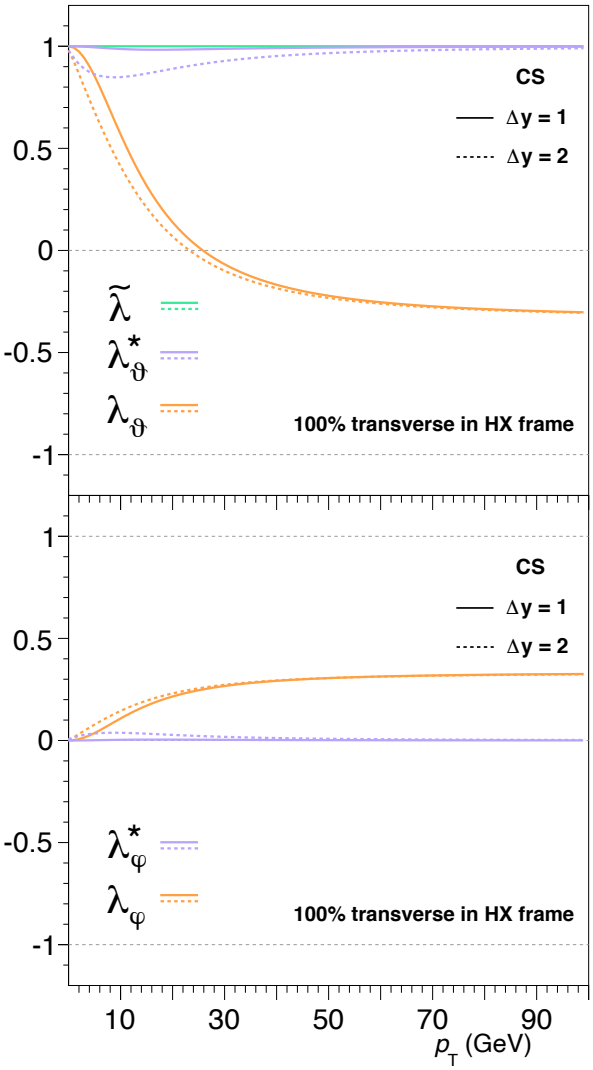

Fig. 4.15 The parameters $\tilde{\lambda}$, $\lambda_\vartheta^\star$, and λ_ϑ (top), as well as $\lambda_\varphi^\star$ and λ_φ (bottom), as a function of p_T, as seen in the CS frame, for a state of mass 25 GeV produced transversely polarized in the HX frame. Two cases are shown, with the same average rapidity, $\langle y \rangle = 1$, and only differing in the width of the rapidity window over which the measurement is integrated, $\Delta y = 1$ or 2.

because it provides the magnitude of the *maximum observable* parity asymmetry, that is, the net asymmetry measured along the polarization axis that maximizes it.

As mentioned in Chapter 1 (Eq. 1.30), the parameter A_ϑ is related to the "forward-backward asymmetry" between the numbers of events with $\cos\vartheta > 0$ and $\cos\vartheta < 0$ (according to the adopted definition of $\cos\vartheta$), studied, for example, in experimental analyses of direct Z/γ^* and W production. This asymmetry is usually

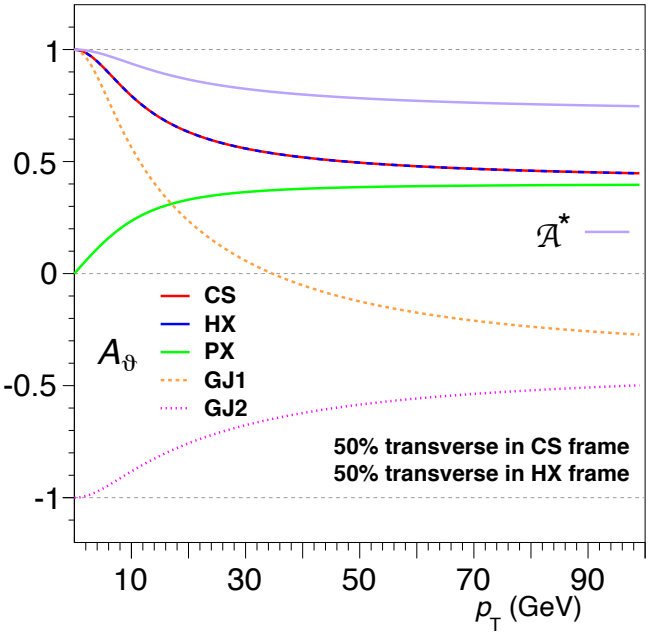

Fig. 4.16 The parameters $\mathcal{A}^\star$ and A_ϑ, as a function of p_T, as seen in the five frames indicated in the legends, when the decaying state, of $m = 25$ GeV and $y = +0.5$, is produced with an equal and constant mixture of purely transverse polarizations in the CS and HX frames, and the parity violation asymmetry is maximal in both kinds of processes. $\mathcal{A}^\star$ is identical in all frames.

defined in the CS frame. However, at high p_T, where processes beyond leading order contribute significantly, the CS frame no longer closely reflects the topology of the decay process. As previously discussed, the polarization parameter undergoes a strong reduction from its leading-order expectation for direct production, $\lambda_\vartheta^{CS} = +1$. In a similar way, the polar "projection" of the asymmetry becomes smaller than the maximum observable asymmetry. For example, the processes shown in the panels (a), (b), and (d) of Fig. 2.2 have natural transverse polarizations and, therefore, natural parity asymmetries along the GJ or HX axes; the transformation to the CS frame leads to a reduction of the corresponding A_ϑ contributions and to the appearance of an azimuthal component A_φ.

In such situations, the significance of the measured parity-violating effect can be improved, independently of the choice of the polarization frame, by measuring $\mathcal{A}^\star$, which can be done with the parameter substitutions of Eq. 3.49. This is illustrated in Fig. 4.16, corresponding to the same process and conditions of Fig. 4.14: we see that $\mathcal{A}^\star$ always represents a more significant parity-violating effect than A_ϑ, whatever direction is chosen as quantization axis.

However, it is important to note that $\mathcal{A}^\star$ is actually a "quasi-invariant", so that its measurement is affected by the same caveat noticed for $\lambda_\vartheta^\star$ and $\lambda_\varphi^\star$. This is shown in Fig. 4.17, prepared for the same conditions as assumed in Fig. 4.15, where we

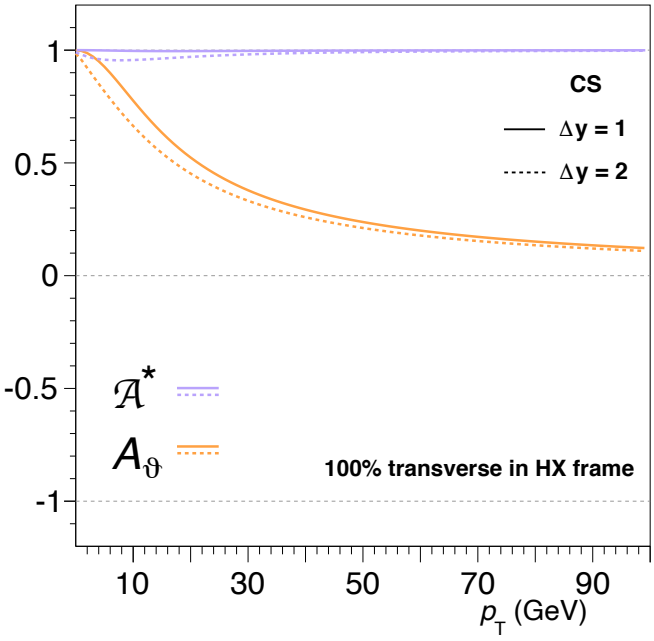

Fig. 4.17 The parameters $\mathcal{A}^\star$ and A_ϑ, as a function of p_T, as seen in the CS frame, for a state of mass 25 GeV produced transversely polarized in the HX frame and decaying with maximum parity violation. Two cases are shown, with the same average rapidity, $\langle y \rangle = 1$, and only differing in the width of the rapidity window over which the measurement is integrated, $\Delta y = 1$ or 2.

clearly see that $\mathcal{A}^\star$ deviates from the frame independence expectation. While it remains true that $\mathcal{A}^\star$ is always larger than $|A_\vartheta|$ in any frame (just like $|\lambda_\vartheta^\star|$ is always larger than $|\lambda_\vartheta|$ when the correct convention is used), a rigorous use of its frame-independence (for example, as a data-analysis crosscheck) can only be made in cases where one can avoid integrations over broad kinematic ranges.

4.6 Recapitulation

When the production of the particle under study results from two or more fundamental processes, characterized by natural polarization axes having distinct directions, the frame-dependent parameters λ_ϑ, λ_φ and $\lambda_{\vartheta\varphi}$ always show a significant dependence on the particle momentum, in whatever frame they are measured (Figs. 4.1–4.3 and 4.6–4.8). The measurement also depends on the experimental acceptance, just as described in Section 2.14, but, this time, no frame exists, in general, where two experiments with different acceptances obtain the same results (Fig. 4.4). In fact, in the considered hypothesis the chosen observation frame differs from at least one of the natural ones and to calculate (for example) the λ_ϑ value resulting from the

sum over processes, given by Eq. 4.1, we must first transform at least one of the individual $\lambda_\vartheta^{(i)}$ values, introducing a kinematic dependence. The invariant polarization parameter $\mathcal{F}$ (or $\tilde{\lambda}$) solves this problem: the analogous addition rule (Eq. 4.2 or 4.4) only involves frame-independent quantities, which can be determined, therefore, choosing either always the same frame or a different frame for each term, with the same the result in both cases. If the natural polarizations are intrinsically independent of the kinematics, their simplicity will be strongly disrupted in the observation of λ_ϑ, λ_φ and $\lambda_{\vartheta\varphi}$, but fully recovered in that of $\mathcal{F}$ or $\tilde{\lambda}$.

The production of Drell–Yan dileptons and of Z or W bosons offers an interesting application of these concepts, because the different contributing subprocesses provide examples of natural polarizations in the CS, GJ and HX frames (Fig. 2.2). While very low p_T measurements are not sensitive to the variety of topologies and a measurement in the CS frame simply shows a constant polarization (Fig. 4.9), the CDF (W) and LHC (Z) data are ideally suited to illustrate the strong kinematic dependence observed (Figs. 4.10 and 4.11) despite the underlying constant natural transverse polarization characterizing each individual subprocess.

To reproduce the data as a superposition of such processes requires attention in the modelling of the *s*-channel processes, whose natural quantization axis is actually the particle direction with respect to the parton-parton rest frame, significantly different from the proton-proton frame. The longitudinal parton motion must be taken into account in the transformation from the unobservable parton-parton-HX frame to the experimental (proton-proton based) polarization frame, so that λ_ϑ (or A_0) and the other frame-dependent parameters cannot be predicted without using as input the proton PDFs. On the other hand, the transformation from the parton-parton to the proton-proton HX frame is a simple rotation in the production plane, if the intrinsic parton k_T is neglected (a justified approximation at high p_T). For this reason, $\mathcal{F}$ and $\tilde{\lambda}$ are identical in those two frames: interestingly, the invariant polarization returns the natural polarization even when it arises along an experimentally unobservable direction.

More generally, each of the subprocesses depicted in Fig. 2.2 yields exactly $\mathcal{F} = 1/2$, or $\tilde{\lambda} = +1$, independently of the frame and of the kinematics. This condition is nothing else than the Lam–Tung relation, previously considered as a surprising coincidence in the results of perturbative QCD calculations, while it can simply be explained as a manifestation of helicity conservation (determining the intrinsic transverse polarization of all participating processes) and rotational invariance. The Lam–Tung relation, as well as $\mathcal{F}$ and $\tilde{\lambda}$, are actually *insensitive* to the details of the process topologies used in the calculations. Such important physical details are reflected, instead, in the kinematics-dependent values of λ_ϑ and of the other frame-dependent shape parameters: frame-dependent and frame-independent measurements complement each other.

In the presence of a superposition of processes with different natural polarization axes, the invariant $\lambda_\vartheta^\star$ no longer equals the (average) natural polarization and, together with $\lambda_\varphi^\star$, becomes kinematics dependent (Fig. 4.14). These two parameters can be defined (with a suitable choice of the alternative sign definition inside $\Lambda^\star$ in Eq. 3.41) so as to represent, respectively, the maximum λ_ϑ and the minimum

λ_φ values measurable in any frame. They are related to $\tilde{\lambda}$ by Eq. 4.9 and may replace λ_ϑ and λ_φ without loss of information. Similarly, the frame-independent parity asymmetry $\mathcal{A}^\star$ represents the maximum observable asymmetry when varying the observation frame (Fig. 4.16). There is a limitation, not affecting $\mathcal{F}$ and $\tilde{\lambda}$, in the use of the parameters $\lambda_\vartheta^\star$, $\lambda_\varphi^\star$ and $\mathcal{A}^\star$: because of their non-linear dependence on the coefficients of the angular distribution, a measurement averaged over a large kinematic interval can violate frame-independence (Figs. 4.15 and 4.17). Their use should be, therefore, limited to cases where the effects of kinematic integrations are under control.

References

[1] CDF Collaboration, "Polarization of J/ψ and ψ(2S) mesons produced in $p\bar{p}$ collisions at $\sqrt{s}$ = 1.96 TeV", *Phys. Rev. Lett.* **99** (2007) 132001, doi:10.1103/PhysRevLett.99.132001, arXiv:0704.0638.

[2] E866 Collaboration, "Observation of polarization in bottomonium production at $\sqrt{s}$ = 38.8 GeV", *Phys. Rev. Lett.* **86** (2001) 2529, doi:10.1103/PhysRevLett.86.2529, arXiv:hep-ex/0011030.

[3] CDF Collaboration, "Measurement of the polar-angle distribution of leptons from W boson decay as a function of the W transverse momentum in $p\bar{p}$ collisions at $\sqrt{s}$ = 1.8 TeV", *Phys. Rev. D* **70** (2004) 032004, doi:10.1103/PhysRevD.70.032004, arXiv:hep-ex/0311050.

[4] D0 Collaboration, "Measurement of the angular distribution of electrons from $W \to e\nu$ decays observed in $p\bar{p}$ collisions at $\sqrt{s}$ = 1.8 TeV", *Phys. Rev. D* **63** (2001) 072001, doi:10.1103/PhysRevD.63.072001, arXiv:hep-ex/0009034.

[5] CMS Collaboration, "Angular coefficients of Z bosons produced in pp collisions at $\sqrt{s}$ = 8 TeV and decaying to $\mu^+\mu^-$ as a function of transverse momentum and rapidity", *Phys. Lett. B* **750** (2015) 154, doi:10.1016/j.physletb.2015.08.061, arXiv:1504.03512.

[6] ATLAS Collaboration, "Measurement of the angular coefficients in Z-boson events using electron and muon pairs from data taken at $\sqrt{s}$ = 8 TeV with the ATLAS detector", *JHEP* **08** (2016) 159, doi:10.1007/JHEP08(2016)159, arXiv:1606.00689.

[7] C.-S. Lam and W.-K. Tung, "A systematic approach to inclusive lepton pair production in hadronic collisions", *Phys. Rev. D* **18** (1978) 2447, doi:10.1103/PhysRevD.18.2447.

[8] E. Mirkes and J. Ohnemus, "Angular distributions of Drell–Yan lepton pairs at the Tevatron: order α_s^2 corrections and Monte Carlo studies", *Phys. Rev. D* **51** (1995) 4891, doi:10.1103/PhysRevD.51.4891, arXiv:hep-ph/9412289.

[9] E. L. Berger, J.-W. Qiu, and R. A. Rodriguez-Pedraza, "Transverse momentum dependence of the angular distribution of the Drell–Yan process", *Phys. Rev. D* **76** (2007) 074006, doi:10.1103/PhysRevD.76.074006, arXiv:0708.0578.

[10] NA10 Collaboration, "Angular distributions of muon pairs produced by negative pions on deuterium and tungsten", *Z. Phys. C* **37** (1988) 545, doi:10.1007/BF01549713.

[11] E615 Collaboration, "Experimental study of muon pairs produced by 252 GeV pions on tungsten", *Phys. Rev. D* **39** (1989) 92, doi:10.1103/PhysRevD.39.92.

[12] D. Boer, "Investigating the origins of transverse spin asymmetries at RHIC", *Phys. Rev. D* **60** (1999) 014012, doi:10.1103/PhysRevD.60.014012, arXiv:hep-ph/9902255.

[13] D. Boer and P. J. Mulders, "Time reversal odd distribution functions in leptoproduction", *Phys. Rev. D* **57** (1998) 5780, doi:10.1103/PhysRevD.57.5780, arXiv:hep-ph/9711485.

[14] A. Brandenburg, S. J. Brodsky, V. V. Khoze, and D. Müller, "Angular distributions in the Drell–Yan process: a closer look at higher twist effects", *Phys. Rev. Lett.* **73** (1994) 939, doi:10.1103/PhysRevLett.73.939, arXiv:hep-ph/9403361.

[15] F. Gelis and J. Jalilian-Marian, "Drell–Yan production and Lam–Tung relation in the color glass condensate formalism", *Phys. Rev. D* **76** (2007) 074015, doi:10.1103/PhysRevD.76.074015, arXiv:hep-ph/0609066.

[16] P. Faccioli, C. Lourenço, and J. Seixas, "Rotation-invariant relations in vector meson decays into fermion pairs", *Phys. Rev. Lett.* **105** (2010) 061601, doi:10.1103/PhysRevLett.105.061601, arXiv:1005.2601.

Chapter 5
Smearing effects in non-planar processes

In certain physical cases, the angular momentum of a vector particle may naturally align with a direction no longer exactly contained in the production plane, leading to an attenuation of the polarization magnitude observable in any experimentally defined frame.

In this chapter we consider two possible causes of this phenomenon: the higher-order, nonplanar processes contributing to Drell–Yan, W and Z production, and the intrinsic transverse momentum of the partons inside the colliding hadrons.

We will address the following questions.

- How are the polar and azimuthal anisotropies affected by the non-planarity of the production process?
- What happens to the Lam–Tung relation and to the frame-independent polarization? What kind of qualitative and quantitative information is provided by their modifications with respect to the purely planar case?
- How can the existing measurements of Z polarization at the LHC be interpreted?
- For what particles and in what kinematic conditions does the effect of the intrinsic transverse parton momentum become important?

P. Faccioli and C. Lourenço, *Particle Polarization in High Energy Physics*,
Lecture Notes in Physics 1002,
https://doi.org/10.1007/978-3-031-08876-6_5

5.1 When the natural axis escapes experimental observation

In the previous chapter we saw that the invariant parameter $\tilde{\lambda}$ provides, independently of the chosen frame, the value of the "natural" polarization parameter λ_0, when the decay distribution is of the kind $\propto 1 + \lambda_0 \cos^2 \vartheta$ along some natural quantization direction, even when such direction is not uniquely defined because of the superposition of different underlying production mechanisms. We have mentioned that this happens under a condition: the natural quantization axis (or axes) must belong to the production plane (zx), that is, the plane containing all meaningful experimental definitions of the polarization axis for inclusive production measurements. In fact, $\tilde{\lambda}$ is invariant only by rotations about the zx plane. We will now focus on that condition and discuss in detail what happens when it is not satisfied.

There are, in fact, important physical cases where the natural polarization axis does not necessarily belong to the production plane. The process leading to the production of the observed particle can often deviate from a planar topology. For example, it can have more than two final states ("$2 \to N$ processes", with $N > 2$), a case illustrated in the next section as a possible cause of violation of the Lam–Tung relation. Similarly, it may involve more than two incident objects, as when three or four partons of the colliding protons actively participate in the process.

Even in the case of $2 \to 1$ or $2 \to 2$ processes, if the incoming partons have non-negligible transverse momenta with respect to the particle's mass (and, therefore, with respect to their own longitudinal momenta), they may collide along a line of flight no longer contained in the production plane, so that the plane they form together with the outgoing vector particle represents an additional physical reference. Another example, which will be the subject of the next chapter, is the entire category of "two-step" or "cascade" processes, as the case of J/ψ mesons produced from the decays of B or χ_c mesons.

All these processes are no longer "two-dimensional", as those shown in Fig. 2.2. Their intrinsically three-dimensional topology allows for the meaningful definition of more than one reference plane for the "theoretical" description of the decay distribution of the observed particle. It is to one of such distinct planes, not necessarily the production plane, that the natural polarization axis may belong.

However, the measurement is often limited to the two-dimensional "view" of the process; in inclusive production studies (as in the cases that we will consider here) the additional degrees of freedom of the non-planar topology are averaged out. This means that only the final, decaying vector particle is detected and no information is acquired on the accompanying objects, such as the additional products of a $2 \to 3$ process, or the recoil particle in the decay of a cascade process, for example the photon in $\chi_{c0} \to \mathrm{J}/\psi\,\gamma$ decays (discussed in the next chapter). Also, the parton-parton collision direction and, in particular, its tilt with respect to the production plane are not even accessible experimentally. In these cases, the only possible reference for the study of the decay distribution remains the production plane, formed by the only two directions that are known in the decaying particle's rest frame, those of the colliding hadrons. Therefore, the angular momentum of the particle will have, in general, its definite or preferred projection along an axis *intersecting* the production plane at an

unknown angle, which varies from one event to another. As a consequence of this uncertainty in the geometry of the process, the observed angular distribution will only be a "smeared" version of the original one.

5.2 Non-planar processes: violations of the Lam–Tung relation

As discussed in Section 4.4, the production of Drell–Yan lepton pairs and elementary vector bosons satisfies, up to the leading order (order-α_s^1) QCD corrections shown in Fig. 2.2, a simple polarization identity, $\lambda_\vartheta + 4\lambda_\varphi = 1$ (that is, $\mathcal{F} = 1/2$ or $\tilde{\lambda} = 1$), known as the Lam–Tung relation, valid in any reference frame. This result is today understood as a simple consequence of the helicity-conserving couplings between light fermions and elementary vector bosons (gluon, virtual photon, or Z and W bosons), as appearing in the relevant elementary processes, and the rotational covariance of angular momentum states.

Processes including higher-order QCD corrections, like those shown in Fig. 5.1, can lead to the observation of a violation of the Lam–Tung relation, as has indeed been reported in the LHC measurements of Z decay distributions already considered in Section 4.3.

In the parametrization adopted by the ATLAS and CMS collaborations, the angular distribution, considering the relevant azimuthal components but, for simplicity, only including parity-conserving terms, is written as

$$\begin{aligned} W(\cos\vartheta,\varphi) \;\propto\; 1 \;+\; \cos^2\vartheta \;+\; \frac{1}{2}A_0\,(1-3\cos^2\vartheta) \\ +\; A_1\,\sin 2\vartheta\cos\varphi \;+\; \frac{A_2}{2}\,\sin^2\vartheta\cos 2\varphi\,, \end{aligned} \tag{5.1}$$

where the coefficients correspond to the ones of the usual expression (Eq. 2.1) according to the relations

$$\lambda_\vartheta = \frac{1-\frac{3}{2}A_0}{1+\frac{1}{2}A_0}\,, \quad \lambda_\varphi = \frac{\frac{1}{2}A_2}{1+\frac{1}{2}A_0} \qquad \text{and} \quad \lambda_{\vartheta\varphi} = \frac{A_1}{1+\frac{1}{2}A_0}\,. \tag{5.2}$$

The full expression of the distribution and the properties of the parameters A_i are reported in Appendix A.

The invariant polarization parameter becomes

$$\mathcal{F} = \frac{1}{2}\left(1-\frac{A_0-A_2}{2}\right). \tag{5.3}$$

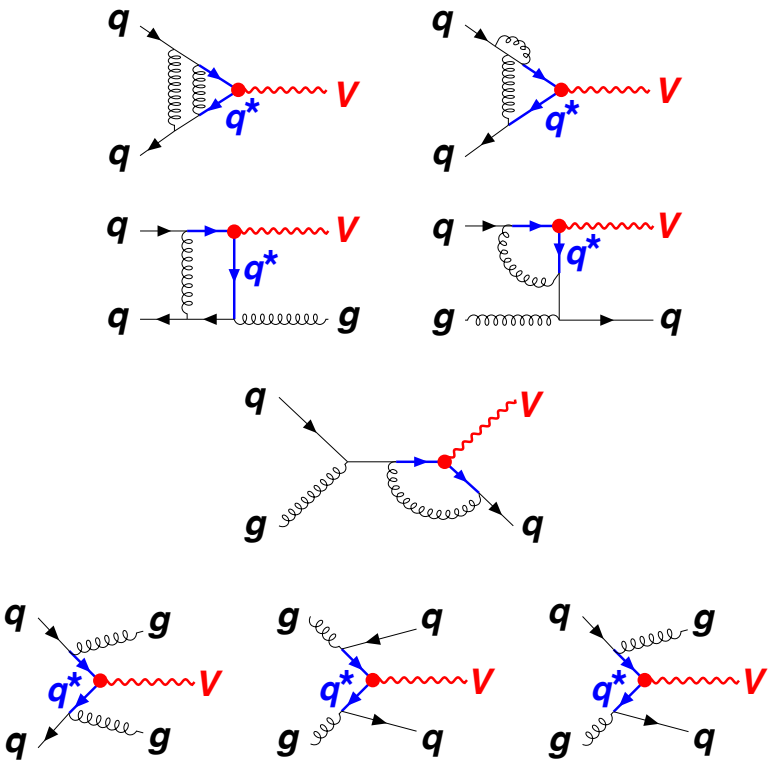

Fig. 5.1 Two categories of Feynman diagrams contributing to Drell–Yan, Z and W production at higher perturbative orders than those shown in Fig. 2.2: planar ($2 \to 1$ or $2 \to 2$) processes (top three rows); and non-planar ($2 \to 3$) processes (bottom row).

From this expression, we see that the quantity $(A_0 - A_2)\,/\,2$ itself, included in the interval $[-1, +1]$, is invariant, that is, it must be identical in the CS, HX, PX, and GJ frames, independently of the underlying production mechanisms.

The Lam–Tung relation, $\mathcal{F} = 1/2$, is written as

$$\frac{A_0 - A_2}{2} = 0\,. \tag{5.4}$$

The relation $A_2 = A_0$ is significantly violated in nature, as clearly seen by comparing the p_{T} dependences of the A_0 and A_2 parameters measured by CMS [1] and ATLAS [2], in two rapidity intervals, shown in Fig. 5.2. The red curves, previously shown in Fig. 4.11, represent the analytical model described in Section 4.3), only considering the existence of leading order production processes, for which $A_2 = A_0$. We see that, as already discussed in Section 4.3, the $O(\alpha_s^1)$ processes of Fig. 2.2 are sufficient to provide a good description of A_0 but clearly overestimate the A_2 measurements.

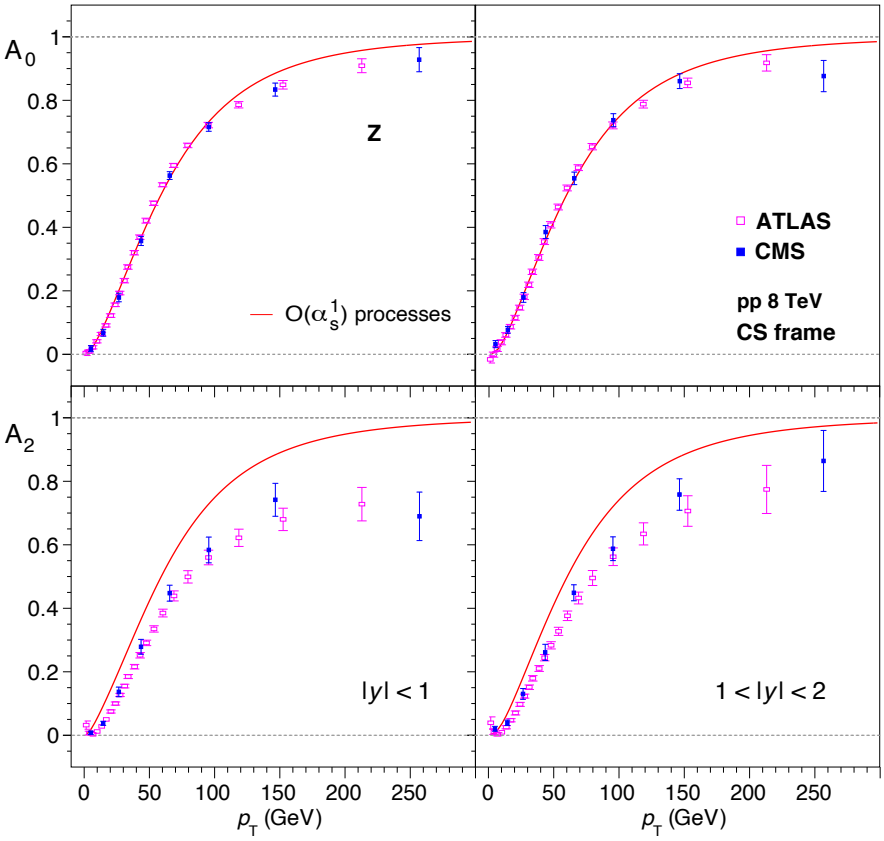

Fig. 5.2 The anisotropy parameters A_0 (top) and A_2 (bottom), in the CS frame, for Z bosons produced in proton-proton collisions at $\sqrt{s} = 8$ TeV, as measured by CMS [1] and ATLAS [2], in two ranges of rapidity: $|y| < 1$ (left) and $1 < |y| \lesssim 2$ (right). The curves only reflect production processes with leading order QCD corrections, for which $A_2 = A_0$.

The significance of the violation $A_2 \neq A_0$ is more clearly seen in the measurement of $A_0 - A_2$, presented in Fig. 5.3; the difference is always positive, meaning that $\mathcal{F} < 1/2$.

The monotonic decrease to zero towards $p_T = 0$ is also an important physical indication: it confirms that the underlying natural polarization is indeed fully transverse in all involved processes. In fact, in that limit no azimuthal anisotropy can physically exist and $A_0 - A_2 = 0$ implies $A_0 = 0$, that is, $\lambda_\vartheta = +1$. It is important to remark that $(A_0 - A_2) / 2$, even when it is not zero as in the case of leading-order production, must anyhow remain a frame-independent quantity in any (small or large) integrated kinematic range, a check unfortunately not reported by the experiments.

While, in general, the reasons for a violation of the Lam–Tung relation in Drell–Yan production can be manifold and, in some cases, are still today not fully understood, the ATLAS and CMS results do have a geometrical interpretation, involving

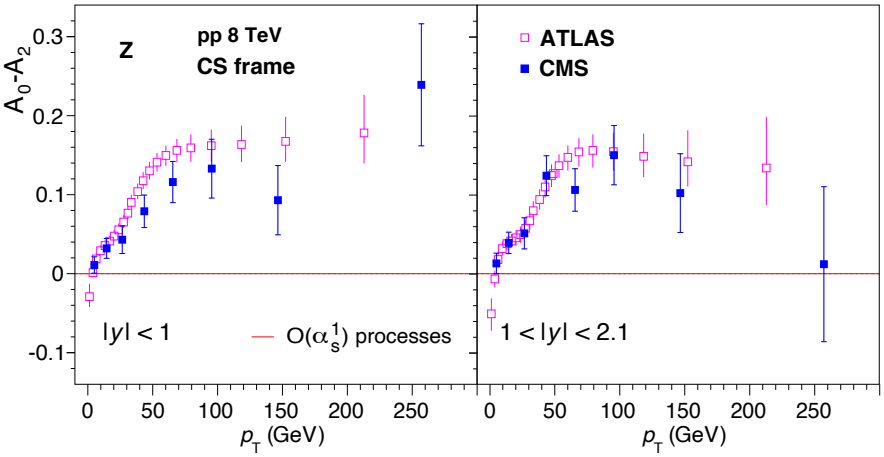

Fig. 5.3 The difference $A_0 - A_2$, directly expressing the violation of the Lam–Tung relation, corresponding to the measurements shown in the previous figure.

higher-order QCD production processes, which is as simple and intuitive as the explanation of why the Lam–Tung relation itself is satisfied by leading-order processes [3–7]. In particular, the natural polarization continues to be fully transverse, as a reflection of helicity conservation, which still represents the polarizing mechanism. In fact, as can be seen in each diagram of Fig. 5.1, the final vector state always originates from the same kind of coupling to quarks seen in the leading order processes. The blue quark line represents, just as it did in Fig. 2.2, the physical direction along which the polarization of the observed particle is fully transverse.

What is crucially different with respect to the leading order case is that this direction is not always contained in the production plane. Actually, this condition is a geometrical criterion distinguishing two categories of higher-order processes. The top three rows of Fig. 5.1 show diagrams that are topologically identical to the leading order ones of Fig. 2.2, because any additional emission of a gluon is followed by its internal re-absorption, preserving the same momentum relations between final and initial partons as at leading order. Instead, in the diagrams of the bottom row the emitted gluons lead to the presence of additional particles in the event, in this case belonging to the final state. In other words, the latter kind of diagrams does not represent $2 \to 1$ or $2 \to 2$ topologies, as those of Figs. 2.2 and 5.1-a: they are "$2 \to 3$" processes, leading, for example, to the production of Z bosons accompanied by two jets. More generally, the present considerations apply to any kind of *non-planar* topology (including, for example, $N \to 2$ or $2 \to N$ processes, with $N > 2$), where the momentum vectors of the initial and final states are no longer forced by momentum conservation to belong to one plane.

With respect to the production plane, containing the directions of the incoming hadrons, the natural polarization direction in the non-planar processes of Fig. 5.1-b forms an angle $\hat{\phi}$, changing from one event to the next. In inclusive Z or DY studies,

where the production plane is the only meaningful reference and the polarization axis chosen in the measurement must belong to it, the transformation from natural to experimental frame (for a given subprocess) is no longer the simple rotation around the y axis relating, for example, the CS and HX frames. It can be described as a composition of rotations, as illustrated in Fig. 2.22, where the first rotation around the z axis is superfluous when applied to a natural, cylindrically symmetric distribution of the kind $1 + \lambda_0 \cos^2\vartheta$ (it maintains the distribution unchanged).

The general relation between natural polarization and observed one, for a single subprocess, depends, therefore, on the rotation angles ζ and ω; it can be obtained from Table 2.2, setting to zero the initial values of all parameters except λ_ϑ, which should be set to λ_0.

The resulting relations are

$$\lambda_\vartheta = \frac{1 - \frac{3}{2}\sin^2\zeta}{1 + \frac{1}{2}\lambda_0 \sin^2\zeta}\,\lambda_0\,,$$

$$\lambda_\varphi = \frac{\frac{1}{2}\sin^2\zeta\cos 2\omega}{1 + \frac{1}{2}\lambda_0 \sin^2\zeta}\,\lambda_0\,, \quad \lambda_\varphi^\perp = \frac{-\frac{1}{2}\sin^2\zeta\sin 2\omega}{1 + \frac{1}{2}\lambda_0 \sin^2\zeta}\,\lambda_0\,, \tag{5.5}$$

$$\lambda_{\vartheta\varphi} = \frac{-\frac{1}{2}\sin 2\zeta\cos\omega}{1 + \frac{1}{2}\lambda_0 \sin^2\zeta}\,\lambda_0\,, \quad \lambda_{\vartheta\varphi}^\perp = \frac{\frac{1}{2}\sin 2\zeta\sin\omega}{1 + \frac{1}{2}\lambda_0 \sin^2\zeta}\,\lambda_0\,.$$

In the case under study, the natural polarization λ_0 is +1, but these more general relations are reported for later reference.

The analogous transformation between two reference frames both having z axis belonging to the production plane, as the experimentally defined HX and CS frames, is obtained from these relations by setting $\omega = 0$, and depends only on the angle ζ defining the rotation around the y axis. In particular, the relations for $\lambda_\varphi^\perp$ and $\lambda_{\vartheta\varphi}^\perp$ vanish identically, illustrating how these parameters reflect a tilt of the distribution with respect to the azimuthal reference plane (not observable, when the latter coincides with the production plane, in inclusive studies of parity-conserving processes). The crucial difference between the two kinds of transformation is that the rotation between two "experimental" reference frames depends in a known way on p_T and rapidity, as detailed in Table 2.1, where δ coincides with ζ. On the contrary, when the natural z axis is not bound to lie on the production plane ($\omega \neq 0$), the rotation angles are unmeasurable and event-dependent, even if the experiment considers the narrowest possible ranges of p_T and rapidity.

The relation between $\hat{\phi}$, describing the event-dependent tilt of the natural polarization axis with respect to the production plane, and the rotation angles ζ and ω is

$$\sin\hat{\phi} = \sin\zeta\,\sin\omega\,. \tag{5.6}$$

This relation can be obtained by considering that the unit vector describing the direction of the natural axis is $(\sin\zeta\cos\omega, \sin\zeta\sin\omega, \cos\zeta)$ and forms an angle ξ,

such that $\cos\xi = \sin\zeta \sin\omega$, with respect to the y axis; $\hat{\phi}$ is the complementary of ξ, so that $\sin\hat{\phi} = \cos\xi$.

The angle $\hat{\phi}$ is the one appearing in the relations we will find when we verify what happens to the invariant polarization parameters. In fact, from Eqs. 5.5 and 5.6 the analogous of the covariant relations of Eq. 3.9 is found to be, for the transformation now under study,

$$\begin{aligned} 3 + \lambda_\vartheta &= \frac{1}{1+\Lambda}\,(3+\lambda_0)\,, \\ 1 - \lambda_\varphi &= \frac{1}{1+\Lambda}\,\left(1 + \lambda_0\,\sin^2\hat{\phi}\right)\,, \end{aligned} \tag{5.7}$$

with $\Lambda = \frac{1}{2}\lambda_0 \sin^2\zeta$.

The expressions for the variants $\mathcal{F} \equiv \mathcal{F}_{\{1,-2,1,0\}}$ (Eq. 3.10), $\tilde{\lambda} \equiv -(1-3\mathcal{F})\,/\,(1-\mathcal{F})$ and $\frac{1}{2}(A_0 - A_2) \equiv 1 - 2\mathcal{F}$ of the frame-independent polarization are

$$\begin{aligned} \mathcal{F} &= \frac{1 + \lambda_0 \cos 2\hat{\phi}}{3+\lambda_0}\,, \quad \tilde{\lambda} = \frac{1 - 3\sin^2\hat{\phi}}{1 + \lambda_0 \sin^2\hat{\phi}}\,\lambda_0\,, \\ \text{and} \quad \frac{1}{2}(A_0 - A_2) &= \frac{1 + \lambda_0\,\left(1 - 2\cos 2\hat{\phi}\right)}{3+\lambda_0}\,. \end{aligned} \tag{5.8}$$

These quantities depend not only on λ_0 but also on the tilt angle $\hat{\phi}$, appearing in the expressions $\sin^2\hat{\phi}$ and $\cos 2\hat{\phi}$, which have to be averaged over all the events and are both positive (being $\hat{\phi}$ distributed around zero). Only when $\hat{\phi} \equiv 0$ (for all events) they directly reflect the natural polarization, being in particular $\tilde{\lambda} = \lambda_0$ and $\frac{1}{2}(A_0 - A_2)$ representing the corresponding longitudinal fraction $(1-\lambda_0)\,/\,(3+\lambda_0)$. In fact, these observables, while always remaining anyhow invariant by transformation among two observation frames (CS and HX, etc.), are *not* invariant by the transformation from natural to observation frame. Given that $|\tilde{\lambda}| < \lambda_0$, as can be deduced from Eq. 5.8 for a reasonably small $\sin^2\hat{\phi}$, this transformation leads to a *smearing* of the magnitude of the overall polarization observed in the experimental frame.

As suggested by the fact that the covariant transformation of $3 + \lambda_\vartheta$ in Eq. 5.7 remains actually unchanged with respect to the transformations between experimental frames and only $1 - \lambda_\varphi$ becomes dependent on the tilt angle $\hat{\phi}$, the smearing effect is due to the loss of an event-by-event coherent reference for the azimuthal angle measurement: it is essentially an attenuation of the observable *azimuthal* anisotropy. The transformation of λ_ϑ is formally identical to the transformation between any pair of experimental frames sharing the same y axis (HX, CS, etc.): it depends only on the angle ζ between the initial and final polarization axes, whether they both belong or not to the production plane. Instead, the transformed λ_φ depends on *both* rotation angles ζ and ω, and, when the natural axis is tilted with respect to the production plane, that is $\hat{\phi} \neq 0$, λ_φ is systematically (therefore, also on average), *smaller* than if the natural axis could only rotate *within* the production plane. In fact, even if $\hat{\phi}$ changes sign event after event and its distribution is, in parity conserving cases, symmetric around zero, the average quantity $\langle\sin^2\hat{\phi}\rangle$ is not zero unless the process

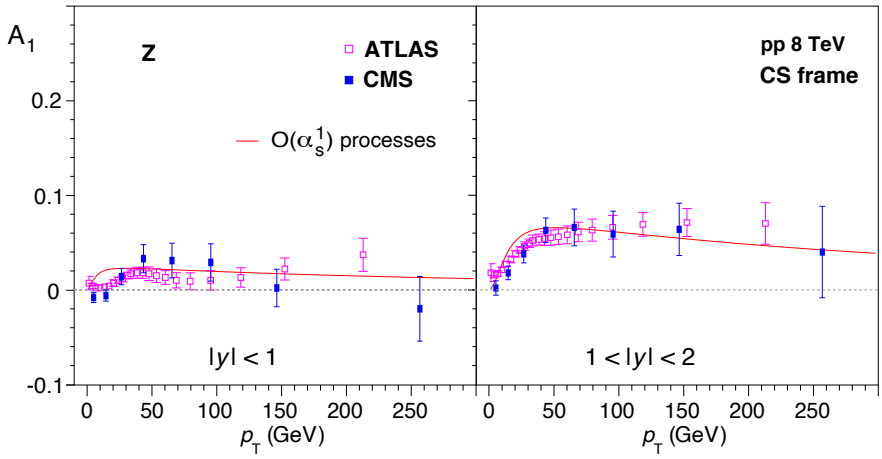

Fig. 5.4 The azimuthal anisotropy parameter A_1, in the CS frame, for Z bosons produced in proton-proton collisions at $\sqrt{s} = 8$ TeV [1, 2], in two ranges of rapidity: $|y| < 1$ (left) and $1 < |y| \lesssim 2$ (right). The curve represents the same analytical model as previously shown in Fig. 5.2.

is intrinsically planar. Therefore, in non-planar processes the maximum azimuthal anisotropy that can be observed in any experimentally accessible polarization frame has generally smaller magnitude than in planar ones.

Similarly, the parameter $\lambda_{\vartheta\varphi}$, or, equivalently, A_1,

$$A_1 \equiv \frac{4\,\lambda_{\vartheta\varphi}}{3+\lambda_\vartheta} = -\frac{2\,\lambda_0}{3+\lambda_0}\sin 2\zeta\cos\omega\,, \tag{5.9}$$

tends to be reduced in magnitude with respect to the prediction for planar processes ($\omega = 0$), because the factor $\cos\omega$ has module, on average, always smaller than 1. This effect is clearly seen in Fig. 5.4, where most of the data points are below the curve, especially in the $p_{\mathrm{T}} \lesssim 100$ GeV range, where the measurements have the best precision.

The fact that we are essentially seeing a smearing of the azimuthal anisotropy can be further appreciated through the following considerations. It is possible, in fact, to define a polarization-related quantity that is invariant, unlike $\tilde{\lambda}$ and its analogues, by the full "3D" transformation of the natural polarization λ_0, written in Eq. 5.5. Being

$$\sqrt{\lambda_\varphi^2 + \lambda_\varphi^{\perp 2}} = \frac{|\lambda_0|}{2}\,\frac{\sin^2\zeta}{1+\frac{1}{2}\lambda_0\sin^2\zeta}\,, \tag{5.10}$$

we see that the quantity

$$\tilde{\lambda}^{3\mathrm{D}} \equiv \frac{\lambda_\vartheta + 3\,\frac{\lambda_0}{|\lambda_0|}\sqrt{\lambda_\varphi^2+\lambda_\varphi^{\perp 2}}}{1-\frac{\lambda_0}{|\lambda_0|}\sqrt{\lambda_\varphi^2+\lambda_\varphi^{\perp 2}}} \tag{5.11}$$

(where the sign of λ_0 is easily inferred from the sign of the "planar" $\tilde{\lambda}$: $\lambda_0/|\lambda_0| = \tilde{\lambda}/|\tilde{\lambda}|$, except for extreme cases not worth discussing) reproduces exactly the natural polarization:

$$\tilde{\lambda}^{3D} = \lambda_0 \,. \tag{5.12}$$

In other words, if it were possible to determine experimentally the full shape of the distribution, including the parameter $\lambda_\varphi^\perp$, we would recover, in any frame, the full unsmeared natural polarization. However, the measurement of $\lambda_\varphi^\perp$ is not meaningful in inclusive observations of parity-conserving processes, as it must always yield exactly zero, because of the event averaging of equally probable, opposite anisotropies with respect to the production plane, as already discussed in more than one occasion (throughout this chapter we are assuming the absence of effects caused by polarizations of the colliding hadrons).

In the case of parity violating processes, $\lambda_\varphi^\perp$ may acquire small nonzero values in extreme kinematic conditions, but would anyhow be significantly smeared. To determine the unsmeared $\lambda_\varphi^\perp$ and, therefore, λ_0, it would be necessary to study the decay using reference axes based on the full non-planar topology of the production mechanism, keeping track, for each event, of the momenta of all particles produced in the hard scattering process together with the decaying particle. It can be easily seen that the suppression of $\lambda_\varphi^\perp$ in Eq. 5.11 leads to an underestimation of the full natural polarization: $|\tilde{\lambda}| < |\tilde{\lambda}^{3D}|$.

In summary, while it is possible to reproduce the measured polar anisotropy (A_0) assuming a suitable superposition of planar processes, the corresponding predictions for A_2 and A_1 overestimate the measured values when non-planar processes contribute: the measurement is not sensitive to the full magnitude of the intrinsic azimuthal anisotropies existing event after event and only returns a smeared version of these, as resulting from the event average. In order to spot the existence of contributing non-planar processes it is not necessary to compare the individual A_0 (λ_ϑ) and A_2 (λ_φ) values with calculations of these parameters accurately reproducing their peculiar p_T and rapidity dependences: the simplicity of the Lam–Tung relation allows for an immediate recognition of the effect, resulting in its violation. Actually, however, the violation alone does not provide indications on what category of effects can be the main cause. Moreover, it does not represent a means of quantification for the magnitude of the effect. In the next section we discuss how the Lam–Tung relation can be generalized in a form that can provide better qualitative and quantitative information about the underlying physics.

5.3 A generalization of the Lam–Tung relation

As discussed in the previous section, a violation of the Lam–Tung relation can be the signal of effects beyond the leading-order perturbative-QCD description of the production of elementary vector bosons. However, in its original form, $\lambda_\vartheta + 4\lambda_\varphi = 1$, the relation does not provide a quantification of the importance of the effects. To

start with, it is not frame-independent and cannot, therefore, provide any estimate of the fractional contribution of the processes responsible for the violation: a well-defined event fraction should be rotation-invariant and, hence, be represented by a frame-independent quantity.

Figure 5.5 shows values of the quantity $G = \lambda_\vartheta + 4\lambda_\varphi - 1 = \lambda + 2\nu - 1$, sometimes used to test the relation (often in conjunction with the alternative notation $\lambda \equiv \lambda_\vartheta$, $\nu \equiv 2\lambda_\varphi$), calculated for several points in the plane $\lambda_\vartheta^{\rm HX}, \lambda_\varphi^{\rm HX}$. The corresponding values in the CS frame are also indicated, in the assumed kinematic limit $p_{\rm T} \gg p_{\rm L}$, for which the two frames have perpendicular z axes, independently of the particle mass: $\delta^2_{\rm HX \leftrightarrows CS} = E^2 p_{\rm T}^2 \,/\, (p^2 m_{\rm T}^2)$ (see Table 2.1). The values in the two frames are completely different, except for $G = 0$, that is, when the Lam–Tung relation is indeed satisfied, and in the trivial cases when $\lambda_\varphi = \lambda_\vartheta$, for which λ_ϑ and λ_φ themselves are individually frame-independent, as mentioned in Section 3.3 (invariant configurations shown in Fig. 3.1). Moreover, their difference would vary with the kinematic conditions, as a function of $p_{\rm T}$, $p_{\rm L}$ and also of the mass of the particle.

Figure 5.6 shows the values of $\tilde{\lambda}$ and $\mathcal{F}$ for the same configurations as shown in Fig. 5.5: they are always identical in the two frames and in any other experimental frame, as they would be in any other chosen kinematic condition and for any mass of the decaying particle; labels specifying the frame, needed in the case of G, are in this case omitted.

As an illustration of the interesting quantitative information provided by the measurement of $\mathcal{F}$ (or $\tilde{\lambda}$) when the Lam–Tung relation is violated, we consider again the case of vector boson production discussed in Section 5.2. We indicate with $f_{\rm NP}$ the fraction of contributing non-planar processes (production in association with two or more quark/gluon jets), responsible for the violation. Imposing in Eq. 5.8 that the natural polarization is always fully transverse ($\lambda_0 = 1$) we write the invariant polarization of the higher-order, non-planar processes as $\mathcal{F}_{\rm NP} = 1/4\ (1 + \cos 2\hat{\phi})$, while for planar ones $\mathcal{F}_{\rm P} = 1/2$. The observable overall combination of the two complementary topologies is, therefore, characterized by the parameter $\mathcal{F} = f_{\rm NP}\, \mathcal{F}_{\rm NP} + (1 - f_{\rm NP})\, \mathcal{F}_{\rm P}$, where the sum rule in Eq. 4.2 was used.

The resulting "smeared" polarization is

$$\mathcal{F} = \frac{1}{2} \left(1 - f_{\rm NP} \langle \sin^2 \hat{\phi} \rangle \right), \tag{5.13}$$

or, in terms of "invariant longitudinal fraction" (using Eq. 5.3),

$$\frac{1}{2} (A_0 - A_2) = f_{\rm NP} \langle \sin^2 \hat{\phi} \rangle, \tag{5.14}$$

where we have now explicitly introduced the symbols indicating that the relevant angular quantity is actually the average over the "non-planar" events used in the measurement.

According to the CMS and ATLAS data, for Z production $A_0 - A_2$ tends to an asymptotic high-$p_{\rm T}$ value of order 0.1, that is, $f_{\rm NP} \langle \sin^2 \hat{\phi} \rangle \sim 0.05$. Given that there is no reason for $\langle \sin^2 \hat{\phi} \rangle$ to be particularly small in the effectively "three-dimensional"

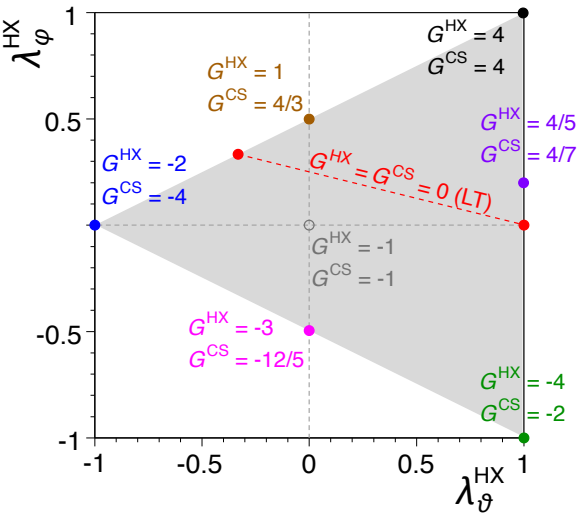

Fig. 5.5 Map of the values of $G = \lambda_\vartheta + 4\lambda_\varphi - 1 = \lambda + 2\nu - 1$, in the λ_φ vs. λ_ϑ plane. The λ_ϑ and λ_φ values are considered in the HX frame and then transformed to the CS frame with the hypothesis that they are perpendicular to each other ($p_T \gg p_L$): G depends on the frame.

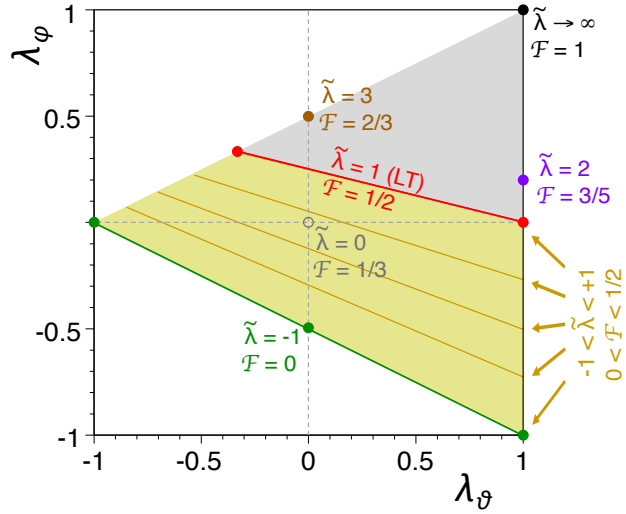

Fig. 5.6 Map of the values of $\tilde{\lambda}$ and $\mathcal{F}$, in the λ_φ vs. λ_ϑ plane. The values are completely independent of the experimental polarization frame.

events with two or more "jets" and that the population of events is concentrated towards low p_T, where the effect is progressively smaller, we can state that the overall fraction f_{NP} of events responsible for the observed violation of the Lam–Tung relation is relatively small (at the percent level). Interestingly, a Monte Carlo simulation

of the relevant non-planar topologies can potentially provide an estimate of $\langle \sin^2 \hat{\phi} \rangle$ as a function of, for example, p_T and translate the polarization measurement into a measurement of f_{NP}, that is, of how many Z bosons are produced together with two or more jets. As an accompanying check, the rejection/selection of events with higher jet multiplicity should reduce/enhance the violation of the Lam–Tung relation, leading to correspondingly smaller/larger f_{NP} values.

In the example just considered, the use of the invariant polarization allows us to recognize, in a rather straightforward way, that we are observing phenomena representing only a higher-order correction to the basic theoretical description. We can wonder if a similar explanation is compatible with other known cases of violation of the Lam–Tung relation. Drell–Yan production in pion-nucleus collisions is one such case.

Particularly significant effects were evidenced by the E615 experiment [8], using 252 GeV pions colliding on a tungsten target to study muon pairs in the invariant mass range $4.05 < m < 8.55$ GeV. Results obtained by NA10 [9] and, very recently, by COMPASS [10] are, at least qualitatively, very similar and the following discussion can also be applied to them with analogous conclusions.

Figure 5.7 shows the E615 p_T-dependent measurements of the anisotropy parameters λ_ϑ $(= \lambda)$ and λ_φ $(= \nu/2)$, as well as the combination $G = \lambda + 2\nu - 1$, which was used in the E615 publication to express the violation. The results were provided in the CS frame and also in the equivalent of what, in this book, we call the GJ1 and GJ2 frames; given the rather low p_T/m ratio of the muon pairs ($p_T < 3$ GeV), the geometrical difference between the three frames is not sufficiently large to be interesting (see Table 2.1) and here we will only consider the CS results, practically representing the average of the other two, which are indeed very similar. The values of $\mathcal{F}$ and $\tilde{\lambda}$, which we derived, are also shown.

At first sight, we could think that we are viewing a rather conventional transverse polarization scenario ($\lambda \simeq 1$), as expected for Drell–Yan production, while the definite increase of ν with increasing p_T may seem analogous to that of A_2, seen in the bottom panels of Fig. 5.2. At the same time, the Lam–Tung relation $\lambda + 2\nu - 1 = 0$ is increasingly violated with increasing p_T, a result qualitatively similar to the progressive deviation of $A_0 - A_2$ from zero.

However, a look at $\mathcal{F}$ (and $\tilde{\lambda}$) reveals that we are seeing a completely different kind of effect, both qualitatively and quantitatively. First, $\mathcal{F}$ *increases* monotonically above the low-p_T value $1/2$, corresponding to the Lam–Tung relation: this is the opposite behaviour with respect to the LHC observation of a *reduction* in the observable Z polarization, indicated by $\mathcal{F} < 1/2$ (and $\tilde{\lambda} < +1$). The value of $\mathcal{F}$ seems to even approach the maximum physical value, 1, in its increasing trend. As seen in Section 3.3, this limit corresponds to the rather uncommon angular momentum state represented by a pure $J_y = 0$ projection on the axis perpendicular to the production plane. Equivalently, it can be interpreted as the coherent superposition $\frac{1}{\sqrt{2}} |1, +1\rangle + \frac{1}{\sqrt{2}} |1, -1\rangle$ of $J_z = +1$ and $J_z = -1$ states ($a_{+1} = a_{-1} = 1/\sqrt{2}$ in Eq. 1.13). An alternative way to appreciate the peculiarity of the result is to consider that all data points have $\tilde{\lambda} > +1$. This means that the angular distribution is *never* the superposition of n elementary distributions of the kind $1 + \lambda_0^{(i)} \cos^2 \vartheta$

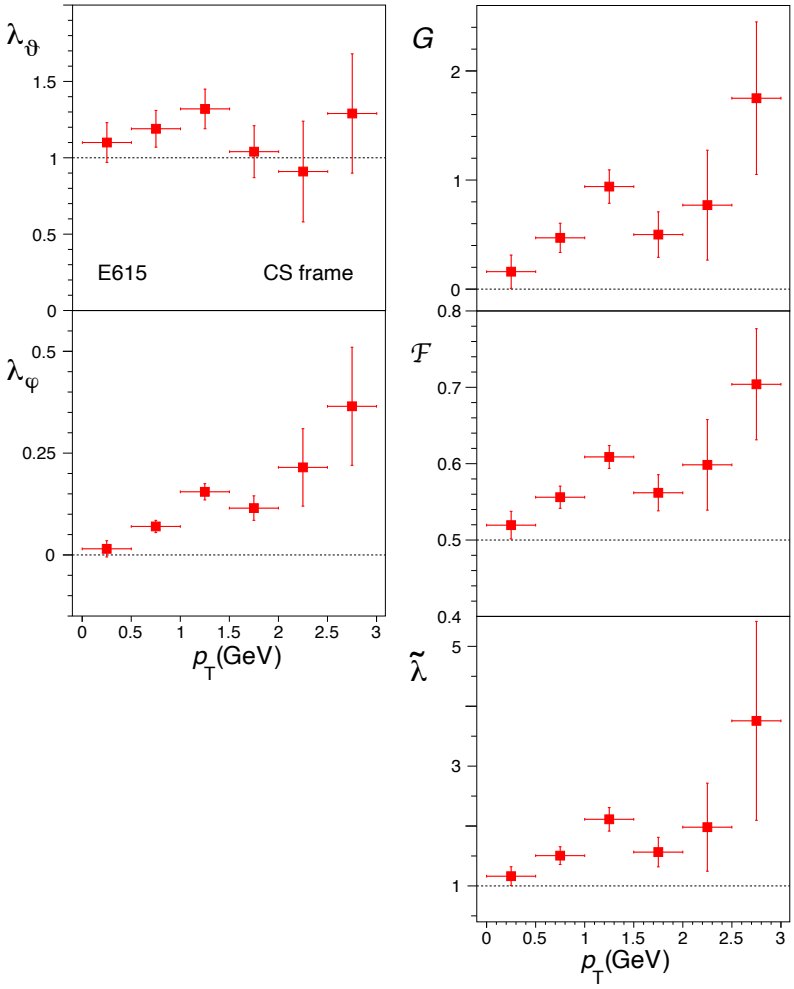

Fig. 5.7 The E615 measurements [8] of the Drell–Yan angular distribution parameters λ_ϑ (= λ) and λ_φ (= $\nu/2$), on the left, and the combinations $G = \lambda + 2\nu - 1$, $\mathcal{F}$ and $\tilde{\lambda}$, on the right, as functions of p_T, in the CS frame. The average $\lambda_\vartheta \sim 1$ and $\lambda_\varphi \sim 0.2$ values correspond to the purple point in Figs. 5.5 and 5.6.

(with $|\lambda_0^{(i)}| \leq +1$), which would imply, according to Eq. 4.5, that $|\tilde{\lambda}| \leq 1$: part of the contributing processes produce states that, instead of having simple "natural" polarizations, are coherent superpositions of states, with *intrinsic* azimuthal anisotropies (not eliminable by rotation).

Several theoretical speculations exist [11–14] about the nature of the processes determining this puzzling "anomaly", and simply adding $\mathcal{F}$ to the tools does not solve the mystery. Nevertheless, using $\mathcal{F}$ we easily find that such processes are very different from the non-planar but always fully *transverse* ones leading to the

smeared Z polarization observed at the LHC: in this case we are seeing contributions of events where the dilepton pairs are *longitudinally* polarized. This is an example of how, when the violation is expressed as $\mathcal{F} - 1/2 \neq 0$, its sign provides an immediate qualification of the possible physics processes responsible for the violation.

Furthermore, it becomes possible to quantify *how much* the "anomalous" processes contribute to the observed yield and also in this respect the two considered examples differ significantly. We saw that the maximum violation observed as a function of p_{T} in the Z case is around 5%, $\mathcal{F} - 1/2 \simeq 0.025$. It is definitely larger in the Drell–Yan data: the most significant deviation, $\mathcal{F} - 1/2 = 0.109 \pm 0.015$ (for the p_{T} range from 1 to 1.5 GeV), allows us to deduce, using the relation $\mathcal{F} = f_{\mathrm{anom}} \times 1 + (1 - f_{\mathrm{anom}}) \times 1/2$, that the fraction f_{anom} of dilepton events violating the condition $\mathcal{F} = 1/2$ is *at least* as large as 0.22 ± 0.03. Considering the highest-p_{T} point, the minimum fraction is $f_{\mathrm{anom}} = 0.40 \pm 0.15$.

These should already be considered very large contributions to the Drell–Yan production yield, certainly not "perturbations". However, the real values of such fractions must be even larger, because the deduced lower limit corresponds to an extreme hypothesis: $\mathcal{F}$ is always either $1/2$, in the case of standard $O(\alpha_s^0)$ and $O(\alpha_s^1)$ processes, or 1, in the case of the anomalous processes violating the Lam–Tung relation. In reality, the anomalous processes can very well have $\mathcal{F}$ values smaller than the $\mathcal{F} = 1$ extreme limit. Allowing for these more realistic conditions, we can say that, in order to reproduce the E615 measurement, the fraction of Drell–Yan dileptons produced by the anomalous processes needs to be *comparable* to the contribution of the standard processes. A "perturbative" interpretation of the phenomenon is, therefore, ruled out.

In summary, the frame-independent polarization $\mathcal{F}$ (or any of its variants) allows us to write a generalization of the Lam–Tung identity, in the form

$$\mathcal{F} - 1/2 = \epsilon\,. \tag{5.15}$$

Unlike $\lambda + 2\nu - 1$, this expression remains always frame-independent, that is, the violation amount ϵ is a rotation-invariant quantity, "homogeneous" to a fractional particle yield, and can, therefore, be used to estimate the magnitude of the violation.

In other words, thanks to the information it contains on both sign and magnitude of the violation, the measurement of $\mathcal{F}$ (or $\tilde{\lambda}$) in studies of the production of vector particles can be used as a discriminant of physics cases [5].

1. A value of $\mathcal{F}$ compatible with $1/2$ (or of $\tilde{\lambda}$ compatible with $+1$) means that we are not observing any deviation from the most basic picture of vector boson production. The Lam–Tung relation is satisfied: the underlying processes involve helicity-conserving couplings between light quarks and vector bosons in planar processes, as foreseen at QED and leading-order QCD levels and in several higher-order QCD contributions.
2. If ϵ is small and negative ($\mathcal{F}$ and $\tilde{\lambda}$ slightly smaller than, respectively, $1/2$ and $+1$), effectively requiring a rather precise measurement for its detection, *and* vanishes in the limit $p_{\mathrm{T}} \to 0$, as is the case of the Z measurements at the LHC, we are most probably in the presence of the same, "ordinary" couplings between vector

bosons and quark pairs as mentioned above, but with higher-order contributions containing non-planar processes.
Since non-planar processes correspond, for example in the case of Z production, to the presence of more than one jet in the final state, the measurement of $\mathcal{F} - 1/2$ can provide an estimate of the average jet multiplicity in the considered data sample.
We can include in this category also another kind of phenomenon, equally involving a deviation from the planarity of the process topology, which is the smearing of the observable polarization due to the transverse motion of the colliding partons. As discussed in the next section, this effect becomes significant for states having mass comparable to 1 GeV.

3. Values of $\mathcal{F}$ significantly smaller than $1/2$ (but always positive), or remaining (even slightly) smaller than $1/2$ in the $p_{\mathrm{T}} \to 0$ limit, indicate a significant deviation from the scenario where vector bosons are produced in the coupling with light quarks and have, therefore, natural transverse polarizations. Completely different production mechanisms have to be expected, where longitudinal contributions coexist with transverse ones or dominate. This is, at least conceptually, a large category of scenarios, including practically all cases where, for a variety of reasons, the decaying particle tends to be produced with natural angular momentum projections that include the $J_z = 0$ case as a significant component.
One example is the production of a Z boson pair in the decay of a Higgs boson. The intermediate Higgs, which couples directly to the vector bosons, cuts all links with light-quark helicity fluxes and eliminates the raison d'être of a preferred intrinsic transverse polarization of the observed Z bosons. For analogous reasons, also the polarization of W bosons produced from the decays of top quarks is far from being fully transverse. More generally, vector bosons produced indirectly, as products of the decay of another particle, can in principle have a wide range of polarizations, depending on the production mechanism of the mother particle. This is, for example, the case of J/ψ mesons coming from decays of χ_{c1} and χ_{c2} mesons, which we will encounter in Section 6.6. Further examples will be the subject of Sections 6.1–6.4, discussing extreme smearing effects that can even result in the observation of a seemingly unpolarized production scenario ($\mathcal{F} \simeq 1/3$).
4. The last physical category that we consider includes more exotic mechanisms, which lead to $\mathcal{F}$ larger than $1/2$ and $\tilde{\lambda}$ larger than $+1$, up to even extremely large values (given that $\tilde{\lambda}$ is not bound by an upper limit).
The pion-nucleus Drell–Yan data provide an example (possibly the only one existing so far) seemingly pointing to a significant contribution of processes creating a longitudinal polarization along the axis perpendicular to the production plane, a rather unexpected phenomenon with no clear and intuitive explanation.
5. Finally, measured values significantly trespassing the limits of the physical domains, $0 \leq \mathcal{F} \leq 1$ and $\tilde{\lambda} \geq -1$, indicate a mistake in the analysis or calculation. Similarly, as discussed in Section 3.12, if the invariant parameter is found to be different in, for example, the HX and CS frames, we know with certainty that something went wrong in the analysis or computation procedure.

5.4 Effects of the parton transverse momentum

We saw in Section 4.3 how the longitudinal motion of the system of colliding partons in the proton-proton centre-of-mass frame influences the outcome of polarization measurements for vector states produced in *s*-channel processes, where the direction of the quantization axis is naturally referred to the unobserved parton-parton system, rather than to the proton-proton one.

We will now discuss how also the *transverse* component of the parton motion inside the colliding hadrons has an effect on the observable polarization. The effect is relevant in measurements performed at low p_T and small x_F (or rapidity), that is, when the momentum of the decaying particle is not significantly larger than the intrinsic transverse momenta of the partons. For the same reason, it is more important in the production of relatively light particles.

For particles produced with p_T comparable to (or smaller than) the transverse momenta of the scattering partons, k_T, the natural polarization axis is, most often, represented by the relative direction of the partons themselves. This is the case, for example, of the leading order process for Drell–Yan production (Fig. 2.2-c) and, more generally, of any $2 \to 1$ process.

Moreover, even in the presence of a recoil particle conferring an "extrinsic" transverse momentum component to the observed decaying particle ($2 \to 2$ processes and beyond), different natural polarization directions always converge to the parton-parton scattering direction if that extrinsic component is negligible with respect to the k_T value.

It is also important to remark that, at least for the scope of the present discussion, we should not restrict the meaning of k_T to the bare intrinsic momentum that the partons have for being confined inside a hadron of finite dimensions ($\Delta p \approx 1$ fm$^{-1} \approx$ 200 MeV). Doing so, we would be considering k_T values that are clearly too small to account for the p_T spectra typically measured in fixed-target experiments. For instance, the J/ψ mesons produced in proton-nucleus collisions with proton beam energies between 400 and 920 GeV have average p_T squared, $\langle p_T^2 \rangle$, in the range 1.6–2.5 GeV^2, depending on the collision energy and on the mass number of the target nucleus, as shown in Fig. 5.8.

In fact, during the scattering process the intrinsic momentum component is effectively augmented by other effects, ranging from more or less soft gluon emissions to the multiple scattering of the incoming proton inside the nuclear target ("p_T broadening"). In our illustrations we will assume that, thanks to extra sources of transverse momentum kick, the parton average k_T squared reaches a magnitude of order 1 GeV^2, compatible with the measured p_T distribution, given that $\langle p_T^2 \rangle \simeq 2 \langle k_T^2 \rangle$, with no need of a significant "extrinsic" recoil component.

While in all examples considered until here we have always identified the direction of the scattering partons with the one of the colliding protons, that is, with the CS axis as experimentally definable using the beam momenta, we are now going to study possible effects of this approximation.

In the laboratory frame (centre of mass of the colliding hadrons) the angle Ω between the two directions is given by

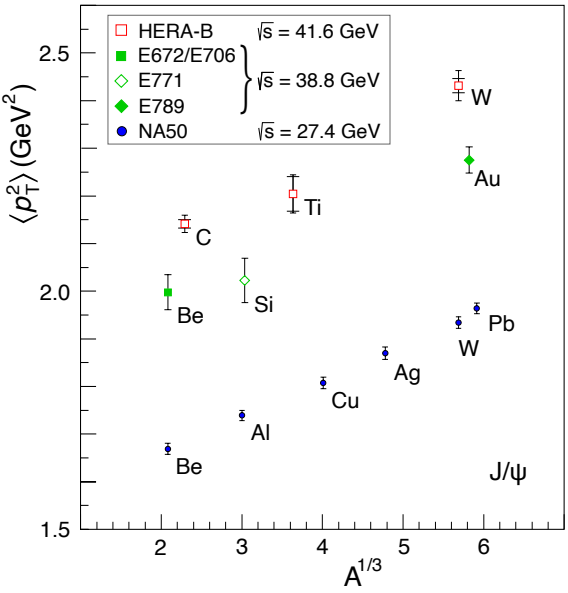

Fig. 5.8 The J/ψ average p_T squared, $\langle p_T^2 \rangle$, measured in proton-nucleus collisions at three beam energies, 400 GeV [15], 800 GeV [16], and 920 GeV [17], as a function of the cubic root of the mass number of the target nucleus [18].

$$\sin^2 \Omega \;=\; \frac{(\mathbf{k}_{1T} - \mathbf{k}_{2T})^2}{(\mathbf{k}_1 - \mathbf{k}_2)^2}\,, \tag{5.16}$$

where $\mathbf{k}_1$, $\mathbf{k}_2$, $\mathbf{k}_{1T}$, and $\mathbf{k}_{2T}$ are the partons' momentum and transverse momentum vectors. When the production is dominated by $2 \to 1$ processes, $(\mathbf{k}_{1T} + \mathbf{k}_{2T})^2 \simeq p_T^2$, so that $(\mathbf{k}_{1T} - \mathbf{k}_{2T})^2 = 2\,(k_{1T}^2 + k_{2T}^2) - p_T^2$. Moreover, assuming the approximation that the partons collide on average with antiparallel directions, the denominator becomes $(\mathbf{k}_1 - \mathbf{k}_2)^2 \simeq E^2$, where E is the total energy of the studied particle. The average over the transverse momentum component, with $\langle k_{T1}^2 \rangle = \langle k_{T2}^2 \rangle \simeq \frac{1}{2}\langle p_T^2 \rangle$, leads to the approximate relation

$$\langle \sin^2 \Omega \rangle \;\simeq\; \frac{2\,\langle k_T^2 \rangle}{m^2 + p_L^2 + 2\,\langle k_T^2 \rangle}\,, \tag{5.17}$$

where m and $p_L = \frac{\sqrt{s}}{2}\, x_F$ are the mass and longitudinal momentum of the particle.

This expression, with its inherent simplifications, is only meant to show that the parton and proton directions are seen as effectively coinciding ($\sin^2 \Omega \simeq 0$) when we study the production of a particle having m^2 much larger than $\langle k_T^2 \rangle$. The angle Ω is, however, not yet the relevant angle between the "parton-parton CS axis" (in the following denoted by pCS) and the usual proton-proton axis, which has to be determined in the rest frame of the decaying particle. The boost to the particle's rest

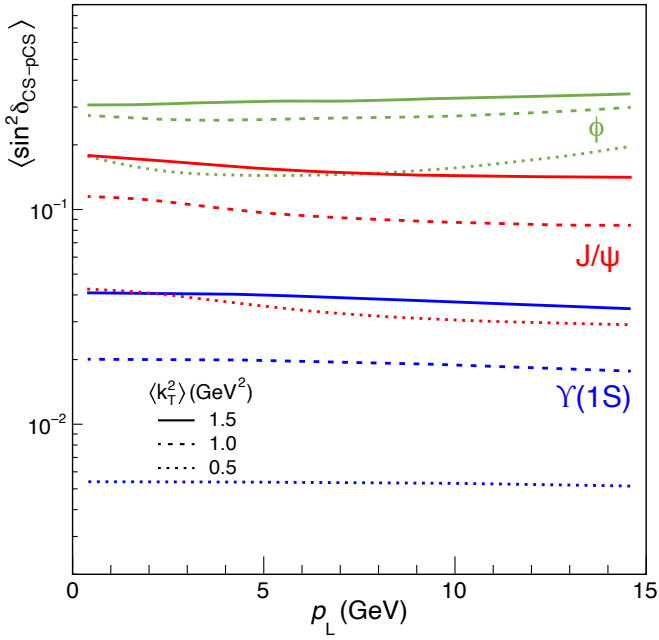

Fig. 5.9 The p_{T}-averaged angle between the CS and pCS axes, $\langle \sin^2 \delta_{\mathrm{CS-pCS}} \rangle$, as a function of p_{L}, for the $\phi(1020)$, J/ψ, and Υ(1S) mesons, and three assumed values of $\langle k_{\mathrm{T}}^2 \rangle$.

frame attenuates considerably the dependence on p_{L} seen in the above equations. The boost effect does not only depend on the longitudinal and transverse parton momentum components, but also on their azimuthal angles. To determine the angle $\delta_{\mathrm{CS-pCS}}$ between the CS and pCS axes, we used, therefore, a toy Monte Carlo (MC) model, generating, for given m and p_{L} values, the vectors $\mathbf{k}_{1\mathrm{T}}$ and $\mathbf{k}_{2\mathrm{T}}$ with moduli $k_{1\mathrm{T}}$ and $k_{2\mathrm{T}}$ following a Gaussian distribution of variance $\langle k_{\mathrm{T}}^2 \rangle$ and azimuthal angles ϕ_1 and ϕ_2 distributed uniformly.

The results for the relevant average angular quantity, $\langle \sin^2 \delta_{\mathrm{CS-pCS}} \rangle$, are shown in Fig. 5.9, which illustrates the dependences on its three ingredients: the mass, for the cases of the $\phi(1020)$, J/ψ, and Υ(1S) mesons, the average k_{T}^2, for which we have selected the values 0.5, 1, and 1.5 GeV^2, and the longitudinal momentum, shown on the horizontal axis.

The quantity $\langle \sin^2 \delta_{\mathrm{CS-pCS}} \rangle$ determines how the polar anisotropy λ_ϑ of the dilepton decay distribution is modified by a change of polarization axis from the pCS (natural) frame to the CS (observation) frame As seen in the first relation of Eq. 5.5, even if the transformation is not a rotation in the production plane (around the y axis), the natural polarization ($\lambda_\vartheta^{\mathrm{pCS}} \equiv \lambda_0$ with no azimuthal anisotropies) transforms always in the same way for a given angular displacement towards any spatial direction (indicated there by the angle ζ, here by $\delta_{\mathrm{CS-pCS}}$). In this case, $\lambda_\vartheta^{\mathrm{CS}} = \lambda_\vartheta^{\mathrm{pCS}} \left(1 - \frac{3}{2} \sin^2 \delta_{\mathrm{CS-pCS}}\right) \Big/ \left(1 + \frac{1}{2} \lambda_\vartheta^{\mathrm{pCS}} \sin^2 \delta_{\mathrm{CS-pCS}}\right)$, which, for small values of

$\langle \sin^2\delta_{\mathrm{CS-pCS}}\rangle$, can be written as

$$\lambda_\vartheta^{\mathrm{CS}} \simeq \left(1 - \frac{3+\lambda_\vartheta^{\mathrm{pCS}}}{2}\,\langle \sin^2\delta_{\mathrm{CS-pCS}}\rangle\right)\lambda_\vartheta^{\mathrm{pCS}}. \tag{5.18}$$

This means that $\langle \sin^2\delta_{\mathrm{CS-pCS}}\rangle$ equals the relative decrease of the observed λ_ϑ magnitude with respect to a natural longitudinal polarization, while a natural transverse polarization decreases twice as much. The effect can be quite large in the study of low-p_{T} $\phi(1020)$ production, where, for $\langle k_{\mathrm{T}}^2\rangle = 1$ GeV^2, fully longitudinal and transverse polarizations would be seen as $\lambda_\vartheta^{\mathrm{CS}} \simeq -0.7$ and $+0.5$, respectively.

In existing low-p_{T} measurements for the heavier J/ψ and Υ states, subtler effects are expected. Figures 5.10 and 5.11 show measurements by the HERA-B [20] and E866 [19] experiments, in fixed-target proton-nucleus collisions with beam energies of, respectively, 920 and 800 GeV ($\sqrt{s} = 41.6$ and 38.8 GeV) and $0 < p_{\mathrm{T}} \lesssim 4$ GeV. The polarization parameters are shown as a function of x_{F}, averaged over p_{T}. The HERA-B results, for J/ψ, were reported in three polarization frames, CS, GJ and HX, and for the three polarization parameters. The hierarchy of λ_ϑ values, with the largest magnitude measured in the CS frame and the smallest one in the HX frame, confirms that the natural quantization axis is closest to the CS frame.

As shown by the curves, obtained with the toy MC for $\langle k_{\mathrm{T}}^2\rangle = 1\,\mathrm{GeV}^2$, the assumption of a natural polarization $\lambda_\vartheta^{\mathrm{pCS}} = -0.3$, independent of x_{F}, along the parton-parton direction (black curve) describes reasonably well the patterns observed in the three experimental frames for λ_ϑ, λ_φ and $\lambda_{\vartheta\varphi}$. The MC model shows that, as a consequence of the parton k_{T} effect, the magnitude of the maximum observed λ_ϑ, in the CS frame, is reduced by about 15% with respect to the natural value. The invariant parameter $\tilde{\lambda}$ (grey curve) is only slightly closer to the natural value, reflecting the

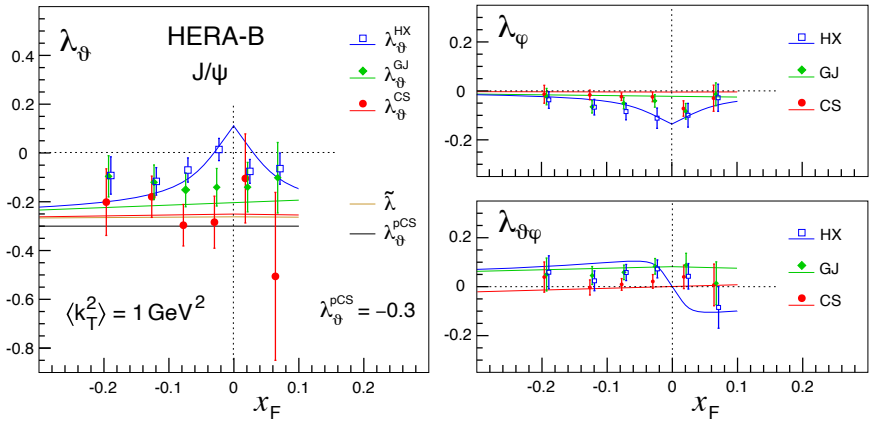

Fig. 5.10 J/ψ polarization parameters, λ_ϑ, λ_φ, and $\lambda_{\vartheta\varphi}$, measured by the HERA-B experiment and calculated in the k_{T}-smearing model described in the text, shown as functions of x_{F}, averaged over the $p_{\mathrm{T}} < 4$ GeV range.

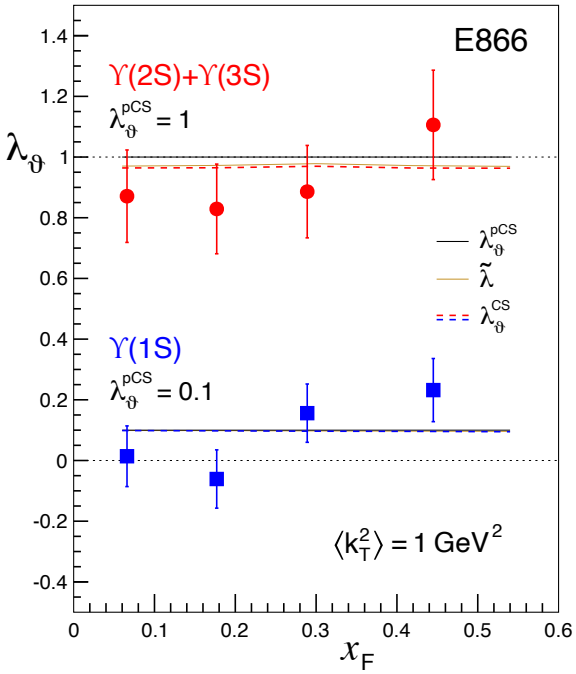

Fig. 5.11 Υ(1S) and Υ(2S)+Υ(3S) polarization parameters measured by the E866 experiment [19] and calculated in the k_T-smearing model described in the text, shown as functions of x_F, averaged over p_T within the 0–4 GeV range.

fact that the transformation from the pCS frame to the CS frame is not a simple rotation: while the magnitude of the polar anisotropy decreases as in an ordinary rotation, the correspondingly arising azimuthal anisotropy does not fully compensate for such decrease. In fact, the rotation plane (formed by the parton-parton and proton-nucleon relative momentum directions) does not coincide with the experimentally defined production plane. The angle between the two planes changes from one event to the next, so that the azimuthal anisotropy deriving from the tilt between the "natural" polarization axis and the experimental axis tends to be smeared out in the integration over all events.

The almost maximal polarization observed by E866 for the Υ(2S) and Υ(3S) states (not distinguished experimentally) in the CS frame is a further confirmation that quarkonia produced at low p_T are naturally polarized along the direction of the colliding objects. As shown by the MC model results, assuming a natural polarization $\lambda_\vartheta^{pCS} = +1$, the k_T-smearing effect is very small in this case, because of the large mass of the produced particle. The effect becomes undetectable for smaller polarizations like the one measured for the Υ(1S) state, for which a natural value of $\lambda_\vartheta^{pCS} = +0.1$ was assumed.

The reader may rightfully be puzzled by the very different natural polarizations that have to be assumed to describe the results in the three cases (J/ψ, Υ(1S), and

Υ(2S+3S)), a scenario that seemingly contradicts a very reasonable expectation: all S-wave quarkonia should have similar production mechanisms. A possible interpretation of these differences is given in Ref. [21], where it is argued that these measurements are compatible with being the reflection of the interplay between the same basic $q\bar{q}$ and gg production mechanisms, with the Drell–Yan-like (transversely polarized) $q\bar{q}$ annihilation process becoming increasingly important at larger mass and $|x_F|$ values. At the same time, indirect production via decays from χ_b states may be prevalent over direct production processes in the Υ(1S) case, and the two mechanisms lead, in general, to very different polarizations.

Before wrapping up this chapter, we will add a comment regarding a misconception sometimes found in publications reporting measurements of the forward-backward asymmetries in the angular distributions of Drell–Yan dileptons of very high masses (similar to or larger than the mass of the Z boson). The message has been conveyed through some form of the following phrasing: "when the dilepton has non-vanishing p_T, the momentum of the incoming quark or antiquark is not known, because it is no longer collinear with the incoming beams; the CS frame is chosen for the angular analysis, to minimize the impact of this effect on the asymmetry measurement". A more concise version is "this measurement uses the CS frame to minimize uncertainties caused by the unknown transverse momenta of the incoming quarks".

As can be deduced from the comparison between the cases considered in this section, the effect of the intrinsic parton momentum becomes completely negligible in studies of the angular distributions of dileptons of a sufficiently high mass, and even a mass as low as 10 GeV (the Υ(1S) mass) is already large enough. In fact, for $p_T > 0$ the *beams* themselves are not collinear in the dilepton rest frame, and this should be the reason why the CS frame might be considered as a suitable choice, being more "democratic" than selecting one of the two GJ frames, as the latter option could be seen as an arbitrary selection of one of the two beams (having said that, one might even consider more interesting to try matching the incoming quark, antiquark or gluon with its beam of origin, on a statistical basis, by exploiting events in the higher-rapidity domain, as mentioned in Section 2.2).

Nevertheless, the lack of collinearity between parton and proton momenta, caused by the intrinsic transverse momentum, does not induce any "uncertainty" or "effect" in the analysis, for measurements at such high mass values: if the partons had zero k_T, the result would remain identical. Furthermore, even for low mass dileptons the importance of the effect on the observable angular distribution is the same in any chosen frame and there is no experimentally-definable frame (using only the dilepton information) that is less sensitive to the parton-proton non-collinearity (or to any other observable physics effect). Actually, a measurement of the polar anisotropy (or of the polar projection of the parity asymmetry) in the CS frame would even be the one showing with maximum sensitivity the difference between two hypothetical scenarios, where the parton k_T effects either exist or are absent, in the very low p_T domain, where $2 \to 1$ processes dominate, given that only the CS frame is directly comparable to the natural partonic frame (pCS), as seen in the HERA-B example. In the HX frame, for example, the effect would be distributed

between the polar and azimuthal anisotropies, so that it would seem milder in analyses that only consider the polar dimension. Moreover, at not-too-low p_T it is the HX frame (or, even better, the PX frame) that best approximates the natural frame, as shown in Fig. 4.12 (based on LHC data) for the parity conserving parameter λ_ϑ (or A_0); similar hierarchies are expected for the forward-backward asymmetries.

As already emphasized several times in this book, a better approach would be to perform the measurement in more than one reference frame, a procedure that is particularly important in analyses that ignore the azimuthal dimension. Still, the ultimate method to obtain the most information from the data, independently of the frame choice, is to perform a two-dimensional analysis, considering both projections of the parity-violating asymmetry, A_ϑ and A_φ, as well as their combination into the quasi-invariant $\mathcal{A}^\star$.

5.5 Recapitulation

When the production process transcends the planar topology of the basic $2 \to 1$ and $2 \to 2$ mechanisms, the natural polarization axis no longer always belongs to the production plane. Its angle with respect to the experimental polarization axis (which always stays in the production plane) changes, in general, from one event to another and is not experimentally determinable in an inclusive measurement. Therefore, a *smeared* version of the natural polarization is observed.

Also the invariant polarization parameter loses, at least in part, sensitivity to the true magnitude of the polarization, because the transformation from natural to experimental frame is not a rotation around the y axis (perpendicular to the production plane).

One interesting example of this effect is the contribution of nonplanar processes to Drell–Yan, W and Z production, as described for example by the diagrams in the last row of Fig. 5.1. While the natural polarization remains fully transverse because of helicity conservation, it is never seen as such in any of the experimental frames, because of the relative tilt between natural and observation axis and the rotational smearing of the resulting azimuthal anisotropy.

As described by Eq. 5.5, the tilt (by an angle ζ) reduces λ_ϑ just as in a transformation between two experimental frames. On the other hand, the azimuthal anisotropy parameters λ_φ, $\lambda_{\vartheta\varphi}$, etc., depend on a further rotation angle (ω), which is zero on average but not in individual events, with the result that their observed magnitudes are smaller than in a conventional frame rotation within the production plane. Therefore, $\mathcal{F} < 1/2$, or $\tilde{\lambda} < +1$, and the Lam–Tung identity is violated.

This phenomenon has been observed in ATLAS and CMS measurements of inclusive Z production: while the polar anisotropy (A_0) can be described well with the same polarization composition rules suitable for planar processes, as was seen in Fig. 4.11, the azimuthal parameters (A_1 and A_2) calculated in that way overestimate the measured ones significantly, as shown in Figs. 5.2 and 5.4.

The resulting violation of the Lam–Tung relation (Eq. 5.4), absent at $p_T = 0$ and increasing with p_T (Fig. 5.2) in the direction corresponding to a decreasing observable polarization magnitude ($A_0 - A_2 > 0$, that is, $\mathcal{F} < 1/2$, Eq. 5.3, or $\tilde{\lambda} < 1$), is qualitatively consistent with the progressive contribution of higher-order processes with two or more accompanying particles (or "jets").

The frame-independent polarization parameter $\mathcal{F}$ (or $\tilde{\lambda}$) allows us to recognize not only the qualitative features of the phenomenon, but also its magnitude. In fact, the relative deviation of $\mathcal{F}$ from $1/2$ is at most 5% according to the Z data, being consistent with a higher-order effect. More precisely, it equals $f_{NP} \langle \sin^2 \hat{\phi} \rangle$, where f_{NP} is the fraction of events due to non-planar processes and $\hat{\phi}$ the tilt angle of the natural axis with respect to the production plane. Through a simulation of the non-planar topologies, providing an estimate of $\langle \sin^2 \hat{\phi} \rangle$, it is possible to determine f_{NP} and, therefore, the contribution of events where the Z boson is accompanied by more than one jet.

More generally, the invariant polarization parameter allows us to replace the Lam–Tung relation with a family of relations, becoming a discriminant of physics cases for the production of vector particles (Section 5.3). For example, violations of the Lam–Tung relation observed in fixed-target pion-induced collisions lead to $\mathcal{F}$ values significantly exceeding $1/2$, indicating that the phenomenon observed in that case has a different physical origin, involving non-transverse natural polarizations, and that the "anomalous" effect is quantitatively much more important than a higher-order correction.

The intrinsic transverse parton momentum, k_T, of the partons inside the colliding hadrons is another common cause producing a "tilt" of the natural polarization axis along a direction not contained in the production plane and changing event after event. The expected result is, also in this case, a *reduction* of the observed polarization magnitude, that is, in the Drell–Yan case, $\mathcal{F} < 1/2$ or $\tilde{\lambda} < 1$. However, the effect is important only when the mass of the produced particle is comparable to the magnitude of k_T: it will, for example, smear significantly the polarization of $\phi(1020)$ mesons, for which the angle between the proton-proton and the parton-parton CS axes is large on average (Fig. 5.9), but it should be small in the above-mentioned Drell–Yan measurements ($m_{\mu^+\mu^-} > 4$ GeV) as well as in more recent measurements of COMPASS and other fixed-target experiments. Already for J/ψ production the expected effects are subtle and would require high-precision measurements to become significant in the interpretation of the data, as shown by the comparison to the HERA-B measurement in Fig. 5.10.

References

[1] CMS Collaboration, "Angular coefficients of Z bosons produced in pp collisions at $\sqrt{s} = 8$ TeV and decaying to $\mu^+\mu^-$ as a function of transverse momentum and rapidity", *Phys. Lett. B* **750** (2015) 154, doi:10.1016/j.physletb.2015.08.061, arXiv:1504.03512.

[2] ATLAS Collaboration, "Measurement of the angular coefficients in Z-boson events using electron and muon pairs from data taken at $\sqrt{s} = 8$ TeV with the ATLAS detector", *JHEP* **08** (2016) 159, doi:10.1007/JHEP08(2016)159, arXiv:1606.00689.

[3] P. Faccioli, C. Lourenço, and J. Seixas, "Rotation-invariant relations in vector meson decays into fermion pairs", *Phys. Rev. Lett.* **105** (2010) 061601, doi:10.1103/PhysRevLett.105.061601, arXiv:1005.2601.

[4] P. Faccioli, C. Lourenço, J. Seixas, and H. K. Wöhri, "Model-independent constraints on the shape parameters of dilepton angular distributions", *Phys. Rev. D* **83** (2011) 056008, doi:10.1103/PhysRevD.83.056008, arXiv:1102.3946.

[5] P. Faccioli, "Angular momentum and decay distributions in high energy physics: an introduction and use cases for the LHC", in *"HEPHY-SMI Seminar", HEPHY, Vienna, April 18th, 2013,* and *"CERN EP Seminar", CERN, Geneva, April 23rd, 2013*. https://indico.cern.ch/event/246009/.

[6] Y. Lyu et al., "Lepton angular distribution of W boson productions", *Phys. Rev. D* **103** (2021) 034011, doi:10.1103/PhysRevD.103.034011, arXiv:2010.01826.

[7] W.-C. Chang, R. E. McClellan, J.-C. Peng, and O. Teryaev, "QCD effects in lepton angular distributions of Drell–Yan/Z production and jet discrimination", *PoS* **ICHEP2020** (2021) 465, doi:10.22323/1.390.0465, arXiv:2101.11160.

[8] E615 Collaboration, "Experimental study of muon pairs produced by 252 GeV pions on tungsten", *Phys. Rev. D* **39** (1989) 92, doi:10.1103/PhysRevD.39.92.

[9] NA10 Collaboration, "Angular distributions of muon pairs produced by negative pions on deuterium and tungsten", *Z. Phys. C* **37** (1988) 545, doi:10.1007/BF01549713.

[10] COMPASS Collaboration, "Measurement of target spin (in)dependent asymmetries in dimuon production in pion-nucleon collisions at COMPASS", in *"XXVIII Int. Workshop on Deep-Inelastic Scattering and Related Subjects", Stony Brook Univ., New York, USA, 12–16 April 2021*. https://indico.bnl.gov/event/9726/contributions/46025/.

[11] E. L. Berger and S. J. Brodsky, "Quark structure functions of mesons and the Drell–Yan process", *Phys. Rev. Lett.* **42** (1979) 940, doi:10.1103/PhysRevLett.42.940.

[12] E. L. Berger, "Quark structure functions of mesons, fragmentation functions, higher twist effects in QCD, Deep Inelastic Scattering, and the Drell–Yan process", *Z. Phys. C* **4** (1980) 289, doi:10.1007/BF01421570.

[13] A. Brandenburg, S. J. Brodsky, V. V. Khoze, and D. Müller, "Angular distributions in the Drell–Yan process: a closer look at higher twist effects", *Phys. Rev. Lett.* **73** (1994) 939, doi:10.1103/PhysRevLett.73.939, arXiv:hep-ph/9403361.

[14] K. J. Eskola, P. Hoyer, M. Vanttinen, and R. Vogt, "Higher twist effects in the Drell–Yan angular distribution", *Phys. Lett. B* **333** (1994) 526, doi:10.1016/0370-2693(94)90178-3, arXiv:hep-ph/9404322.

[15] NA50 Collaboration, "Quarkonium production and suppression in Pb-Pb and p-A collisions at SPS energies", *Nucl. Phys. A* **774** (2006) 59, doi:10.1016/j.nuclphysa.2006.06.029.

[16] NuSea Collaboration, "Measurement of J/ψ and ψ(2S) suppression in p-A collisions at 800 GeV", *Phys. Rev. Lett.* **84** (2000) 3256, doi:10.1103/PhysRevLett.84.3256, arXiv:nucl-ex/9909007.

[17] HERA-B Collaboration, "Kinematic distributions and nuclear effects of J/ψ production in 920 GeV fixed-target proton-nucleus collisions", *Eur. Phys. J. C* **60** (2009) 525, doi:10.1140/epjc/s10052-009-0965-7, arXiv:0812.0734.

[18] C. Lourenço, "Open questions in quarkonium and electromagnetic probes", *Nucl. Phys. A* **783** (2007) 451, doi:10.1016/j.nuclphysa.2006.11.096, arXiv:nucl-ex/0612014.

[19] E866 Collaboration, "Observation of polarization in bottomonium production at $\sqrt{s}$ = 38.8 GeV", *Phys. Rev. Lett.* **86** (2001) 2529, doi:10.1103/PhysRevLett.86.2529, arXiv:hep-ex/0011030.

[20] HERA-B Collaboration, "Angular distributions of leptons from J/ψ's produced in 920 GeV fixed-target proton-nucleus collisions", *Eur. Phys. J. C* **60** (2009) 517, doi:10.1140/epjc/s10052-009-0957-7, arXiv:0901.1015.

[21] P. Faccioli, "Charmonium polarization in pp collisions", in *Workshop "Gluon content of proton and deuteron with the Spin Physics Detector at the NICA collider", JINR, Dubna, September 30th to October 1st, 2020.* https://indico.jinr.ru/event/1428/contributions/10162/.

Chapter 6
Polarization in cascade decays

It often happens that vector particles are not produced directly from the partonic collision but are, together with an accompanying "recoil" system, the fruit of the decay or transformation of another particle or object. In inclusive production studies the two-step process usually remains unobserved and the dilepton decay distribution is studied as if the vector particle were produced directly.

The basic, intuitive expectation is that the isotropic decay from a $J = 0$ (mother) state should lead to the observation of a rotationally smeared angular distribution of the (daughter) vector particle decay, while, for $J > 0$, the observed polarization of the vector particle should somehow reflect the one of the mother particle.

We will address the following specific questions.

- In what kind of measurement and kinematic conditions can we indeed expect that a vector particle indirectly produced from the decay of a $J = 0$ particle ($\chi_{c0} \to \mathrm{J}/\psi\,\gamma$, $\mathrm{B} \to \mathrm{J}/\psi\,\mathrm{K}$, $\mathrm{H} \to \mathrm{Z}\,\gamma$, etc.) tends to look as unpolarized?
- How can the observation, made at the LHC, of almost unpolarized "directly" produced J/ψ mesons be justified in terms of fundamental production mechanisms? Is it not true that those coming from the decays of ($J = 0$) B mesons are the ones most reasonably expected to be unpolarized?
- How do the polarizations of $J = 1$ or $J = 2$ mother particles transform into the observed polarization of the vector particle ($\chi_{c1,2} \to \mathrm{J}/\psi\,\gamma$, $\mathrm{Z} \to \mathrm{J}/\psi\,\gamma$, etc.)?
- What polarization frame definitions can be adopted to describe the two-step process and what are their respective advantages?

P. Faccioli and C. Lourenço, *Particle Polarization in High Energy Physics*,
Lecture Notes in Physics 1002,
https://doi.org/10.1007/978-3-031-08876-6_6

6.1 Observing unpolarized vector-particle production

In this chapter we describe how the polarization is transferred from the mother particle to the daughter particle in a cascade (two-step) decay, where the daughter is a vector particle further decaying into a lepton-antilepton pair. Most of the chapter is devoted to the detailed discussion of the simplest case, the one where the mother particle is a $J = 0$ state. This is not only the easiest possible template of a general description, but it also corresponds to several interesting physics cases. Moreover, it represents a bridge to the subject of the previous chapter, where we proposed examples of "smearing" effects reducing the "amount" of the observed polarization. In fact, we can see the cascade production from a $J = 0$ particle as the potential source of the most extreme of the smearing effects, leading, in certain limits and conditions, to an effectively unpolarized production, thereby seemingly violating the unavoidable mathematical constraint that vector particles are necessarily intrinsically polarized (Theorem 1.1, Section 1.10).

We will consider examples of the cascade process $O \to V + X$, $V \to \ell^+\ell^-$, where O is (in the first part of the chapter) a particle of spin $J = 0$, V the vector state of which we want to study the polarization, and X an accompanying particle. The process has four degrees of freedom, represented by the angles Θ and Φ, describing the direction of V in the O rest frame, and ϑ and φ, the lepton emission angles in the V rest frame.

Figure 6.1 illustrates the definitions of these variables. The angles Θ and Φ are defined with respect to the polarization frame chosen for O (such as the GJ, CS, HX, and PX frames introduced in Chapter 2), referred to external physical directions (the colliding hadrons). For V we take as polarization axis the V direction in the O rest frame and, as a reference for the azimuthal anisotropy, the plane containing the polarization axes (z and z') of the two particles: we will refer to this frame as the "cascade helicity frame" (cHX).

In our specific case, the fact that O has zero angular momentum reduces considerably the complexity of the problem. Any $J = 0$ state, when it decays, emits its products isotropically. In fact, the spherical symmetry of a $J = 0$ wave function does not provide any possible reference for the definition of what an angular anisotropy could be. The calculation of the decay distribution involves the $\mathcal{D}^0_{LL'}(\Theta, \Phi)$ matrix, which has, actually, only one element, $\mathcal{D}^0_{00}$, constant and independent of the angles. As a result, the full angular distribution, $W(\cos\Theta, \Phi, \cos\vartheta, \varphi)$, is actually independent of $\cos\Theta$ and of Φ.

In several concrete cases it is also straightforward to write the $\cos\vartheta$ and φ dependence of W. We will consider a series of examples, where V is either a vector quarkonium or a Z boson and O is either a χ_0 quarkonium ($\chi_{c0} \to \mathrm{J}/\psi\,\gamma$ and $\chi_{b0} \to \Upsilon\,\gamma$), a B meson ($\mathrm{B} \to \mathrm{J}/\psi\,\mathrm{K}$), or a Higgs boson ($\mathrm{H} \to \mathrm{J}/\psi\,\gamma$, $\mathrm{H} \to \mathrm{Z}\,\gamma$). Some of these decays happen quite frequently in high-energy experiments; others are rare or even so-far unobserved processes. Together, they cover a large spectrum of possible observable manifestations of the polarization of V, thanks to the wide range of masses of the mother and daughter particles. In fact, and as we will see

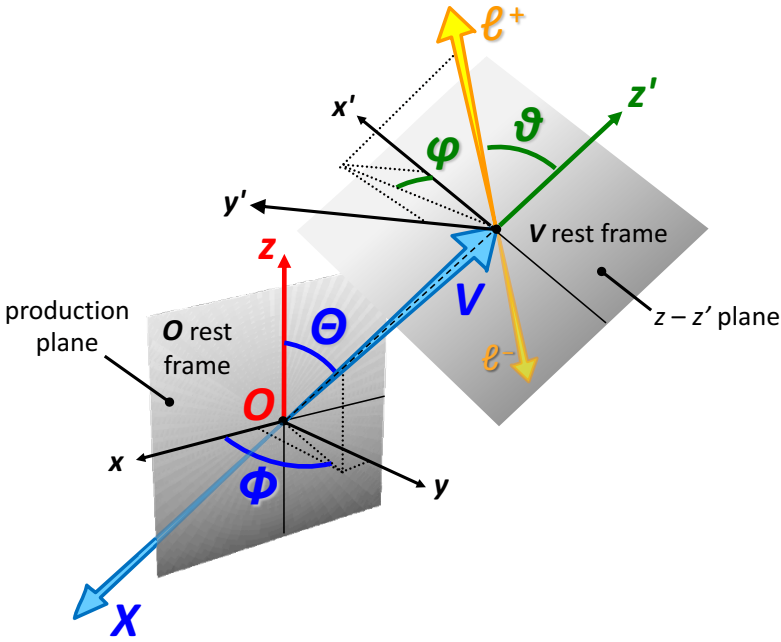

Fig. 6.1 Definition of the four angles used in the description of the cascade decay $O \to V + X$, $V \to \ell^+\ell^-$: the Θ and Φ angles are measured in the O polarization frame (x, y, z), defined as one of the usual frames (HX, CS, etc.) introduced in Chapter 2, while ϑ and φ are the dilepton emission angles in the V rest frame, with respect to the "cascade helicity" (cHX) system of axes (x', y', z').

in detail in Section 6.3, the results that can be observed in a real (or simulated) experiment are strongly dependent on the mass difference between O and V.

In all these examples the polarization of V, when measured in the cHX frame, is either fully transverse or fully longitudinal, depending on the accompanying daughter particle X (a photon or a kaon), as a pure consequence of angular momentum conservation: no role is played by the different interaction couplings involved.

The $O \to V + X$ decay in the O rest frame is illustrated in Fig. 6.2-top. The $V + X$ system has angular momentum $J = 0$ and, therefore, projection $J_z = 0$ on any z axis, so that, in general,

$$J_z^V + J_z^X + I_z^{V-X} = 0\,. \tag{6.1}$$

This relation includes a possible orbital angular momentum component $\mathbf{I}^{V-X}$ between the final states, which is, in particular, mandatory and well determined ($I = 1$) in the decay B($J = 0$) $\to$ J/ψ($J = 1$) K($J = 0$), where, otherwise, angular momentum conservation would be violated. The cHX axis z', defined by the common direction of the back-to-back V and X momenta, is a privileged axis to study the composition of angular momenta, because $\mathbf{I}^{V-X}$ is perpendicular to the linear momenta and $I_{z'}^{V-X}$ vanishes: only the individual spins of V and X have to be considered in the projected sum. The component $J_{z'}^X$ is well defined in all considered cases: it

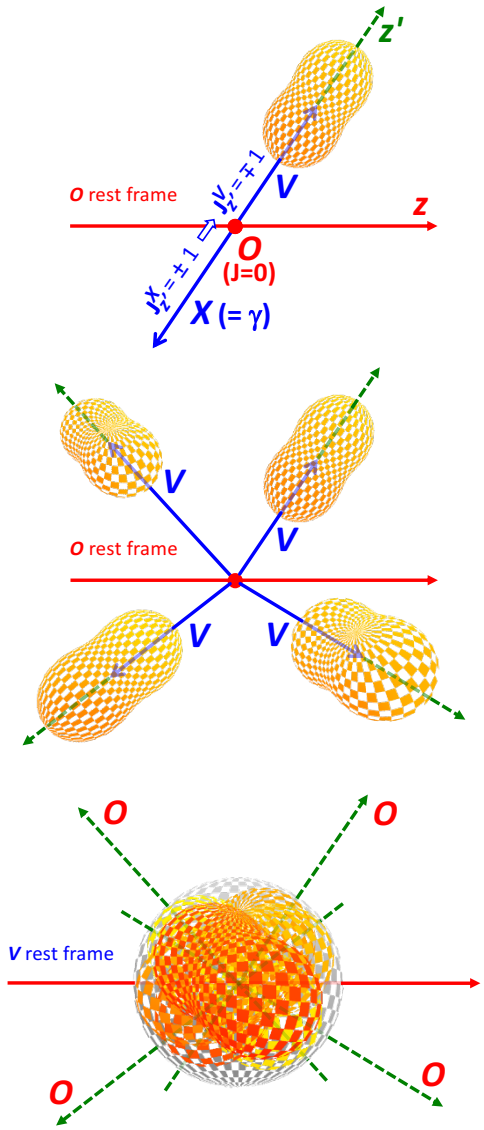

Fig. 6.2 How the vector particle V, produced in the $O \to V + X$ decay, acquires or loses its observable polarization, depending on the kind of measurement. Top: the process observed with respect to the O rest frame, in a measurement where both V and X are detected and the cHX axis z' is adopted as V polarization axis. For illustration, the case of a transverse polarization is shown, corresponding for example to $X = \gamma$ (transversely polarized photon): V is transversely polarized. Middle: the same kind of observation, for different directions of the outgoing V (different orientations of z'). Bottom: X is not observed or not used in the determination of the angular distribution; the measurement does not distinguish between directly and indirectly produced V and uses the same laboratory-referred frame as in inclusive studies. The average over all event configurations smears the shape of the V decay angular distribution towards the spherical symmetry.

can only be ±1 when X is a (transversely polarized) photon and 0 when X is a kaon or another $J = 0$ particle.

With these constraints, Eq. 6.1 implies, respectively, $J^V_z = \mp 1$ and 0 in the photon and kaon cases. As expected for a vector particle (Theorem 1.1), V is intrinsically polarized. The four-dimensional angular distribution is

$$W_{\mathrm{cHX}}(\cos\Theta, \Phi, \cos\vartheta, \varphi) \propto 1 + \lambda_0 \cos^2\vartheta\,, \tag{6.2}$$

where λ_0 is the "natural" polarization, $\lambda_0 = +1$ (photon) or -1 (kaon), and, as discussed above, there is no dependence on the Θ and Φ angles. To be measured, this distribution requires that the experiment reconstructs not only V but also X, using the momenta of both to determine the momentum and rest frame of O, needed for the definition of the cHX polarization axis.

The smearing effect that we will be studying arises when the V polarization measurement neglects (i.e. implicitly integrates out) the degrees of freedom of X, one possible reason being that X is not even observed and the $O \to V + X$ events are collected in the analysed data sample together with many other events where V represents *the* detected final state, independently of how it was produced.

To this category of measurement, which we will call "inclusive", belong, for example, most quarkonium ("prompt") production measurements, such as those published in Refs. [1–11], where J/ψ or Υ mesons are studied without distinguishing between directly produced states and those coming from the "feed-down" decays of χ_c or χ_b mesons: the analysed sample includes a fraction of such indirectly produced states, whose yields and (usually different) polarization properties must then be addressed, through hypotheses or analysis of further data, in the theoretical interpretation of the results.

The so-called "non-prompt" J/ψ (or ψ(2S)), produced in the decays of B mesons at an experimentally significant distance from the partonic interaction point, can, instead, be effectively distinguished from the prompt ones through suitable selection and subtraction procedures, as described hereafter, and are generally considered in separate measurements addressing their different production mechanisms (and different polarizations).

A second class of measurements, which we will refer to as "exclusive", is performed on the basis of event samples selected by fully reconstructing the final state. In particular, measurements of χ_c and χ_b cross sections (or cross-section ratios or polarizations), such as those reported in Refs. [12–19], reconstruct the photon emitted in the radiative decays, $\chi_c \to \mathrm{J}/\psi\,\gamma$ and $\chi_b \to \Upsilon\,\gamma$, and only select events where the final state has an invariant mass compatible with the χ_c or χ_b masses. Also in this case, the photon (X) momentum is, generally (and as assumed in our discussion), ignored in the angular analysis, i.e. it is not translated into values of $\cos\Theta$ and Φ.

Even when these variables are, in nature, uniformly distributed and the problem "looks" like a two-dimensional one (Eq. 6.2), acceptance and efficiency limitations in the detection of the involved particles can sculpt the four-dimensional distribution introducing correlations between the four angles. Integrating out the variables $\cos\Theta$ and Φ can be a necessity when the analysis cannot afford a four-dimensional anal-

ysis, typically because the data sample is too small. However, this analysis choice has consequences on the observable $\cos\vartheta, \varphi$ distribution, which we will illustrate in detail.

Considering the two kinds of measurements, inclusive and exclusive, allows us to address the following questions, here, for clarity of exposition, only formulated for the quarkonium case.

a) What are the polarizations of J/ψ or Υ mesons produced in the decays of χ_{c0} or χ_{b0} states, as they contribute to the inclusively observed prompt J/ψ or Υ production (that is, when radiative decay photons are not detected or are ignored)?

b) If, using the measured γ momentum, we exclusively select samples of J/ψ or Υ mesons coming from the decays of χ_{c0} or χ_{b0} states, and submit them to the same kind of analysis applied to the corresponding "inclusive" samples, what polarizations are we expected to measure and why?

We can already anticipate here that, contrary to what common sense may at first suggest, the two questions have different answers.

Of these two examples, the first one (a) can only be addressed theoretically or through simulated events: it cannot be investigated experimentally in a direct way, since restricting the analysis to the vector quarkonia coming from χ states requires that some selection is applied to $X = \gamma$, but this procedure is the one defining the second example (b).

When, instead, we consider the case of J/ψ mesons produced in decays of B mesons, the measurement of the corresponding polarization can actually be made also using "inclusive" samples. In fact, experiments often identify inclusive event samples dominated by $B \to J/\psi$ decays by selecting the "non-prompt" J/ψ mesons, i.e. the events in which the distance between the primary vertex (the proton-proton interaction point, where the B is produced), and the dimuon vertex, where the J/ψ is produced and immediately decays, is significantly larger than the uncertainty in the measurement of that distance. This method is justified by the relatively large decay length of B mesons (the $B^{\pm}$ lifetime is around 500 μm), with respect to the measurement resolution of most modern experiments, of around 10 μm.

In this case we can, therefore, ask the questions: what do we expect as an outcome of a real polarization measurement of J/ψ mesons produced in decays of B mesons, when using either an inclusive sample of non-prompt J/ψ mesons, or the exclusive events where the accompanying particle X (a kaon, for example) is identified? In both cases, it is meant that the angular degrees of freedom of the B decay are integrated out and the angular measurement is made in the two-dimensional $(\cos\vartheta, \varphi)$ space of the dilepton decay in the J/ψ rest frame.

Finally, we will also discuss the polarizations of the J/ψ or Z bosons emitted in radiative Higgs decays ($H \to J/\psi\,\gamma$ or $H \to Z\,\gamma$), measured with respect to the usual CS and HX frames, defined in terms of the momenta of the colliding protons without using the momentum of the daughter photon, that is, without referring, at each given event, to the rest frame of the specific Higgs boson that generated the observed particle.

We will discuss these questions gradually, until the end of this chapter, starting here with a first, simple and intuitive answer, quantitatively valid under conditions and limitations that will be studied in the next sections.

The idea is illustrated in Fig. 6.2. We know that V is emitted isotropically in the rest frame of the $J = 0$ particle O, as illustrated in the middle drawing. With a "Copernican" change of point of view, adopting as observation platform the rest frame of V (where the polarization measurement is made), we will see, event after event, O departing in all possible directions, a situation illustrated in the bottom drawing and described by uniformly distributed spherical coordinates $\cos\Theta$ and Φ. Along each of these individual directions (represented by the event-dependent z' cHX axis) we see a lepton decay distribution of shape $1 + \lambda_0 \cos^2\vartheta$, according to Eq. 6.2. With respect to a hypothetical "absolute" set of x, y, z axes fixed in space (for example, the laboratory axes), this distribution appears, each time, as rotated in a different direction. The convolution of all these rotated distributions leads to a spherical overall distribution. In other words, by referring to the "absolute" axes we lose the connection to the natural frame and the polarization orientation is fully "randomized", resulting in the apparent absence of any anisotropy of the decay distribution.

The intuitive concept that the decay distribution undergoes a full rotational smearing, concealing any underlying polarization, if the direction of the polarization axis is randomized with respect to the natural one, is formalized mathematically by Eq. 5.5. Here, $\cos\zeta$ and ω are the analogous of the spherical coordinates $\cos\Theta$ and Φ, describing how the observation frame (the "absolute" one in the present case) is rotated with respect to the natural one. All terms in $\sin(n\,\omega)$ or $\cos(n\,\omega)$, with $n = 1$ or 2, have zero average over the ω interval $[-\pi, +\pi]$, implying that λ_φ, $\lambda_\varphi^\perp$, $\lambda_{\vartheta\varphi}$, and $\lambda_{\vartheta\varphi}^\perp$ vanish. Concerning λ_ϑ, we notice that the uniform integration over the polar coordinate $\cos\zeta = \cos\Theta$ is actually not the only operation leading to a perfectly isotropic distribution. While there are in principle several ad hoc possibilities producing the same result, we consider here a case that will be seen as physically relevant in the subsequent discussion, namely a linear distribution of the kind $1/2\ (1 + B\cos\zeta)$ with $|B| \leq 1$ (normalized to unity over the $[-1, +1]$ range). In fact, the average of $\sin^2\zeta$ over this distribution is

$$\langle \sin^2\zeta \rangle = \frac{1}{2}\int_{-1}^{1} (1 - \cos^2\zeta)\,(1 + B\cos\zeta)\,\mathrm{d}\cos\zeta = \frac{2}{3}\,, \tag{6.3}$$

independently of B, leading to $\lambda_\vartheta = 0$ in Eq. 5.5: a constant distribution ($B = 0$) or a linear one ($0 < |B| \leq 1$), the latter option corresponding to a non-spherical smearing, both lead to the unpolarized scenario.

The actual reason why the linear $\cos\zeta$ distribution is equivalent to a flat one is that it corresponds to a flat distribution of $|\cos\zeta|$, and the sign of $\cos\zeta$ is not relevant for our present considerations (this argument would not be valid in studies of parity-violating effects).

This simple reasoning, leading to the prediction of unpolarized vector particles, does have counterparts in possible physical scenarios. However, depending on the

case, a fully isotropic smearing will be observed only in very specific kinematic conditions and/or with specific analysis choices. In fact, we have used two hypotheses that require case-by-case validation:

a) the laboratory-referred frames HX, CS, etc., are good approximations of an "absolute" frame;
b) the two-dimensional $(\cos\Theta, \Phi)$ distribution remains uniform, as it is in nature, in the data sample used for the measurement or, at most, its $\cos\Theta$ projection becomes linear.

How are these hypotheses affected by the experimental selections? The next sections address this problem and illustrate what kinds of observable distributions are expected in real experiments.

6.2 Kinematics of cascade decays

We have seen that the observation of an unpolarized vector particle becomes possible, at least conceptually, when the particle is produced from the decay of a $J = 0$ state O, in specific kinds of measurements where the observer is blind to the angular degrees of freedom of the O decay. The full smearing leading to a complete lack of measurable anisotropy, is, however, only an extreme case, occurring when, in the collected event sample, the (unobserved) $\cos\Theta$ distribution remains uniform as it is in nature, or becomes linear, the latter condition practically including, as approximations, cases where it is only slightly and smoothly shaped by experimental selections.

We are now going to study how the measurement itself, by sculpting the $\cos\Theta$ distribution, can perturb the spherical smearing naturally produced by the decay of a $J = 0$ particle, and actually find a more or less anisotropic dilepton distribution. The four-dimensional distribution W of Eq. 6.2 does not depend explicitly on $\cos\Theta$ and does not give any hint on how the dilepton distribution can be (more or less) smeared as a consequence of a (more or less) uniform randomization of the $\cos\Theta$ variable; in fact, it remains true that, even when such a randomization occurs, the V polarization along the cHX axis, built with the *per-event* knowledge of the O momentum, is immune to it and remains maximal and unsmeared.

In order to study the geometry of the smearing mechanism, it is convenient, therefore, to use an alternative configuration of the V polarization frame. Figure 6.3 shows the new definition, which, like the previous one, is adoptable, more generally, for the description of any two-step cascade decay. The x, y, z axes, with respect to which the emission angles Θ and Φ of the $O \to V + X$ decay are measured, are the same as in the previous definition: z is, for example, the polarization axis in the HX or CS frame of O. Instead, the x'', y'', z'' axes, the double-prime sign indicating the new references for the dilepton decay in the V rest frame, are now exact geometrical clones of the x, y, z axes, obtained by a simple, undistorted translation, not involving any Lorentz boosts of the physical references. In practice, the dimensionless unit

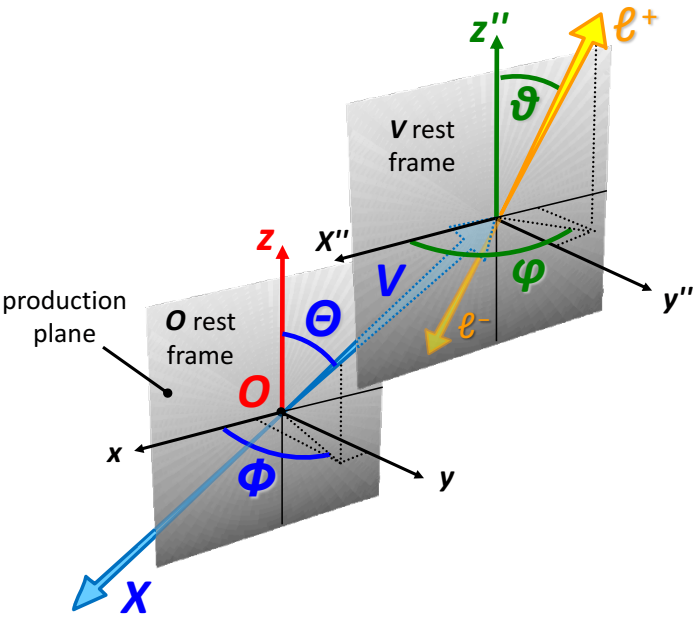

Fig. 6.3 An alternative definition of the polarization frame used in the description of the cascade decay $O \to V + X$, $V \to \ell^+\ell^-$: the x, y, z axes, and therefore the angles Θ and Φ, are the same as in the usual definition of Fig. 6.1, while ϑ and φ, dilepton emission angles in the V rest frame, are now defined with respect to a system of axes, x'', y'', z'', geometrically identical to x, y, z (the "cloned cascade frame", CC).

vectors of the x, y, z axes, defined in the O rest frame (O must, in principle, be reconstructed) are used with no modification as unit vectors of the x'', y'', z'' axes in the V rest frame.

This choice, hereafter referred to as the "cloned cascade frame" (CC) may sound physically abstract and perhaps counter-intuitive, but there is a limit in which the x'', y'', z'' axes simply reduce to the axes of the "ordinary" HX or CS frame (or any other frame adopted for x, y, z) of V, that is, the one "properly" defined in terms of beam directions Lorentz-boosted to the V rest frame: when the momenta of O and V in the laboratory are much larger than the mass difference between O and V, they become almost indistinguishable and the directions of, say, the HX axis in the O rest frame and the HX axis in the V rest frame tend to coincide (as is more quantitatively described later in this section).

We note that the definition of the CC frame requires the specification of the frame used for the decay of O, that is, of what frame is being "cloned": we can refer, for example, to the HX CC or CS CC frame. When this specification is absent, we will imply that we are using the HX frame as "master" frame.

For the decays $\chi_c \to \mathrm{J}/\psi\,\gamma$, $\chi_b \to \Upsilon\,\gamma$ or $\mathrm{B} \to \mathrm{J}/\psi\,\mathrm{K}$, given the relatively small differences between the masses of the mother and daughter particles, this condition is satisfied in most of the kinematic domain of the LHC measurements. In this limit,

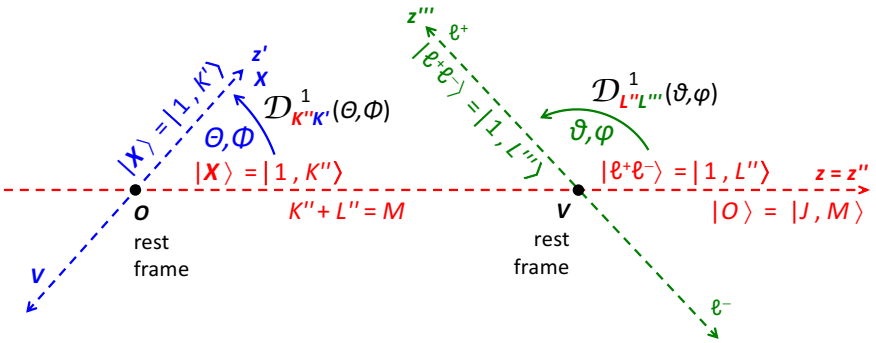

Fig. 6.4 Representation of the cascade decay $O \to V + X$, $V \to \ell^+\ell^-$, indicating the reference axes (CC frame), the decay angles, the angular momentum states of the involved particles, and the Wigner matrix elements used for their rotation. The red axis represents the common direction of the O and V polarization axes (z and z'', respectively) in the CC frame.

the determination of the x'', y'', z'' axes decouples from the knowledge of the O momentum and the polarization measurement in the CC frame can effectively be performed without observing the accompanying particle X and reconstructing the O rest frame.

To determine the expression of the four-dimensional angular distribution, we start by writing the amplitude of the process $O \to V+X$, following a procedure analogous to the one used in Section 1.7 to derive the dilepton distribution of a J/ψ.

Figure 6.4 summarizes the notations used for the angular momentum states of the involved particles, the axes and their rotations; for later use (Section 6.6), the diagram represents the general case where the mother particle O has angular momentum quantum number J.

As mentioned in the previous section, in the considered examples X has a definite angular momentum projection, which we indicate here with K', along the z' (cHX) axis, while there is, in general, also an orbital momentum component that now, with respect to the CC polarization axis z'', we will not be able to ignore. In order to use simple two-body angular momentum sum rules, we then attribute the orbital angular momentum to X: in practice, we consider X as a state that has, whatever its identity (a photon, a spin-0 kaon), total angular momentum $J = 1$, including the orbital part, as required so that its sum with the, also unitary, spin of V yields the zero angular momentum of O.

The Wigner matrix needed to rotate the angular momentum of X from the x', y', z' axes to the x'', y'', z'' axes is, therefore, $\mathcal{D}^1_{K'' K'}(\Theta, \Phi)$, where K'' is the $J_{z''}$ projection of X on the z'' axis:

$$|X; 1, K'\rangle_{z'} = \sum_{K''=0,\pm1} \mathcal{D}^1_{K'' K'}(\Theta, \Phi)\, |X; 1, K''\rangle_{z''} \,. \tag{6.4}$$

Since we will only be considering parity-conserving terms of the decay distribution, Θ and Φ indifferently denote the direction of V or of X, while to obtain correct

signs for the parity-violating terms, following the notations of Fig. 6.3 where it is the direction of V that defines Θ and Φ, the Wigner matrix for the rotation of X should read $\mathcal{D}^1_{K'' K'}(\pi - \Theta, \pi + \Phi)$.

Indicating with L'' the generic $J_{z''}$ projection of V on z'', the decay amplitude is given by

$$\begin{aligned} &\mathcal{A}(O \to V_{L''} + X_{K'}) \\ &= \sum_{K''=0,\pm1} {}_{z''}\langle V\, X;\ 1, L'',\ 1, K'' \,|\, \mathcal{B} \,|\, O; 0, 0\rangle_{z''}\ \mathcal{D}^{1*}_{K'' K'}(\Theta, \Phi) \\ &= \langle 1, L'',\ 1, -L'' \,|\, 0, 0\rangle\ \mathcal{D}^{1*}_{-L'' K'}(\Theta, \Phi)\ , \end{aligned} \tag{6.5}$$

where the operator $\mathcal{B}$, containing the dynamics of the decay, can, in general, impose relations between the angular momentum states of O, V, and X. In the cases here considered, the relevant physical constraints are two: a) along z'', the V and X particles have opposite angular momentum projections, being the two daughters of a $J = 0$ state, as expressed in the relation used in the second equality above:

$${}_{z''}\langle V\, X;\ 1, L'',\ 1, K'' \,|\, \mathcal{B} \,|\, O; 0, 0\rangle_{z''} \ \propto\ \delta_{K'', -L''}\ \langle 1, L'',\ 1, -L'' \,|\, 0, 0\rangle\ ; \tag{6.6}$$

b) the nature of X, being either a transversely polarized photon or another $J = 0$ particle (a condition that we will impose below, while summing over the squared amplitudes), effectively determines, by angular momentum conservation, a definite natural polarization of V.

The Clebsch–Gordan coefficient $\langle 1, L'',\ 1, -L'' \,|\, 0, 0\rangle$ is $\sqrt{3}/3$ or $-\sqrt{3}/3$, respectively for $L'' = 0$ or ±1. The amplitude of the two-step process can then be written by including a factor expressing the rotation of the dilepton angular momentum state, which has projection $L''' = \pm1$ along its own flight direction in the V rest frame (z''' axis), onto the z'' axis (where it has projection identical to the V one, L''), and summing over the possible L'' components of V:

$$\begin{aligned} &\mathcal{A}[\, O \to V + X_{K'},\ V \to (\ell^+\ell^-)_{L'''}] \\ &\propto \sum_{L''=0,\pm1} \langle 1, L'',\ 1, -L'' \,|\, 0, 0\rangle\ \mathcal{D}^{1*}_{-L'' K'}(\Theta, \Phi)\ \mathcal{D}^{1*}_{L'' L'''}(\vartheta, \varphi)\ . \end{aligned} \tag{6.7}$$

This latter expression can also be read, by comparison with Eq. 1.10, as the amplitude of the dilepton decay of V, when V has (Θ, Φ)-dependent angular momentum components (referred to z'') $a_{L''} = \langle 1, L'',\ 1, -L'' \,|\, 0, 0\rangle\ \mathcal{D}^{1*}_{-L'' K'}(\Theta, \Phi)$. The final expression of the angular distribution is obtained by squaring Eq. 6.7 and summing over $L''' = \pm1$ and over the relevant K' values, which depend on what the final state X is. In the cases we will consider, $K' = 0$ if X is a kaon (or other $J = 0$ particle), and $K' = \pm1$ if X is a photon. Therefore, V has a fully longitudinal natural polarization in the cHX frame, $\lambda_0 = -1$, in the first case and a fully transverse one, $\lambda_0 = +1$, in the second.

The resulting distribution for a generic natural polarization of V is:

$$\begin{aligned} & W_{\mathrm{CC}}(\cos\Theta, \Phi, \cos\vartheta, \varphi) \\ & \propto \frac{1}{3+\lambda_0}\Big(2 + \lambda_0\,(1 - \cos^2\Theta - \cos^2\vartheta + 3\cos^2\Theta\,\cos^2\vartheta\,) \\ & + \lambda_0\,\sin^2\Theta\,\sin^2\vartheta\,\cos 2(\varphi - \Phi) \\ & + \lambda_0\,\sin 2\Theta\,\sin 2\vartheta\,\cos(\varphi - \Phi)\Big)\,. \end{aligned} \tag{6.8}$$

Only the difference between azimuthal angles, $\varphi - \Phi$, enters this expression, which is, moreover, fully symmetric by exchange between the O and V decay angles: $(\Theta, \Phi) \leftrightharpoons (\vartheta, \varphi)$. It is, however, possible to rewrite the result giving emphasis to the dilepton part, by defining $(\cos\Theta, \Phi)$-dependent anisotropy parameters and obtaining the same usual expression of Eq. 1.16, with

$$\begin{aligned} \lambda_\vartheta &= \frac{-\lambda_0\,(1 - 3\cos^2\Theta)}{2 + \lambda_0\,(1 - \cos^2\Theta)}\,, \\ \lambda_\varphi &= \frac{\lambda_0\,\sin^2\Theta\cos 2\Phi}{2 + \lambda_0\,(1 - \cos^2\Theta)}\,, \quad \lambda_\varphi^\perp = \frac{\lambda_0\,\sin^2\Theta\sin 2\Phi}{2 + \lambda_0\,(1 - \cos^2\Theta)}\,, \\ \lambda_{\vartheta\varphi} &= \frac{\lambda_0\,\sin 2\Theta\cos\Phi}{2 + \lambda_0\,(1 - \cos^2\Theta)}\,, \quad \lambda_{\vartheta\varphi}^\perp = \frac{\lambda_0\,\sin 2\Theta\sin\Phi}{2 + \lambda_0\,(1 - \cos^2\Theta)}\,. \end{aligned} \tag{6.9}$$

The distribution becomes obviously isotropic if $\lambda_0 = 0$. We can also recognize from Eq. 6.8 that the average over a uniform (or linear) $\cos\vartheta$ distribution (giving $\langle\cos^2\vartheta\rangle = 1/3$) and over the azimuthal dimension leads to an isotropic $(\cos\Theta, \Phi)$ distribution, as expected from the decay of a $J = 0$ particle. Vice versa and more interestingly, the (uniform or linear) average over $\cos\Theta$ leads to an isotropic dilepton decay distribution of the vector particle V, providing a further illustration of the concepts discussed in the previous section. However, it is now apparent that, if the $\cos\Theta$ distribution is, for some reason, not uniform or linear, so that $\langle\cos^2\Theta\rangle \neq 1/3$, the resulting dilepton distribution measured in the CC frame will not be isotropic and the presence of a nonzero natural polarization λ_0 will somehow be revealed.

It is not difficult to realize that a measurement usually introduces sculpting effects on the $\cos\Theta$ distribution. If all V particles produced by the decay of O were included in the analysed data sample, the distribution would remain uniform, as it is naturally. In general, however, this is not possible in a real experiment, and not only because of the selection criteria applied to improve the quality of the signal reconstruction. The simple fact that we are *observing* a sample of V particles (instead of a sample of O particles) and we are, therefore, delimiting the range of their (transverse and/or longitudinal) momenta in the laboratory, reshapes the $\cos\Theta$ distribution. To understand how, we need to open a brief parenthesis on the relations between the relevant kinematic variables: the momenta of O and V in the laboratory, $\mathbf{P}$ and $\mathbf{p}$, with moduli P and p; the momentum of V in the rest frame of O, $\mathbf{p}'$, with

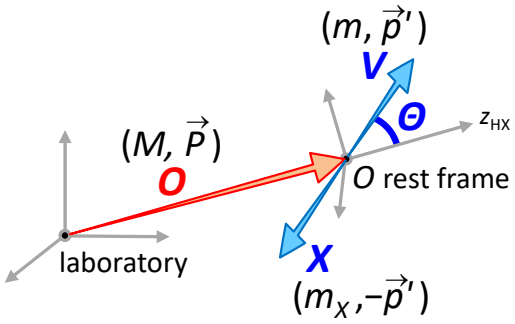

Fig. 6.5 Kinematic variables used in the description of the decay $O \to V + X$.

modulus p'; the masses M, m, and m_X of O, V, and X; and $\cos\Theta$. The notations are illustrated in Fig. 6.5, where the angle Θ is seen to be defined in the HX frame of O. In all relations until the end of this section, we imply $\Theta \equiv \Theta_{\rm HX}$.

The components of the V momentum perpendicular, $p_\perp$, and parallel, $p_\parallel$, to the direction of **P** transform from the O rest frame to the laboratory frame according to the Lorentz boost defined by $\beta = P/\sqrt{M^2 + P^2}$, so that:

$$p_\perp = p'_\perp = p' \sin\Theta \tag{6.10}$$

and

$$\begin{aligned} p_\parallel &= \frac{1}{\sqrt{1-\beta^2}} \left(p'_\parallel + \beta \sqrt{p'^2 + m^2} \right) \\ &= \sqrt{1 + \frac{P^2}{M^2}}\, p' \cos\Theta + \frac{P}{M} \sqrt{p'^2 + m^2}\,. \end{aligned} \tag{6.11}$$

The momentum p' is

$$p' = \frac{1}{2M} \sqrt{(M^2 + m^2 - m_X^2)^2 - 4M^2 m^2} \simeq \frac{M^2 - m^2}{2M}\,, \tag{6.12}$$

where the approximate equality corresponds to $m_X^2 \ll M^2 + m^2$, a relation satisfied in all the cases hereafter considered, either exactly ($X = \gamma$) or up to 1%-order corrections ($X = $ K in B decays).

For an easier illustration of the concept we will make the temporary assumption that we are considering high-momentum measurements, that is, the momenta of O and V in the laboratory are significantly bigger than their masses. This condition, which will not be used in the computations of the next section, can be considered to be satisfied, for example, in most charmonium measurements at the LHC. The relations seen in the remaining of this section are, therefore, applicable quantitatively to the decays $\chi_{c0} \to {\rm J}/\psi\,\gamma$ and ${\rm B} \to {\rm J}/\psi\,{\rm K}$, but not, in general, to the Higgs decays.

Equations 6.10 and 6.12 imply the general inequality $p_\perp < (M - m)\sin\Theta$ and, therefore,

$$p_\perp \ll p \quad \text{if} \quad M - m \ll p\,. \tag{6.13}$$

This means that, in the assumed approximation, we have $p \simeq p_\parallel$, so that the vectors $\mathbf{p}$ and $\mathbf{P}$ can be considered to be parallel. In this approximation, as previously mentioned, the CC frame becomes coincident with the corresponding laboratory-referred frame, for example the HX frame.

We can now quantify the effect of this approximation on a polarization measurement, considering that the angle δ_{CC} between the two polarization axes is, by definition of such axes, the angle between the vectors $\mathbf{p}$ and $\mathbf{P}$, given by $\sin\delta_{\mathrm{CC}} = p_\perp/p$. Assuming that the decay distribution is of the kind $\propto 1 + \lambda_\vartheta^{\mathrm{CC}}\cos^2\vartheta$ in the HX-CC frame (that is, $\lambda_\vartheta^{\mathrm{CC}} \equiv \lambda_0$), the corresponding λ_ϑ value in the HX frame is (Eq. 2.13, setting λ_φ and $\lambda_{\vartheta\varphi}$ to zero)

$$\lambda_\vartheta^{\mathrm{HX}} \;=\; \lambda_\vartheta^{\mathrm{CC}}\,\frac{1 - \frac{3}{2}\sin^2\delta_{\mathrm{CC}}}{1 + \frac{1}{2}\lambda_\vartheta^{\mathrm{CC}}\sin^2\delta_{\mathrm{CC}}} \;\simeq\; \left[1 - \frac{3 + \lambda_\vartheta^{\mathrm{CC}}}{2}\sin^2\delta_{\mathrm{CC}}\right]\lambda_\vartheta^{\mathrm{CC}}\,, \tag{6.14}$$

where the approximate equality is valid in the limit of a small angle. Therefore,

$$\left|\lambda_\vartheta^{\mathrm{HX}} - \lambda_\vartheta^{\mathrm{CC}}\right| \;\simeq\; \frac{3 + \lambda_\vartheta^{\mathrm{CC}}}{2}\left|\lambda_\vartheta^{\mathrm{CC}}\right|\sin^2\delta_{\mathrm{CC}} \;\le\; \frac{3 + \lambda_\vartheta^{\mathrm{CC}}}{2}\left|\lambda_\vartheta^{\mathrm{CC}}\right|\left(\frac{M - m}{p}\right)^2\,. \tag{6.15}$$

For example, the relative deviation, $\left|(\lambda_\vartheta^{\mathrm{HX}} - \lambda_\vartheta^{\mathrm{CC}})/\lambda_\vartheta^{\mathrm{CC}}\right|$, of a λ_ϑ measurement in the HX frame from its CC expectation is at most of order 2–4% (depending on λ_ϑ) for the polarization of J/ψ mesons from B decays at $p_{\mathrm{T}} = 10$ GeV and rapidity $y = 1$, and decreases with increasing p_{T} and $|y|$.

We will now assume that the condition $\mathbf{p} \parallel \mathbf{P}$ is satisfied. Taking then $p_\parallel$ in Eq. 6.11 as expression for p, with

$$\sqrt{p'^2 + m^2} = \frac{M^2 + m^2}{2M} \quad \text{and} \quad \sqrt{1 + \frac{P^2}{M^2}}\,\frac{p'}{P} \simeq \frac{p'}{M}\,,$$

the first relation deriving from Eq. 6.12 and the second from the assumption that $P \gg M$, we find that

$$\mathbf{p} \;\simeq\; \mathbf{P}\; f(\cos\Theta)\,, \tag{6.16}$$

$$\text{with} \quad f(\cos\Theta) \;=\; \left(\frac{1 - \cos\Theta}{2}\,\frac{m^2}{M^2} \;+\; \frac{1 + \cos\Theta}{2}\right), \tag{6.17}$$

where we note the linear dependence on $\cos\Theta$.

This vector relation can be rewritten, remaining formally identical, with $\mathbf{p}$ and $\mathbf{P}$ replaced by their moduli, or their transverse or longitudinal components. The mathematical passages throughout this section will use the symbols p and P to denote either of the three possibilities. The one relevant for the case under study is the variable with respect to which the polarization parameters λ_ϑ, λ_φ and $\lambda_{\vartheta\varphi}$ in the CC

frame (that is, in its corresponding laboratory-referred frame) are observed. In our illustrative studies we will consider hypothetical measurements made as a function of p_{T}. Correspondingly, all the following relations should be considered with the substitutions $p \to p_{\mathrm{T}}$, $P \to P_{\mathrm{T}}$.

Equation 6.17 can be read as follows: if we consider a sample of events where O is always produced with the same laboratory momentum, of modulus (or component) P, the laboratory momentum (component) p of V is distributed uniformly between the values $m^2/M^2\, P$ and P, corresponding to the extremes of the natural uniform distribution of $\cos\Theta$ between -1 and $+1$.

Having a sample of events distributed within a defined narrow interval around a value of P is not a realistic situation for the considered examples, where the experiment may not even reconstruct O and, in general, does not perform the measurement as a function of P. Instead, the experiment observes V and at each event determines its momentum (component) p, so that the sample is characterized by a distribution of p values. However, while fixing P leads to a uniform $\cos\Theta$ distribution, fixing p does not. In fact, for a narrow interval in p, neither the $\cos\Theta$ nor the P distributions are uniform, their ratio being

$$\frac{\mathrm{d}N}{\mathrm{d}\cos\Theta} \Big/ \frac{\mathrm{d}N}{\mathrm{d}P} \equiv \left|\frac{\mathrm{d}P}{\mathrm{d}\cos\Theta}\right| = \begin{cases} \frac{1}{2}\, p \left(1 - (m/M)^2\right) f(\cos\Theta)^{-2} \\ \frac{1}{2}\, p^{-1} \left(1 - (m/M)^2\right) P^2 \end{cases} , \tag{6.18}$$

where the dependence on either $\cos\Theta$ or P has been made explicit.

From this relation we see that, given a value of p, the $\cos\Theta$ distribution could only be uniform (constant $\mathrm{d}N/\mathrm{d}\cos\Theta$) if the sample were chosen with a P distribution of the kind $\mathrm{d}N/\mathrm{d}P \propto P^{-2}$ (and it would be possible to obtain a uniform P distribution, constant $\mathrm{d}N/\mathrm{d}P$, only if $\cos\Theta$ would be distributed as $\mathrm{d}N/\mathrm{d}\cos\Theta \propto f(\cos\Theta)^{-2}$). But the P distribution is obviously not chosen by us: on the contrary, it is precisely what physically determines the p distribution of the event sample under analysis.

In summary, given a collected sample of V particles, how the $\cos\Theta$ distribution of the studied event sample departs from a constant distribution depends on the underlying shape of the unobserved P distribution, that is, on the shape of the observed p distribution. To figure out how, we start by writing the "original" two-dimensional $(P, \cos\Theta)$ distribution as

$$\frac{\mathrm{d}N}{\mathrm{d}P\, \mathrm{d}\cos\Theta} \propto \left(\frac{M}{P}\right)^{\rho} , \tag{6.19}$$

where there is no $\cos\Theta$ dependence (constant distribution) and the P dependence is parametrized with a power-law function, an always reliable shape approximation in a sufficiently narrow kinematic domain. Equation 6.19 means that, in measurements made as a function of the B momentum, the $\cos\Theta$ distribution would remain flat (apart from other perturbing effects) and, thus, a fully smeared J/ψ polarization should be seen (P-independent and negligible λ parameters).

We want to find the corresponding two-dimensional $(p, \cos\Theta)$ distribution, which is the one relevant for the description of an experimental data sample where p, and

not P, is the focus of the measurement. In the variable replacement

$$P \to p = P\, f(\cos\Theta)\,, \quad \cos\Theta \to \cos\Theta \tag{6.20}$$

the measure changes as

$$\mathrm{d}P\,\mathrm{d}\cos\Theta = 1/f(\cos\Theta)\;\mathrm{d}p\;\mathrm{d}\cos\Theta\,, \tag{6.21}$$

so that Eq. 6.19 is transformed into

$$\frac{\mathrm{d}N}{\mathrm{d}p\,\mathrm{d}\cos\Theta} \;\propto\; \left(\frac{m}{p}\right)^{\rho} f(\cos\Theta)^{\rho-1}\,. \tag{6.22}$$

Apart from finding an unchanged power-law dependence on momentum, we see from this expression and from the $f(\cos\Theta)$ definition (Eq. 6.17) that the effective $\cos\Theta$ distribution will, in general, depart from a flat or linear shape. Examples of $\cos\Theta$ distributions are shown in Fig. 6.6-left for the cases of the decays $\mathrm{B} \to \mathrm{J}/\psi\,\mathrm{K}$ (top) and $\chi_{c0} \to \mathrm{J}/\psi\,\gamma$ (bottom), for some chosen values of ρ. In their analytical description, the two decays differ only for the value of m/M, which fully determines the shape of $f(\cos\Theta)$. The corresponding $|\cos\Theta|$ distributions,

$$\frac{\mathrm{d}N}{\mathrm{d}\,|\cos\Theta|} \;\propto\; \frac{\mathrm{d}N}{\mathrm{d}\cos\Theta}(\cos\Theta) + \frac{\mathrm{d}N}{\mathrm{d}\cos\Theta}(-\cos\Theta)\,, \tag{6.23}$$

are shown in the right panels. As mentioned above, the latter distributions are the ones relevant for the effect under study: whether or not they are flat, and to what degree, determines if we will see a fully smeared or only attenuated polarization in the HX or CS frame approximating the CC frame. The cases $\rho = 1$ and $\rho = 2$ lead, for both decays, to a flat $|\cos\Theta|$ distribution and are not shown in the figure.

The deviation from a flat distribution is larger for larger values of $|\rho - 1|$. It is important to understand that ρ is the (locally defined) "slope" of the p distribution of the collected sample of V particles, affected by experimental acceptance and efficiency effects. Even if the measurement of the dilepton angular distribution implies that the dilepton acceptance and efficiency are taken into account and/or corrected for, and even if the correction of the dilepton events brings the p distribution close to its natural shape, the $\cos\Theta$ distribution, defined in the O rest frame and additionally affected by the acceptance and reconstruction efficiency for X, is, by hypothesis, not observed and cannot, obviously, be corrected. It is, therefore, the "raw" experimental distribution of p that determines the shaping of the $\cos\Theta$ distribution.

For example, as a consequence of the lepton selection criteria (minimum p_{T} requirement) we can expect to see a turn-down shape towards the lowest detected values of p, meaning that ρ can be negative at low p (number of events increasing with p), passing through zero at the maximum of the distribution and changing to positive values at higher p. Correspondingly, with varying p the shape of the $\cos\Theta$ distribution will change, according to Eq. 6.17, from decreasing to increasing, leading to varying degrees of smearing of the polarization observed in the CC (that is, HX or CS) frame.

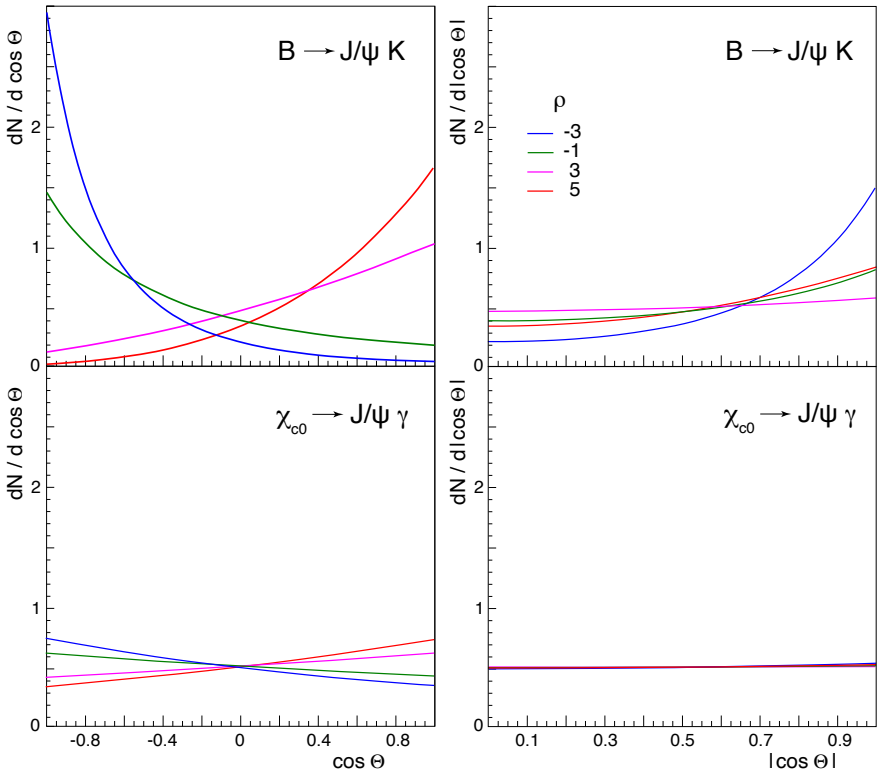

Fig. 6.6 Examples of the underlying $\cos\Theta$ and (corresponding) $|\cos\Theta|$ distributions for the decays B $\rightarrow$ J/ψ K and $\chi_{c0} \rightarrow$ J/$\psi\,\gamma$, when the experiment selects samples of J/ψ mesons having p distributions $\propto (p/m)^{-\rho}$, for different values of ρ.

Effectively, therefore, the smearing of the polarization is strongly influenced by purely experimental features of the measurement, which may be difficult to be accounted for. This fact can lead to disagreements between experiments performing the same measurement with different detectors and selection criteria, as illustrated in the next section.

Equation 6.17 shows another factor that influences the strength of the smearing: the dependence of f on $\cos\Theta$ tends to vanish in the limit $m/M \rightarrow 1$. We expect, for example, a significantly stronger polarization smearing for J/ψ mesons from $\chi_{c0} \rightarrow$ J/$\psi\,\gamma$ than from B $\rightarrow$ J/ψ K, given the proximity of the χ_{c0} and J/ψ masses, as shown by the comparison between the upper and lower panels of Fig. 6.6.

The above description is appropriate for measurements made at a high momentum-to-mass ratio. In particular, in the decay from χ_{c0} the condition of Eq. 6.13, leading to $\mathbf{p} \parallel \mathbf{P}$, is practically always satisfied and the "ordinary" J/ψ HX or CS axis, adopted in the measurement, becomes coincident with the corresponding CC axis over the entire momentum range of the measurement; moreover, for $p_{\mathrm{T}} \gtrsim 10$ GeV

and even at mid rapidity, the analytical relation of Eq. 6.17 is almost exact and the previous discussion should faithfully reproduce the reality. In the case of B decays, a slightly higher threshold in p_{T} and/or $|y|$ is necessary.

Instead, this description does not apply to the typical events produced by decays of the much heavier Higgs boson. The decay $\mathrm{H} \rightarrow \mathrm{J}/\psi\,\gamma$ is the one departing the most from the assumed approximations. It remains true that a smearing of the natural polarization is expected, because the direction of the z axis of the J/ψ HX frame (the observation frame) is certainly not fully correlated with the emission direction of the J/ψ in the Higgs rest frame (natural polarization axis). However, the sizeable J/ψ momentum $p' \simeq M/2 \simeq 62.5$ GeV in the Higgs rest frame must play an important role, determining different observations when the laboratory momentum p is much smaller than, or much larger than, or comparable to p': a complex smearing pattern is expected.

In general, realistic descriptions of the considered decays, moving away from the kinematic approximations mentioned in this section, are important to predict more accurately not only the effects of differences in the masses of the mother and daughter particles but also the transitions between scenarios where the smearing is more or less effective, depending on the laboratory momentum of V and on how the events are selected in the analyses (of measured or simulated event samples). This is the subject of the next section.

6.3 A wide spectrum of possible observations

In this section we will illustrate, using simulated events, a range of possible smearing effects occurring in the polarization measurement of a vector particle produced from the decay of another particle. As described in the previous section, the effects depend, among other things, on the distribution of the V momentum component with respect to which the polarization is measured. In what follows, we have chosen the transverse component, p_{T}. Since the kinematics of V are a direct reflection of those of the mother particle O, to produce a realistic event sample we must use realistic p_{T} distributions for the considered mother particles. The distributions are obtained by interpolating existing quarkonium, B meson and Higgs-boson cross section measurements from LHC experiments, shown in Fig. 6.7 as a function of p_{T}/M. The B meson cross section measured by CDF is also shown, as it will be used for the corresponding prediction in Section 6.5.

As illustrated in the left panel, the quarkonium data, available for seven states (including χ_{c1} and χ_{c2}), do not show deviations from a "universal" p_{T}/M spectrum. This observation allows us to assume, at least for illustration, that this universal shape also characterizes the χ_{c0} and χ_{b0} distributions, for which no data exist. Since a finite-p_{T} V can come from the decay of a "zero"-p_{T} O, especially if the mass difference (that is, p') is large, as in the Higgs decays, it is important that the mother particle is generated in the simulation down to low p_{T}. Extrapolated shapes are used for this purpose, but it must be kept in mind that these are only empirical guesses

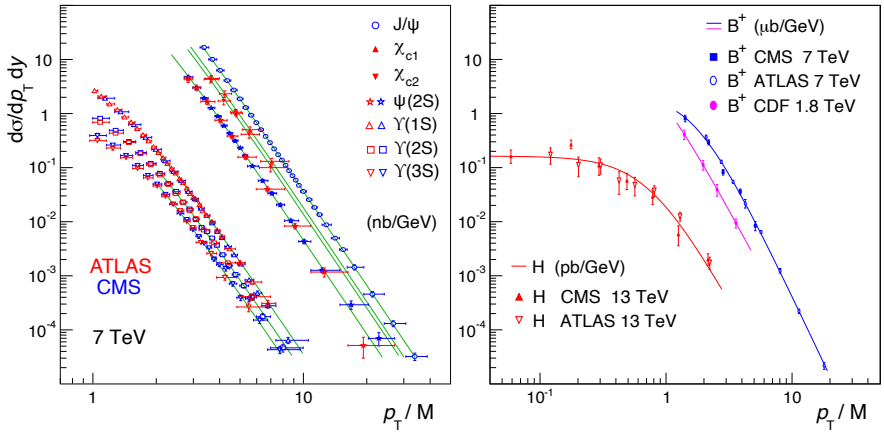

Fig. 6.7 Left: Prompt quarkonium double-differential cross sections, $\mathrm{d}\sigma/\mathrm{d}p_\mathrm{T}\,\mathrm{d}y$, measured at midrapidity, in pp collisions at $\sqrt{s}$ = 7 TeV, by CMS (blue markers) [1, 2] and ATLAS (red markers) [5, 12, 20]. All the green curves have identical shapes and represent the result of a fit to all quarkonium cross sections of $p_\mathrm{T}/M > 2$ [21]. Right: Midrapidity double-differential cross sections for the production of B^+ mesons at $\sqrt{s}$ = 1.8 TeV (pink circles) and at $\sqrt{s}$ = 7 TeV (blue markers), and Higgs bosons at $\sqrt{s}$ = 13 TeV (red markers), measured by CDF [22], ATLAS (open symbols) [23, 24] and CMS (closed symbols) [25, 26]. The curves represent empirical parametrizations.

made in an illustrative context. In the event generation, O decays isotropically into $V + X$ and V to $\mu^+\mu^-$ according to the distribution of Eq. 6.2 in the cHX frame. No approximations are made in the generation of the decay distributions.

We start by analysing the case of J/ψ production from B decays, for which both the "inclusive" and "exclusive" kinds of measurement are realistic experimental options. The inclusive case corresponds to measurements which select samples of J/ψ mesons from $\mathrm{B} \to \mathrm{J}/\psi\, X$ decays by applying a threshold on the distance between the primary and dimuon vertices, thus presumably rejecting all the "prompt" events. Ideally, this selection has no effect on the momentum of the accompanying particle X. Instead, the exclusive measurement selects events where X is identified as (for example) a kaon and its momentum enters, therefore, the domain of acceptance of the detector, here parametrized with the rapidity and p_T selections $|y_\mathrm{K}| < 2.5$ and $p_\mathrm{T}^\mathrm{K} > 1.3$ GeV, representative of those applied in typical analyses of the LHC experiments.

For the modelling of the inclusive scenario we are making a series of simplifying hypotheses that need to be clearly specified. First, we assume that X is a $J = 0$ particle (kaon, pion, eta meson, etc.), conferring a definite "natural" polarization to the J/ψ, longitudinal along the cHX axis, as discussed in Section 6.1, just as in the exclusive case. In reality, $\mathrm{B} \to \mathrm{J}/\psi\, X$ decays include cases where X is a second vector particle or a multi-body system (possibly having an invariant mass that can be significantly larger than the "small" mass of a kaon), and, in the lack of the strong $J(X) = 0$ constraint, the resulting natural polarization can become

less than fully longitudinal: the simulation provides, in this case, an upper limit for the *magnitude* of the observed polarization. Additionally, inclusive non-prompt production actually includes more complex decay chains, where the B meson first decays into a χ_{c1}, χ_{c2} or $\psi(2S)$ meson, which then decays into a J/ψ. Also this kind of further complexity, leading to a reduction in the observed polarization, will be neglected in our illustration.

As a further, more technical note we clarify that we are assuming that the J/ψ is produced in the B decay as a ${}^3S_1$ $c\bar{c}$ state, already having the quantum numbers of the final colour-neutral hadron (core hypothesis of the "colour singlet model", see Section 6.4). However, it can also happen that the J/ψ exits the decay through an intermediate coloured $c\bar{c}$ state,

However, it can also happen that the J/ψ exits the decay through an intermediate coloured $c\bar{c}$ state, possibly having an angular momentum configuration different from the final one (for example, ${}^1S_0$); in this case, the subsequent gluon emission(s) necessary to produce the observable meson will tend to attenuate its observed polarization, so that λ_0 will, also for this kind of contributing mechanism, deviate from its extreme value, -1.

All these simplifications are functional to the purpose of this section, where we want to illustrate the difference between two kinds of observation methods (inclusive vs. exclusive) on the observed polarization, applied to the same underlying process; it is, therefore, important that the physical cascade process is modelled in exactly the same way in the two cases. In Section 6.5 we will revise these assumptions in a more realistic description of the non-prompt case, also in the light of some basic notions, presented in Section 6.4, about the existing hypotheses on the mechanisms of J/ψ production.

The resulting polarization parameters of the J/ψ dilepton decay distribution, λ_ϑ, λ_φ, and $\lambda_{\vartheta\varphi}$, in the HX and CS frames, as well as $\tilde{\lambda}$, are shown in Fig. 6.8 for the inclusive and exclusive measurements. Both cases reveal a strong smearing of the natural longitudinal polarization (represented by the flat green line at $\lambda_\vartheta = -1$). The residual polarizations are, however, quite significant and, furthermore, p_T-dependent. The dashed and dotted lines illustrate the effect of performing the measurement on a sample where the decay muons are required to have minimum p_T values of 5 and 10 GeV, respectively. The application of these thresholds, inspired by selection criteria applied in some typical LHC analyses, leads to non-negligible variations of the obtained patterns.

We note that all the curves considered in the present chapter become asymptotically constant at very high p_T, where, in comparison, the relevant physical scales determining the natural polarization (the masses of mother and daughter particles) become indefinitely small. This also happens because the p_T distributions assumed in our simulation have a definite asymptotical power-law behaviour. The high-p_T flatness of the parameters can be disrupted whenever the p_T distribution changes its power-law slope for whatever reason not considered here, for example because a different production mechanism of the mother particle starts dominating, or in the proximity of a kinematic end point, or as a consequence of experimental selections affecting the high-p_T spectrum. It can be seen, in particular, that the lepton

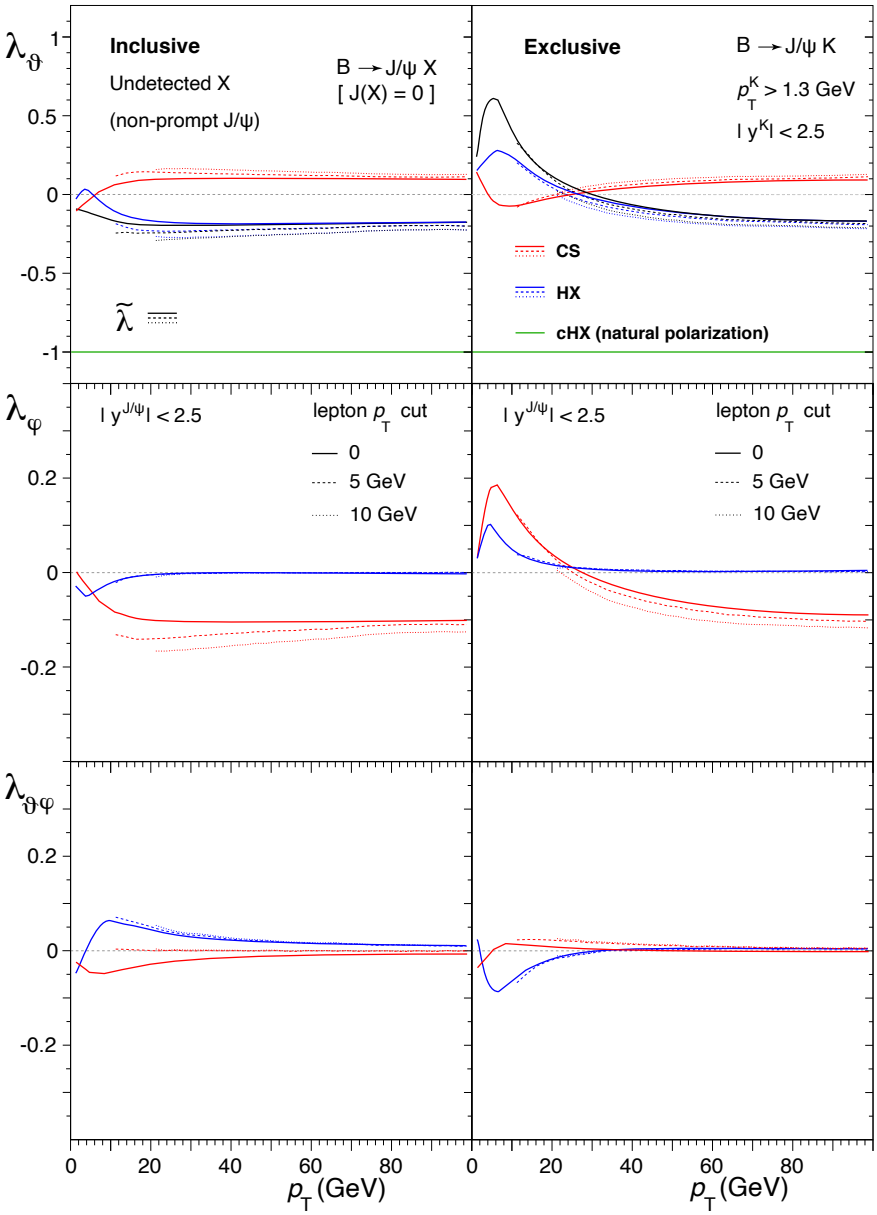

Fig. 6.8 The frame-dependent anisotropy parameters λ_ϑ, λ_φ, and $\lambda_{\vartheta\varphi}$ (top to bottom rows), as well as the frame-invariant parameter $\tilde{\lambda}$ (top row), of the dilepton decay distribution of inclusively observed "non-prompt" J/ψ mesons (left) and of J/ψ mesons observed in fully reconstructed exclusive B decays (right), requiring the detection of the daughter K meson. The results are shown in the HX (blue) and CS (red) frames, as functions of the J/ψ p_T, with no further selection (solid) and when minimum p_T values are required in the analysis for the decay muons (dashed and dotted). The green line represents the natural polarization of the generated events, $\lambda_0 = -1$.

selections and the momentum requirements on X in the exclusive case extend the non-flat behaviour to higher p_{T} values in comparison to the inclusive curves with no experimental selections.

The observed effects can be interpreted in the light of the analytical description made in the previous section. For this purpose we consider the J/ψ p_{T} range 25–30 GeV, where the high-momentum approximation, adopted in that discussion, is well satisfied. Figure 6.9-top shows the p_{T} distribution in the considered interval, well reproduced by a power-law function with best-fit exponent $\rho = 4.7 \pm 0.4$.

The fitted central value of the exponent can be univocally converted (Eqs. 6.17, 6.22 and Fig. 6.6) into the prediction of the $\cos\Theta$ distribution, $f(\cos\Theta)^{\rho-1}$, always meant here, as in the previous section, to be measured in the HX frame. As shown in the middle panel of Fig. 6.9, this prediction is in good agreement with the simulated data for the inclusive case, where no selections are applied to the data. The $|\cos\Theta|$ distribution (shown in the bottom panel of the same figure) is not flat, implying that the smearing effect is only partial and motivating the nonzero observed polarization.

Also the difference between the two experimental approaches can be explained in terms of the $\cos\Theta$ distribution. As seen in Fig. 6.10-top, where the exclusive and inclusive cases are shown by the red and blue histograms, respectively, the additional selection on the K momentum, in particular on p_{T}, further sculpts the distribution in the exclusive measurement, removing events close to $\cos\Theta = +1$. This is, in fact, the configuration where the J/ψ and K are emitted, respectively, forward and backward with respect to the B meson direction and, therefore, where the kaon is most likely to have a laboratory momentum too small to pass the acceptance threshold, so that the event is rejected. The $|\cos\Theta|$ distribution, shown in the middle panel, becomes less sharply unbalanced towards high values when the K momentum selection is applied, that is, its average becomes closer to the average of a uniform distribution, meaning that a fuller smearing should be expected. In fact, a smaller anisotropy is seen in Fig. 6.8, between 25 and 30 GeV, with respect to the inclusive case.

Figure 6.10 also shows, in the bottom panel, how the corresponding $\cos\vartheta$ distributions can be reproduced by integrating the angular distribution W (Eq. 6.8) over $\cos\Theta$. The integration would lead to a flat $\cos\vartheta$ distribution if the $\cos\Theta$ distribution were flat (or linear), while the resulting $\cos\vartheta$ modulation (different in the two cases) is a reflection of how non-uniform the $\cos\Theta$ distribution is. The slightly longitudinal polarization observed in the inclusive case is turned by the K selection criteria into a practically unpolarized result, a coincidence ($\langle\cos^2\Theta\rangle$ turns out to be close to $1/3$ even if the $\cos\Theta$ distribution is not flat nor linear) caused by the fact that inside the considered p_{T} interval the polarization is changing from transverse to longitudinal (as can be seen in Fig. 6.8).

Figures 6.11–6.13 illustrate the effects of requiring minimum p_{T} values on the muons used in the J/ψ reconstruction, referring to the inclusive case. As discussed in Section 2.13 and shown in Fig. 2.18, such requirements strongly sculpt the dilepton distribution. Figure 6.11-left shows the $\cos\vartheta$ distribution, in the HX frame, before (blue) and after (green and red) applying selection cuts on the p_{T} of the muons; the corresponding "acceptance ratios", representing the fraction of events that survive those selection cuts, are presented in Fig. 6.11-right.

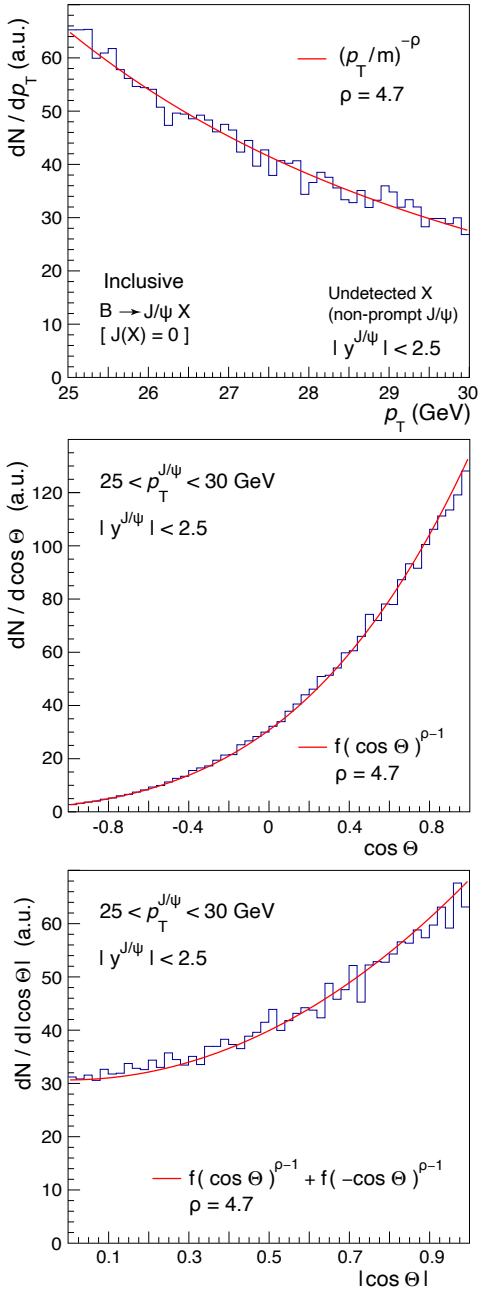

Fig. 6.9 The J/ψ p_{T} distribution (top), as well as the cos Θ (middle) and $|\cos\Theta|$ (bottom) distributions, of simulated B $\rightarrow$ J/ψ X events with unobserved X, for 25 $< p_{\mathrm{T}}^{\mathrm{J}/\psi} <$ 30 GeV. The exponent ρ, determined by fitting the p_{T} distribution, provides a good analytical description of the angular distributions.

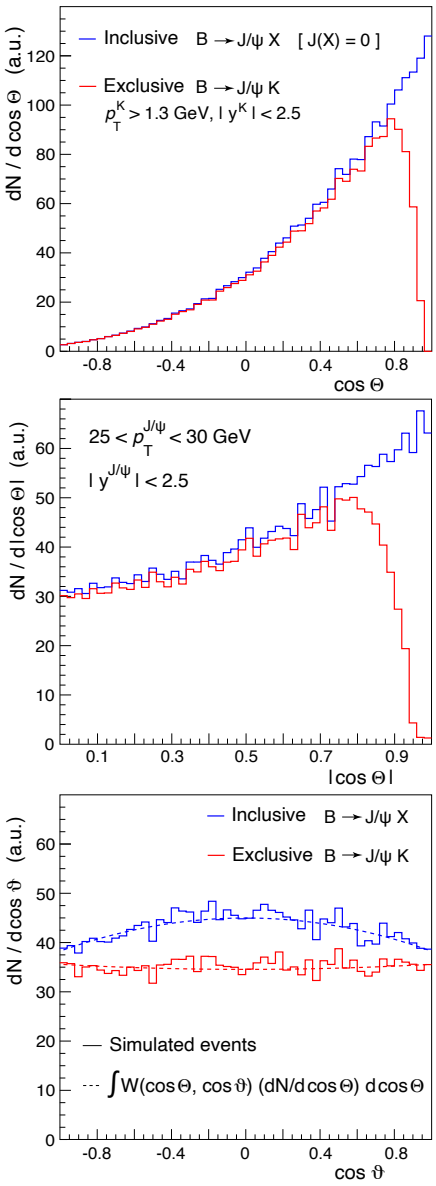

Fig. 6.10 The underlying distributions of $\cos\Theta$ (top) and $|\cos\Theta|$ (middle), in the B HX frame, and the corresponding measured distributions of $\cos\vartheta$ (bottom), in the J/ψ HX frame, for simulated B $\to$ J/ψ X events in the range $25 < p_T^{J/\psi} < 30$ GeV. The blue distributions correspond to measurements using a sample of non-prompt J/ψ events, where X remains unobserved, while the red ones represent analyses of exclusively reconstructed B $\to$ J/ψ K decays, with selection cuts applied on the K momentum. The curves (dashed lines) reproducing the shapes of the $\cos\vartheta$ distributions are obtained by integrating the full angular distribution W (Eq. 6.8) over $\cos\Theta$, taking into account the modulation in the latter distribution.

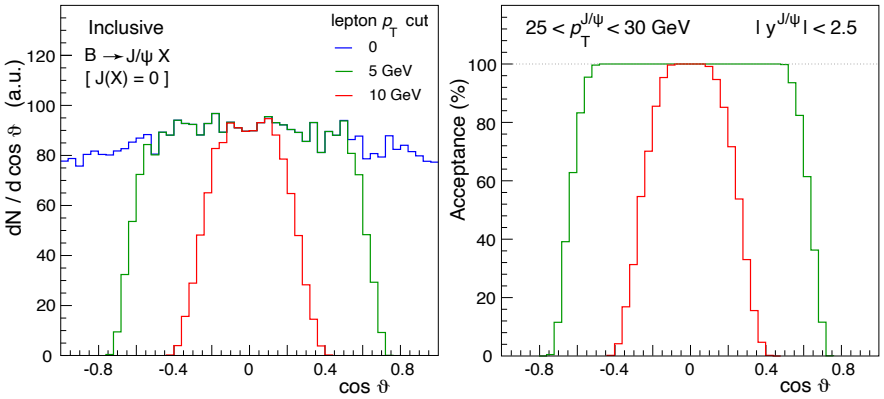

Fig. 6.11 The cos ϑ distribution in the J/ψ HX frame (left), applying (green and red) or not (blue) selection cuts on the p_T of the muons, and corresponding "acceptance ratios" (right), representing the fractions of events surviving the two considered muon p_T cut values.

Naturally, an accurate correction procedure must be applied for the recovery of the physical result. The dashed and dotted lines in Fig. 6.8 indicate the results that an experiment would obtain *after* such corrections have been successfully applied in the data-analysis procedure: they represent the *physical* polarization of the selected sample of J/ψ mesons and their values will always remain, irrespectively of how strong the applied selections are, within the boundaries of the physical domain of the polarization parameters.

Interestingly, however, we see that the obtained polarization result still reflects residual traces of how the sample was selected. This also implies that two experiments applying different selection criteria will obtain different physical results. We could even say, therefore, that there is no such thing as *the* polarization of J/ψ mesons from B decays, at a given collision energy and in given kinematic conditions: the experiment-dependent event selection criteria must concur to an extended definition of the "kinematic domain". This is, actually, a general feature of analyses where the polarization of an indirectly-produced particle is studied ignoring the event-by-event correlations between the mother's and the daughter's decay angles.

Before continuing with the discussion of this interesting and delicate problem, it is worth pausing to explain that these "corrected results" were determined using Eq. 6.9, with the (cos Θ, Φ)-dependent quantities replaced by average values calculated using the events around each considered p_T value. The dilepton decay parameters in the HX (CS) frame are obtained from these relations when the B decay angles in the HX (CS) frame are used for cos Θ and Φ. This procedure assumes that the CC frame can be replaced by the ordinary HX (CS) frame, an approximation valid in the high-momentum limit, with associated uncertainty quantified by Eq. 6.15 (and not applicable, for example, in the study of Higgs decays).

To clarify and explain why experiments applying different selection criteria will obtain different physical results we need to study how the sculpting of the (J/ψ de-

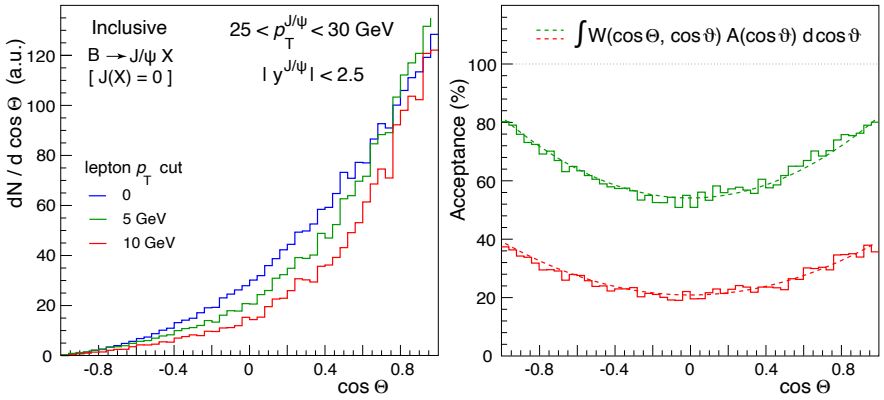

Fig. 6.12 Left: The cos Θ distributions (in the B HX frame) for simulated B $\rightarrow$ J/ψ X events with unobserved X and 25 < $p_T^{J/\psi}$ < 30 GeV, before (blue) and after (green and red) rejecting events with muon p_T smaller than some cut value. The distributions are arbitrarily normalized, to emphasize the shape differences. Right: Corresponding "acceptance ratios", representing the fractions of events surviving the muon selections. See the text for details on the superimposed curves.

cay) cos ϑ distribution affects the (B decay) cos Θ distribution. The concept is the same as illustrated above for the "inverse" effect of how different cos Θ modulations determine different resulting cos ϑ distributions: the two distributions are intimately correlated and any experiment-induced modification of one will have an effect on the other.

We remind that, in the considered high-momentum limit, the variables cos ϑ defined in the CC and HX frames (being cos Θ here defined in the HX frame) are effectively equivalent, so that the dilepton decay angles appearing in Eq. 6.8 can be calculated in the HX frame.

Figure 6.12-left compares the cos Θ distributions obtained before (blue) and after (green and red) muon selections. They are arbitrarily normalized so that the effect on the shapes can be more easily seen: removing low p_T muons induces a loss of events that is more pronounced as cos $\Theta \rightarrow 0$, and the higher is the cut threshold, the bigger is the event loss. The net result, symmetric in cos Θ, is best represented by the acceptance ratios, shown in Fig 6.12-right.

To confirm that it is the sculpting of the observed dilepton cos ϑ distribution that causes this shaping of the unobserved cos Θ distribution, we use the acceptance ratios A(cos ϑ) shown in Fig. 6.11-right as weights in the integration of the four-dimensional angular distribution W (Eq. 6.8) over cos ϑ. While we know that a full and uniform cos ϑ coverage would lead to a uniform cos Θ distribution (in the absence of all other effects mentioned above), using the distribution of the actually accepted dimuon events, A(cos ϑ), to perform the average over cos ϑ leads to the green and red curves shown in the right panel of Fig. 6.12, which reproduce perfectly well the the shapes of the acceptances as functions of cos Θ. Indeed, we can

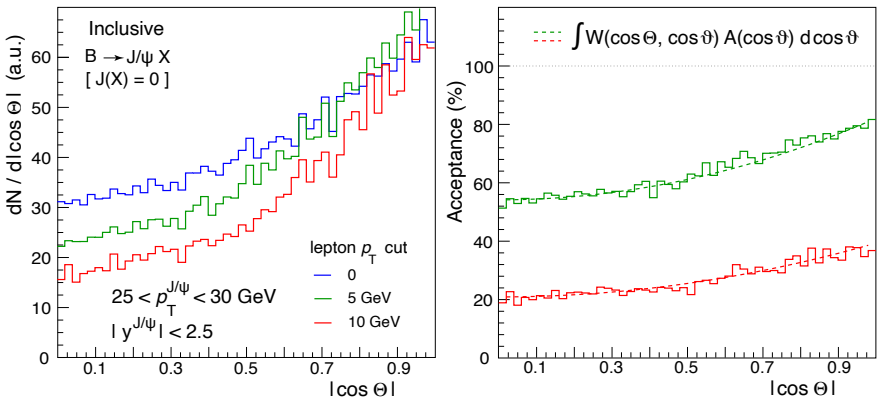

Fig. 6.13 Left: The $|\cos\Theta|$ distributions (in the B HX frame) for simulated $B \to J/\psi\, X$ events with unobserved X and $25 < p_T^{J/\psi} < 30$ GeV, before (blue) and after (green and red) rejecting events with muon p_T smaller than some cut value. The distributions are arbitrarily normalized, to emphasize the shape differences. Right: Corresponding "acceptance ratios", representing the fractions of events surviving the muon selections. See the text for details on the superimposed curves.

conclude that the $\cos\Theta$ modulations induced by the muon selections are a direct reflection of the sculpting of the $\cos\vartheta$ distribution.

As clearly shown by the $|\cos\Theta|$ distributions, and even more visibly by their ratios, both shown in Fig. 6.13, the muon selections accentuate the unevenness of the B decay angular distribution, therefore decreasing the smearing effect and increasing the magnitude of the observed polarization, just as seen in Fig. 6.8. The only way to remove the dependence of the measurement outcome on the event selections specifically applied by the experiment is to adopt a fully four-dimensional analysis approach, taking into account acceptance correlations between the angular variables $(\cos\Theta, \Phi)$ and $(\cos\vartheta, \varphi)$. This is not possible, by definition, when X is not observed (inclusive case) or when the angular analysis is anyhow restricted to its dilepton "projection", as in our definition of the exclusive scenario.

The conclusion of this discussion is that both kinds of measurement should report a full and reproducible definition of the dilepton and single-lepton kinematic phase space where the analysis is made. Two different experimental measurements (or a measurement and a theory prediction) can only be reliably compared if those kinematical constraints are carefully taken into account. In fact, the exact comparison between two results may require detailed simulations of the experimental conditions, including any specific event selections that may affect the $\cos\Theta$ distribution.

As a variation on the theme, Fig. 6.14 shows the result of a simulation of non-prompt $\psi(2S)$ mesons (right panels), made in the same conditions as the J/ψ simulation (left panels). The comparison between the two cases, focusing on the low-p_T region, illustrates the important role of the mother-daughter mass difference. With the decrease of the momentum of the charmonium in the B rest frame, $p' \approx (M_B^2 - M_\psi^2) / (2\, M_B)$, from $p' \simeq 1.7$ GeV for the J/ψ to $\simeq 1.3$ GeV for the $\psi(2S)$,

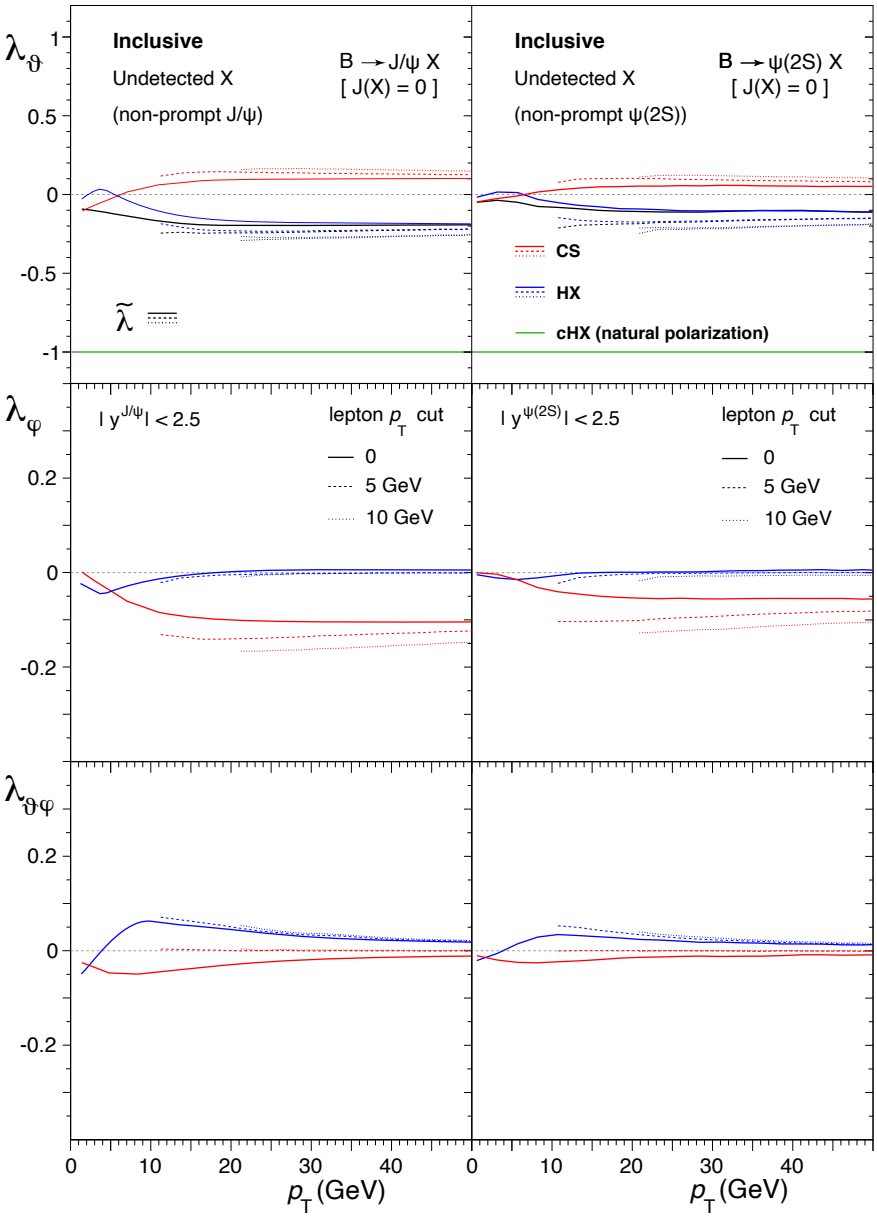

Fig. 6.14 The frame-dependent anisotropy parameters λ_ϑ, λ_φ, and $\lambda_{\vartheta\varphi}$ in the HX and CS frames (top to bottom rows), as well as the frame-invariant parameter $\tilde{\lambda}$ (top row), of the dilepton decay distribution for the inclusive observation of "non-prompt" J/ψ (left) and ψ(2S) (right). The curves (blue, red, and green; solid, dashed and dotted), shown as functions of the p_{T} of the J/ψ or ψ(2S), have the same meaning as those shown in Fig. 6.8. Comparing the non-prompt J/ψ (left) and ψ(2S) (right) patterns illustrates the sensitivity of the results to the difference between the masses of the mother (B mesons) and daughter (J/ψ or ψ(2S)) particles.

the smearing increases significantly and the magnitude of the observed ψ(2S) polarization is only about half of that seen in the J/ψ case.

We turn now to the case of the cascade process $\chi_{c0} \rightarrow \mathrm{J}/\psi\,\gamma$, with $\mathrm{J}/\psi \rightarrow \ell^+\ell^-$, where ℓ represents a muon or an electron. Inclusive and exclusive scenarios are formally defined as previously, except for the selection of the photon in the exclusive case, for which the lower p_{T} threshold of 0.4 GeV is used, as a realistic emulation of typical data analyses in the LHC experiments.

Conceptually, the "inclusive" case no longer represents a realistic measurement, since it is not possible to measure the polarization of J/ψ mesons emitted in χ_{c0} decays without applying selections on the photon momentum to obtain an event sample dominated by χ_{c0} decays. However, the scenario remains interesting, since it depicts the polarization of the (small) fraction of J/ψ mesons coming from χ_{c0} decays in all existing J/ψ polarization measurements, which always address the total "prompt" production, including undistinguished contributions from the feed-down decays of heavier charmonium states. The results for the two scenarios are shown in Fig. 6.15. The differences with respect to the $\mathrm{B} \rightarrow \mathrm{J}/\psi\,X$ case are the input p_{T} distribution, the natural polarization in the cHX frame (transverse, in this case) and, most importantly, the significantly smaller mass difference between mother and daughter particles. In fact, a practically full smearing happens in the inclusive scenario, as anticipated from the almost flat $\cos\Theta$ distributions seen in Fig. 6.6, as a consequence of the sole reduction in mass difference: χ_{c0} decays do give an unpolarized contribution to the inclusive prompt J/ψ production. However, the selection of events with minimum photon p_{T} leads to a slight polarization, according to the mechanism described above for the B decays.

The difference between the χ_{c0} feed-down contribution to inclusive J/ψ polarization and the measured polarization of J/ψ coming from χ_{c0} decays may be at first sight counter-intuitive, but becomes comprehensible as a consequence of the two different selection criteria applied to the $\chi_{c0} \rightarrow \mathrm{J}/\psi\,\gamma$ events. Even if small, the difference is conceptually non-negligible.

While radiative χ_{c0} decays actually play a minor role in J/ψ production, because of their small branching ratio, the decays from χ_{c1} and χ_{c2} produce a fraction of order 25% of the observed J/ψ mesons [27]. It should not be forgotten that a mismatch between the contribution to inclusive polarization and the exclusive polarization of J/ψ from χ_{c1} and/or χ_{c2} has to be expected and should, in principle, be taken into account when "subtracting" the latter from the total inclusive result to deduce the polarization of the directly produced J/ψ mesons. This problem will be addressed in the next sections.

One may wonder what happens if we change the masses of *both* the mother and the daughter particles. As shown in Fig. 6.16 for the exclusive measurement, going from the charmonium to the bottomonium system, which implies an increase in the masses by a factor of three, does not lead to significantly different smearing patterns. The relevant parameter is not the absolute mass of each of the two particles but rather the mass difference or, more precisely, the p' value, which remains in this case rather similar, only changing from 0.30 to 0.39 GeV. The inclusive case is

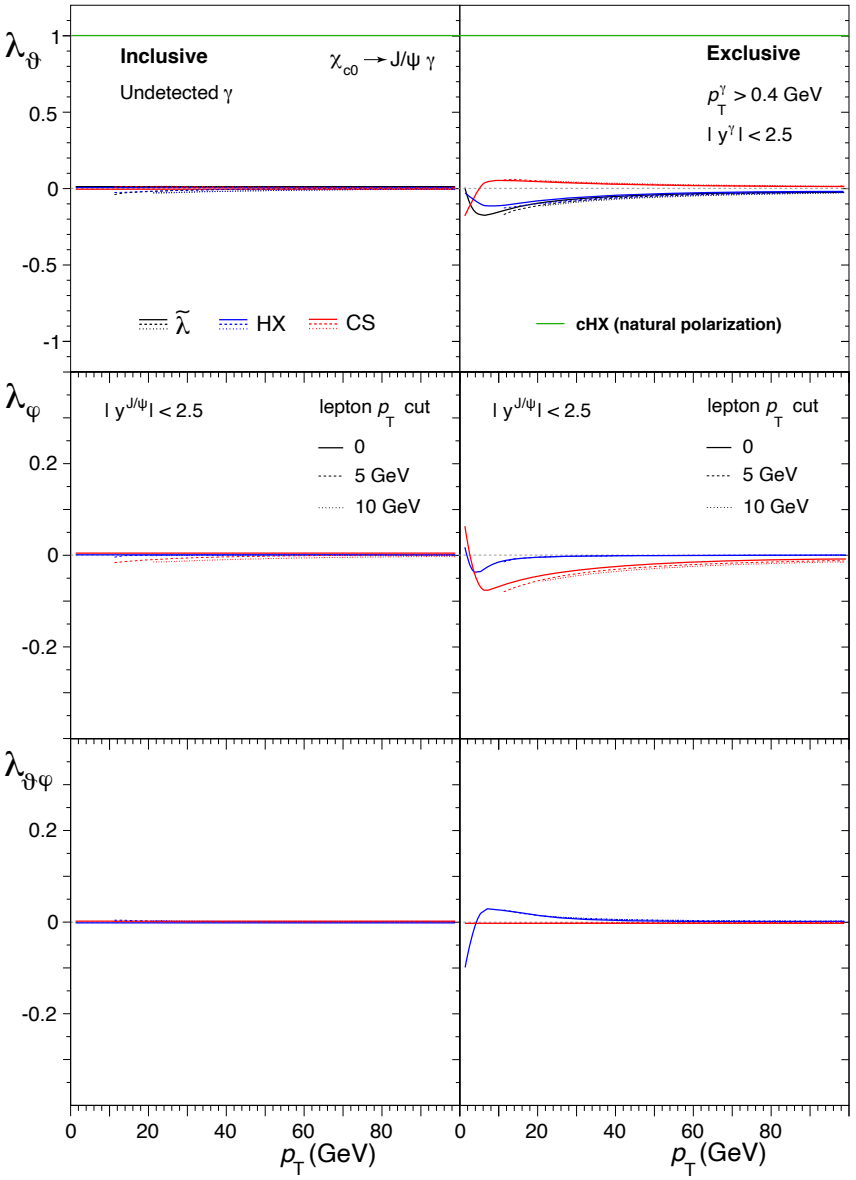

Fig. 6.15 The frame-dependent anisotropy parameters λ_ϑ, λ_φ, and $\lambda_{\vartheta\varphi}$ in the HX and CS frames (top to bottom rows), as well as the frame-invariant parameter $\tilde{\lambda}$ (top row), of the dilepton decay distribution of J/ψ mesons produced in the radiative decays of χ_{c0} mesons, as functions of the J/ψ p_T. The curves (blue, red, and green; solid, dashed and dotted), shown as functions of the p_T of the J/ψ, have the same meaning as those shown in Fig. 6.8, the natural polarization of the generated events being $\lambda_0 = +1$. The inclusively observed J/ψ mesons (left) show essentially no polarization, while those selected by fully reconstructing the exclusive decays (right), requiring the detection of the radiated photon, do not suffer from a full rotational smearing and, hence, lead to a slight, p_T-dependent polarization.

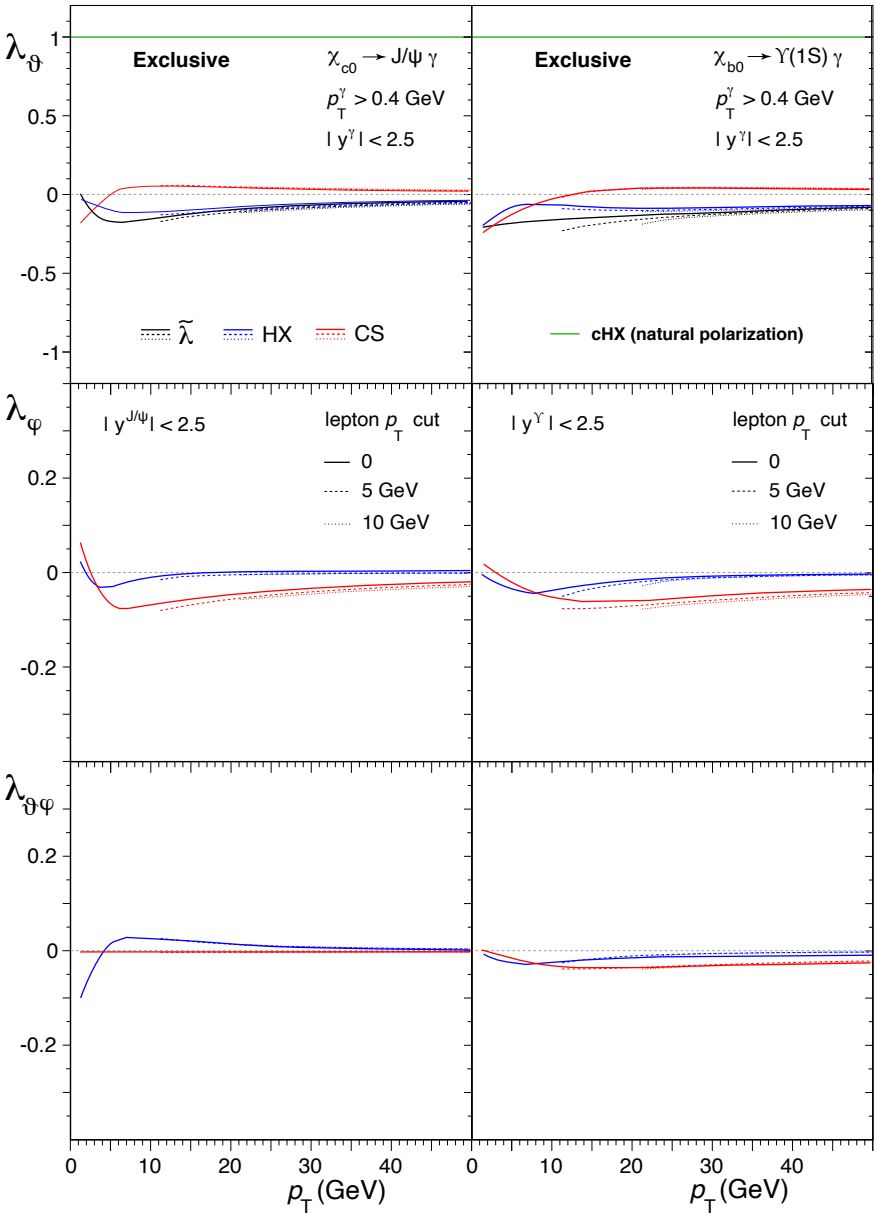

Fig. 6.16 The frame-dependent anisotropy parameters λ_ϑ, λ_φ, and $\lambda_{\vartheta\varphi}$ in the HX and CS frames (top to bottom rows), as well as the frame-invariant parameter $\tilde{\lambda}$ (top row), of the dilepton decay distribution of J/ψ (left) and Υ(1S) (right) mesons observed in fully reconstructed exclusive radiative decays of χ_{c0} and χ_{b0} mesons, respectively. The curves (blue, red, and green; solid, dashed and dotted), shown as functions of the p_T of the J/ψ or Υ(1S), have the same meaning as those shown in Fig. 6.15. Comparing the J/ψ and Υ(1S) patterns illustrates the sensitivity of the results to the difference between the masses of the mother and daughter mesons.

omitted in the comparison given its simplicity: the contribution of $\chi_{b0}(1P)$ decays to inclusive $\Upsilon(1S)$ production remains fully unpolarized.

Finally, Fig. 6.17 shows the results of an exclusive simulation of the decays $H \to J/\psi\,\gamma$ and $H \to Z\,\gamma$, with the requirement that the photon has a minimum p_T of 15 GeV, a realistic value for analyses of experimental data. While in the previous examples p' was smaller than the minimum dilepton momentum accessible to the experiment, now its value falls inside the measured p_T spectrum ($p' \simeq 62$ and 29 GeV, respectively), creating complex polarization patterns. The most significant polarization magnitude is seen, with a resonance-like effect, for $p_T \simeq p'$, as well as in the limit $p_T \to 0$ for the $H \to J/\psi\,\gamma$ case. The decay with larger mass difference produces the less smeared polarization, even approaching the fully transverse limit of the natural one, as shown by the variable $\tilde{\lambda}$, which combines the polar and azimuthal anisotropies.

The decay with larger mass difference produces the less smeared polarization, even approaching the fully transverse limit of the natural one, as shown by the variable $\tilde{\lambda}$, which combines the polar and azimuthal anisotropies. The decay $H \to \Upsilon\,\gamma$ leads to a Υ polarization of a magnitude similar to that of the J/ψ, given the negligible decrease in p' value.

6.4 The unique case of J/ψ production

We have discussed how the observation of an unpolarized (or almost unpolarized) vector particle is indeed possible: the particle must be produced *indirectly*, in the decay of a heavier $J = 0$ particle, which the experiment is unable to fully reconstruct or decides to not take into account in a multi-dimensional angular study, to minimize the complexity of the analysis. The cancellation between oppositely polarizing production processes remains an alternative possibility as explanation of an unpolarized observation, even if it is not only improbable, but also reasonably limited to a restricted transition domain between kinematic regions where individual processes dominate. Most often, different production mechanisms tend to be charactrized, for example, by different p_T distributions. In fact, the existence of concurring processes having exactly opposite polarizations and otherwise indistinguishable kinematic properties should rather be interpreted as the existence of deeper underlying symmetries than those conjectured in the production model.

There is one case where a vector particle appears to be produced unpolarized, even when produced *directly*: the J/ψ meson, as observed by LHC experiments [32]. While at first sight this phenomenon seems to pose a serious challenge to the considerations exposed above, in reality, and as we will see in this section, it provides the most paradigmatic example of what we have discussed in the previous sections.

In fact, the "promptly produced" J/ψ mesons (i.e. after subtracting the contribution from B meson decays) are mostly produced directly: the feed-down decays of the $\psi(2S)$ and χ_c states are responsible for, respectively, around 8 and 25% of the J/ψ yield [27], and the corresponding polarizations are known or constrained exper-

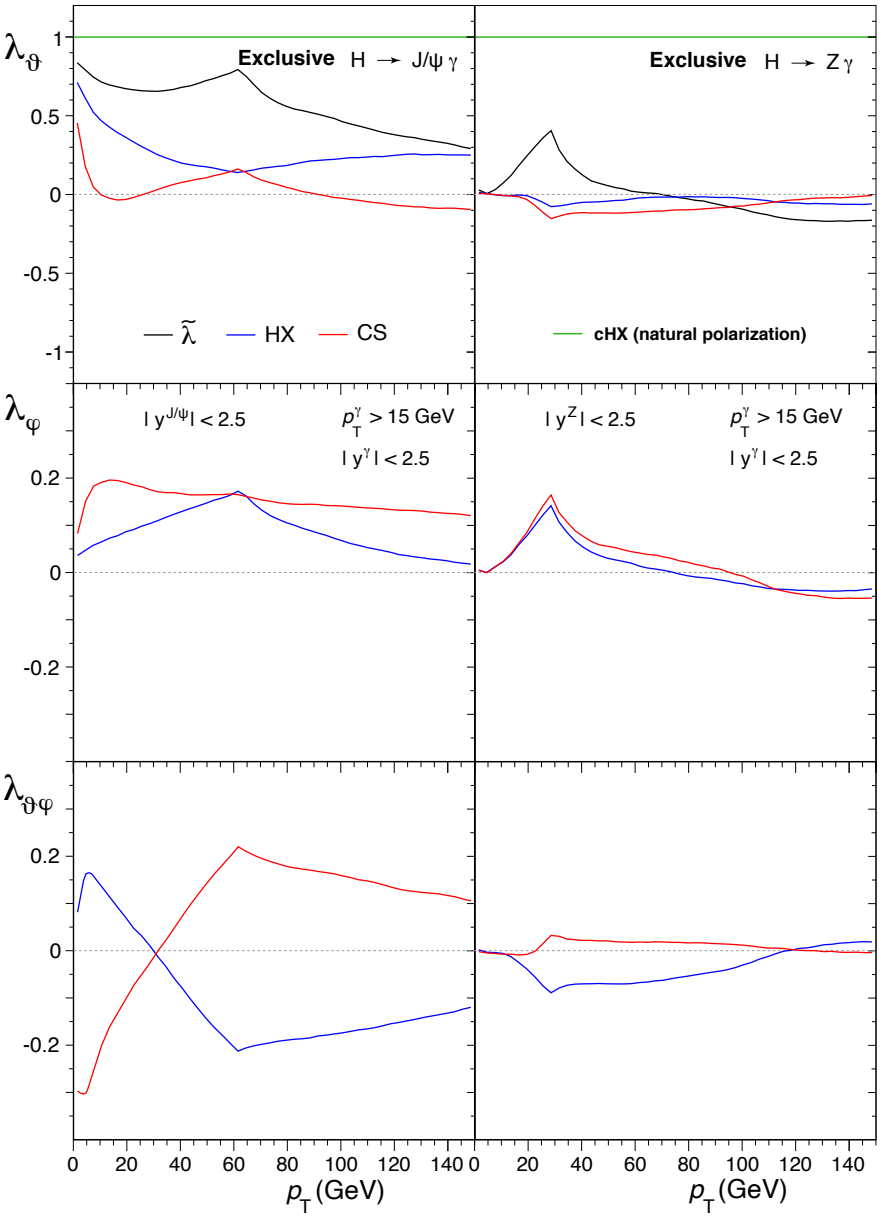

Fig. 6.17 The frame-dependent anisotropy parameters λ_ϑ, λ_φ, and $\lambda_{\vartheta\varphi}$ in the HX and CS frames (top to bottom rows), as well as the frame-invariant parameter $\tilde{\lambda}$ (top row), of the dilepton decay distribution of J/ψ mesons (left) and of Z bosons (right) produced in the decays of Higgs bosons, and selected by fully reconstructing the exclusive decays. The parameters are shown as functions of the p_{T} of the J/ψ or Z.

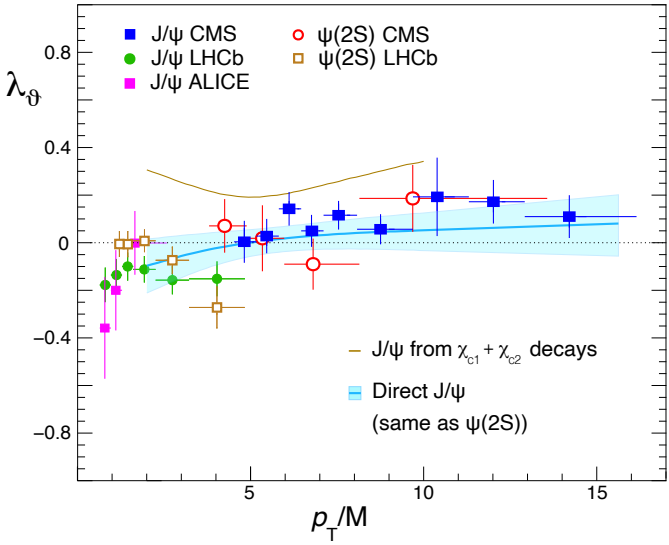

Fig. 6.18 Measurements of J/ψ and ψ(2S) polarizations (λ_ϑ in the HX frame) from LHC experiments [28–31]. The band represents the best-fit result for the polarization of the *directly* produced J/ψ, obtained in a global analysis of charmonium data [32], including χ_c cross sections [12–14] and constraints on the polarization of the J/ψ mesons emitted in χ_c decays [19].

imentally. Moreover, its radial excitation, the ψ(2S) state, is always produced directly, presumably by the same partonic processes as the direct 1S state, and shows a similar polarization pattern: above a certain p_{T} both states are very close to the unpolarized conditions, with no significant kinematic dependence.

Figure 6.18 shows the J/ψ and ψ(2S) polarizations measured by LHC experiments [28–31], as well as the result of a global data fit analysis [32] that also uses experimental constraints on the polarizations of J/ψ mesons emitted in χ_{c1} and χ_{c2} decays [19], providing a reasonably precise determination of the *direct* J/ψ polarization: above $p_{\mathrm{T}}/m \simeq 3$ the J/ψ is produced unpolarized over a wide range of laboratory momentum, making the hypothesis of a polarization cancellation implausible.

The mechanism behind the production of vector quarkonia has always been a matter of debate. The conceptually simplest idea, that a $c\bar{c}$ pair is produced by the parton scattering process as an already colour-neutral state in the "right" spin-angular-momentum configuration $^3S_1$ ("colour singlet' model" [35]), underestimates by a large factor the J/ψ and ψ(2S) production yields seen in hadron collider experiments. This data-to-theory discrepancy was originally seen in the mid-1990's by CDF [36, 37]. Figure 6.19 provides a more modern illustration of this observation by showing the data-theory comparison for the two states, as measured at the LHC [1, 20] and as computed in perturbative QCD at next-to-leading order [33, 34].

While for the J/ψ case part of the large discrepancy can be attributed to the contribution from (prompt) feed-down decays of heavier quarkonia, which corresponds to around one third of the total prompt cross section and is not considered in the cal-

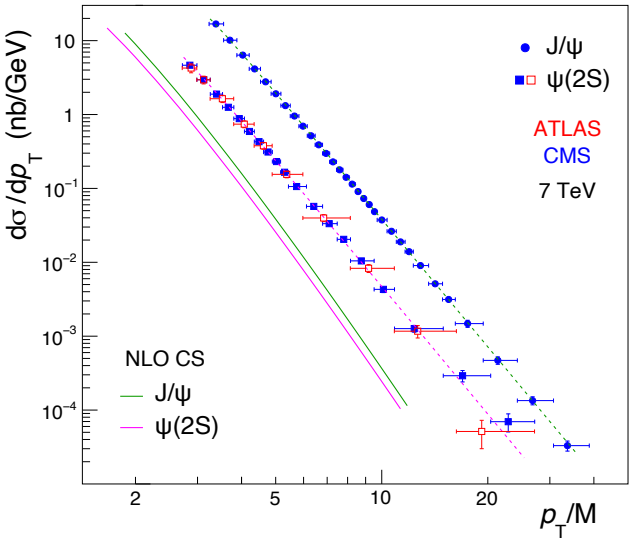

Fig. 6.19 The J/ψ and ψ(2S) production cross sections, as measured at the LHC [1, 20] compared with the next-to-leading order (NLO) predictions of the colour-singlet model [33, 34].

culated curves, the ψ(2S) comparison is free from those contaminations, justifying why the early results became known as "the CDF ψ(2S) anomaly". Clearly, there must exist additional sources of quarkonium production, besides colour-singlet production, dominating at least in high-energy collisions and at high p_T. Also in the mid-1990's, an improved and more general quarkonium production model was developed: the non-relativistic QCD (NRQCD) approach [38].

In NRQCD, the J/ψ (or the $\psi(2S)$) bound state is considered in its superposition of Fock states, consisting not only of a simple $c\bar{c}$ pair, but also of combinations of $c\bar{c}$ pairs with gluons (or light $q\bar{q}$ pairs):

$$\begin{aligned}\left|\psi\left({}^3S_1\right)\right\rangle \;=\; & a_{{}^3S_1^{[1]}}\left|c\bar{c}\left({}^3S_1^{[1]}\right)\right\rangle \\ & +\; a_{{}^3P_0^{[8]}}\left|c\bar{c}\left({}^3P_0^{[8]}\right)\,g\right\rangle \;+\; a_{{}^3P_1^{[8]}}\left|c\bar{c}\left({}^3P_1^{[8]}\right)\,g\right\rangle \;+\; a_{{}^3P_2^{[8]}}\left|c\bar{c}\left({}^3P_2^{[8]}\right)\,g\right\rangle \\ & +\; a_{{}^3S_1^{[8]}}\left|c\bar{c}\left({}^3S_1^{[8]}\right)\,gg\right\rangle \;+\; a_{{}^1S_0^{[8]}}\left|c\bar{c}\left({}^1S_0^{[8]}\right)\,gg\right\rangle \;+\; \ldots\end{aligned} \tag{6.24}$$

The first term, representing an already colour-neutral (singlet) state and having the spin and angular momentum quantum numbers of a vector particle, is the dominant one. In each term of the remaining expansion only the $c\bar{c}$-gluon(s) combination must be colour neutral; the $c\bar{c}$ pair itself is, in general, coloured ("octet" state) and can have any spin and angular momentum quantum numbers, provided that it combines with the gluon(s) into a ${}^3S_1$ state.

The colour-octet terms are suppressed by powers of v, the velocity of the c quark in the $c\bar{c}$ rest frame, which is assumed to be only moderately relativistic. In fact, the

kinetic energy $T \simeq mv^2$ of the bound state is estimated as $T \approx 0.4$–0.6 GeV from the energy splittings between radial and orbital angular momentum excitations of the quarkonium system, which are very similar for charmonium and bottomonium. For the J/ψ, the lightest of the vector quarkonia, v is the largest, at around 0.4.

The probability that the final-state hadron has been produced as the result of the transition from an initial octet $c\bar{c}$ state is evaluated to be of order v^4 smaller than the probability that it came from a singlet $c\bar{c}$. This means that, if in a given experiment $c\bar{c}$ pairs were produced with the same probability in the ${}^3S_1^{[1]}$ singlet as in any octet state, the production via colour-octet $c\bar{c}$ would be responsible for only a few percent of the observed J/ψ mesons, and an even smaller fraction should be expected for the three-times heavier Υ mesons coming from coloured $b\bar{b}$ pairs ($v^4 \approx 10^{-3}$).

These proportions are opposite to what is necessary to explain the LHC observation of cross sections one order of magnitude larger than the singlet-only ones. However, perturbative calculations confirm that the existence of colour-octet processes represents a solution to the problem: the partonic cross sections for the production of colour-octet $c\bar{c}$ pairs are orders of magnitude larger than the colour-singlet one and their inclusion completely overturns the proportion, leading to predicted quarkonium yields dominated by the octet processes.

Furthermore, octet mechanisms offer a potential and interesting solution to another problem of the colour-singlet model: the singlet channel alone leads to a practically fully polarized J/ψ [39], as is the case of all mechanisms producing vector particles directly, a prediction in clear contradiction with the quarkonium polarization measurements made at the LHC.

The production via colour-octet quark-antiquark states is a perfect example of what happens in a cascade process where the mother state is unobserved and, at the same time, the daughter's mass is only slightly smaller than the mother's. The mass difference between the octet state and the physical quarkonium must be, in fact, of the same order as the typical splittings of the mass spectrum (of the order of 0.5 GeV). If the mother happens to be a $J = 0$ state, a complete smearing of the polarization should be expected, in analogy with the $\chi_{c0} \to \mathrm{J}/\psi\,\gamma$ and $\chi_{b0} \to \Upsilon\,\gamma$ decays seen in the previous section (inclusive case). For example, the ${}^3P_0^{[8]} \to \mathrm{J}/\psi\, g$ transition is completely equivalent to the $\chi_{c0} \to \mathrm{J}/\psi\,\gamma$ decay and leads to an unpolarized J/ψ, considering that the gluon is not observed. The most relevant $J = 0$ octet state is, however, the ${}^1S_0^{[8]}$ one. Even if its transition to J/ψ has a more complex topology because it involves the emission of (at least) two gluons and the natural J/ψ polarization in the ${}^1S_0^{[8]}$ rest frame is not easily characterized, the resulting dilepton decay distribution is isotropic. In fact, it should be clear from the considerations in the previous sections that the full rotational smearing occurring for small mass differences with respect to a $J = 0$ mother state is a pure consequence of the flatness of the $|\cos\Theta|$ distribution and is independent of the value of λ_0. Above all, however, it is important to remember that the condition that the mother is a $J = 0$ state remains the most crucial one for the explanation of the observed unpolarized production. Other octet terms, for example the ${}^3S_1^{[8]}$ one, lead, instead, to a full polarization, transverse in this case. It is, therefore, important to determine which of the octet terms are actually significant.

Each individual octet contribution to the cross section includes a non-perturbative constant factor (the long-distance matrix element, LDME), representing the probability of transition from the considered coloured $c\bar{c}$ state to the J/ψ and considered to be "universal", that is, independent of the nature of the short-distance partonic process and equal, for example, in hadroproduction, photoproduction or in indirect production via decays of heavier particles. The LDMEs have not yet been theoretically calculated, and their values are currently determined in the very process of theory-data comparison, through global fit analyses [33, 40–46].

All octet LDMEs corresponding to the terms shown in Eq. 6.24 are equally "small", of order v^4 smaller than the singlet LDME (as discussed above with other words), and it would not be surprising if one of these "corrective" terms were actually dominating over the others: this could not be reasonably considered as a failure of the v hierarchy, which is only an order-of-magnitude expectation. However, a reliable answer to the question of how the octet terms actually compare to one another in magnitude is only recently and gradually coming to light. After several years of difficulties and contradictory or even puzzling results shown by theory studies of the experimental data [47], the results of recent global-fit analyses comparing NRQCD calculations with experimental measurements show that the ${}^1S_0^{[8]}$ octet mechanism is indeed the dominant contribution to direct J/ψ production in high-energy hadron colliders [21, 48–50].

While the explanation of the unique and puzzling observation of the unpolarized production of the J/ψ meson, as a directly produced vector particle, is the result of a long path of understanding, we could, a posteriori, look at the problem from a different perspective and realize that this polarization measurement has always been implying, by itself, an almost unequivocal physical indication: in the considered conditions, the J/ψ must have a "two-step" production mechanism, where the intermediate stage is a $J = 0$ state. This is a good example of how polarization measurements can provide deep insights into the underlying physics.

It remains true that the J/ψ case is rather special and results from concurrent causes. Despite being a "heavy quarkonium" state, the J/ψ is rather light and the v hierarchy does not penalize the octet terms with respect to the singlet ones as it could happen for heavier states. For example, it will be interesting to see if future high-precision polarization measurements for the Υ states will show the same p_{T}-independent lack of polarization or will rather denote the presence of more competing processes by showing a non-negligible kinematic variation. Above all, the overwhelming importance of partonic processes producing octet quark-antiquark pairs is a peculiarity of direct quarkonium production in hadron collider experiments.

This dominance of octet processes does not seem to be present in low-p_{T} measurements made in fixed-target experiments, which actually show significant polarizations of vector quarkonia, as seen in Section 5.4.

It is also reasonably absent in several cases of indirect production, a clear example being when the parent particle (with its constituents) and the accompanying particles have zero colour charge, as in the previously considered $\mathrm{H} \rightarrow \mathrm{J}/\psi\,\gamma$ case, so that the gluon emissions enabling the transformation of a coloured $c\bar{c}$ into the final observable state cannot be reabsorbed within the isolated process. For similar

reasons, the purely electromagnetic transitions from χ_c states do not involve intermediate octet states. In fact, in these examples (as considered in Section 6.3 and in the following Section 6.6), the J/ψ does have a strong natural polarization, potentially observable by choosing the cHX frame. The non-prompt production of J/ψ is a more complex case, as denoted by the several simplifying assumptions we adopted for its description in Section 6.3, and will be further discussed in the next section.

Another counterexample is the production of vector quarkonia in the electromagnetic process $e^+e^- \to Q\overline{Q}$ (with $Q = c, b$), where the quark-antiquark pair is formed through a virtual photon as a colour singlet state and is fully transversely polarized, as shown by the BES experiment [51]. In summary, the unpolarized production of J/ψ mesons in high energy proton-proton collisions is an exceptional observation resulting from exceptional circumstances.

6.5 Non-prompt charmonium production

In the comparison between the two measurement scenarios discussed in Section 6.3 for the polarization of J/ψ mesons emitted in B decays we assumed that the non-prompt J/ψ events, addressed by the "inclusive" measurement without observing or selecting a specific accompanying state X, are due to decays of the kind B $\to$ J/ψ K (with K possibly replaced by another relatively light $J = 0$ state), just as in the "exclusive" measurement, which explicitly selects these decays through additional requirements on the X = K candidates. In reality, non-prompt events result from a spectrum of different B decay channels. In this section we want to address this problem and provide a more realistic description of the phenomenon.

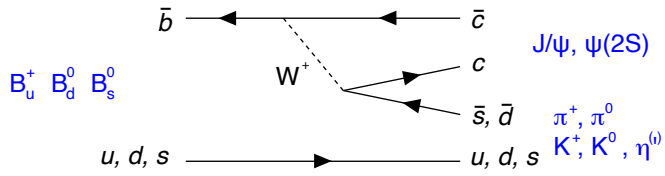

Fig. 6.20 Feynman diagram for the decay B $\to$ J/ψ X, with X = K, π or η.

In an exclusive two-body decay as, for example, B $\to$ J/ψ X, with X = K, π or η, it is reasonable to assume that the formation of the J/ψ bound state often happens through the colour-singlet mechanism, where the decay, represented in Fig 6.20, produces a $c\bar{c}$ state that is already a colour neutral $^3S_1$ state [52, 53]. In fact, the production of an intermediate coloured state (with possibly different quantum numbers) would imply its subsequent emission of soft gluons, necessary for the colour neutralization into a physical hadron; these gluons should then recombine with the spectator quark of the B meson, to form exactly the "right" accompanying particle X, for example a kaon: the probability that this happens should be relatively small.

However, intermediate octet $c\bar{c}$ states are also expected to contribute to the "cocktail" of decay configurations composing the sample of non-prompt events. These cases generally lead to "multi-body" final states, where X is a system of two or more particles (for example, two or more pions). Complex final states are also produced by multiple decay chains, of the kind $\mathrm{B} \to \chi_{c1}/\chi_{c2}/\psi(2\mathrm{S})\,X$, with, for example, $\chi_{c1}/\chi_{c2} \to \mathrm{J}/\psi\,\gamma$ and $\psi(2\mathrm{S}) \to \mathrm{J}/\psi\,\pi^+\pi^-$.

From the point of view of the expected J/ψ polarization, as it can be measured in an inclusive analysis, the variety of the processes described above can be reduced to two categories: the one of the two-body B decays where X is a single kaon (or another relatively light particle) and $J(X) = 0$ (or, more generally, the J/ψ has a natural longitudinal polarization), and the one represented by the ensemble of all the remaining $\mathrm{B} \to \mathrm{J}/\psi$ decays, mostly including multi-body configurations and complex cascade sequences. We will denote these two cases with the expressions "two-body" and "multi-body".

The relevant differences between the two kinds of processes can be summarised as follows. 1) While the J/ψ has a maximally longitudinal natural polarization ($J_{z'} = 0$ in the cHX frame) when it comes from the two-body decays (given how we defined them), the multi-body case represents a mixture of several decays, favouring, in general, all kinds of J/ψ $J_{z'}$ projections: a significantly reduced polarization magnitude is, hence, expected. 2) For the two-body case, the hypothesis that X is, for instance, a kaon or a pion determines the value of the J/ψ momentum p' in the B rest frame, which is one of the parameters determining how the natural polarization is "smeared" when observed, for example, in the J/ψ HX frame. In Eq. 6.12, the second, approximate relation shows that any relatively light X leads to the same $p' \simeq 1.7$ GeV. Instead, in multi-body decays the invariant mass m_X of the accompanying system assumes a distribution of values, possibly significantly larger than the mass of a kaon, and p' is smaller. Also this effect, increasing the uniformity of the smearing (as seen in Section 6.3 when the mother-daughter mass difference, hence p', are smaller), should lead to a smaller observable polarization.

To quantify the importance of these different properties, we will examine results reported by the CLEO [54] and BaBar [55] experiments, which measured the momentum distribution of J/ψ mesons, daughters of B^+ and B^0 mesons produced "almost at rest" in the decay of the $\Upsilon(4\mathrm{S})$ resonance. To interpret these measurements, shown in Fig. 6.21, we will first have a look at some kinematic relations. The B mesons have a momentum of only 0.33 GeV in the $\Upsilon(4\mathrm{S})$ rest frame, and, therefore, the J/ψ momentum (p) distribution measured in the $\Upsilon(4\mathrm{S})$ "laboratory" is a slightly smeared version of the one observed in the B rest frame (p'). The mathematical relations between p' and p, and between m_X and p, are shown in the top and middle panels of Fig. 6.22, where the blue dashed lines represent the hypothetical limit case where the B meson is produced exactly at rest, that is, $p = p'$ (and the relation between m_X and p is simply the one described by Eq. 6.12), while the coloured bands describe the effect of the momentum smearing produced by the small boost of the B meson in the laboratory. The red lines indicate the case of the specific decay $\mathrm{B} \to \mathrm{J}/\psi\,\mathrm{K}$. It can be seen that, for masses comparable to or lighter than the one of a kaon, the p range does not change significantly: we can assume, therefore, that

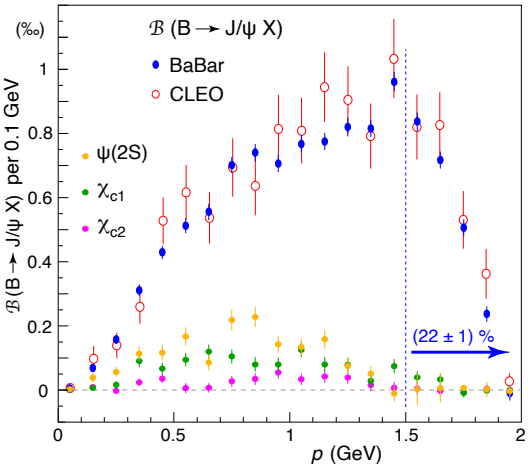

Fig. 6.21 Laboratory momentum distribution of J/ψ mesons emitted in decays of B mesons that are themselves produced by Υ(4S) decays. Besides the inclusive spectrum, the individual contributions (measured by BaBar) from the feed-down decays B $\to [\chi_{c1}|\chi_{c2}|\psi(2S)]\,X$ are also shown.

the ensemble of two-body decays, with $m_X \lesssim 0.5$ GeV, is responsible for the events with $p \gtrsim 1.5$ GeV. The measured p distribution (Fig. 6.21) shows that a large part of the spectrum covers a domain complementary to this, clearly indicating the important role of multi-body decays. For example, the decay chains B $\to \chi_{c1} \to$ J/ψ, B $\to \chi_{c2} \to$ J/ψ, and B $\to \psi(2S) \to$ J/ψ, individually determined by BaBar and also shown in Fig. 6.21, contribute mostly to the region $p < 1.5$ GeV.

In these experimental conditions, very different from those of LHC measurements, it also happens that the polarization measured in the HX frame, that is, taking the direction of **p** as polarization axis, will tend to be very close to the one measured in the cHX frame, with polarization axis along **p′**, given the similarity of the two momenta. Figure 6.22-bottom shows how λ_ϑ is smeared in the HX frame with respect to the hypothetical natural polarization cases $\lambda_\vartheta^{\rm cHX} \equiv \lambda_0 = -1, -0.6$, and -0.2. The first case corresponds to our hypothesis for the two-body processes: the full longitudinal polarization for $p > 1.5$ GeV remains practically unsmeared. BaBar reported the values $\lambda_\vartheta^{\rm HX} = -0.196 \pm 0.044$ for $p < 1.1$ GeV and -0.592 ± 0.032 for $p > 1.1$ GeV. The former value, in the low-p region, refers to multi-body configurations, with no contamination from two-body ones. In Fig. 6.22-bottom we see that the polarization smearing for the case closest to this, $\lambda_\vartheta^{\rm cHX} = -0.2$, leads to a difference $\lambda_\vartheta^{\rm HX} - \lambda_\vartheta^{\rm cHX}$ of order 0.01 on average, considering that the bulk of the events has $0.4 < p < 1.1$ GeV. We will, therefore, assume the range from -0.25 to -0.15 for the average natural polarization of the J/ψ mesons produced in multi-body decays.

As a cross check, we can try to interpret the result in the high-p region, which reflects a mixture of two-body and multi-body events. Assuming, for simplicity, that all the events in the range $p > 1.5$ GeV are due to two-body processes, we derive that these processes contribute $(40 \pm 1)\%$ of the events in the $p > 1.1$ GeV region.

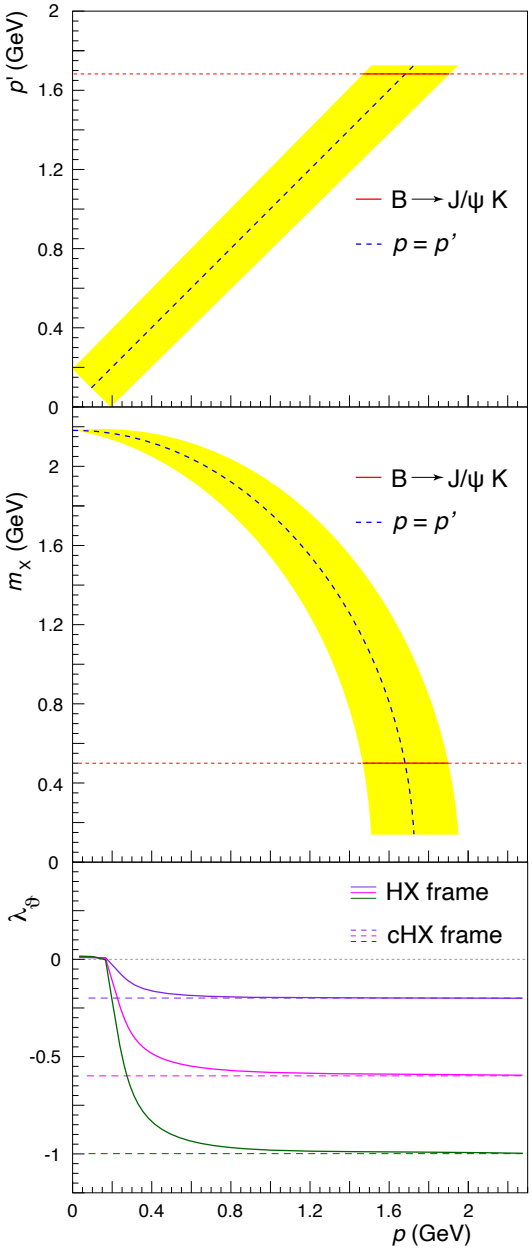

Fig. 6.22 Relations between kinematic variables used in the description of the process $B \to J/\psi X$. Top: momentum smearing from the B rest frame (p') to the $\Upsilon(4S)$ rest frame (laboratory, p). Middle: invariant mass of the X system as a function of p. The $p = p'$ limit is indicated by the blue dashed line, while the red line describes the $B \to J/\psi$ K case. Bottom: polarization smearing from the cHX to the HX frame, for three different natural polarizations: $\lambda_\vartheta^{\mathrm{cHX}} \equiv \lambda_0 = -1$ (green), -0.6 (pink), and -0.2 (purple).

Assuming $\lambda_\vartheta^{\mathrm{cHX}} = \lambda_\vartheta^{\mathrm{HX}} = -0.592 \pm 0.032$ for the average natural polarization of the mixture in the broader range (where the smearing is completely negligible, as seen in Fig. 6.22-bottom) and taking $\lambda_\vartheta^{\mathrm{cHX}}$ between -0.25 and -0.15 for the subsample of multi-body decays, the sum rule of Eq. 1.17, inverted, leads to a value between -1.1 and -0.9 for the two-body polarization, which is in perfect agreement with our assumption that this category of processes leads to fully longitudinal J/ψ mesons.

We will now convert this information, derived from measurements made at the Υ(4S) resonance, into realistic expectations for the non-prompt J/ψ polarization as measurable in a high-energy collider experiment. Here the B meson, generally produced with a large laboratory momentum, emits the J/ψ almost collinearly (Eq. 6.13), so that the HX axis adopted for the observation of the dilepton decay loses its correlation to the natural (cHX) one, and a significantly smeared polarization is observed, as we saw in Section 6.3.

From the spectra measured by BaBar and CLEO, shown in Fig. 6.21, and assuming that the transition from multi-body to two-body events happens at $p \simeq 1.5$ GeV, we see that the fraction of two-body events is $f_{2-\mathrm{body}} = (22 \pm 1)\%$. However, the relative contribution of two- and multi-body processes in (high-energy) hadron collisions is probably not the same as the one observed in the conditions of BaBar and CLEO, given that a different admixture of parent hadron species containing b quarks (additionally including B_s mesons and b baryons) contributes to the non-prompt J/ψ sample. Moreover, it should be kept in mind that, at least hypothetically, certain event selection criteria may alter the proportions between the two kinds of processes in the collected and/or analysed sample, given that, in general, a multi-body event should lead to a higher number of particles traversing the detector. It would be very interesting, in fact, to probe experimentally if the polarization of the non-prompt J/ψ mesons tends to become more significantly longitudinal when stricter selection criteria are applied to retain an event sample that corresponds more closely to the two-body decay limit. For these reasons, besides the realistic mixture using $f_{2-\mathrm{body}}$ we will also report the predictions for the two-body and multi-body individual cases. The measurement itself should be able to consider the two physical options and determine their relative contributions.

The two-body expectation is obtained, as was done in Section 6.3, assuming $\lambda_\vartheta^{\mathrm{cHX}} = -1$ and $m_X = m_K = 0.5$ GeV. For the multi-body case, from the p distribution of Fig. 6.21 and the m_X-to-p correlation shown in Fig. 6.22-middle, we deduce that the 1–2 GeV range of average m_X values is a good representation of the spectrum of physical possibilities. Taking into account that a higher m_X value leads to a more strongly smeared polarization in the experimental frames, we can define reasonable upper and lower margins for the observable polarization magnitude: they correspond, respectively, to the pairs of parameter values $\lambda_\vartheta^{\mathrm{cHX}} = -0.15$, $\langle m_X \rangle = 2$ GeV and $\lambda_\vartheta^{\mathrm{cHX}} = -0.25$, $\langle m_X \rangle = 1$ GeV. The only existing measurement in the case of hadron collisions was performed by CDF [56], which reported λ_ϑ in the HX frame as a function of p_{T}. As shown in Fig. 6.23, where the predictions reflect the specific conditions of the experiment ($|y| < 0.6$), the precision of the data is not sufficient to indicate if one or the other mechanism is predominant. The intermediate prediction assumes the same mixture of processes as in the Υ(4S)

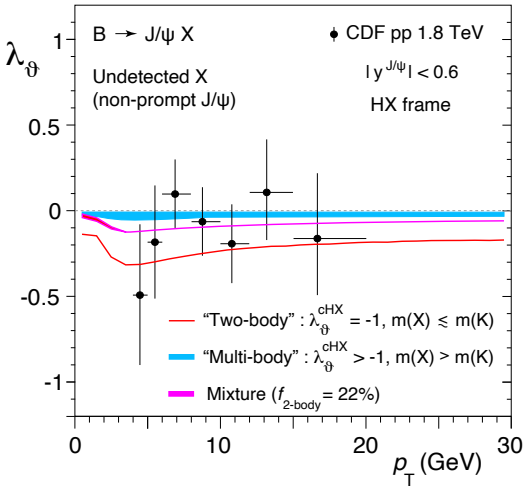

Fig. 6.23 The non-prompt J/ψ polarization (λ_ϑ in the HX frame) measured by CDF in $p\bar{p}$ collisions at $\sqrt{s} = 1.8$ TeV, as a function of p_T, in the rapidity range $|y| < 0.6$, compared to predictions assuming that the J/ψ is produced in "two-body" (red curve) or "multi-body" (blue band) B decays, the width of the band reflecting the variation of the relevant parameters, λ_ϑ^{cHX} and $\langle m_X \rangle$. The pink band represents a mixture of the two kinds of processes, as motivated in the text. The B meson p_T distribution measured by CDF (Fig. 6.7) was used in the simulation. For improved visibility, curves including the small effects of the selection criteria applied to the decay leptons are not shown.

measurements. The multi-body prediction is compatible with the (octet-dominated) NRQCD calculations of non-prompt J/ψ polarization reported in Refs. [57, 58].

Figure 6.24 shows the predictions of all parameters, in the HX and CS frames, calculated for conditions typical of a LHC experiment, already considered in Section 6.3; in fact, the curves for the two-body case were already shown in Fig. 6.8 (we do not report again the lepton selection effects, which are invisible in the multi-body case). The J/ψ mesons produced in multi-body decays look practically unpolarized, This also means that this prediction is, in substance, insensitive to the assumptions made to obtain it: further adjustments in the input parameters λ_ϑ^{cHX} and $\langle m_X \rangle$ are unlikely to change the conclusion that multi-body decays lead to a barely detectable degree of polarization. The almost p_T-independent difference with respect to the polarization of the two-body case, $\Delta\lambda_\vartheta^{HX} \simeq 0.2$, is not negligible, so that some LHC experiments should be able to perform significant measurements of the relative importance of the two kinds of processes.

6.6 Decays from $J > 0$ particles and the "cloning" effect

Among the physical examples considered in Section 6.3, the decay $\chi_{c0} \to J/\psi\,\gamma$, followed by $J/\psi \to \ell^+\ell^-$, illustrates in a paradigmatic way, by virtue of the small

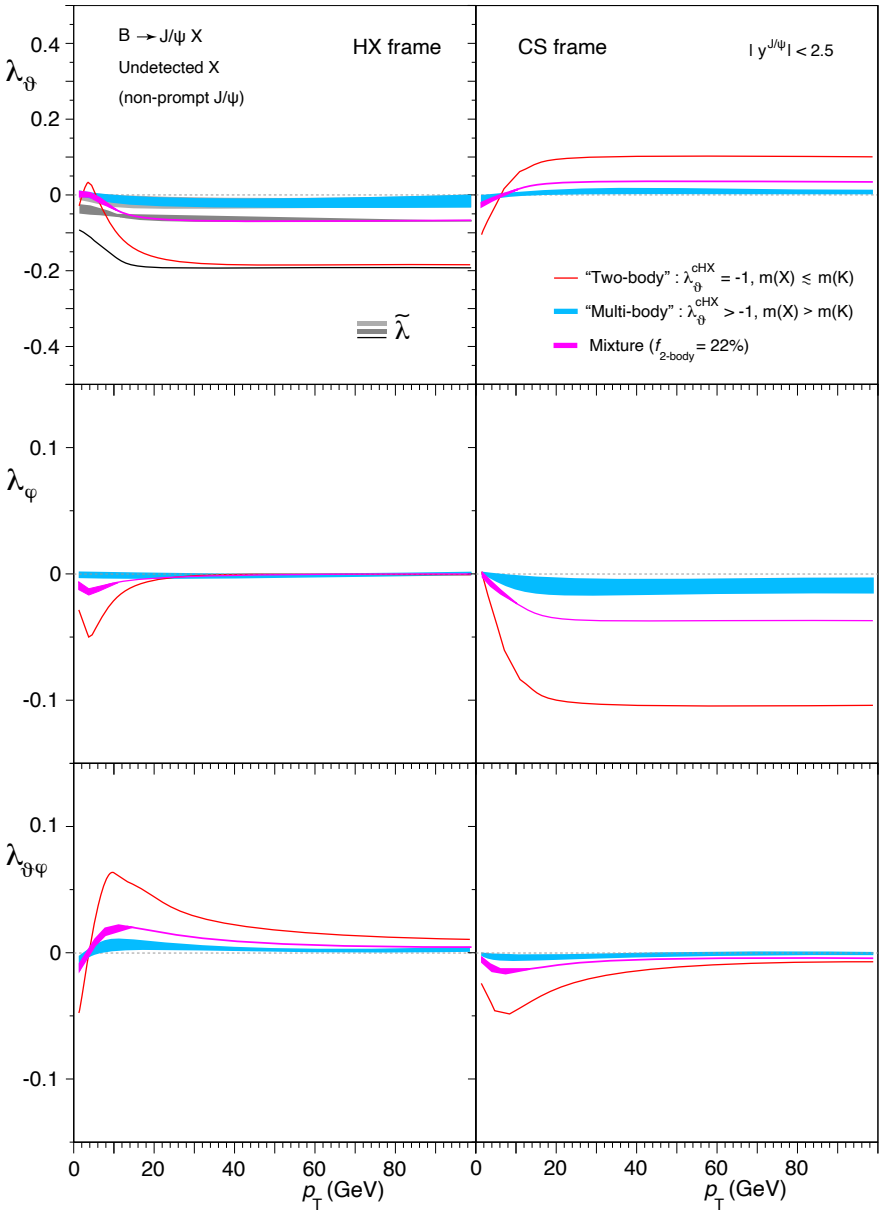

Fig. 6.24 The frame-dependent anisotropy parameters λ_ϑ, λ_φ, and $\lambda_{\vartheta\varphi}$ (top to bottom rows), as well as the frame-invariant parameter $\tilde{\lambda}$ (top row), of the dilepton decay distribution of inclusively observed "non-prompt" J/ψ mesons, in the two complementary assumptions that the J/ψ is produced in "two-body" B decays (same curves as in Fig. 6.8) or in "multi-body" B decays (blue bands, their widths representing the variation of the relevant input parameters, $\lambda_\vartheta^{\mathrm{cHX}}$ and $\langle m_X \rangle$). The pink bands represent a mixture of these two kinds of processes, as motivated in the text. The results are shown in the HX (left) and CS (right) frames, as functions of the J/ψ p_{T}.

mass difference between the χ_{c0} and J/ψ mesons, the randomization effect leading to a zero-polarization contribution in the inclusive dilepton observation. In this section we address its $J = 1$ and 2 counterparts, the χ_{c1} and $\chi_{c2} \to \mathrm{J}/\psi\,\gamma$ decays, as prototype cases to illustrate how the previous considerations can be extended to a wider category of cascade processes, by releasing the crucial $J = 0$ condition. Just as seen in the $J = 0$ case, the following discussion also applies to the bottomonium counterparts, $\chi_{b1,2} \to \Upsilon\,\gamma$.

We should reasonably expect to see, in these cases, a generally polarized vector quarkonium, reflecting the J_z state of the χ. In fact, the first step is to generalize Eq. 6.7, by introducing the sum over the amplitudes a_M defining the angular momentum state of the mother particle O with respect to the system of axes (x, y, z) of Fig. 6.3, with M representing the eigenvalues:

$$|\,O\,\rangle = \sum_{M=-J}^{+J} a_M\,|\,J,\,M\,\rangle_z\ . \tag{6.25}$$

Figure 6.4 provides a visual aid also for the description of this case. The general amplitude for the description of the two-step process is

$$\begin{aligned}
&\mathcal{A}\Big[\,O \to V + X_{K'},\ V \to (\ell^+\ell^-)_{L'''}\Big] \ \propto \\
&\sum_{M=-J}^{+J} a_M \sum_{L''=0,\pm1} \sum_{K''=0,\pm1} {}_{z''}\langle V\,X; 1, L'',\ 1, K''\,|\,\mathcal{B}|\,O; J, M\rangle_{z''} \\
&\qquad\qquad \times \mathcal{D}^{1*}_{K''\,K'}(\Theta, \Phi)\ \mathcal{D}^{1*}_{L''\,L'''}(\vartheta, \varphi)\ ,
\end{aligned} \tag{6.26}$$

where $\mathcal{B}$ represents the underlying dynamics of the decay. In the radiative transition we are studying, we just have to take into account that the $J_{z''}$ projections of V (L'') and X (K'') must sum to M, because the z'' and z axes represent the same direction in the definition of the CC frame:

$$\begin{aligned}
&\mathcal{A}\Big[\,O \to V + X_{K'},\ V \to (\ell^+\ell^-)_{L'''}\Big] \ \propto \\
&\sum_{M=-J}^{+J} a_M \sum_{L''=0,\pm1} \sum_{K''=0,\pm1} \langle 1, L'',\ 1, K''\,|\,J, M\,\rangle\ \delta_{L''+K'',\,M} \\
&\qquad\qquad \times \mathcal{D}^{1*}_{K''\,K'}(\Theta, \Phi)\ \mathcal{D}^{1*}_{L''\,L'''}(\vartheta, \varphi)\ .
\end{aligned} \tag{6.27}$$

Moreover, the squared amplitude must be summed over $K' = \pm1$ ($J_{z'}$ projection of X = photon over the cHX z' axis of Fig. 6.1; corresponding to setting $\lambda_0 = +1$ in the formulas for the $J = 0$ case) and $L''' = \pm1$ (dilepton decay of V).

In reality, we are making an approximation in the derivation of the anisotropies of the χ_c and subsequent J/ψ decays. In these transitions the photon emission is sensitive to the internal electromagnetic charge structure of the quarkonium state. As a result, the photon can effectively have an orbital angular momentum component and, therefore, a total angular momentum of up to $J_\gamma = 2$ (in $\chi_{c1} \to \mathrm{J}/\psi\,\gamma$) and up to $J_\gamma = 3$ (in $\chi_{c2} \to \mathrm{J}/\psi\,\gamma$). To account for the contributions of these higher

J_γ values, the total amplitude should be calculated summing also over J_γ, using the corresponding photon $\mathcal{D}$ matrix and the Clebsch–Gordan coefficients for $J \to (J = 1) + J_\gamma$, and the partial amplitudes would now have a dependence on J and J_γ, contained in the matrix elements of $\mathcal{B}$. However, these effects can be neglected, since they only cause a small change of the values of the anisotropy parameters [59] and do not have a significant influence in the illustrative considerations that follow.

The resulting expression of the four-dimensional angular distribution for the most generic χ_{c1} angular momentum state of Eq. 6.25, depending on the complex amplitudes a_M, can be found in Appendix B. The corresponding χ_{c2} distribution is not included in that appendix because its much more complex expression extends over almost two pages, without offering particularly original insights into the properties of the observable polarization. Here we report the much simpler distributions produced by the χ_{c1} and χ_{c2} mesons when they are pure eigenstates of J_z, i.e., $|J, M\rangle_z$:

$$W_{\mathrm{CC}}(\cos\Theta, \Phi, \cos\vartheta, \varphi) \propto \tag{6.28}$$

$$\begin{cases} (1+\cos^2\Theta)(1+\cos^2\vartheta) - \sin^2\Theta\,\sin^2\vartheta\,\cos2(\varphi-\Phi) & \text{for } \chi_{c1}\,,\ M=0\,, \\ 1-\cos^2\Theta\cos^2\vartheta - \frac{1}{4}\sin2\Theta\,\sin2\vartheta\,\cos(\varphi-\Phi) & \text{for } \chi_{c1}\,,\ M=\pm1\,, \\ 9\,(1+\cos^2\Theta\cos^2\vartheta) - 7\,(\cos^2\Theta+\cos^2\vartheta) + \\ \sin^2\Theta\,\sin^2\vartheta\,\cos2(\varphi-\Phi) - 2\sin2\Theta\,\sin2\vartheta\,\cos(\varphi-\Phi) & \text{for } \chi_{c2}\,,\ M=0\,, \\ 1-\cos^2\Theta\cos^2\vartheta + \frac{1}{4}\sin2\Theta\,\sin2\vartheta\,\cos(\varphi-\Phi) & \text{for } \chi_{c2}\,,\ M=\pm1\,, \\ (1+\cos^2\Theta)(1+\cos^2\vartheta) & \text{for } \chi_{c2}\,,\ M=\pm2\,. \end{cases}$$

As already noticed for the $J = 0$ case, the distribution is in all cases invariant by exchange between $(\cos\Theta, \Phi)$ and $(\cos\vartheta, \varphi)$. The origin of the symmetry is in fact visible in the amplitude of Eq. 6.28, where L'' and K'' are completely equivalent as running variables of two identical sums (with the Clebsch–Gordan coefficient reflecting the commutative property of the sum) and, therefore, exchanging the upper and lower case angles is equivalent to exchanging L''' with K'. As long as the square amplitude is summed over the same set of values for L''' and K' (±1, in this case), the exchange has no effect on the final result.

Figure 6.25 gives an intuitive illustration of the symmetry. The adopted frame (Fig. 6.3) has *one* set of axes providing the reference directions for both angular distributions, the one of the photon (and J/ψ) emission in the χ_c rest frame and the one of the dilepton emission in the J/ψ rest frame. In this situation, it is evident from the figure that exchanging the "names" of γ and $\ell^+\ell^-$ (i.e., the blue and green colours), two equivalent objects from the point of view of angular momentum, only modifies the individual event configuration, but not the resulting event distribution.

Equation 6.28 can be translated into a form that uses the coefficients of the dilepton distribution (similarly to what was done in Eq. 6.9), as measured in the CC frame (coinciding, in the case considered, with the corresponding laboratory-referred frame, HX or CS) and as functions of Θ and Φ. The λ_ϑ, λ_φ, $\lambda_\varphi^\perp$, $\lambda_{\vartheta\varphi}$, and $\lambda_{\vartheta\varphi}^\perp$ parameters are reported in Table 6.1, including the χ_{c0} case (Eq. 6.9 with $\lambda_0 = +1$).

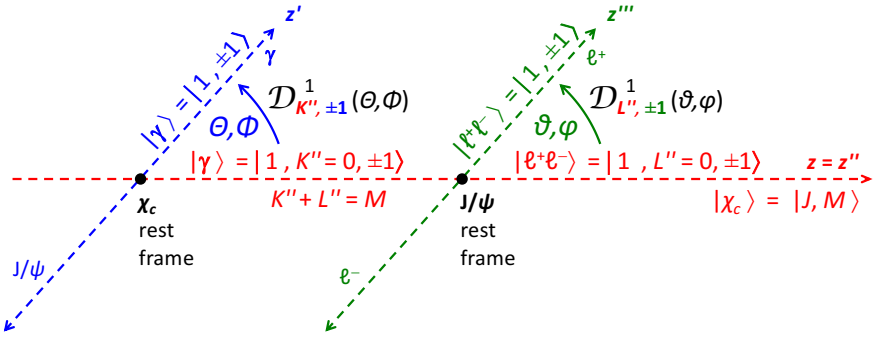

Fig. 6.25 Illustration of the origin of the $(\Theta, \Phi) \rightleftarrows (\vartheta, \varphi)$ exchange symmetry for the angular distribution of the cascade decay $\chi_{cJ} \to \mathrm{J}/\psi\,\gamma$, followed by $\mathrm{J}/\psi \to \ell^+\ell^-$.

Table 6.1 The (Θ, Φ)-dependent J/ψ decay anisotropy parameters for the cascade process $\chi_{cJ} \to \mathrm{J}/\psi\,\gamma$, $\mathrm{J}/\psi \to \ell^+\ell^-$, when the χ_{cJ} is an eigenstate of J_z with eigenvalue M.

	χ_{c0}	χ_{c1}		χ_{c2}		
	$(M=0)$	$M=0$	$M=\pm1$	$M=0$	$M=\pm1$	$M=\pm2$
λ_ϑ	$\frac{-1+3\cos^2\Theta}{3-\cos^2\Theta}$	$+1$	$-\cos^2\Theta$	$\frac{-7+9\cos^2\Theta}{9-7\cos^2\Theta}$	$-\cos^2\Theta$	$+1$
λ_φ	$\frac{\sin^2\Theta\cos 2\Phi}{3-\cos^2\Theta}$	$\frac{-\sin^2\Theta\cos 2\Phi}{1+\cos^2\Theta}$	0	$\frac{\sin^2\Theta\cos 2\Phi}{9-7\cos^2\Theta}$	0	0
$\lambda^\perp_\varphi$	$\frac{\sin^2\Theta\sin\Phi}{3-\cos^2\Theta}$	$\frac{-\sin^2\Theta\sin 2\Phi}{1+\cos^2\Theta}$	0	$\frac{\sin^2\Theta\sin 2\Phi}{9-7\cos^2\Theta}$	0	0
$\lambda_{\vartheta\varphi}$	$\frac{\sin 2\Theta\cos\Phi}{3-\cos^2\Theta}$	0	$-\frac{\sin 2\Theta\cos\Phi}{4}$	$-\frac{2\sin 2\Theta\cos\Phi}{9-7\cos^2\Theta}$	$\frac{\sin 2\Theta\cos\Phi}{4}$	0
$\lambda^\perp_{\vartheta\varphi}$	$\frac{\sin 2\Theta\sin\Phi}{3-\cos^2\Theta}$	0	$-\frac{\sin 2\Theta\sin\Phi}{4}$	$-\frac{2\sin 2\Theta\sin\Phi}{9-7\cos^2\Theta}$	$\frac{\sin 2\Theta\sin\Phi}{4}$	0

If the distribution is integrated over $\cos\Theta$ and Φ uniformly, that is, in the absence of modulations created by experimental selections as those discussed in Section 6.3, it can be seen that all azimuthal terms vanish (not a surprising result, as we are in the special case when the χ_{cJ} is in a pure J_z state) and λ_ϑ in the CC frame assumes (being $\langle\cos\Theta\rangle = 1/3$) nonzero values, except for the χ_{c0} case. In particular, we see that the J/ψ mesons produced in decays of χ_{c1} mesons with $M = 0$ or of χ_{c2} mesons with $M = \pm2$ are fully transverse ($\lambda_\vartheta = +1$), those from decays of χ_{c1} or χ_{c2} mesons with $M = \pm1$ are half transverse and half longitudinal ($\lambda_\vartheta = -1/3$), and those from decays of χ_{c2} mesons with $M = 0$ are $2/3$ longitudinal and $1/3$ transverse ($\lambda_\vartheta = -3/5$). As anticipated, the "smearing" effect leading to the unpolarized observation

only happens when the mother particle has $J = 0$, while the decay from a polarized $J > 0$ particle produces, in general, a polarized daughter reflecting the mother's polarization.

There is no obvious pattern of correspondence between the χ_{cJ} and J/ψ polarizations. However, a common denominator can be recognized in how the *shape* of the distribution is "propagated" from mother to daughter. In fact, the previously mentioned $(\Theta, \Phi) \leftrightharpoons (\vartheta, \varphi)$ exchange symmetry implies that the integrated distributions $W(\cos\Theta, \Phi)$ and $W(\cos\vartheta, \varphi)$ are functionally identical: the two-body decay distribution $\chi_{cJ} \to \mathrm{J}/\psi\,\gamma$ can be written exactly as in Eq. 1.16, replacing the lower-case angles with the upper-case ones and using the coefficients of Table 6.1 with the opposite replacement of symbols. Integrating uniformly over $\cos\vartheta$ and φ, we obtain that both the χ_{c1} with $M = 0$ and the χ_{c2} with $M = \pm 2$ decay into J/$\psi\,\gamma$ with a $\cos\Theta$ distribution of polar parameter $\lambda_\Theta = +1$, the χ_{c1} or χ_{c2} with $M = \pm 1$ produce a distribution with $\lambda_\Theta = -1/3$ and the χ_{c2} with $M = 0$ has $\lambda_\Theta = -3/5$. Comparing these numbers with those reported a few lines above, we see that the anisotropy parameters are the same for the decays of mother and daughter, even if the polarization states are very different. Also the χ_{c0} decay fits this interpretation: both the decay $\chi_{c0} \to \mathrm{J}/\psi\,\gamma$ and the following $\mathrm{J}/\psi \to \ell^+\ell^-$ are isotropic. What unifies all these cases is, therefore, that the shape of the two-body distribution is "cloned" from the mother's to the daughter's decay, as illustrated in Fig. 6.26.

Just as seen for the "smearing" effect in Section 6.3, deviations from the "cloning" condition are expected in real experiments. For χ_{c1} and χ_{c2}, as for χ_{c0}, the J/ψ CC frame is well approximated by, for example, the HX one (when the HX frame is chosen for the χ_c), at least in LHC experiments, where the laboratory momenta of the involved particles are always much larger than their masses. Therefore, the four-dimensional angular distributions reported above can effectively be measured defining $\cos\vartheta$ and φ as the angular variables in the experimental J/ψ HX frame. Consequently, no large "anti-smearing" (or, rather, "anti-cloning") effects as those seen in Higgs decays (especially close to the limits $p_\mathrm{T} \simeq p'$ and $p_\mathrm{T} \ll M$, not relevant in here) should be observed.

What can still moderately perturb the cloning effect in the χ_c decays is the shaping of the $\cos\Theta$ distribution induced by experimental selections in the exclusive observations where the photon is reconstructed. However, as seen in Table 6.1, several of the anisotropy parameters for J/ψ from χ_{c1} and χ_{c2} are $\cos\Theta$-independent (λ_ϑ for $M = \pm 1$ as well as λ_φ and/or $\lambda_{\vartheta\varphi}$ in several cases), so that deviations from an exact cloning should be moderate. In particular, no visible deviations exist in inclusive observations, as already seen for the χ_{c0} case.

Figures 6.27 and 6.28 show, respectively for the χ_{c1} and χ_{c2}, the resulting J/ψ anisotropy parameters for exclusive measurements in the HX frame (blue curves) or in the CS frame (red curves), when the χ_c mesons are produced with J_z projections $M = 0, \pm 1$ and ± 2 (panels from left to right) along the HX axis. The solid, dashed and dotted curves represent the effect of applying threshold values of 0.4, 1 and 2 GeV, respectively, on the p_T of the detected photon. The differences with respect to the cloned parameter values, represented by the green (HX frame) and magenta (CS frame) curves, corresponding to the inclusive measurements, are relatively small.

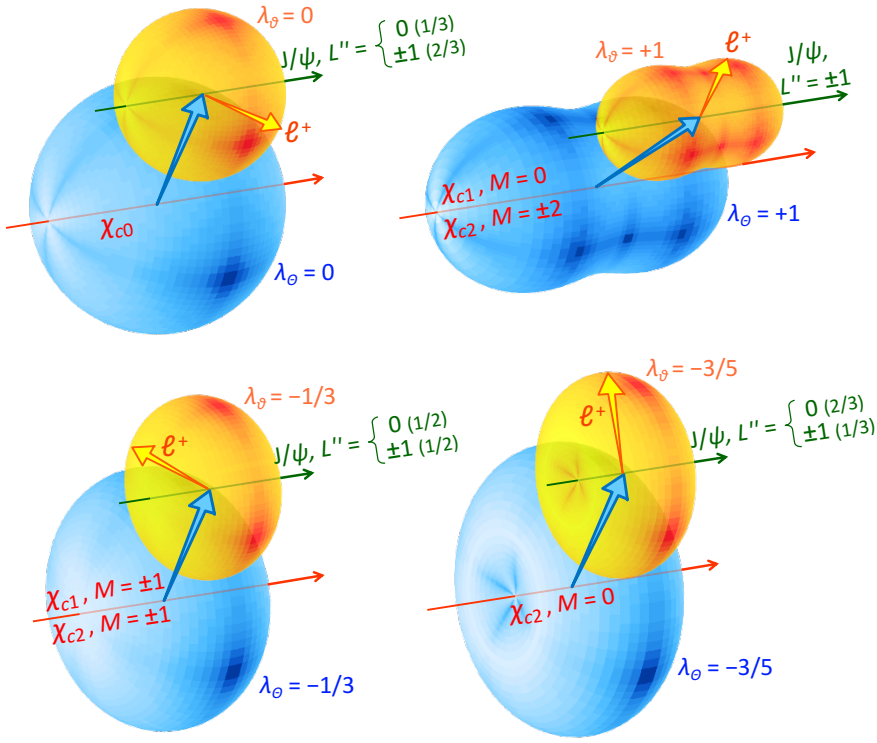

Fig. 6.26 Illustration of the "cloning" effect: the $\chi_{cJ} \to \mathrm{J}/\psi\,\gamma$ decay and the subsequent $\mathrm{J}/\psi \to \ell^+\ell^-$ decay have identical distributions of the products' directions.

Nevertheless, they are not zero, meaning that the polarization parameters determined in an exclusive measurement of J/ψ mesons produced in χ_c decays are not always identical to those describing the contribution of χ_c feed-down to inclusive prompt J/ψ production.

In particular, we even see values of $\tilde{\lambda}$ larger than +1 towards low p_{T} in the χ_{c1} case for $M = 0$. This is a spurious effect of the requirement that the photon p_{T} must be larger than 0.4 GeV, which, besides removing configurations with $\cos\Theta$ close to +1 (for any p_{T} value), as mentioned in Section 6.3, also sculpts the azimuthal distribution of the J/ψ emission direction when p_{T} is small, rejecting events with Φ around ±180°, for which the photon is emitted at $\Phi \to 0°$, that is, towards the beam direction. This leads to negative values of the average $\langle \cos 2\Phi \rangle$ and, therefore, to a positive λ_φ, according to the corresponding formula in Table 6.1. Since λ_ϑ remains unchanged, being independent of the J/ψ emission angles, this experimentally induced azimuthal component results in an increase of $\tilde{\lambda}$ beyond +1. This is not an unphysical effect (in fact, $\tilde{\lambda}$ has no upper limit, unlike λ_ϑ); it is created by the selection of a peculiar (but physical) subset of events.

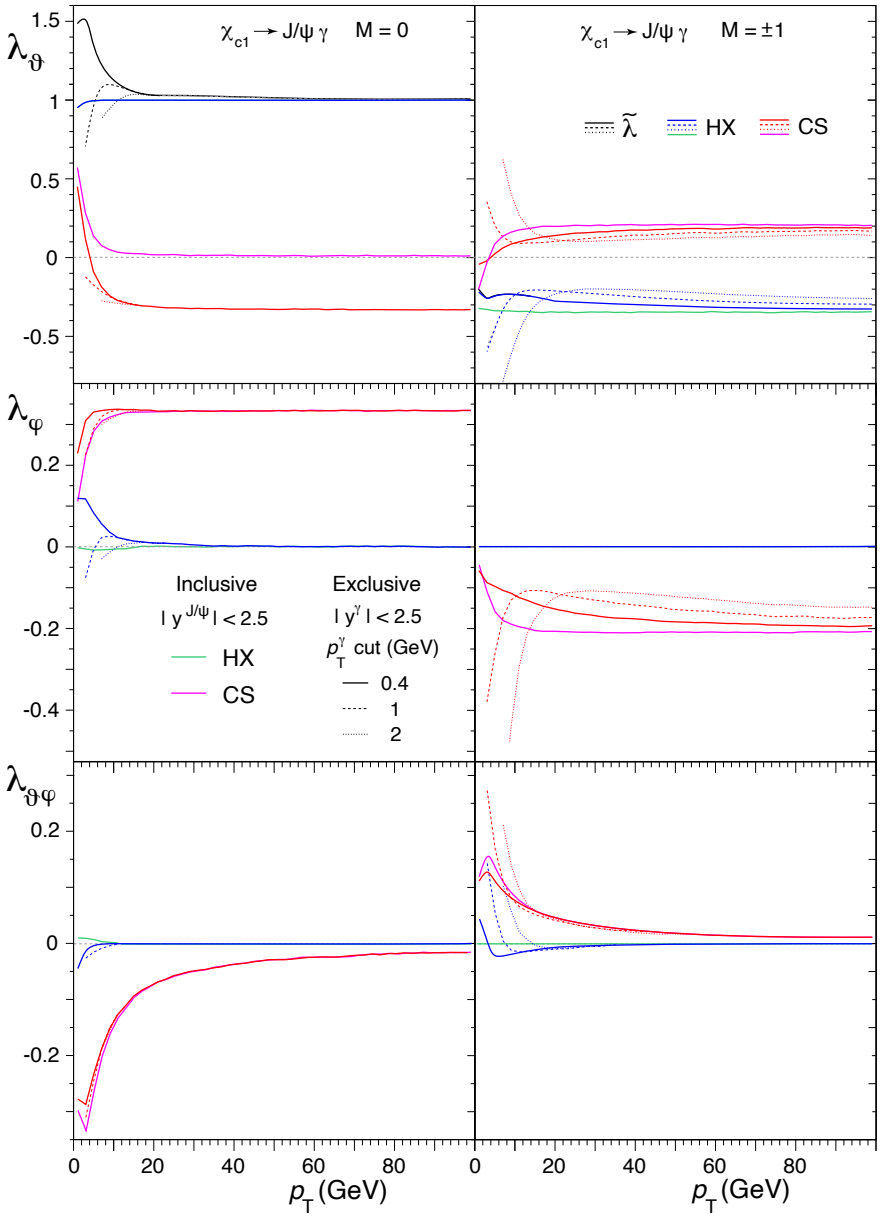

Fig. 6.27 The frame-dependent anisotropy parameters λ_ϑ, λ_φ and $\lambda_{\vartheta\varphi}$ (top to bottom rows), in the HX (blue) and CS (red) frames, as well as the frame-invariant parameter $\tilde{\lambda}$ (top row), of the dilepton decay distribution of J/ψ mesons observed in fully reconstructed exclusive radiative decays of χ_{c1} mesons produced with J_z projections $M = 0$ (left) and $M = \pm 1$ (right) along the HX axis. The solid, dashed and dotted curves correspond to increasing cuts on the photon p_T. The corresponding curves for inclusive measurements, where the cloning effect occurs almost exactly, are also shown, in green (HX) and magenta (CS).

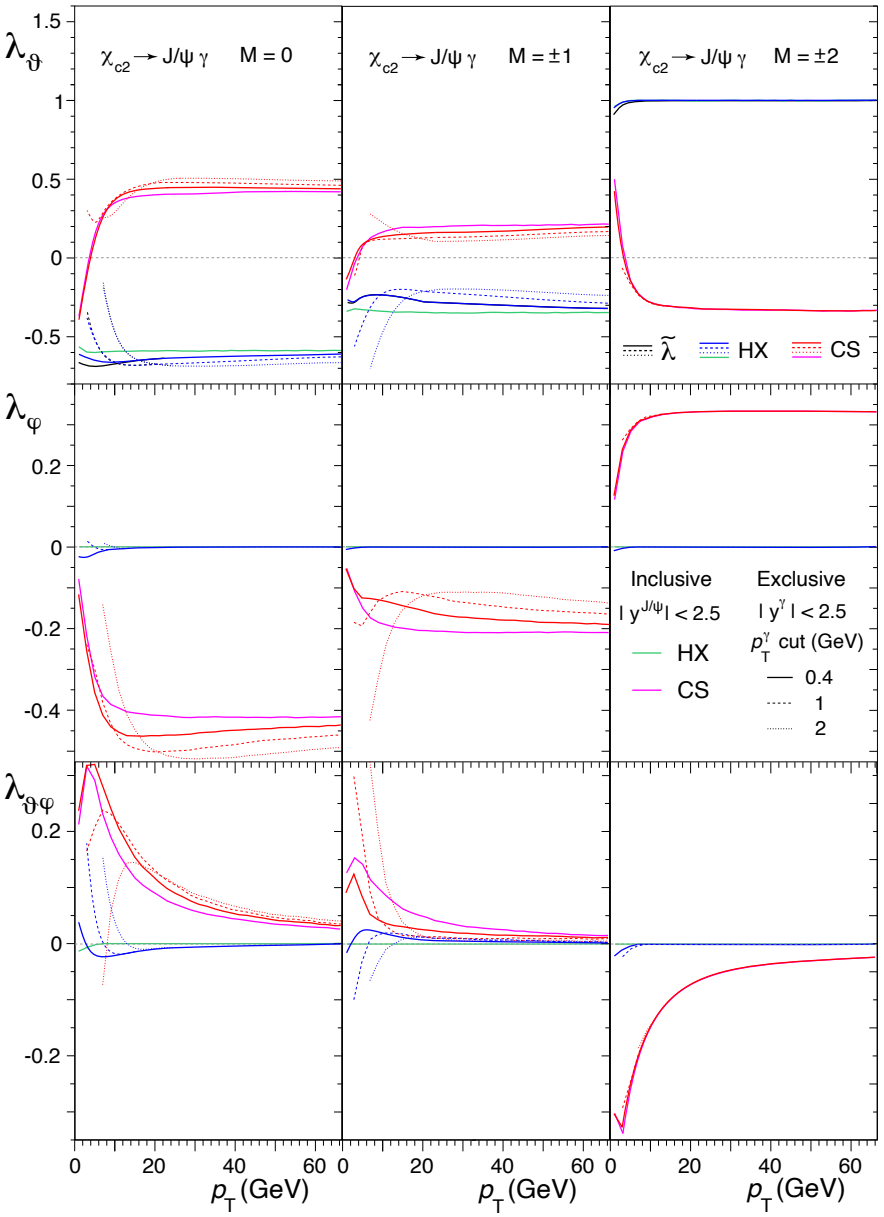

Fig. 6.28 The frame-dependent anisotropy parameters λ_ϑ, λ_φ and $\lambda_{\vartheta\varphi}$ (top to bottom rows), in the HX (blue) and CS (red) frames, as well as the frame-invariant parameter $\tilde{\lambda}$ (top row), of the dilepton decay distribution of J/ψ mesons observed in fully reconstructed exclusive radiative decays of χ_{c2} mesons produced with J_z projections $M = 0$ (left), $M = \pm 1$ (centre), and $M = \pm 2$ (right) along the HX axis. The solid, dashed and dotted curves correspond to increasing cuts on the photon p_T. The corresponding curves for inclusive measurements, where the cloning effect occurs almost exactly, are also shown, in green (HX) and magenta (CS).

The difference between the results of inclusive and exclusive observations has to be taken into account when sufficiently precise measurements of the polarization of J/ψ mesons produced in χ_c decays are used in a subtraction procedure to extract the polarization of the directly produced J/ψ, as was done to obtain the band in Fig. 6.18.

Similarly, accurate comparisons of exclusive measurements with theoretical predictions must account for the impact of the experimental selections on the photon (and leptons), either by applying the same selection criteria in the theoretical calculations or by performing a full-dimensional acceptance correction of the experimental data.

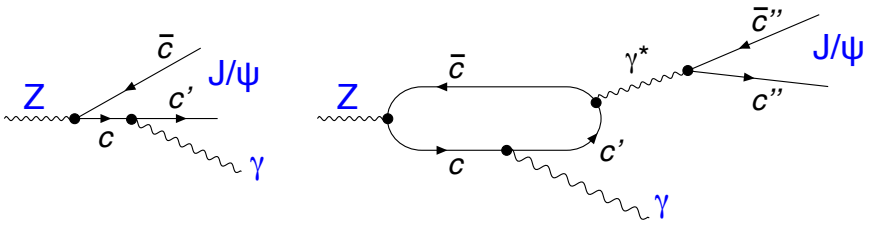

Fig. 6.29 Diagrams describing the decay Z $\rightarrow$ J/$\psi\,\gamma$. The same processes, replacing the c quarks with b quarks, also describe the analogous decay Z $\rightarrow \Upsilon\,\gamma$.

As in the $J = 0$ case, a more variegated scenario is expected when the mother particle has a much larger mass. As a prototype example of this case we consider the decay Z $\rightarrow$ J/$\psi\,\gamma$, which is formally analogous to the radiative decay of the χ_{c1} meson. In fact, as can be seen in Fig. 6.29, in the diagrams describing the processes [63–65] the Z boson transforms into an initial $c\bar{c}$ pair; one of the quarks then radiates a photon and the pair turns into the final J/ψ. The diagram on the right side, representing a higher-order process, adds a further step, where the quarks annihilate into a virtual photon, which transforms into a J/ψ, but the momentum (**P**) and angular momentum (**J**) of the J/ψ are the same as those of the pair that has just produced the photon. In both processes we hence have an initial $c\bar{c}$ state having the same **P** and **J** as the Z and a post-radiation one having the same **P** and **J** as the J/ψ: from the point of view of energy and angular-momentum conservation among the involved particles, the process is identical to an electromagnetic transition between "quarkonium" states, $c\bar{c} \rightarrow c'\bar{c}\gamma$. The four-dimensional angular distribution in the CC frame has, therefore, the same expression for the Z and χ_{c1} decays, for all polarization cases. Figure 6.30 shows the p_{T} distribution used for the generation of the simulated Z events.

The Z polarization is well measured, as seen in Sections 4.3 and 5.2, and can in principle be used to completely determine $W(\cos\Theta, \Phi, \cos\vartheta, \varphi)$ and, therefore, obtain one definite prediction for the polarization of the J/ψ mesons produced in Z decays. The necessary formulas, depending on a completely generic polarization state of the mother particle, are reported in Appendix B, for this and analogous decays where the J/ψ is replaced by another vector particle (ϕ, ρ) decaying into

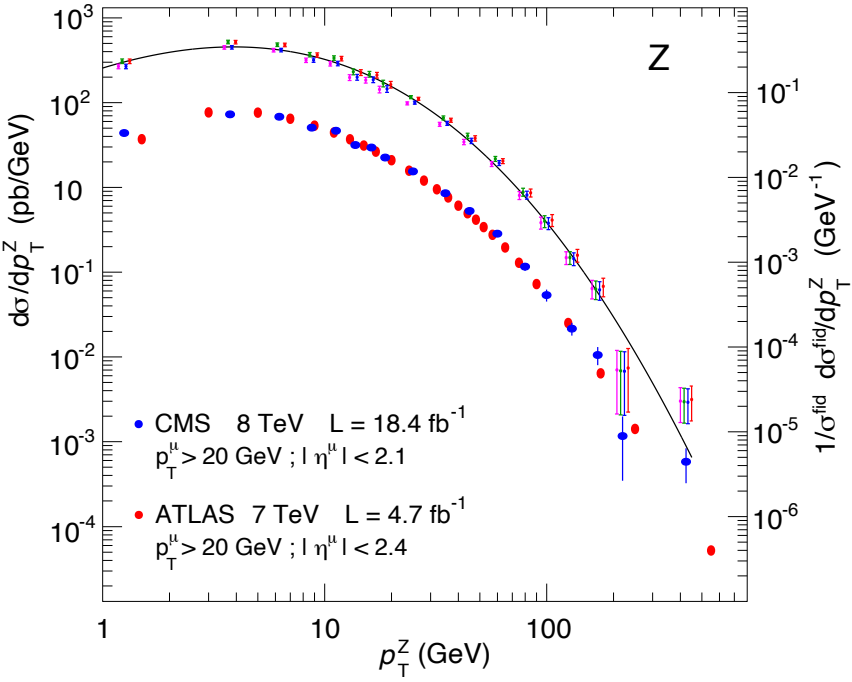

Fig. 6.30 The Z boson fiducial normalized p_{T}-differential cross section, $1/\sigma^{\mathrm{fid}}\mathrm{d}\sigma^{\mathrm{fid}}/\mathrm{d}p_{\mathrm{T}}$ (right y-axis), measured by ATLAS [60] (red bullets) and CMS [61] (blue bullets), in the phase space domain defined by the single muon cuts $p_{\mathrm{T}}^{\mu} > 20$ GeV and $|\eta^{\mu}| < 2.4$ (ATLAS) or 2.1 (CMS). The corresponding absolute fiducial cross sections, in pb/GeV (left y-axis), were obtained using the σ^{fid} value reported (for $|y^{\mathrm{Z}}| < 2$) by CMS [62]. The curve represents the absolute acceptance-corrected p_{T}-differential cross section that we used in the generation of simulated events. It provides a faithful interpolation of four sets of data points (slightly shifted horizontally for visibility reasons), acceptance-corrected assuming four different Z polarization scenarios. While the procedure usually depends on the assumed polarization, the results obtained in the four scenarios are almost identical, the residual differences being negligible for our purposes.

either $\ell^+\ell^-$ (or $\pi^0\,\gamma$) or $\pi^+\pi^-/\mathrm{K}^+\mathrm{K}^-$, and/or where W is the decaying boson, for example in $\mathrm{W}^{\pm} \to \rho^{\pm}\,\gamma$, with $\rho^{\pm} \to \pi^{\pm}\pi^0$ (or $\to \pi^{\pm}\,\gamma$).

Here, for simplicity, and for immediateness of comparison with the χ_{c1} case, we still consider the two distinct hypotheses of pure polarization states, $M = 0$ and ± 1, both in the HX frame. The anisotropy parameters expected as a function of the J/ψ p_{T} for exclusive measurements in the HX and CS frames are shown in Fig. 6.31. In this case, with the experimental frame deviating substantially from the CC frame, given the large p' value ($p' \simeq 46$ GeV), we see more complex patterns: the cloning phenomenon is visibly disrupted. However, the different λ_{ϑ}, λ_{φ} and $\lambda_{\vartheta\varphi}$ values and p_{T} dependences still univocally characterize the $M = 0$ and ± 1 cases. The analogous decay $\mathrm{Z} \to \Upsilon\,\gamma$ leads to very similar results, given the only slightly smaller p' value.

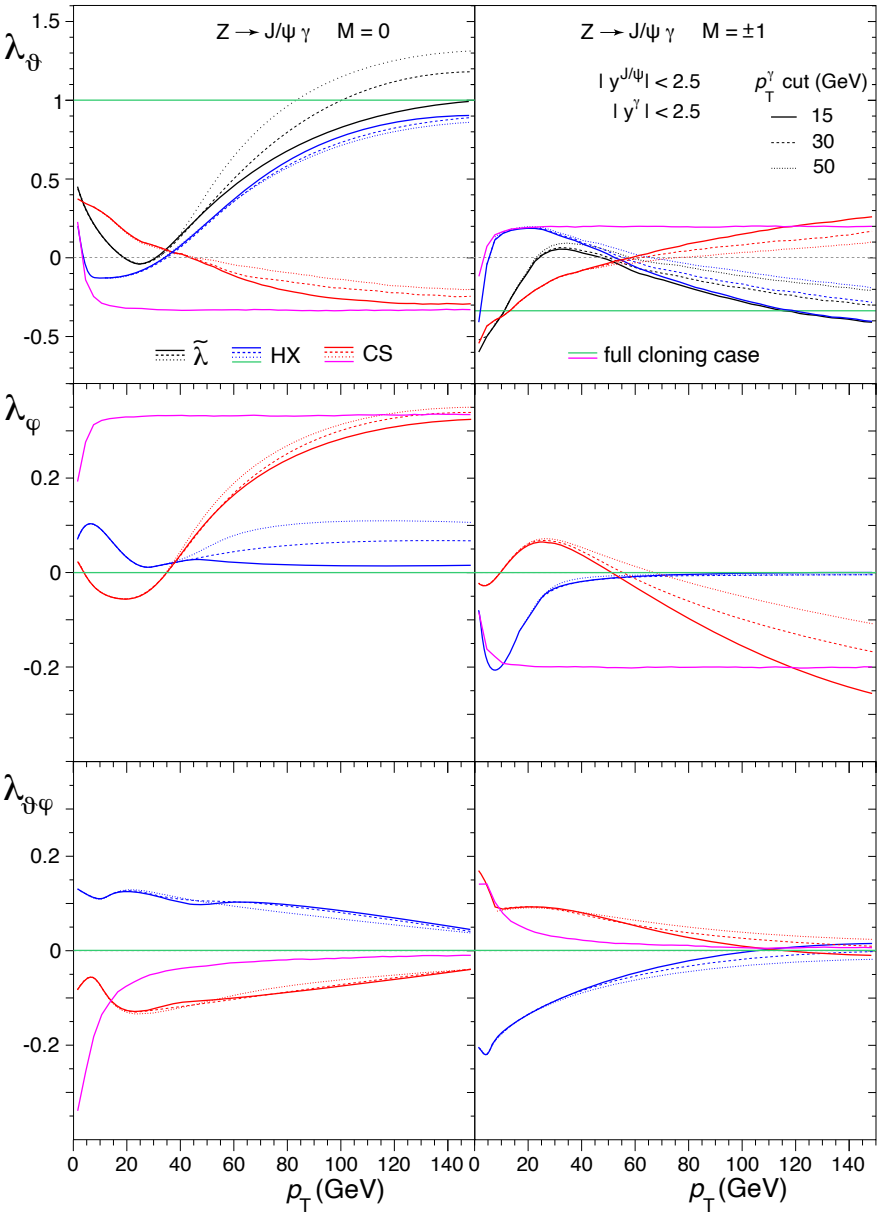

Fig. 6.31 The frame-dependent anisotropy parameters λ_ϑ, λ_φ and $\lambda_{\vartheta\varphi}$ (top to bottom rows), in the HX (blue) and CS (red) frames, as well as the frame-invariant parameter $\tilde{\lambda}$ (top row), of the dilepton decay distribution of J/ψ mesons observed in the decays of Z bosons produced with J_z projections $M = 0$ (left) and $M = \pm 1$ (right) along the HX axis. The results corresponding to an exact cloning effect are also shown, in green (HX) and magenta (CS). The solid, dashed and dotted curves correspond to increasing cuts on the p_T of the accompanying decay photon, also detected by the experiment.

6.7 The importance of the reference frame

In our discussion of the cascade decays we have adopted, as a reference for the dilepton decay of V, the CC frame, represented in Fig. 6.3, instead of the one more usually found in the literature, and perhaps a priori more intuitive, which is the cHX frame, defined in Fig. 6.1. This choice has allowed us to illustrate in an almost "visual" way, through the concepts of smearing and cloning, how the polarization properties are transferred from mother to daughter particle. The discussion would remain somehow incomplete without a brief account of what happens when, instead, we choose the cHX frame.

To address this point, we will determine the polarization of the J/ψ produced in the decays $\chi_{cJ} \to \mathrm{J}/\psi\,\gamma$ for $J = 0, 1, 2$, using the cHX frame. For simplicity, we limit the illustration to the polar anisotropy. This allows us to avoid dealing with rotations and $\mathcal{D}$-matrices and follow a simple shortcut, only considering the possible combinations of angular momentum projections $J_{z'}$ of J/ψ (L') and γ (K') along their common emission direction in the χ_c rest frame, represented by the z' axis, that is, the cHX axis, as illustrated in Fig. 6.32.

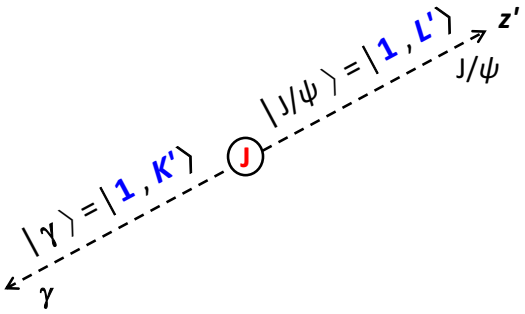

Fig. 6.32 The decay $\chi_{cJ} \to \mathrm{J}/\psi\,\gamma$ seen in the χ_{cJ} rest frame, where J/ψ and γ have angular momentum projections L' and K' along their common direction (z' axis).

The relative probabilities of these combinations are expressed by the corresponding Clebsch–Gordan coefficients, squared. The numbers are listed in Table 6.2 for the generic decay of a $J = 0$, 1 or 2 particle into two $J = 1$ particles.

The configurations where $K' = 0$ correspond to the forbidden case of a longitudinally polarized photon and must be excluded for the present examples. In the case of the decay $\chi_{c0} \to \mathrm{J}/\psi\,\gamma$, we find, as expected, that in the only two remaining configurations the J/ψ has $L' = +1$ and -1: it is, like the photon, transversely polarized along z', so that $\lambda_\vartheta = +1$: this reproduces the result amply discussed in the previous sections (Eq. 6.2).

We consider now the $\chi_{c1} \to \mathrm{J}/\psi\,\gamma$ case. Taking $J = 1$ and excluding the forbidden configurations where $K' = 0$, besides $L' + K' = \pm 2$, we find that in the four allowed ones the J/ψ has 50% probability of being transverse ($L' = +1$ or -1) and 50% of

Table 6.2 The squared Clebsch–Gordan coefficients weighing the angular momentum configurations of the decay $|J,\, L' + K'\rangle \to |1,\, L'\rangle + |1,\, K'\rangle$, with $J = 0$, 1, and 2, along the z' axis.

L'	K'	$L' + K'$	weight = C^2		
			$J = 0$	$J = 1$	$J = 2$
+1	+1	+2	–	–	1
+1	0	+1	–	1/2	1/2
+1	−1	0	1/3	1/2	1/6
0	+1	+1	–	1/2	1/2
0	0	0	1/3	0	2/3
0	−1	−1	–	1/2	1/2
−1	+1	0	1/3	1/2	1/6
−1	0	−1	–	1/2	1/2
−1	−1	−2	–	–	1

being longitudinal ($L' = 0$): therefore, its dilepton distribution along z' is

$$w(\cos\vartheta) \propto \frac{1}{2}\frac{1+\cos^2\vartheta}{4} + \frac{1}{2}\frac{1-\cos^2\vartheta}{2} \propto 1 - \frac{1}{3}\cos^2\vartheta\,, \tag{6.29}$$

that is, $\lambda_\vartheta = -1/3$. This result is *independent* of the polarization state of the χ_{c1}. For the χ_{c2} decay, by summing the relevant coefficients in the table we find that the J/ψ is 70% transverse and 30% longitudinal with respect to the z' axis,

$$w(\cos\vartheta) \propto \frac{7}{10}\frac{1+\cos^2\vartheta}{4} + \frac{3}{10}\frac{1-\cos^2\vartheta}{2} \propto 1 + \frac{1}{13}\cos^2\vartheta\,, \tag{6.30}$$

that is, $\lambda_\vartheta = +1/13$, irrespectively of the χ_{c2} polarization state. In summary, by adopting the cHX axis for the observation of the J/ψ decay distribution, the measurement remains completely blind to the χ_c polarization. This is a result of the implicit integration we made over the emission angles Θ, Φ of the J/ψ itself in the χ_c rest frame. In fact, the full information on the χ_c polarization state remains available in the four-dimensional distribution $W(\cos\Theta, \Phi, \cos\vartheta, \varphi)$ of the cascade $\chi_{cJ} \to \mathrm{J}/\psi\,\gamma$ with $\mathrm{J}/\psi \to \ell^+\ell^-$, which can of course be determined, with a method analogous to the one used in Section 6.6, adopting the cHX axis for the J/ψ.

Anyhow, in the light of these examples, the results seen in Section 6.6 imply a clear advantage in the use of the CC frame: with this choice the dilepton anisotropy alone, even after integration over $\cos\Theta$ and Φ, is fully sensitive to the χ_c polarization, because it "clones" the polarization-dependent anisotropy of the J/$\psi\,\gamma$ emission

in the χ_c rest frame. The difference between the results obtained with the two frame choices is illustrated in Fig. 6.33.

This crucial advantage of the CC frame remains present also when the cloning effect is disrupted by the deviation of the HX from the CC frame at typical p_T values and by the effects of exclusive selection cuts, as in the measurement of the J/ψ polarization in the decay $Z \to J/\psi\,\gamma$, discussed in the previous section. In fact, the calculation of the J/ψ dilepton distribution in the cHX frame leads to the same polarization-insensitive result as in the χ_{c1} case, $\lambda_\vartheta = -1/3$. Instead, even if the cloning is now visually unrecognizable (Fig. 6.31), the λ_ϑ, λ_φ and $\lambda_{\vartheta\varphi}$ patterns in the HX (or CS) frame remain very different in the $M = 0$ and $M = \pm 1$ cases, allowing for a clear discrimination between Z polarization cases.

The title of this section alludes to the previous discussion of Chapter 2 about the dependence of a polarization measurement on the reference frame and how it is convenient to test more than one frame in the search for possibly simpler (and, therefore, more physically revealing) "patterns". However, it is important to remark that, in that case, we were considering polarization frames (HX, CS, GJ, PX) that are mutually related by simple spatial rotations around the y axis and, for this reason, the measurement in one frame could always be translated into a corresponding result in any other frame, provided that all anisotropy parameters are measured and effects caused by integrations over kinematic intervals (e.g. p_T and/or rapidity bins) can be neglected. In the present case, the choice between cHX and CC frames for the measurement of the J/ψ polarization is irreversible, at least if only the dilepton distribution is measured (and, of course, if the analysis is not repeated with the other choice): it is not possible to transform mathematically the measurement made in the cHX frame to the CC frame, as can be understood by the simple fact that only the destination frame gives an anisotropy that depends on the χ_c polarization, while this information is irrecoverably occulted in the frame of origin. In fact, the relation between the cHX and CC frames at fixed p_T and rapidity is not a rotation, but the convolution of a continuous series of event-dependent rotations, where the *shape* of the distribution changes and some of the original information it contained gets lost.

6.8 A counterexample for the cloning effect

We have presented the χ_c radiative decays as prototypes for the illustration of the cloning mechanism, which can be seen at work when the measurement adopts, for example, the HX frame, as an almost perfect replica of the CC frame: the dilepton decay in the J/ψ rest frame will be practically identical to the distribution of the J/ψ emission in the χ_c rest frame and, therefore, fully and univocally reflect the χ_c polarization in its HX frame (this is exactly true when higher order multiple radiations are neglected, as previously mentioned and as discussed in detail in Ref. [59]).

When the mother-daughter mass difference is large, as in the otherwise analogous $Z \to J/\psi\,\gamma$ decay, the cloning effect is no longer clearly recognizable as such in the "usual" HX frame. However, the J/ψ dilepton distribution continues to be a

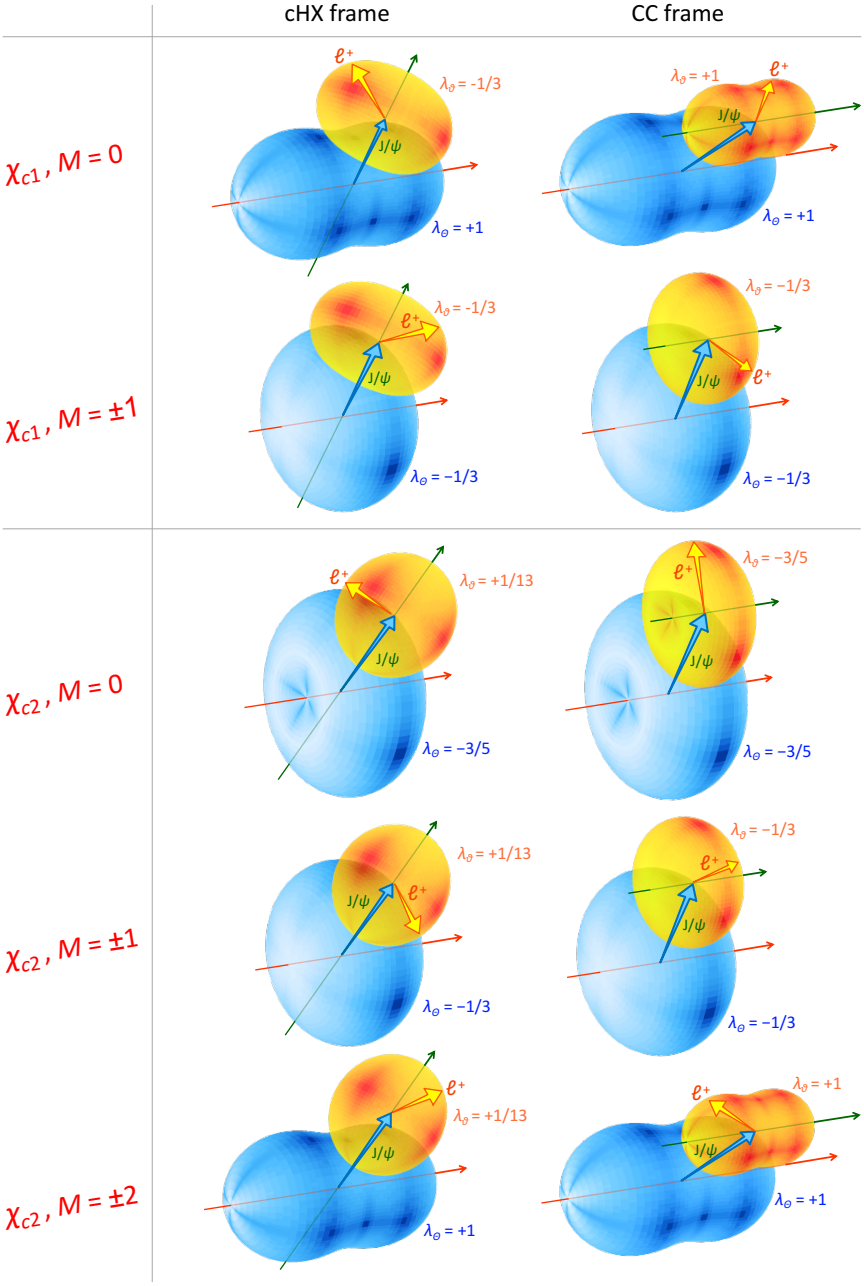

Fig. 6.33 Illustration of how the observation of the angular distribution of the decay $J/\psi \to \ell^+\ell^-$, subsequent to $\chi_{cJ} \to J/\psi\,\gamma$, is substantially different in the cHX and CC frames. In the CC frame the shape of the dilepton distribution is univocally correlated to the χ_{cJ} polarization state, making its measurement possible even when the decay distribution of the χ_{cJ} itself is not observed. Instead, in the CC frame the J/ψ polarization is blind to the χ_{cJ} polarization.

definite indicator of the Z polarization. Above all, it is important to remind that the cloning mechanism remains present in this decay and is, in principle, observable: it is sufficient to adopt for the J/ψ the exact CC frame, that is, to calculate the polarization direction in the Z rest frame and translate it with no change into the J/ψ rest frame.

It is now natural to wonder about what happens in the decays where this kind of cloning is absent: does in such cases the CC axis still provide its advantage in terms of sensitivity to the mother's polarizations? Fortunately, our $\chi_{cJ} \to \mathrm{J}/\psi\,\gamma$ "prototype" admits a very close counterpart, providing a particularly instructive answer. We simply have to release the constraint that the radiated photon is transversely polarized: we replace it with a virtual photon γ^*, which eventually produces a second, non-resonant, lepton-antilepton pair. The corresponding physical cases are the rarer decays $\chi_{cJ} \to \mathrm{J}/\psi\,\gamma^*$, where both J/$\psi$ and γ^* further decay into $\ell^+\ell^-$ pairs. The exchange symmetry $(\Theta, \Phi) \leftrightharpoons (\vartheta, \varphi)$ illustrated in Fig. 6.25 is broken by the replacement of γ with γ^*, since this latter admits a $J_{z'} = 0$ component along z' and ceases to be perfectly analogous to the J/ψ's $\ell^+\ell^-$ system as observed with respect to the z''' axis: no cloning is expected in this case.

The amplitude of the process is unchanged with respect to the one of Eq. 6.28. The difference in the observable angular distribution results from extending the sum of the squared amplitudes to include the $K' = 0$ term. The four-dimensional angular distribution for pure χ_{cJ} polarizations, corresponding to Eq. 6.28, becomes

$$W_{\mathrm{CC}}(\cos\Theta, \Phi, \cos\vartheta, \varphi) \propto \begin{cases} 1 + \cos^2\vartheta & \text{for } \chi_{c1}\,,\ M = 0\,, \\ 1 - \frac{1}{3}\cos^2\vartheta & \text{for } \chi_{c1}\,,\ M = \pm 1\,, \\ 1 - \frac{3}{5}\cos^2\vartheta & \text{for } \chi_{c2}\,,\ M = 0\,, \\ 1 - \frac{1}{3}\cos^2\vartheta & \text{for } \chi_{c2}\,,\ M = \pm 1\,, \\ 1 + \cos^2\vartheta & \text{for } \chi_{c2}\,,\ M = \pm 2\,. \end{cases} \tag{6.31}$$

These expressions are independent of the angles Θ and Φ, implying that the integration over ϑ (and φ) leads to a constant distribution: the J/ψ is emitted *isotropically* in the χ_c polarization frame. This means that the measurement of the two-body decay angular distribution of the χ_c is blind to its polarization state.

Additionally, we can recognize, with the method used in Section 6.7 (Fig. 6.32), that also the dilepton decay in the J/ψ cHX frame is isotropic for $J = 0$, 1 and 2 (the same is true, incidentally, for the one in the γ^* cHX rest frame): with no restriction on K', the summed Clebsch–Gordan weights (Table 6.2) become identical for the three configurations $L' = -1$, 0 and $+1$, in all three J cases. No trace of the χ_{cJ} polarization would be seen, therefore, in *either* integrated two-dimensional distribution by adopting the cHX frame. Only the four-dimensional distribution $W_{\mathrm{cHX}}(\cos\Theta, \Phi, \cos\vartheta, \varphi)$ will contain such information, in terms correlating the upper- and lower-case angles.

The CC frame continues, instead, to provide for the J/ψ decay the same distribution as in the $\chi_{cJ} \to \mathrm{J}/\psi\,\gamma$ case: the polar anisotropy parameters implied by Eq. 6.31,

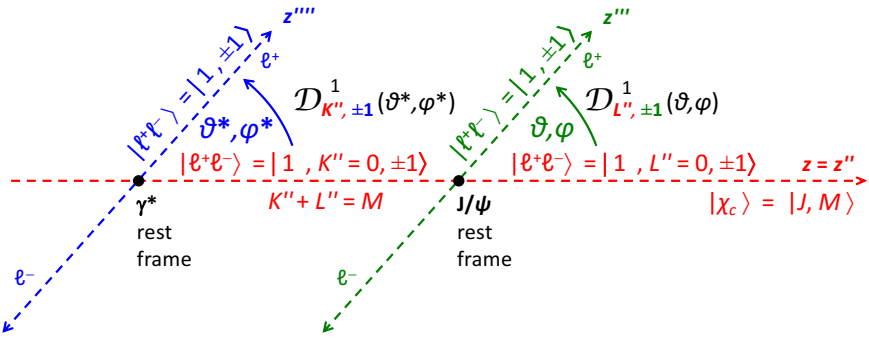

Fig. 6.34 Illustration of the $(\vartheta', \varphi') \rightleftharpoons (\vartheta, \varphi)$ exchange symmetry for the angular distribution of the cascade decay $\chi_{cJ} \to \mathrm{J}/\psi\, \gamma^*$, followed by $\mathrm{J}/\psi \to \ell^+\ell^-$ and $\gamma^* \to \ell^+\ell^-$.

$\lambda_\vartheta = -3/5$ (χ_{c2} for $M = 0$), $-1/3$ (χ_{c1} or χ_{c2} for $M = \pm 1$), and $+1$ (χ_{c1} for $M = 0$ or χ_{c2} for $M = \pm 2$) are the same as those found in Section 6.6 for the decays with a real photon.

Moreover, for understandable reasons of symmetry, that same polarization information is also carried by the additional dilepton distribution produced by the γ^* decay, when observed with respect to the CC axis. In fact, another clone symmetry can be discerned, as illustrated in Fig. 6.34, between the two dilepton systems, which are completely equivalent and exchangeable (they only differ for their invariant masses, which do not affect the determination of the angular distribution): the four dimensional angular distribution $W(\cos\vartheta, \varphi, \cos\vartheta', \varphi')$ is symmetric with respect to a change of the J/ψ decay angles (ϑ and φ) by those of the virtual photon (ϑ' and φ').

It is now immediate to determine the correlated distribution of the four angular coordinates $\cos\vartheta$, φ, $\cos\vartheta'$, and φ'. In fact, we can reuse the passages of Section 6.6 that lead to the derivation of the distribution of $\chi_{cJ} \to \mathrm{J}/\psi\, \gamma$, $\mathrm{J}/\psi \to \ell^+\ell^-$ (Eq. 6.28), replacing the rotation of the γ eigenstate from the z' to the z'' (CC) axis, by angles Θ and Φ, with the rotation of the second dilepton system, coming from the γ^* decay, from the z'''' axis (where lepton and antilepton are back-to-back) to the z'' axis, by angles ϑ' and φ'. Along z'''' the γ^* dilepton has allowed angular momentum projections ± 1, just like γ had along z'. Moreover, the involved Wigner matrices are exactly the same.

The replacement, therefore, does not change the functional dependence of the result on the angles: it only leads to the substitution of Θ, Φ with ϑ', φ'. This means that, with only a change of names of the angles, Eq. 6.28 represents the correlated angular distribution of the two dilepton systems of the J/ψ and γ^* decays, being the angles measured in the respective CC rest frames of the two particles. In particular, by integrating this four-dimensional distribution $W(\cos\vartheta, \varphi, \cos\vartheta', \varphi')$ over either $\cos\vartheta'$ and φ', or $\cos\vartheta$ and φ, to derive, respectively, the J/ψ decay distribution $w(\cos\vartheta, \varphi)$ or the γ^* one, $w(\cos\vartheta', \varphi')$, we obviously obtain the same result

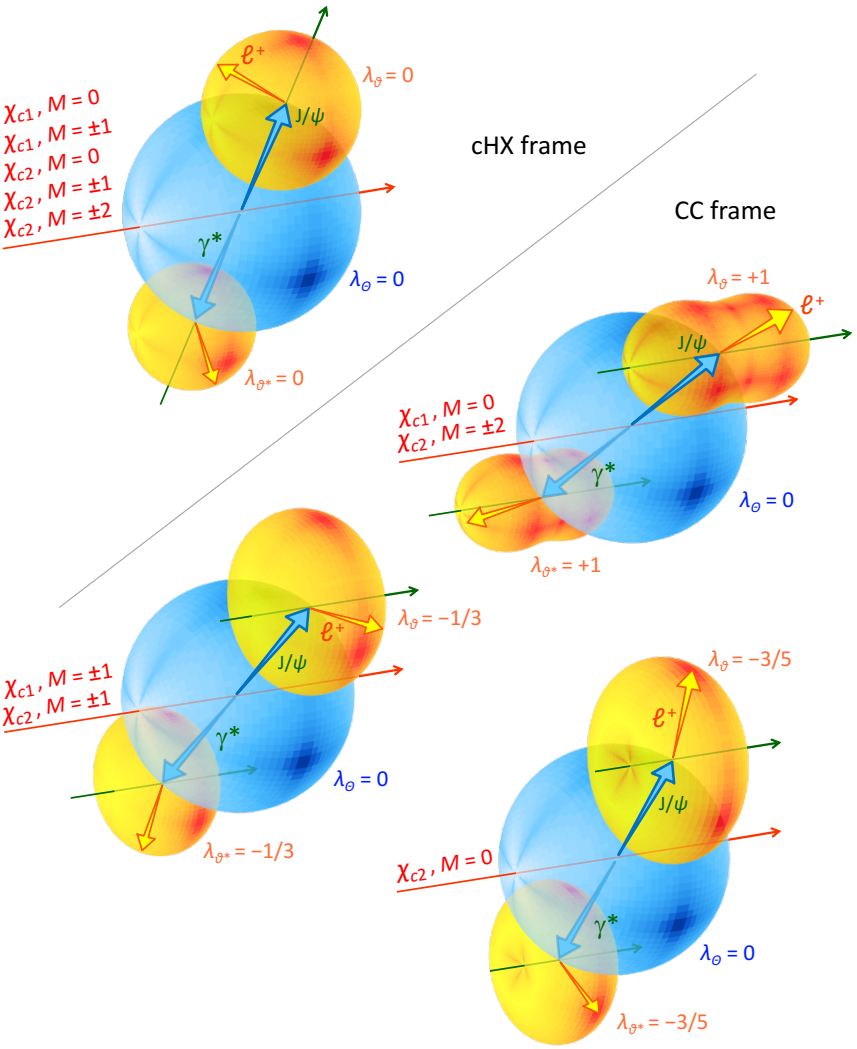

Fig. 6.35 Illustration of how the angular distribution of the decay $\chi_{cJ} \to \mathrm{J}/\psi\,\gamma^*$, with $\mathrm{J}/\psi \to \ell^+\ell^-$ and $\gamma^* \to \ell^+\ell^-$, is observed in the cHX and CC frames. The χ_{cJ} decay is isotropic in all cases and both frames. Concerning the dilepton distributions, all χ_{cJ} polarization cases lead to an undistinguished, fully isotropic result in the cHX frame, while both J/ψ and γ^* decay distributions in the CC frame univocally reflect the χ_{cJ} polarization state, being two identical replicas of the $\mathrm{J}/\psi \to \ell^+\ell^-$ distribution in the $\chi_{cJ} \to \mathrm{J}/\psi\,\gamma$ case (Fig. 6.26).

as when we integrate the distribution $W(\cos\Theta, \Phi, \cos\vartheta, \varphi)$ of the $\chi_{cJ} \to \mathrm{J}/\psi\,\gamma$ case over $\cos\Theta$ and Φ.

Figure 6.35 gives a pictorial summary of how the measurements in the cHX and CC frames differ for integrated two-dimensional distributions: in the cHX frame

every distribution is isotropic, independently of the χ_c polarization; in the CC frame both the distribution of the J/ψ decay and that of the γ^* are exactly the same as in the dilepton distribution in the $\chi_{cJ} \to \mathrm{J}/\psi\,\gamma$ case (Fig. 6.33), and both fully reflect the χ_c polarization.

We have exploited the close parallelism between the two alternative χ_{cJ} decays, $\chi_{cJ} \to \mathrm{J}/\psi\,\gamma$ and $\chi_{cJ} \to \mathrm{J}/\psi\,\gamma^*$, to further illustrate the concept of cloning and the roles of different frame definitions, taking advantage of existing and experimentally observed decay channels. The latter decay channel may, however, not be a good alternative for the measurement of the χ_c polarization. First, because the event sample would certainly be much smaller than the $\chi_{cJ} \to \mathrm{J}/\psi\,\gamma$ sample, given the lower branching fraction. Second, because it remains necessary to carefully evaluate the effects of the integration over $\cos\vartheta'$ and φ' in the presence of experimental selections.

As previously described in detail, the selection criteria applied to the photon lead to sculpting effects on the $(\cos\Theta, \Phi)$ distribution in the $\chi_{cJ} \to \mathrm{J}/\psi\,\gamma$ case, thereby creating slight deviations from the full-cloning expectation. In exactly the same way, the selections applied to the lepton pair produced by the γ^* will affect the observed J/ψ dilepton distribution (and vice-versa), since the functional correlation between $(\cos\vartheta', \varphi')$ and $(\cos\vartheta, \varphi)$ is the same as the one between $(\cos\Theta, \Phi)$ and $(\cos\vartheta, \varphi)$. This problem should not be more easily addressed in the γ^* decay case, because the invariant mass of the γ^* is very small, of the order of only 1 MeV, so that the two resulting leptons will be produced with very low laboratory momenta, making their detection a big challenge.

6.9 Recapitulation

In this chapter we have studied the dilepton decay distribution of a vector particle V produced indirectly, in the decay $O \to V + X$ of a heavier particle O, to answer the following question: what polarization does V inherit in this two-step production process?

We started by developing in detail the description of the vector particle production from the decay of a $J = 0$ particle, including cases like $\chi_{c0} \to \mathrm{J}/\psi\,\gamma$, $\chi_{b0} \to \Upsilon\,\gamma$, $\mathrm{B} \to \mathrm{J}/\psi\,\mathrm{K}$, $\mathrm{H} \to \mathrm{J}/\psi\,\gamma$, and $\mathrm{H} \to Z\,\gamma$. In certain experimental and kinematic conditions, these processes represent extreme examples of polarization "smearing", potentially leading to the extraordinary observation of a fully unpolarized vector particle. In fact, V is intrinsically polarized along the direction of its emission in the O rest frame (the cHX frame, Fig. 6.1) having, for example, a natural polarization $\lambda_0 = +1$ when X is a real photon and $\lambda_0 = -1$ when X is a $J = 0$ particle.

However, in "inclusive" studies, where the production of V is observed by reconstructing only its dilepton decay, and not the underlying $O \to V + X$ step, the dilepton distribution is necessarily referred to the directions of the colliding beams, taking for example the HX axis as polarization axis. Given that V is emitted isotropically in the O rest frame, in the V rest frame the directions of the HX and cHX axes

are distributed in a spherically uniform way with respect to one another, leading, in principle, to a fully smeared dilepton distribution as seen with respect to the HX axis (Fig. 6.2).

The four-dimensional distribution of the V emission angles Θ, Φ in the O rest frame and the dilepton emission angles ϑ, φ in the V rest frame is given by Eq. 6.2 in the cHX frame and by Eq. 6.8 in the "cloned cascade" (CC) frame of Fig. 6.3, where the V polarization axis is a geometrical clone of the O polarization axis and approximates the HX or CS axis (the same chosen for O) when the laboratory momentum of V is large with respect to the $O - V$ mass difference (Eq. 6.15). In this latter frame we see that the uniform integration over the angular variables of either step of the cascade leads indeed to a constant. However, when the integration is not uniform, the result is, in general, an anisotropic two-dimensional distribution.

It actually happens that the measurement process disrupts the spherical symmetry of the smearing, by sculpting the $\cos\Theta$ distribution. If, for example, V is reconstructed in intervals of its p_{T}, the $\cos\Theta$ distribution ceases to be uniform and assumes a shape depending on the slope of the p_{T} distribution within the considered interval (Eqs. 6.17 and 6.22, Fig. 6.9). The effect increases with the mass difference between O and V, as shown in Fig. 6.6, comparing the cases $\mathrm{B} \to \mathrm{J}/\psi\,\mathrm{K}$ and $\chi_{c0} \to \mathrm{J}/\psi\,\gamma$. When the $|\cos\Theta|$ distribution is no longer uniform (that is, the $\cos\Theta$ distribution is not uniform or linear) in the HX or CS frame of O, a non-uniform dilepton decay distribution will be observed in the CC frame, HX or CS, of V.

The resulting anisotropy parameters as observable in inclusive measurements (ignoring the $O \to V$ step) at the LHC are shown in Fig. 6.14 ($\mathrm{B} \to \mathrm{J}/\psi\,\mathrm{K}$, $\mathrm{B} \to \psi(2\mathrm{S})\,\mathrm{K}$) and in the left panels of Fig. 6.15 ($\chi_{c0} \to \mathrm{J}/\psi\,\gamma$): a practically isotropic dilepton distribution is observed only when the mass difference is as small as for the J/ψ from χ_{c0} decays.

It is important to notice that, as seen in those figures, the results depend on the experimental selections. For example, also the minimum-p_{T} requirements on the decay leptons sculpt the $\cos\Theta$ distributions (Figs. 6.12 and 6.13). Since the $\cos\Theta$ distribution is not observed and, therefore, not corrected for the lepton acceptance, this effect leads to an increase of the observed anisotropies. The selection criteria must become an integral part of the measurement definition.

In most measurements, additional criteria are applied to isolate events corresponding to the specific decay channel $O \to V + X$. Even if only the dilepton decay distribution of V is analysed, such selections, effectively requiring the presence of X with a laboratory momentum in a given acceptance domain, strongly sculpt the $\cos\Theta$ distribution (Fig. 6.10). In such "exclusive" measurements, stronger kinematic modulations are expected for the dilepton decay parameters of V, as shown by the comparison between the right and left panels in Figs. 6.8 and 6.15. Processes like $\mathrm{H} \to \mathrm{J}/\psi\,\gamma$ and $\mathrm{H} \to \mathrm{Z}\,\gamma$, which must be isolated with suitable selections on the photon, show particularly strong deviations from the isotropic limit (Fig. 6.17), because the mass difference is large with respect to the typical values of the observed V momentum spectrum.

The same smearing mechanism occurring in the decay $\chi_{c0} \to \mathrm{J}/\psi\,\gamma$ provides a key for the interpretation of the surprising observation, made at the LHC, that *di-*

rectly produced J/ψ mesons show polarization parameters compatible with being zero and with no significant dependence on p_{T} (Fig. 6.18). An exact cancellation of oppositely polarized mechanisms, leading to a p_{T}-independent result, is improbable, and a more natural explanation is provided by the colour-octet mechanism (a basic feature of NRQCD), where the observable vector meson results from the transformation of an unobserved ("pre-resonance") coloured $Q\overline{Q}$ pair, having a mass only slightly different from the final one and possibly different quantum numbers. The binding transition, happening via emission of soft gluons, leads to a seemingly unpolarized J/ψ if the pre-resonance $Q\overline{Q}$ has $J = 0$. Measurements in hadron collider experiments do indeed support the hypothesis of a dominance of partonic processes creating coloured $Q\overline{Q}$ pairs with respect to those producing already colour neutral states (Fig. 6.19). Moreover, recent global analyses of LHC data indicate that the ${}^1S_0^{[8]}$ colour-octet channel (of $J = 0$) is the prevalent one. It is, therefore, the peculiar nature of the J/ψ, a composite particle made of two heavy quarks, and the marked process hierarchy characterizing the high-energy domain explored at the LHC, that allow for the exceptional observation of unpolarized production.

Colour-octet dominance and unpolarized J/ψ production are not necessarily foreseen, nor observed, in low-p_{T} fixed-target production, in electromagnetic processes and, as exemplified by the several cases analysed in this chapter, in indirect production. In particular, the indirect J/ψ production from decays of B mesons, which can be studied inclusively by selecting "non-prompt" events, should show a significant longitudinal polarization if the sample is dominated by two-body decays of the kind $\mathrm{B} \to \mathrm{J}/\psi\,\mathrm{K}$. Multi-body decays, including processes producing a colour-octet $Q\overline{Q}$ state and more complex chains starting with $\mathrm{B} \to \chi_c$ or $\mathrm{B} \to \psi(2\mathrm{S})$ decays, may, however, dilute the overall polarization (Figs. 6.23 and 6.24).

The generalization of the previous considerations to the cases of a $J = 1$ or $J = 2$ mother particle ($\chi_{c1,2} \to \mathrm{J}/\psi\,\gamma$, $\mathrm{Z} \to \mathrm{J}/\psi\,\gamma$) shows the "smearing" effect turning into another phenomenon, where the shape of the mother's decay distribution is "cloned" into the one of the daughter's as observed in the CC frame (Fig. 6.26), reflecting the invariance of the four-dimensional angular distribution by exchange of the O and V decay angles (Eq. 6.28 and Fig. 6.25). Therefore, while the polarization (J_z composition) changes from mother to daughter, the one of the mother is still univocally reflected by the dilepton decay distribution of V, even when the O decay angles are integrated out. Also the $J = 0$ case, where both mother and daughter have isotopic decays distributions, is actually a case of cloning.

The cloning is verified in the CC frame, meaning that, at sufficiently high laboratory momentum, it is possible to measure the χ_{c1} and χ_{c2} polarizations in the "ordinary" HX or CS frames, by only determining the dilepton distribution of the daughter J/ψ and without performing a four-dimensional analysis including the χ_c decay angles. Just as the full spherical smearing in the $J = 0$ case, also the exact cloning is partially disrupted by experimental selections affecting the momentum of the accompanying particle X. The effect is small for J/ψ from χ_c decays (Figs. 6.27 and 6.28), but significant for large mother-daughter mass differences, as in the case of the decay $\mathrm{Z} \to \mathrm{J}/\psi\,\gamma$, where strong kinematic modulations appear for the dilepton

anisotropy parameters; the Z polarization is, however, still unequivocally reflected in the observable patterns.

Both the cHX ($x'y'z'$) and CC ($x''y''z''$) frames of Figs. 6.1 and 6.3, alternative choices for the measurement of the V decay distribution, require, in principle, the knowledge of the O (or X) momentum, besides the V one: for example, z' (cHX) and z'' (CC HX) represent the direction of O, respectively, in the V rest frame and in the laboratory. Correspondingly, the measurement of the correlated four-dimensional distribution of the cascade process provides the same amount of physics information with both frame choices.

However, for V momenta larger than the $O - V$ mass difference, the CC HX frame is simply determined as the V HX frame, using only the V momentum in the laboratory. Measurements of the dilepton distribution using the CC (HX or CS) frame and integrating over the O decay angles, as those considered in all examples of this chapter, require, therefore, significantly less experimental information than those choosing the cHX frame, which always rely on the knowledge of the O momentum. Apart from being more "economical" from the experimental point of view, the choice of the CC frame is also the only one of the two allowing the experiment to determine the polarization of O simply using the dilepton degrees of freedom, as was illustrated by the χ_{c1} and χ_{c2} examples. In fact, after integration over $\cos\Theta$ and Φ, the dilepton distribution in the cHX frame is blind to the O polarization (Eqs. 6.29 and 6.30, Fig. 6.33).

Interestingly, the dilepton measurement in the CC frame continues to provide the same full sensitivity to the O polarization even in the seemingly evasive example of the $\chi_{c1,2} \to J/\psi\,\gamma^*$ decays (Fig. 6.35), where the $\cos\Theta, \Phi$ distribution itself is always measured as isotropic independently of the χ_c polarization, an observation not to be mistaken as an indication that the χ_c is produced unpolarized.

References

[1] CMS Collaboration, "Measurement of J/ψ and ψ(2S) prompt double-differential cross sections in pp collisions at $\sqrt{s} = 7$ TeV", *Phys. Rev. Lett.* **114** (2015) 191802, doi:10.1103/PhysRevLett.114.191802, arXiv:1502.04155.

[2] CMS Collaboration, "Measurements of the Υ(1S), Υ(2S), and Υ(3S) differential cross sections in pp collisions at $\sqrt{s} = 7$ TeV", *Phys. Lett. B* **749** (2015) 14, doi:10.1016/j.physletb.2015.07.037, arXiv:1501.07750.

[3] CMS Collaboration, "Measurement of quarkonium production cross sections in pp collisions at $\sqrt{s}$ = 13 TeV", *Phys. Lett. B* **780** (2018) 251, doi:10.1016/j.physletb.2018.02.033, arXiv:1710.11002.

[4] ATLAS Collaboration, "Measurement of the differential cross-sections of prompt and non-prompt production of J/ψ and ψ(2S) in pp collisions at $\sqrt{s}$ = 7 and 8 TeV with the ATLAS detector", *Eur. Phys. J. C* **76** (2016) 283, doi:10.1140/epjc/s10052-016-4050-8, arXiv:1512.03657.

[5] ATLAS Collaboration, "Measurement of Υ production in 7 TeV pp collisions at ATLAS", *Phys. Rev. D* **87** (2013) 052004, doi:10.1103/PhysRevD.87.052004, arXiv:1211.7255.

[6] LHCb Collaboration, "Measurement of J/ψ production in pp collisions at $\sqrt{s}$ = 7 TeV", *Eur. Phys. J. C* **71** (2011) 1645, doi:10.1140/epjc/s10052-011-1645-y, arXiv:1103.0423.

[7] LHCb Collaboration, "Measurement of Υ production in pp collisions at $\sqrt{s}$ = 7 TeV", *Eur. Phys. J. C* **72** (2012) 2025, doi:10.1140/epjc/s10052-012-2025-y, arXiv:1202.6579.

[8] LHCb Collaboration, "Forward production of Υ mesons in pp collisions at $\sqrt{s}$ = 7 and 8 TeV", *JHEP* **11** (2015) 103, doi:10.1007/JHEP11(2015)103, arXiv:1509.02372.

[9] LHCb Collaboration, "Production of J/ψ and Υ mesons in pp collisions at $\sqrt{s}$ = 8 TeV", *JHEP* **06** (2013) 064, doi:10.1007/JHEP06(2013)064, arXiv:1304.6977.

[10] LHCb Collaboration, "Measurement of forward J/ψ production cross-sections in pp collisions at $\sqrt{s}$ = 13 TeV", *JHEP* **10** (2015) 172, doi:10.1007/JHEP10(2015)172, arXiv:1509.00771. [Erratum: *JHEP* **05** (2017) 063].

[11] LHCb Collaboration, "Measurement of Υ production in pp collisions at $\sqrt{s}$ = 13 TeV", *JHEP* **07** (2018) 134, doi:10.1007/JHEP07(2018)134, arXiv:1804.09214. [Erratum: *JHEP* **05** (2019) 076].

[12] ATLAS Collaboration, "Measurement of χ_{c1} and χ_{c2} production with $\sqrt{s}$ = 7 TeV pp collisions at ATLAS", *JHEP* **07** (2014) 154, doi:10.1007/JHEP07(2014)154, arXiv:1404.7035.

[13] CMS Collaboration, "Measurement of the relative prompt production rate of χ_{c2} and χ_{c1} in pp collisions at $\sqrt{s}$ = 7 TeV", *Eur. Phys. J. C* **72** (2012) 2251, doi:10.1140/epjc/s10052-012-2251-3, arXiv:1210.0875.

[14] CMS Collaboration, "Measurement of the production cross section ratio $\sigma(\chi_{b2}(1P))$ / $\sigma(\chi_{b1}(1P))$ in pp collisions at $\sqrt{s}$ = 8 TeV", *Phys. Lett. B* **743** (2015) 383, doi:10.1016/j.physletb.2015.02.048, arXiv:1409.5761.

[15] LHCb Collaboration, "Measurement of the cross-section ratio $\sigma(\chi_{c2})$ / $\sigma(\chi_{c1})$ for prompt χ_c production at $\sqrt{s}$ = 7 TeV", *Phys. Lett. B* **714** (2012) 215, doi:10.1016/j.physletb.2012.06.077, arXiv:1202.1080.

[16] LHCb Collaboration, "Measurement of the relative rate of prompt χ_{c0}, χ_{c1} and χ_{c2} production at $\sqrt{s} = 7$ TeV", *JHEP* **10** (2013) 115, doi:10.1007/JHEP10(2013)115, arXiv:1307.4285.

[17] LHCb Collaboration, "Measurement of the ratio of prompt χ_c to J/ψ production in pp collisions at $\sqrt{s} = 7$ TeV", *Phys. Lett. B* **718** (2012) 431, doi:10.1016/j.physletb.2012.10.068, arXiv:1204.1462.

[18] LHCb Collaboration, "Study of χ_b meson production in pp collisions at $\sqrt{s} = 7$ and 8 TeV and observation of the decay $\chi_b(3P) \to \Upsilon(3S)\gamma$", *Eur. Phys. J. C* **74** (2014) 3092, doi:10.1140/epjc/s10052-014-3092-z, arXiv:1407.7734.

[19] CMS Collaboration, "Constraints on the χ_{c1} versus χ_{c2} polarizations in proton-proton collisions at $\sqrt{s} = 8$ TeV", *Phys. Rev. Lett.* **124** (2020) 162002, doi:10.1103/PhysRevLett.124.162002, arXiv:1912.07706.

[20] ATLAS Collaboration, "Measurement of the production cross-section of $\psi(2S) \to J/\psi(\to \mu^+\mu^-)\pi^+\pi^-$ in pp collisions at $\sqrt{s} = 7$ TeV at ATLAS", *JHEP* **09** (2014) 079, doi:10.1007/JHEP09(2014)079, arXiv:1407.5532.

[21] P. Faccioli et al., "Quarkonium production at the LHC: a data-driven analysis of remarkably simple experimental patterns", *Phys. Lett. B* **773** (2017) 476, doi:10.1016/j.physletb.2017.09.006, arXiv:1702.04208.

[22] CDF Collaboration, "Measurement of the B^+ total cross section and B^+ differential cross section $d\sigma/dp_T$ in $p\bar{p}$ collisions at $\sqrt{s} = 1.8$ TeV", *Phys. Rev. D* **65** (2002) 052005, doi:10.1103/PhysRevD.65.052005, arXiv:hep-ph/0111359.

[23] ATLAS Collaboration, "Measurement of the differential cross-section of B^+ meson production in pp collisions at $\sqrt{s} = 7$ TeV at ATLAS", *JHEP* **10** (2013) 042, doi:10.1007/JHEP10(2013)042, arXiv:1307.0126.

[24] ATLAS Collaboration, "Combined measurement of differential and total cross sections in the $H \to \gamma\gamma$ and the $H \to ZZ^* \to 4\ell$ decay channels at $\sqrt{s} = 13$ TeV with the ATLAS detector", *Phys. Lett. B* **786** (2018) 114, doi:10.1016/j.physletb.2018.09.019, arXiv:1805.10197.

[25] CMS Collaboration, "Measurement of the B^+ production cross section in pp collisions at $\sqrt{s} = 7$ TeV", *Phys. Rev. Lett.* **106** (2011) 112001, doi:10.1103/PhysRevLett.106.112001, arXiv:1101.0131.

[26] CMS Collaboration, "Measurement and interpretation of differential cross sections for Higgs boson production at $\sqrt{s} = 13$ TeV", *Phys. Lett. B* **792** (2019) 369, doi:10.1016/j.physletb.2019.03.059, arXiv:1812.06504.

[27] P. Faccioli, C. Lourenço, M. Araújo, and J. Seixas, "Universal kinematic scaling as a probe of factorized long-distance effects in high-energy quarkonium production", *Eur. Phys. J. C* **78** (2018) 118, doi:10.1140/epjc/s10052-018-5610-x, arXiv:1802.01102.

[28] CMS Collaboration, "Measurement of the prompt J/ψ and $\psi(2S)$ polarizations in pp collisions at $\sqrt{s} = 7$ TeV", *Phys. Lett. B* **727** (2013) 381, doi:10.1016/j.physletb.2013.10.055, arXiv:1307.6070.

[29] LHCb Collaboration, "Measurement of J/ψ polarization in pp collisions at $\sqrt{s}$ = 7 TeV", *Eur. Phys. J. C* **73** (2013) 2631, doi:10.1140/epjc/s10052-013-2631-3, arXiv:1307.6379.

[30] LHCb Collaboration, "Measurement of ψ(2S) polarisation in pp collisions at $\sqrt{s}$ = 7 TeV", *Eur. Phys. J. C* **74** (2014) 2872, doi:10.1140/epjc/s10052-014-2872-9, arXiv:1403.1339.

[31] ALICE Collaboration, "J/ψ polarization in pp collisions at $\sqrt{s}$ = 7 TeV", *Phys. Rev. Lett.* **108** (2012) 082001, doi:10.1103/PhysRevLett.108.082001, arXiv:1111.1630.

[32] P. Faccioli, C. Lourenço, and T. Madlener, "From prompt to direct J/ψ production: new insights on the χ_{c1} and χ_{c2} polarizations and feed-down contributions from a global-fit analysis of mid-rapidity LHC data", *Eur. Phys. J. C* **80** (2020) 623, doi:10.1140/epjc/s10052-020-8201-6, arXiv:2006.15446.

[33] Y.-Q. Ma, K. Wang, and K.-T. Chao, "J/ψ (ψ') production at the Tevatron and LHC at $O(\alpha_s^4 v^4)$ in nonrelativistic QCD", *Phys. Rev. Lett.* **106** (2011) 042002, doi:10.1103/PhysRevLett.106.042002, arXiv:1009.3655.

[34] M. Butenschön and B. A. Kniehl, "Next-to-leading-order tests of NRQCD factorization with J/ψ yield and polarization", *Mod. Phys. Lett. A* **28** (2013) 1350027, doi:10.1142/S0217732313500272, arXiv:1212.2037.

[35] R. Baier and R. Rückl, "Hadronic collisions: a quarkonium factory", *Z. Phys. C* **19** (1983) 251, doi:10.1007/BF01572254.

[36] CDF Collaboration, "Quarkonia production at CDF", *Nucl. Phys. A* **610** (1996) 373c, doi:10.1016/S0375-9474(96)00371-5.

[37] CDF Collaboration, "J/ψ and ψ(2S) production in p$\bar{\text{p}}$ collisions at $\sqrt{s}$ = 1.8 TeV", *Phys. Rev. Lett.* **79** (1997) 572, doi:10.1103/PhysRevLett.79.572.

[38] G. T. Bodwin, E. Braaten, and P. Lepage, "Rigorous QCD analysis of inclusive annihilation and production of heavy quarkonium", *Phys. Rev. D* **51** (1995) 1125, doi:10.1103/PhysRevD.51.1125, arXiv:hep-ph/9407339. [Erratum: *Phys. Rev. D* **55** (1997) 5853].

[39] J.-P. Lansberg, "J/ψ production at $\sqrt{s}$ = 1.96 and 7 TeV: Color-Singlet Model, NNLO* and polarisation", *J. Phys. G* **38** (2011) 124110, doi:10.1088/0954-3899/38/12/124110, arXiv:1107.0292.

[40] Y.-Q. Ma, K. Wang, and K.-T. Chao, "A complete NLO calculation of the J/ψ and ψ(2S) production at hadron colliders", *Phys. Rev. D* **84** (2011) 114001, doi:10.1103/PhysRevD.84.114001, arXiv:1012.1030.

[41] M. Butenschön and B. A. Kniehl, "Reconciling J/ψ production at HERA, RHIC, Tevatron, and LHC with NRQCD factorization at next-to-leading order", *Phys. Rev. Lett.* **106** (2011) 022003, doi:10.1103/PhysRevLett.106.022003, arXiv:1009.5662.

[42] K.-T. Chao et al., "J/ψ polarization at hadron colliders in nonrelativistic QCD", *Phys. Rev. Lett.* **108** (2012) 242004, doi:10.1103/PhysRevLett.108.242004, arXiv:1201.2675.

[43] M. Butenschön and B. A. Kniehl, "J/ψ polarization at Tevatron and LHC: nonrelativistic-QCD factorization at the crossroads", *Phys. Rev. Lett.* **108** (2012) 172002, doi:10.1103/PhysRevLett.108.172002, arXiv:1201.1872.

[44] B. Gong, L.-P. Wan, J.-X. Wang, and H.-F. Zhang, "Polarization for prompt J/ψ and ψ(2S) production at the Tevatron and LHC", *Phys. Rev. Lett.* **110** (2013) 042002, doi:10.1103/PhysRevLett.110.042002, arXiv:1205.6682.

[45] M. Butenschön and B. A. Kniehl, "World data of J/ψ production consolidate NRQCD factorization at NLO", *Phys. Rev. D* **84** (2011) 051501, doi:10.1103/PhysRevD.84.051501, arXiv:1105.0820.

[46] G. T. Bodwin, H. S. Chung, U.-R. Kim, and J. Lee, "Fragmentation contributions to J/ψ production at the Tevatron and the LHC", *Phys. Rev. Lett.* **113** (2014) 022001, doi:10.1103/PhysRevLett.113.022001, arXiv:1403.3612.

[47] P. Faccioli, C. Lourenço, J. Seixas, and H. K. Wöhri, "Towards the experimental clarification of quarkonium polarization", *Eur. Phys. J. C* **69** (2010) 657, doi:10.1140/epjc/s10052-010-1420-5, arXiv:1006.2738.

[48] P. Faccioli et al., "Quarkonium production in the LHC era: a polarized perspective", *Phys. Lett. B* **736** (2014) 98, doi:10.1016/j.physletb.2014.07.006, arXiv:1403.3970.

[49] G. T. Bodwin et al., "Fragmentation contributions to hadroproduction of prompt J/ψ, χ_{cJ}, and ψ(2S) states", *Phys. Rev. D* **93** (2016) 034041, doi:10.1103/PhysRevD.93.034041, arXiv:1509.07904.

[50] P. Faccioli et al., "From identical S- and P-wave p_{T} spectra to maximally distinct polarizations: probing NRQCD with χ states", *Eur. Phys. J. C* **78** (2018) 268, doi:10.1140/epjc/s10052-018-5755-7, arXiv:1802.01106.

[51] BES Collaboration, "ψ(2S) $\to \pi^+\pi^-$J/ψ decay distributions", *Phys. Rev. D* **62** (2000) 032002, doi:10.1103/PhysRevD.62.032002, arXiv:hep-ex/9909038.

[52] M. Beneke, F. Maltoni, and I. Z. Rothstein, "QCD analysis of inclusive B decay into charmonium", *Phys. Rev. D* **59** (1999) 054003, doi:10.1103/PhysRevD.59.054003, arXiv:hep-ph/9808360.

[53] M. Beneke, G. A. Schuler, and S. Wolf, "Quarkonium momentum distributions in photoproduction and B decay", *Phys. Rev. D* **62** (2000) 034004, doi:10.1103/PhysRevD.62.034004, arXiv:hep-ph/0001062.

[54] CLEO Collaboration, "Inclusive decays of B mesons to charmonium", *Phys. Rev. D* **52** (1995) 2661, doi:10.1103/PhysRevD.52.2661.

[55] BaBar Collaboration, "Study of inclusive production of charmonium mesons in B decay", *Phys. Rev. D* **67** (2003) 032002, doi:10.1103/PhysRevD.67.032002, arXiv:hep-ex/0207097.

[56] CDF Collaboration, "Measurement of J/ψ and ψ(2S) polarization in $\mathrm{p\bar{p}}$ collisions at $\sqrt{s} = 1.8$ TeV", *Phys. Rev. Lett.* **85** (2000) 2886, doi:10.1103/PhysRevLett.85.2886, arXiv:hep-ex/0004027.

[57] S. Fleming, O. F. Hernandez, I. Maksymyk, and H. Nadeau, "NRQCD matrix elements in polarization of J/ψ produced from b decay", *Phys. Rev. D* **55** (1997) 4098, doi:10.1103/PhysRevD.55.4098, arXiv:hep-ph/9608413.

[58] V. Krey and K. R. S. Balaji, "Polarized J/ψ production from B mesons at the Tevatron", *Phys. Rev. D* **67** (2003) 054011, doi:10.1103/PhysRevD.67.054011, arXiv:hep-ph/0209135.

[59] P. Faccioli, C. Lourenço, J. Seixas, and H. K. Wöhri, "Determination of χ_c and χ_b polarizations from dilepton angular distributions in radiative decays", *Phys. Rev. D* **83** (2011) 096001, doi:10.1103/PhysRevD.83.096001, arXiv:1103.4882.

[60] ATLAS Collaboration, "Measurement of the Z/γ^* boson transverse momentum distribution in pp collisions at $\sqrt{s} = 7$ TeV with the ATLAS detector", *JHEP* **09** (2014) 145, doi:10.1007/JHEP09(2014)145, arXiv:1406.3660.

[61] CMS Collaboration, "Measurement of the transverse momentum spectra of weak vector bosons produced in proton-proton collisions at $\sqrt{s} = 8$ TeV", *JHEP* **02** (2017) 096, doi:10.1007/JHEP02(2017)096, arXiv:1606.05864.

[62] CMS Collaboration, "Measurement of the Z boson differential cross section in transverse momentum and rapidity in proton-proton collisions at 8 TeV", *Phys. Lett. B* **749** (2015) 187, doi:10.1016/j.physletb.2015.07.065, arXiv:1504.03511.

[63] B. Guberina, J. H. Kühn, R. D. Peccei, and R. Rückl, "Rare decays of the Z^0", *Nucl. Phys. B* **174** (1980) 317, doi:10.1016/0550-3213(80)90287-4.

[64] T.-C. Huang and F. Petriello, "Rare exclusive decays of the Z-boson revisited", *Phys. Rev. D* **92** (2015) 014007, doi:10.1103/PhysRevD.92.014007, arXiv:1411.5924.

[65] G. T. Bodwin, H. S. Chung, J.-H. Ee, and J. Lee, "Z-boson decays to a vector quarkonium plus a photon", *Phys. Rev. D* **97** (2018) 016009, doi:10.1103/PhysRevD.97.016009, arXiv:1709.09320.

Chapter 7
Two-body decay distributions beyond the dilepton case

Throughout the previous chapters we explored in detail the properties of the angular distribution of the dilepton decay of a vector particle. We will now illustrate a general method to calculate the shape of the angular distribution for any considered two-body decay, and survey examples for different kinds of initial particles, with integer or half-integer J.

We will focus on the following questions.

- How does the shape of the angular distribution depend on J and J_z? What are the observable parameters and their allowed physical values? How does the distribution depend on the identity of the decay products?
- If the nature of the decaying particle has not yet been identified and its angular momentum properties are unknown, how (and with what assumptions) can the measurement of the angular distribution lead to the determination of J?
- Apart from the previously discussed smearing effects in the indirect production from the decay of a $J = 0$ state, how can a $J > 0$ particle produce a completely isotropic two-body decay distribution, irrespectively of its polarization? Why is such an observation not a paradox?

P. Faccioli and C. Lourenço, *Particle Polarization in High Energy Physics*,
Lecture Notes in Physics 1002,
https://doi.org/10.1007/978-3-031-08876-6_7

7.1 Wigner rotation matrices

We saw in Chapter 1 how to calculate the dilepton decay angular distribution of a vector particle produced in a certain angular momentum configuration (its "polarization"), namely $|J, J_z\rangle = |1, 0\rangle_z$ or $|1, \pm 1\rangle_z$, or a superposition of these three cases, with respect to a given quantization axis z. In the following chapters we discussed in detail the properties of this distribution. In this chapter we consider several more decay distributions, involving initial and final particles of different categories, focusing on how they can be calculated in their general form and on how they reflect the angular momentum properties of the decaying particle.

The principal tool in all these calculations is the set of rotation transformations represented by the Wigner matrices [1]. Each matrix is identified by the value of the total angular momentum of the decaying particle, J. Its elements, $\mathcal{D}^J_{LL'}(\vartheta, \varphi)$, describe how an angular momentum state, with J_z projection L along a given axis z, transforms to a superposition of states of all possible projections L' along a different set of axes, rotated with respect to the original one by the spherical coordinates ϑ and φ. We introduced the Wigner matrices in Eq. 1.1 and defined them in Eq. 1.2, here reproduced for completeness:

$$\mathcal{D}^J_{LL'}(\vartheta, \varphi) = e^{-iL\varphi}\, d^J_{LL'}(\vartheta)\, e^{iL'\varphi}\,. \tag{7.1}$$

Before continuing with the description of these matrices, we will make a parenthesis to clarify that we use in this book a simpler notation than the one found in Refs. [2, 3] and other publications, where the rotation matrix elements are functions of the *three* Euler angles necessary to define a *completely generic* rotation in space, $D(\alpha, \beta, \gamma)$. That general transformation is the succession of a rotation around the z axis by the angle α, followed by a rotation around the (new) y axis by the angle β, and by a third rotation around, again, the (latest) z axis, this time by the angle γ, just as illustrated (except for the names of the angles) in Fig. 2.22, for the most generic change of reference frame.

In all calculations considered in this book, and in the general method used to calculate decay distributions, more examples of which will be seen in this chapter, the Wigner matrices are employed to rotate a *direction*, the one of the quantization axis, and not a three-dimensional shape; the number of angles parametrizing the rotation of a direction is two, not three, as would be needed to fully define the rotation of a generic three dimensional object with its own (not cylindrically symmetric) shape, like a generic wave function.

In fact, while the measurement of the decay angular distribution of a particle can be considered as a measurement of the particle's wave function, the wave functions of the decay products, which are the objects to which we apply the rotations in the calculation procedure, are not observed, unless they, in turn, decay *and* this further step is included as component of a higher-dimensional angular analysis.

Examples of the latter case are the cascade processes seen in Chapter 6, where the further decaying "daughter" (a J/ψ or Υ meson, or a Z boson) was represented by an additional Wigner matrix element changing the polarization axis of the dilepton

system as seen in the daughter's rest frame, therefore "giving life" to the daughter's three-dimensional nature and adding two more angles to the list of the observable degrees of freedom.

However, when the decay product is the "final" one, it has no associated "three-dimensional" structure that would justify the use of three angles for its rotation from a quantization "frame" to another: what we rotate in this case is only its quantization *axis* z and this operation depends only on the two angular coordinates defining the direction of the new axis with respect to the old axis.

To obtain this "minimal" rotation from the potentially more generic one described by the Wigner matrix, we have to impose that the two rotation components (first and third) around the z axis are the opposite of each other, i.e. $\gamma = -\alpha$. In this way, as can be recognized by observing the passages of the "cartoon" in Fig. 2.22 and inverting the direction of the last rotation step, the net effect is effectively a rotation made around the axis perpendicular to the plane containing the old and the new z axes, which is, in fact, the only meaningful option when no information exists about the shape of the rotated object. This is why we can use a simpler notation than the general one:

$$D^J_{LL'}(\varphi, \vartheta, -\varphi) \quad \rightarrow \quad \mathcal{D}^J_{LL'}(\vartheta, \varphi)\,. \tag{7.2}$$

It can now be observed that the complex exponential terms in Eq. 7.1 correspond to the two opposite rotations around the z axis (which, as explained in Section 2.15 and represented by Eq. 2.40, can be seen as shifts of the φ coordinate), while the ("reduced") d-matrix elements, $d^J_{LL'}(\vartheta)$, represent the polar-angle displacement from the z axis caused by the rotation around the y axis.

As already mentioned in Section 1.3, the reduced Wigner matrices can be computed with the expression

$$\begin{aligned} d^J_{LL'}(\vartheta) = & \sum_{t=\max(0,L-L')}^{\min(J+L,J-L')} (-1)^t \\ & \times \frac{\sqrt{(J+L)!\,(J-L)!\,(J+L')!\,(J-L')!}}{(J+L-t)!\,(J-L'-t)!\,t!\,(t-L+L')!} \\ & \times \left(\cos\frac{\vartheta}{2}\right)^{2J-(L'-L+2t)} \left(\sin\frac{\vartheta}{2}\right)^{L'-L+2t}. \end{aligned} \tag{7.3}$$

We alert the reader to the fact that two alternative conventions exist in the literature for this definition [1–4], only differing for a sign in certain configurations. They are entirely equivalent for the final physical results provided that, naturally, the same convention is systematically used in all the steps of the calculations. In this book we adopted and consistently used the convention of Ref. [2].

The number of computations can be significantly reduced through the use of the following relations (equivalent to Eq. 1.4):

$$\begin{aligned} d^J_{L,L'}(\vartheta) &= d^J_{-L',-L}(\vartheta)\,, \\ d^J_{L,L'}(\vartheta) &= (-1)^{L'-L}\, d^J_{L',L}(\vartheta)\,. \end{aligned} \tag{7.4}$$

The $d^J_{L,L'}(\vartheta)$ matrices are shown in Tables 7.1–7.6, respectively for $J = 1/2$, $3/2$, 1, 2, 3, and 4. In all tables we used two abbreviations, $c \equiv \cos(\vartheta/2)$ and $s \equiv \sin(\vartheta/2)$ (so that $c^2 + s^2 = 1$), to provide more compact expressions. It is worth noting that, since $0 < \vartheta < \pi$, both c and s are always positive. With this notation, $d^J_{J,J} = c^{2J}$ and $d^J_{-J,J} = s^{2J}$. As clearly seen in the definition of Eq. 7.3, all matrix elements are polynomials of order $2J$ in c and s.

Obviously, no table is needed for the $J = 0$ case, given that the only matrix element appearing in the formulas for its calculation, $d^0_{0,0}$, is independent of the

Table 7.1 The reduced Wigner matrix for the $J = 1/2$ case, $d^{1/2}_{L,L'}(\vartheta)$, with $c \equiv \cos(\vartheta/2)$ and $s \equiv \sin(\vartheta/2)$.

L	L'	
	$-1/2$	$+1/2$
$-1/2$	c	s
$+1/2$	$-s$	c

Table 7.2 The reduced Wigner matrix for the $J = 3/2$ case, $d^{3/2}_{L,L'}(\vartheta)$.

L	L'			
	$-3/2$	$-1/2$	$+1/2$	$+3/2$
$-3/2$	c^3	$\sqrt{3}\,c^2\,s$	$\sqrt{3}\,c\,s^2$	s^3
$-1/2$	$-\sqrt{3}\,c^2\,s$	$c\,(1-3s^2)$	$-(1-3c^2)\,s$	$\sqrt{3}\,c\,s^2$
$+1/2$	$\sqrt{3}\,c\,s^2$	$(1-3c^2)\,s$	$c\,(1-3s^2)$	$\sqrt{3}\,c^2\,s$
$+3/2$	$-s^3$	$\sqrt{3}\,c\,s^2$	$-\sqrt{3}\,c^2\,s$	c^3

Table 7.3 The reduced Wigner matrix for the $J = 1$ case, $d^1_{L,L'}(\vartheta)$.

L	L'		
	-1	0	$+1$
-1	c^2	$\sqrt{2}\,c\,s$	s^2
0	$-\sqrt{2}\,c\,s$	$2\,c^2-1$	$\sqrt{2}\,c\,s$
$+1$	s^2	$-\sqrt{2}\,c\,s$	c^2

Table 7.4 The reduced Wigner matrix for the $J = 2$ case, $d^2_{L,L'}(\vartheta)$.

L	L'				
	-2	-1	0	$+1$	$+2$
-2	c^4	$2\,c^3 s$	$\sqrt{6}\,c^2 s^2$	$2\,cs^3$	s^4
-1	$-2\,c^3 s$	$c^2\,(1-4\,s^2)$	$-\sqrt{6}\,cs\,(1-2\,c^2)$	$-(1-4\,c^2)\,s^2$	$2\,cs^3$
0	$\sqrt{6}\,c^2 s^2$	$\sqrt{6}\,cs\,(1-2\,c^2)$	$1-6\,c^2 s^2$	$-\sqrt{6}\,cs\,(1-2\,c^2)$	$\sqrt{6}\,c^2 s^2$
$+1$	$-2\,cs^3$	$-(1-4\,c^2)\,s^2$	$\sqrt{6}\,cs\,(1-2\,c^2)$	$c^2\,(1-4\,s^2)$	$2\,c^3 s$
$+2$	s^4	$-2\,cs^3$	$\sqrt{6}\,c^2 s^2$	$-2\,c^3 s$	c^4

Table 7.5 The reduced Wigner matrix for the $J = 3$ case, $d^3_{L,L'}(\vartheta)$.

L	L'						
	-3	-2	-1	0	$+1$	$+2$	$+3$
-3	c^6	$\sqrt{6}\,c^5 s$	$\sqrt{15}\,c^4 s^2$	$2\sqrt{5}\,c^3 s^3$	$\sqrt{15}\,c^2 s^4$	$\sqrt{6}\,cs^5$	s^6
-2	$-\sqrt{6}\,c^5 s$	c^4 $(1-6\,s^2)$	$\sqrt{10}\,c^3 s$ $(1-3\,s^2)$	$-\sqrt{30}\,c^2 s^2$ $(1-2\,c^2)$	$-\sqrt{10}\,cs^3$ $(1-3\,c^2)$	$-s^4$ $(1-6\,c^2)$	$\sqrt{6}\,cs^5$
-1	$\sqrt{15}\,c^4 s^2$	$-\sqrt{10}\,c^3 s$ $(1-3\,s^2)$	$c^2\,(1+5\,s^2$ $(1-3\,c^2))$	$2\sqrt{3}\,cs$ $(1-5\,c^2 s^2)$	$s^2\,(1+5\,c^2$ $(1-3\,s^2))$	$-\sqrt{10}\,cs^3$ $(1-3\,c^2)$	$\sqrt{15}\,c^2 s^4$
0	$-2\sqrt{5}\,c^3 s^3$	$-\sqrt{30}\,c^2 s^2$ $(1-2\,c^2)$	$-2\sqrt{3}\,cs$ $(1-5\,c^2 s^2)$	$-(1-2\,c^2)$ $(1-10\,c^2 s^2)$	$2\sqrt{3}\,cs$ $(1-5\,c^2 s^2)$	$-\sqrt{30}\,c^2 s^2$ $(1-2\,c^2)$	$2\sqrt{5}\,c^3 s^3$
$+1$	$\sqrt{15}\,c^2 s^4$	$\sqrt{10}\,cs^3$ $(1-3\,c^2)$	$s^2\,(1+5\,c^2$ $(1-3\,s^2))$	$-2\sqrt{3}\,cs$ $(1-5\,c^2 s^2)$	$c^2\,(1+5\,s^2$ $(1-3\,c^2))$	$\sqrt{10}\,c^3 s$ $(1-3\,s^2)$	$\sqrt{15}\,c^4 s^2$
$+2$	$-\sqrt{6}\,cs^5$	$-s^4$ $(1-6\,c^2)$	$\sqrt{10}\,cs^3$ $(1-3\,c^2)$	$-\sqrt{30}\,c^2 s^2$ $(1-2\,c^2)$	$-\sqrt{10}\,c^3 s$ $(1-3\,s^2)$	c^4 $(1-6\,s^2)$	$\sqrt{6}\,c^5 s$
$+3$	s^6	$-\sqrt{6}\,cs^5$	$\sqrt{15}\,c^2 s^4$	$-2\sqrt{5}\,c^3 s^3$	$\sqrt{15}\,c^4 s^2$	$-\sqrt{6}\,c^5 s$	c^6

polar and azimuthal decay angles, always resulting in an isotropic angular decay distribution.

To compare these compact expressions with those used in Chapter 1 and elsewhere, it is useful to keep in mind a few trigonometric identities, such as $\sin(\vartheta) = 2\cos(\vartheta/2)\sin(\vartheta/2)$, $\cos^2(\vartheta/2) = 1/2\,(1+\cos\vartheta)$, and $\sin^2(\vartheta/2) = 1/2\,(1-\cos\vartheta)$.

For visibility purposes, Table 7.6 is reported in truncated form, omitting the columns corresponding to $+1 \le L' \le +4$ and several of the terms in the displayed

Table 7.6 The reduced Wigner matrix for the $J = 4$ case, $d^4_{L,L'}(\vartheta)$. The missing matrix elements can be obtained using Eq. 7.4, as shown in the inset.

L \ L'	−4	−3	−2	−1	0
−4	c^8				
−3	$-2\sqrt{2}\,c^7 s$	$c^6(1-8s^2)$			
−2	$2\sqrt{7}\,c^6 s^2$	$-\sqrt{14}\,c^5 s(1-4s^2)$	$c^4(15-42c^2+28c^4)$		
−1	$-2\sqrt{14}\,c^5 s^3$	$\sqrt{7}\,c^4 s^2(3-8s^2)$	$-\sqrt{2}\,c^3 s(10-35c^2+28c^4)$	$c^2(-10+60c^2-105c^4+56c^6)$	
0	$\sqrt{70}\,c^4 s^4$	$2\sqrt{35}\,c^3 s^3(1-2c^2)$	$\sqrt{10}\,c^2(3-17c^2+28c^4-14c^6)$	$2\sqrt{5}\,cs(1-9c^2+21c^4-14c^6)$	$1-10\,c^2 s^2(2-7c^2+7c^4)$
+1	$-2\sqrt{14}\,c^3 s^5$	$-\sqrt{7}\,c^2 s^4(3-8c^2)$	$-\sqrt{2}\,cs^3(3-21c^2+28c^4)$	$-s^2(1-18c^2+63c^4-56c^6)$	
+2	$2\sqrt{7}\,c^2 s^6$	$\sqrt{14}\,cs^5(1-4c^2)$	$s^4(1-14c^2+28c^4)$		
+3	$-2\sqrt{2}\,cs^7$	$-s^6(1-8c^2)$			
+4	s^8				

L \ L'	−4	−3	−2	−1	0	+1	+2	+3	+4
−4	$\mathbf{d_{4,4}}$	$-d_{4,3}$	$d_{4,2}$	$-d_{4,1}$	$d_{4,0}$	$-d_{4,-1}$	$d_{4,-2}$	$-d_{4,-3}$	$d_{4,-4}$
−3	$\mathbf{d_{4,3}}$	$\mathbf{d_{3,3}}$	$-d_{3,2}$	$d_{3,1}$	$-d_{3,0}$	$d_{3,-1}$	$-d_{3,-2}$	$d_{3,-3}$	$-d_{4,-3}$
−2	$\mathbf{d_{4,2}}$	$\mathbf{d_{3,2}}$	$\mathbf{d_{2,2}}$	$-d_{2,1}$	$d_{2,0}$	$-d_{2,-1}$	$d_{2,-2}$	$-d_{3,-2}$	$d_{4,-2}$
−1	$\mathbf{d_{4,1}}$	$\mathbf{d_{3,1}}$	$\mathbf{d_{2,1}}$	$\mathbf{d_{1,1}}$	$-d_{1,0}$	$d_{1,-1}$	$-d_{2,-1}$	$d_{3,-1}$	$-d_{4,-1}$
0	$\mathbf{d_{4,0}}$	$\mathbf{d_{3,0}}$	$\mathbf{d_{2,0}}$	$\mathbf{d_{1,0}}$	$\mathbf{d_{0,0}}$	$-d_{1,0}$	$d_{2,0}$	$-d_{0,3}$	$d_{4,0}$
+1	$\mathbf{d_{4,-1}}$	$\mathbf{d_{3,-1}}$	$\mathbf{d_{2,-1}}$	$\mathbf{d_{1,-1}}$	$d_{1,0}$	$d_{1,1}$	$-d_{2,1}$	$d_{3,1}$	$-d_{4,1}$
+2	$\mathbf{d_{4,-2}}$	$\mathbf{d_{3,-2}}$	$\mathbf{d_{2,-2}}$	$d_{2,-1}$	$d_{2,0}$	$d_{2,1}$	$d_{2,2}$	$-d_{3,2}$	$d_{4,2}$
+3	$\mathbf{d_{4,-3}}$	$\mathbf{d_{3,-3}}$	$d_{3,-2}$	$d_{3,-1}$	$d_{3,0}$	$d_{3,1}$	$d_{3,2}$	$d_{3,3}$	$-d_{4,3}$
+4	$\mathbf{d_{4,-4}}$	$d_{4,-3}$	$d_{4,-2}$	$d_{4,-1}$	$d_{4,0}$	$d_{4,1}$	$d_{4,2}$	$d_{4,3}$	$d_{4,4}$

columns. The missing elements can be easily derived from those shown, using the symmetry relations presented in Eq. 7.4, as illustrated in the inset table.

7.2 Generic formulas for two-body decay distributions

To derive the shape of the dilepton decay distribution of the J/ψ, in Chapter 1, we used the following relevant physical constraints: a) the decaying particle has total angular momentum $J = 1$; b) the products are a fermion and an anti-fermion, of spin $1/2$ and mass negligible with respect to that of the mother particle; c) an intermediate vector boson (a virtual photon) couples to the final fermions preserving their helicities. These strong requirements effectively meant that we were considering a transition between two $J = 1$ (vector) systems, with the final one being "transversely polarized" ($J_{z'} = \pm 1$ along the common flight direction of the two fermions in the J/ψ rest frame). The resulting distributions and the meaning of their shape parameters were, obviously, specific to this well defined physical case.

We will now consider the *most general* case of two-body decays, $O \to X_1 X_2$, without any a priori constraint on the underlying physics. The result will depend on several amplitudes, in growing number with increasing values of the angular momentum quantum numbers of the initial (J) and final (J_1 and J_2) states. In this approach, physical hypotheses can be applied a posteriori, by restricting the possible number and values of the relevant amplitudes. Vice versa, an experimental measurement determining the observable shape parameters will put constraints on such amplitudes and, therefore, on the admissible hypotheses for the process being observed, sometimes even helping in the determination of the properties of the decaying particle.

For our completely generic description, we define a set of amplitudes, $\mathcal{A}_{M,G'_1,G'_2}$. As illustrated in Fig. 7.1-left, each coefficient represents the combined probability that O has angular momentum projection M along the chosen quantization axis z

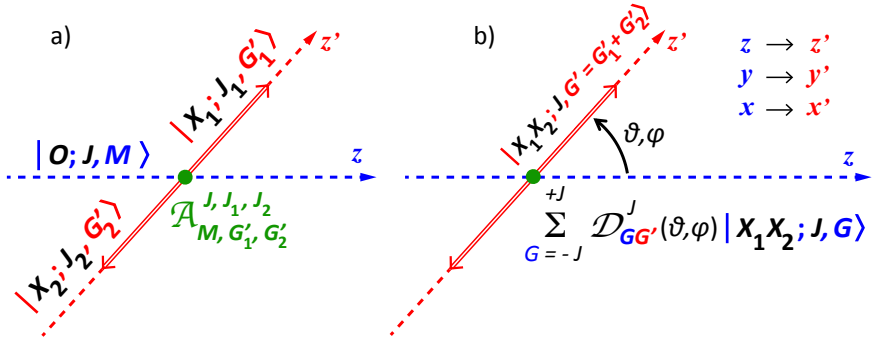

Fig. 7.1 Diagram of the $O \to X_1 X_2$ decay as seen in the O rest frame, specifying notations for axes, angles and angular momentum states of the initial and final particles.

(for example its momentum in the laboratory, that is the HX axis, or the direction of one or the other colliding beams, the two GJ axes, or the average of the two, the CS axis) and X_1 and X_2 have angular momentum projections G'_1 and G'_2 along the z' axis, defined by their common flight direction in the O rest frame (with a purely conventional orientation along the X_1 momentum).

We will consider the $\mathcal{A}_{M,G'_1,G'_2}$ amplitudes as generic complex numbers, without imposing any specific constraints. These are the coefficients that contain information on the underlying process dynamics, determining both the polarization state of O (the amplitudes a_M used in Chapter 1 are included in $\mathcal{A}_{M,G'_1,G'_2}$) and the angular momentum configurations of the decay products. They depend on the elementary couplings in the considered production and decay processes, which determine the allowed combinations of initial- and final-state "helicities" (angular momentum projections) and their probabilities. For example, in the decays of Standard Model vector gauge bosons (virtual photon, Z, W, gluon) into sufficiently light fermions, helicity conservation forbids terms with opposite fermion spin projections along z', so that $\mathcal{A}_{M,+1/2,-1/2} = \mathcal{A}_{M,-1/2,+1/2} = 0$. Moreover, considering for simplicity the leading-order process of Fig. 2.2-c, dominating towards low p_{T}, and choosing the CS frame, helicity conservation also forbids the J_z projection $M = 0$ for the initial state, that is, $\mathcal{A}_{0,G'_1,G'_2} = 0$.

We start by calculating the amplitude of the transition $O(M) \to X_1(G'_1)\,X_2(G'_2)$, which, by definition, involves the individual coefficient $\mathcal{A}_{M,G'_1,G'_2}$. Similarly to what we did in Chapter 1, and as illustrated in Fig. 7.1-right, we use the Wigner matrix to "project" the angular momentum state of the X_1X_2 system from the z' axis to the z axis:

$$|X_1X_2;\, J,\, G'_1 + G'_2\,\rangle_{z'} = \sum_{G=-J}^{+J} \mathcal{D}^{J}_{G,\,G'_1+G'_2}(\vartheta,\varphi)\;|X_1X_2;\, J,\, G\,\rangle_z\,. \tag{7.5}$$

Indicating with $\mathcal{B}_{M,G'_1,G'_2}$ the transition operator, the probability amplitude of the process can be written as

$$\begin{aligned}
\mathcal{A}\Big[O(M) \to X_1(G'_1)\,X_2(G'_2)\Big] \;&=\; {}_{z'}\langle X_1X_2;\, J,\, G'_1 + G'_2\,|\,\mathcal{B}_{M,\,G'_1,G'_2}\,|\,O;\, J,\, M\rangle_z \\
&= \sum_{G=-J}^{+J} \mathcal{D}^{J*}_{G,\,G'_1+G'_2}(\vartheta,\varphi)\;{}_z\langle X_1X_2;\, J,\, G\,|\,\mathcal{B}_{M,\,G'_1,G'_2}\,|\,O;\, J,\, M\rangle_z \\
&= \sum_{G=-J}^{+J} \mathcal{D}^{J*}_{G,\,G'_1+G'_2}(\vartheta,\varphi)\;\delta_{M,G}\,\mathcal{A}_{M,\,G'_1,G'_2} \\
&= \mathcal{D}^{J*}_{M,\,G'_1+G'_2}(\vartheta,\varphi)\;\mathcal{A}_{M,\,G'_1,G'_2}\,,
\end{aligned} \tag{7.6}$$

where the relation ${}_z\langle X_1X_2;\, J,\, G\,|\,\mathcal{B}_{M,\,G'_1,G'_2}\,|\,O;\, J,\, M\rangle_z = \delta_{M,G}\,\mathcal{A}_{M,\,G'_1,G'_2}$ contains the conservation of J_z, in the Kronecker delta, and the process dynamics, in $\mathcal{A}_{M,G'_1,G'_2}$.

The following step in making the calculations more and more general consists in considering O to be produced not as a pure state having $J_z = M$, but as a superposition of J_z eigenstates; this is equivalent to taking the sum of all possible transition

amplitudes given by the previous equation:

$$\mathcal{A}\left[O \to X_1(G_1')\, X_2(G_2')\right] \;=\; \sum_{M=-J}^{+J} \mathcal{A}\left[O(M) \to X_1(G_1')\, X_2(G_2')\right] . \tag{7.7}$$

We note that, having defined $\mathcal{A}_{M,G_1',G_2'}$ to include the probability that O has J_z projection M, the sum does not contain the further coefficient a_M as it did, for example, in Eq. 1.10.

The square modulus of this amplitude gives the partial angular distribution for the specific angular momentum configurations G_1' and G_2' of the decay products:

$$\begin{aligned} &W_{G_1',G_2'}(\cos\vartheta,\varphi) = \\ &\sum_{|M|\le J,\,|N|\le J} \mathcal{A}^*\left[O(M) \to X_1(G_1')\, X_2(G_2')\right] \mathcal{A}\left[O(N) \to X_1(G_1')\, X_2(G_2')\right] \\ &= \sum_{|M|\le J,\,|N|\le J} \mathcal{D}^{J}_{M,\,G_1'+G_2'}(\vartheta,\varphi)\, \mathcal{D}^{J*}_{N,\,G_1'+G_2'}(\vartheta,\varphi)\, \mathcal{A}^*_{M,G_1',G_2'}\, \mathcal{A}_{N,G_1',G_2'} . \end{aligned} \tag{7.8}$$

As the final step, we sum over all allowed X_1 and X_2 angular momentum configurations (which are not observed, because eventual decay distributions of X_1 and X_2 are not part of the analysis):

$$W(\cos\vartheta,\varphi) \;=\; \sum_{\substack{|G_1'|\le J_1,\,|G_2'|\le J_2 \\ |G_1'+G_2'|\le \min\{J,\,J_1+J_2\}}} W_{G_1',G_2'}(\cos\vartheta,\varphi) . \tag{7.9}$$

The sum is made over all values of G_1' and G_2' satisfying angular momentum conservation. Besides the obvious relations $|G_1'| \le J_1$ and $|G_2'| \le J_2$, the inequality $|G_1' + G_2'| \le \min\{J,\, J_1 + J_2\}$ accounts for the fact that the relation $|J_1 - J_2| \le J \le J_1 + J_2$ is not necessarily satisfied when the decay products X_1 and X_2 have a relative orbital angular momentum $\mathbf{I_{1,2}}$, i.e. $\mathbf{J} = \mathbf{J_1} + \mathbf{J_2} + \mathbf{I_{1,2}}$. The presence of a nonzero $\mathbf{I_{1,2}}$ explains, for example, the existence of decays like $B^+ \to \mathrm{J}/\psi\, K^+$, where $J = 0$ and $|J_1 - J_2| = 1$, so that $J < |J_1 - J_2|$. In the next sections we will address several more cases, for example those where a particle of $J = 2$ decays to two spin-1/2 fermions, or a particle of $J = 1$ decays to two $J = 0$ particles, for which $J > J_1 + J_2$. When this latter condition happens, $|G_1' + G_2'|$ never reaches the value J, because the orbital angular momentum $\mathbf{I_{1,2}}$ has always projection zero along the quantization axis of the decay products (z') and does not contribute to a possible larger magnitude of $G_1' + G_2'$.

The dependence of the distribution on the dynamical amplitudes $\mathcal{A}_{M,G_1',G_2'}$ is usually reorganized into a set of complex coefficients,

$$\rho^{G'}_{M,N} \;=\; \sum_{\substack{|G_1'|\,\le\, J_1,\,|G_2'|\,\le\, J_2 \\ G_1'+G_2'=G'}} \mathcal{A}^*_{M,G_1',G_2'}\, \mathcal{A}_{N,G_1',G_2'} , \tag{7.10}$$

which form, for each G', the so-called "spin density matrix", a hermitian matrix ($\rho^{G'}_{M,N} = \rho^{G'*}_{N,M}$) with trace

$$\sum_{\substack{|G'_1| \le J_1,\, |G'_2| \le J_2 \\ G'_1+G'_2=G',\, |M| \le J}} \left|\mathcal{A}_{M,G'_1,G'_2}\right|^2 = 1\,. \tag{7.11}$$

Therefore, the angular distribution is written, combining Eqs. 7.8, 7.9 and 7.10, as

$$\begin{aligned} W(\cos\vartheta,\varphi) &= \sum_{\substack{|G'| \le \min(J,J_1+J_2) \\ |M| \le J,\, |N| \le J}} \rho^{G'}_{M,N}\; \mathcal{D}^{J}_{M,G'}(\vartheta,\varphi)\, \mathcal{D}^{J*}_{N,G'}(\vartheta,\varphi) \\ &= \sum_{\substack{|G'| \le \min(J,J_1+J_2) \\ |M| \le J,\, |N| \le J}} \rho^{G'}_{M,N}\; d^{J}_{M,G'}(\cos\vartheta)\, d^{J}_{N,G'}(\cos\vartheta)\, e^{-i\,(M-N)\,\varphi}\,. \end{aligned} \tag{7.12}$$

The ultimate generalization consists in considering the sum over all possible subprocesses contributing to the production of O, with weights proportional to their relative yields. For this purpose it is sufficient to define the corresponding weighted average of the density matrix,

$$\rho^{G'}_{M,N} = \sum_{\substack{|G'_1| \le J_1,\, |G'_2| \le J_2 \\ G'_1+G'_2=G'}} \left\langle \mathcal{A}^{*}_{M,G'_1,G'_2}\; \mathcal{A}_{N,G'_1,G'_2} \right\rangle\,, \tag{7.13}$$

while the final expression of the angular distribution remains formally the one of Eq. 7.12.

A note of caution is due about the possibly misleading notation used for the dynamical amplitudes $\mathcal{A}_{M,G'_1,G'_2}$ and for the spin density matrix elements $\rho^{G'}_{M,N}$. These objects appear in expressions like Eqs. 7.8 and 7.12, where we see them together with Wigner matrix elements, which are the only ones explicitly having "J" as index. However, they actually depend on all the details of the production and decay dynamics and, in particular, on J, J_1, and J_2, despite the fact that these symbols are not explicitly shown as indices.

7.3 The polar projection of the decay distribution

There are cases where only the polar angle dependence of the decay distribution is effectively interesting for the study of the process under consideration. The azimuthal dependence of the distribution obviously vanishes when the particle is produced in $2 \to 1$ processes and the polarization axis z is chosen along the only meaningful direction, that of the relative momentum of the colliding particles (CS frame). The same happens along any other polarization axis if the particle is produced in a single, pure J_z eigenstate along that direction. For these cases, it is convenient to

consider directly the generic expression of the $\cos\vartheta$ distribution, as obtained by averaging Eq. 7.12 over φ. Given that the azimuthal dependence is exclusively contained in the complex exponential factor of that expression, and that

$$\frac{1}{2\pi}\int_{-\pi}^{+\pi} e^{-i\,(M-N)\,\varphi}\; d\varphi = \delta_{M,N}\;, \tag{7.14}$$

the resulting averaged distribution is

$$w(\cos\vartheta) \;=\; \sum_{\substack{|G'|\leq \min(J,J_1+J_2)\\ |M|\leq J}} \sigma_M^{G'}\left[d^J_{M,G'}(\cos\vartheta)\right]^2\;, \tag{7.15}$$

which only depends on the squared moduli of the helicity amplitudes, that is, on the "diagonal" (and real) $\rho^{G'}_{M,M}$ terms:

$$\sigma_M^{G'} \;\equiv\; \rho^{G'}_{M,M} \;=\; \sum_{\substack{|G'_1|\,\leq\, J_1,\; |G'_2|\,\leq\, J_2\\ G'_1+G'_2\,=\,G'}} \left\langle \left|\mathcal{A}_{M,G'_1,G'_2}\right|^2 \right\rangle\,. \tag{7.16}$$

As can be seen in Tables 7.1–7.6, the square of any reduced d-matrix element is, for all cases of J, both integer and half-integer, a linear combination of terms of the kind $\sin^Q(\vartheta/2)\,\cos^P(\vartheta/2)$ with *even* Q and P values, that is, of terms of the kind $(1-\cos\vartheta)^{Q/2}\,(1+\cos\vartheta)^{P/2}$. The maximum overall power $Q+P$ in each d^2 expression is $4J$. Therefore, the polar angle distribution will be a polynomial of order $2J$ in $\cos\vartheta$, with $2J$ independent observable coefficients, λ_i,

$$w(\cos\vartheta \mid \boldsymbol{\lambda}) \;=\; \frac{1}{\mathcal{N}}\left[\,1+\sum_{i=1}^{2J}\lambda_i\,(\cos\vartheta)^i\,\right], \tag{7.17}$$

where the normalization $\mathcal{N}$ is equal to $1+\sum\lambda_j\,/\,(j+1)$, with the sum being made only over the *even* natural numbers $j\leq 2J$. The terms with odd powers of $\cos\vartheta$ are parity violating.

We should keep in mind that any information about the interference between the different angular momentum eigenstates composing the initial state is lost in the polar projection of the distribution. The decaying particle can be a coherent or an incoherent superposition of eigenstates. As seen in Chapter 1, these two physically different cases lead to different azimuthal anisotropies, properly reflected in Eq. 7.12, but not to different polar anisotropies, thereby being indistinguishable in the polar projection. As has been discussed a number of times in this book, *neglecting* the possible existence of significant azimuthal anisotropies can create problems, both for the accuracy of the measurement and for the interpretation of the results.

On the other hand, as we study cases of increasing J, the simplification of considering only the $\cos\vartheta$ dimension becomes more and more convenient. For $J=1$, in the most general case, including parity-violating effects, the maximum number of observable parameters of the full distribution is eight (five of them potentially non-

negligible if the particle is observed inclusively, without referring the polarization axes to possible accompanying particles in the event), while the polar projection only has two measurable parameters, clearly allowing for a substantial simplification of the analysis procedure.

In the $J = 2$ case, the total number of parameters increases from 8 to 24, their measurement requiring very challenging procedures, and even in the simpler option of inclusive observation we still need to consider 14 "significant parameters". Instead, when only considering the $\cos\vartheta$ distribution, the number of parameters drops to four, vastly reducing the complexity of the experimental analysis.

7.4 The general $J = 1$ two-body decay distribution

In the derivation of the decay distribution of a vector particle into two leptons, in Chapter 1, we have used the physical constraint of helicity conservation, which imposes that the final dilepton has projection $G' = G'_1 + G'_2 = \pm 1$ along the decay direction in the mother's rest frame. By removing this constraint we can obtain, using Eq. 7.12, the most general two-body decay distribution of any $J = 1$ state. Its parametrization is formally unchanged with respect to the dilepton case (Eq. 1.29):

$$\begin{aligned} W(\cos\vartheta,\varphi) \;=\; & \frac{3}{4\pi}\frac{1}{(3+\lambda_\vartheta)}\,(1+\lambda_\vartheta\cos^2\vartheta \\ & + \lambda_\varphi \sin^2\vartheta\cos 2\varphi + \lambda_{\vartheta\varphi}\sin 2\vartheta\cos\varphi \\ & + \lambda^{\perp}_{\varphi}\sin^2\vartheta\sin 2\varphi + \lambda^{\perp}_{\vartheta\varphi}\sin 2\vartheta\sin\varphi \\ & + 2A_\vartheta\cos\vartheta + 2A_\varphi\sin\vartheta\cos\varphi + 2A^{\perp}_{\varphi}\sin\vartheta\sin\varphi)\,. \end{aligned} \tag{7.18}$$

Compared to those of Eq. 1.28, however, the shape parameters have now the additional dependence on the $G' = 0$ amplitudes (through the elements $\rho^0_{M,N}$ of the spin density matrix):

$$\begin{aligned} \lambda_\vartheta \;&=\; 1/D\,\Big[\rho^{+1}_{+1,+1} + \rho^{-1}_{+1,+1} - 2\rho^{0}_{+1,+1} + \rho^{+1}_{-1,-1} + \rho^{-1}_{-1,-1} - 2\rho^{0}_{-1,-1} \\ &\qquad - 2\left(\rho^{+1}_{0,0} + \rho^{-1}_{0,0} - 2\rho^{0}_{0,0}\right)\Big], \\ \lambda_\varphi \;&=\; 2/D\,\mathrm{Re}\left(\rho^{+1}_{+1,-1} + \rho^{-1}_{+1,-1} - 2\rho^{0}_{+1,-1}\right), \\ \lambda^{\perp}_{\varphi} \;&=\; 2/D\,\mathrm{Im}\left(\rho^{+1}_{+1,-1} + \rho^{-1}_{+1,-1} - 2\rho^{0}_{+1,-1}\right), \\ \lambda_{\vartheta\varphi} \;&=\; \sqrt{2}/D\,\mathrm{Re}\left[\rho^{+1}_{+1,0} + \rho^{-1}_{+1,0} - 2\rho^{0}_{+1,0} - \left(\rho^{+1}_{0,-1} + \rho^{-1}_{0,-1} - 2\rho^{0}_{0,-1}\right)\right], \\ \lambda^{\perp}_{\vartheta\varphi} \;&=\; \sqrt{2}/D\,\mathrm{Im}\left[\rho^{+1}_{+1,0} + \rho^{-1}_{+1,0} - 2\rho^{0}_{+1,0} - \left(\rho^{+1}_{0,-1} + \rho^{-1}_{0,-1} - 2\rho^{0}_{0,-1}\right)\right], \end{aligned} \tag{7.19}$$

$$A_\vartheta = 1/D \left(\rho^{+1}_{+1,+1} - \rho^{-1}_{+1,+1} + \rho^{-1}_{-1,-1} - \rho^{+1}_{-1,-1}\right),$$

$$A_\varphi = \sqrt{2}/D \,\mathrm{Re}\left(\rho^{+1}_{+1,0} - \rho^{-1}_{+1,0} + \rho^{+1}_{0,-1} - \rho^{-1}_{0,-1}\right),$$

$$A^\perp_\varphi = \sqrt{2}/D \,\mathrm{Im}\left(\rho^{+1}_{+1,0} - \rho^{-1}_{+1,0} + \rho^{+1}_{0,-1} - \rho^{-1}_{0,-1}\right),$$

where the denominator is

$$D = \rho^{+1}_{+1,+1} + \rho^{-1}_{+1,+1} + 2\,\rho^{0}_{+1,+1} + \rho^{+1}_{-1,-1} + \rho^{-1}_{-1,-1} + 2\,\rho^{0}_{-1,-1} + 2\left(\rho^{+1}_{0,0} + \rho^{-1}_{0,0}\right).$$

The parameters transform from one reference frame to another exactly as in the dilepton case (Section 2.15). Their physically allowed domain is shown in Fig. 7.2, where its two-dimensional projections are represented by the blue areas. Superimposed to these are, in gold, the corresponding projections (reproduced from Fig. 3.4) for the dilepton (or light quark-antiquark) decay via intermediate vector boson, illustrating how the additional requirement of helicity conservation ($\rho^0_{M,N} = 0$) restricts the parameter domain. We also remind that the same constraint is present in the decays to a $J = 0$ particle accompanied by a real photon; for example, the decays $\rho^0 \to \ell^+\ell^-$ and $\rho^0 \to \pi^0\gamma$ have identical angular distributions.

Frame-independent polarization parameters exist and are formally defined, as functions of the λ and A parameters, exactly as those of the dilepton distribution (Chapter 3), even if their meaning in terms of natural polarizations can be different.

This generalized $J = 1$ decay distribution can be used to describe many physical decays beyond the dilepton case, such as, for instance, $\mathrm{Z} \to \mathrm{J}/\psi\,\gamma$, the radiative transitions of $J = 1$ mesons, like $\chi_{c1} \to \mathrm{J}/\psi\,\gamma$ or $\psi(2\mathrm{S}) \to \chi_{cJ}\,\gamma$ (with $J = 0, 1, 2$), and several hadronic decays [5].

As an illustration, we will calculate the polar anisotropy parameter of the decays $\chi_{c1} \to \mathrm{J}/\psi\,\gamma$ and $\mathrm{Z} \to \mathrm{J}/\psi\,\gamma$ (and the equivalent ones with the charmonium states replaced by the corresponding bottomonium ones). The decaying particle is the generic combination $|\,O\,\rangle = \sum_{M=-1}^{+1} a_M\ |1,\ M\,\rangle$. As done in Section 6.7 to calculate the J/ψ decay anisotropy, we refer to the axis z' (Fig. 6.32), along which the J/ψ and the γ have back-to-back momenta in the mother's rest frame, and to the coefficients listed in Table 6.2, expressing the relative probabilities of the configurations with specific $J_{z'}$ projections of J/ψ and γ. This time, the method is applied to calculate the anisotropy of the χ_{c1} or Z two-body decay.

Considering the column $J = 1$ of Table 6.2 and keeping only the lines with $K' = \pm 1$ (transversely polarized photon), we see that there are two allowed configurations with $G' = L' + K' = 0$, having total weight $1/2 + 1/2 = 1$, while the cases $G' = +1$ and $G' = -1$ only have one configuration each, with weight $1/2$. The J/$\psi\,\gamma$ state is then "polarized", because the three cases, $G' = -1$, 0 and $+1$, have unequal weights: as will be discussed in Section 7.8, this is a condition for the observability of the polarization of the mother particle. The diagonal spin densities (i.e. the squared amplitudes) $\sigma^{G'}_M = \rho^{G'}_{M,M}$ are proportional to those weights, times the probability $|a_M|^2$ that the decaying state $|\,O\,\rangle$ has $J_z = M$:

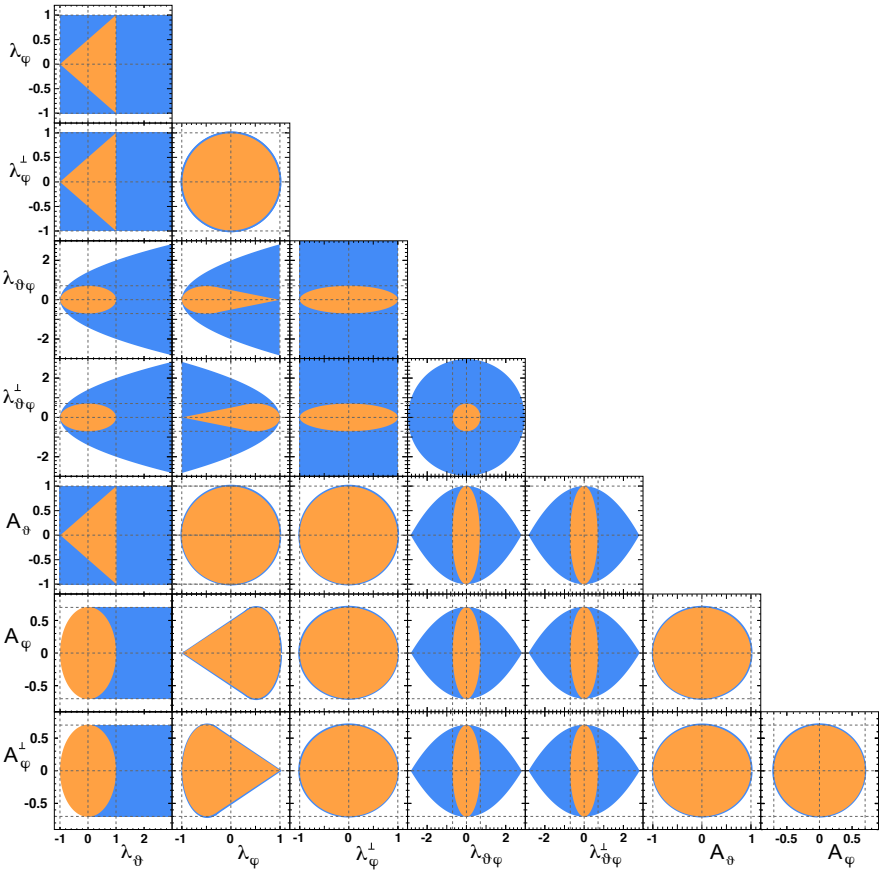

Fig. 7.2 Allowed parameter regions of the two-body decay distribution of a $J = 1$ particle. The largest areas (blue) represent the most general domain while the inner areas (gold) represent the dilepton decay case. In the most general case there are no upper bounds on λ_ϑ and $|\lambda_{\vartheta\varphi}|$, but the bound $\lambda_\vartheta < 3$ was added to enable the graphical representation.

$$\sigma_M^{+1} = \sigma_M^{-1} \propto \frac{1}{2}|a_M|^2\,, \quad \sigma_M^0 \propto |a_M|^2\,. \tag{7.20}$$

Substituted in Eq. 7.19, with the normalization $|a_{-1}|^2 + |a_0|^2 + |a_{+1}|^2 = 1$, these give

$$\lambda_\vartheta = -\frac{1 - 3\,|a_0|^2}{3 - |a_0|^2}\,. \tag{7.21}$$

This is the polar anisotropy of the J/ψ (or photon) emission direction in the χ_{c1} rest frame, equal (as already seen in Section 6.6) to $-1/3$, 0 and $+1$ when, respectively, $|a_0|^2 = 0$, $1/3$ and 1, while values of λ_ϑ smaller than $-1/3$ or larger than $+1$ are forbidden. Repeating the exercise for the decay where the emitted photon is virtual (as in the case $\chi_{c1} \to \mathrm{J}/\psi\,\gamma^*$), this time including in the count, therefore,

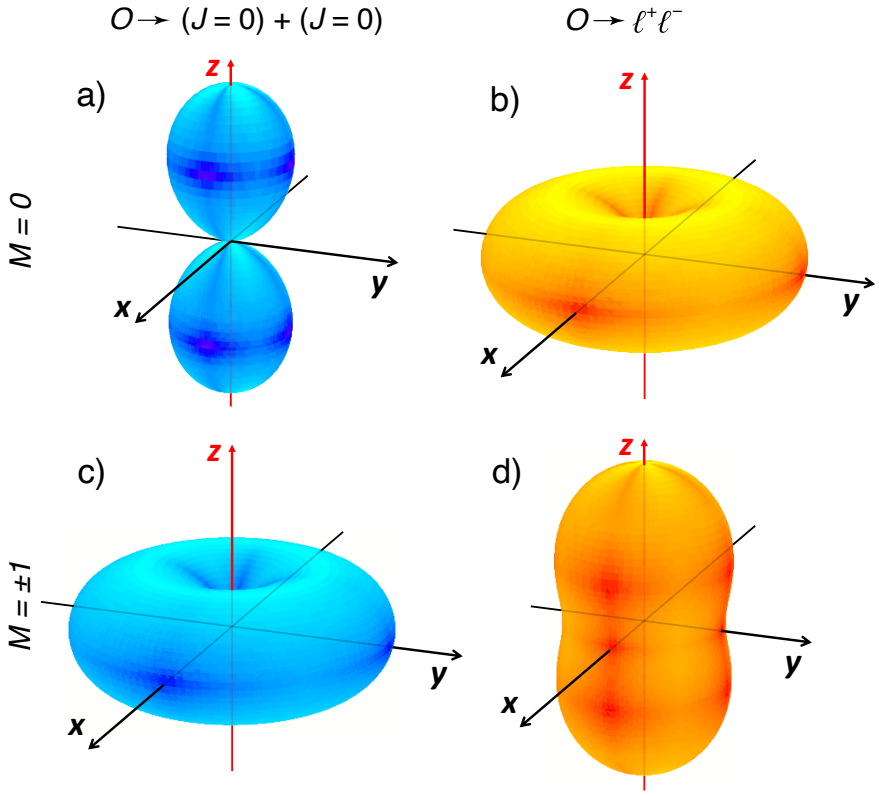

Fig. 7.3 A longitudinally (top panels) or transversely (bottom panels) polarized vector particle O produces two different decay angular distributions when it decays into a $J = 0$ meson and its antimeson (left panels) or into a lepton-antilepton pair (right panels).

the $K' = 0$ term, we can see that now the three cases, $G' = -1$, 0 and $+1$, are equiprobable and, for any M, the anisotropy parameters are zero: the J/ψ is emitted isotropically in the χ_c rest frame, independently of the χ_c polarization. This confirms the result found, with a different method, in Section 6.8.

It is interesting to consider the case where the two final particles have both spin $J = 0$, illustrated by the left drawings of Fig. 7.3. This example is "complementary" to the dilepton one (shown in the right drawings of the same figure): the $J_{z'}$ projection $G' = 0$ of the final system is not only allowed, but is now the *only* physical possibility, given that the relative orbital component $I = 1$, required by angular momentum conservation, has zero projection along the common direction of two back-to-back products. The maximum allowed domain is not different from the general case shown in blue in Fig. 7.2, except that the parity-violating asymmetries A_ϑ, A_φ, and $A_\varphi^\perp$ must always vanish, for the same reason why A_ϑ can only be zero when the *initial* state has zero J_z projection (Sections 1.3 and 1.4): the squared matrix element $(d^1_{M,0})^2$, just like $(d^1_{0,G'})^2$, is a function of only the parity conserving expres-

sion $\cos^2\vartheta$ (Table 7.3). Relevant physical cases include, for example, the decays $\rho(770)^{\pm,0} \to \pi^{\pm}\pi^0$ / $\pi^+\pi^-$, $\phi(1020) \to K^+K^-$, and $\Upsilon(4S) \to B\overline{B}$ [5].

The particles $\rho(770)$, $\phi(1020)$, and $\Upsilon(4S)$ also decay to dileptons and it is interesting to compare the shapes of the angular distributions of two decay channels. The decay into a pair of $J = 0$ mesons gives an interesting illustration of the seemingly strange fact that, as seen in Fig. 7.2, λ_ϑ (and therefore $|\lambda_{\vartheta\varphi}|$) can assume values larger than +1. Actually, λ_ϑ even tends to $+\infty$ when the spin density matrix element $\rho^0_{0,0}$ dominates over all others, given that, as seen in Eq. 7.19, it is the only element not appearing in the denominator (or constant factor) D, which therefore tends to vanish. This limit corresponds to the hypothetical case when the vector particle $\rho(770)$, $\phi(1020)$, or $\Upsilon(4S)$ is produced *longitudinally* polarized ($M = 0$) in the chosen frame. Equations 7.18 and 7.19 are then simply replaced by

$$W(\cos\vartheta, \varphi) \;=\; \frac{3}{4\pi}\,\cos^2\vartheta\,, \tag{7.22}$$

a shape very different from the one of the dilepton decay distribution (where, for any λ_ϑ, a significant fraction of events is emitted at around $\cos\vartheta = 0$) and in particular, as shown in Fig. 7.3-a, from the one of the dilepton decay of a longitudinally polarized vector particle, which is $\propto 1 - \cos^2\vartheta$ (Fig. 7.3-b).

In the case of transverse polarization the roles are inverted: in the di-meson decay, when only the $\rho^0_{M,N}$ matrix elements with $M, N = \pm 1$ are nonzero λ_ϑ assumes the maximum possible negative value, -1 (Fig. 7.3-c), while $\lambda_\vartheta = +1$ in the dilepton decay, where the nonzero elements are $\rho^{\pm 1}_{M,N}$ (Fig. 7.3-d). For example, the $\Upsilon(4S)$ resonance is produced transversely polarized in e^+e^- colliders because of helicity conservation in the coupling between the colliding leptons and the intermediate virtual photon; Fig. 7.3-c represents, therefore, the distribution of the emission directions of the B and $\overline{B}$ mesons with respect to the direction, z, of the beams.

A further example leading to this distribution shape is represented by the decays of ρ and ϕ mesons to pion or kaon pairs, when the ρ and ϕ are produced (always transversely polarized) in the radiative decays $H \to \rho\gamma$ or $H \to \phi\gamma$; in this case the natural axis with respect to which $\lambda_\vartheta = -1$ is the meson direction in the H rest frame (cHX frame).

7.5 Polar anisotropy of the $J = 2$ two-body decay distribution

Expanding Eq. 7.15 and reordering the result according to Eq. 7.17, we obtain the polar projection of the two-body decay distribution of a $J = 2$ particle, described by four independent parameters:

$$\lambda_1 = 4\,(\beta_{22} - 2\beta_{11} + 4\beta_{12})\,/\,D\,,$$

$$\lambda_2 = 6\,(\alpha_{22} - \alpha_{00} - 2\,\alpha_{02} - 2\,\alpha_{11} + 4\,\alpha_{01})\,/\,D\,,$$

$$\lambda_3 = 4\,(\beta_{22} + 4\beta_{11} - 4\beta_{12})\,/\,D\,, \tag{7.23}$$

$$\lambda_4 = (\alpha_{22} + 9\,\alpha_{00} + 6\,\alpha_{02} + 16\,\alpha_{11} - 24\,\alpha_{01} - 8\,\alpha_{12})\,/\,D\,,$$

$$\text{with}\;\; D = \alpha_{22} + \alpha_{00} + 6\,\alpha_{02} + 4\,\alpha_{11} + 8\,\alpha_{12}\,,$$

and

$$\begin{aligned} \alpha_{i,j} &= \sigma_i^j + \sigma_j^i + \sigma_{-i}^{-j} + \sigma_{-j}^{-i} + \sigma_i^{-j} + \sigma_{-j}^i + \sigma_{-i}^j + \sigma_j^{-i} \\ \beta_{i,j} &= \sigma_i^j + \sigma_j^i + \sigma_{-i}^{-j} + \sigma_{-j}^{-i} - \left(\sigma_i^{-j} + \sigma_{-j}^i + \sigma_{-i}^j + \sigma_j^{-i}\right). \end{aligned} \tag{7.24}$$

Given the, respectively, symmetric and antisymmetric definitions of $\alpha_{i,j}$ and $\beta_{i,j}$ by exchange between initial- and final-state helicities, λ_2 and λ_4 are parity-conserving, while λ_1 and λ_3 are parity-violating.

As a simple application of these relations, along the line of the previous section, where we considered the radiative χ_{c1} or Z decays to J/ψ, we examine here the analogous decay $\chi_{c2} \to \mathrm{J}/\psi\,\gamma$, where now $|\chi_{c2}\rangle = \sum_{M=-2}^{+2} a_M\,|2,\,M\rangle$. The relevant weights in Table 6.2 are 1, 1, 1/2, 1/2, and 1/6 + 1/6 = 1/3, respectively for the J/$\psi\,\gamma$ configurations $G' = L' + K' = +2, -2, +1, -1$, and 0. Therefore,

$$\sigma_M^{+2} = \sigma_M^{-2} \propto |a_M|^2\,, \quad \sigma_M^{+1} = \sigma_M^{-1} \propto \frac{1}{2}\,|a_M|^2\,, \quad \sigma_M^{0} \propto \frac{1}{3}\,|a_M|^2\,, \tag{7.25}$$

and Eq. 7.23 gives, after some algebra, the polar anisotropy of the J/ψ emission in the χ_{c2} rest frame:

$$\lambda_2 = \frac{3\left[\,2\left(|a_{+2}|^2\,|a_{-2}|^2\right) - \left(|a_{+1}|^2\,|a_{-1}|^2\right) - 2\,|a_0|^2\,\right]}{6\left(|a_{+2}|^2\,|a_{-2}|^2\right) + 9\left(|a_{+1}|^2\,|a_{-1}|^2\right) + 10\,|a_0|^2}\,, \tag{7.26}$$

$$\lambda_1 = \lambda_3 = \lambda_4 = 0\,.$$

The parameter λ_2 has values between $-3/5$ and $+1$, being equal to $-3/5$, $-1/3$, and $+1$ when the χ_{c2} is produced with the respective J_z projections $M = 0, \pm 1$, and ± 2, as already found in Section 6.6. When the emitted photon is virtual ($\chi_{c2} \to \mathrm{J}/\psi\,\gamma^*$) and the cases with $K' = 0$ are allowed, the same procedure leads to the fully isotropic and polarization-independent result $\lambda_1 = \lambda_2 = \lambda_3 = \lambda_4 = 0$, as in the χ_{c1} case and as already found in Section 6.8.

The physical domain of parameter space depends on the type of decay products and on the production mechanism; some examples are shown in Figs. 7.4 and 7.5. The grey contours in both figures represent the allowed regions including all possible physical cases: they reflect only angular momentum conservation and rotation invariance, which shape the general dependences of the parameters λ_i on the different process amplitudes, as described by Eq. 7.23. The more restricted, coloured areas represent specific physics hypotheses.

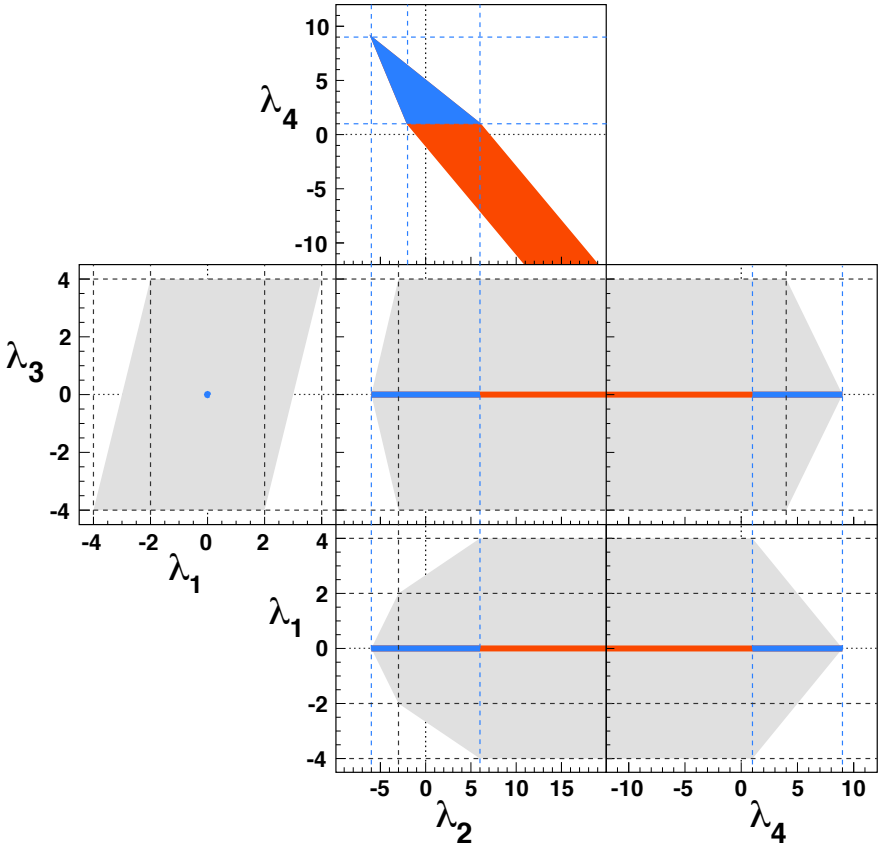

Fig. 7.4 Allowed parameter regions of the polar projection of the two-body decay distribution of a $J = 2$ particle O. The largest areas (grey) represent the most general domain. The intermediate areas (red+blue) represent any of two equivalent cases: O decays into two real photons; O is produced alone from the scattering of two real gluons (and the measurement is made in the CS frame). The smallest areas (blue) represent the case where both hypotheses are satisfied. There is no upper bound on λ_2 and no lower bound on λ_4.

The union of the blue and red areas in Fig. 7.4 corresponds to the case where the decay products are two real photons, a condition translating into $\sigma_M^{\pm 1} = 0$ for any M, given that $G' = \pm 1$ would mean that one of the two photons is not transversely polarized. Known $J = 2$ particles seen in the photon-photon channel are, for example, $a_2(1320)$, $a_2(1700)$, $\eta_2(1870)$, and $X(3915)$, the latter with spin assignment still uncertain between $J = 0$ and $J = 2$ [5].

Given the symmetry of the equations in Eq. 7.23, in particular the properties of $\alpha_{i,j}$ and $\beta_{i,j}$ (Eq. 7.24) by exchange of the i and j indices, identical contours (blue plus red) are obtained by reversing the role of initial and final states, forbidding this time that the decaying particle is produced in the $M = \pm 1$ state ($\sigma_{\pm 1}^{G'} = 0$ for any G'). This corresponds, for example, to the production via scattering of two real gluons

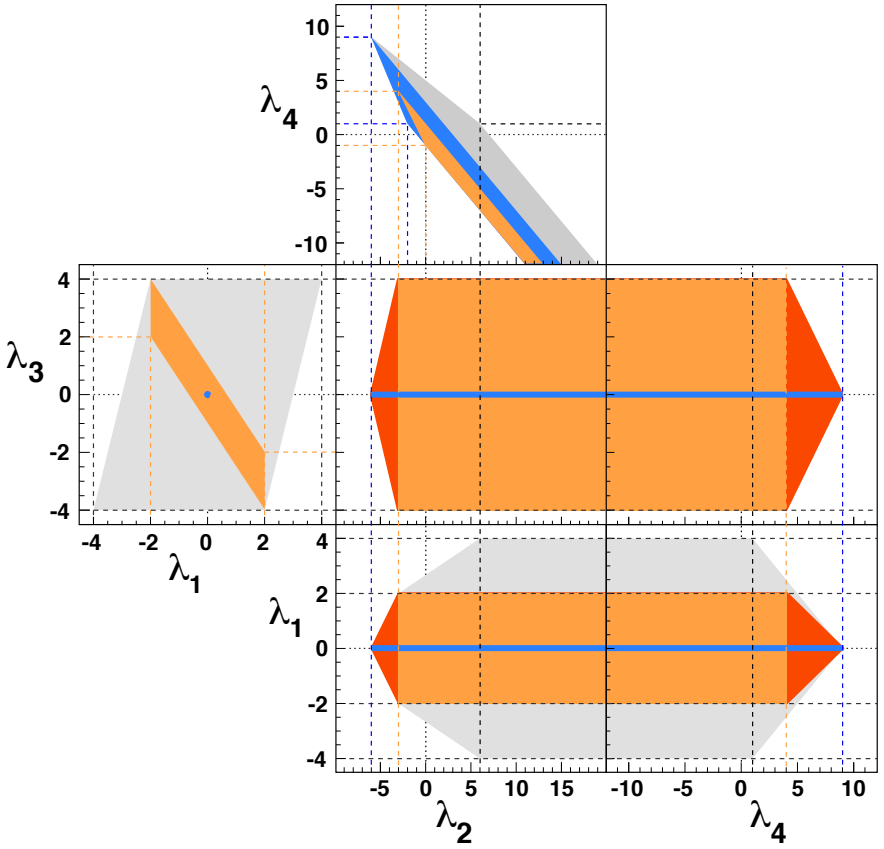

Fig. 7.5 Allowed parameter regions of the polar projection of the two-body decay distribution of a $J = 2$ particle O. The largest areas (grey) represent the most general domain. The intermediate areas (red+blue+orange) represent the case in which O decays into two $J = 1/2$ fermions. The blue areas correspond to the hypothesis that O is produced alone from the scattering of two real gluons *and* decays into two $J = 1/2$ fermions, for measurements made in the CS frame; alternatively, they describe the decay into two $J = 0$ particles. The orange areas refer to the $G' = \pm 1$ case, for example a decay into $J = 0$ particle plus photon. There is no upper bound on λ_2 and no lower bound on λ_4.

in $2 \to 1$ processes (that is, with no recoiling particle); in this case, however, the contours refer only to a measurement where the polarization axis is chosen along the scattering direction of the gluons (CS frame).

When either the elementary production process is initiated by two identical particles or the decay products are two identical particles, the parity-violating terms λ_1 and λ_3 obviously vanish, resulting in simple lines or dots as allowed regions in the two-dimensional projected domains. The smallest, blue areas show the case when *both* of these hypotheses apply: the particle is produced in gluon-gluon fusion and decays into two photons.

This intersection is particularly interesting in the search for unknown boson resonances of mass, m, higher than the mass of any known particle, as discussed in the next section; in fact, such objects would be observed in the domain of very low p_T/m values, where the presence of a recoiling particle is not necessary nor probable. The di-photon decay represented, for example, the discovery channel of the Higgs boson.

Hypotheses on the properties of the fundamental couplings involved can, obviously, further restrict the allowed regions or even fix the values of the λ_i parameters. For example, considering the gluon-gluon to photon-photon case (where $\lambda_1 = \lambda_3 = 0$), the hypothesis of a graviton-like $J = 2$ particle interacting with SM bosons with no helicity flip [6] (corresponding to the *additional* conditions $\sigma_0^{G'} = \sigma_M^0 = 0$ for any G' and M: overall, only $G' = \pm 2$ and $M = \pm 2$ are allowed) leads to $\lambda_2 = 6$ and $\lambda_4 = 1$, the rightmost vertex of the blue triangle in the λ_2–λ_4 plane.

Further examples are shown in Fig. 7.5. Here the intermediate areas, in colour (union of blue, red, and orange), represent the case in which the particle decays into two $J = 1/2$ fermions, but with no assumption of helicity conservation, therefore only forbidding the $G' = \pm 2$ projection: $\sigma_M^{\pm 2} = 0$.

The blue areas (blue plus orange in the λ_4 vs. λ_2 case) are obtained by, additionally, imposing that also the $G' = \pm 1$ component is absent, $\sigma_M^{\pm 1} = \sigma_M^{\pm 2} = 0$: this case corresponds, for example, to decays into two $J = 0$ particles, as in the decays of $a_2(1320)$ and $a_2(1700)$ to $\eta\pi$ or $\mathrm{K\overline{K}}$ [5].

Because of the symmetry of these conditions by exchange of final and initial state, as mentioned above, the same blue contours also refer to the joint requirement that the particle is produced alone from the scattering of two real gluons (suppression of $M = \pm 1$, in the CS frame) and decays into two $J = 1/2$ fermions, so that $\sigma_{\pm 1}^{G'} = \sigma_M^{\pm 2} = 0$.

The orange areas describe the case of a decay to a final state having always $J_{z'}$ projection $G' = \pm 1$. This happens, for example, if the daughters are a $J = 0$ particle and a photon, as in the decay $a_2(1320) \to \pi^{\pm}\gamma$ [5].

Figure 7.6 shows the shapes assumed by the angular distribution for the different combinations of initial and final state angular momentum projections, in the parity-conserving case ($\lambda_1 = \lambda_3 = 0$). Only the examples with $|G'| \leq |M|$ are drawn: the remaining ones are related to these through the above-mentioned symmetry by exchange of M with G'.

Parity violation is possible in three out of the six distinct cases shown in Fig. 7.6. The parity asymmetry is parametrized by the amplitude combinations β_{11}, β_{12} and β_{22} in Eq. 7.23: whenever the initial or final state have zero J_z or J'_z projections, λ_1 and λ_3 vanish. The corresponding distributions are shown in Fig. 7.7 for the two maximal and opposite asymmetry effects.

The anisotropy parameters corresponding to the shapes shown in Figs. 7.6 and 7.7 are indicated on the $\lambda_2 - \lambda_4$ and $\lambda_1 - \lambda_3$ maps of Fig. 7.8. The Grail-shaped distribution defined by $M = \pm 1, G' = 0$ (or vice-versa) represents the asymptotic vertex of the domain area at $\lambda_2 \to +\infty, \lambda_4 \to -\infty$, where $w(\cos\vartheta) \propto \cos^2\vartheta \sin^2\vartheta$.

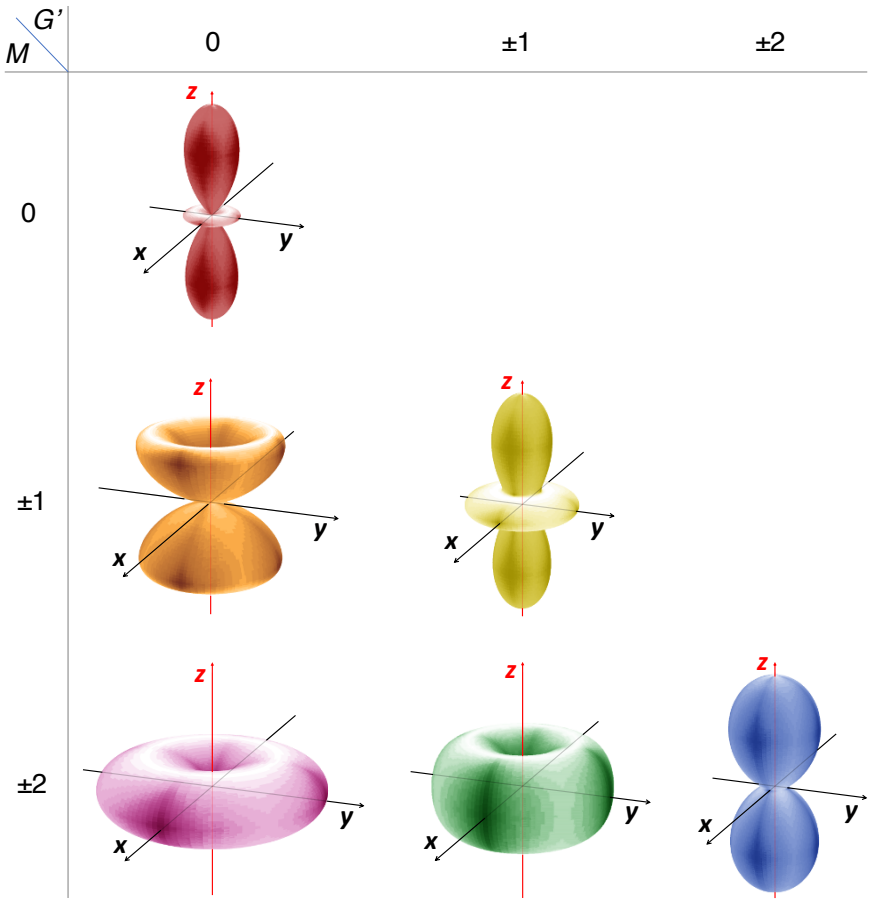

Fig. 7.6 Shapes of the angular distributions of the parity-conserving two-body decay $O \to X_1X_2$ of a $J = 2$ particle, for all combinations of angular momentum projections of O along z (M) and of the X_1X_2 system along z' (G'). Off-diagonal combinations with $|G'| > M$, here omitted, can be obtained by exchanging M with G'.

7.6 Case study: spin characterization of a heavy di-photon resonance

The above-mentioned graviton hypothesis was one of the several models considered as possible interpretations of the "Higgs-like" resonance observed by the ATLAS and CMS experiments [7, 8], before its definitive identification. We will now examine this latter physical example as an illustration of how the determination of the shape of the decay distribution can lead, with minimal assumptions, to the characterization of an unknown particle.

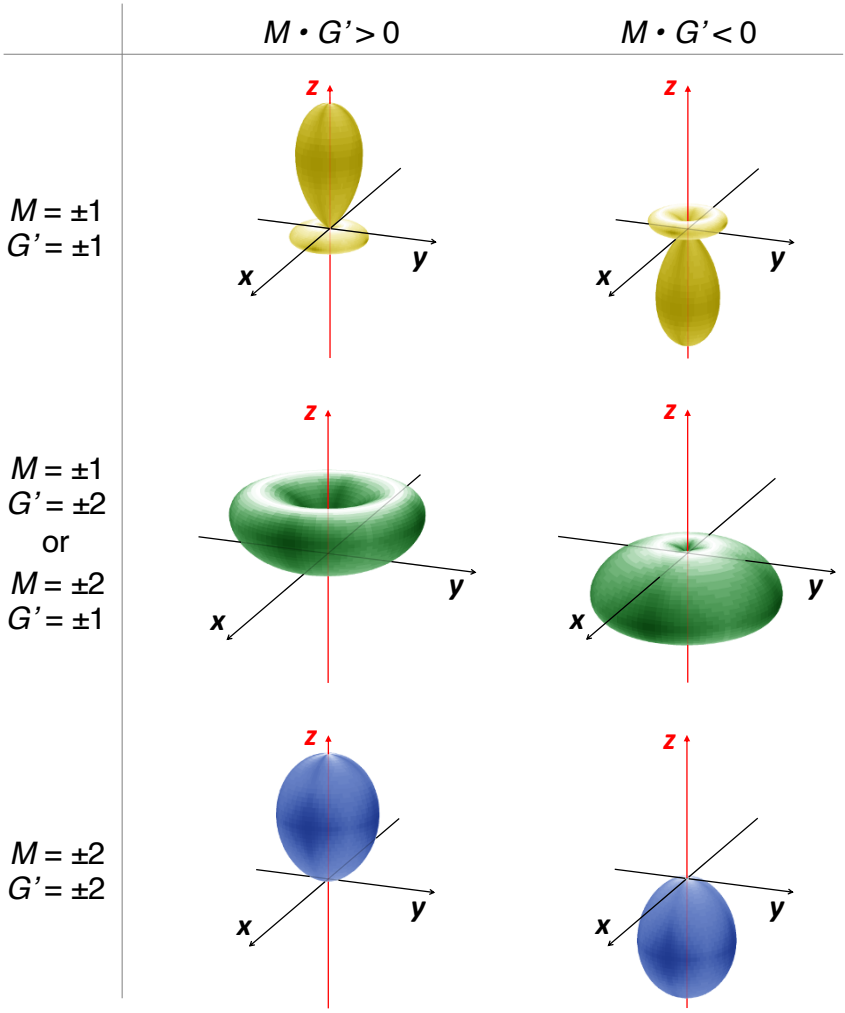

Fig. 7.7 Shapes of the angular distributions of the maximally parity violating two-body decay $O \to X_1X_2$ of a $J = 2$ particle, for the three relevant combinations (rows) of angular momentum projections of O along z (M) and of the X_1X_2 system along z' (G'), and for the two opposite signs of the effect (columns).

As a first step in the determination of the angular momentum quantum number of the hypothetical new resonance, it is interesting to note that a particle assumed to be produced with no recoil from the fusion of two real gluons and decaying into two real photons always produces a significant polar anisotropy ($\lambda_i \neq 0$ for some i) with respect to the scattering direction of the gluons, except, obviously, in the $J = 0$ case, corresponding to $\mathrm{H} \to \gamma\gamma$.

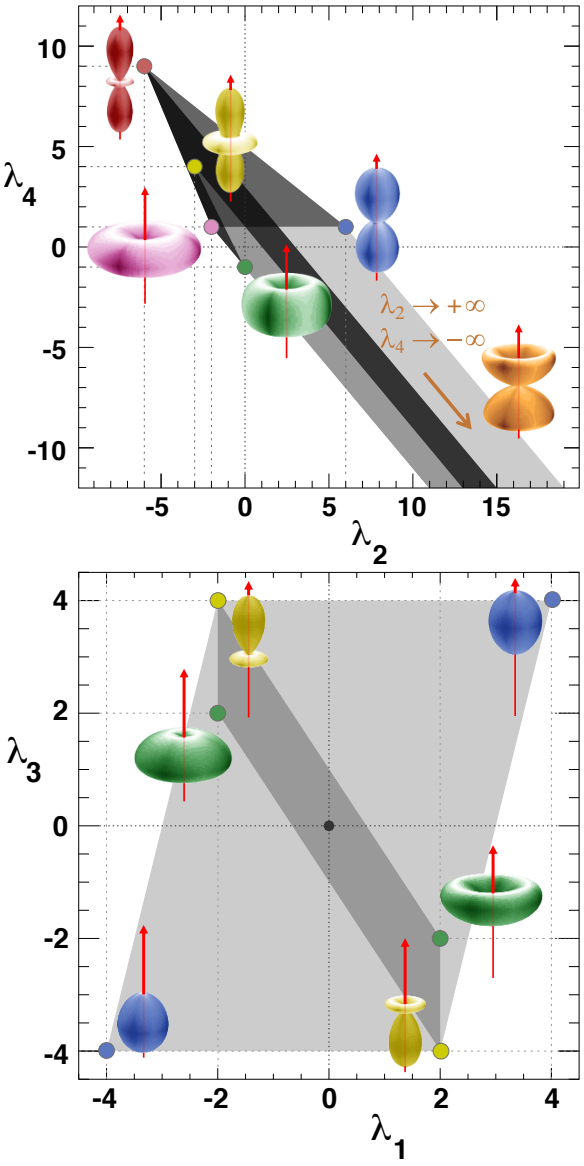

Fig. 7.8 The (λ_2, λ_4) and (λ_1, λ_3) coordinates of the polarization examples shown in Figs. 7.6 and 7.7.

This effect is seen in Fig. 7.4 for the $J = 2$ case, being λ_4 always ≥ 1. It can, moreover, be generalized to other J values. The $J = 1$ case is excluded by the Landau–Yang theorem [9, 10], stating that a $J = 1$ particle cannot decay into two

real (transversely polarized) photons (nor, equivalently, be produced alone by two transversely polarized gluons). Let us consider then $J = 3$ and $J = 4$.

The polar projection of the di-photon decay distribution of a $J = 3$ particle produced by gluon-gluon fusion is described by the parameters

$$\begin{aligned} \lambda_2 &= 3\,(3\,\alpha_{00} + 10\,\alpha_{02} - 5\,\alpha_{22})\,/\,D\,, \\ \lambda_4 &= 10\,(-3\,\alpha_{00} - 6\,\alpha_{02} + \alpha_{22})\,/\,D\,, \\ \lambda_6 &= (25\,\alpha_{00} + 30\,\alpha_{02} + 9\,\alpha_{22})\,/\,D\,, \end{aligned} \tag{7.27}$$

with $D = 4\,\alpha_{22}$ and α_{ij} defined as in Eq. 7.24.

The corresponding $J = 4$ decay parameters are

$$\begin{aligned} \lambda_2 &= 4\,(-45\,\alpha_{00} - 160\,\alpha_{02} + 52\,\alpha_{22})\,/\,D\,, \\ \lambda_4 &= 10\,(111\,\alpha_{00} + 312\,\alpha_{02} - 32\,\alpha_{22})\,/\,D\,, \\ \lambda_6 &= -140\,(15\,\alpha_{00} + 32\,\alpha_{02} + 4\,\alpha_{22})\,/\,D\,, \\ \lambda_8 &= 49\,(25\,\alpha_{00} + 40\,\alpha_{02} + 16\,\alpha_{22})\,/\,D\,, \\ \text{with}\quad D &= 9\,\alpha_{00} + 40\,\alpha_{02} + 16\,\alpha_{22}\,. \end{aligned} \tag{7.28}$$

In both cases the parity-violating λ_i parameters (odd i) vanish. The parameter domains for $J = 2$, 3 and 4 in the CS frame are shown in Fig. 7.9. The minimum distance from the origin ($\lambda_i = 0$ for any i, corresponding to $J = 0$) increases from $J = 2$ to $J = 3$ to $J = 4$ and, in general, should increase with J, reflecting the higher level of relative polarization represented by the limitation of the initial- and final-state helicities to $M = 0, \pm 2$ and $G' = 0, \pm 2$: the larger is the modulus of $\mathbf{J}$, the more of its projections become forbidden (for example, ± 3 in the $J = 3$ case, ± 3 and ± 4 in the $J = 4$ case, etc.).

It is interesting to note that, as shown in Fig. 7.10, the three domains have no intersections between them and also not with the $J = 0$ point ($\lambda_i = 0$ for any i). Therefore, a sufficiently-precise measurement of the di-photon decay distribution can provide an unambiguous spin characterization, independent of further specific hypotheses on the identity of the particle and how it is produced and interacts.

Figure 7.11 illustrates the dependence of the observable $\cos\vartheta$ distribution on J, for the $J = 2$, 3 and 4 cases. The curves were obtained by scanning the (respectively, two-, three- and four-dimensional) physical domains of the λ_i parameters.

A more immediate geometrical illustration of the J dependence of the angular distribution is given by Fig. 7.12, for each of the three allowed combinations of gluon-gluon and photon-photon polarizations: ($M = 0, G' = 0$), ($M = \pm 2, G' = 0$) (or vice-versa), and ($M = \pm 2, G' = \pm 2$). The recognizable shape differences seen in these figures show that it is always possible to unambiguously resolve the value of J between the three options.

The experimental precision needed to achieve a significant discrimination obviously depends on J and on the actual values of the polarization parameters, that is,

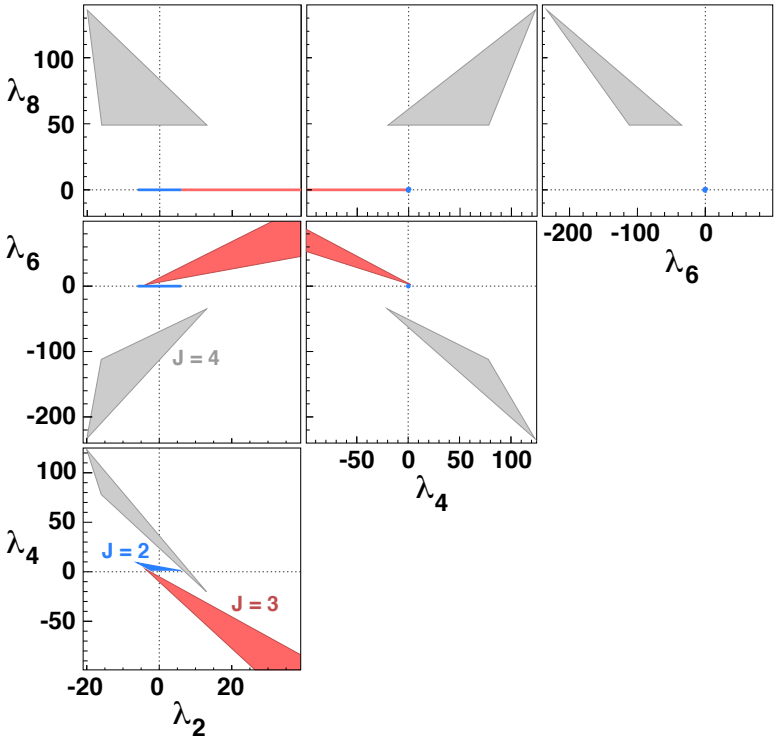

Fig. 7.9 Allowed regions for the polar anisotropy parameters (in the CS frame) of the decay distribution of a particle produced by gluon-gluon fusion and decaying into two photons. The three different shades indicate, from darkest (blue) to lightest (grey), the $J = 2$, 3 and 4 cases. In the $J = 3$ case there are no upper bounds on λ_2 and λ_6 and no lower bound on λ_4.

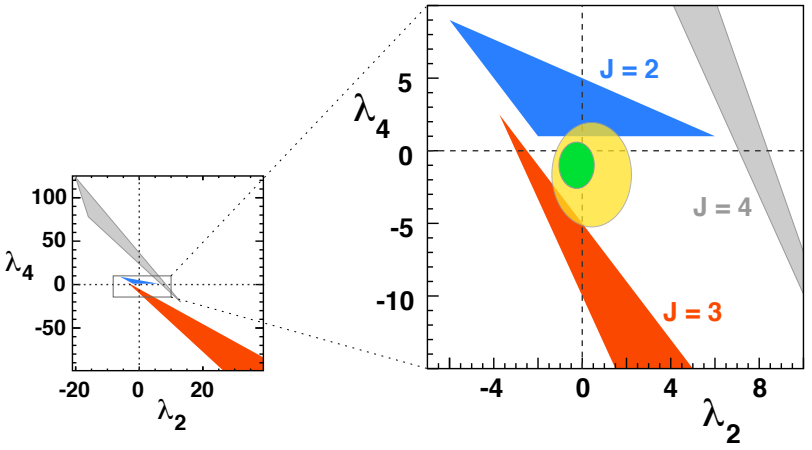

Fig. 7.10 Zoom of the top plot of Fig. 7.9 around the origin, with ellipses representing hypothetical measurements favouring the $J = 0$ hypothesis.

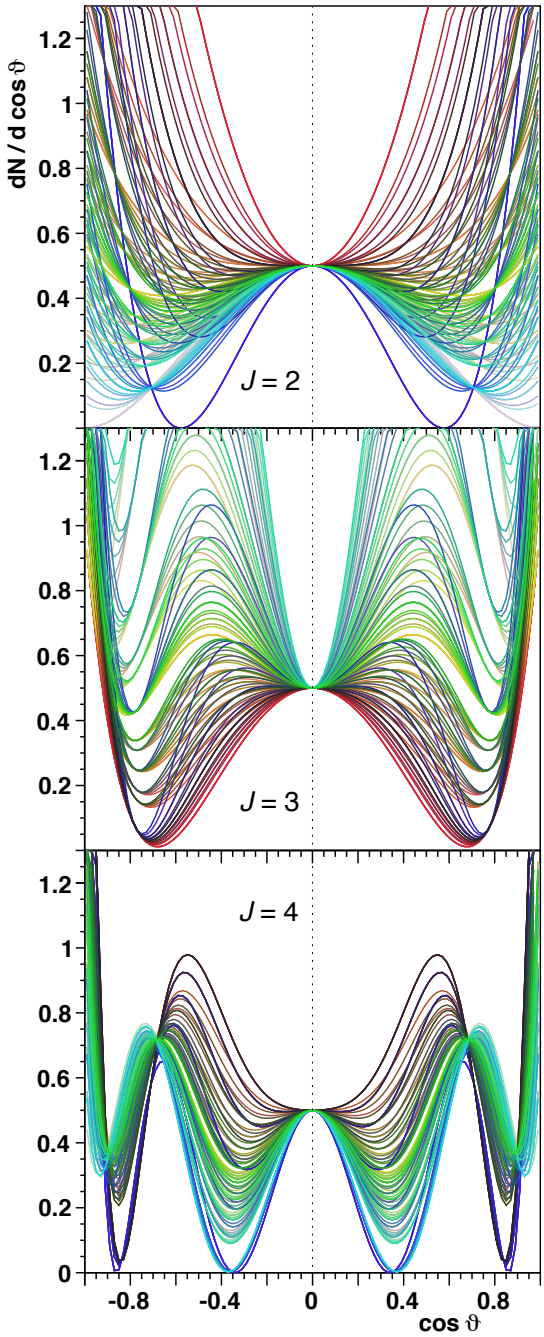

Fig. 7.11 Physically allowed $\cos\vartheta$ distributions in the CS frame for (from top to bottom) $J = 2$, 3 and 4 bosons produced by gluon-gluon fusion and decaying into two photons. For clarity of representation, all distributions are normalized to the same (arbitrary) value at $\cos\vartheta = 0$.

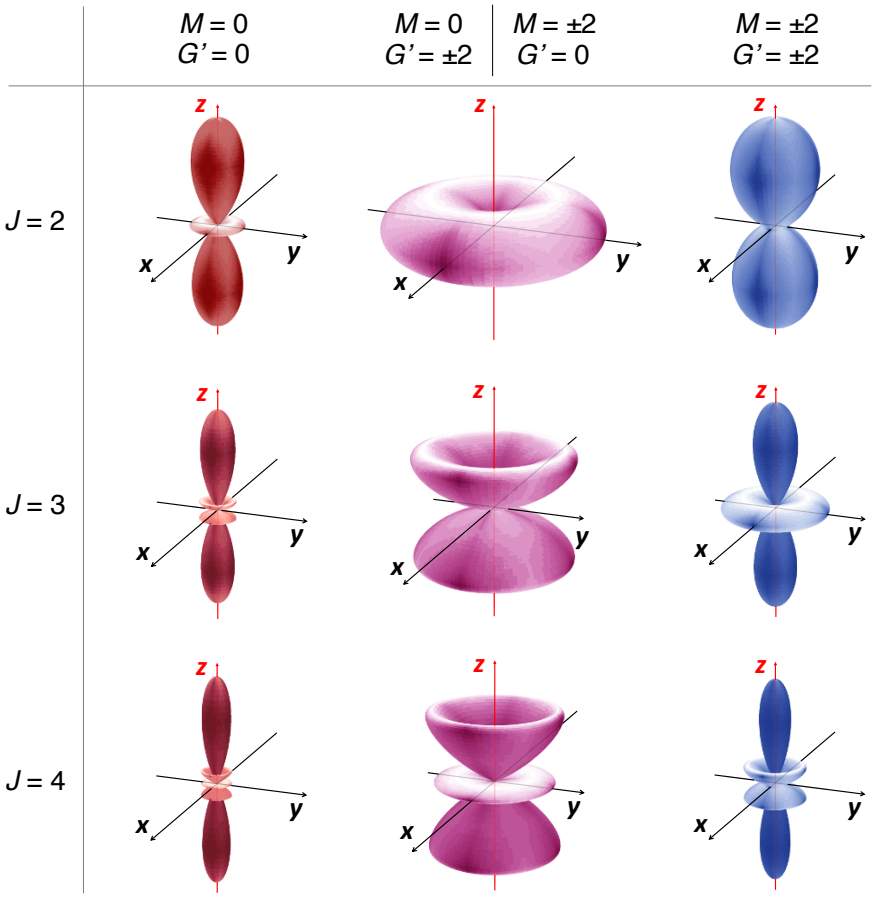

Fig. 7.12 Shapes of the angular distributions for $J = 2$, 3, and 4 bosons produced by gluon-gluon fusion and decaying into two photons, for the three allowed combinations of initial- and final-state polarizations.

on the identity of the particle. Figure 7.10 includes two ellipses representing putative measurements of different uncertainties. Both include the origin $\lambda_2 = \lambda_4 = 0$, which corresponds to the isotropic distribution that only a $J = 0$ particle can yield if produced by gluon-gluon fusion. The larger experimental contour excludes the $\lambda_2 = 6$, $\lambda_4 = 1$ point, eliminating the hypothesis that the decaying boson is a graviton-like $J = 2$ particle of the kind mentioned above. However, it does not rule out hypothetical $J = 2$ (or even $J = 3$) boson identities corresponding to the smallest values that λ_2 and λ_4 can have for those angular momentum values. The inner ellipse illustrates another hypothetical measurement, sufficiently precise to exclude the full $J = 2$ and $J = 3$ domains, thereby leading to the model-independent spin characterization of a $J = 0$ particle.

7.7 Decay distributions of half-integer spin particles

Expanding Eq. 7.12 for $J = 1/2$, we find that the most general distribution is

$$\begin{aligned} W(\cos\vartheta, \varphi) \;=\; \frac{1}{4\pi}\,(1 &+ \nu_\vartheta \cos\vartheta \\ &+ \nu_\varphi \sin\vartheta\cos\varphi \\ &+ \nu_\varphi^\perp \sin\vartheta\sin\varphi)\,, \end{aligned} \tag{7.29}$$

with

$$\begin{aligned} \nu_\vartheta &= \frac{1}{D}\left(\rho^{+\frac{1}{2}}_{+\frac{1}{2},+\frac{1}{2}} - \rho^{-\frac{1}{2}}_{+\frac{1}{2},+\frac{1}{2}} + \rho^{-\frac{1}{2}}_{-\frac{1}{2},-\frac{1}{2}} - \rho^{+\frac{1}{2}}_{-\frac{1}{2},-\frac{1}{2}}\right) \\ \nu_\varphi &= \frac{2}{D}\,\mathrm{Re}\left(\rho^{+\frac{1}{2}}_{+\frac{1}{2},-\frac{1}{2}} - \rho^{-\frac{1}{2}}_{+\frac{1}{2},-\frac{1}{2}}\right), \\ \nu_\varphi^\perp &= \frac{2}{D}\,\mathrm{Im}\left(\rho^{+\frac{1}{2}}_{+\frac{1}{2},-\frac{1}{2}} - \rho^{-\frac{1}{2}}_{+\frac{1}{2},-\frac{1}{2}}\right), \\ \text{where}\;\; D &= \rho^{+\frac{1}{2}}_{+\frac{1}{2},+\frac{1}{2}} + \rho^{-\frac{1}{2}}_{-\frac{1}{2},-\frac{1}{2}} + \rho^{-\frac{1}{2}}_{+\frac{1}{2},+\frac{1}{2}} + \rho^{+\frac{1}{2}}_{-\frac{1}{2},-\frac{1}{2}}\,. \end{aligned} \tag{7.30}$$

The three parameters measure differences between yields characterized by a given spin orientation of the final state and those with the opposite spin orientation, with respect to a given initial state configuration. They clearly represent parity asymmetries. In fact only parity-violating decays show anisotropic decay distributions. This is the case, for example, of the decays of the top quark into a W boson and a b quark, and of the Λ hyperon into a proton and a pion.

The decay anisotropy due to parity violation is measurable only if the particle is also produced polarized, with its spin preferentially aligned along a certain "positive" or "negative" direction in the chosen polarization frame; if this does not happen, the decay angles cannot be referred to a reference direction maintaining consistent orientation event after event and the corresponding parity violation becomes unobservable. In fact, each anisotropy parameter can be thought as the product of two parameters, one expressing the polarization induced by the production mechanism, the other being the parity-violating asymmetry of the decay, and it is nonzero only when both are.

For example, the top quark seemingly decays almost isotropically in $t\bar{t}$ production [11, 12], because of lack of the polarization of the corresponding QCD production mechanism; however, its intrinsic left-handed nature is revealed with significant decay anisotropies in single-t events [13], where it is produced polarized.

The polarization of the Λ is an exception to the rule that the natural polarization axis tends to stay, at least on average, inside the production plane. In fact, since the mid-1970's fixed-target experiments have been showing [14] that the polariza-

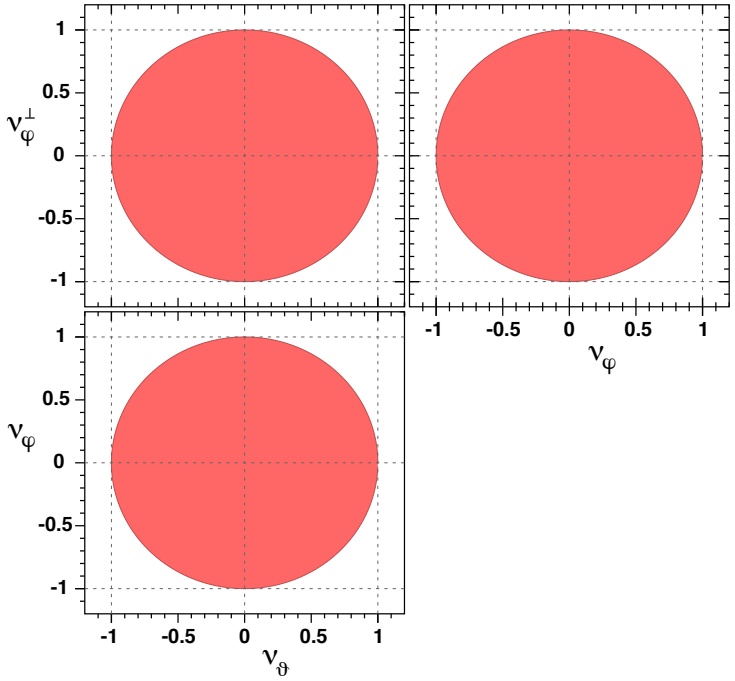

Fig. 7.13 Allowed parameter regions of the two-body decay distribution of a $J = 1/2$ particle.

tion is largest along a quantization axis *perpendicular* to the production plane. The implications of this unexpected observation on the underlying QCD mechanisms, which must confer a polarization to the s quark, have been the subject of several experimental and theoretical studies [15], but the question is still open. It remains true that in symmetric collisions and in the limit of zero longitudinal momentum (x_F or y) the anisotropy along such axis vanishes, as confirmed by the small polarization measured by the ALICE experiment at the LHC [16].

The physically allowed domain of the ν parameters, shown in Fig. 7.13 in its three projections, is simply a sphere defined by the relation

$$\tilde{\nu} = \sqrt{\nu_\vartheta^2 + \nu_\varphi^2 + \nu_\varphi^{\perp 2}} \leq 1\,. \tag{7.31}$$

It is easy to recognize that, under a generic rotation of the polarization frame $R_z(\omega)\,R_y(\zeta)\,R_z(\psi)$ (see Section 2.15), the parameters ν_ϑ, ν_φ, and $\nu_\varphi^\perp$ simply transform according to the same rotation as the vector (z, x, y):

$$\begin{pmatrix} \nu'_\vartheta \\ \nu'_\varphi \\ \nu_\varphi^{\perp\prime} \end{pmatrix} = \begin{pmatrix} \cos\zeta & \sin\zeta\cos\psi & \sin\zeta\sin\psi \\ -\sin\zeta\cos\omega & \cos\zeta\cos\omega\cos\psi - \sin\omega\sin\psi & \cos\zeta\cos\omega\sin\psi + \sin\omega\cos\psi \\ \sin\zeta\sin\omega & -\cos\zeta\sin\omega\cos\psi - \cos\omega\sin\psi & -\cos\zeta\sin\omega\sin\psi + \cos\omega\cos\psi \end{pmatrix} \begin{pmatrix} \nu_\vartheta \\ \nu_\varphi \\ \nu_\varphi^\perp \end{pmatrix}.$$

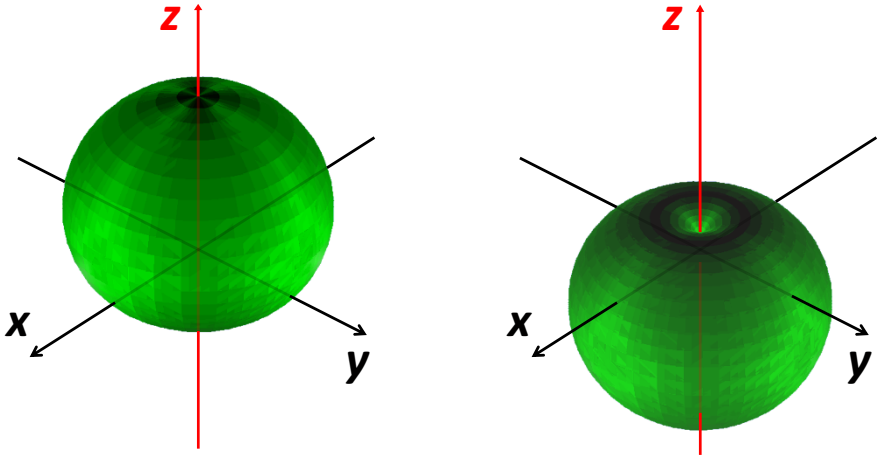

Fig. 7.14 Shape of the decay distribution of a $J = 1/2$ particle produced fully polarized and decaying with maximum parity asymmetry along the chosen z axis, when the initial and final states have same-sign (left) or opposite-sign (right) projections M and G'.

The rotation preserves $\tilde{\nu}$, which, therefore, represents the maximum measurable value of the asymmetry ν_ϑ along any chosen reference axis z and is obviously invariant for any frame transformation, while ν_ϑ, ν_φ and $\nu_\varphi^\perp$ are themselves invariant by rotations around, respectively, the z, x and y axes.

Another way of expressing these considerations on the rotational property of the distribution is that the three angular expressions $\cos\vartheta$, $\sin\vartheta\cos\varphi$ and $\sin\vartheta\sin\varphi$ entering Eq. 7.29 are equal, respectively, to the direction cosines $\cos\theta_z$, $\cos\theta_x$ and $\cos\theta_y$. It is an option for the experimental analysis to consider, in fact, the three one-dimensional distributions of these variables, which have the form $w(\cos\theta_z) \propto 1 + \nu_\vartheta \cos\theta_z$, etc., and yield the three parameters ν_ϑ, ν_φ and $\nu_\varphi^\perp$ individually, even if with statistical correlations more difficult to be accounted for, since the number of independent angular degrees of freedom remains only two.

Figure 7.14 shows the shape of the distribution in the extreme cases when the production and decay asymmetries are (for best visualization) maximum along the chosen axis, that is, $w(\cos\vartheta) = \frac{1}{2}(1 \pm \cos\vartheta)$.

We finally report the expressions for the polar anisotropy parameters of the decay of a $J = 3/2$ particle:

$$\begin{aligned}
\lambda_1 &= \left(-5\beta_{\frac{1}{2}\frac{1}{2}} + 3\beta_{\frac{3}{2}\frac{3}{2}} + 6\beta_{\frac{1}{2}\frac{3}{2}}\right)/D\,,\\
\lambda_2 &= \left(3\alpha_{\frac{1}{2}\frac{1}{2}} + 3\alpha_{\frac{3}{2}\frac{3}{2}} - 6\alpha_{\frac{1}{2}\frac{3}{2}}\right)/D\,,\\
\lambda_3 &= \left(9\beta_{\frac{1}{2}\frac{1}{2}} + \beta_{\frac{3}{2}\frac{3}{2}} - 6\beta_{\frac{1}{2}\frac{3}{2}}\right)/D\,,\\
\text{with}\quad D &= \alpha_{\frac{1}{2}\frac{1}{2}} + \alpha_{\frac{3}{2}\frac{3}{2}} + 6\alpha_{\frac{1}{2}\frac{3}{2}}\,,
\end{aligned} \tag{7.32}$$

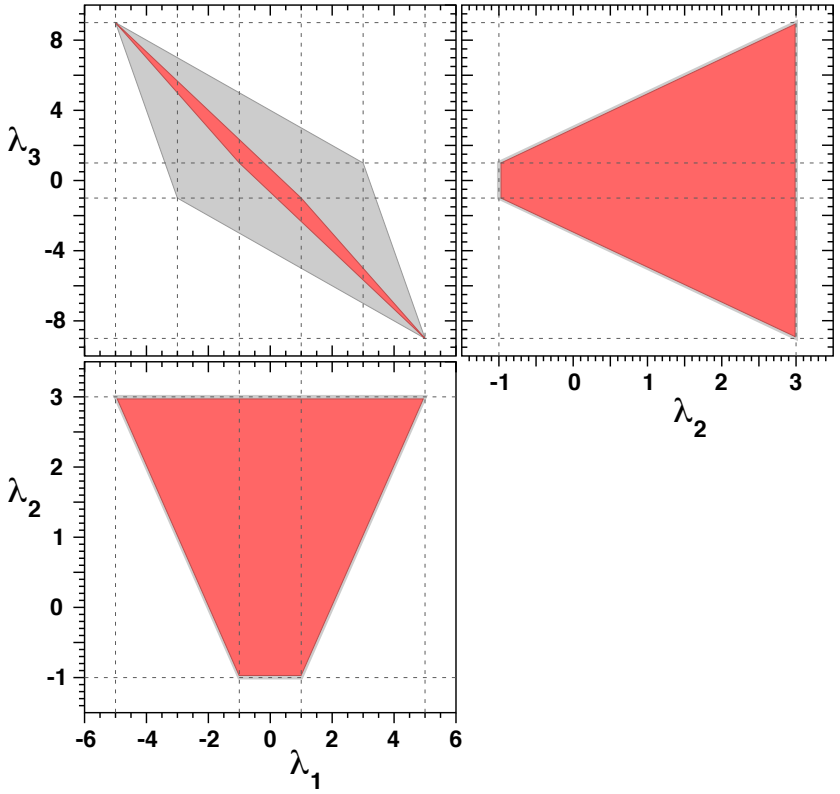

Fig. 7.15 Allowed parameter regions for the polar anisotropy parameters of the two-body decay distribution of a $J = 3/2$ particle. The largest areas (grey) represent the most general domain while the inner areas (red) represent the case of the decay into a system having G' projection $\pm 1/2$, as in the proton–pion and proton–kaon channels.

where α_{ij} and β_{ij} are the parity-conserving and parity-violating amplitude combinations defined in Eq. 7.24. The most general domain of these parameters is represented by the grey areas in Fig. 7.15, while the smaller red areas refer to the decay where $G' = \pm 1/2$, corresponding for example to the decays of the $J = 3/2$ N, Δ, and Λ baryons into proton–pion and proton–kaon, and of the Ω to Λ–kaon [5].

While the decay of a $J = 1/2$ particle is always isotropic in the absence of parity-violating effects, this is not true for the $J = 3/2$ case, where the angular distribution in the parity-conserving case has the form $\propto 1 + \lambda_2 \cos^2 \vartheta$, with λ_2 included between -1 and $+3$.

The shapes assumed by the distribution for all combinations of natural polarizations of the initial state (along z) and of the final state (along z') are shown in Fig. 7.16. The first two columns refer to the maximally parity-violating cases where initial- and final- state helicities have, respectively, always the same or always opposite signs, while the third column shows the parity-conserving distributions where

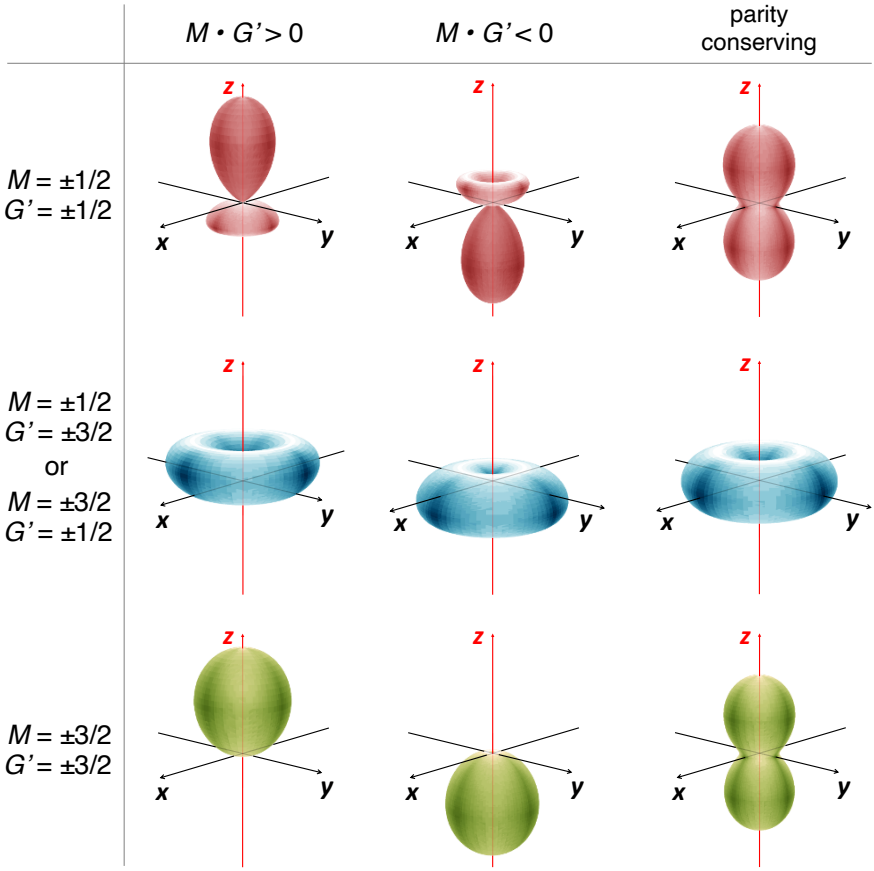

Fig. 7.16 Shape of the angular distribution produced by a $J = 3/2$ particle in a pure J_z state (M) decaying into a two-body system being a pure $J_{z'}$ state (G'); the colums represent, respectively, the two maximally and oppositely parity-violating cases and the parity-conserving case.

the signs of the helicities are uncorrelated. The $(\lambda_1, \lambda_2, \lambda_3)$ values corresponding to these shapes are shown in Fig. 7.17.

7.8 When "polarized" and "anisotropic" are seemingly not equivalent

After seeing expressions of the angular distribution parameters for generic decay channels, we can discuss the relation between the concepts of "particle polarization" and "decay anisotropy" in a more complete way, with respect to what was possible by examining the dilepton decay case in the previous chapters. Referring

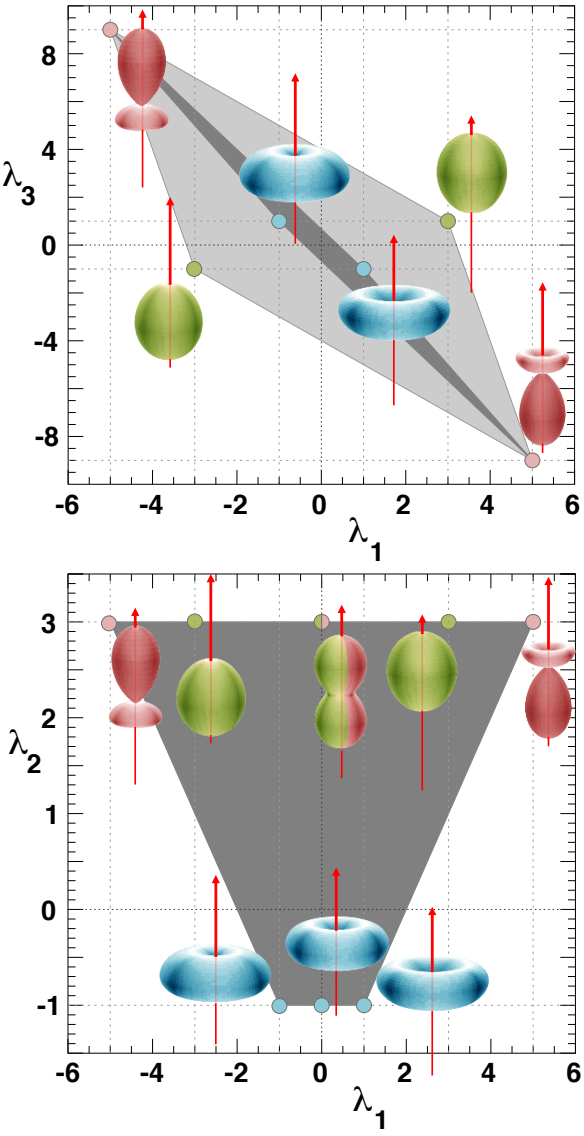

Fig. 7.17 The shape-parameter values of the polarization examples shown in Fig. 7.16.

in particular to the $J = 1$ case (Eq. 7.19), we now see a general feature: even considering one individual production process, where the particle is fully polarized, for example in the (longitudinal) $J_z = 0$ state (that is, the matrix elements $\rho^{G'}_{0,0}$ are the only nonzero ones), if the final state can have $G' = -1$, 0, or $+1$ with identical probabilities ($\rho^{-1}_{0,0} = \rho^{0}_{0,0} = \rho^{+1}_{0,0}$), then the distribution appears to be isotropic. The same result can be seen for any other angular momentum configuration of the initial

particle, being, for example, λ_ϑ a sum of terms of the kind $\rho^{+1}_{M,M} + \rho^{-1}_{M,M} - 2\rho^{0}_{M,M}$. In other words and more generally, the polarization of the decaying particle is observable through a measurable anisotropy of its two-body decay distribution only if also the *final* state is "polarized", being a superposition of $J_{z'}$ eigenstates with unequal weights. This is a completely general condition, satisfied, for example, also by the expressions of the polar anisotropy parameters of the distribution for a $J = 2$ particle (Eq. 7.23): all λ_i coefficients can be seen to vanish when it is imposed that $\sigma^j_i = \sigma^k_i$ for any i, j, and k. As we already mentioned in Section 7.7, each anisotropy parameter of the $J = 1/2$ decay reflects the product of initial state polarization and partity-violating decay asymmetry.

It remains true that a $J = 1$ particle is always produced intrinsically polarized, in the sense defined by Theorem 1.1, presented in Section 1.10: in every individual event it has always angular projection $M = \pm 1$ along some direction. As we have seen in Chapters 5 and 6, smearing effects, happening when that direction changes event after event with respect to the chosen reference frame, can attenuate or even completely hide the natural polarization. Assuming that none of such effects is at play here, there is a general condition for the observability of the polarization of a particle in its two-body decay: the final state must have a non-uniform pattern of spin orientations G', effectively providing the "analyzing power" of the decay. This is what usually happens, as seen in the examples considered, thanks to either the coupling properties of the involved particles (as helicity conservation in the dilepton decay) or simply because of angular momentum conservation, which often forbids certain $J_{z'}$ configurations of the final state.

Concerning the latter case, we have seen, in the previous sections, examples where the polarization becomes observable because $J_1 + J_2 < J$. Another possibility is that one of the decay particles has a definite polarization, as in the case of the transverse photon.

This fact is well illustrated by the already noticed difference between the angular distributions of the decays $\chi_{cJ} \to \mathrm{J}/\psi\,\gamma$ and $\chi_{cJ} \to \mathrm{J}/\psi\,\gamma^*$. In the first decay the emitted photon is real and transverse. Its $J_{z'}$ projection (Fig. 6.32), which can only be ± 1, rules out, because of angular momentum conservation, certain $J_{z'}$ projections of the J/ψ, which is, therefore, polarized. Above all, the J/$\psi\,\gamma$ system is polarized, that is, the values of its total $J_{z'}$ projection, $G' = L' + K' = -J, \ldots, +J$, are not equally probable, leading, as seen in Sections 7.4 (χ_{c1}) and 7.5 (χ_{c2}), to anisotropic χ_c decay distributions with shapes univocally correlated to the polarization.

When, instead, the photon is virtual, there is no constraint on its polarization and these $J \to (J = 1) + (J = 1)$ transitions become a "natural" illustration of the angular momentum addition rule $J = 1 \oplus 1$, where all possible G' combinations of the decay system compatible with $|G'| \leq J$ participate with equal weights, without any restriction imposed by the physical interaction driving the decay. This "unpolarized" final state does not provide any analyzing power for the determination of the mother particle's polarization. The J/ψ is, hence, emitted isotropically in the χ_c polarization frame, leading to the seemingly paradoxical case where the measurement of the two-body decay angular distribution is blind to the polarization state of the decaying particle.

The solution of the paradox is that this conclusion is true only when the measurement ignores the information contained in the subsequent decays of the final-state particles. A suitable analysis of the shapes of their own decay angular distributions *will* provide the necessary analyzing power.

The full information on the χ_c polarization state remains available in the higher-dimensional distribution of the cascade process $\chi_{cJ} \to \mathrm{J}/\psi\,\gamma^*$, $\mathrm{J}/\psi \to \ell^+\ell^-$, $\gamma^* \to \ell^+\ell^-$, determinable either in the frame (cHX) defined in Fig. 6.1 or in the one (CC) defined with the alternative J/ψ polarization axes of Fig. 6.3. Exploiting the full dimensionality of the process with its underlying variable correlations is always beneficial, also from the experimental point of view, since it minimizes the risks of analysis biases, presented by the blind integration over physical degrees of freedom (as we have seen in Section 2.13). In this case, however, as seen in Section 6.8, with the choice of the CC frame the anisotropy of the J/ψ dilepton decay alone, after integration over the angles of the χ_c decay, is fully sensitive to the χ_c polarization. Moreover, with the same axis definition, the dilepton distribution produced by the virtual photon is identical to the J/ψ one and carries a further "duplicate" of the χ_c polarization information.

7.9 Recapitulation

In the calculation of a decay angular distribution, the functional dependence on the decay angles is determined by the elements of the Wigner matrix, $\mathcal{D}^J_{LL'}$, corresponding to the total angular momentum J of the decaying particle O. In the considered case of a two-body decay, the matrix transforms the angular momentum projection (L') of the final state, as defined along the common direction, z', of the decay products X_1 and X_2 in the O rest frame, into the projection (L) on the quantization axis z chosen for O (Fig. 7.1-right), allowing us to impose the conservation $J_z(X_1 + X_2) = J_z(O)$. Section 7.1 describes the Wigner matrices in a form suitable for these calculations, which depends on the two spherical angles ϑ and φ defining the relative orientations of z' and z. The dependence is factorized as $\mathcal{D}^J_{LL'}(\vartheta,\varphi) = \exp[-i(L-L')\,\varphi]\; d^J_{LL'}(\vartheta)$, with the "reduced" elements $d^J_{LL'}(\vartheta)$ defined in Eq. 7.3. Explicit analytical expressions of the reduced matrix elements for J between $1/2$ and 4 are given in Tables 7.1–7.6.

The decay amplitude is a linear combination of Wigner matrix elements (Eqs. 7.6 and 7.7); the coefficients, $\mathcal{A}_{M,G'_1,G'_2}$, are complex amplitudes representing the dynamics of both the production and the decay of O (Fig. 7.1-left). In fact they express, on one hand, the probability of a given J_z projection, M, of O, that is, the polarization that O inherited in the production process. On the other hand, they reflect the properties of the final states X_1 and X_2, as well as of their coupling to O, by representing the probabilities of their possible $J_{z'}$ projections, G'_1 and G'_2.

The general expression of the angular distribution, squared modulus of the amplitude (Eq. 7.12), depends linearly on the "spin" density matrix elements $\rho^{G'}_{M,M}$, defined in Eq. 7.13 as the sum of all relevant products between an amplitude and a

complex-conjugate amplitude, also averaged over all possible contributing mechanisms.

The polar projection of the distribution (Eq. 7.15), depending only on the diagonal (and real) density matrix elements $\sigma_M^{G'} \equiv \rho_{M,M}^{G'}$ (Eq. 7.16), is a polynomial of order $2J$ in $\cos\vartheta$ and its $2J$ observable parameters are certainly much easier to handle in a measurement than those of the full distribution, which, for example, for $J = 2$ are 24 instead of 4.

The most general decay distribution of a $J = 1$ particle into any two-body final state (Eq. 7.18) is formally the same as for the dilepton decay of a vector particle (Eq. 1.29), depending on eight observable parameters, three of which parity-violating and two more vanishing in inclusive observations. The difference is in the dependence on the amplitudes (Eq. 7.19): the dilepton (helicity-conserving) case (Eq. 1.28) corresponds to setting the density matrix elements $\rho_{M,M}^0$ to zero. The allowed parameter space is, therefore, different (Fig. 7.2). For a given initial particle and polarization (M), the angular distributions of the decays into dilepton and into, for example, two $J = 0$ particles are as different as they could be, as shown by the comparison made in Fig. 7.3, which applies, for example, to the decays $\Upsilon(4S) \to B\overline{B}$ and $\Upsilon(4S) \to \ell^+\ell^-$.

Further examples of how the distribution changes for different final state particles and, also, for different production channels (which determine different possible polarizations of O) are given in Section 7.5 for the $J = 2$ case, considering, for simplicity, only the polar component, that is, the pure J_z eigenstates of the decaying particle (Fig. 7.6), and maximal parity violation effects (Fig. 7.7). Section 7.6 illustrates, with an example, how the identity of the production and decay channels strongly constrains the allowed shapes of the decay distributions. In particular, an unidentified particle produced by gluon-gluon fusion and decaying into two photons can be characterized with a measurement of its decay distribution without the need of injecting further theoretical hypotheses on it production mechanism. The allowed physical domains of the $J = 0$, 2, 3, and 4 cases ($J = 1$ being excluded by the Landau–Yang theorem) are disjointed from one another and can be experimentally discriminated (Fig. 7.10). In fact, the shapes of the distributions have characteristic differences, essentially in the number of changes of sign of the derivative of the $\cos\vartheta$ distribution (Fig 7.11), that is, in the number of "lobes" of the three-dimensional shape (Fig. 7.12). Clearly, more specific hypotheses, completely fixing the polarization of the produced particle, can be tested and rejected with higher significance, since they correspond to one point, instead of a region, in the parameter domain and to *one* of the possible curves or shapes seen in those figures.

The decays of half-integer spin particles are briefly illustrated in Section 7.7. In particular, in the $J = 1/2$ case the $\cos\vartheta, \varphi$ distribution (Eq. 7.29) is either isotropic or parity-violating, that is, its three parameters are asymmetries (Eq. 7.30), vanishing when either the production mechanism or the decay are parity-conserving. Instead, for the $J = 3/2$ distribution, parity-conserving but strongly anisotropic physical cases exist, where it assumes the form $1 + \lambda_2 \cos^2\vartheta$, with $\lambda_2 = -1$ for $|M| = 1/2$ and $|G'| = 3/2$, or vice-versa, and $\lambda_2 = +3$ for $|M| = |G'| = 3/2$ or $1/2$ (Figs. 7.16 and 7.17).

We saw in the previous chapter that an intrinsically polarized vector particle can appear as unpolarized if it is produced in the decay of a $J = 0$ state and the existence of this first decay step is ignored in the analysis. The natural polarization of the vector particle can, however, at least in principle, be measured, by reconstructing the two-step decay chain in its full dimensionality. In this chapter we have provided a further example of how an isotropic decay distribution can be observed even if the particle is naturally polarized.

A common feature recognizable in all formulas expressing the shape parameters of the two-body decay distribution as functions of the spin density matrix elements is that, for any J, a fully isotropic distribution is obtained not only when O is produced as an identical mixture of $J_z = -J, \ldots, +J$ states, but also (alternatively) when all $J_{z'}$ projections of the system of the decay products are equally probable. In other words, even if the decaying particle is polarized, the resulting two-body angular distribution will appear as isotropic if the final state is "unpolarized", and the polarization of O will seemingly be unobservable. This is a fairly rare occurrence, since the presence of leptons, real photons or $J = 0$ particles in the final state is generally sufficient to provide the $X_1 + X_2$ system with its required "polarization".

As concrete example we considered the decays $\chi_{cJ} \to \mathrm{J}/\psi\,\gamma^*$, where a measurement of the J/ψ emission angles in the χ_{cJ} rest frame always yields an isotropic result, irrespectively of the χ_{cJ} polarization. As in the case of the cascade decay from a $J = 0$ particle, it is actually always possible to perform an experiment that will determine the particle's polarization, by recovering neglected dimensions in the problem. In this case, such dimensions are those of the *subsequent* step in the decay: the angular analysis of the decays of X_1 and X_2, considering correlations with the $O \to X_1X_2$ distribution, will necessarily reveal the polarization of O, provided that X_1 and/or X_2 decay into "polarized" final states. This is the case of the considered example, where the J/ψ and γ^* produce lepton pairs having angular momentum projections ± 1 along their own directions in the J/ψ and γ^* rest frames, because of helicity conservation. Otherwise, the analysis of the cascade should, hypothetically, be further extended to subsequent decay steps.

References

[1] E. P. Wigner, "Group theory and its application to the quantum mechanics of atomic spectra". Pure and applied physics. Academic Press, New York, USA, 1959. ISBN 0127505504.

[2] D. M. Brink and G. R. Satchler, "Angular momentum". Oxford science publications. Clarendon Press, third edition, 1993. ISBN 0198517599.

[3] M. E. Rose, "Elementary theory of angular momentum". Wiley, New York, USA, 1957. ISBN 9780471735243.

[4] E. U. Condon and G. H. Shortley, "The theory of atomic spectra". Cambridge University Press, Cambridge, United Kingdom, 1951. ISBN 9780521092098.

[5] Particle Data Group Collaboration, "Review of Particle Physics", *PTEP* **2020** (2020) 083C01, doi:10.1093/ptep/ptaa104.

[6] Y. Gao et al., "Spin determination of single-produced resonances at hadron colliders", *Phys. Rev. D* **81** (2010) 075022, doi:10.1103/PhysRevD.81.075022, arXiv:1001.3396.

[7] ATLAS Collaboration, "Observation of a new particle in the search for the Standard Model Higgs boson with the ATLAS detector at the LHC", *Phys. Lett. B* **716** (2012) 1, doi:10.1016/j.physletb.2012.08.020, arXiv:1207.7214.

[8] CMS Collaboration, "Observation of a new boson at a mass of 125 GeV with the CMS experiment at the LHC", *Phys. Lett. B* **716** (2012) 30, doi:10.1016/j.physletb.2012.08.021, arXiv:1207.7235.

[9] L. D. Landau, "On the angular momentum of a system of two photons", *Dokl. Akad. Nauk SSSR* **60** (1948) 207, doi:10.1016/B978-0-08-010586-4.50070-5.

[10] C.-N. Yang, "Selection rules for the dematerialization of a particle into two photons", *Phys. Rev.* **77** (1950) 242, doi:10.1103/PhysRev.77.242.

[11] ATLAS Collaboration, "Measurement of top quark polarization in top-antitop events from proton-proton collisions at $\sqrt{s} = 7$ TeV using the ATLAS detector", *Phys. Rev. Lett.* **111** (2013) 232002, doi:10.1103/PhysRevLett.111.232002, arXiv:1307.6511.

[12] CMS Collaboration, "Measurements of $t\bar{t}$ spin correlations and top quark polarization using dilepton final states in pp collisions at $\sqrt{s} = 8$ TeV", *Phys. Rev. D* **93** (2016) 052007, doi:10.1103/PhysRevD.93.052007, arXiv:1601.01107.

[13] CMS Collaboration, "Measurement of top quark polarisation in t-channel single top quark production", *JHEP* **04** (2016) 073, doi:10.1007/JHEP04(2016)073, arXiv:1511.02138.

[14] G. Bunce et al., "Λ^0 hyperon polarization in inclusive production by 300 GeV protons on beryllium", *Phys. Rev. Lett.* **36** (1976) 1113, doi:10.1103/PhysRevLett.36.1113.

[15] A. D. Panagiotou, "Λ^0 polarization in hadron-nucleon, hadron-nucleus and nucleus-nucleus interactions", *Int. J. Mod. Phys. A* **5** (1990) 1197, doi:10.1142/S0217751X90000568.

[16] ALICE Collaboration, "Global polarization of $\Lambda\bar{\Lambda}$ hyperons in Pb-Pb collisions at $\sqrt{s_{NN}}$ = 2.76 and 5.02 TeV", *Phys. Rev. C* **101** (2020) 044611, doi:10.1103/PhysRevC.101.044611, arXiv:1909.01281.

Appendix A
Alternative parametrization of the dilepton decay distribution

The angular distribution of the dilepton decay of a vector particle is often parametrized in the form [1–3]

$$\begin{aligned} W(\cos\vartheta,\varphi) \;\propto\; & 1 \;+\; \cos^2\vartheta \;+\; \frac{A_0}{2}\,(1-3\cos^2\vartheta) \\ & +\; \frac{A_2}{2}\,\sin^2\vartheta\cos 2\varphi \;+\; A_1\,\sin 2\vartheta\cos\varphi \\ & +\; \frac{A_5}{2}\,\sin^2\vartheta\sin 2\varphi \;+\; A_6\,\sin 2\vartheta\sin\varphi \\ & +\; A_4\,\cos\vartheta \;+\; A_3\,\sin\vartheta\cos\varphi \;+\; A_7\,\sin\vartheta\sin\varphi\,, \end{aligned} \tag{A.1}$$

which is equivalent to the expression given in Eq. 1.29, simply replacing its coefficients by the corresponding A_i versions.

The two alternative sets of coefficients are related to each other according to the following relations:

$$\begin{pmatrix} \lambda_\vartheta \\ \lambda_\varphi \\ \lambda_{\vartheta\varphi} \\ \lambda^\perp_\varphi \\ \lambda^\perp_{\vartheta\varphi} \\ A_\vartheta \\ A_\varphi \\ A^\perp_\varphi \end{pmatrix} = \frac{1}{1+A_0/2} \begin{pmatrix} 1-3\,A_0/2 \\ A_2/2 \\ A_1 \\ A_5/2 \\ A_6 \\ A_4/2 \\ A_3/2 \\ A_7/2 \end{pmatrix}. \tag{A.2}$$

Inversely, we can compute the A_i parameters from the λ values, using the following relations:

P. Faccioli and C. Lourenço, *Particle Polarization in High Energy Physics*,
Lecture Notes in Physics 1002,
https://doi.org/10.1007/978-3-031-08876-6

$$\begin{pmatrix} A_0/2 \\ A_2/2 \\ A_1 \\ A_5/2 \\ A_6 \\ A_4/2 \\ A_3/2 \\ A_7/2 \end{pmatrix} = \frac{4}{3+\lambda_\vartheta} \begin{pmatrix} (1-\lambda_\vartheta)/4 \\ \lambda_\varphi \\ \lambda_{\vartheta\varphi} \\ \lambda_\varphi^\perp \\ \lambda_{\vartheta\varphi}^\perp \\ A_\vartheta \\ A_\varphi \\ A_\varphi^\perp \end{pmatrix} . \tag{A.3}$$

The reader should note that we are here considering (and recommending) a modified version of the parametrization actually used in the previous literature, where the term $\sin^2\vartheta \sin 2\varphi$ appears with the coefficient A_5 (instead of $A_5/2$), introducing a spurious asymmetry with respect to the term $\sin^2\vartheta \cos 2\varphi$ with its coefficient $A_2/2$. In the parametrization used throughout this book the corresponding coefficients, $\lambda_\varphi^\perp$ and λ_φ, are defined in a symmetric way, reflecting their geometrical analogy. In fact, these two parameters represent the same kind of geometrical anisotropy of the distribution, as we have seen in at least two occasions. First, they transform into one another (in modulus) by a rotation of the reference frame of $\pm\pi/4$ around the z axis, as can be seen in Eqs. 2.38 and 2.40. Second, they appear as "homogeneous" quantities also in the definition of the "3D" invariant polarization of Eq. 5.11.

It is true that the smearing effects of the event averaging in inclusive observations, which suppress reflection asymmetries with respect to the production plane, introduce an asymmetry between the effective domains of the parameters λ_φ and $\lambda_\varphi^\perp$ (or $A_2/2$ and $A_5/2$), with the latter being reduced in magnitude with respect to its "natural" value. The appreciation of this effect — of possible interest when parity-violating effects and/or a polarization of the colliding hadrons prevent the *complete* suppression of $\lambda_\varphi^\perp$ (and of $A_5/2$) — benefits from a properly symmetric definition.

We also remark the not very helpful ordering of the numerical indices of the parameters A_i, requiring attention in their identification with the coefficients of the parity conserving and parity-violating terms of the distribution. Moreover, their definitions would be more coherent and practical if some of them were divided by two. The first relation of Eq. A.3,

$$A_0/2 = \frac{1-\lambda_\vartheta}{3+\lambda_\vartheta} , \tag{A.4}$$

shows that $A_0/2$, included between 0 and 1, is the longitudinal polarization fraction ($|a_0|^2$ in Eq. 3.1), that is, the proportion of events that are longitudinally polarized in the chosen frame. Figure A.1 shows the shapes of the parameter domain (determined from Eq. 3.24 using Eq. A.2). We can observe that, except for $A_0/2$, all the coefficients take values in the range between -1 and $+1$, if we divide by two the parameters A_2, A_5, A_4, A_3, and A_7.

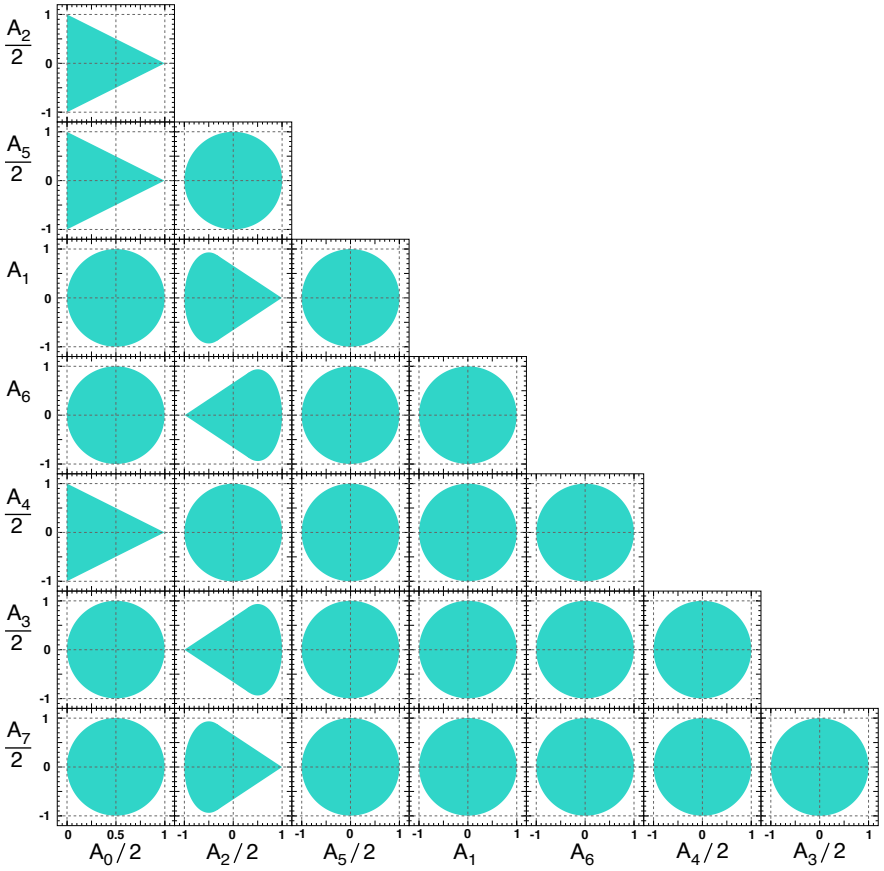

Fig. A.1 Two-dimensional projections of the allowed domain for the parameters A_i, corresponding, in their order, to those shown in Fig. 3.4 for the parameters λ_ϑ, λ_φ, $\lambda_\varphi^\perp$, $\lambda_{\vartheta\varphi}$, $\lambda_{\vartheta\varphi}^\perp$, A_ϑ, A_φ.

Despite the somewhat counter-intuitive conventions used in the definition of its coefficients, the A_i parametrization (Eq. A.1) offers several advantages with respect to "the λ version" (Eq. 1.29).

To start with, the average over concurring production processes follows a linear addition rule which is, for each individual parameter, independent of all others,

$$A_i = \frac{\sum_{j=1}^{n} f^{(j)} A_i^{(j)}}{\sum_{j=1}^{n} f^{(j)}}, \tag{A.5}$$

contrary to the analogous rule for $\lambda_{\vartheta|\varphi|\vartheta\varphi}^{(\perp)}$ and $A_{\vartheta|\varphi}^{(\perp)}$ (given in Eq. 1.17).

In the determination of the parameters from one-dimensional projections of the distribution, the coefficients of the azimuthal components no longer depend on the polar anisotropy parameter (contrary to what happens in Eqs. 1.18, 1.19 and 1.20):

$$w(\cos\vartheta) \;\propto\; 1 \,+\, \cos^2\vartheta \,+\, \frac{A_0}{2}(1-3\cos^2\vartheta)\,, \tag{A.6}$$

$$w(\varphi) \;\propto\; 1 \,+\, \frac{A_2}{4}\cos 2\varphi \,+\, \frac{A_5}{4}\sin 2\varphi\,, \tag{A.7}$$

$$w(\tilde{\varphi}) \;\propto\; 1 \,+\, \frac{\sqrt{2}}{4}A_1\,\cos\tilde{\varphi} \,+\, \frac{\sqrt{2}}{4}A_6\,\sin\tilde{\varphi}\,. \tag{A.8}$$

The same kind of decoupling characterizes the parameter dependences of the event asymmetries (to be compared with Eq. 1.22),

$$\begin{aligned}
\frac{P(|\cos\vartheta|>1/2)-P(|\cos\vartheta|<1/2)}{P(|\cos\vartheta|>1/2)+P(|\cos\vartheta|<1/2)} &= \frac{3}{16}\left(1-3\frac{A_0}{2}\right),\\
\frac{P(\cos 2\varphi>0)-P(\cos 2\varphi<0)}{P(\cos 2\varphi>0)+P(\cos 2\varphi<0)} &= \frac{A_2}{2\pi},\\
\frac{P(\sin 2\varphi>0)-P(\sin 2\varphi<0)}{P(\sin 2\varphi>0)+P(\sin 2\varphi<0)} &= \frac{A_5}{2\pi},\\
\frac{P(\sin 2\vartheta\cos\varphi>0)-P(\sin 2\vartheta\cos\varphi<0)}{P(\sin 2\vartheta\cos\varphi>0)+P(\sin 2\vartheta\cos\varphi<0)} &= \frac{A_1}{\pi},\\
\frac{P(\sin 2\vartheta\sin\varphi>0)-P(\sin 2\vartheta\sin\varphi<0)}{P(\sin 2\vartheta\sin\varphi>0)+P(\sin 2\vartheta\sin\varphi<0)} &= \frac{A_6}{\pi},
\end{aligned} \tag{A.9}$$

and of the averages of angular combinations (to be compared with Eq. 1.23),

$$\begin{aligned}
\langle\cos^2\vartheta\rangle &= \frac{1}{5}\left(2-\frac{A_0}{2}\right),\\
\langle\cos 2\varphi\rangle &= \frac{1}{4}\frac{A_2}{2},\\
\langle\sin 2\varphi\rangle &= \frac{1}{4}\frac{A_5}{2},\\
\langle\sin 2\vartheta\,\cos\varphi\rangle &= \frac{1}{5}A_1\,,\\
\langle\sin 2\vartheta\,\sin\varphi\rangle &= \frac{1}{5}A_6\,.
\end{aligned} \tag{A.10}$$

As an example of the benefits of dealing with linear and uncorrelated relations, $A_0/2$, $A_2/2$ and A_1 can be determined (in event samples not requiring acceptance and efficiency corrections or background subtraction) simply as the average values of suitable variables:

$$\begin{aligned} A_0/2 &= \langle\, 2 - 5\cos^2\vartheta \,\rangle\,, \\ A_2/2 &= \langle\, 4\,\cos 2\varphi \,\rangle\,, \\ A_1 &= \langle\, 5\,\sin 2\vartheta\,\cos\varphi \,\rangle\,. \end{aligned} \tag{A.11}$$

Also the frame transformations are represented by linear (but not homogeneous) equations,

$$\begin{pmatrix} A_0'/2 \\ A_2'/2 \\ A_1' \\ A_5'/2 \\ A_6' \end{pmatrix} = \begin{pmatrix} \frac{1}{2}\sin^2\delta \\ \frac{1}{2}\sin^2\delta \\ -\frac{1}{2}\sin 2\delta \\ 0 \\ 0 \end{pmatrix} + \begin{pmatrix} 1-\frac{3}{2}\sin^2\delta & -\frac{1}{2}\sin^2\delta & -\frac{1}{2}\sin 2\delta & 0 & 0 \\ -\frac{3}{2}\sin^2\delta & 1-\frac{1}{2}\sin^2\delta & -\frac{1}{2}\sin 2\delta & 0 & 0 \\ \frac{3}{2}\sin 2\delta & \frac{1}{2}\sin 2\delta & \cos 2\delta & 0 & 0 \\ 0 & 0 & 0 & \cos\delta & -\sin\delta \\ 0 & 0 & 0 & \sin\delta & \cos\delta \end{pmatrix} \begin{pmatrix} A_0/2 \\ A_2/2 \\ A_1 \\ A_5/2 \\ A_6 \end{pmatrix} \tag{A.12}$$

and

$$\begin{pmatrix} A_4'/2 \\ A_3'/2 \\ A_7'/2 \end{pmatrix} = \begin{pmatrix} \cos\delta & \sin\delta & 0 \\ -\sin\delta & \cos\delta & 0 \\ 0 & 0 & 1 \end{pmatrix} \begin{pmatrix} A_4/2 \\ A_3/2 \\ A_7/2 \end{pmatrix}, \tag{A.13}$$

whereas the corresponding transformations of $\lambda^{(\perp)}_{\vartheta|\varphi|\vartheta\varphi}$ and $A^{(\perp)}_{\vartheta|\varphi}$ (Eqs. 2.32 and 2.33) additionally contain the overall denominator $1 + A_y$, itself a function of the parameters (Eq. 2.34). Thanks to the absence of that denominator, the A_i transformations form three completely independent sets, for the groups of parameters (A_0, A_2, A_1), (A_5, A_6), and (A_4, A_3, A_7).

In particular, A_0 and A_2 transform according to the relations

$$\begin{aligned} A_0' &= A_0 + \Delta\,, \\ A_2' &= A_2 + \Delta\,, \\ \text{with}\quad \Delta &= \left(1 - 3\,\frac{A_0}{2} - \frac{A_2}{2}\right)\sin^2\delta \;-\; A_1\sin 2\delta\,, \end{aligned} \tag{A.14}$$

immediately showing that $A_0 - A_2$ is invariant. In fact, the quantity

$$\frac{A_0 - A_2}{2} \;=\; 1 - 2\mathcal{F} \;=\; \frac{1-\tilde{\lambda}}{3+\tilde{\lambda}} \tag{A.15}$$

represents a frame-independent definition of the longitudinal fraction, expressing the proportion of events where the vector particle is produced longitudinally polarized along some direction belonging to the production plane ($\tilde{\lambda} = -1$), while the complementary fraction represents the proportion of "intrinsically" transversely polarized events ($\tilde{\lambda} = +1$).

The frame-independent version of the Lam–Tung relation (Chapter 4) can in fact be written as

$$\frac{A_0 - A_2}{2} = 0\,, \tag{A.16}$$

with the meaning that all involved processes are intrinsically fully transverse.

However, we also note that this "frame-independent longitudinal fraction" is, in the most general case, not a proper fraction of events, since it is included between -1 and $+1$. The domain of negative values corresponds to the peculiar physical scenarios discussed in Section 5.3, where $\mathcal{F} > 1/2$ and $\tilde{\lambda} > +1$, indicating a preferred orientation of the angular momentum vector along the direction perpendicular to the production plane.

The quasi-invariant parameters (introduced and discussed in Sections 3.9 and 4.5) can be defined in the A_i notation as

$$\begin{aligned} A_0^\star &= A_0 + B\,, \\ A_2^\star &= A_2 + B\,, \\ \text{with} \quad B &= \frac{1}{2}\left[1 - 3\,\frac{A_0}{2} - \frac{A_2}{2} \pm \sqrt{\left(1 - 3\,\frac{A_0}{2} - \frac{A_2}{2}\right)^2 + 4\,A_1^2}\right], \end{aligned} \tag{A.17}$$

where the sign can be chosen according to some convention, for example the one giving the smaller modulus of A_2, in which case $A_0^\star$ and $A_2^\star$ represent the distribution as seen in the (always existing) frame where the diagonal terms A_1 and A_6 vanish *and* the azimuthal anisotropy (A_2) is minimized.

The frame-independent parity-violating asymmetry (discussed in Section 3.10), normalized so that $0 \leq \mathcal{A}^\star \leq 1$, can be written as

$$\mathcal{A}^\star = \sqrt{\left(\frac{A_4}{2}\right)^2 + \left(\frac{A_3}{2}\right)^2 + \left(\frac{A_7}{2}\right)^2}\,. \tag{A.18}$$

It can be determined directly in a fit to the measured distribution through the substitutions

$$\begin{aligned} \frac{A_4}{2} &\to \mathcal{A}^\star \cos\xi\,, \\ \frac{A_3}{2} &\to \mathcal{A}^\star \sin\xi\cos\chi\,, \\ \frac{A_7}{2} &\to \mathcal{A}^\star \sin\xi\sin\chi\,, \end{aligned} \tag{A.19}$$

where the angles ξ and χ express the rotation relating the current polarization axis to the one where the partity-violation effect is maximal, i.e., the axis where the vector (A_4, A_3, A_7) has maximal projection. Both the definition of $\mathcal{A}^\star$ and the above substitutions are free from the dependence on the polar anisotropy parameter, contrary to what happens in the corresponding relations in the usual parametrization (Eqs. 3.46 and 3.49).

Also the forward-backward asymmetry and the accompanying parity-violating asymmetries between azimuthal configurations (Eq. 1.30) can be obtained by simply rescaling A_4, A_3, and A_7:

$$\begin{aligned} \mathcal{A}_{\cos\vartheta} &= \frac{3}{8} A_4 \,, \\ \mathcal{A}_{\cos\varphi} &= \frac{3}{8} A_3 \,, \\ \mathcal{A}_{\sin\varphi} &= \frac{3}{8} A_7 \,. \end{aligned} \tag{A.20}$$

References

[1] E. Mirkes, "Angular decay distribution of leptons from W bosons at NLO in hadronic collisions", *Nucl. Phys. B* **387** (1992) 3, doi:10.1016/0550-3213(92)90046-E.

[2] CMS Collaboration, "Angular coefficients of Z bosons produced in pp collisions at $\sqrt{s} = 8$ TeV and decaying to $\mu^+\mu^-$ as a function of transverse momentum and rapidity", *Phys. Lett. B* **750** (2015) 154, doi:10.1016/j.physletb.2015.08.061, arXiv:1504.03512.

[3] ATLAS Collaboration, "Measurement of the angular coefficients in Z-boson events using electron and muon pairs from data taken at $\sqrt{s} = 8$ TeV with the ATLAS detector", *JHEP* **08** (2016) 159, doi:10.1007/JHEP08(2016)159, arXiv:1606.00689.

Appendix B
Angular distributions of $O \to V\,\gamma$, with $J(O) = J(V) = 1$ and $V \to \ell^+\ell^- \,|\, \pi\gamma \,|\, \pi\pi \,|\, \ldots$

The formulas presented in Section 6.6 for the decay $\chi_{c1} \to \mathrm{J}/\psi\,\gamma$, followed by the dilepton decay of the J/ψ, Eq. 6.28, only considered the case of pure J_z states of O. In the more general case, where O is the superposition defined in Eq. 6.25, the angular distribution in the CC frame becomes

$$
\begin{aligned}
W^{\ell^+\ell^-}_{\mathrm{CC}}&(\cos\Theta, \Phi, \cos\vartheta, \varphi) \propto \\
&\quad 2\left[|a_0|^2 + 2\left(|a_{+1}|^2 + |a_{-1}|^2\right)\right] \\
&+ 2\,|a_0|^2\,(\cos^2\Theta + \cos^2\vartheta) \\
&+ 2\left[|a_0|^2 - 2\left(|a_{+1}|^2 + |a_{-1}|^2\right)\right]\cos^2\Theta\cos^2\vartheta \\
&- 2\,|a_0|^2\,\sin^2\Theta\sin^2\vartheta\cos 2(\Phi - \varphi) \\
&- \left(|a_{+1}|^2 + |a_{-1}|^2\right)\sin 2\Theta\sin 2\vartheta\cos(\Phi - \varphi) \\
&- 2\,\mathrm{Re}[a^*_{+1}a_{-1}]\left[\sin 2\Theta\sin 2\vartheta\cos(\Phi + \varphi) + 2\sin^2\Theta\sin^2\vartheta\,(\cos 2\Phi + \cos 2\varphi)\right] \\
&- 2\,\mathrm{Im}[a^*_{+1}a_{-1}]\left[\sin 2\Theta\sin 2\vartheta\sin(\Phi + \varphi) + 2\sin^2\Theta\sin^2\vartheta\,(\sin 2\Phi + \sin 2\varphi)\right] \\
&- \sqrt{2}\,\mathrm{Re}[a^*_{+1}a_0 - a^*_0a_{-1}]\left\{2\,(\sin 2\Theta\cos\Phi + \sin 2\vartheta\cos\varphi)\right. \\
&\qquad\qquad + \sin^2\Theta\sin 2\vartheta\,[\cos(2\Phi - \varphi) - \cos\varphi] \\
&\qquad\qquad \left. + \sin^2\vartheta\sin 2\Theta\,[\cos(2\varphi - \Phi) - \cos\Phi]\right\} \\
&- \sqrt{2}\,\mathrm{Im}[a^*_{+1}a_0 - a^*_0a_{-1}]\left\{2\,(\sin 2\Theta\sin\Phi + \sin 2\vartheta\sin\varphi)\right. \\
&\qquad\qquad + \sin^2\Theta\sin 2\vartheta\,[\sin(2\Phi - \varphi) - \sin\varphi] \\
&\qquad\qquad \left. + \sin^2\vartheta\sin 2\Theta\,[\sin(2\varphi - \Phi) - \sin\Phi]\right\}\,.
\end{aligned}
\tag{B.1}
$$

The superscript "$\ell^+\ell^-$" is included in the symbol $W^{\ell^+\ell^-}_{\mathrm{CC}}$ to clearly specify the J/ψ decay channel under consideration: $\mathrm{J}/\psi \to \ell^+\ell^-$.

P. Faccioli and C. Lourenço, *Particle Polarization in High Energy Physics*,
Lecture Notes in Physics 1002,
https://doi.org/10.1007/978-3-031-08876-6

The same expression also describes the case of any decay of the kind $O \to V\gamma$, with $J(O) = J(V) = 1$. Moreover, the decay channel $V \to \ell^+\ell^-$ can be replaced with, for example, $V \to \pi^{0,\pm}\gamma$ or $V \to \mathrm{K}^{0,\pm}\gamma$, or any other process where the decay products have angular momentum projection $J_{z'''} = \pm 1$ along their common direction in the V rest frame (Fig. 6.4, $L''' = \pm 1$ in Eq. 6.28), with the same resulting distribution. Parity violating effects are here always assumed to be absent.

We are now going to consider the further case where V decays into two $J = 0$ particles, such as, for example, two pions or two kaons, or, more generally, any pair of particles having, for some reason, $J_{z'''} = 0$.

The distribution for $V \to \pi^+\pi^-$ (neutral O and V) or $V \to \pi^\pm\pi^0$ (charged O and V), or with any other pair of $J = 0$ particles replacing the pions, can be derived from the same amplitude of Eq. 6.28, calculating this time its square modulus for $L''' = 0$. The result is

$$
\begin{aligned}
&W^{\pi\pi}_{\mathrm{CC}}(\cos\Theta, \Phi, \cos\vartheta, \varphi) \propto \\
&\quad 2\left(|a_0|^2 + |a_{+1}|^2 + |a_{-1}|^2\right) \\
&- 2\,|a_0|^2 \cos^2\vartheta \\
&+ 2\left[|a_0|^2 - \left(|a_{+1}|^2 + |a_{-1}|^2\right)\right]\cos^2\Theta \\
&+ 2\left[2\left(|a_{+1}|^2 + |a_{-1}|^2\right) - |a_0|^2\right]\cos^2\Theta\cos^2\vartheta \\
&+ 2\,|a_0|^2 \sin^2\Theta \sin^2\vartheta \cos 2(\Phi - \varphi) \\
&+ \left(|a_{+1}|^2 + |a_{-1}|^2\right)\sin 2\Theta \sin 2\vartheta \cos(\Phi - \varphi) \\
&+ 2\,\mathrm{Re}[a^*_{+1}a_{-1}]\Big[\sin 2\Theta \sin 2\vartheta \cos(\Phi + \varphi) + 2\sin^2\Theta \sin^2\vartheta\ (\cos 2\Phi + \cos 2\varphi) \\
&\qquad\qquad -2\ \sin^2\Theta \cos 2\Phi\Big] \\
&+ 2\,\mathrm{Im}[a^*_{+1}a_{-1}]\Big[\sin 2\Theta \sin 2\vartheta \sin(\Phi + \varphi) + 2\sin^2\Theta \sin^2\vartheta\ (\sin 2\Phi + \sin 2\varphi) \\
&\qquad\qquad -2\ \sin^2\Theta \sin 2\Phi\Big] \\
&+ \sqrt{2}\,\mathrm{Re}[a^*_{+1}a_0 - a^*_0 a_{-1}]\Big\{2\ \sin 2\vartheta \cos\varphi \\
&\qquad\qquad + \sin^2\Theta \sin 2\vartheta\ [\cos(2\Phi - \varphi) - \cos\varphi] \\
&\qquad\qquad + \sin^2\vartheta \sin 2\Theta\ [\cos(2\varphi - \Phi) - \cos\Phi]\Big\} \\
&+ \sqrt{2}\,\mathrm{Im}[a^*_{+1}a_0 - a^*_0 a_{-1}]\Big\{2\ \sin 2\vartheta \sin\varphi \\
&\qquad\qquad + \sin^2\Theta \sin 2\vartheta\ [\sin(2\Phi - \varphi) - \sin\varphi] \\
&\qquad\qquad + \sin^2\vartheta \sin 2\Theta\ [\sin(2\varphi - \Phi) - \sin\Phi]\Big\}\ .
\end{aligned}
\tag{B.2}
$$

It can be verified, as a crosscheck, that both distributions, Eqs. B.1 and B.2, when integrated over $\cos\vartheta$ and φ, reduce to the same $\cos\Theta, \Phi$ distribution, representing

the two-body decay $O \to V\,\gamma$ (obviously independent of the subsequent decay channel of V):

$$\begin{aligned} w^{O\to V\,\gamma}(\cos\Theta,\Phi) \;\propto\; & D \;+\; D\,\lambda_\Theta\,\cos^2\Theta \\ & +\; D\,\lambda_\Phi\,\sin^2\Theta\cos 2\Phi \;+\; D\,\lambda_\Phi^\perp\,\sin^2\Theta\sin 2\Phi \\ & +\; D\,\lambda_{\Theta\Phi}\,\sin 2\Theta\cos\Phi \;+\; D\,\lambda_{\Theta\Phi}^\perp\,\sin 2\Theta\sin\Phi\;, \end{aligned} \tag{B.3}$$

where

$$\begin{aligned} D &= 2\,|a_0|^2 + 3\left(|a_{+1}|^2 + |a_{-1}|^2\right)\;, \\ D\,\lambda_\Theta &= 2\,|a_0|^2 - \left(|a_{+1}|^2 + |a_{-1}|^2\right)\;, \\ D\,\lambda_\Phi &= -2\,\mathrm{Re}[a_{+1}^* a_{-1}]\;, \\ D\,\lambda_\Phi^\perp &= -2\,\mathrm{Im}[a_{+1}^* a_{-1}]\;, \\ D\,\lambda_{\Theta\Phi} &= -\sqrt{2}\,\mathrm{Re}[a_{+1}^* a_0 - a_0^* a_{-1}]\;, \\ D\,\lambda_{\Theta\Phi}^\perp &= -\sqrt{2}\,\mathrm{Im}[a_{+1}^* a_0 - a_0^* a_{-1}]\;. \end{aligned} \tag{B.4}$$

In particular, and as already shown in Section 6.6 (Table 6.1 and related text), we see that $W^{O\to V\,\gamma} \propto 1 + \lambda_\Theta\,\cos^2\Theta$ with $\lambda_\Theta = +1$ and $-1/3$ when O is, respectively, a pure $J_z = 0$ or $J_z = \pm 1$ eigenstate.

When V decays to $\ell^+\ell^-$ or to $\pi^{0,\pm}\,\gamma$, the $(\cos\vartheta,\varphi)$ angular distribution is formally identical to Eqs. B.3–B.4, with the replacement of the upper-case angles with the lower-case ones, thanks to the cloning symmetry described in Section 6.6. The cloning symmetry is, instead, broken when V decays to $\pi\pi$ or, in principle, to any other pair of particles no longer having definite $J_{z'''} = \pm 1$ projection along their common direction in the V rest frame (Fig. 6.25). The $\pi\pi$ distribution, with coefficients expressed in terms of the angular momentum composition of the original mother particle O, is

$$\begin{aligned} w^{V\to\pi\pi}(\cos\vartheta,\varphi) \;\propto\; & D \;+\; D\,\lambda_\vartheta\,\cos^2\vartheta \\ & +\; D\,\lambda_\varphi\,\sin^2\vartheta\cos 2\varphi \;+\; D\,\lambda_\varphi^\perp\,\sin^2\vartheta\sin 2\varphi \\ & +\; D\,\lambda_{\vartheta\varphi}\,\sin 2\vartheta\cos\varphi \;+\; D\,\lambda_{\vartheta\varphi}^\perp\,\sin 2\vartheta\sin\varphi\;, \end{aligned} \tag{B.5}$$

where

$$\begin{aligned} D &= 2\,|a_0|^2 + |a_{+1}|^2 + |a_{-1}|^2\;, \\ D\,\lambda_\vartheta &= -2\,|a_0|^2 + |a_{+1}|^2 + |a_{-1}|^2\;, \\ D\,\lambda_\varphi &= 2\,\mathrm{Re}[a_{+1}^* a_{-1}]\;, \\ D\,\lambda_\varphi^\perp &= 2\,\mathrm{Im}[a_{+1}^* a_{-1}]\;, \\ D\,\lambda_{\vartheta\varphi} &= \sqrt{2}\,\mathrm{Re}[a_{+1}^* a_0 - a_0^* a_{-1}]\;, \\ D\,\lambda_{\vartheta\varphi}^\perp &= \sqrt{2}\,\mathrm{Im}[a_{+1}^* a_0 - a_0^* a_{-1}]\;. \end{aligned} \tag{B.6}$$

This distribution turns out to be identical to the one defined by Eqs. 1.12 and 1.13: the $V \to \pi\pi$ decay distribution observed in the CC frame, while being different from the actual decay distribution of $O \to V\gamma$, happens to clone the *dilepton* decay distribution of O.

Incidentally, the $\pi\pi$ distribution can also be provided in terms of a generic V angular momentum state ($|\,V\rangle = \sum_{M=-1}^{+1} b_M \;|\,1,\, M\,\rangle_z$), starting from Eq. 7.19 and keeping only the terms $\rho^0_{M,N}$, expressed as $b^*_M b_N$.

The formulas reported here can be used to study Z and W boson production in several decays channels. Among the processes described by the distribution $W^{\ell^+\ell^-}_{\rm CC}$ (Eq. B.1) we can mention the decays $\mathrm{Z} \to \mathrm{J}/\psi\,\gamma$, $\mathrm{Z} \to \phi\,\gamma$, and $\mathrm{Z} \to \rho^0\,\gamma$, with the $\mathrm{J}/\psi \,|\, \phi \,|\, \rho^0$ mesons observed in the $\ell^+\ell^-$ decay channel or in any radiative decay to a $J = 0$ particle. The distribution $W^{\pi\pi}_{\rm CC}$ (Eq. B.2), on the other hand, describes, for example, the Z decays with $\phi \to \mathrm{K}^+\mathrm{K}^-$ or $\rho^0 \to \pi^+\pi^-$, as well as the analogous W decay, $\mathrm{W}^\pm \to \rho^\pm\,\gamma$, with $\rho^\pm \to \pi^\pm\pi^0$.

Rare decays of this kind have been studied at the LHC [1, 2], to probe the Standard Model. The measurement of their branching fractions represents an example of an application of Eqs. B.1 and B.2. Indeed, the Z and W yields observed in the considered $V\gamma$ decay channels must be corrected for the corresponding experimental acceptances, both for the photon and for the further decay products of V. The results depend, therefore, on the shapes of the four-dimensional decay angular distributions, similarly to what was discussed in Section 1.6.

The coefficients in the above expressions can be constrained using Z (and W) polarization measurements performed using the dilepton (and lepton-neutrino) decay channels. The Z polarization has been measured precisely by ATLAS [3] and CMS [4] (see Sections 4.3 and 5.2). In first approximation, reasonably valid for the purpose of acceptance correction studies, the W polarization parameters A_i (detailed in Appendix A) can be determined to be the same as the Z ones, as a function of $p_{\rm T}/M$ and rapidity. In fact, the vector boson polarization is, as described in Section 4.3, always intrinsically transverse along certain natural directions, and the parameters A_i in a chosen experimental frame are simply determined by suitable rotations (Appendix A) of naturally transverse polarizations, by angles depending only on (dimensionless) combinations of $p_{\rm T}/M$ and y (Table 2.1).

Using Eqs. 1.13 and A.3 we can express the combinations of amplitudes appearing in Eqs. B.1 and B.2 (with $\mathcal{N} = |a_0|^2 + |a_{+1}|^2 + |a_{-1}|^2$) in terms of the coefficients A_i of the angular distribution of the *dilepton* decay:

$$
\begin{aligned}
\frac{|a_0|^2}{\mathcal{N}} &= \frac{A_0}{2}\,, \quad & \frac{|a_{+1}|^2 + |a_{-1}|^2}{\mathcal{N}} &= 1 - \frac{A_0}{2}\,, \\
\frac{2\,\mathrm{Re}[a^*_{+1}a_{-1}]}{\mathcal{N}} &= \frac{A_2}{2}\,, \quad & \frac{2\,\mathrm{Im}[a^*_{+1}a_{-1}]}{\mathcal{N}} &= \frac{A_5}{2}\,, \\
\frac{\sqrt{2}\,\mathrm{Re}[a^*_{+1}a_0 - a^*_0 a_{-1}]}{\mathcal{N}} &= A_1\,, \quad & \frac{\sqrt{2}\,\mathrm{Im}[a^*_{+1}a_0 - a^*_0 a_{-1}]}{\mathcal{N}} &= A_6\,.
\end{aligned}
\tag{B.7}
$$

The angular distribution for processes of the kind $\mathrm{Z} \to V\gamma$, followed by the dilepton decay of V, becomes, therefore,

$$
\begin{aligned}
W_{\mathrm{CC}}^{\ell^+\ell^-}&(\cos\Theta, \Phi, \cos\vartheta, \varphi) \propto \\
&\quad 4 - A_0 \\
&+ A_0 \left(\cos^2\Theta + \cos^2\vartheta\right) \\
&- (4 - 3A_0)\, \cos^2\Theta \cos^2\vartheta \\
&- A_0\, \sin^2\Theta \sin^2\vartheta \cos 2(\Phi - \varphi) \\
&- \left(1 - \frac{A_0}{2}\right) \sin 2\Theta \sin 2\vartheta \cos(\Phi - \varphi) \\
&- \frac{A_2}{2} \left[\sin 2\Theta \sin 2\vartheta \cos(\Phi + \varphi) + 2 \sin^2\Theta \sin^2\vartheta\, (\cos 2\Phi + \cos 2\varphi)\right] \\
&- \frac{A_5}{2} \left[\sin 2\Theta \sin 2\vartheta \sin(\Phi + \varphi) + 2 \sin^2\Theta \sin^2\vartheta\, (\sin 2\Phi + \sin 2\varphi)\right] \\
&- A_1 \Big\{2\, (\sin 2\Theta \cos\Phi\, +\, \sin 2\vartheta \cos\varphi) \\
&\qquad + \sin^2\Theta \sin 2\vartheta\, [\cos(2\Phi - \varphi) - \cos\varphi] \\
&\qquad + \sin^2\vartheta \sin 2\Theta\, [\cos(2\varphi - \Phi) - \cos\Phi]\Big\} \\
&- A_6 \Big\{2\, (\sin 2\Theta \sin\Phi\, +\, \sin 2\vartheta \sin\varphi) \\
&\qquad + \sin^2\Theta \sin 2\vartheta\, [\sin(2\Phi - \varphi) - \sin\varphi] \\
&\qquad + \sin^2\vartheta \sin 2\Theta\, [\sin(2\varphi - \Phi) - \sin\Phi]\Big\}\ .
\end{aligned}
\tag{B.8}
$$

Correspondingly, the angular distribution for the $V\gamma$ decays of the Z and W bosons, with V decaying to two $J = 0$ particles, can be written as

$$
\begin{aligned}
W_{\mathrm{CC}}^{\pi\pi}&(\cos\Theta, \Phi, \cos\vartheta, \varphi) \propto \\
&\quad 2 - A_0\, \cos^2\vartheta + 2\,(A_0 - 1) \cos^2\Theta \\
&+ (4 - 3A_0)\, \cos^2\Theta \cos^2\vartheta \\
&+ A_0\, \sin^2\Theta \sin^2\vartheta \cos 2(\Phi - \varphi) \\
&+ \left(1 - \frac{A_0}{2}\right) \sin 2\Theta \sin 2\vartheta \cos(\Phi - \varphi) \\
&+ \frac{A_2}{2} \Big[\sin 2\Theta \sin 2\vartheta \cos(\Phi + \varphi) \\
&\qquad + 2\, \sin^2\Theta \sin^2\vartheta\, (\cos 2\Phi + \cos 2\varphi) - 2\, \sin^2\Theta \cos 2\Phi\Big] \\
&+ \frac{A_5}{2} \Big[\sin 2\Theta \sin 2\vartheta \sin(\Phi + \varphi) \\
&\qquad + 2\, \sin^2\Theta \sin^2\vartheta\, (\sin 2\Phi + \sin 2\varphi) - 2\, \sin^2\Theta \sin 2\Phi\Big]
\end{aligned}
\tag{B.9}
$$

$$
\begin{aligned}
&+ A_1 \Big\{ 2\, \sin 2\vartheta \cos\varphi \\
&\qquad + \sin^2\Theta \sin 2\vartheta \, [\cos(2\Phi - \varphi) - \cos\varphi] \\
&\qquad + \sin^2\vartheta \sin 2\Theta \, [\cos(2\varphi - \Phi) - \cos\Phi] \Big\} \\
&+ A_6 \Big\{ 2\, \sin 2\vartheta \sin\varphi \\
&\qquad + \sin^2\Theta \sin 2\vartheta \, [\sin(2\Phi - \varphi) - \sin\varphi] \\
&\qquad + \sin^2\vartheta \sin 2\Theta \, [\sin(2\varphi - \Phi) - \sin\Phi] \Big\} \; .
\end{aligned}
$$

We remind that, when using the existing ATLAS and CMS measurements of the coefficients A_i, performed in the CS frame, the angles $\cos\Theta$ and Φ in these formulas must be defined with respect to the CS frame of the Z or W bosons. According to the definition of the CC frame, the angles $\cos\vartheta$ and φ of the V decay must be referred to that *same* system of axes, identically translated from the Z or W rest frame to the V rest frame.

As seen in Figs. 4.11, 5.2, and 5.4, the coefficients A_i are rapidly varying functions of p_{T}. Considerably simplified formulas are obtained in two limit scenarios, low p_{T} and high p_{T}, which may correspond, to a very good approximation, to the conditions where specific measurements are actually performed. When p_{T} is significantly smaller than the boson mass, the polarization is approximately purely transverse in the CS frame, where all coefficients A_i tend to vanish. In the high-p_{T} limit, instead, the condition $A_i \to 0$ tends to be verified in the HX frame, as seen in Fig. 4.12. In both limits, the angular distributions of the two decay chains reduce to

$$
W_{\mathrm{CC}}^{\ell^+\ell^-} \propto 1 \, - \, \cos^2\Theta \, \cos^2\vartheta \, - \, \frac{1}{4} \sin 2\Theta \sin 2\vartheta \cos(\Phi - \varphi) \, , \tag{B.10}
$$

$$
W_{\mathrm{CC}}^{\pi\pi} \propto 1 \, - \, \cos^2\Theta \, + 2 \, \cos^2\Theta \, \cos^2\vartheta \, + \, \frac{1}{2} \sin 2\Theta \sin 2\vartheta \cos(\Phi - \varphi) \, , \tag{B.11}
$$

where the CC frame is defined using the axes of the W or Z CS frame at low p_{T} and those of the W or Z HX frame at high p_{T}.

We remark for completeness that, as can be deduced from previous considerations (see also Section 1.2), the analogous Z radiative decays to a $J = 0$ particle (e.g., $\mathrm{Z} \to \pi^0 \,|\, \mathrm{K}^0\gamma$, with $\pi^0 \to \gamma\gamma$ and $\mathrm{K}^0 \to \pi^+\pi^-$) lead to the four-dimensional angular distribution

$$
\begin{aligned}
&W_{\mathrm{CC}}(\cos\Theta, \Phi, \cos\vartheta, \varphi) \\
&\quad \propto \; 1 \; + \; \cos^2\Theta \; + \; \frac{A_0}{2} \, (1 - 3\cos^2\Theta) \\
&\quad + \; \frac{A_2}{2} \; \sin^2\Theta \cos 2\Phi \; + \; A_1 \; \sin 2\Theta \cos\Phi \\
&\quad + \; \frac{A_5}{2} \; \sin^2\Theta \sin 2\Phi \; + \; A_6 \; \sin 2\Theta \sin\Phi \\
&\quad + \; A_4 \; \cos\Theta \; + \; A_3 \; \sin\Theta \cos\Phi \; + \; A_7 \; \sin\Theta \sin\Phi \, ,
\end{aligned} \tag{B.12}
$$

which is formally identical to the expression of the (two-dimensional) dilepton decay distribution in Eq. A.1, except for the substitution of the lower-case angles by the upper-case ones. There is no dependence on the angles (ϑ, φ) of the decay of the pion or kaon, which is always identically isotropic.

References

[1] ATLAS Collaboration, "Search for exclusive Higgs and Z boson decays to $\phi\gamma$ and $\rho\gamma$ with the ATLAS detector", *JHEP* **07** (2018) 127, doi:10.1007/JHEP07(2018)127, arXiv:1712.02758.

[2] CMS Collaboration, "Search for rare decays of Z and Higgs bosons to J/ψ and a photon in proton-proton collisions at $\sqrt{s} = 13$ TeV", *Eur. Phys. J. C* **79** (2019) 94, doi:10.1140/epjc/s10052-019-6562-5, arXiv:1810.10056.

[3] ATLAS Collaboration, "Measurement of the angular coefficients in Z-boson events using electron and muon pairs from data taken at $\sqrt{s} = 8$ TeV with the ATLAS detector", *JHEP* **08** (2016) 159, doi:10.1007/JHEP08(2016)159, arXiv:1606.00689.

[4] CMS Collaboration, "Angular coefficients of Z bosons produced in pp collisions at $\sqrt{s} = 8$ TeV and decaying to $\mu^+\mu^-$ as a function of transverse momentum and rapidity", *Phys. Lett. B* **750** (2015) 154, doi:10.1016/j.physletb.2015.08.061, arXiv:1504.03512.

Index

acceptance and efficiency, effects of
  in B → J/ψ decays, 189–191
  in dilepton decays, **12**, **19**
acceptance coverage effects in the observed polarization, *72*
addition rule for polarization parameters, 25, 118
ALICE
  J/ψ polarization, *111*, 112, *198*
  Λ polarization, 259
allowed parameter values, *see* parameter domain
ATLAS
  B cross section, *183*
  χ_{c2} / χ_{c1} cross-section ratio, *20*
  Higgs cross section, *183*
  Lam–Tung relation, 145, *146*
  quarkonium cross sections, *183*, *199*
  Z boson cross sections, *217*
  Z boson A_0, *129*, 144, *145*
  Z boson A_1, *149*, 149
  Z boson A_2, 144, *145*
  Z boson $A_0 - A_2$, *146*, 151
azimuthal angle φ, *7*
azimuthal anisotropy, 24

BaBar
  B → J/ψ decays at the Υ(4S), *204*, 203–206
BES
  $e^+e^- \to Q\overline{Q}$, 202

cascade decay, 166
  reference axes for the description of, *167*, *173, 174*
CDF
  B cross section, *183*
  non-prompt J/ψ polarization, 206, *207*
  prompt J/ψ polarization, 64, *65*, 122
  ψ(2S) anomaly, 199
  Υ polarization, 112, *113*
  W polarization, *128*
χ_{c1} and χ_{c2} polarizations, 22, **207**, 243, 247
χ_{c2} / χ_{c1} cross-section ratio, *20*
chirality, 4
Clebsch–Gordan coefficients, 175, 210, 219
CLEO
  B → J/ψ decays at the Υ(4S), *204*, 203–206
CMS
  B cross section, *183*
  χ_{c1} and χ_{c2} polarizations, 22, *198*
  χ_{c2} / χ_{c1} cross-section ratio, *20*
  Higgs cross section, *183*
  J/ψ polarization, *198*
  Lam–Tung relation, 145, *146*
  ψ(2S) polarization, *198*
  quarkonium cross sections, *183*, *199*
  Z boson cross sections, *217*
  Z boson A_0, *129*, 144, *145*
  Z boson A_1, *149*, 149
  Z boson A_2, 144, *145*
  Z boson $A_0 - A_2$, *146*, 151
colour-octet mechanism, 199
colour-singlet mechanism, 199
COMPASS
  Lam–Tung relation violation, 153
covariance relations for polarization parameters, 89, 104, 105
cross section vs. polarization correlation, **19**

D0
  W polarization, *128*
decays
  $a_2(1320) \to \eta\pi$, 250
  $a_2(1320) \to K\overline{K}$, 250

P. Faccioli and C. Lourenço, *Particle Polarization in High Energy Physics*,
Lecture Notes in Physics 1002,
https://doi.org/10.1007/978-3-031-08876-6

$a_2(1320) \to \pi^{\pm}\gamma$, 250
$a_2(1700) \to \eta\pi$, 250
$a_2(1700) \to K\overline{K}$, 250
$a_2(1320) \to \gamma\gamma$, 248
$a_2(1700) \to \gamma\gamma$, 248
$B \to J/\psi\, K$, 173–191, *192*, **202**
$\chi_b \to \Upsilon\,\gamma$, 173
$\chi_{b0} \to \Upsilon\,\gamma$, *195*, 196
$\chi_{b1} \to \Upsilon\,\gamma$, 209
$\chi_{b2} \to \Upsilon\,\gamma$, 209
$\chi_c \to J/\psi\,\gamma$, 173
$\chi_{c0} \to J/\psi\,\gamma$, 180–181, 193, *194, 195*, 212
$\chi_{c1} \to J/\psi\,\gamma$, 207–216, 219–221, 243
$\chi_{c1} \to J/\psi\,\ell^+\ell^-$, *225*, 223–226, 264
$\chi_{c2} \to J/\psi\,\gamma$, 207–216, 219–221, 247
$\chi_{c2} \to J/\psi\,\ell^+\ell^-$, *225*, 223–226, 264
$\Delta \to p\pi$ or $\Delta \to pK$, 261
$\eta_2(1870) \to \gamma\gamma$, 248
graviton $\to \gamma\gamma$, 251, 257
$H \to \gamma\gamma$, 252
$H \to J/\psi\,\gamma$, 182, 196, *197*
$H \to \Upsilon\,\gamma$, 196
$H \to Z\,\gamma$, 196, *197*
$H \to ZZ^*$, 2, 156
$J/\psi \to \ell^+\ell^-$, *9*, 9–12
$\Lambda \to p\pi$ or $\Lambda \to pK$, 258, 261
$N \to p\pi$ or $N \to pK$, 261
$\Omega \to \Lambda K$, 261
$\phi(1020) \to \ell^+\ell^-$, *159*, 159, 246
$\phi(1020) \to K^+K^-$, 246
$\psi(2S) \to \chi_{cJ}\,\gamma$, 243
$\rho(770) \to \ell^+\ell^-$, 246
$\rho(770)^{\pm,0} \to \pi^{\pm}\pi^0 \,/\, \pi^+\pi^-$, 246
$t \to W\,b$, 258
$\Upsilon(4S) \to \ell^+\ell^-$, 246
$\Upsilon(4S) \to B\overline{B}$, 246
$W \to \rho\,\gamma$, 280
$X(3915) \to \gamma\gamma$, 248
$Z \to J/\psi\,\gamma$, 216–217, *218*, 243, 280
$Z \to K^0\,\gamma$, 282
$Z \to \phi\,\gamma$, 280
$Z \to \pi^0\,\gamma$, 282
$Z \to \rho\,\gamma$, 280
$Z \to \Upsilon\,\gamma$, 217
detection effects, *see* acceptance and efficiency
detection efficiency, 26
diagonalization of the angular distribution, **94**, **100**
Drell–Yan, 2, **124**
  E615, *154*
  E866, *127*
  elementary production processes, 42, *43*, *144*
  in polarized collisions, 32
E615
  Lam–Tung relation violation, 153, *154*
E866
  Drell–Yan polarization, 126, *127*
  Υ polarization, 160, *161*
eigenstate of angular momentum, 3, **6**
experimental selections, *see* acceptance and efficiency

feed-down fractions for J/ψ production, 193, 198
Fermilab fixed target experiments
  J/ψ average p_T squared, *158*
forward-backward asymmetry, 11, 33
frame, *see* polarization frame
frame-independent
  geometrical parameters, **100**, **132**
  line in the parameter domain, *86*, 87
  parameter domain, **82**, **85**, **93**
  parity asymmetry, **106**, 135–138
  planes in the parameter domain, **85**, *86*, 89
  polarization, 89, 91, **108, 109**

helicity conservation
  as a transversely polarizing mechanism, 42, 45, 146, 238, 246
  in the decay to fermion-antifermion, **4**, *5*, 238, 242
HERA-B
  J/ψ average p_T squared, *158*
  J/ψ polarization, *160*

inclusive observation of particle production
  choice of polarization axis, 38, 45–46
  symmetry of angular distribution, 31–32
  vs. exclusive, in cascade processes, 169–170, 183–193, *194*
invariant, *see* frame-independent
isotropic decay distribution
  due to angular momentum configuration, **27**
  due to smearing effects, **166**
  of polarized particle, **262**

jet multiplicity, 153, 156
J/ψ cross sections
  ATLAS, *199*
  CMS, *199*
J/ψ polarization
  ALICE, *111*, 112, *198*
  CDF, 64, *65*, 122
  CMS, *198*
  HERA-B, *160*
  LHCb, *111*, 112, *198*

Lam–Tung relation, **131**, 135

generalization, **150**
violation, **143**
violation in Drell–Yan measurements
COMPASS, 153
E615, 153, *154*
NA10, 153
violation in Z boson measurements
ATLAS, *146*
CMS, *146*
Λ polarization, 258
LHCb
χ_{c2} / χ_{c1} cross-section ratio, *20*
J/ψ polarization, *111*, 112, *198*
ψ(2S) polarization, *198*

NA10
Lam–Tung relation violation, 153
NA50
J/ψ average p_T squared, *158*
non-prompt J/ψ, 170, 183–191, *192*, **202**, *208*
non-prompt ψ(2S), 191, *192*
NRQCD, 199–201

one-dimensional polarization measurements
caveats, 33, 51, 64, 66, 68, **69**
formulas for, **25**, 32, 92, **240**

parameter domain
decay of $J = 1/2$ particle, *259*
decay of $J = 1$ particle, *244*
decay of $J = 3/2$ particle, *261*, *263*
decay of $J = 2$ particle, *248, 249*, *253*
dilepton decay, **82**, **85**, **93**
in canonical form, *103*
two-photon decay of heavy $J = 0$, 2, 3 or 4 resonance, *255*
parity violation
in dilepton decay distribution
asymmetries, 32
diagonalization of parity-violating term, 98
frame transformation of parameters, 74
frame-independent parameters, **106**
general shape of the distribution, 31
origin, **10**
parameter domain, **93**
quasi-invariants, 136–138
in generic two-body decay
$J = 1/2$, 258, 260
$J = 1$, 242
$J = 2$, 247, *252*
$J = 3/2$, *262*
parity-violating polar anisotropy terms, 241
parton k_T, effects of, 156, **157**
parton motion, effects of
longitudinal, 128
transverse, 156, **157**
polar angle ϑ, *7*
polarization frame
cascade helicity frame (cHX), 166, *167*
centre-of-mass helicity (HX), **45**
cloned cascade (CC), *173*
Collins–Soper (CS), **44**
experimental definition, *40*
Gottfried–Jackson (GJ), **40**
parton-parton Collins–Soper (pCS), 158
parton-parton helicity, 128
perpendicular helicity (PX), **46**
transformations, **48**, *55*, **74**, *84*
polarized (vs. unpolarized) hadron collisions
additional terms in the decay distribution, 32, 38, 39, 93
processes
non-planar, **143**, *144*, 151, 156
planar, 88, *144*, 155
s-channel, 45, 127, 129
t/*u*-channel, 42, 123, 124
$2 \to 1$, 45, 126, *144*, 240
$2 \to 2$, 127, *144*
with more than two final states, 142, *144*, 146
production mechanisms, *see* processes
production plane, 38
ψ(2S) cross sections
ATLAS, *199*
CMS, *199*
ψ(2S) polarization
CMS, *198*
LHCb, *198*

QCD corrections to Drell–Yan, Z and W production, 127, 132, 143, 145
quantization axis, change of, **6**
quasi-invariants, **132**

rotation
of an angular momentum eigenstate, **6**, **232**
of reference axes, **48**, **74**

spherical coordinates, *7*
spin alignment, 2
spin characterization, **251**
spin density matrix, 240

top quark polarization (single and $t\bar{t}$), 258

unpolarized

angular momentum configuration, **27**
observation due to smearing, **166**
unpolarized vs. isotropic, **262**
Υ polarization
CDF, 112, *113*
E866, 160, *161*
vector particles, **2**
theorem on the polarization of, 27, 95

Wigner D-matrices, **6**, **232**